



ISSN 1580-3155

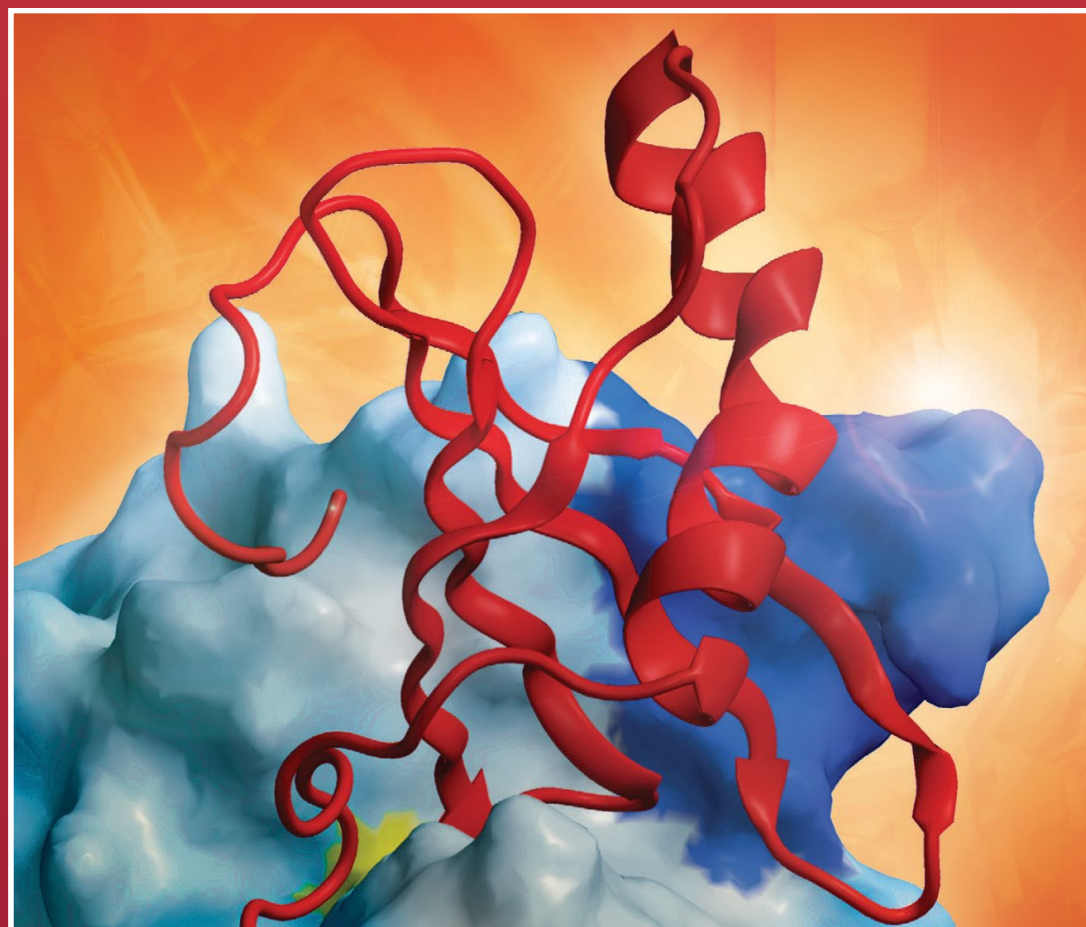
Pages 1-245 ■ Year 2019, Vol. 66, No. 1

Slovensko kemijsko društvo
Slovenian Chemical Society



Acta Chimica Slo Acta Chimica Slo Slovenica Acta C

1



66/2019

EDITOR-IN-CHIEF

KSENIJA KOGEJ

Slovenian Chemical Society, Hajdrihova 19, SI-1000 Ljubljana, Slovenija,

E-mail: ACSi@fkk.uni-lj.si, Telephone: (+386)-1-479-8538

ASSOCIATE EDITORS

Janez Cerkovnik, University of Ljubljana, Slovenia

Krištof Kranjc, University of Ljubljana, Slovenia

Ksenija Kogej, University of Ljubljana, Slovenia

Franc Perdih, University of Ljubljana, Slovenia

Aleš Podgornik, University of Ljubljana, Slovenia

Helena Prosen, University of Ljubljana, Slovenia

Damjana Rozman, University of Ljubljana, Slovenia

Melita Tramšek, Jožef Stefan Institute, Slovenia

Irena Vovk, National Institute of Chemistry, Slovenia

GUEST-EDITOR

Vito Turk, Jožef Stefan Institute, Slovenia

Borut Štrukelj, Faculty of Pharmacy, Slovenia

Aleš Berlec, Jožef Stefan Institute, Slovenia

ADMINISTRATIVE ASSISTANT

Marjana Gantar Albreht, National Institute of Chemistry, Slovenia

EDITORIAL BOARD

Wolfgang Buchberger, Johannes Kepler University, Austria

Alojz Demšar, University of Ljubljana, Slovenia

Stanislav Gobec, University of Ljubljana, Slovenia

Marko Goličnik, University of Ljubljana, Slovenia

Günter Grampp, Graz University of Technology, Austria

Wojciech Grochala, University of Warsaw, Poland

Danijel Kikelj, Faculty of Pharmacy, Slovenia

Janez Košmrlj, University of Ljubljana, Slovenia

Blaž Likozar, National Institute of Chemistry, Slovenia

Mahesh K. Lakshman, The City College and

The City University of New York, USA

Janez Mavri, National Institute of Chemistry, Slovenia

Friedrich Sreenc, University of Minnesota, USA

Walter Steiner, Graz University of Technology, Austria

Jurij Svete, University of Ljubljana, Slovenia

Ivan Švancara, University of Pardubice, Czech Republic

Jiri Pinkas, Masaryk University Brno, Czech Republic

Gašper Tavčar, Jožef Stefan Institute, Slovenia

Christine Wandrey, EPFL Lausanne, Switzerland

Ennio Zangrando, University of Trieste, Italy

ADVISORY EDITORIAL BOARD

Chairman

Branko Stanovnik, Slovenia

Members

Josef Barthel, Germany

Udo A. Th. Brinkman, The Netherlands

Attilio Cesaro, Italy

Dušan Hadži, Slovenia

Vida Hudnik, Slovenia

Venčeslav Kaučič, Slovenia

Željko Knez, Slovenia

Radovan Komel, Slovenia

Janez Levec, Slovenia

Stane Pejovnik, Slovenia

Anton Perdih, Slovenia

Slavko Pečar, Slovenia

Andrej Petrič, Slovenia

Boris Pihlar, Slovenia

Milan Randič, Des Moines, USA

Jože Škerjanc, Slovenia

Miha Tišler, Slovenia

Đurđa Vasić-Racki, Croatia

Marjan Veber, Slovenia

Gorazd Vesnaver, Slovenia

Jure Zupan, Slovenia

Boris Žemva, Slovenia

Majda Žigon, Slovenia

Acta Chimica Slovenica is indexed in: *Chemical Abstracts Plus*, *Current Contents (Physical, Chemical and Earth Sciences)*, *PubMed*, *Science Citation Index Expanded* and *Scopus*. Impact factor for 2017 is IF = 1.104.



Articles in this journal are published under Creative Commons Attribution 3.0 License

<http://creativecommons.org/licenses/by/3.0/>

Izdaja - Published by:

SLOVENSKO KEMIJSKO DRUŠTVO – SLOVENIAN CHEMICAL SOCIETY

Naslov redakcije in uprave – Address of the Editorial Board and Administration

Hajdrihova 19, SI-1000 Ljubljana, Slovenija

Tel.: (+386)-1-476-0252; Fax: (+386)-1-476-0300; E-mail: chem.soc@ki.si

Izdajanje sofinancirajo – Financially supported by:

Slovenian Research Agency, Ljubljana, Slovenia

National Institute of Chemistry, Ljubljana, Slovenia

Jožef Stefan Institute, Ljubljana, Slovenia

Faculty of Chemistry and Chemical Technology at University of Ljubljana, Slovenia

Faculty of Chemistry and Chemical Engineering at University of Maribor, Slovenia

Faculty of Pharmacy at University of Ljubljana, Slovenia

University of Nova Gorica, Nova Gorica, Slovenia

Slovensko kemijsko društvo
Slovenian Chemical Society



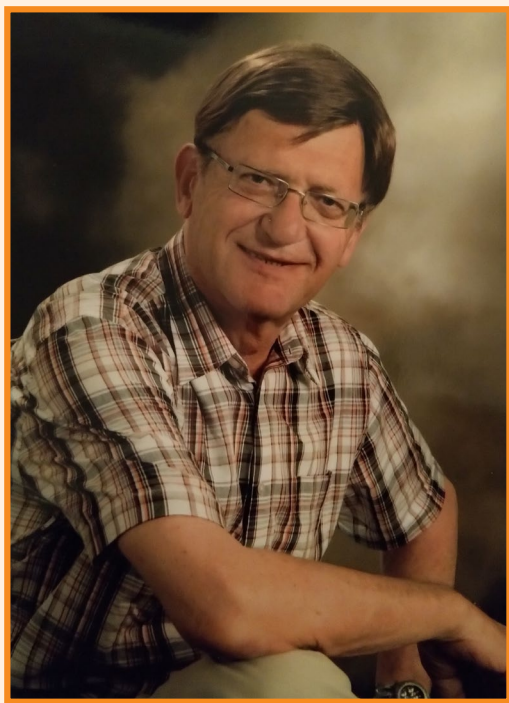
Acta Chimica Slovenica izhaja štirikrat letno v elektronski obliki na spletni strani <http://acta.chem-soc.si>. V primeru posvečenih števil izhaja revija tudi v tiskani obliki v omejenem številu izvodov.

Acta Chimica Slovenica appears quarterly in electronic form on the web site <http://acta.chem-soc.si>. In case of dedicated issues, a limited number of printed copies are issued as well.

Transakcijski račun: 02053-0013322846 Bank Account No.: SI56020530013322846-Nova Ljubljanska banka d. d., Trg republike 2, SI-1520 Ljubljana, Slovenia, SWIFT Code: LJBA SI 2X

Oblikovanje ovitka – Design cover: KULT, oblikovalski studio, Simon KAJTNA, s. p. Grafična priprava za tisk: Majanafin, d. o. o.

© Copyright by Slovenian Chemical Society



Dedicated to the memory of the late Prof. Dr. Igor Kregar (1937–2017)

Igor Kregar, Slovenian and an internationally renowned biochemist in the field of proteolysis and plant molecular biology, unexpectedly passed away on April 11, 2017 in Ljubljana at the age of 79. After almost 40 years of conducting excellent research, teaching and mentoring of undergraduate and graduate students at the Jožef Stefan Institute and Biotechnical faculty at Ljubljana University, he had retired in year 1997 to enjoy his family, friends, travel and some hobbies.

Igor was born on September 11, 1937 in Ljubljana, the son of architect Rado and mother Antonija. In his family reigned an intellectual atmosphere, which resulted in his broad interests for reading books, enjoying traveling, classical music, art and culture in general. Interestingly, as a boy he was highly motivated to read adventure novels set in the American Wild West written by German writer Karl May. Many of May's novels were translated into the Slovenian language, but unfortunately those editions were not accessible in our libraries after World War II for unknown reasons, most probably political. However, Igor did have access to the German editions, which stimulated him to learn the German language. At the same time Igor enjoyed competitive swimming at a local swimming pool. After completing high school with an excellent degree, he decided to study chemistry at the University of Ljubljana. At that time we first met. Soon we established a friendship

that included my classmate Franček Gubenšek. Igor was one of the best students in his class. He chose organic chemistry for his diploma at the Faculty of Chemistry at Ljubljana University. Then Igor joined the Department of Radiobiology at the Nuclear Institute Jožef Stefan (now Jožef Stefan Institute) by enrolling in a master's degree program and completed his PhD dissertation in December 1965 under the mentorship of Prof. Drago Lebez, working on the characterization of intracellular proteinases from the small intestinal mucosa of the rat. At that time intracellular proteases were poorly understood. The main enzyme studied was an acidic hemoglobin-splitting enzyme, called Anson's enzyme in laboratory jargon after the pioneering protein biochemist M. L. Anson. After the lysosome organelle was discovered by C. de Duve, it became clear that this acid protease is a lysosomal enzyme, and in 1960 it was characterized and named cathepsin D. Igor and the author started to collaborate primarily on cathepsin D and also on cathepsin E soon after its discovery. This was at that time an almost unexplored field of research and we were one of the pioneering groups to work in this field.

In 1968 Igor received a Fulbright scholarship to study in Professor John A. Rupley's laboratory in the Department of Chemistry at the University of Arizona, Tucson, USA. Coming from Yugoslavia at that time was for Igor (and later for the author) a completely new world. The Rupley laboratory was modern and very well equipped with adequate funding to buy chemicals. Igor studied the pH dependence of lysozyme-catalyzed hydrolysis of the N-acetylglucosamine hexasaccharide. These kinetic experiments were time consuming and required precise measurements, but later resulted in a high quality publication (1973). Rupley was an excellent biochemist with a great and warm but serious personality. Not to forget, Rupley and his lovely wife, Ila, organized nice parties in their

home, thus keeping and promoting friendly relations in his international laboratory. I can say as one of Rupley's postdocs that those working with him were very fortunate and learned to enjoy hard work and at the same time to be happy. Igor established many friendships in the USA, especially with Rupley's graduate student, Karl Kramer and his wife Virginia, which lasted until Igor's death. In 1968 Igor joined the Kramers on a unique train trip to Mexico where they visited Guadalajara, Mexico City and Taxco. On that trip the train passed through many small Mexican communities, some with bullet-riddled buildings, which were perhaps a reflection of past political conflicts. Igor learned to love Mexican cuisine in part through his many visits to the Kramer's apartment, where Virginia made mouth-watering dishes such as enchiladas, refried beans, flautas, green chiles and spicy meats. Upon his return to Yugoslavia, these experiences motivated Igor to learn how to replicate Mexican meals and to share them with his family and good friends. There was a problem, however, in that many of the ingredients required for Mexican cooking were not readily available in Yugoslavia in the 1970s. Nevertheless, the Kramers were able to supply Igor with Mexican food items such as masa harina, a special red chile powder and various types of chiles in care packages until he was later able to obtain them locally.

Returning to our Department at the Institute after his Fulbright-sponsored study in the USA, Igor continued his research on cathepsins. Development of the first purification of cathepsin D by affinity chromatography allowed him to obtain large quantities of the pure enzyme for numerous biochemical studies including structural and denaturation studies. Almost at the same time an acid sulphhydryl protease was discovered (1973) and later named cathepsin S. This discovery was not immediately recognized and many believed that cathepsin S and L were identical enzymes. Ultimately, this problem was solved by isolating both proteins from the same species and determining their amino acid sequences. Cathepsin S is involved in antigen processing and presentation, degradation of the extracellular matrix, tumor progression, cardiovascular disease and obesity among other roles. A new method for cathepsin B purification from bovine lymph nodes yielded sufficient enzyme for biochemical characterization. All advances in the field resulted in the Second International Symposium on Intracellular Protein Catabolism organized in Ljubljana in 1975. A brief document was prepared by Alan Barrett, Fred Woessner, Igor Kregar and Vito Turk, which highlighted all known 23 intracellular proteases. This modest beginning resulted finally with the establishment of a new classification system and the MEROPS database, which now includes well over 1000 peptidases (Handbook of Proteolytic Enzymes, N.D. Rawlings and G. Salvesen, Preface, Acad. Press, 2013). Igor then extended his research on proteases to those present in the ergot fungus *Claviceps purpurea* and bacterium *Streptomyces rimosus* as well as proteases and their inhibitors from plants

such as the potato. Igor and his coworkers discovered the potato cysteine proteinase inhibitor gene family and characterized some of the expressed recombinant proteins.

Igor was a highly respected scientist and personality. His research resulted in approximately 80 original research papers and reviews published primarily in international journals. He attended many domestic and international symposia and congresses as an invited lecturer. In parallel to his contributions to science, he was an excellent teacher and popular among many students. Most of his students who obtained their PhD degree under his guidance went on to become successful researchers and professors at different universities and institutes. Igor served on various committees at the Institute. He was also the first Secretary General of the Slovenian Biochemical Society (1972–1987) and then Secretary General of the Union of Biochemical Societies of Yugoslavia (1987–1992) until the collapse of Yugoslavia. In 1987 the 18th meeting of the Federation of European Biochemical Societies (FEBS) was held for the first time in Ljubljana, which was a great success from the organizational and scientific points of view. Igor contributed greatly to this success, serving as secretary of this prestigious meeting with more than 1800 scientists attending from all over the world. For his achievements in science, Igor received several distinguished recognitions including the Yugoslav Order of Labour with Silver Wreath Award (1978), Slovenian Boris Kidrič Fund Award (1979) and Lapanje Plaque from the Slovenian Biochemical Society (2009).

Igor's remarkable wife, Anka, died several months after he did. He is survived by two sons, Zlato and Robert, three grandchildren and their families. For us and for those who knew him, Igor always will be remembered. His scientific legacy will live on.

Vito Turk
Jožef Stefan Institute

Graphical Contents



ActaChimicaSlo
ActaChimicaSlo
SlovenicaActaC

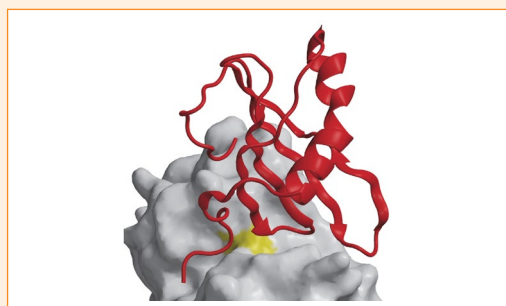
Year 2019, Vol. 66, No. 1

REVIEW

5–17 Biochemistry and molecular biology

Characteristics, Structure, and Biological Role of Stefins (Type-1 Cystatins) of Human, Other Mammals, and Parasite Origin

Vito Turk, Dušan Turk, Iztok Dolenc and Veronika Stoka

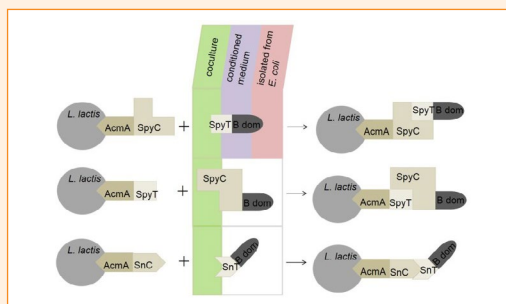


SCIENTIFIC PAPER

18–27 Biochemistry and molecular biology

Surface Anchoring on *Lactococcus lactis* by Covalent Isopeptide Bond

Tina Vida Plavec and Aleš Berlec



28–36 Biochemistry and molecular biology

β -Trefoil Protease Inhibitors Unique to Higher Fungi

Jerica Sabotič, Miha Renko and Janko Kos

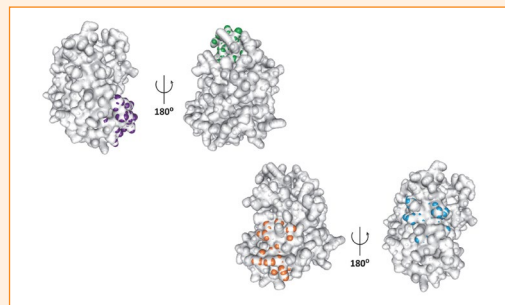
β -Trefoil protease inhibitors unique to higher fungi



- high genetic heterogeneity
- distinct inhibitory profiles
- structural plasticity of the β -trefoil fold
- diversity of functions
- resistance to extremes of pH
- resistance to high temperatures
- resistance to proteolytic digestion

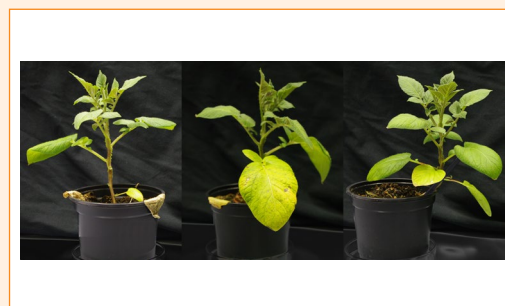
37–44 Biochemistry and molecular biology
Epitope Mapping of Major Ragweed Allergen Amb a 1

Abida Zahirović, Borut Štrukelj, Peter Korošec and Mojca Lunder



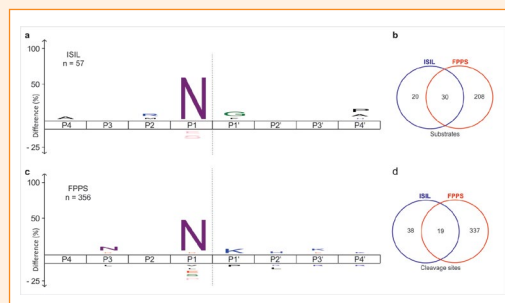
45–49 Biochemistry and molecular biology
The Titre of the Virus in the Inoculum Affects the Titre of the Viral RNA in the Host Plant and the Occurrence of the Disease Symptoms

Maruša Pompe-Novak, Maja Križnik and Kristina Gruden



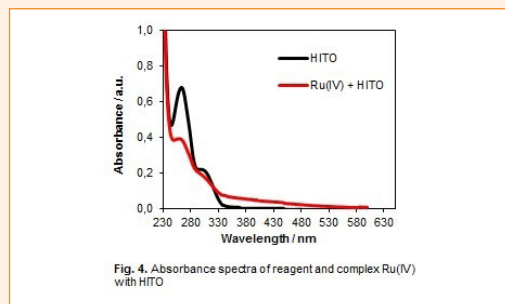
50–57 Biochemistry and molecular biology
Characterization of Legumain Degradome Confirms Narrow Cleavage Specificity

Robert Vidmar, Matej Vizovišek, Dušan Turk, Boris Turk, and Marko Fonović



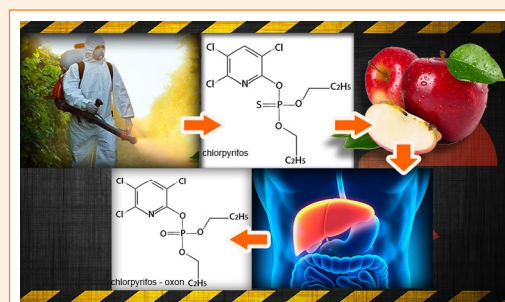
62–69 Analytical chemistry
Spectrophotometric Determination of Ru(IV) Using 5-Hydroxyimino-4-imino-1,3-thiazolidin-2-one as a Novel Analytical Reagent

Oleksandr Tymoshuk, Lesia Oleksiv, Liudmyla Khvalbota, Taras Chaban and Ihor Patsay



70–77 Analytical chemistry
Atmospheric Solids Analysis Probe with Mass Spectrometry for Chlorpyrifos and Chlorpyrifos-Oxon Determination in Apples

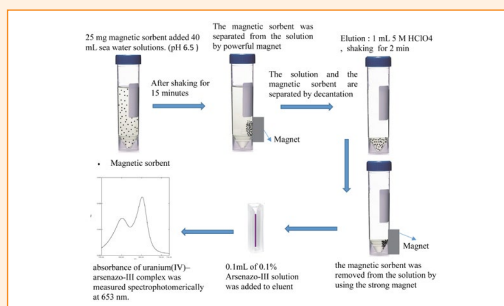
Mirjana R. Cvijović, Valerio Di Marco, Srboljub J. Stanković, Zoran P. Nedić, Ljubinka G. Joksović and Nevena R. Mihailović



78–84 Analytical chemistry

Solid-Phase Extraction Method by Magnetic Nanoparticles Functionalized with Murexide for Trace U(VI) from Sea Water Prior to Spectrophotometric Determination

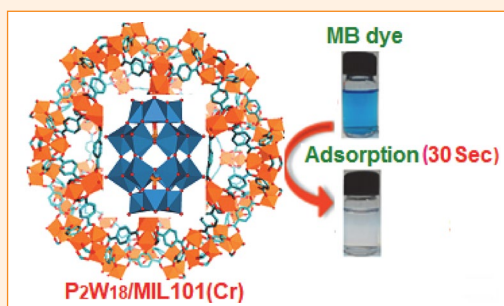
Tülay Oymak



85–102 Materials science

Dawson-Type Polyoxometalate Incorporated into Nanoporous MIL-101(Cr): Preparation, Characterization and Application for Ultrafast Removal of Organic Dyes

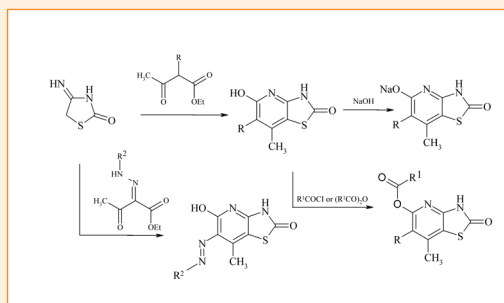
Afsoon Jarrah and Saeed Farhadi



103–111 Organic chemistry

Synthesis, Anti-Inflammatory and Antioxidant Activities of Novel 3H-Thiazolo[4,5-b]Pyridines

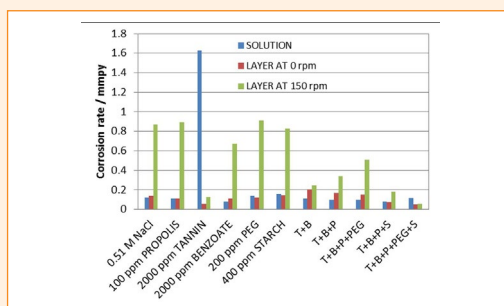
Taras I. Chaban, Volodymyr V. Ogurtsov, Vasyl S. Matyichuk, Ihor G. Chaban, Inna L. Demchuk and Ihor A. Nektegayev



112–122 Physical chemistry

A Novel Environmentally Friendly Synergistic Mixture for Steel Corrosion Inhibition in 0.51 M NaCl

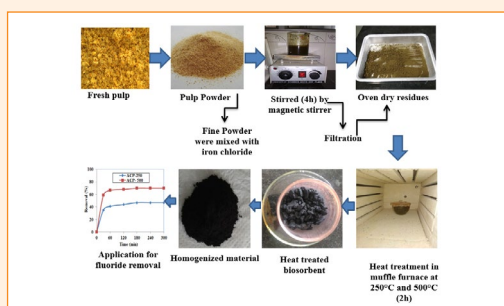
Stojan Božović, Sanja Martinez and Veselinka Grudić



123–136 Chemical, biochemical and environmental engineering

Adsorptive Removal of Fluoride from Aqueous Solution by Biogenic Iron Permeated Activated Carbon Derived from Sweet Lime Waste

Mohd. Ibrahim, Adil Siddique, Lata Verma, Jiwan Singh and Janardhan Reddy Koduru



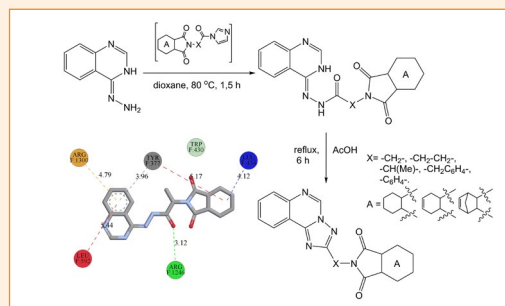
136–144 Chemical, biochemical and environmental engineering
Fabrication of Silver-Modified Halloysite Nanotubes and their Catalytic Performance in Rhodamine 6G and Methyl Orange Reduction

Maryam Akhondi and Effat Jamalizadeh



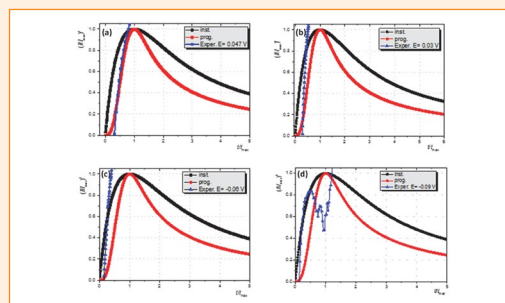
145–154 Organic chemistry
Directed Search of Biologically Active Compounds among Hydrogenated Isoindolylalkyl(alkylaryl-,aryl-)carboxylic Acids with Quinazoline Fragment that ...

Yulya Victorivna Martynenko, Oleksii Mykolayovich Antypenko, Oleksandr Anatolievich Brazhko, Irina Borisivna Labenska and Sergii Ivanovich Kovalenko



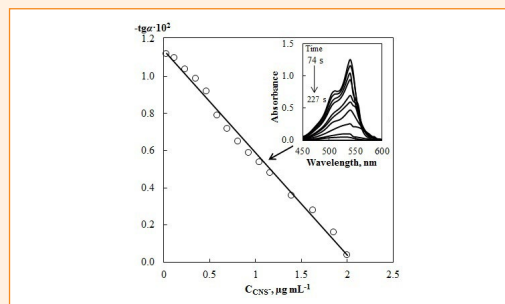
155–162 Physical chemistry
Investigation of the Electrochemical Reduction Process of the Molybdate Ions in the Tartaric Electrolytes

Vusala Asim Majidzade, Akif Shikhan Aliyev, Dunya Mahammad Babanly, Mahmood Elrouby and Dilgam Babir Tagiyev



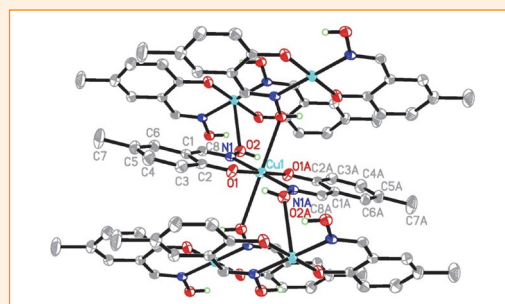
163–167 Analytical chemistry
Kinetic-Spectrophotometric Determination of Thiocyanate in Human Saliva Based on Landolt Effect in Presence of Astrafloxine FF

Alexander Chebotarev, Vitaliy Dubovyi, Dmytro Barbalat, Elena Guzenko, Kateryna Bevziuk and Denys Snigur



168–172 Inorganic chemistry
Synthesis and Crystal Structure of a Polymeric Copper(II) Complex Derived from 2-Hydroxy-5-methylbenzaldehyde Oxime with Antibacterial Activities

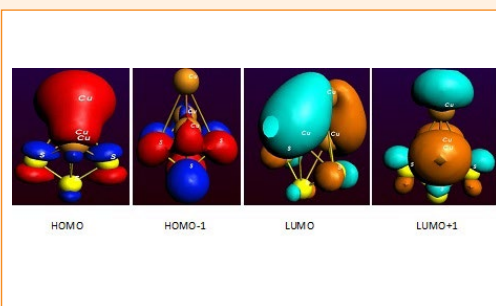
Ya-Li Sang and Xue-Song Lin



173–181 Materials science

Density Functional Approach: To Study Copper Sulfide Nanoalloy Clusters

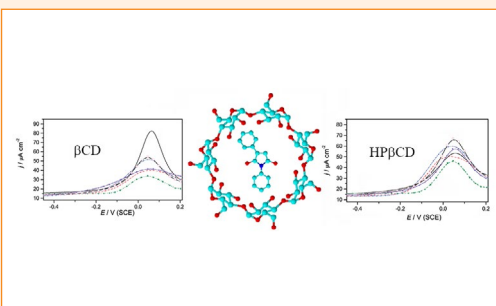
Prabhat Ranjan and Tanmoy Chakraborty



182–189 Physical chemistry

Voltammetric Investigation of Inclusion Complexes of the Selected Succinimides with β -Cyclodextrin and (2-Hydroxypropyl)- β -Cyclodextrin

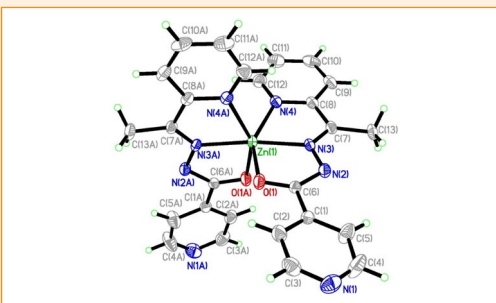
Jelena Lović, Milka Avramov Ivić, Bojan Božić, Jelena Lađarević and Dušan Mijin



190–195 Inorganic chemistry

Synthesis, Crystal Structures, and Antimicrobial Activity of Zinc(II) and Manganese(II) Complexes Derived from N' -(1-(Pyridin-2-yl)Ethylidene)Isonicotinohydrazide

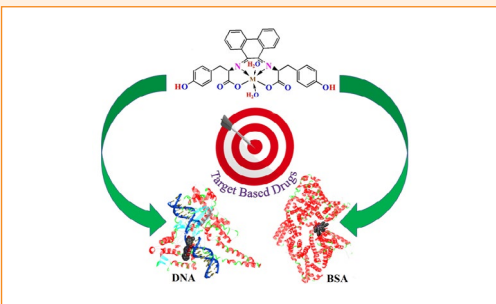
Ling-Wei Xue, Hui-Jie Zhang and Pan-Pan Wang



196–207 Inorganic chemistry

Evaluation of DNA/BSA Binding and Chemical Nuclease Activity of L-Tyrosine-Based Mn(III) and Fe(III) Metallo-Intercalators

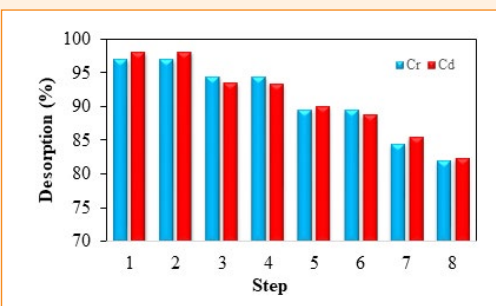
Biju Bennie Rajaretnam, Joel Chellappa, Daniel Abraham Solomon, Iyyam Pillai Subramanian and Theodore David Manickam Selvanayagam



208–216 Chemical, biochemical and environmental engineering

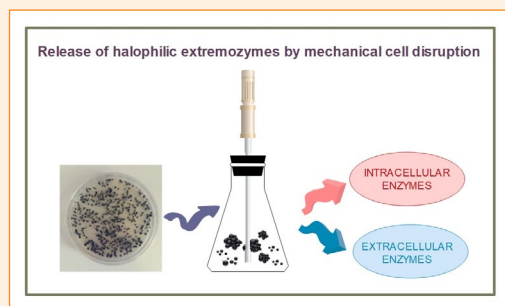
Adsorption of Cr (III) and Cd (II) Ions using Mesoporous Cobalt-Ferrite Nanocomposite from Synthetic Wastewater

Iman Khoshkerdar and Hossein Esmaeili



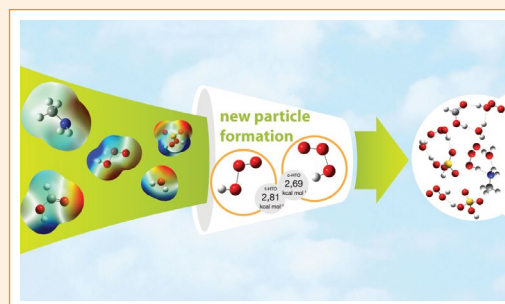
217–228 Chemical, biochemical and environmental engineering
Release of Halophilic Extremozymes by Mechanical Cell Disruption

Mateja Primožič, Maja Čolnik, Željko Knez, and Maja Leitgeb



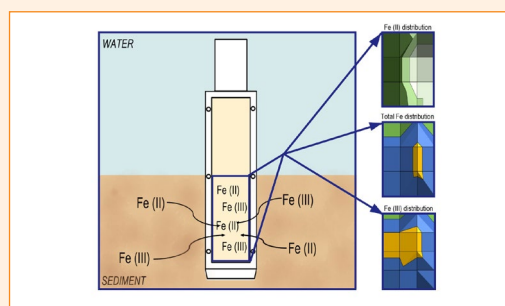
229–238 Physical chemistry
Characterization and Atmospheric Implication of Hydroxy Radical-Water-Methylamine-Formic Acid-Sulphuric Acid Complexes

Matjaž Dlouhy and Antonija Lesar



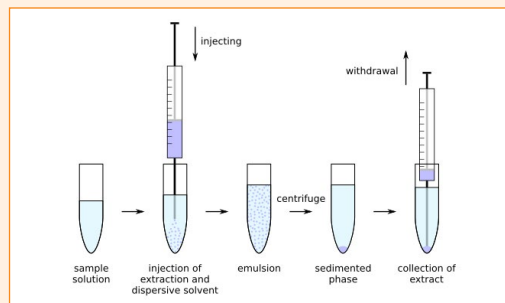
239–246 Chemical, biochemical and environmental engineering
Determination of Dissolved Iron Redox Species in Freshwater Sediment using DGT Technique Coupled to BDS

Hanna Budasheva, Aleksander Kravos, Dorota Korte, Arne Bratkič, Yue Gao and Mladen Franko



247–254 Analytical chemistry
Development of a Dispersive Liquid-Liquid Microextraction Followed by LC-MS/MS for Determination of Benzotriazoles in Environmental Waters

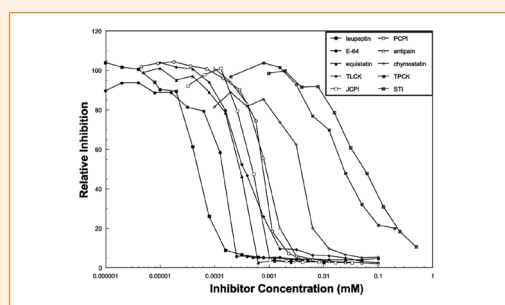
Ida Kraševc and Helena Prosen



SHORT COMMUNICATION

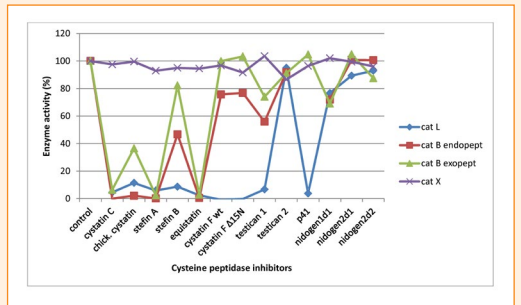
1–4 Chemical, biochemical and environmental engineering
My Times with Professor Igor Kregar and some Hydrolytic Enzymes

Karl J. Kramer



The Carboxypeptidase Activity of Cathepsin X is not Controlled by Endogenous Inhibitors

Urša Pečar Fonović, Milica Perišić Nanut, Nace Zidar, Brigita Lenarčič and Janko Kos



Short communication

My Times with Professor Igor Kregar and some Hydrolytic Enzymes

Karl J. Kramer*

Department of Biochemistry and Molecular Biophysics, Chalmers Hall, Kansas State University,
Manhattan, Kansas 66506 USA

* Corresponding author: E-mail: kkramer1@cox.net;
Tel: +1 785 5395975

Received: 01-21-2019

Dedicated to the memory of Prof. Dr. Igor Kregar

Abstract

The late Professor Igor Kregar and this author had several overlapping biochemical research interests. One focus was the glycoside hydrolase, lysozyme, and the other was proteolytic enzymes and their inhibitors, in particular those present in tissues from insects and plants. Regarding lysozyme our results helped to understand its catalytic mechanism and the carboxylic acid functional groups involved. Another area was insect-plant interactions involving defensive responses of plants to insect feeding via proteolytic enzyme inhibitors. Those results can be utilized in transgenic plant and seed biotechnological applications, which would help to reduce damage to plants and seeds caused by coleopteran and other insect pests. Also described are some cultural and travel interactions that the author benefited from his friendship with Professor Kregar.

Keywords: Lysozyme; catalysis; mechanism; proteases; inhibitors; beetles; potato; resistance

1. Introduction

My interactions with the late Slovenian scientist Professor Igor Kregar began more than 50 years ago. We met in Tucson, Arizona, USA, where he had arrived in the late 1960s from Ljubljana, Slovenia (then Yugoslavia) to begin working in the Department of Chemistry at the University of Arizona with Professor John A. Rupley. Igor was the second of three postdoctoral researchers from the Jozef Stefan Institute in Ljubljana to work in Rupley's laboratory during my tenure there as a graduate student. Franc Gubensek was the first postdoctoral scholar to work there and Vito Turk the third. After each initial meeting, valued friendships were established with all three Slovenes, all of which were maintained long thereafter, and in Igor's case, our friendship lasted a very long time until his untimely death in 2017.

2. Research Time

Igor had a long list of scientific publications.¹ In Rupley's laboratory Igor and I both worked on protein chemistry projects focused on the structure and function of a

glycosidic enzyme, hen's egg white lysozyme, he on the dependence of pH on the hydrolysis of the chitohexasaccharide substrate² and myself on the relative chemical reactivity in aqueous solution and acidic methanol of its ten carboxylic acids, several of which are involved in substrate binding and the catalytic mechanism.^{3,4} Results from Igor's research supported the hypothesis that non-productive enzyme-substrate complexes are of kinetic importance and that the structure of the productive complex and the catalytic mechanism were those suggested by results obtained from the x-ray crystallographic enzyme and enzyme-substrate complex structures. Results from my experiments revealed that the two carboxyl groups present in the active site of lysozyme, which were indicated by the crystallographic structures to participate in the catalytic mechanism, were more reactive to nucleophilic chemical modification than any of the other eight carboxyl groups.

During our subsequent scientific careers, both Igor and I became interested in another type of hydrolytic enzyme, the proteolytic enzymes and also their inhibitors. He studied several kinds of proteases and inhibitors obtained from a wide array of sources such as microbes, cows, rats, pigs, sheep, marine animals, plants and insects. My labo-

ratory was more focused on proteases and their inhibitors that were present in insect and plant tissues. Our interests overlapped in the area of insect-plant interactions involving defensive responses of plants to insect feeding via proteolytic enzyme inhibitors. Igor published several papers dealing with proteolytic enzymes and inhibitors in the potato, *Solanum tuberosum* as well as the cysteine proteases in the gut of Colorado potato beetle, *Leptinotarsa decemlineata*.^{5–10} He and his collaborators found that the beetle's cysteine proteolytic activity was insensitive to potato protease inhibitors, enabling the insects to overcome this defense mechanism of potato plants. They then looked for inhibitors from other sources that would be more effective against the beetle's proteases.⁵ After testing several proteinaceous inhibitors of different structural types for their ability to inhibit the beetle's proteolytic activities *in vitro*, most members of the cystatin superfamily of inhibitors¹¹ were found to be poor inhibitors of the beetle's induced endoproteolytic activities except for the third domain of human kininogen, which was a fairly strong inhibitor. The best inhibitor of the beetle's induced endoproteolytic activity was one of the structurally different thyroglobulin type-1 domain-like inhibitors, equistatin, a protease inhibitor from the sea anemone, *Actinia equine*.^{12–14} The stefin family of inhibitors in the cystatin superfamily was inhibitory of the beetle's induced aminopeptidase-like activity. In *in vivo* feeding experiments, larvae of the Colorado potato beetle fed on equistatin-coated potato leaves were strongly retarded in their growth and development with about half of the larvae dying after only a few days. Igor's results

demonstrated the potential of using thyroglobulin type-1 domain-like and stefin family-like inhibitors as potential field crop protectants against insect attack.⁵

A related insect control project involved a collaboration between not only Slovenian and American scientists but also several Japanese scientists on a study of the effects of proteinase inhibitors on the growth and digestive proteolysis of another coleopteran, the red flour beetle, *Tribolium castaneum*.¹⁵ Inhibitors of *T. castaneum* digestive proteinases were examined to identify potential biopesticides for incorporation into transgenic plants and seeds thereof. Cysteine proteinase inhibitors from potato, Job's tears and sea anemone (equistatin) were effective inhibitors of *in vitro* casein hydrolysis by *T. castaneum* proteinases (Fig. 1).

Similar to Igor's findings with the Colorado potato beetle, the thyroglobulin type-1 domain was the inhibitor domain most active toward red flour beetle gut proteases. Casein hydrolysis was inhibited weakly by chymostatin and soybean trypsin inhibitor. The soybean trypsin inhibitor had no significant effect on growth when it was bioassayed alone, but it was effective when used in combination with a potato cysteine proteinase inhibitor. In oral feeding bioassays with single inhibitors, larval growth was suppressed by the cysteine proteinase inhibitors from potato, Job's tears and sea anemone. Levels of inhibition were similar to that observed with a low molecular weight model cysteine protease inhibitor, E-64, although the moles of proteinaceous inhibitors tested were many fold less. These proteinaceous inhibitors were identified to be candidates

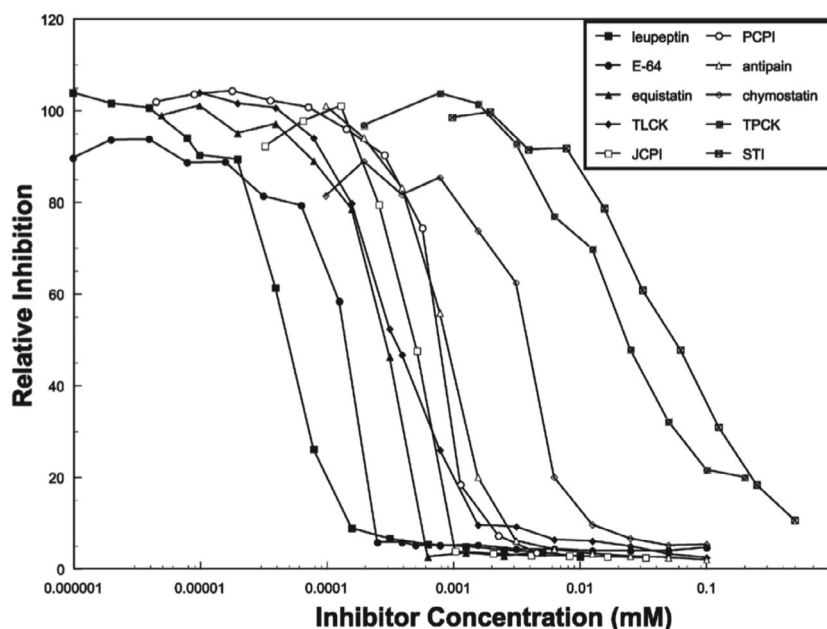


Figure 1. Relative inhibition (as a percent of the control activity) of casein hydrolysis by *Tribolium castaneum* larval gut proteinases with selected proteinase inhibitors¹⁵ including E-64: L-trans-epoxysuccinylleucylamido w4-guanidinobutane; JCPI, Job's tears cysteine proteinase inhibitor; TLCK, tosyl-L-lysine chloromethyl ketone; TPCK, N-tosyl-L-phenylalanine chloromethyl ketone; PCPI, potato cysteine proteinase inhibitor and STI, soybean trypsin inhibitor (Kunitz). Leupeptin, E-64, equistatin and TLCK were the most potent caseinolytic enzyme inhibitors. In feeding bioassays, equistatin and PCPI were the most potent peptides in inhibiting larval growth of the red flour beetle.¹⁵

for transgenic plant and seed technology to reduce damage by coleopteran pests such as the red flour beetle and Colorado potato beetle.

Overall, from a practical viewpoint, Igor's and other findings further illustrated the striking diversity of possible protease-inhibitor interactions in insect-plant systems and underline the relevance of protease inhibitor activity-based protease profiling to characterize the inhibitory range of recombinant inhibitors considered for insect pest control. For example, a straightforward way to use cystatin-like inhibitors against coleopteran insects might be to combine them with serine protease inhibitors in such a way as to significantly broaden the overall spectrum of target protease types and minimize the effectiveness of any physiological compensatory processes in the herbivores.^{16,17}

3. Cultural and Travel Times

In addition to our scientific interactions, I gained much information from not only Igor but also Vito and Franc about the history, politics and geography of Slovenia/Yugoslavia and the Balkan region. Until that time, I knew very little about their country, but because of their generosity, I came to appreciate its greatness and wonderful citizens. All three are/were very good ambassadors for Slovenia.

One of the more memorable times spent with Igor was when he joined my wife Virginia and myself on a Mexican railroad trip south to Guadalajara and Mexico City where we enjoyed many cultural attractions and savored many kinds of delicious Mexican dishes. Afterwards, Igor became quite the connoisseur of Mexican cooking and loved to prepare Mexican food for his family and friends in Slovenia. We would even mail him care packages containing Mexican food items that at that time were hard to find in Slovenia. A very special travel time with Igor for me was a visit to Ljubljana when he helped to host me and to enjoy the natural beauty and culture of that area of Slovenia. Another happy travel memory of Igor was one regarding the car he had bought and drove in Tucson. He was very delighted to be the owner of a 1961 white Buick LeSabre convertible and enjoyed cruising around Arizona very much with the top down while taking in the warm southwestern sunshine.

4. Quality of Life Time

One of the greatest gifts of life is friendship, and I received that and more from Professor Kregar. He added much to my quality of life overall. As we grew older and in spite of living far apart, we spent many hours visiting via Skype on the internet, updating our activities, sharing stories and trying to find solutions to the world's problems.

Not only did I benefit scientifically from our friendship, I also became better educated in international history, geography, politics and culture because of Igor. I will always remember him as a wonderful colleague and friend with great love and respect.

5. References

1. PubMed, 2018, <https://www.ncbi.nlm.nih.gov/pubmed?cmd=Search&term=Kregar%20I%5BAuth%5D>
2. S. K. Banerjee, I. Kregar, V. Turk and J. A. Rupley, *J. Biol. Chem.* **1973**, *248*, 4786–92.
3. K. J. Kramer and J. A. Rupley, *Arch. Biochem. Biophys.* **1973**, *156*, 414–25. DOI:10.1016/0003-9861(73)90290-7
4. K. J. Kramer and J. A. Rupley, *Arch. Biochem. Biophys.* **1973**, *158*, 566–76. DOI:10.1016/0003-9861(73)90549-3
5. K. Gruden, B. Strukelj, T. Popovic, B. Lenarcic, T. Bevec, J. Brzin, I. Kregar, J. Herzog-Velikonja, W. J. Stiekema, D. Bosch and M. A. Jongsma, *Insect Biochem. Mol. Biol.* **1998**, *28*, 549–60. DOI:10.1016/S0965-1748(98)00051-4
6. K. Gruden, B. Strukelj, M. Ravnikar, M. Poljsak-Prijatelj, I. Mavric, J. Brzin, J. Pungercar and I. Kregar, *Plant Mol. Biol.* **1997**, *34*, 317–23. DOI:10.1023/A:1005853026333
7. S. Kreft, M. Ravnikar, P. Mesko, J. Pungercar, A. Umek, I. Kregar and B. Strukelj, *Phytochemistry* **1997**, *44*, 1001–6. DOI:10.1016/S0031-9422(96)00668-1
8. D. B. Maganja, B. Strukelj, J. Pungercar, F. Gubensek, V. Turk and I. Kregar, *Plant Mol. Biol.* **1992**, *20*, 311–3. DOI:10.1007/BF00014499
9. U. Schluter, M. Benchabane, A. Munger, A. Kiggundu, J. Vorster, M. C. Goulet, C. Cloutier and D. Michaud, *J. Exp. Bot.* **2010**, *61*, 4169–83. DOI:10.1093/jxb/erq166
10. B. Strukelj, J. Pungercar, P. Mesko, D. Barlic-Maganja, F. Gubensek, I. Kregar and V. Turk, *Biol. Chem. Hoppe Seyler* **1992**, *373*, 477–82. DOI:10.1515/bchm3.1992.373.2.477
11. V. Turk, V. Stoka and D. Turk, *Front. Biosci.* **2008**, *13*, 5406–20. DOI:10.2741/3089
12. B. Lenarcic, A. Ritonja, B. Strukelj, B. Turk and V. Turk, *J. Biol. Chem.* **1997**, *272*, 13899–903. DOI:10.1074/jbc.272.21.13899
13. T. Bevec, V. Stoka, G. Pungercic, I. Dolenc and V. Turk, *J. Exp. Med.* **1996**, *183*, 1331–8. DOI:10.1084/jem.183.4.1331
14. T. Ogrinc, I. Dolenc, A. Ritonja and V. Turk, *FEBS Lett.* **1993**, *336*, 555–9. DOI:10.1016/0014-5793(93)80875-U
15. B. Oppert, T. D. Morgan, K. Hartzler, B. Lenarcic, K. Galesa, J. Brzin, V. Turk, K. Yoza, K. Ohtsubo and K. J. Kramer, *Comp. Biochem. Physiol. C Toxicol. Pharmacol.* **2003**, *134*, 481–90.
16. B. Oppert, T. D. Morgan, K. Hartzler and K. J. Kramer, *Comp. Biochem. Physiol. C Toxicol. Pharmacol.* **2005**, *140*, 53–8.
17. J. Vorster, A. Rasoolizadeh, M. C. Goulet, C. Cloutier, F. Sainsbury and D. Michaud, *Insect Biochem. Mol. Biol.* **2015**, *65*, 10–9. DOI:10.1016/j.ibmb.2015.07.017

Povzetek

Nekateri interesi pokojnega profesorja Igorja Kregarja ter avtorja tega prispevka so se na področju biokemijskih raziskav prekrivali. Na eni strani glikozidne hidrolaze in lizocim na drugi strani pa proteolizni encimi in njihovi inhibitorji, prisotni v tkivih insektov in rastlin. V primeru lizocima so naši rezultati doprinesli k razumevanju njegovega katalitskega mehanizma, pri katerem funkcionalne skupine karboksilne kisline sodelujejo. Drugo področje pa zajema interakcije med insektom in rastlino, ki vključuje obrambne odgovore rastlin na prehrano insektov s pomočjo inhibitorjev proteoliznih encimov. Dobljeni rezultati so lahko uporabni pri biotehnološki aplikaciji transgenih rastlin in semen, kar naj bi pripomoglo k zmanjšanju škode, ki jo povzročajo *Coleoptere* in drugi insekti. Iz prikazanih skupnih interesov na področju kulture in potovanj avtor tega prispevka ocenjuje, da je veliko pridobil s prijateljstvom s profesor Kregarjem.

Review

Characteristics, Structure, and Biological Role of Stefins (Type-1 Cystatins) of Human, Other Mammals, and Parasite Origin

Vito Turk,^{1,2*} Dušan Turk,^{1,3*} Iztok Dolenc¹ and Veronika Stoka^{1,2*}

¹ Department of Biochemistry and Molecular and Structural Biology, J. Stefan Institute, Jamova 39, SI-1000 Ljubljana, Slovenia

² Jožef Stefan International Postgraduate School, Jamova 39, SI-1000 Ljubljana, Slovenia

³ Centre of Excellence CIPKEBIP, Jamova 39, SI-1000 Ljubljana, Slovenia

* Corresponding author: E-mail: vito.turk@ijs.si; dusan.turk@ijs.si; veronika.stoka@ijs.si
Tel: +386 1 4773 365 Fax: + 386 1 4773 984

Received: 08-02-2018

Dedicated to the memory of Prof. Dr. Igor Kregar

Abstract

The majority of lysosomal cysteine cathepsins are ubiquitously expressed enzymes. However, some of them differ in their specific cell or tissue distribution and substrate specificity, suggesting their involvement in determining normal cellular processes, as well as pathologies. Their proteolytic activities are potentially harmful if uncontrolled. Therefore, living organisms have developed several regulatory mechanisms such as endogenous protein inhibitors of the cystatin family, including the group of small cytosolic proteins, the stefins. The main focus of this review is stefins of various origins and their properties, structure, and mechanism of interaction with their target enzymes. Furthermore, oligomerization and fibrillogenesis in stefins and/or cystatins provide insights into conformational diseases. The present status of the knowledge in this field and current trends might contribute to identifying novel therapeutic targets and approaches to treat various diseases.

Keywords: Mammalian stefins; parasite stefins; cystatins; cysteine cathepsins; mechanism of interaction; oligomerization

1. Introduction

The discovery of the lysosome was crucial for understanding intracellular protein degradation processes.¹ Clearly, this finding subsequently contributed to the rapid progress in studies on lysosomal proteases and led to the discovery of a great variety of their endogenous protein inhibitors and small-molecule inhibitors. Among lysosomal proteases are cysteine cathepsins, the most thoroughly studied enzymes that require a slightly acidic and reducing lysosomal environment. There are 11 human cysteine cathepsins, cathepsins B, C, F, H, K, L, O, S, V, X, and W, and they were identified at the sequence level and later confirmed by bioinformatic analysis of the genome sequence and mRNA expression levels.² Some of the cathepsins, such as cathepsins B, H, L, C, and O, are ubiquitously expressed in a wide variety of cells and tissues, whereas

cathepsins F, K, S, V, X, and W show a more restricted cell- or tissue-specific distribution and expression.^{2–4} Most of the cathepsins exhibit predominantly endopeptidase activity, while cathepsins B, C, H, and X are exopeptidases. Lysosomal cysteine cathepsins resemble the papain family of cysteine peptidases (C1A). The crystal structure of papain includes two adjacent structural domains separated by a V-shaped active site cleft, with Cys25, His159, and Asn175 residues essential for catalysis. Compared to the crystal structures of true endopeptidases such as cathepsins L⁵, S⁶, and K⁷, the additional features found in the crystal structures of exopeptidases enable their exopeptidase activity by modifying the active-site cleft of these enzymes, such as an occluding loop in cathepsins B and X or an additional exclusion domain in cathepsin C and an octapeptide in cathepsin H.^{8–11} The determined crystal structures of cathepsins and their substrate specific-

ties^{12–14} can provide clues about the biological function of these enzymes. Human cysteine cathepsins, in addition to intracellular protein degradation, participate and control many important physiological processes such as antigen presentation,³ aging,¹⁵ bone remodeling,¹⁶ apoptosis,^{17,18} prohormone activation,¹⁹ and cell signaling.^{13,20} However, more recent studies demonstrated the presence of the lysosomal cathepsins in the extracellular environment, nucleus, nuclear and plasma membrane, and cytosol, where they play a crucial role in the pathogenesis of cardiovascular diseases,²¹ cancer,^{22,23} neurodegeneration,^{15,24} and other diseases.

Cathepsins are synthesized as inactive precursors; however, once activated, these enzymes are potentially hazardous to their environment.²⁵ Therefore, their proteolytic activities *in vivo* must be strictly regulated at multiple levels by various control mechanisms, including pH, zymogen activation, and endogenous protein inhibitors, to prevent improper cleavage of signaling molecules.^{26,27} The nature of zymogen activation was elucidated from procathepsin structures,^{28,29} which revealed that the propeptide folds on the surface of the enzyme and runs through the active site cleft, thus blocking the access of the substrate. In the final step, the propeptide unfolds at acidic pH and opens the catalytic site of the mature enzyme.³⁰ Propeptides differ in their length. Cathepsin X propeptide contains only 38 residues,³¹ while cathepsin C and F propeptides contain 206 and 251 residues, respectively.^{32,33} In most cathepsins, the N-terminal propeptide is proteolytically removed by various proteases³⁴ or autocatalytically under acidic conditions.^{30,35,36} Very recently was demonstrated that procathepsin H is not autoactivated but requires other proteases, such as endopeptidase cathepsin L for its activation.³⁷ It was found that glycosaminoglycans (GAGs) can accelerate the autocatalytic removal of the propeptide and subsequent activation of cathepsin B³⁸ and some other cathepsins.²⁸ The released propeptides from endopeptidases exhibit a limited selectivity of inhibition against their cognate cathepsins *in vitro*,³⁹ whereas the true exopeptidases cathepsins C and X require endopeptidases, such as cathepsins L and S, for their activation but not autocatalytic processing.⁴⁰

The main regulators of cysteine cathepsins and other papain-like enzymes are their endogenous protein inhibitors, cystatins. The main function of cystatins is to protect the organism against their endogenous enzymes when released from the lysosomes to the extracellular environment, as well as to serve as a defense mechanism against proteases of invading pathogens. In the immune system, parasite stefins and cystatins modulate host's cysteine cathepsin activities by inhibiting processing of exogenous antigens and the MHC class II – Ii, carried out by lysosomal cysteine cathepsins and legumain.^{41–43} Stefins and cystatins upregulate nitric oxide (NO) production by interferon γ -activated murine macrophages. NO inhibits cysteine proteases, particularly those from parasitic protozoa.^{44–46}

Parasite inhibitors contribute to the innate and adaptive immunity by targeting host's cysteine peptidases. It is evident that cystatin thus exerts several immunomodulatory functions.⁴¹

The cystatins are generally non-selective, competitive, reversible, and tight-binding inhibitors.²⁸ They are widely found in all living organisms, from humans, animals, plants, parasites, bacteria, and archaea.⁴⁷ Based on their protein sequences and tertiary structure, the cystatin family (clan IH) is divided into three inhibitory subfamilies: the stefins (type-1 cystatins or I25A), cystatins (type-2 cystatins or I25B), and kininogens (type-3 cystatins or I25C), as seen in the MEROPS database (<http://merops.sanger.ac.uk>). However, the classification of protein peptidase inhibitors, including the cystatin family, is continually being revised.⁴⁸ Stefins are primarily intracellular single-chain proteins of about 100 amino acid residues that lack carbohydrate and disulfide bonds. Cystatins are extracellular single-chain proteins of about 115 amino acid residues and contain a signal peptide for secretion and two intracellular disulfide bridges, with the exception of human cystatin F, which contains an additional disulfide bridge. The most well-studied member is human cystatin C.⁴⁹ The third subfamily of inhibitors is the kininogens, also known as kinin precursor proteins.⁵⁰ They are large multifunctional and multi-domain proteins and are predominantly found in the blood plasma, with different biological functions attributable to each different domain. In humans, there are two types of kininogens: high-molecular-weight kininogen (HK) and low-molecular-weight inhibitor (LK). Both HK and LK are composed of three tandemly repeated type-2 cystatin domains (designated 1, 2, and 3) containing eight disulfide bridges. Only domains 2 and 3 of HK and LK bind and inhibit various cysteine proteases, including cathepsins and cruzipain.^{51–53} Additional information about cystatins can be found in a recent review²⁸ and in several older review papers.^{54–57}

In addition to the cystatins, there are other known protein inhibitors of papain-like enzymes. Structurally unrelated to cystatins are thyropepsins, which are assigned according to the MEROPS database to the family I31 of clan IX⁴⁸ and show significant homology to thyroglobulin type-1 domains.⁵⁸ The main representatives are the p41 fragment of the invariant chain of MHC class II molecules^{59,60} and the equistatin from the sea anemone *Actinia equina*.^{61,62} The equistatin is composed of the three structurally related domains; the N-terminal domain inhibits cysteine cathepsins,⁶³ whereas the second domain inhibits lysosomal cathepsin D.^{61,63} The p41 fragment strongly inhibits various cysteine cathepsins⁶⁴ and cruzipain.⁶⁵ The crystal structure of the cathepsin L-p41 inhibitory fragment complex possesses a novel fold of p41, which enables specificity to their target enzymes, in contrast to rather non-selective cystatins.⁶⁶ It was demonstrated that mammalian serpins are involved in cross-class inhibition with cysteine proteases. Thus, the serpin endopin 2C demon-

strates selective inhibition of cathepsin L and elastase-like serine protease,⁶⁷ while the serpin squamous cell carcinoma antigen (SCCA) inhibits cathepsins K, L, and S,⁶⁸ suggesting a novel inhibitory pathway.

Many small-molecule protease inhibitors of clinical significance and applicability were synthesized using a number of reactive groups, which interact with enzymes. For example, the pioneering group of Elliott Shaw exploited, among others, the diazomethyl ketone functional group to inhibit irreversibly cysteine proteases, including cathepsins.^{69,70} The discovery of the epoxysuccinyl-based inhibitor E-64⁷¹ as a non-selective irreversible inhibitor of cysteine cathepsins led to its wide use in a variety of biological studies and as a diagnostic tool to assess the proteolytic activity of cysteine cathepsins and some other related enzymes. E-64 does not inhibit aspartic, serine, and metallo-proteases. Many E-64 derivatives were systematically synthesized by Katunuma's group that targeted various cysteine cathepsins such as CA-030, CA-074, and several CLIK inhibitors (reviewed in⁷²). It was reported that CA-074 as a specific inhibitor of cathepsin B suppressed the degradation of collagen in rheumatoid arthritis fluid.⁷³ The crystal structure of cathepsin B in complex with CA030 revealed for the first time a substrate-like interaction in the S1' and S2' sites of the active site cleft of the enzyme.⁷⁴ The binding geometry of the double-headed inhibitors was confirmed by the crystal structure of the papain-CLIK complex⁷⁵ and the cathepsin B-NS-134 complex.⁷⁶ More details about small-molecule inhibitors can be found in previous reviews^{28,77,78} and in numerous original publications. Recent advances in the field of cysteine cathepsins as suitable drug targets are providing valuable research avenues for the treatment of various diseases that result from uncontrolled elevated cathepsin activity.⁷⁹

In this review, after the introduction to the lysosomal cysteine cathepsins and the regulation of their activities by various protein and chemically synthesized inhibitors, we discuss the current knowledge of the properties, structural characteristics, and oligomerization of protein inhibitors belonging to the stefin subfamily (type-1 cystatins) of the cystatin family.

2. Stefins

2.1. Human and Other Mammalian Stefins

The first protein inhibitor of papain-like cysteine protease was isolated and characterized from chicken egg white, and later, the name "cystatin" was proposed to designate its function.⁸⁰ The first intracellular protein inhibitors were isolated and partially characterized from pig leukocytes,⁸¹ human epidermis,⁸² and human spleen.⁸³ The stefin inhibitor (later named stefin A) was isolated from human polymorphonuclear granulocytes, and the amino-acid sequence was determined^{84,85} as well as that of chicken cystatin from egg white.⁸⁶ Both sequences con-

firmed structural differences between these two homologous protein inhibitors. In addition, a protein inhibitor of cysteine cathepsins was isolated from the sera of patients with Balkan endemic nephropathy, and the first 47 residues of the N-terminal sequence⁸⁶ was identical to that of human γ -trace,⁸⁷ and the name human cystatin was proposed.^{86,88} Soon after, it was renamed human cystatin C.⁸⁹ These and other accumulated data were of great importance for the nomenclature and classification of the cystatin superfamily, comprising three families.⁹⁰ The inhibitor cystatin B/stefin B was isolated from human liver⁹¹ and human spleen,⁹² and the resulting sequences of the first 65 residues were identical, thus strongly suggesting that both inhibitors, isolated from different tissues, are structurally identical proteins.⁹² The stefin B dimer was confirmed for the first time from human spleen.⁹² Structurally homologous inhibitors to human stefins A and B have been identified and characterized in mammals, such as rats^{93,94} and mice.⁹⁵ Stefin A,⁹⁶ stefin B,⁹⁷ and stefin C⁹⁸ are found in bovines. Interestingly, bovine stefin C was identified as the first tryptophan-containing stefin with a prolonged N-terminus. Four different porcine stefin-type inhibitors, namely A, B, D1, and D2, have been isolated and characterized.⁹⁹ Porcine stefins A, B, and D1 were sequenced, revealing that porcine D1 and the previously characterized pig leukocyte cysteine proteinase inhibitor-PLCPI¹⁰⁰ were identical proteins. Most of the stefins occur in multiple isoelectric forms in acidic or close to neutral pH and are mostly stable in the pH range 3–10 and temperatures up to 80 °C, thus avoiding protein denaturation.⁵⁴

Among mammals, human stefins A and B are clearly the main representatives and most studied protein inhibitors of the stefin subfamily. However, homologues of both human stefins have been found in various mammals, as mentioned above. Human stefins are intracellular proteins that are present in the cytosol of many cell types and tissues, but they also appear extracellularly in body fluids.¹⁰¹ They are synthesized without signal peptides. It seems that stefin B is generally more widely spread in various cell types and tissues than stefin A. Stefins are the smallest among the members of the cystatin family of inhibitors.

2.2. Stefins from Parasite Origin

Little is known about stefins, cystatins, and other protease inhibitors in parasites and their role to protect themselves from degradation by host proteases and to manipulate the host response to the parasite.¹⁰² Stefins have been identified and characterized in a wide range of organisms.^{47,103,104} Currently, about 700 members of the stefin subfamily can be found in the MEROPS database. They are involved in the regulation of their own proteolytic activities and processing of their host proteins. Two inhibitors were isolated from the liver fluke *Clonorchis sinensis*, CsStefin-1 and CsStefin-2, which have sequence similarities to human stefins.^{105,106} It was suggested that both in-

hibitors share functionally redundant regulatory functions to modulate activity and processing of CsCathepsin F. In addition, two inhibitors were isolated from the tropical liver fluke *Fasciola gigantica*, FgStefin-1¹⁰⁷ and FgStefin-2, which contain a signal peptide.^{107,108} The cystatin B homologue SmCytB from turbot *Scophthalmus maximus* enhances macrophage bactericidal activity.¹⁰⁹ Three different stefins, designated rFhStf-1, rFhStf-2, and rFhStf-3, expressed by the trematode *Fasciola hepatica* exhibited differences in their inhibition profile against various tested enzymes.¹¹⁰ Immunomodulatory properties of FhStefins could be used in order to evaluate their therapeutic potential against inflammatory diseases. The inhibitors FhStf-2 and FhStf-3 fall into an atypical subgroup of stefins due to the presence of a signal peptide, similar to the previously mentioned FgStefin-2.¹⁰⁸ The cysteine protease inhibitor AcStefin was identified and characterized from *Acanthamoeba*, the causative agent of granulomatous amoebic encephalitis and amoebic keratitis.¹¹¹ The human stefin homolog as SmCys expressed by *Schistosoma mansoni* is involved in hemoglobin degradation and its regulation¹¹². Very recently, the novel stefin-type inhibitor EnStef was found in the sanguinivorous fish parasite *Eudiplozoon nipponicum*, and it was found to inhibit endogenous cathepsins and, surprisingly, legumain, asparaginyl endopeptidase (family C13), from the *Ixodes ricinus* tick.¹¹³ Notably, only limited knowledge about the characteristics and roles of fish stefins and other endogenous inhibitors are available.^{114–116} It is well known that fish and shellfish quality depend on the meat texture, which is mainly controlled by proteolysis and autolysis and storage conditions. Endogenous proteases and their inhibitors play crucial roles in these processes, as do fish parasite proteases and their inhibitors. Therefore, more biochemical and molecular biology studies in this direction are of great economic importance in order to improve and ensure the quality of fish and their products.¹¹⁷

3. Stefin Inhibitory Profile

3.1. Mammalian Stefins

Members of the stefin subfamily are rather non-specific inhibitors of mammalian cysteine cathepsins. They are competitive, reversible inhibitors that form tight, equimolar complexes with their target enzymes.^{54,55} However, they are able to differentiate between endopeptidases and exopeptidases because of the differences in the structures of the interacting regions of the enzymes. Human and other mammalian stefins mostly act as fast and tight-binding inhibitors of typical endopeptidases, cathepsins L and S, papain, and cruzipain, inhibiting with K_i values in the pM to nM range.^{28,51} However, human stefin B is generally a weaker inhibitor than stefin A. In contrast, the exopeptidases cathepsins B, X, C, and H possess structural features that restrain the binding of the inhibitors to the parts of

the active site cleft.¹¹⁸ In mice, there are at least three variants of stefin A (Stfa1, Stfa2, and Stfa3); the first two are a result of polymorphisms.⁹⁵ Two variants, Stfa1 and Stfa2, act as fast and tight-binding inhibitors of endopeptidases such as cathepsins L and S (K_i values ranging 0.07–0.16 nM); however, their interaction with the exopeptidases cathepsins B, C, and H is several orders of magnitude weaker compared to that of human, porcine, and bovine stefins, suggesting that in mice, stefin A variants are involved predominantly in the regulation of endopeptidases. Bovine stefin A binds tightly and rapidly to cathepsin L ($K_i = 0.03$ nM), binds weaker to cathepsin H ($K_i = 0.4$ nM), and binds to cathepsin B slower but still tight ($K_i = 1.9$ nM), indicating different mechanisms of inhibition of various cathepsins by stefin A.⁹⁶ Bovine stefin B strongly inhibits cathepsin S ($K_i = 8.0$ pM) as a tight-binding inhibitor.⁹⁷ Similar to bovine stefins A and B, bovine stefin C strongly inhibits cathepsin L and papain (K_i of about 0.18 nM) and weakly inhibits exopeptidase cathepsin B.⁹⁸ Interestingly, porcine stefins A and B bind tightly and rapidly to exopeptidase cathepsin H ($K_i = 0.02$ and 0.07 nM, respectively), stefins D1 and D2 are poorer inhibitors of the same enzyme ($K_i = 102$ – 125 nM) and weak inhibitors of cathepsin B ($K_i = 335$ and 195 nM, respectively), and all four stefins (A, B, D1, and D2) are fast-acting and tight-binding inhibitors to the endopeptidases cathepsins L and S and papain (K_i values ranging 0.01–0.19 nM), as expected.⁹⁹ These results suggest that in addition to the differences in the enzyme active sites, which are used to classify proteases as endo- and exopeptidases, minor specific structural features of the porcine stefins, in particular, play an important role in binding.

3.2. Stefins of Parasite Origin

In non-mammalian species, there are some important differences in the potency and selectivity of their target enzymes compared to human and other mammalian stefins. There are several examples listed in this context. Two stefins (CsStefin-1 and CsStefin-2) from the parasite *Clonorchis sinensis* almost equally inhibit the endopeptidase plant papain, human cathepsin L, two endogenous cathepsin F variants (CsCF-4 and CsCF-4-6), and surprisingly human cathepsin B. All enzymes are inhibited in the range of K_i 0.03–0.06 nM.^{105,106} Nanomolar inhibitions of bovine cathepsins B and L, human cathepsin S, and the released cysteine protease of the parasite were observed with the fluke *Fasciola gigantica* inhibitors FgStefin-1 and FgStefin-2.^{107,108} The *Fasciola hepatica* recombinant stefin inhibitors rFhStf-1, rFhStf-2, and rFhStf-3 strongly inhibit two variants of endogenous cathepsin L (FhCL-1,-3) and human cathepsin L (K_i 1.52–52 nM); variants rFhStf-1 and rFhStf-2 inhibit human cathepsin C (K_i 35–57 nM); and human cathepsin B is inhibited only by rFhStf-2 ($K_i = 15$ nM).¹⁰⁸ The *S. mansoni* inhibitor SmCys strongly inhibits papain ($K_i = 0.065$ nM).¹¹² However, the N-terminally

truncated forms of SmCys with deletions of 10 and 20 amino acid residues resulted in much weaker papain inhibition ($K_i = 0.739$ nM and 4.915 nM, respectively). A similar effect was observed in truncated forms of human cystatin C of the first ten residues¹¹⁹ and chicken cystatin upon deletion of the first eight residues preceding Gly9.¹²⁰ In summary, it is evident that some stefin-type parasite inhibitors are strong and tight-binding inhibitors of their endogenous cysteine proteases-cathepsins as well as human and other mammalian cathepsins, suggesting their involvement in the immune regulation and inflammatory diseases.^{121–125} Furthermore, they demonstrate different inhibitory potencies against their endogenous cathepsins with endo- and exopeptidases activities compared to those of

human and other mammalian cathepsins. This might be of importance for the successful accommodation and reproduction of parasites in their host organisms.

4. Structure of Stefins and the Mechanism of Interaction with Their Target Enzymes

4.1. Interaction Between Stefins and Cathepsin Endopeptidases

Based on the known 3D structures of the chicken egg white cystatin¹²⁶ and human stefin B-papain complex,¹²⁷ the

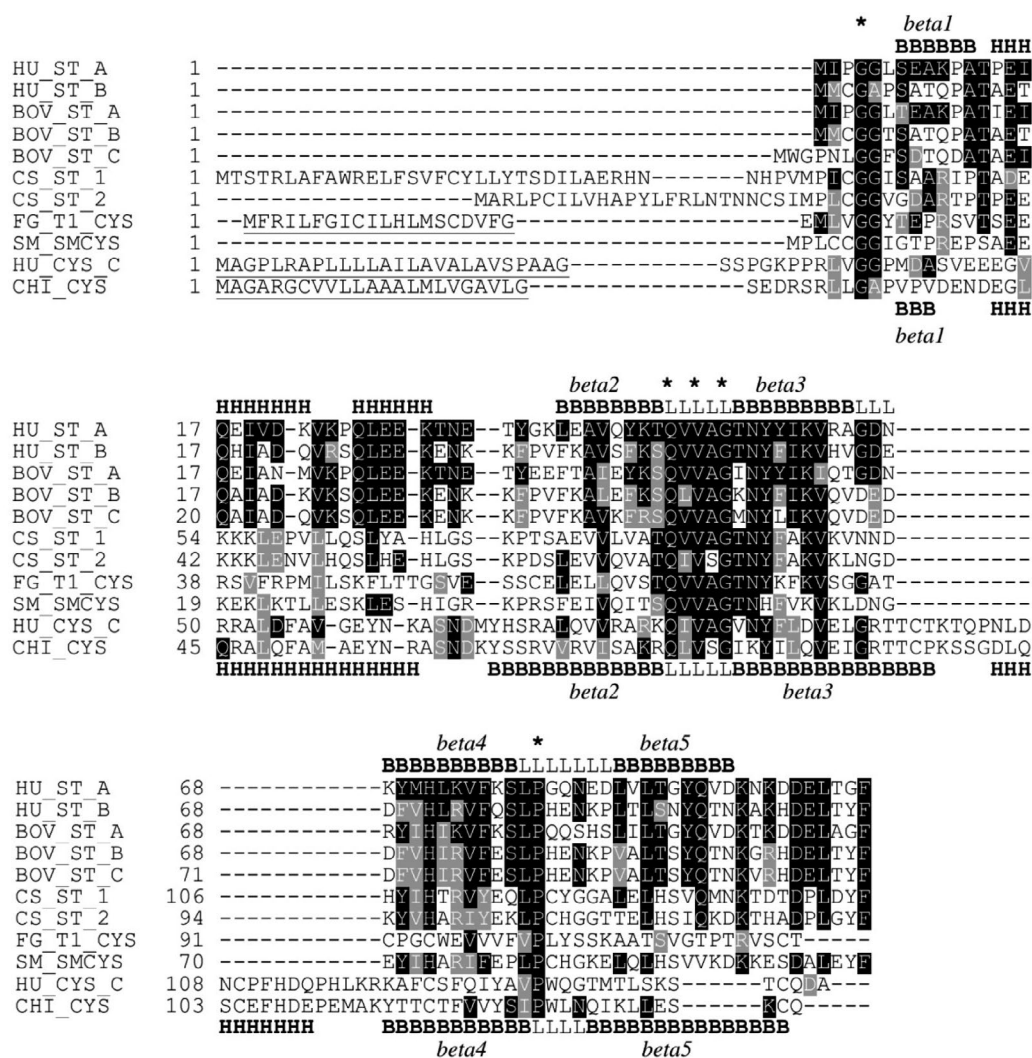


Figure 1. Multiple sequence alignment of stefins and cystatins. The alignment was performed by Clustal Omega using sequences obtained from UniProt.¹²⁸ Conserved residues in comparison to human stefin A (HU_ST_A, P01040) are marked using BoxShade as black background, and similar residues have gray background. Asterisks represent conserved residues forming tripartite wedge-shaped edge interacting with the active site of an enzyme. Signal sequences are underlined. Secondary structure elements alpha-helices (H) and beta-sheets (B), and loops (L) are indicated for stefin A (above) and for chicken cystatin (below). Five-stranded antiparallel beta-sheets are numbered. Other aligned inhibitors are: human stefin B (HU_ST_B, P04080), bovine stefin A (BOV_ST_A, P80416), B (BOV_ST_B, P25417), and C (BOV_ST_C, P35478), stefins 1 (CS_ST_1, A6YID9) and 2 (CS_ST_2, A6YE0) from *Clonorchis sinensis*, Type-1 cystatin cysteine protease inhibitor from *Fasciola gigantica* (FG_T1_CYS, K4P3W9), cystatin B (stefin type) from *Schistosoma mansoni* (SM_SMCYS, Q7YW72), human cystatin C (HU_CYS_C, P01034), and chicken cystatin (CHI_CYS, P01038).

amino acid sequences of several stefins of mammalian and parasite origin have been aligned. The conserved residues in equivalent positions confirmed the relationships between stefin and cystatin subfamilies, although some differences are evident (Figure 1). Moreover, the correct alignment of the stefins and the cystatins revealed that the previous sequence alignments were partly incorrect because of the deletion of the shorter α -helical segment in the stefins.

The first and the most important step in the elucidation of the mechanism of inhibition of cysteine proteases was the determination of the crystal structure of chicken cystatin.¹²⁶ The chicken cystatin molecule consists mainly of a five-stranded antiparallel β -pleated sheet that is twisted and wrapped around a long central α -helix and an appending shorter α -helical segment. The partially flexible N-terminal highly conserved GG residues, an exposed first hairpin loop with the sequence QLVSG (the prototype of the highly conserved QVVAG sequence in almost all stefins), and a second hairpin loop with PW residues form a wedge-shaped hydrophobic tripartite edge that has high complementarity to the V-shaped active site cleft of papain, as shown in a docking experiment.¹²⁶ Based on this docking model, the mechanism of interaction between cysteine proteases and their cystatin-like inhibitors was proposed¹²⁶ and later essentially confirmed by the crystal structure of the recombinant human stefin B-papain complex.¹²⁷ The main-chain interactions are provided by the N-terminal segment occupying the non-primed subsites S3 to S1 of the enzyme in a substrate-like manner, but the peptide segment afterwards turns away at P1 from the ac-

tive site preventing cleavage. The two hairpin loops bind to the primed-sites (S1' to S4') of the enzyme (Figure 2). In stefin B, there are only minor contributions from the second hairpin loop, but the carboxyl terminus provides an additional interaction region compared to chicken cystatin. These results provide firm evidence that the inhibition by the protein inhibitors of cysteine proteases is fundamentally different from that obtained with serine protease inhibitors.¹²⁹

4. 2. Interaction Between Stefins and Cathepsin Exopeptidases

Binding of the cystatin-type inhibitors to cathepsin exopeptidases cannot be explained by the stefin B-papain complex.¹²⁷ Cathepsin H acts as an aminopeptidase and endopeptidase; however, it exhibits strong aminopeptidase activity and is inhibited by various cystatins, including the tight-binding inhibitor stefin A, with $K_i = 0.31$ nM.²⁸ The crystal structure of native porcine cathepsin H shows a typical papain fold.¹¹ In addition, it contains the octapeptide EPQNCSAT derived from the propeptide, called a mini-chain, which is covalently attached to the main body of the enzyme by the disulfide bond to the narrowed active site cleft in the substrate-binding direction in non-primed binding sites from S2 backwards (Figure 3). The major reason for the narrowing feature is a unique insertion loop of four residues. The carbohydrate moiety attached to the main body of the enzyme participates in the positioning of the mini-chain in the active-site cleft.

The displacement of the residues in the active site cleft results in the exopeptidase activity of cathepsin H. From the crystal structure of the stefin A-cathepsin H complex,¹²⁷ it is evident that stefin A binds to the active site cleft of the en-

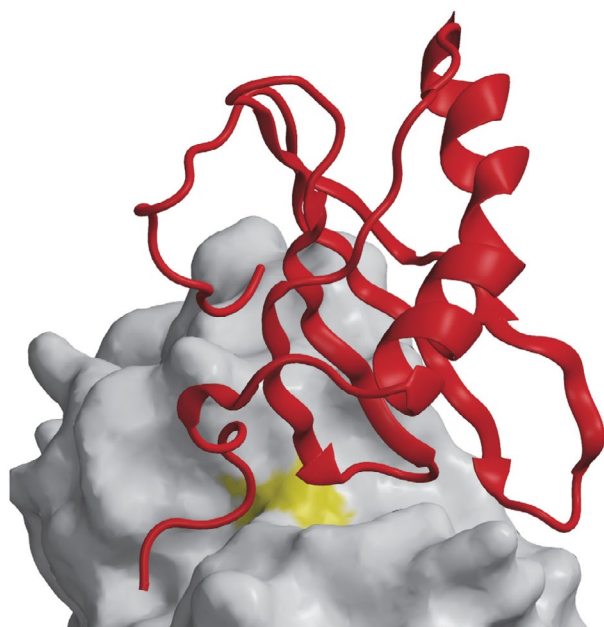


Figure 2. Papain – stefin B complex¹²⁷ (1STF). Stefins B fold is shown in red bound to papain shown as white surface with catalytic Cys area in yellow. All images (Figure 2–6) were made with MAIN software.¹³⁰

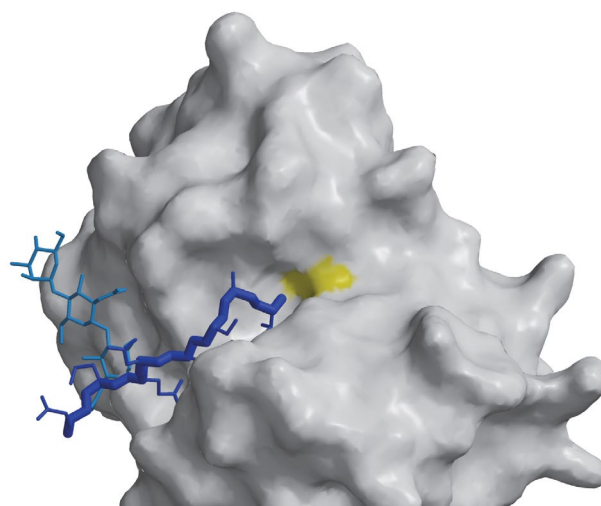


Figure 3. Cathepsin H¹¹ (8PCH). Cathepsin H is shown as white surface with catalytic Cys area in yellow. Mini chain and carbohydrate rings responsible for its stabilization are shown as sticks in dark and bright blue, respectively.

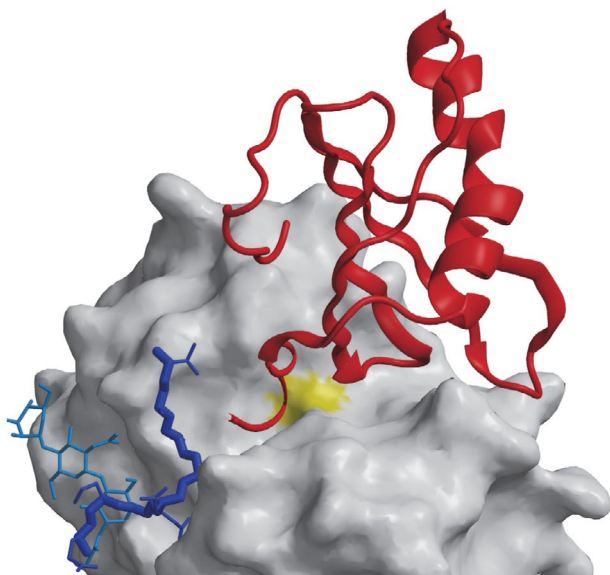


Figure 4. Cathepsin H - stefin A complex¹³¹ (1NB5). Cathepsin H is shown as in the figure 3, whereas stefin A fold is shown as red ribbon.

zyme. However, the N-terminal residues of stefin A adopt the form of a hook, which pushes away the cathepsin H mini-chain residues and distorts the structure of an insertion loop that is unique to cathepsin H (Figure 4).

The crucial role of the human cathepsin H mini-chain was further confirmed by the expression of the recombinant cathepsin H in *Escherichia coli* as a nonglycosylated protein lacking the mini-chain after autocatalytic processing.¹³² Removal of the mini-chain resulted in endopeptidase activity only. The recombinant cathepsin H was inhibited by human stefins A and B with K_i values in the range of 0.05–0.1 nM, which is stronger than the inhibition of native cathepsin H. Another example that possesses both exopeptidase and endopeptidase activities is human cathepsin B⁸ (Figure 5).

Although its overall structure and the arrangement of the active site residues are similar to those of endopeptidase papain, there are several insertion loops on the surface of the molecule that modify its properties. Some of the primed subsites are occluded by a novel 20 residue peptide segment, termed the occluding loop with two histidine residues (H110 and H111), which provide positively charged anchors for the C-terminal carboxylate group of the polypeptide substrates. The occluding loop restricts access to the active site cleft of cathepsin B by occupying part of the active site cleft on the primed side and blocking access to the active site cleft beyond the S2' substrate binding site.^{8,12} These structural features explain the unique peptidyl-di-peptidase activity of exopeptidase cathepsin B. Deletion of the occluding loop by site-directed mutagenesis resulted in an enzyme with endopeptidase activity but completely lacking exopeptidase activity.¹³⁴ The crystal structure of the human stefin A-human cathepsin B complex revealed that occluding loop residues are displaced, thus allowing the in-

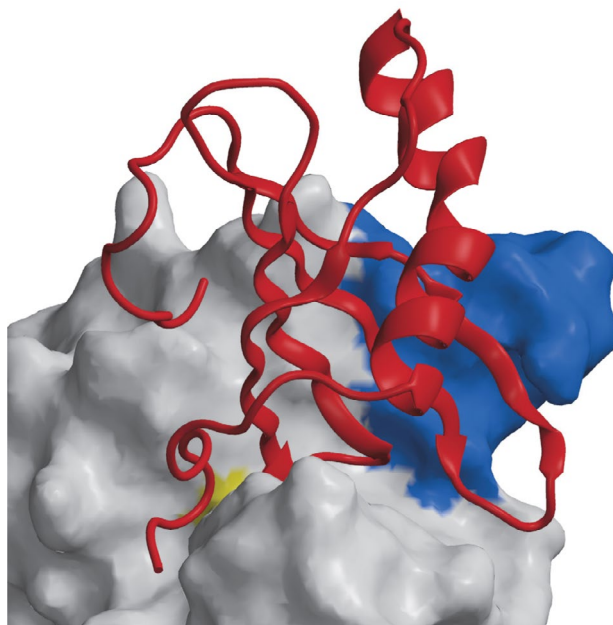


Figure 5. Cathepsin B - stefin A complex¹³³ (3K9M). Cathepsin B is shown as white surface with the catalytic Cys area yellow and occluding loop displaced from the active site cleft in blue. Stefin A is shown as red ribbon.

teraction with inhibitors in the binding region¹³³ and indicating that the occluding loop flexibility must be responsible for the cathepsin B endopeptidase activity.

Most of the protein structures were determined by X-ray crystallography with comparisons to NMR spectroscopy. Structures determined by both techniques, in the solid state and in solution, are usually very similar. However, two NMR structures of chicken cystatin, the native phosphorylated and recombinant non-phosphorylated variants,^{135,136} showed the same overall fold and the flexible N-terminal part, but there were also some significant differences in the structurally variable segments of the polypeptide chain compared to the crystal structure.¹²⁶ The NMR analysis revealed that the second α -helix determined in the crystal is not present in the solution. Similarly, the solution structure of human stefin A¹³⁷ showed similarity to the homologous protein stefin B in complex with papain,¹²⁷ but some important differences in the binding regions such as in the mobile N-terminal region and the second binding loop were observed. The crystal structure of the stefin B type inhibitor CsStefin-1 from the liver fluke *C. sinensis* was just reported, indicating some minor structural differences to human stefin B such as a four-stranded antiparallel β -pleated sheet and an additional short α -helix not present in human stefin B.¹³⁸

4. 3. Oligomerization and Fibrillogenesis of Stefins and Cystatins

Small-sized proteins, also termed mini-proteins, represent a useful and relatively simple model for studies on

oligomeric proteins. They are composed of two or more subunits, and most of them are symmetrical homo-oligomers, which are on average tetramers.¹³⁹ Oligomerization results from a variety of mechanisms and can provide insights into the evolution of proteins. Suitable examples are stefins (I25A) and cystatins (I25B), members of the cystatin family of inhibitors. The phyletic distribution of the cystatin family indicates the presence of only two ancestral lineages, stefins and cystatins, in eukaryotes and prokaryotes.⁴⁷ Stefins are present as single copy genes or small multigene families throughout the eukaryotes and underwent small changes in function during evolution. In contrast to stefins, the cystatins went through a more complex evolution involving numerous gene and domain duplications.

Stefins and cystatins share a rather high sequence similarity and nearly the same fold, as already discussed. The early finding that human stefin B⁹² and rat TPI-2 (cystatin β /stefin B)¹⁴⁰ form dimers indicated for the first time the possible appearance of the oligomerization of these proteins. Later, it was found that the trematode parasitic *C. sinensis* native stefin-type inhibitor CsStefin-2 exists in monomer, dimer, and tetramer forms, which are not the result of interchain disulfide bond interactions.¹⁰⁵ Similarly, the oligomerization from monomers (10 kDa) to oligomers of various sizes (over 100 kDa) in *F. hepatica* stefin-type inhibitors (rFhStf-1, rFhStf-2, and rFhStf-3) was reported very recently.¹¹⁰

An important step in elucidating the oligomerization of cystatins was determining the crystal structure of dimerized domain-swapped human cystatin C¹⁴¹ and of chicken cystatin and human stefin A in solution.¹⁴² Then, it was demonstrated that the domain-swapped dimer of chicken cystatin oligomerizes to a tetramer as a transient intermediate prior to oligomerization.¹⁴³ Furthermore, it was shown that human cystatin C oligomers are intermediates in fibrillogenesis, indicating that the propagation of three-dimensional domain swapping is crucial to oligomerization processes.¹⁴⁴ A variant of human cystatin C (L68Q mutant) found in patients with hereditary cystatin C amyloid angiopathy (HCCAA) causes massive amyloidosis as a result of amyloid fibrils in the cerebral arteries, with fatal consequences for young adults^{145,146}. It has just been reported that the conformational destabilization of human cystatin E (I25B) results in a domain-swapped dimer that can convert to amyloid fibrils.¹⁴⁷ This dimer inhibits legumain by forming a trimeric complex but does not inhibit papain and human cathepsin S. Furthermore, it was shown that recombinant human stefin B, in contrast to stefin A, dimerizes, oligomerizes, and forms amyloid fibrils under *in vitro* conditions.^{148,149} Soon afterwards, the crystal structures of the tetrameric human stefin B and of stefin B in solution were determined.¹⁵⁰ The structures revealed that the formation of the stefin B tetramer is not a further domain swapping process, as it was proposed earlier for cystatins,^{151,152} but a new mechanism, termed hand shaking, through which 3D domain-swapped dimers be-

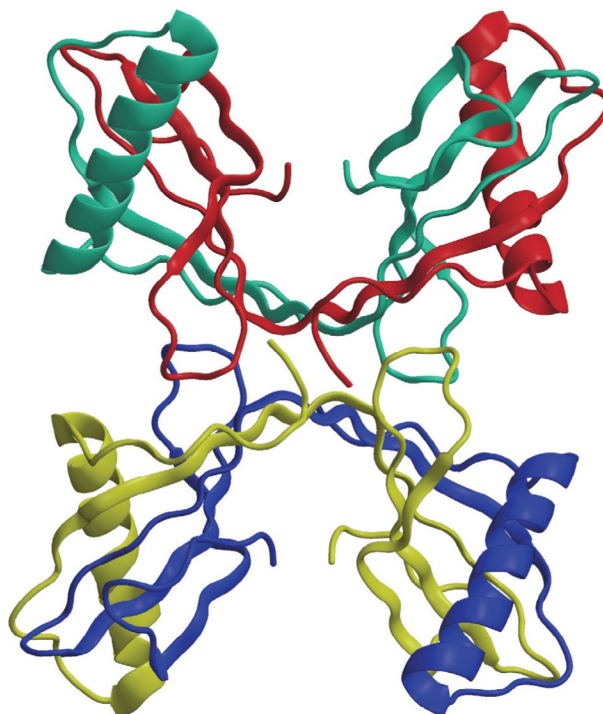


Figure 6. Stefins A tetramer¹⁵⁰ (2OCT). Each chain in the tetramer is shown as ribbon with own color. The dimers of the two domain swapped dimers are shown at the top and bottom of the figure. The two dimers interlink with loop handshake shown in the middle.

come entwined as a consequence of concurrent *trans* to *cis* isomerization of proline 74,¹⁵⁰ as can be seen in Figure 6.

This proline residue is widely conserved throughout the stefins and cystatins. It was found that the tetrameric structure of stefin B in solution correlates with that of the crystal. These and other experimental data suggest that the isomerization of proline residues is a crucial component in tetramerization and very likely involved in other steps of amyloid formation. Taken together, the similarities in structure, sequence, and oligomerization processes between stefins and cystatins suggest that in addition to domain swapping there is an additional mechanism called, hand shaking, in which the *trans* to *cis* isomerization of proline 74 is leading from may be on the path of formation of the mature fibrils. Additional information about oligomerization and amyloid formation can be found in previous reports.^{151–153} The recent progress in sample preparation due to their polymorphic purity, as well as solid state NMR and cryo-EM methods, recently provided insight in high-resolution 3D structures of amyloids.^{154,155}

5. Conclusions and Future Trends

Lysosomal cysteine cathepsins and the precise regulation of their harmful proteolytic activities are of crucial importance to prevent improper cleavage(s) of signaling molecules.^{55,156} There are several means for this regulation, one of which is the use of endogenous protein inhib-

itors, such as stefins and cystatins. We understand a great deal about the mechanisms of interaction with their target enzymes. However, low specificity of inhibitors for their target proteases indicates that we still do not understand their exact individual physiological roles.

On the other hand, most of the cathepsins are ubiquitously expressed, exhibit relatively wide specificity, and have multiple functions. Therefore, it is crucial to understand the diseases in which cathepsins play critical roles and the roles of individual cathepsins in these diseases. Interestingly, mutations in two endogenous protein inhibitors of cysteine cathepsins, stefin B, and cystatin C, are critical for the development of two neurological disorders, such as Unverricht-Lundborg disease-EPM1^{157,158} and Hereditary cystatin C amyloid angiopathy (HCCAA).^{159,143,160} Insight into the interplay of stefins and cathepsins may encourage the development of selective cathepsin inhibitors as candidates for clinical studies and eventually new drugs.⁷⁹ Furthermore, studies on parasites induced immune regulation and inflammatory diseases should also be encouraged in order to develop new therapeutic drugs.^{161–163} Another important area is the identification of physiological substrates using proteomic strategies and chemical tools.^{164,165} Although the understanding of the complexity of the numerous vital biological processes, both physiological and pathological, is best illustrated by the current trends in a number of ongoing research projects, it is likely that studies on the regulation of proteolysis in the light of the structure-function relationship will reveal valuable information in the near future.

6. Acknowledgments

Funding was provided by Slovenian Research Agency to research programs P1-0140 (B. Turk) and P1-0048 (D. Turk), and to the Infrastructural Funds to Centre of Excellence CIPKeBiP IO-0048 (D. Turk).

7. References

- C. de Duve, *Nat. Cell Biol.* **2005**, *7*, 847–9. DOI: 10.1038/ncb0905-847
- A. Rossi, Q. Deveraux, B. Turk and A. Sali, *Biol. Chem.* **2004**, *385*, 363–72. DOI: 10.1515/bc.2004.040
- E. R. Unanue, V. Turk and J. Neeffes, *Annu. Rev. Immunol.* **2016**, *34*, 265–97. DOI: 10.1146/annurev-immunol-041015-055420
- J. Kos, A. Sekirnik, A. Premzl, V. Zavasnik Bergant, T. Langerholc, B. Turk, B. Werle, R. Golouh, U. Repnik, M. Jeras and V. Turk, *Exp. Cell Res.* **2005**, *306*, 103–13. DOI: 10.1016/j.yexcr.2004.12.006
- A. Fujishima, Y. Imai, T. Nomura, Y. Fujisawa, Y. Yamamoto and T. Sugawara, *FEBS Lett.* **1997**, *407*, 47–50.
- M. E. McGrath, J. T. Palmer, D. Bromme and J. R. Somoza, *Protein Sci.* **1998**, *7*, 1294–302. DOI: 10.1002/pro.5560070604
- M. E. McGrath, J. L. Klaus, M. G. Barnes and D. Bromme, *Nat. Struct. Biol.* **1997**, *4*, 105–9.
- D. Musil, D. Zucic, D. Turk, R. A. Engh, I. Mayr, R. Huber, T. Popovic, V. Turk, T. Towatari, N. Katunuma and et al., *EMBO J.* **1991**, *10*, 2321–30.
- G. Guncar, I. Klemencic, B. Turk, V. Turk, A. Karaoglanovic-Carmona, L. Juliano and D. Turk, *Structure* **2000**, *8*, 305–13.
- D. Turk, V. Janjic, I. Stern, M. Podobnik, D. Lamba, S. W. Dahl, C. Lauritzen, J. Pedersen, V. Turk and B. Turk, *EMBO J.* **2001**, *20*, 6570–82. DOI: 10.1093/emboj/20.23.6570
- G. Guncar, M. Podobnik, J. Pungercar, B. Strukelj, V. Turk and D. Turk, *Structure* **1998**, *6*, 51–61.
- Y. Choe, F. Leonetti, D. C. Greenbaum, F. Lecaille, M. Bogyo, D. Bromme, J. A. Ellman and C. S. Craik, *J. Biol. Chem.* **2006**, *281*, 12824–32. DOI: 10.1074/jbc.M513331200
- B. Turk, D. Turk and V. Turk, *EMBO J.* **2012**, *31*, 1630–43. DOI: 10.1038/emboj.2012.42
- M. Vizovisek, R. Vidmar, E. Van Quickenberghe, F. Impens, U. Andjelkovic, B. Sobotic, V. Stoka, K. Gevaert, B. Turk and M. Fonovic, *Proteomics* **2015**, *15*, 2479–90. DOI: 10.1002/pmic.201400460
- V. Stoka, V. Turk and B. Turk, *Ageing Res Rev* **2016**, *32*, 22–37. DOI: 10.1016/j.arr.2016.04.010
- M. Fonovic and B. Turk, *Biochim. Biophys. Acta* **2014**, *1840*, 2560–70. DOI: 10.1016/j.bbagen.2014.03.017
- V. Stoka, B. Turk, S. L. Schendel, T. H. Kim, T. Cirman, S. J. Snipas, L. M. Ellerby, D. Bredesen, H. Freeze, M. Abrahamson, D. Bromme, S. Krajewski, J. C. Reed, X. M. Yin, V. Turk and G. S. Salvesen, *J. Biol. Chem.* **2001**, *276*, 3149–57. DOI: 10.1074/jbc.M008944200
- V. Stoka, B. Turk and V. Turk, *IUBMB Life* **2005**, *57*, 347–53. DOI: 10.1080/15216540500154920
- V. Hook, L. Funkelstein, D. Lu, S. Bark, J. Wegrzyn and S. R. Hwang, *Annu. Rev. Pharmacol. Toxicol.* **2008**, *48*, 393–423. DOI: 10.1146/annurev.pharmtox.48.113006.094812
- B. Turk and V. Stoka, *FEBS Lett.* **2007**, *581*, 2761–7. DOI: 10.1016/j.febslet.2007.05.038
- C. L. Liu, J. Guo, X. Zhang, G. K. Sukhova, P. Libby and G. P. Shi, *Nat. Rev. Cardiol.* **2018**, *15*, 351–370. DOI: 10.1038/s41569-018-0002-3
- O. C. Olson and J. A. Joyce, *Nat. Rev. Cancer* **2015**, *15*, 712–29. DOI: 10.1038/nrc4027
- V. Turk, J. Kos and B. Turk, *Cancer Cell* **2004**, *5*, 409–10.
- J. R. Lowry and A. Klegeris, *Brain Res. Bull.* **2018**, *139*, 144–156. DOI: 10.1016/j.brainresbull.2018.02.014
- B. Wiederanders, G. Kaulmann and K. Schilling, *Curr Protein Pept Sci* **2003**, *4*, 309–26.
- B. Turk, J. G. Bieth, I. Bjork, I. Dolenc, D. Turk, N. Cimerman, J. Kos, A. Colic, V. Stoka and V. Turk, *Biol. Chem. Hoppe Seyler* **1995**, *376*, 225–30.
- V. Turk, B. Turk and D. Turk, *EMBO J.* **2001**, *20*, 4629–33. DOI: 10.1093/emboj/20.17.4629
- V. Turk, V. Stoka, O. Vasiljeva, M. Renko, T. Sun, B. Turk and D. Turk, *Biochim. Biophys. Acta* **2012**, *1824*, 68–88. DOI: 10.1016/j.bbapap.2011.10.002

29. M. R. Groves, R. Coulombe, J. Jenkins and M. Cygler, *Proteins* **1998**, 32, 504–14.
30. R. Jerala, E. Zerovnik, J. Kidric and V. Turk, *J. Biol. Chem.* **1998**, 273, 11498–504.
31. D. K. Nagler and R. Menard, *FEBS Lett.* **1998**, 434, 135–9.
32. A. Paris, B. Strukelj, J. Pungercar, M. Renko, I. Dolenc and V. Turk, *FEBS Lett.* **1995**, 369, 326–30.
33. B. Wang, G. P. Shi, P. M. Yao, Z. Li, H. A. Chapman and D. Bromme, *J. Biol. Chem.* **1998**, 273, 32000–8.
34. K. Nissler, S. Kreusch, W. Rommerskirch, W. Strubel, E. Weber and B. Wiederanders, *Biol. Chem.* **1998**, 379, 219–24.
35. L. Mach, J. S. Mort and J. Glossl, *J. Biol. Chem.* **1994**, 269, 13030–5.
36. J. Rozman, J. Stojan, R. Kuhelj, V. Turk and B. Turk, *FEBS Lett.* **1999**, 459, 358–62.
37. Y. Hao, W. Purtha, C. Cortesio, H. Rui, Y. Gu, H. Chen, E. A. Sickmier, P. Manzanillo and X. Huang, *PLoS One* **2018**, 13, e0200374.
38. D. Caglic, J. R. Pungercar, G. Pejler, V. Turk and B. Turk, *J. Biol. Chem.* **2007**, 282, 33076–85.
DOI: 10.1074/jbc.M705761200
39. J. Guay, J. P. Falguyet, A. Ducret, M. D. Percival and J. A. Mancini, *Eur. J. Biochem.* **2000**, 267, 6311–8.
40. S. W. Dahl, T. Halkier, C. Lauritzen, I. Dolenc, J. Pedersen, V. Turk and B. Turk, *Biochemistry* **2001**, 40, 1671–8.
41. B. Vray, S. Hartmann and J. Hoebeke, *Cell. Mol. Life Sci.* **2002**, 59, 1503–12.
42. N. Kopitar-Jerala, *FEBS Lett.* **2006**, 580, 6295–301.
DOI: 10.1016/j.febslet.2006.10.055
43. D. Knox, *Parasite Immunol.* **2007**, 29, 57–71.
44. L. Verdot, G. Lalmanach, V. Vercruysee, J. Hoebeke, F. Gauthier and B. Vray, *Eur. J. Biochem.* **1999**, 266, 1111–7.
45. L. Verdot, G. Lalmanach, V. Vercruysee, S. Hartmann, R. Lucius, J. Hoebeke, F. Gauthier and B. Vray, *J. Biol. Chem.* **1996**, 271, 28077–81.
46. Y. Wang, L. Wu, X. Liu, S. Wang, M. Ehsan, R. Yan, X. Song, L. Xu and X. Li, *Parasit Vectors* **2017**, 10, 425.
DOI: 10.1186/s13071-017-2368-1
47. D. Kordis and V. Turk, *BMC Evol. Biol.* **2009**, 9, 266.
DOI: 10.1186/1471-2148-9-266
48. N. D. Rawlings, *Biochimie* **2010**, 92, 1463–83.
DOI: 10.1016/j.biochi.2010.04.013
49. P. M. Mathews and E. Levy, *Ageing Res Rev* **2016**, 32, 38–50.
DOI: 10.1016/j.arr.2016.06.003
50. G. Lalmanach, C. Naudin, F. Lecaille and H. Fritz, *Biochimie* **2010**, 92, 1568–79. DOI: 10.1016/j.biochi.2010.03.011
51. V. Stoka, M. Nycander, B. Lenarcic, C. Labriola, J. J. Cazzulo, I. Bjork and V. Turk, *FEBS Lett.* **1995**, 370, 101–4.
52. B. Turk, V. Stoka, V. Turk, G. Johansson, J. J. Cazzulo and I. Bjork, *FEBS Lett.* **1996**, 391, 109–12.
53. B. Turk, V. Stoka, I. Bjork, C. Boudier, G. Johansson, I. Dolenc, A. Colic, J. G. Bieth and V. Turk, *Protein Sci.* **1995**, 4, 1874–80. DOI: 10.1002/pro.5560040922
54. V. Turk and W. Bode, *FEBS Lett.* **1991**, 285, 213–9.
55. B. Turk, D. Turk and G. S. Salvesen, *Curr. Pharm. Des.* **2002**, 8, 1623–37.
56. M. Abrahamson, M. Alvarez-Fernandez and C. M. Nathanson, *Biochem. Soc. Symp.* **2003**, 179–99.
57. V. Turk, V. Stoka and D. Turk, *Front. Biosci.* **2008**, 13, 5406–20.
58. B. Lenarcic and T. Bevec, *Biol. Chem.* **1998**, 379, 105–11.
59. T. Bevec, V. Stoka, G. Pungercic, I. Dolenc and V. Turk, *J. Exp. Med.* **1996**, 183, 1331–8.
60. T. Ogrinc, I. Dolenc, A. Ritonja and V. Turk, *FEBS Lett.* **1993**, 336, 555–9.
61. B. Lenarcic and V. Turk, *J. Biol. Chem.* **1999**, 274, 563–6.
62. B. Lenarcic, A. Ritonja, B. Strukelj, B. Turk and V. Turk, *J. Biol. Chem.* **1997**, 272, 13899–903.
63. B. Strukelj, B. Lenarcic, K. Gruden, J. Pungercar, B. Rogelj, V. Turk, D. Bosch and M. A. Jongmsma, *Biochem. Biophys. Res. Commun.* **2000**, 269, 732–6. DOI: 10.1006/bbrc.2000.2356
64. M. Mihelic, A. Dobersek, G. Guncar and D. Turk, *J. Biol. Chem.* **2008**, 283, 14453–60. DOI: 10.1074/jbc.M801283200
65. T. Bevec, V. Stoka, G. Pungercic, J. J. Cazzulo and V. Turk, *FEBS Lett.* **1997**, 401, 259–61.
66. G. Guncar, G. Pungercic, I. Klemencic, V. Turk and D. Turk, *EMBO J.* **1999**, 18, 793–803. DOI: 10.1093/emboj/18.4.793
67. S. R. Hwang, V. Stoka, V. Turk and V. Y. Hook, *Biochemistry* **2005**, 44, 7757–67. DOI: 10.1021/bi050053z
68. C. Schick, P. A. Pemberton, G. P. Shi, Y. Kamachi, S. Cataltepe, A. J. Bartuski, E. R. Gornstein, D. Bromme, H. A. Chapman and G. A. Silverman, *Biochemistry* **1998**, 37, 5258–66.
DOI: 10.1021/bi972521d
69. H. Angliker, P. Wikstrom, H. Kirschke and E. Shaw, *Biochem. J.* **1989**, 262, 63–8.
70. E. Shaw, S. Mohanty, A. Colic, V. Stoka and V. Turk, *FEBS Lett.* **1993**, 334, 340–2.
71. K. Hanada, M. Tamai, M. Yamagishi, S. Ohmura, L. Sawada and I. Tanaka, *Agric. Biol. Chem.* **1978**, 42, 523–528.
DOI: 10.1080/00021369.1978.10863014
72. N. Katunuma, *Proc. Jpn. Acad. Ser. B Phys. Biol. Sci.* **2011**, 87, 29–39.
73. Y. Hashimoto, H. Kakegawa, Y. Narita, Y. Hachiya, T. Hayakawa, J. Kos, V. Turk and N. Katunuma, *Biochem. Biophys. Res. Commun.* **2001**, 283, 334–9. DOI: 10.1006/bbrc.2001.4787
74. D. Turk, M. Podobnik, T. Popovic, N. Katunuma, W. Bode, R. Huber and V. Turk, *Biochemistry* **1995**, 34, 4791–7.
75. H. Tsuge, T. Nishimura, Y. Tada, T. Asao, D. Turk, V. Turk and N. Katunuma, *Biochem. Biophys. Res. Commun.* **1999**, 266, 411–6. DOI: 10.1006/bbrc.1999.1830
76. I. Stern, N. Schaschke, L. Moroder and D. Turk, *Biochem. J.* **2004**, 381, 511–7. DOI: 10.1042/bj20040237
77. E. Shaw, *Adv. Enzymol. Relat. Areas Mol. Biol.* **1990**, 63, 271–347.
78. J. C. Powers, J. L. Asgian, O. D. Ekici and K. E. James, *Chem. Rev.* **2002**, 102, 4639–750.
79. L. Kramer, D. Turk and B. Turk, *Trends Pharmacol. Sci.* **2017**, 38, 873–898. DOI: 10.1016/j.tips.2017.06.003
80. L. C. Sen and J. R. Whitaker, *Arch. Biochem. Biophys.* **1973**, 158, 623–32.
81. M. Kopitar, J. Brzin, T. Zvonar, P. Locnikar, I. Kregar and V. Turk, *FEBS Lett.* **1978**, 91, 355–9.
82. M. Jarvinen, *J. Invest. Dermatol.* **1978**, 71, 114–8.

83. M. Jarvinen and A. Rinne, *Biochim. Biophys. Acta* **1982**, *708*, 210–7.
84. J. Brzin, M. Kopitar, V. Turk and W. Machleidt, *Hoppe Seylers Z. Physiol. Chem.* **1983**, *364*, 1475–80.
85. W. Machleidt, U. Borchart, H. Fritz, J. Brzin, A. Ritonja and V. Turk, *Hoppe Seylers Z. Physiol. Chem.* **1983**, *364*, 1481–6.
86. V. Turk, J. Brzin, M. Longer, A. Ritonja, M. Eropkin, U. Borchart and W. Machleidt, *Hoppe Seylers Z. Physiol. Chem.* **1983**, *364*, 1487–96.
87. A. Grubb and H. Lofberg, *Proc. Natl. Acad. Sci. U. S. A.* **1982**, *79*, 3024–7.
88. J. Brzin, T. Popovic, V. Turk, U. Borchart and W. Machleidt, *Biochem. Biophys. Res. Commun.* **1984**, *118*, 103–9.
89. A. J. Barrett, M. E. Davies and A. Grubb, *Biochem. Biophys. Res. Commun.* **1984**, *120*, 631–6.
90. A. J. Barrett, H. Fritz, A. Grubb, S. Isemura, M. Jarvinen, N. Katunuma, W. Machleidt, W. Muller-Esterl, M. Sasaki and V. Turk, *Biochem. J.* **1986**, *236*, 312.
91. A. Ritonja, W. Machleidt and A. J. Barrett, *Biochem. Biophys. Res. Commun.* **1985**, *131*, 1187–92.
92. B. Lenarčič, Ritonja, A., Sali, A., Kotnik, M., Turk, V. and Machleidt, W. in: V. Turk (Ed.): Cysteine Proteinases and Their Inhibitors, Walter De Gruyter, Berlin, **1986**, pp. 473–487.
93. K. Takio, E. Kominami, N. Wakamatsu, N. Katunuma and K. Titani, *Biochem. Biophys. Res. Commun.* **1983**, *115*, 902–8.
94. K. Takio, E. Kominami, Y. Bando, N. Katunuma and K. Titani, *Biochem. Biophys. Res. Commun.* **1984**, *121*, 149–54.
95. M. Mihelic, C. Teuscher, V. Turk and D. Turk, *FEBS Lett.* **2006**, *580*, 4195–9. DOI: 10.1016/j.febslet.2006.06.076
96. B. Turk, A. Ritonja, I. Bjork, V. Stoka, I. Dolenc and V. Turk, *FEBS Lett.* **1995**, *360*, 101–5.
97. B. Turk, A. Colic, V. Stoka and V. Turk, *FEBS Lett.* **1994**, *339*, 155–9.
98. B. Turk, I. Krizaj, B. Kralj, I. Dolenc, T. Popovic, J. G. Bieth and V. Turk, *J. Biol. Chem.* **1993**, *268*, 7323–9.
99. B. Lenarcic, I. Krizaj, P. Zunec and V. Turk, *FEBS Lett.* **1996**, *395*, 113–8.
100. B. Lenarcic, A. Ritonja, I. Dolenc, V. Stoka, S. Berbic, J. Pungercar, B. Strukelj and V. Turk, *FEBS Lett.* **1993**, *336*, 289–92.
101. M. Abrahamson, A. J. Barrett, G. Salvesen and A. Grubb, *J. Biol. Chem.* **1986**, *261*, 11282–9.
102. D. P. Knox, *Parasite Immunol.* **2007**, *29*, 57–71. DOI: 10.1111/j.1365-3024.2006.00913.x
103. M. Castagnola, R. Inzitari, C. Fanali, F. Iavarone, A. Vitali, C. Desiderio, G. Vento, C. Tirone, C. Romagnoli, T. Cabras, B. Manconi, M. T. Sanna, R. Boi, E. Pisano, A. Olianias, M. Pellegrini, S. Nemolato, C. W. Heizmann, G. Faa and I. Meszana, *Mol. Cell. Proteomics* **2011**, *10*, M110.003467. DOI: 10.1074/mcp.M110.003467
104. R. Vitorino, M. J. Lobo, A. J. Ferrer-Correira, J. R. Dubin, K. B. Tomer, P. M. Domingues and F. M. Amado, *Proteomics* **2004**, *4*, 1109–15. DOI: 10.1002/pmic.200300638
105. J. M. Kang, H. L. Ju, K. H. Lee, T. S. Kim, J. H. Pak, W. M. Sohn and B. K. Na, *Parasitol. Res.* **2014**, *113*, 47–58. DOI: 10.1007/s00436-013-3624-8
106. J. M. Kang, K. H. Lee, W. M. Sohn and B. K. Na, *Mol. Biochem. Parasitol.* **2011**, *177*, 126–34. DOI: 10.1016/j.molbiopara.2011.02.010
107. M. Tarasuk, S. Vichasri Grams, V. Viyanant and R. Grams, *Mol. Biochem. Parasitol.* **2009**, *167*, 60–71. DOI: 10.1016/j.molbiopara.2009.04.010
108. S. Siricoon, S. V. Grams and R. Grams, *Mol. Biochem. Parasitol.* **2012**, *186*, 126–33. DOI: 10.1016/j.molbiopara.2012.10.003
109. P. P. Xiao, Y. H. Hu and L. Sun, *Dev. Comp. Immunol.* **2010**, *34*, 1237–41. DOI: 10.1016/j.dci.2010.07.008
110. M. Cancela, I. Corvo, D. A. S. E, A. Teichmann, L. Roche, A. Diaz, J. F. Tort, H. B. Ferreira and A. Zaha, *Parasitology* **2017**, *144*, 1695–1707. DOI: 10.1017/s0031182017001093
111. J. Y. Lee, S. M. Song, E. K. Moon, Y. R. Lee, B. K. Jha, D. B. Danne, H. J. Cha, H. S. Yu, H. H. Kong, D. I. Chung and Y. Hong, *Eukaryot. Cell* **2013**, *12*, 567–74. DOI: 10.1128/ec.00308–12
112. F. C. Morales, D. R. Furtado and F. D. Rumjanek, *Mol. Biochem. Parasitol.* **2004**, *134*, 65–73.
113. J. Ilgová, L. Jedličková, H. Dvořáková, M. Benovics, L. Mikeš, L. Janda, J. Vorel, P. Roudnický, D. Potěšil and Z. Zdráhal, *Sci. Rep.* **2017**, *7*, 17526.
114. S. J. Ahn, H. J. Bak, J. H. Park, S. A. Kim, N. Y. Kim, J. Y. Lee, J. H. Sung, S. J. Jeon, J. K. Chung and H. H. Lee, *Comp. Biochem. Physiol. B Biochem. Mol. Biol.* **2013**, *165*, 211–8. DOI: 10.1016/j.cbpb.2013.04.007
115. H. K. Premachandra, I. Whang, Y. D. Lee, S. Lee, M. De Zoyssa, M. J. Oh, S. J. Jung, B. S. Lim, J. K. Noh, H. C. Park and J. Lee, *Comp. Biochem. Physiol. B Biochem. Mol. Biol.* **2012**, *163*, 138–46. DOI: 10.1016/j.cbpb.2012.05.012
116. S. Li, Z. Yang, J. Ao and X. Chen, *Dev. Comp. Immunol.* **2009**, *33*, 1268–77. DOI: 10.1016/j.dci.2009.07.008
117. S. Avtar and B. Soottawat, *Compr. Rev. Food Sci. Food Saf.* **2018**, *17*, 496–509. DOI: 10.1111/1541-4337.12337
118. D. Turk and G. Guncar, *Acta Crystallogr. D Biol. Crystallogr.* **2003**, *59*, 203–13.
119. M. Abrahamson, A. Ritonja, M. A. Brown, A. Grubb, W. Machleidt and A. J. Barrett, *J. Biol. Chem.* **1987**, *262*, 9688–94.
120. W. Machleidt, U. Thiele, B. Laber, I. Assfalg-Machleidt, A. Esterl, G. Wiegand, J. Kos, V. Turk and W. Bode, *FEBS Lett.* **1989**, *243*, 234–8.
121. R. A. Whelan, S. Rausch, F. Ebner, D. Gunzel, J. F. Richter, N. A. Hering, J. D. Schulzke, A. A. Kuhl, A. Keles, P. Janczyk, K. Nockler, L. H. Wieler and S. Hartmann, *Mol. Ther.* **2014**, *22*, 1730–40. DOI: 10.1038/mt.2014.125
122. M. J. Schuijs, S. Hartmann, M. E. Selkirk, L. B. Roberts, P. J. Openshaw and C. Schnoeller, *PLoS One* **2016**, *11*, e0161885. DOI: 10.1371/journal.pone.0161885
123. Y. Sun, G. Liu, Z. Li, Y. Chen, Y. Liu, B. Liu and Z. Su, *Immunology* **2013**, *138*, 370–81. DOI: 10.1111/imm.12049
124. C. Klotz, T. Ziegler, A. S. Figueiredo, S. Rausch, M. R. Hepworth, N. Obsivac, C. Sers, R. Lang, P. Hammerstein, R. Lucius and S. Hartmann, *PLoS Pathog.* **2011**, *7*, e1001248. DOI: 10.1371/journal.ppat.1001248

125. C. Aranzamendi, L. Sofronic-Milosavljevic and E. Pinelli, *J Parasitol Res* **2013**, 2013, 329438. DOI: 10.1155/2013/329438
126. W. Bode, R. Engh, D. Musil, U. Thiele, R. Huber, A. Karshikov, J. Brzin, J. Kos and V. Turk, *EMBO J.* **1988**, 7, 2593–9.
127. M. T. Stubbs, B. Laber, W. Bode, R. Huber, R. Jerala, B. Lencarc and V. Turk, *EMBO J.* **1990**, 9, 1939–47.
128. R. Apweiler, A. Bairoch, C. H. Wu, W. C. Barker, B. Boeckmann, S. Ferro, E. Gasteiger, H. Huang, R. Lopez, M. Magrane, M. J. Martin, D. A. Natale, C. O'Donovan, N. Redaschi and L. S. Yeh, *Nucleic Acids Res.* **2004**, 32, D115–9. DOI: 10.1093/nar/gkh131
129. W. Bode and R. Huber, *Biochim. Biophys. Acta* **2000**, 1477, 241–52.
130. D. Turk, *Acta Crystallogr. D Biol. Crystallogr.* **2013**, 69, 1342–57. DOI: 10.1107/s0907444913008408
131. S. Jenko, I. Dolenc, G. Guncar, A. Dobersek, M. Podobnik and D. Turk, *J. Mol. Biol.* **2003**, 326, 875–85.
132. O. Vasiljeva, M. Dolinar, V. Turk and B. Turk, *Biochemistry* **2003**, 42, 13522–8. DOI: 10.1021/bi035355k
133. M. Renko, U. Pozgan, D. Majera and D. Turk, *FEBS J.* **2010**, 277, 4338–45. DOI: 10.1111/j.1742-4658.2010.07824.x
134. C. Illy, O. Quraishi, J. Wang, E. Purisima, T. Vernet and J. S. Mort, *J. Biol. Chem.* **1997**, 272, 1197–202.
135. T. Dieckmann, L. Mitschang, M. Hofmann, J. Kos, V. Turk, E. A. Auerswald, R. Jaenicke and H. Oschkinat, *J. Mol. Biol.* **1993**, 234, 1048–59. DOI: 10.1006/jmbi.1993.1658
136. R. A. Engh, T. Dieckmann, W. Bode, E. A. Auerswald, V. Turk, R. Huber and H. Oschkinat, *J. Mol. Biol.* **1993**, 234, 1060–9. DOI: 10.1006/jmbi.1993.1659
137. J. R. Martin, C. J. Craven, R. Jerala, L. Kroon-Zitko, E. Zerovnik, V. Turk and J. P. Waltho, *J. Mol. Biol.* **1995**, 246, 331–43.
138. S. Y. Park, M. S. Jeong, S. A. Park, S. C. Ha, B. K. Na and S. B. Jang, *Biochem. Biophys. Res. Commun.* **2018**, 498, 9–17. DOI: 10.1016/j.bbrc.2018.02.196
139. D. S. Goodsell and A. J. Olson, *Annu. Rev. Biophys. Biomol. Struct.* **2000**, 29, 105–53. DOI: 10.1146/annurev.biophys.29.1.105
140. N. Wakamatsu, E. Kominami, K. Takio and N. Katunuma, *J. Biol. Chem.* **1984**, 259, 13832–8.
141. R. Janowski, M. Kozak, E. Jankowska, Z. Grzonka, A. Grubb, M. Abrahamson and M. Jaskolski, *Nat. Struct. Biol.* **2001**, 8, 316–20. DOI: 10.1038/86188
142. R. A. Staniforth, S. Giannini, L. D. Higgins, M. J. Conroy, A. M. Hounslow, R. Jerala, C. J. Craven and J. P. Waltho, *EMBO J.* **2001**, 20, 4774–81. DOI: 10.1093/emboj/20.17.4774
143. A. Sanders, C. Jeremy Craven, L. D. Higgins, S. Giannini, M. J. Conroy, A. M. Hounslow, J. P. Waltho and R. A. Staniforth, *J. Mol. Biol.* **2004**, 336, 165–78.
144. M. Wahlbom, X. Wang, V. Lindstrom, E. Carlemalm, M. Jaskolski and A. Grubb, *J. Biol. Chem.* **2007**, 282, 18318–26. DOI: 10.1074/jbc.M611368200
145. A. Palsdottir, M. Abrahamson, L. Thorsteinsson, A. Arnason, I. Olafsson, A. Grubb and O. Jensson, *Lancet* **1988**, 2, 603–4.
146. J. Ghiso, O. Jensson and B. Frangione, *Proc. Natl. Acad. Sci. U. S. A.* **1986**, 83, 2974–8.
147. E. Dall, J. C. Hollerweger, S. O. Dahms, H. Cui, K. Haussermann and H. Brandstetter, **2018**, 293, 13151–65. DOI: 10.1074/jbc.RA118.002154
148. S. Jenko, M. Skarabot, M. Kenig, G. Guncar, I. Musevic, D. Turk and E. Zerovnik, *Proteins* **2004**, 55, 417–25. DOI: 10.1002/prot.20041
149. E. Zerovnik, M. Pompe-Novak, M. Skarabot, M. Ravnikar, I. Musevic and V. Turk, *Biochim. Biophys. Acta* **2002**, 1594, 1–5.
150. S. Jenko Kokalj, G. Guncar, I. Stern, G. Morgan, S. Rabzelj, M. Kenig, R. A. Staniforth, J. P. Waltho, E. Zerovnik and D. Turk, *J. Mol. Biol.* **2007**, 366, 1569–79. DOI: 10.1016/j.jmb.2006.12.025
151. E. Zerovnik, V. Stoka, A. Mirtic, G. Guncar, J. Grdadolnik, R. A. Staniforth, D. Turk and V. Turk, *FEBS J.* **2011**, 278, 2263–82. DOI: 10.1111/j.1742-4658.2011.08149.x
152. R. Kolodziejczyk, K. Michalska, A. Hernandez-Santoyo, M. Wahlbom, A. Grubb and M. Jaskolski, *FEBS J.* **2010**, 277, 1726–37. DOI: 10.1111/j.1742-4658.2010.07596.x
153. P. Jurczak, P. Groves, A. Szymanska and S. Rodziewicz-Motowidlo, *FEBS Lett.* **2016**, 590, 4192–4201. DOI: 10.1002/1873-3468.12463
154. B. H. Meier, R. Riek and A. Bockmann, *Trends Biochem. Sci.* **2017**, 42, 777–787. DOI: 10.1016/j.tibs.2017.08.001
155. A. W. P. Fitzpatrick, B. Falcon, S. He, A. G. Murzin, G. Murshudov, H. J. Garringer, R. A. Crowther, B. Ghetti, M. Goedert and S. H. W. Scheres, *Nature* **2017**, 547, 185–190. DOI: 10.1038/nature23002
156. B. Turk, *Nat. Rev. Drug Discov.* **2006**, 5, 785–99. DOI: 10.1038/nrd2092
157. A. Crespel, E. Ferlazzo, S. Franceschetti, P. Genton, R. Gouider, R. Kalviainen, M. Korja, M. K. Lehtinen, E. Mervaala, M. Simonato and A. Vaarmann, *Epileptic Disord.* **2016**, 18, 28–37. DOI: 10.1684/epd.2016.0841
158. T. Joensuu, M. Kuronen, K. Alakurtti, S. Tegelberg, P. Hakala, A. Aalto, L. Huopaniemi, N. Aula, R. Michellucci, K. Eriksson and A. E. Lehesjoki, *Eur. J. Hum. Genet.* **2007**, 15, 185–93. DOI: 10.1038/sj.ejhg.5201723
159. W. Mi, M. Pawlik, M. Sastre, S. S. Jung, D. S. Radvinsky, A. M. Klein, J. Sommer, S. D. Schmidt, R. A. Nixon, P. M. Mathews and E. Levy, *Nat. Genet.* **2007**, 39, 1440–2. DOI: 10.1038/ng.2007.29
160. I. Olafsson and A. Grubb, *Amyloid* **2000**, 7, 70–9.
161. C. Klotz, T. Ziegler, E. Danilowicz-Luebert and S. Hartmann, *Adv. Exp. Med. Biol.* **2011**, 712, 208–21. DOI: 10.1007/978-1-4419-8414-2_13
162. S. L. Ranasinghe and D. P. McManus, *Trends Parasitol.* **2017**, 33, 400–413. DOI: 10.1016/j.pt.2016.12.013
163. S. Coronado, L. Barrios, J. Zakzuk, R. Regino, V. Ahumada, L. Franco, Y. Ocampo and L. Caraballo, **2017**, 39. DOI: 10.1111/pim.12425
164. L. E. Sanman and M. Bogyo, *Annu. Rev. Biochem.* **2014**, 83, 249–73. DOI: 10.1146/annurev-biochem-060713-035352
165. M. Vizovisek, R. Vidmar, M. Drag, M. Fonovic, G. S. Salvesen and B. Turk, *Trends Biochem. Sci.* **2018**, 43, 829–44. DOI: 10.1016/j.tibs.2018.07.003

Povzetek

Večina lizosomskih cisteinskih katepsinov je splošno izražena. Razlikujejo pa se v specifični celični in/ali tkivni porazdelitvi ter substratni specifičnosti. Vse to vpliva na njihovo delovanje v normalnih celičnih procesih, kot tudi v patologiji. Če njihova proteolizna aktivnost ni kontrolirana, postane potencialno nevarna. V ta namen so živi organizmi razvili regulatorne mehanizme, med katere spadajo tudi endogeni proteinski inhibitorji družine cistatinov, ki vključujejo skupino majhnih citozolnih proteinov, imenovanih stefini. Pregledni članek obravnava predvsem stefine različnih izvorov, njihove lastnosti, strukturo ter mehanizme interakcij z njihovimi tarčnimi encimi. Nadalje obravnava oligomerizacijo in tvorbo fibrilov pri stefinih in cistatinih, kar omogoča boljši vpogled v konformacijske bolezni. Obstoječe znanje na tem področju ter sedanje usmeritve naj bi prispevale k identifikaciji novih terapevtskih tarč in pristopov pri zdravljenju različnih obolenj.

Scientific paper

Surface Anchoring on *Lactococcus lactis* by Covalent Isopeptide Bond

Tina Vida Plavec^{1,2} and Aleš Berlec^{2,*}¹ Faculty of Pharmacy, University of Ljubljana, Aškerčeva 7, Ljubljana, Slovenia² Department of Biotechnology, Jožef Stefan Institute, Jamova 39, Ljubljana, Slovenia* Corresponding author: E-mail: ales.berlec@ijs.si
+ 386 1477 3754

Received: 04-24-2018

Dedicated to the memory of Prof. Dr. Igor Kregar

Abstract

Display of recombinant proteins on the bacterial surface is an emerging research area with wide range of potential biotechnological applications. Because of its GRAS (generally recognized as safe) status, lactic acid bacterium *Lactococcus lactis* represents an attractive host for surface display and promising vector for *in situ* delivery of bioactive proteins. The present study focused on finding a new alternative approach for surface display on *Lactococcus lactis*. We developed a system that enables the formation of irreversible isopeptide bonds on the surface of *Lactococcus lactis*. This was achieved through the following two protein/peptide pairs, SpyCatcher/SpyTag and SnoopCatcher/SnoopTag.^{1–3} Attachment of tagged model protein B domain to the cell surface of *Lactococcus lactis* displaying the corresponding catcher protein was demonstrated using flow cytometry. We demonstrated effective use of aforementioned protein anchors which thus represent a promising alternative to established approaches for surface display on *Lactococcus lactis*.

Keywords: Surface display; *Lactococcus lactis*; isopeptide bond

1. Introduction

Display of recombinant proteins on bacterial surface offers a variety of possible biotechnological applications. Proteins-displaying bacteria can act as bioadsorbents, biosensors, biocatalysts or oral vaccines. They can be used in antibody production and in peptide screening.^{4–6} Several lactic acid bacteria (LAB) are probiotics and are therefore considered valuable hosts in biotechnology due to their beneficial influence on health.^{7,8} Because of the “generally recognized as safe” (GRAS) status which confirms their safety, LAB are attractive not only for industrial application but also therapeutically.⁹ Display of heterologous proteins on the surface of LAB has already been exploited in therapy for the preparation of mucosal vaccines.^{10–12} Moreover, beneficial effects in inflammatory bowel disease could be achieved when displaying binding molecules directed against pro-inflammatory molecules such as TNF α .^{13–17}

Different approaches can be exploited for displaying a protein on the bacterial surface. The protein to be dis-

played is usually fused to an anchoring motif.^{14,18} Five different types of surface anchoring domains have been described for LAB: transmembrane domains, LPXTG-type domains, lysin motif (LysM) domains, surface layer proteins and lipoprotein anchors.^{19–21} The most frequently applied surface anchoring domains in prototype LAB, *Lactococcus lactis*, are the C-terminal part of endogenous AcmA, enabling non-covalent anchoring through peptidoglycan binding LysM repeats,^{22–25} and the LPXTG sequence of M6 protein of *Streptococcus pyogenes* enabling covalent anchoring.^{26,27} Despite these available options, alternative surface display approaches are being sought.

Recently, two peptide/protein pairs known as SpyTag/SpyCatcher, from *Streptococcus pyogenes*, and SnoopTag/SnoopCatcher, from *Streptococcus pneumoniae* have been developed.^{1–3} Interaction between the peptide and the protein leads to the formation of an irreversible isopeptide bond. The reaction is high-yielding and fast while the bond is highly stable. It can survive extreme pH, high ionic strength and exposure to detergents.^{1,28,29} Stable bond formation enables combinatorial assembly of multi-

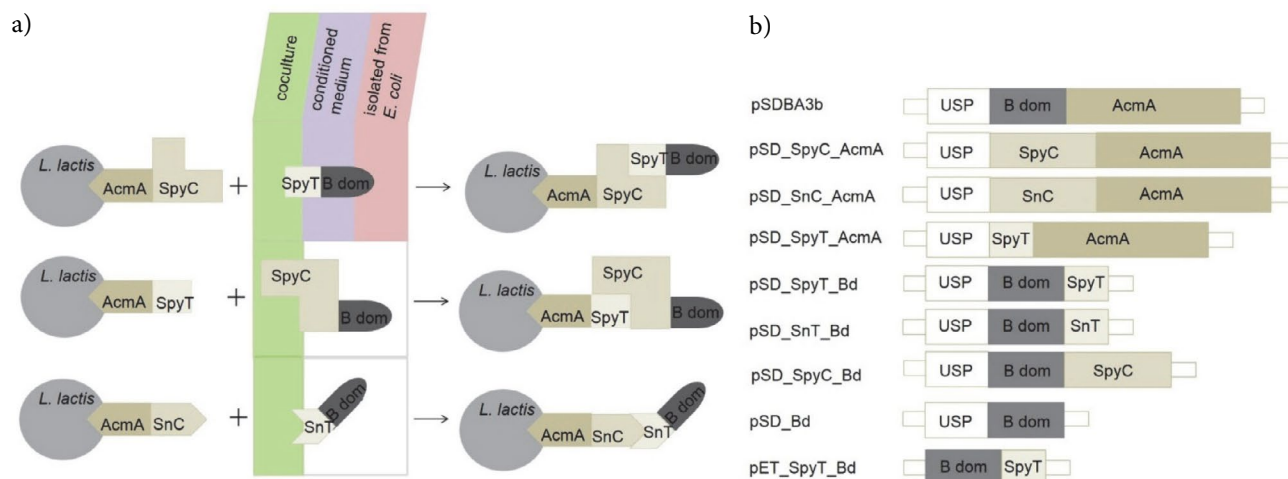


Fig. 1. The principle of surface display of B domain on *L. lactis* by the formation of isopeptide bond (A), and the gene constructs for its implementation (B). A: Surface displayed SpyCatcher (SpyC), SpyTag (SpyT), or SnoopCatcher (SnC), all anchored via AcmA on *L. lactis*, bind fusion proteins consisting of SpyT, SpyC, or SnoopTag (SnT), respectively, and B domain. The fusion proteins were produced by *L. lactis* co-culture, were extracted from *L. lactis* conditioned medium, or were isolated from *E. coli*. B: Gene constructs for lactococcal surface display and isopeptide bond formation. USP: gene for Usp45 signal peptide for secretion to the growth medium (84 bp). B dom: gene for reporter protein B domain of staphylococcal protein A (174 bp). SpyC: gene for protein SpyCatcher which binds SpyT (348 bp). SnC: gene for protein SnoopCatcher which binds SnT (336 bp). SpyT: gene for peptide SpyTag (39 bp). SnT: gene for peptide SnoopTag (36 bp). AcmA: gene for C-terminal part of AcmA protein-containing 3 LysM repeats for surface anchoring to *L. lactis* (642 bp).

protein constructs, and opens an opportunity to use this approach in vaccine production, enzyme substrate channeling, antibody polymerization, cell signaling activation, and biomaterials.^{1,30} The key properties of isopeptide binding are simple and fast procedure, irreversible and stable bond, specificity, and cysteine independence; the latter offering the possibility to use the approach in reducing environment.³

The goal of the present study was to develop a system for surface display on recombinant LAB *L. lactis* by applying the isopeptide bond formation (Fig. 1a). This was achieved by preparing genetic constructs consisting of surface anchor, elements of SpyTag/SpyCatcher or SnoopTag/SnoopCatcher pairs and model passenger protein B domain (Fig. 1b).¹³ B domain is one out of five antibody-binding domains of staphylococcal protein A that can bind antibodies via their Fc region.¹³ The fusion proteins were expressed either in *L. lactis* or in *E. coli*, and assembled on the surface of *L. lactis*, as confirmed by surface localization of B domain.

2. Experimental

2.1. Bacterial Strains, Media and Culture Conditions

Bacterial strains used in this study are listed in Table 1. *E. coli* strains DH5 α and BL21 (DE3) were grown at 37 °C, with aeration in lysogeny broth (LB) medium supplemented with either ampicillin (100 μ g/mL) or kanamycin (50 μ g/mL). *L. lactis* NZ9000 was grown in M-17 medium (Mer-

ck) supplemented with 0.5% glucose (GM-17) and chloramphenicol (10 μ g/mL) at 30 °C without aeration.

2.2. Molecular Cloning

Plasmid DNA was isolated with NucleoSpin Plasmid (Macherey and Nagel, Düren, Germany), with an additional lysozyme treatment step for *L. lactis*. Lactococci were transformed with electroporation using a Gene Pulser II apparatus (Biorad, Hercules, USA) according to the MoBiTec GmbH (Goettingen, Germany) instructions. Nucleotide sequencing was performed by GATC (Constance, Germany).

Gene for SpyTag in fusion with B domain for expression in *E. coli* was amplified from pSDBA3b by PCR using primers B-F-NcoI-Spy and B-R-XhoI, cloned to pGEM-T Easy and then to pET28a via restriction enzymes NcoI/XhoI, yielding pET_SpyT_Bd. Gene for SpyTag in fusion with B domain for secretion from *L. lactis* was amplified from pSDBA3b by PCR using primers B-F-BamHI and B-R-Kpn-Sy-Xba. Gene for SnoopTag in fusion with B domain was prepared likewise using primers B-F-BamHI and B-R-Kpn-So-Xba. Both were first cloned to plasmid pGEM-T Easy and then to plasmid pSDBA3b via restriction enzymes BamHI/XbaI, yielding pSD_SpyT_Bd and pSD_SnT_Bd. Gene for B domain for secretion from *L. lactis* was amplified from pSDBA3b by PCR using primers B-F-BamHI and B-R-Xba, first cloned to plasmid pGEM-T Easy and then to plasmid pSDBA3b via restriction enzymes BamHI/XbaI, yielding pSD_Bd (Table 2–4).

Genes for SpyCatcher and SnoopCatcher were designed and synthesized *de novo* as gBlocks (Table 4) by

Table 1. Strains used in this study

Strain	Relevant features or sequence	Reference
<i>E. coli</i> DH5α	endA1 glnV44 thi-1 recA1 relA1 gyrA96 deoR F ⁻ Φ80dlacZΔM15 Δ(lacZYA-argF)U169, hsdR17(r _K ⁻ m _K ⁺), λ ⁻	Invitrogen
<i>L. lactis</i> NZ9000	MG1363 nisRK ΔpepN	NIZO

Table 2. Plasmids used in this study

Plasmid	Relevant features or sequence	Reference
pET28a	Kan ^r , <i>E. coli</i> expression vector	Novagen
pGEM-T Easy	Ap ^r , cloning vector for PCR products	Promega
pSDBA3b	pNZ8148 containing gene fusion of <i>sp</i> _{Usp45} , <i>b-dom</i> and <i>acmA3b</i>	31
pNZ8148	pSH71 derivative, P _{nisA} , Cm ^r , nisin-controlled expression	32–34
pET_SpyT_Bd	pET28a containing gene fusion of <i>spyt</i> and <i>b-dom</i>	This work
pSD_SpyC_AcmA	pNZ8148 containing gene fusion of <i>sp</i> _{Usp45} , <i>spycatcher</i> and <i>acmA3b</i>	This work
pSD_SnC_AcmA	pNZ8148 containing gene fusion of <i>sp</i> _{Usp45} , <i>snoopcatcher</i> and <i>acmA3b</i>	This work
pSD_Bd	pNZ8148 containing gene fusion of <i>sp</i> _{Usp45} and <i>b-dom</i>	This work
pSD_SpyT_Bd	pNZ8148 containing gene fusion of <i>sp</i> _{Usp45} , <i>spyt</i> and <i>b-dom</i>	This work
pSD_SnT_Bd	pNZ8148 containing gene fusion of <i>sp</i> _{Usp45} , <i>snooptag</i> and <i>b-dom</i>	This work
pSD_SpyC_Bd	pNZ8148 containing gene fusion of <i>sp</i> _{Usp45} , <i>spycatcher</i> and <i>b-dom</i>	This work
pSD_SpyT_AcmA	pNZ8148 containing gene fusion of <i>sp</i> _{Usp45} , <i>spyt</i> and <i>acmA3b</i>	This work

Table 3. Primers used in this study

Primer	Relevant features or sequence	Reference
B-F-NcoI-Spy	5'-CCATGGCTCATATTGTAATGGTCGATGCATATAAACCAACCAAAGCTGATAA CAAATTC AACAAAGAAC-3'	This work
B-R-XhoI	5'-CTCGAGTTTTGGTGCTTGTGCATC-3'	This work
B-F-BamHI	5'-AGGATCCGCTGATAACAAATTC AAC-3'	This work
B-R-Kpn-Sy-Xba	5'-TTCTAGATTATTTGGTTGGTTTATATGCATCGACCATTACA ATATGAGCGGTACCTTTTGGTGCTTGTGCATC-3'	This work
B-R-Kpn-So-Xba	5'-TTCTAGATTATTTGTTAACTTTAATAAATTCGATGTCACCCA ACTTGGTACCTTTTGGTGCTTGTGCATC-3'	This work
B-R-Xba	5'-TTCTAGATTATTTGGTGCTTGTGCATC-3'	This work
SpyC-F-Kpn	5'-AGGTACCGGAGCTATGGTTGATACATTG-3'	This work
SpyC-R-Xba	5'-TTCTAGATTAAATATGAGCATCACCTTTTGTG-3'	This work
AcmA-F-Bam-SpyT	5'-AGGATCCGCTCATATTGTAATGGTCGATGCATATAAACCAACCAA TCTGGTGGCTCGACAACC-3'	This work
AcmA-R-Xba	5'-TTCTAGATTATTTATTTCGTAGATACTGACC-3'	This work
Spy-F-Bam	5'-AGGATCCGAGCTATGGTTGATACATTG-3'	This work
Spy-R-Eco	5'-AGAATTCAATATGAGCATCACCTTTTGTG-3'	This work
Sno-F-Bam	5'-AGGATCCAAACCTTTGCGTGGTGCAG-3'	This work
Sno-R-Eco	5'-AGAATTCCTTTGGTGGGATTGGTTTCGTTTC-3'	This work

IDT (Leuven, Belgium). Gene for secretion of SpyCatcher-B domain fusion from *L. lactis* was amplified from gBlock by PCR using primers SpyC-F-Kpn and SpyC-R-Xba, cloned to pGEM-T Easy and then to pSD_SpyT_Bd via restriction enzymes KpnI/XbaI, yielding pSD_SpyC_Bd (Table 1–4).

Genes for the surface display of SpyCatcher and SnoopCatcher were amplified from gBlocks using primer

pairs Spy-F-Bam/Spy-R-Eco and Sno-F-Bam/Sno-R-Eco, respectively, and were cloned first to pGEM-T Easy and then to plasmid pSDBA3b via restriction enzymes EcoRI/BamHI, yielding pSD_SpyC_AcmA and pSD_SnC_AcmA, respectively. Gene for the display of SpyTag on the *L. lactis* surface was amplified from pSDBA3b by PCR using primers AcmA-F-Bam-SpyT and AcmA-R-Xba, cloned to pGEM-T Easy and then to pSD_SpyC_AcmA via re-

Table 4. Genes used in this study

Gene	Relevant features or sequence	Reference
<i>spycatcher</i>	GGATCCGGAGCTATGGTTGATACATTGTCAGGTTTATCATCAGAACAA GGACAAAGTGGAGATATGACTATGAAAGAAGATTCTGCTACACATATAAA TTTTCAAACCGTGATGAAGATGGAAAAGAATTAGCAGGTGCTACTATGGA ATTGCGTGATTCATCAGGTAACAATTTCAACTTGGATTTTCAGATGGACAA GTAAAGACTTTTATCTGTACCCTGGAAAATATACTTTCGTTGAAACAGCAGCA CCTGACGGATACGAAGTTGCTACTGCTATCACTTTTACAGTTAACGAACAAGG TCAAGTTACAGTTAATGGTAAAGCAACAAAAGGTGATGCTCATATTGAATTC	This work
<i>snoopcatcher</i>	GGATCCAAACCTTTGCGTGGTGCAGTCTTCTCATTACAAAAACAACATCC AGACTACCCTGATATTTATGGTGCCATTGATCAAAAATGGTACTTATCAGAA TGTTCGAACTGGTGAAGACGGAAAATTGACTTTTAAAGAATTGAGTGACGG TAAATATCGTTTATTCGAAAACAGTGAACCAGCTGGATATAAGCCAGTA CAAAATAAACCTATGTGCGCATTTCAAATTGTAAACGGTGAAGTTAGAGACG TTACTTCTATTGTACCTCAGGATATTCCTGCTACTTATGAATTTACTAA TGGAAAACATTATATTACGAA CGAACCAATCCCACCAAAGGAATTC	This work
<i>spytg</i>	GCTCATATTGTAATGGTCGATGCATATAAACCAACCAA	This work
<i>snooptag</i>	AAGTTGGGTGACATCGAATTTATTAAGTTAACAAA	This work

striction enzymes BamHI/XbaI, yielding pSD_SpyT_AcmA (Table 2–4).

2. 3. Expression of SpyTag-B Domain Fusion in *E. coli*

100 μ L of overnight culture of *E. coli* BL21 (DE3) harboring plasmid pET_SpyT_Bd was diluted (1:100) in 10 mL of fresh LB medium and, to determine optimal expression conditions, various parameters were tested: incubation temperature 37 °C or 25 °C, induction at optical densities (A_{600}) 0.5 or 1.0, induction with IPTG in concentration of 0.5 and 1.0 mM.

Large-scale expression of SpyTag-B domain fusion was performed by diluting 10 mL of overnight culture of *E. coli* BL21 (DE3) harboring plasmid pET_SpyT_Bd in 1 L of fresh LB medium. The culture was grown to optical density $A_{600} = 0.5$ at 37 °C. At that point, the expression of SpyTag-B domain fusion, additionally tagged with hexa-histidine (H6), was induced by the addition of 0.5 mM IPTG for 3 h at 37 °C; the conditions that were found to be the most effective in preliminary screen.

2. 4. Purification of SpyTag-B Domain With Hexa-histidine (H6) Tag

The *E. coli* culture expressing SpyTag-B domain with hexa-histidine (H6) tag was centrifuged at $5000 \times g$ for 20 min and the pellet resuspended in 20 mL of equilibration/wash (Eq/W) buffer (50 mM NaH_2PO_4 , 300 mM NaCl, pH 7.0). The cells were lysed with a cycle of freezing and thawing, and with 3 cycles of 5 min sonication with a UPS200S sonifier (Hielscher, Teltow, Germany). After cell lysis, the suspension was centrifuged at $15000 \times g$ for 20 min and the supernatant stored. SpyTag-B domain with H6 tag was iso-

lated with BD Talon metal affinity resin (BD Biosciences), using batch/gravity-flow column purification and imidazole elution (elution buffer: 50 mM NaH_2PO_4 , 300 mM NaCl, 150 mM imidazole, pH 7.0) according to the manufacturer's instructions. Eluted fractions were analyzed by SDS-PAGE, pooled and concentrated by ultrafiltration using Amicon Ultra 1 kDa cut off (Merck Millipore; Darmstadt, Germany). Purified fusion protein was dialyzed against PBS.

2. 5. Expression of Fusion Proteins in *L. lactis*

Overnight cultures of *L. lactis* NZ9000 harboring pSD_SpyC_AcmA, pSD_SnC_AcmA, pSD_SpyT_AcmA, pSD_SpyT_Bd, pSD_SnT_Bd, pSD_SpyC_Bd, or pSD_Bd were diluted (1:100) in 10 mL of fresh GM-17 medium and grown to optical density $A_{600} = 0.8$ –1.0. Fusion protein expression was induced with 25 ng/mL nisin (Fluka AG, Buchs, Switzerland) for 3 h at 30 °C. After incubation, 1 mL of culture was stored at 4 °C for flow cytometric analysis. The remaining cell culture was centrifuged at $5000 \times g$ for 10 min.

2. 6. Formation of Isopeptide Bond Between SpyTag and SpyCatcher / SnoopTag and SnoopCatcher

In order to enable binding of *E. coli*-expressed SpyTag-B domain to *L. lactis* with surface displayed SpyCatcher, we centrifuged 20 μ L of the cell culture of *L. lactis* with surface displayed SpyCatcher for 5 min at $5000 \times g$ at 4 °C, resuspended the pellet in 500 μ L of purified *E. coli*-expressed SpyTag-B domain with concentration of 0.4 mg/mL and incubated for 2 h at RT with constant shaking.

To enable binding of SpyTag-B domain from *L. lactis* conditioned medium to *L. lactis* with surface displayed

SpyCatcher, we separately cultured the SpyTag-B domain-secreting *L. lactis* and SpyCatcher-displaying *L. lactis*. The producer cells of SpyTag-B domain were removed and the conditioned medium containing SpyTag-B domain fusion protein was stored. 20 μL of *L. lactis* cell culture with surface displayed SpyCatcher was centrifuged for 5 min at $5000 \times g$ at 4°C , resuspended in 500 μL of conditioned medium containing SpyTag-B domain and incubated overnight at RT with constant shaking.

Binding of SpyTag-B domain secreted from *L. lactis* to SpyCatcher displayed on *L. lactis* was also achieved during co-culturing of the two strains. 100 μL of overnight cultures of *L. lactis* NZ9000 harboring pSD_SpyT_Bd and pSD_SpyC_AcmA were concomitantly added to 10 mL of fresh GM-17 medium. Simultaneous expression of the two fusion proteins was induced with nisin. Similarly, binding of SpyCatcher-B domain secreted from *L. lactis* to SpyTag displayed on *L. lactis* was achieved by co-culturing *L. lactis* NZ9000 harboring pSD_SpyC_Bd and pSD_SpyT_AcmA, as well as binding of SnoopTag-B domain secreted from *L. lactis* to SnoopCatcher displayed on *L. lactis* by co-culturing *L. lactis* NZ9000 harboring pSD_SnC_AcmA and pSD_SnT_Bd.

2. 7. SDS-PAGE and Western Blot

SDS PAGE was performed with a Mini-Protean II apparatus (Bio-Rad, Hercules, USA). Samples were thawed in an ice bath, briefly sonicated with UPS200S sonicator (Hielscher, Teltow, Germany), mixed with $2\times$ Laemmli Sample buffer and DTT, and denatured by heating at 100°C before loading. Page Ruler Plus (Fermentas, St. Leon-Rot, Germany) pre-stained standard was used for molecular weight comparison. Proteins were stained with Coomassie Brilliant Blue or transferred to polyvinylidene fluoride (PVDF) membranes (Immobilon-P, Millipore) using wet transfer at 100 V for 90 minutes. Membranes were blocked in 5% non-fat dried milk in TBS with 0.05% Tween-20

(TBST; 50 mM Tris-HCl, 150 mM NaCl, 0.05% Tween 20, pH 7.5) and incubated overnight at 4°C with goat anti-protein A antibody (1:2000, Abcam) in 5% non-fat dried milk in TBST. Following three washes with TBST, membranes were incubated for 2 h with HRP conjugated secondary donkey anti-goat IgG (1:5000, Jackson ImmunoResearch) in 5% non-fat dried milk in TBST. After three further washes with TBST, membranes were incubated with Lumi-Light chemiluminescent reagent (Roche). Images were acquired using ChemiDoc MP Imaging System (BioRad).

2. 8. Flow Cytometry

For flow cytometry 20 μL of cell culture in stationary phase was added to 500 μL of Tris-buffered saline (TBS; 50 mM Tris-HCl, 150 mM NaCl, pH 7.5) and centrifuged for 5 min at $5000 \times g$ at 4°C . The pellet was resuspended in 500 μL of TBS with 1 μL of fluorescein-5-isothiocyanate (FITC)-conjugated human IgG antibody (Jackson ImmunoResearch, West Grove, USA) that binds the B domain via Fc region. After 2 h of incubation at RT with constant shaking at 100 rpm, cells were washed three times with 200 μL 0.1% TBST and finally resuspended in 500 μL TBS. Samples were analyzed with a flow cytometer (FACS Calibur; Becton Dickinson, Franklin Lakes, USA) using excitation at 488 nm and emission at 530 nm in the FL1 channel. The geometric mean fluorescence intensity (MFI) of at least 20 000 bacterial cells in the appropriate gate was measured. The average of at least three independent experiments was considered. All the samples went through the same procedures of preparation for flow cytometry analysis.

2. 9. Statistical Analyses

Statistical analyses were performed with GraphPad Prism 5.0 software. Student's t test was used to compare the significance of differences between B domain-displaying bacteria and control.

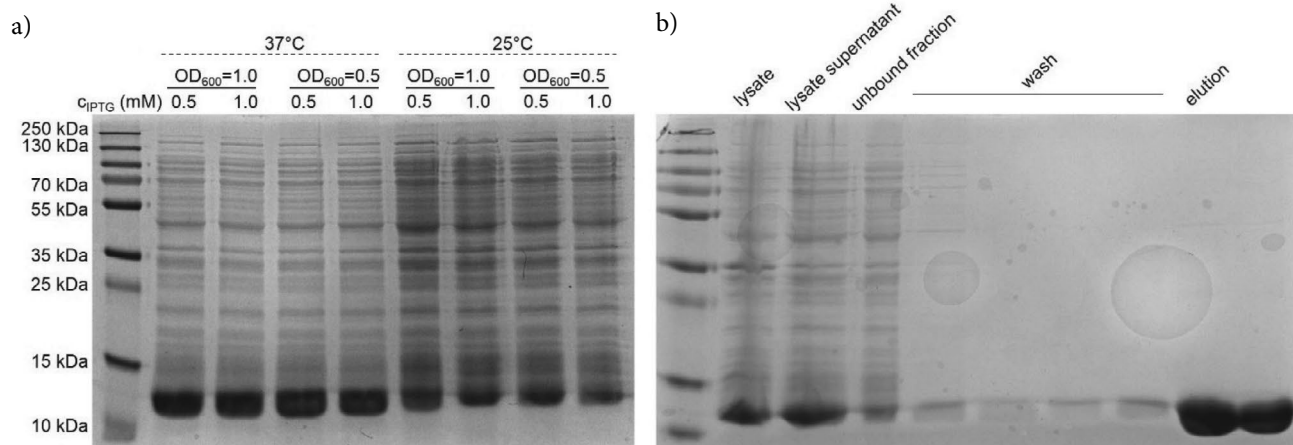


Fig. 2. Coomassie-stained SDS-PAGE of *E. coli* expressing SpyTag-B domain under different culturing conditions (A) and fractions obtained after IMAC purification of SpyTag-B domain from cell lysate (B).

3. Results

3. 1. Expression and Purification of Recombinant SpyTag-B Domain from *E. coli*

Gene for SpyTag-B domain, possessing affinity for the Fc region of human IgG, was cloned into the pET28a plasmid (Fig. 1b) in order to express the protein in *E. coli* and obtain it in sufficient amount and purity. Recombinant SpyT-B domain fusion protein with H6 tag was produced in *E. coli* BL21 DE3. Various expression conditions (growth at 37 °C and 25 °C, induction at optical densities (A_{600}) 0.5 and 1, induction with IPTG concentration of 0.5 and 1.0 mM) were tested. The highest total amount of SpyT-B domain expression was achieved by growing the bacteria at 37 °C to $A_{600} = 0.5$ or 1.0, followed by induction with 0.5 or 1 mM IPTG for 3 h at 37 °C (Fig. 2a). The majority of the fusion protein was produced in the soluble form as it could be detected in the soluble fraction (supernatant) of the cell lysate (Fig. 2b). SpyTag-B domain was isolated with immobilized metal affinity chromatography (IMAC) (Fig. 2b).

3. 2. Binding of *E. coli*-expressed SpyTag-B Domain to *L. Lactis* with Surface Displayed SpyCatcher

SpyCatcher in fusion with Usp45 secretion signal²⁶ and the surface anchoring C-terminal domain of AcmA was displayed on the surface of *L. lactis* as previously reported for other proteins.^{13,35–37} Binding of SpyTag-B domain, isolated from *E. coli*, to recombinant *L. lactis* with surface displayed SpyCatcher was evaluated by flow cytometry using antibody recognizing B domain. Statistical-

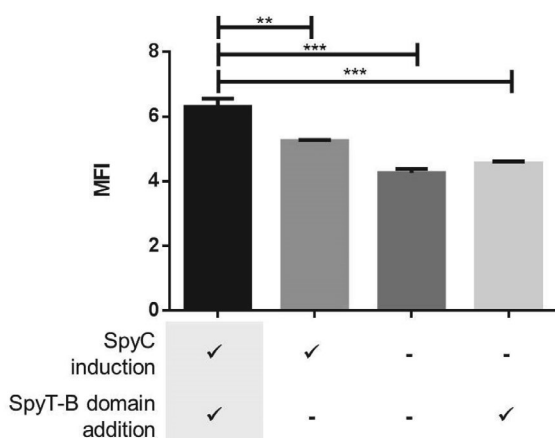


Fig. 3. Flow cytometric analysis of binding of SpyTag (SpyT)-B domain, isolated from *E. coli*, to *L. lactis* cells displaying SpyCatcher (SpyC) on their surface. FITC-conjugated human IgG was used for detection. Mean fluorescence intensity (MFI) value of SpyC-displaying bacteria with added SpyT-B domain was compared to those of the controls by using Student's t test. ** $p < 0.01$, *** $p < 0.001$.

ly significant increase in MFI was observed when SpyT-B domain was incubated with *L. lactis* with induced SpyCatcher expression, in comparison to control non-induced *L. lactis* cells, or induced *L. lactis* cells without the addition of SpyT-B domain (19.9%; Fig. 3).

3. 3. Binding of SpyTag-B Domain from *L. lactis* Conditioned Medium to *L. lactis* with Surface Displayed SpyCatcher

SpyTag in fusion with B domain and Usp45 secretion signal (plasmid pSD_SpyT_Bd) was expressed in *L. lactis* under the control of NisA promoter³⁸ and secreted to the growth medium. The producer cells were removed and the conditioned medium containing SpyTag-B domain fusion protein was incubated with *L. lactis* cells with surface displayed SpyCatcher (plasmid pSD_SpyC_AcMA). Low extent of binding was observed with flow cytometry using antibody recognizing B domain. Small statistically significant increase in MFI was reported when SpyTag-B domain was incubated with SpyCatcher-displaying *L. lactis*, in comparison to empty plasmid pNZ8148-containing control. No difference was observed when non-tagged B domain was incubated with SpyCatcher-displaying *L. lactis* (Fig. 4).

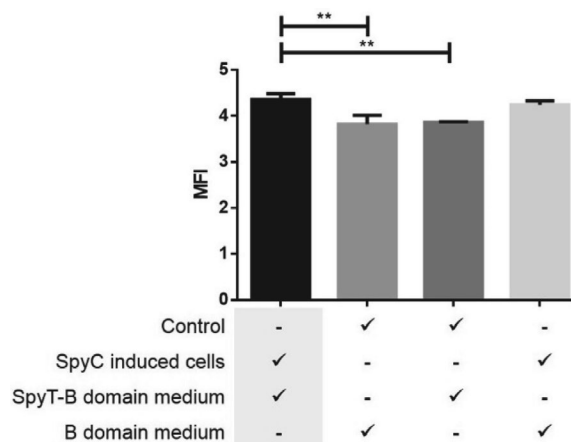


Fig. 4. Flow cytometric analysis of binding of *L. lactis*-secreted SpyTag (SpyT)-B domain to *L. lactis*-displaying SpyCatcher (SpyC). FITC-conjugated human IgG was used for detection. Mean fluorescence intensity (MFI) values of SpyC-displaying bacteria with added SpyT-B domain-containing medium were compared to those of the controls by using Student's t test. * $p < 0.05$, ** $p < 0.01$.

3. 4. Binding of SpyTag-B Domain Secreted from *L. lactis* to SpyCatcher Displayed on *L. lactis* During the Co-culturing of the Two Strains

We co-cultured *L. lactis* secreting SpyTag-B domain fusion (plasmid pSD_SpyT_Bd) with *L. lactis* displaying SpyCatcher (plasmid pSD_SpyC_AcMA) to achieve immediate bond formation between SpyCatcher and SpyTag protein/peptide pair. Binding was evaluated with flow cy-

tometry using antibody recognizing B domain. Statistically significant increase in MFI (40.1%) was observed, when Spy-tagged B domain producing *L. lactis* was co-cultured with SpyCatcher-displaying *L. lactis* cells, in comparison to SpyCatcher-displaying *L. lactis* cells (Fig. 5).

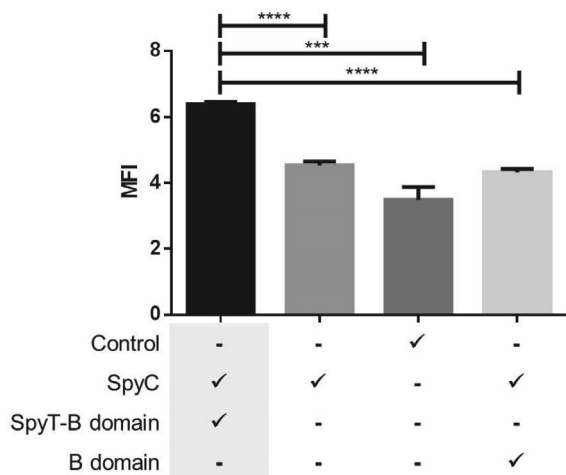


Fig. 5. Flow cytometric analysis of binding of *L. lactis*-secreted SpyTag (SpyT)-B domain to *L. lactis* cells displaying SpyCatcher (SpyC) on their surface after co-culturing of the two strains. FITC-conjugated human IgG was used for detection. Mean fluorescence intensity (MFI) values were compared to those of controls using Student's t test. **** $p < 0.0001$, *** $p < 0.001$.

3. 5. Replacing Tag and Catcher: Binding of SpyCatcher-B Domain Secreted from *L. lactis* to SpyTag Displayed on *L. lactis* During Co-culturing of the Two Strains

The location of interacting protein/peptide pair was reversed by engineering a strain of *L. lactis* to secrete the

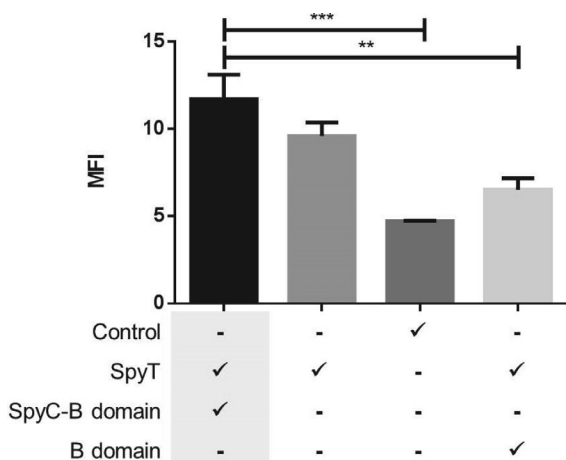


Fig. 6. Flow cytometric analyses of binding of *L. lactis*-secreted SpyCatcher (SpyC)-B domain to *L. lactis* cells displaying SpyTag (SpyT) on their surface. FITC-conjugated human IgG was used for detection. MFI: Mean fluorescence intensity. MFI values were compared to those of controls using Student's t test. ** $p < 0.01$, *** $p < 0.001$.

SpyCatcher fusion protein, and another strain to display the SpyTag. SpyCatcher-B domain fusion-secreting *L. lactis* (plasmid pSD_SpyC_Bd) was co-cultured with SpyTag-displaying *L. lactis* (plasmid pSD_SpyT_AcmA). Statistically significant increase in MFI (22.0%) was observed, when SpyCatcher-B domain producing *L. lactis* was co-cultured with SpyTag-displaying *L. lactis* cells, in comparison to SpyCatcher-displaying *L. lactis* cells (Fig. 6).

3. 6. Introducing SnoopCatcher and Tag: Binding of SnoopTag-B Domain Secreted from *L. lactis* to SnoopCatcher Displayed on *L. lactis* During Co-culturing of the Two Strains

We co-cultured *L. lactis* secreting SnoopTag-B domain fusion (plasmid pSD_SnT_Bd) with *L. lactis* displaying SnoopCatcher (plasmid pSD_SnC_AcmA), respectively, to achieve immediate bond formation, as demonstrated previously for SpyCatcher/SpyTag pair. Binding was evaluated with flow cytometry using antibody recognizing B domain. Statistically significant increase in MFI (21.1%) was observed, when Snoop-tagged B domain-producing *L. lactis* was co-cultured with SnoopTag-displaying *L. lactis* cells, in comparison to SnoopCatcher-displaying *L. lactis* cells (Fig. 7).

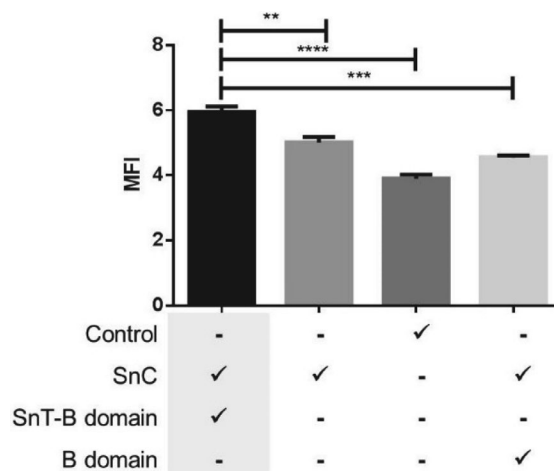


Fig. 7. Flow cytometric analysis of binding of *L. lactis*-secreted SnoopTag (SnoopT)-B domain to *L. lactis* cells displaying SnoopCatcher (SnoopC) on their surface after co-culturing of the two strains. FITC-conjugated human IgG was used for detection. Mean fluorescence intensity (MFI) values were compared to those of controls using Student's t test. ** $p < 0.01$, *** $p < 0.001$, **** $p < 0.0001$.

4. Discussion

Isopeptide bond formation was applied to develop alternative surface display systems for LAB *L. lactis* by enabling a stable covalent bond between a peptide SpyTag

and a protein SpyCatcher or, similarly, between a peptide SnoopTag and a protein SnoopCatcher.^{1,2} The peptide/protein pair has already been employed to stabilize enzymes, for modular vaccine production, vaccine optimization and formation of catalytic biofilms.^{29,39}

To test the feasibility of the isopeptide bond formation, we anchored one of the binding partners to the surface of *L. lactis*, by fusing it with Usp45 secretion signal and peptidoglycan-binding C-terminus of AcmA protein, as previously reported.^{13,35} The second binding partner was fused to a reporter protein B domain that we previously applied for the assessment of surface display.^{13,40} B domain fusion was isolated from *E. coli* or secreted from another recombinant *L. lactis* species (Fig. 1). Formation of the isopeptide bond resulted in the attachment of the B domain to the surface of *L. lactis* and was assessed by flow cytometry. We obtained statistically significant display of B domain on the surface of *L. lactis* with almost all the systems that were constructed.

Firstly, we expressed a fusion peptide SpyTag-B domain-His Tag in *E. coli* to obtain sufficient amount of the fusion protein following IMAC purification. Purified SpyTag-B domain-His Tag was added to SpyCatcher-displaying recombinant *L. lactis*. Statistically significant display of B domain, in comparison to the control, was determined. However, the binding was relatively weak and partially unspecific.

Secondly, we expressed SpyTag-B domain in *L. lactis* and directed it to the growth medium. After removal of the producer cells, the conditioned medium was incubated with SpyCatcher-displaying recombinant *L. lactis*. The display of B domain was lower than that achieved with SpyTag-B domain from *E. coli* and was not statistically significant. This could be due to the lower amount of the fusion protein in the conditioned medium. Moreover, there are several other factors in the medium that could hinder binding, for example pH value of the medium, and the presence of numerous other proteins and peptides. Even though SpyCatcher-SpyTag bond is claimed to be stable under a range of pH values (5–8)²⁹ it is possible that low pH of the conditioned medium hinders the bond formation. Additionally, numerous peptides in the conditioned medium might non-specifically interact with SpyCatcher.

Thirdly, we expected the formation of the isopeptide bond to be more probable if the Spy-tagged B domain was available immediately after induction of the surface display of SpyCatcher, as this would decrease the probability of unspecific interactions. Availability of Spy-tagged B domain was provided by co-culturing two species of *L. lactis*: one displaying SpyCatcher, and the other secreting SpyTag-B domain fusion. Thus achieved surface display of B domain was indeed higher than that achieved by the addition of SpyTag-B domain from *E. coli* or from the conditioned medium of *L. lactis*.

In the above examples the SpyCatcher was immobilized on the surface of *L. lactis*. To test the influence of the

location of binding partners, we reversed the system by displaying SpyTag on *L. lactis*, and co-cultured the strain with *L. lactis* secreting SpyCatcher-B domain fusion protein. The display of B domain was again achieved; however due to relatively high unspecific binding of antibodies with SpyTag-displaying lactococci the display was not statistically significant.

Apart from SpyCatcher/SpyTag pair, the isopeptide bond can also be formed by combining SnoopCatcher and SnoopTag. We applied similar experimental setup as previously described for SpyCatcher/SpyTag by displaying SnoopCatcher on the surface of *L. lactis* and co-culturing the bacteria with a strain of recombinant *L. lactis* secreting SnoopTag-B domain fusion protein. Significant surface display of B domain was again observed; however there was no improvement over SpyCatcher/SpyTag pair.

5. Conclusion

In the present study we demonstrated, for the first time, the surface display of reporter protein on *L. lactis* by exploiting isopeptide bond-forming partners SpyCatcher and SpyTag, as well as SnoopCatcher and SnoopTag. The most effective display was obtained by anchoring SpyCatcher to the bacterial surface, and co-culturing the bacteria with a lactococcal strain that secreted Spy-tagged reporter protein. This represents a proof-of-principle for a new, highly flexible surface display system for *L. lactis* that warrants further studies with an intention to improve the extent of surface display.

6. Acknowledgments

This study was funded by the Slovenian Research Agency (grant number P4-0127).

7. References

1. G. Veggiani, T. Nakamura, M. D. Brenner, R. V. Gayet, J. Yan, C. V. Robinson, M. Howarth, *Proc Natl Acad Sci U S A* **2016**, *113*, 1202–7. DOI:10.1073/pnas.1519214113
2. G. Veggiani, B. Zakeri, M. Howarth, *Trends Biotechnol* **2014**, *32*, 506–12. DOI:10.1016/j.tibtech.2014.08.001
3. B. Zakeri, J. O. Fierer, E. Celik, E. C. Chittock, U. Schwarz-Linek, V. T. Moy, M. Howarth, *Proc Natl Acad Sci U S A* **2012**, *109*, E690–7. DOI:10.1073/pnas.1115485109
4. S. Y. Lee, J. H. Choi, Z. Xu, *Trends Biotechnol* **2003**, *21*, 45–52.
5. S. Stahl, M. Uhlen, *Trends Biotechnol* **1997**, *15*, 185–92. DOI:10.1016/S0167-7799(97)01034-2
6. G. Georgiou, C. Stathopoulos, P. S. Daugherty, A. R. Nayak, B. L. Iverson, R. Curtiss, 3rd, *Nat Biotechnol* **1997**, *15*, 29–34. DOI:10.1038/nbt0197-29
7. V. Laroute, H. Tormo, C. Couderc, M. Mercier-Bonin, P. Le

- Bourgeois, M. Coccain-Bousquet, M. L. Daveran-Mingot, *Microorganisms* **2017**, *5*. DOI:10.3390/microorganisms5020027
8. A. A. Song, L. L. A. In, S. H. E. Lim, R. A. Rahim, *Microb Cell Fact* **2017**, *16*, 55. DOI:10.1186/s12934-017-0669-x
9. M. de Vrese, J. Schrezenmeir, *Adv Biochem Eng Biotechnol* **2008**, *111*, 1–66. DOI:10.1007/10_2008_097
10. A. Berlec, T. Malovrh, P. Zadavec, A. Steyer, M. Ravnikar, J. Sabotic, M. Poljsak-Prijatelj, B. Strukelj, *Appl Microbiol Biotechnol* **2013**, *97*, 4333–42. DOI:10.1007/s00253-013-4722-3
11. A. Berlec, M. Ravnikar, B. Strukelj, *Pharmazie* **2012**, *67*, 891–8.
12. M. de Azevedo, M. Meijerink, N. Taverne, V. B. Pereira, J. G. LeBlanc, V. Azevedo, A. Miyoshi, P. Langella, J. M. Wells, J. M. Chatel, *Vaccine* **2015**, *33*, 4807–12. DOI:10.1016/j.vaccine.2015.07.077
13. M. Ravnikar, B. Strukelj, N. Obermajer, M. Lunder, A. Berlec, *Appl Environ Microbiol* **2010**, *76*, 6928–32. DOI:10.1128/AEM.00190-10
14. C. Michon, P. Langella, V. G. Eijsink, G. Mathiesen, J. M. Chatel, *Microb Cell Fact* **2016**, *15*, 70. DOI:10.1186/s12934-016-0468-9
15. S. Kosler, B. Strukelj, A. Berlec, *Curr Pharm Biotechnol* **2017**, *18*, 318–326. DOI:10.2174/1389201018666170210152218
16. K. Vandenbroucke, H. de Haard, E. Beirnaert, T. Dreier, M. Lauwereys, L. Huyck, J. Van Huysse, P. Demetter, L. Steidler, E. Remaut, C. Cuvelier, P. Rottiers, *Mucosal Immunol* **2010**, *3*, 49–56. DOI:10.1038/mi.2009.116
17. A. Berlec, M. Perse, M. Ravnikar, M. Lunder, A. Erman, A. Cerar, B. Strukelj, *Int Immunopharmacol* **2017**, *43*, 219–226. DOI:10.1016/j.intimp.2016.12.027
18. K. Leenhouts, G. Buist, J. Kok, *Antonie Van Leeuwenhoek* **1999**, *76*, 367–76.
19. G. R. Visweswaran, K. Leenhouts, M. van Roosmalen, J. Kok, G. Buist, *Appl Microbiol Biotechnol* **2014**, *98*, 4331–45. DOI:10.1007/s00253-014-5633-7
20. P. Zadavec, A. Mavric, B. Bogovic Matijasic, B. Strukelj, A. Berlec, *Protein Eng Des Sel* **2014**, *27*, 21–7. DOI:10.1093/protein/gzt059
21. E. K. Call, T. R. Klaenhammer, *Front Microbiol* **2013**, *4*, 73. DOI:10.3389/fmicb.2013.00073
22. S. H. Lim, F. Jahanshahi, R. A. Rahim, Z. Sekawi, K. Yusoff, *Lett Appl Microbiol* **2010**, *51*, 658–64. DOI:10.1111/j.1472-765X.2010.02950.x
23. K. Okano, Q. Zhang, S. Kimura, J. Narita, T. Tanaka, H. Fukuda, A. Kondo, *Appl Environ Microbiol* **2008**, *74*, 1117–23. DOI:10.1128/AEM.02012-07
24. G. Andre, K. Leenhouts, P. Hols, Y. F. Dufrene, *J Bacteriol* **2008**, *190*, 7079–86. DOI:10.1128/JB.00519-08
25. G. Buist, H. Karsens, A. Nauta, D. van Sinderen, G. Venema, J. Kok, *Appl Environ Microbiol* **1997**, *63*, 2722–8.
26. Y. Dieye, S. Usai, F. Clier, A. Gruss, J. C. Piard, *J Bacteriol* **2001**, *183*, 4157–66. DOI:10.1128/JB.183.14.4157-4166.2001
27. A. S. Wiczorek, V. J. Martin, *Microb Cell Fact* **2010**, *9*, 69. DOI:10.1186/1475-2859-9-69
28. L. Li, J. O. Fierer, T. A. Rapoport, M. Howarth, *J Mol Biol* **2014**, *426*, 309–17. DOI:10.1016/j.jmb.2013.10.021
29. S. C. Reddington, M. Howarth, *Curr Opin Chem Biol* **2015**, *29*, 94–9. DOI:10.1016/j.cbpa.2015.10.002
30. S. Thrane, C. M. Janitzek, S. Matondo, M. Resende, T. Gustavsson, W. A. de Jongh, S. Clemmensen, W. Roeffen, M. van de Vegte-Bolmer, G. J. van Gemert, R. Sauerwein, J. T. Schiller, M. A. Nielsen, T. G. Theander, A. Salanti, A. F. Sander, *J Nanobiotechnology* **2016**, *14*, 30. DOI:10.1186/s12951-016-0181-1
31. K. Skrlec, A. Pucer Janez, B. Rogelj, B. Strukelj, A. Berlec, *Microb Biotechnol* **2017**, *10*, 1732–1743. DOI:10.1111/1751-7915.12781
32. P. G. de Ruyter, O. P. Kuipers, W. M. de Vos, *Appl Environ Microbiol* **1996**, *62*, 3662–7.
33. O. P. Kuipers, M. M. Beerthuyzen, R. J. Siezen, W. M. De Vos, *Eur J Biochem* **1993**, *216*, 281–91.
34. I. Mierau, M. Kleerebezem, *Appl Microbiol Biotechnol* **2005**, *68*, 705–17.
35. P. Zadavec, B. Strukelj, A. Berlec, *Appl Environ Microbiol* **2015**, *81*, 2098–106. DOI:10.1128/AEM.03694-14
36. A. Steen, G. Buist, K. J. Leenhouts, M. El Khattabi, F. Grijpstra, A. L. Zomer, G. Venema, O. P. Kuipers, J. Kok, *J Biol Chem* **2003**, *278*, 23874–81. DOI:10.1074/jbc.M211055200
37. A. Steen, G. Buist, G. J. Horsburgh, G. Venema, O. P. Kuipers, S. J. Foster, J. Kok, *FEBS J* **2005**, *272*, 2854–68. DOI:10.1111/j.1742-4658.2005.04706.x
38. J. N. Ahmad, J. Li, L. Biedermannova, M. Kuchar, H. Sipova, A. Semeradtova, J. Cerny, H. Petrokova, P. Mikulecky, J. Polinek, O. Stanek, J. Vondrasek, J. Homola, J. Maly, R. Osicka, P. Sebo, P. Maly, *Proteins* **2012**, *80*, 774–89. DOI:10.1002/prot.23234
39. Z. Liu, H. Zhou, W. Wang, W. Tan, Y. X. Fu, M. Zhu, *Sci Rep* **2014**, *4*, 7266. DOI:10.1038/srep07266
40. T. Bratkovic, A. Berlec, T. Popovic, M. Lunder, S. Kreft, U. Urleb, B. Strukelj, *Biochem Biophys Res Commun* **2006**, *349*, 449–53. DOI:10.1016/j.bbrc.2006.08.078

Povzetek

Predstavitev rekombinantnih proteinov na bakterijski površini postaja pomembno raziskovalno področje s številnimi možnostmi uporabe na področju biotehnologije. Zaradi statusa GRAS (generally recognized as safe – splošno priznana kot varna) predstavlja mlečnokislinska bakterija *Lactococcus lactis* privlačen gostiteljski organizem za površinsko predstavitev in obetaven vektor za *in situ* dostavo proteinov. Opisana raziskava se je osredotočila na iskanje novega alternativnega pristopa za površinsko predstavitev na bakteriji *Lactococcus lactis*. Razvili smo sistem, ki omogoča tvorbo ireverzibilne izopeptidne vezi na površini bakterije *Lactococcus lactis*. To smo dosegli s pomočjo dveh parov protein/peptid, SpyCatcher/SpyTag in SnoopCatcher/SnoopTag.^{1–3} Pritrditev modelnega proteina domene B na površino bakterij *Lactococcus lactis*, ki so imele na površini ustrezen lovilni protein, smo potrdili s pretočno citometrijo. V raziskavi smo prikazali učinkovito uporabo omenjenih proteinskih sidrnih domen, ki tako predstavljajo potencialno alternativo obstoječim načinom površinske predstavitve na bakteriji *Lactococcus lactis*.

Scientific paper

β -Trefoil Protease Inhibitors Unique to Higher Fungi

Jerica Sabotič,^{1,*} Miha Renko² and Janko Kos^{1,3}

¹ Department of Biotechnology, Jožef Stefan Institute, Ljubljana, Slovenia

² MRC Laboratory of Molecular Biology, Cambridge, United Kingdom

³ Faculty of Pharmacy, University of Ljubljana, Ljubljana, Slovenia

* Corresponding author: E-mail: jerica.sabotic@ijs.si;

Tel: +38614773754; Fax: +38614773594

Received: 05-14-2018

Dedicated to the memory of Prof. Dr. Igor Kregar

Abstract

The cysteine protease inhibitors, clitocypin and macrocypins, from higher fungi (mycocypins), together with the serine protease inhibitors highly specific for trypsin cospin and cnispin from higher fungi (mycospins), display several characteristics that distinguish them from protease inhibitors from other sources. Their high genetic heterogeneity affects their functionality and/or stability and results in numerous protein variants with slightly different inhibitory profiles that influence the type of protease inhibited and/or the strength of inhibition. They possess the β -trefoil fold that shows high plasticity in their utilization of the 11 diverse loops for the inhibition of various families of proteases through different mechanisms of inhibition. Their high versatility is also seen in their regulatory and defence functions and in their potential applications in biotechnology, crop protection and medicine.

Keywords: Protease inhibitor; regulation; defence; clitocypin; macrocypin; cospin

1. Introduction

Proteolytic enzymes, also termed proteases or peptidases, are degradative enzymes that catalyse the hydrolysis of peptide bonds. They are ubiquitous and essential for the survival of all organisms, since they enable nutrient acquisition, growth, proliferation and reproduction. Furthermore, they are critical for defence against pathogens and parasites. Since their activity is so essential, it needs to be tightly regulated and dysregulation often leads to disease.^{1–5} Because of their important roles in physiological and pathophysiological processes they are paramount targets and tools in the search for new strategies with applications in medicine, pharmaceutical industry and agriculture.

The regulation of proteolytic enzymes is also vital, because hydrolysis of peptide bonds is irreversible. Specific protease inhibitors play a very important role in their regulation.^{6–9} For this reason, we undertook a search for further protease inhibitors that could exhibit unique inhi-

bitory specificity, provide new mechanisms of inhibition and offer multiple possibilities in medical and biotechnological applications.

We decided to utilize higher fungi or mushrooms as a new and promising source of protease inhibitors¹⁰ since very little was known at the time about the proteolytic systems in higher fungi. A first glimpse of the complexity of these systems was provided by an investigation of the proteolytic activity of mushrooms using gelatin zymography combined with selected protease inhibitors. The number and diversity of proteolytically active bands observed was unexpectedly high. These proteases were classified into different catalytic classes, a large proportion of them showing atypical properties. This indicated the great potential for finding novel protease inhibitors in the proteolytic systems of higher fungi.¹¹

An overview is provided here of the protein protease inhibitors that we have identified in higher fungi, together with their unique features established by characterization at the genetic, molecular, structural and functional levels.

2. Protease Inhibitors from Higher Fungi

Protease inhibitors are indispensable regulators of proteolytic enzymes and are present in all kingdoms of life. They can be classified according to their origin, inhibitory mechanism, structural similarity or their specificity. The last is most often used to group inhibitors according to those that inhibit a number of classes of peptidases, those that inhibit a single class of peptidases, those that inhibit one or more families of peptidases or just a single peptidase.^{6,12} The MEROPS database (<https://www.ebi.ac.uk/merops/>) provides the most extensive classification of protease inhibitors into families, based on sequence homology, and into clans, based on similarity of 3D structure. There are currently 79 families of protease inhibitors in the MEROPS database (release 12.0; April 2018). Of these, 24 include members of fungal origin and only seven include members from higher fungi, of which only four families (I9, I48, I66 and I85) include members that have been characterized at the protein level.¹³ Family I9 comprises subtilisin propeptide-like inhibitors isolated from oyster mushroom (*Pleurotus ostreatus*)^{14,15} and the other three are described in this review (Table 1).

Families I48 and I85 comprise mycocypins, the fungal cysteine protease inhibitors clitocypin¹⁶ (Clt, family I48) from the clouded agaric (*Clitocybe nebularis*), and macrocypin¹⁷ (Mcp, family I85) from parasol mushroom (*Macrolepiota procera*). Mycocypins are small proteins with molecular masses between 16.6 kDa (clitocypin) and 19.0 kDa (macrocypin 1) that have similar biochemical properties. They all exhibit isoelectric points around pH 4.8. An exceptional feature is their apparent resistance to high temperature and to extremes of pH that results from

their ability to unfold reversibly.^{16–20} Furthermore, mycocypins are resistant to proteolytic digestion by the highly non-specific proteinase K although they do not inhibit its proteolytic activity.²¹

Family I66 comprises the trypsin-specific inhibitors mycospins: cnispin²² (Cnp) from *Clitocybe nebularis* and cospin²³ (PIC) from *Coprinopsis cinerea*, as well as a representative from *Lentinula edodes*.²⁴ These inhibitors are small proteins, the molecular mass of cnispin being 16.4 kDa and that of cospin 16.7 kDa and both with a low isoelectric point around pH 5. They are both stable at extreme pH and cospin is resistant to proteolytic digestion.^{21–23}

2. 1. Genetic Heterogeneity

Mycocypins are encoded by small families of genes whose members show sequence heterogeneity. Genes encoding clitocypin in the *C. nebularis* genome are composed of four exons and three short introns. Nucleotide substitutions are evenly distributed throughout the gene sequence. The diversity of amino acid substitutions however is mainly conservative and the isogene sequences for clitocypin share more than 90% identity at the level of the deduced protein sequence.²⁵ A family of clitocypin encoding genes that show similar heterogeneity has also been detected in the *M. procera* genome.¹⁷

Genes encoding macrocypins in the *M. procera* genome are also composed of four exons and three introns. Their diversity is, however, much greater. The deduced amino acid sequences are divided into five groups with 75–86% sequence identity between groups and more than 90% sequence identity within groups. Some of the variable codons have been subject to positive evolutionary selecti-

Table 1. Overview of β -trefoil protease inhibitors from higher fungi.

Protease inhibitor	Mycocypins				Mycospins	
	Clitocypin	Macrocypin 1	Macrocypin 3	Macrocypin 4	Cnispin	Cospin
Origin	<i>Clitocybe nebularis</i>	<i>Macrolepiota procera</i>	<i>Macrolepiota procera</i>	<i>Macrolepiota procera</i>	<i>Clitocybe nebularis</i>	<i>Coprinopsis cinerea</i>
Abbreviation	Clt	Mcp1	Mcp3	Mcp4	Cnp	PIC
MEROPS family	I48	I85	I85	I85	I66	I66
Mass	16582 Da	19062 Da	18900 Da	18639 Da	16407 Da	16713 Da
Isoelectric point (pH)	4.8	4.8	4.8	5.1	5.2	4.9
PDB entry	3H6R, 3H6S	3H6Q	/	/	/	3N0K, 3VWC
Protease family inhibited	C1/C13	C1/C13	C1/C13	C1/S1	S1	S1
Inhibitory loop	β 1– β 2 and β 3– β 4/ β 5– β 6	β 1– β 2 and β 3– β 4/ β 5– β 6	β 1– β 2 and β 3– β 4/ β 5– β 6	β 1– β 2 and β 3– β 4/ β 5– β 6	β 11– β 12	β 2– β 3
Resistant to exposure to	high temperature & extreme pH	alkaline pH	extreme pH			
Resistant to proteolytic digestion by proteinase K	yes	yes	yes	yes	no	yes

on, indicating their importance for the function of the protein.¹⁷ Gene sequences encoding macrocypins are also present in the *C. nebularis* genome, the degree of sequence identity to that of macrocypin 2 from *M. procera* being the highest.²⁶

Deduced amino acid sequences of macrocypins and clitocypin show very low overall sequence identities of 17 to 21% (Table 2 & Figure 1). Furthermore, macrocypin sequences contain sulphur containing amino acids, a cysteine residue being present in most macrocypin sequences and several histidine and methionine residues are present in all macrocypins while they are absent in clitocypin sequences. On the other hand, the deduced amino acid sequences of both clitocypin and macrocypin contain high contents of proline and tyrosine but low contents of leucines.^{16,17,25}

The low sequence identity between different families of mycocypins hinders the search for their homologs in other fungal genomes. Indeed, BLASTP analysis, using clitocypin sequence, across 145 fungal genomes revealed similar protein encoding genes in only four, namely *Botryobasidium botryosum* (10 genes), *Rhizoctonia solani* (4 genes), *Laccaria amethystina* (13 genes) and *Laccaria bicolor* (10 genes), all members of the class Agaricomycetes.²⁷ These genomes include small families of clitocypin analog genes (indicated in brackets) that show low sequence identity between organisms. Given this low sequence identity, it is probable that mycocypins are much more widespread in higher fungi.

The complex regulation of expression of mycocypins at different levels is indicated by the different promoter sequences as well as by differences in 5'UTR, 3'UTR and intron sequences and in their lengths. This was confirmed by the distinct expression levels of clitocypin and macrocypin in both their origin mushrooms and in the model species *C. cinerea*.^{17,25,26}

The expression of clitocypin appeared to be uniform at the protein level in both *C. nebularis* and *M. procera* fruiting bodies. The expression pattern guided by the clitocypin promoter in the model species was very similar to that of the constitutive promoter *gpdII* of glyceraldehyde-3-phosphate dehydrogenase from *Agaricus bisporus*. Some

differences indicating regulatory complexity are seen in the different levels of clitocypin mRNA expression in different parts of fruiting bodies and by variation of expression in mycelium.^{17,25,26}

The complex expression pattern of macrocypin genes reflects and enhances the diversity of their gene sequences. They show tissue specific expression patterns at the promoter, mRNA and protein levels that differ for different macrocypin genes.²⁶

In addition to developmental regulation of mycocypins, environmental factors have influenced their expression, as indicated by the clitocypin genes in *L. bicolor* mycelium, whose expression was upregulated specifically in the presence of an antagonistic soil bacterium, *Collimonas fungivorans*.²⁸

Mycospins are encoded by very small gene families, as indicated by the sequence diversity in natural isolates of cnispin from *C. nebularis* fruiting bodies and confirmed in the *C. cinerea* genome for cospin, where four isogenes were found. Cnispin genes are composed of four exons and three short introns. The sequence identity between the deduced amino acid sequences of cnispin and cospin is 26 to 30% (Table 2 & Figure 2).^{22,23}

Despite the low sequence identity among mycocypins, several homologous sequences have been found in different species. For example, a four-gene family was identified in *L. bicolor* with 17 to 30% amino acid sequence identity to that of cospin.²³ Furthermore, BLASTP analyses across 145 fungal genomes, using cospin sequence, revealed similar protein encoding genes in 21 basidiomycete species from class Agaricomycetes and also in two ascomycetes. Either one gene or small gene families, ranging from 2 to 12 genes, were identified.²⁷ Furthermore, mycocypins were identified and characterized at the protein and functional levels in three additional basidiomycete species: *Armillaria mellea*, *Macrolepiota procera* and *Amanita phalloides*.²⁹ Mycocypins appear to be more widely present in fungi than mycocypins, although this could also be the consequence of more favourable search parameters arising from the higher sequence similarity among mycocypins.

Table 2. A sequence identity matrix of mycocypin and mycospin deduced from amino acid sequences. The percent sequence identity is given for each pair. ID. identical.

	Mcp1	Mcp2	Mcp3	Mcp4	Mcp5	Clt-Kras	Clt-Vrh	PIC	Cnp
Mcp1	ID	82.8	78.6	79.8	76.3	17.4	18.0	10.7	10.9
Mcp2		ID	80.2	85.0	79.6	19.4	19.4	10.8	12.2
Mcp3			ID	80.8	78.4	21.1	21.7	10.8	11.6
Mcp4				ID	82.0	18.2	18.8	10.8	13.9
Mcp5					ID	18.9	18.9	10.2	11.6
Clt-Kras						ID	91.4	12.6	13.9
Clt-Vrh							ID	13.2	15.1
PIC								ID	27.0
Cnp									ID

Cnispin and cospin are expressed in vegetative mycelium and in fruiting bodies and are not secreted. Much (approximately 700 fold) higher expression in fruiting bodies than in mycelium has been determined for cospin.^{22,23}

2. 2. Inhibitory Specificity

Mycocypins inhibit cysteine proteases of plant and animal origins but the strength of inhibition against different proteases differs between members of clitocypin and macrocypin families (Table 3). They are all strong inhibitors of papain-like proteases (family C1), with equilibrium constants for inhibition (K_i) ranging from picomolar to micromolar for various cysteine cathepsins and papain. Cathepsins with endopeptidase activities are strongly inhibited while cathepsins B and H, that exhibit both endopeptidase and exopeptidase activity, are not inhibited by cliticypins and only very weakly by macrocypins. They also inhibit legumain/asparaginyl peptidase with K_i in the nanomolar range, albeit involving a different inhibitory active site (Figure 1 & 3). The latter is, in some macrocypins,

changed and trypsin is inhibited instead of legumain. The sequence heterogeneity in the cliticypin gene family has no influence on the inhibitory activity while the greater sequence heterogeneity in macrocypin sequences is reflected in their inhibitory profiles (Table 3).^{17,20,22,23,30}

Mycospins are strong and highly specific inhibitors of trypsin with values of K_i in the picomolar range for cospin and in the nanomolar range for cnispin. Both are also weak inhibitors of chymotrypsin with K_i in the micromolar range. Other serine proteases are very weakly or not at all inhibited (Table 3).^{22,23}

Natural isolates of cliticypin and macrocypin display inhibitory profiles that differ slightly when (Table 4) compared with those of recombinant variants. This is the effect of the mixture of isoforms in the natural sample isolated from mushrooms growing in the wild.^{16,17,20,25} Despite their sequence heterogeneity, natural isolates of cnispin, CnSPIs, display the same inhibitory profile as cnispin and are very strong inhibitors of trypsin, while inhibition of chymotrypsin is about 40 times weaker and elastase and thrombin are not inhibited at all.²²

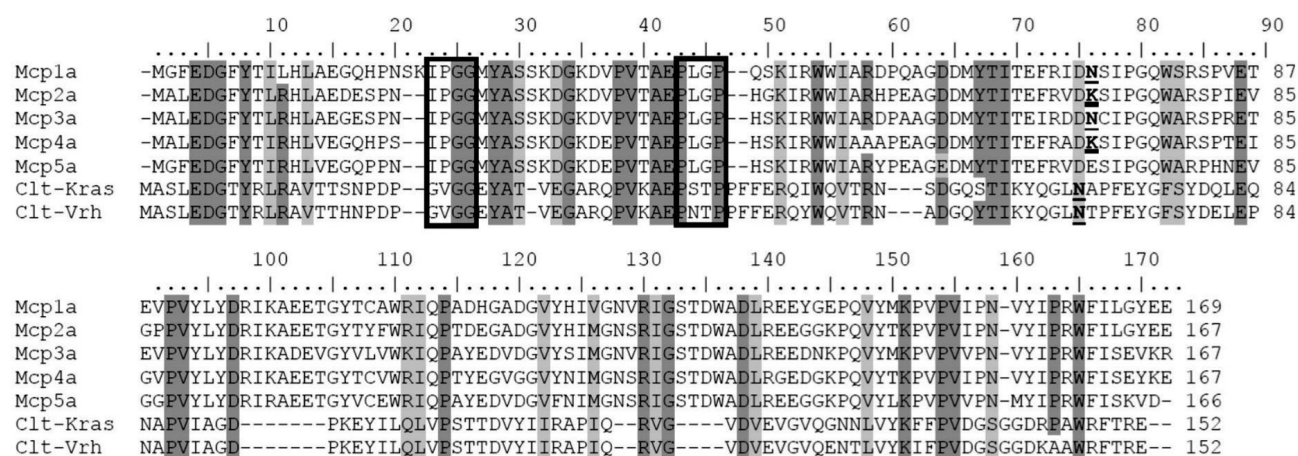


Figure 1. Alignment of mycocypin deduced amino acid sequences. Identical residues are highlighted in dark grey and similar residues in light grey. Amino acid sequences of macrocypins (Mcp) and cliticypins (Clt) were aligned with the BLOSUM62 matrix. Residues forming inhibitory loops that inhibit papain-like proteases are boxed. P1 residues, crucial for the inhibition of legumain or trypsin, are underlined and shown in bold. (Mcp – macrocypin, Clt-Kras and Clt-Vrh are native sequences of cliticypin isolated from fruiting bodies collected in the two widely separated regions, Kras and Vrh in Slovenia.)

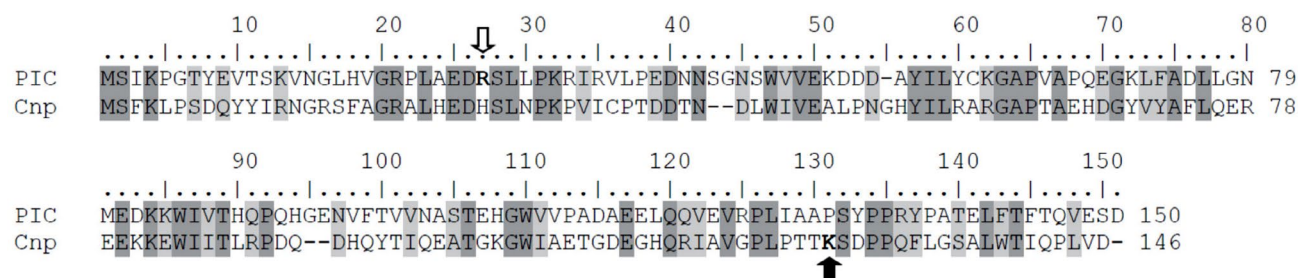


Figure 2. Alignment of deduced amino acid sequences of mycospins. Identical residues are highlighted in dark grey and similar residues in light grey. Amino acid sequences of cnispin (Cnp) and cospin (PIC) are aligned using the BLOSUM62 matrix. The arrows indicate the trypsin reactive P1 residue in cospin (white) and in cnispin (black).

Table 3. Kinetic constants for the interaction of mycocypins and mycospains with various proteases.^{17,20,22,23,30} Standard deviations are given where appropriate. rClT, recombinant clitocypin; rMcp1, recombinant macrocypin 1; rMcp3, recombinant macrocypin 3; rMcp4 recombinant macrocypin 4; Cnp, recombinant cnispin; PIC, recombinant cospin; n.i., no inhibition; ND, not determined.

Protease	Protease family	K_i (nM)					
		rClT	rMcp1	rMcp3	rMcp4	Cnp	PIC
Papain	C1	6.2 ± 0.55	0.95 ± 0.33	0.12 ± 0.05	0.19 ± 0.01	n.i.	n.i.
Cathepsin L	C1	0.02 ± 0.001	0.64 ± 0.22	0.31 ± 0.06	2.76 ± 0.92	ND	ND
Cathepsin V	C1	0.08 ± 0.03	0.69 ± 0.06	0.45 ± 0.01	1.44 ± 0.11	ND	ND
Cathepsin S	C1	2.2 ± 0.3	23.1 ± 1.2	5.1 ± 0.5	6.3 ± 0.6	ND	ND
Cathepsin K	C1	0.03 ± 0.002	170 ± 20	17.5 ± 1.2	21.8 ± 5.2	ND	ND
Cathepsin B	C1	> 1000	490 ± 18	> 1000	125 ± 10	ND	ND
Cathepsin H	C1	n.i.	100 ± 10	24 ± 5	32 ± 6	ND	ND
Legumain	C13	21.5 ± 2.81	3.38 ± 1.44	9.17 ± 1.09	> 1000	n.i.	n.i.
Caspase 3, 6, 9	C14	n.i.	ND	ND	ND	ND	ND
Trypsin	S1	n.i.	n.i.	n.i.	160 ± 14	3.10 ± 0.66	0.022 ± 0.002
Chymotrypsin	S1	ND	ND	ND	ND	120 ± 20	116 ± 8
Kallikrein	S1	ND	ND	ND	ND	> 1000	> 1000
Thrombin	S1	ND	ND	ND	ND	n.i.	n.i.
Subtilisin	S8	ND	ND	ND	ND	> 1000	> 1000
Pepsin	A1	n.i.	n.i.	n.i.	n.i.	n.i.	n.i.

Table 4. Inhibition of various proteases by natural mycocypins. The kinetic data are as reported.¹⁷ Standard deviations are given where appropriate. nMcp, natural macrocypin; nClT, natural clitocypin; n.i., no inhibition.

Enzyme	Protease family	K_i (nM)	
		nClT	nMcp
Papain	C1	2.5 ± 0.94	5.04 ± 0.98
Cathepsin L	C1	0.03 ± 0.002	3.81 ± 1.66
Cathepsin V	C1	0.14 ± 0.01	12.6 ± 3.77
Cathepsin S	C1	3.2 ± 0.3	47.1 ± 3.1
Cathepsin K	C1	0.02 ± 0.005	4.5 ± 0.5
Cathepsin B	C1	> 1000	515 ± 36
Cathepsin H	C1	n.i.	370 ± 11
Legumain	C13	7.1 ± 1.12	110 ± 23
Trypsin	S1	n.i.	n.i.
Pepsin	A1	n.i.	n.i.

2. 3. Structural Plasticity

Mycocypins and mycospains both possess a β -trefoil fold,^{23,31} thus classifying them to clan IC in the MEROPS classification, together with Kunitz serine protease inhibitors from plants (family I3).¹³

The β -trefoil fold consists of a β -barrel composed of three pairs of antiparallel β -strands. An additional three pairs of β -strands cover the β -barrel. The strands are connected by loops of different shapes and compositions (Figure 3). The large surface area of the loops, that accounts for approximately 70% of the protein's total solvent accessible area, enables these proteins to interact with many different binding partners, including proteins, carbohydrates and DNA.^{23,31,32}

For the inhibition of papain-like proteases, mycocypins utilize two loops (β 1– β 2 and β 3– β 4) that bind to

either side of the active site cleft with several hydrogen bonds, occluding the catalytic cysteine. The binding is associated with a glycine-glycine peptide-bond flip (Gly-24-Gly25 in clitocypin) that occurs before or concurrently with inhibitor docking.³¹ The mode of cysteine protease inhibition, as revealed by the cathepsin V – clitocypin complex, is unique in utilizing two loops to achieve inhibition, while other known modes of inhibition by cysteine protease inhibitors, like those of cystatins and thyropepsins, utilize three loops to achieve active site occlusion.^{31,32}

Inhibition of asparaginyl peptidase/legumain by mycocypins is achieved via a second inhibitory active site in the β 5– β 6 loop. Site-directed mutagenesis has confirmed that residues Asn72 in macrocypins and Asn69 in clitocypin mediate inhibition of asparaginyl peptidase.³¹ Furthermore, the same inhibitory active site mediates the inhibition of trypsin when Asn replaces Lys or Arg in different macrocypins but not in clitocypin.³¹ The inhibitory mechanism of the cysteine protease asparaginyl peptidase (family C13) and of the serine protease trypsin (family S1) appears to involve a similar substrate-like binding inhibition.³²

Cospin and cnispin are classic canonical inhibitors that bind to the active site in a substrate-like manner and form a tight and stable complex with trypsin. The trypsin-cospin complex is stable for weeks at 37 °C while the trypsin-cnispin complex is degraded within 24 h. This is also reflected in the stronger inhibition of trypsin by cospin as opposed to that by cnispin (Table 3). Inhibition of trypsin by mycospains is achieved through the different inhibitory reactive sites in cospin and cnispin. The reactive site residue P1 of cospin is Arg27 in the β 2– β 3 loop, while Lys127 in the β 11– β 12 loop of cnispin fulfils the same role (Figure 2 & 3).^{23,30} Inhibitory activity can be mediated by

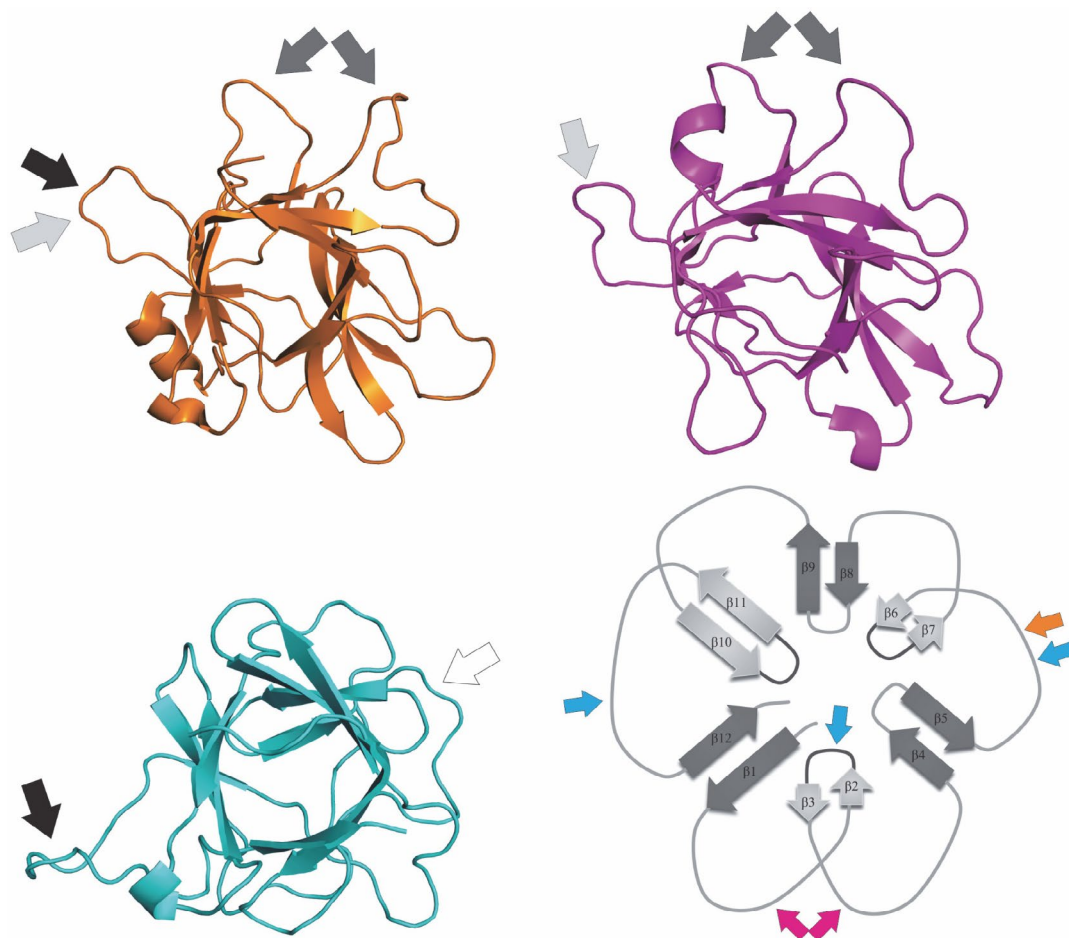


Figure 3. Structures of fungal cysteine protease inhibitors. Ribbon diagrams of the cysteine protease inhibitors macrocypin 1 (PDB code 3H6Q) in orange and clitocypin (PDB code 3H6S) in magenta are shown next to that of the serine protease inhibitor cospin (PDB code 3N0K9) in cyan. Loops with the following inhibitory reactive sites are marked with arrows: light grey arrows indicate asparaginyl protease/legumain inhibition, dark grey arrows indicate papain-like protease inhibition while white and black arrows indicate trypsin inhibition. A schematic representation of the β -trefoil fold loops involved in protease inhibition is shown bottom right. The protease family inhibited by individual loops of the β -trefoil fold in these fungal inhibitors is indicated by coloured arrows as follows: the asparaginyl protease/legumain with orange, papain-like proteases with magenta and trypsin with cyan.

both $\beta 2$ – $\beta 3$ and $\beta 11$ – $\beta 12$ loops in the two inhibitors; engineering of various P1 residues in the aforementioned loops yielded a strong or weak trypsin inhibitor, a chymotrypsin-specific inhibitor, a double headed trypsin inhibitor or a double-headed trypsin and chymotrypsin inhibitor. Other serine proteases are only weakly or not at all inhibited. Cysteine and aspartic proteases were not inhibited and asparaginyl peptidase/legumain inhibition was not achieved by introducing Asn as the P1 residue.³⁰

2. 4. Functional Variability

The proposed function of mycocypins and mycospines is to regulate both the endogenous proteolytic system and the defence against predators and pathogens. Mycocypins and mycospines are cytoplasmic proteins that are not secreted. In addition to the absence, in all the identified genes, of a signal sequence for the classical secretion and to

the low number of cysteine residues and lack of glycosylation in natural samples, no secretion of cnispin and clitocypin has been detected from cultivated mycelium.^{22,23,25}

An obvious biological role for protease inhibitors is the regulation of the endogenous proteolytic system. Activity of several cysteine proteases from fruiting bodies of different basidiomycetes is inhibited by clitocypin.¹¹ Similarly, cnispin and cospin inhibit the activity of various serine proteases from their origin species as well as from other basidiomycetes.^{11,22,23} Regulation of the complex developmental and temporal expression of both mycocypins and mycospines indicates potentially different biological roles for different inhibitors.^{22,6}

Another possible role for protease inhibitors, that is indirectly but strongly supported, is in defence against various antagonists. The strong toxicity of cnispin and cospin against *Drosophila melanogaster* larvae, their cytoplasmic localization and the higher expression in fruiting bodies

compared to that in mycelium indicates their role in the defence of the spore-bearing fruiting body against dipteran larvae that hatch and feed on fruiting bodies.^{22,23} Protection of reproductive tissues from pests and diseases has also been suggested as a defensive role of mycocypins. Thus, cysteine proteases are predominant digestive proteases in many insects and slugs and could be targeted, like trypsin-like digestive proteases in dipteran insects are by mycospains. Furthermore, cysteine proteases are important virulence factors of different pathogenic bacteria, parasites and mycoviruses. These could be targeted by different mycocypins, as indicated by their different expression profiles. Clitocypin, which is constitutively expressed in large amounts in fruiting bodies, represents one line of defence, while the specific pattern of expression localized to the outer layer of the developing fruiting body of some macrocypins constitutes another defence strategy for protection against external attacks by predators or pathogens. The inducible expression of clitocypin analogs in *L. bicolor* when challenged by an antagonistic soil bacterium supports their role in defence. A defensive role is further supported by the high thermal and pH stability and the resistance to proteolytic degradation of these proteins, as well as by their high sequence diversity and versatile inhibitory profile.^{17,22,23,25,26,28}

Another layer of regulation of the β -trefoil fungal protease inhibitors mycocypins and mycospains, is indicated by their interaction *in vitro* with β -trefoil lectins MpL and CNL from the same species, which are also expressed intracellularly and involved in fruiting body defence.^{21,27, 33–36}

2. 5. Diverse Applications

Based on their unique characteristics indicating their function in defence, as described in the previous section, mycocypins have been evaluated for their potential in protecting plants against herbivores. A major pest, Colorado potato beetle (*Leptinotarsa decemlineata*), that utilizes cysteine proteases for protein digestion, has been used as a model. Clitocypin and macrocypins were shown to exhibit adverse effects on Colorado potato beetle larvae, both when expressed as proteins in potato leaves and when recombinant proteins produced in a bacterial expression system were added to the diet. Clitocypin and macrocypins reduced the weight gain of larvae and delayed their development. The effect was linked to inhibition of the special adaptive cysteine proteases, intestains, in larval guts. Moreover, dietary mycocypins did not induce the expression of known adaptation-related genes of digestive enzymes in guts of Colorado potato beetle larvae, as was the case with all other dietary inhibitors from other sources.^{37,38}

The potential of mycocypins and mycospains in biotechnological applications has been confirmed by their use as ligands in affinity chromatography for isolating proteases from various sources. Trypsin was isolated from a complex, partially purified, trypsin sample using cnispin-affi-

nity chromatography. Active cysteine proteases of families C1 (papain-like) and C13 (legumain/asparaginyl protease) have been isolated from plant and animal sources using macrocypin affinity chromatography. Their superior characteristics in terms of stability to pH and temperature make them ideal candidates for use as affinity chromatography ligands. They withstand the harsh conditions during immobilization procedures. For example, following 24h incubation at neutral pH and 45 °C for covalent binding to a monolithic disk, the unoccupied groups are inactivated by incubation for 1 h in 0.5 M H₂SO₄ at 50 °C and macrocypins then retain their inhibitory activity through several elution cycles of extreme pH changes.³⁹

The distinct inhibitory profiles of mycocypins and the highly specific inhibitory profile of mycospains makes them valuable tools in medical research, since many cell processes depend on appropriately regulated proteolytic activity. Protease inhibitors are being studied as promising therapeutic drugs for many types of disease by targeting a variety of deregulated proteases, including those involved in cancer and autoimmune, neurodegenerative, inflammatory, and cardiovascular diseases; secreted bacterial, fungal, and parasite proteases; and viral polyprotein processing proteases.^{7,40}

3. Conclusions and Future Perspectives

Protein protease inhibitors from a number of higher fungi exhibit a variety of unique characteristics when compared to similar protease inhibitors from plant, animal or microbial sources. Distinct inhibitory specificity profiles, coupled with structural plasticity of the β -trefoil fold, afford these inhibitors their diverse functions. Further, their noteworthy stability enables wide-ranging application of mycocypins and mycospains. The uniqueness of these protease inhibitors lies in the combination of the mentioned exceptional features in one protein family promoted by lack of homologues outside of the fungal kingdom.

The protease inhibitors from higher fungi described here just scratch the surface of the immense potential of the fungal proteolytic defence system hidden in forests in Slovenia and in forests worldwide.

In addition to the cysteine protease inhibitors represented by mycocypins and the serine protease inhibitors represented by mycospains, there are most probably protease inhibitors waiting to be identified from higher fungi, possibly with the β -trefoil fold, that inhibit other catalytic classes of proteases, including aspartic and metallo-proteases. Another direction for research, involving the β -trefoil fold proteins with other functionalities such as carbohydrate binding, lies via the β -trefoil fold lectins that have been shown to be versatile and to support unique characteristics. It will be interesting to find more novel multifunctional proteins with both carbohydrate binding and

inhibitory activities. Knowledge of the different functionalities evolved naturally in the β -trefoil scaffold will facilitate the engineering of customized multifunctional proteins.

4. Acknowledgements

We dedicate this paper to prof. Igor Kregar, who was the leader of our group for many years and initiated studies on plant and fungal biochemistry and molecular biology. We are grateful to dr. Jože Brzin who initiated the research on protease inhibitors from mushrooms and guided our investigations until recently. We thank dr. Tatjana Popovič who meticulously determined their kinetics and passed on her knowledge brilliantly. We are indebted to dr. Marjetka Kidrič and prof. Roger H. Pain for numerous discussions and invaluable input. We would also like to acknowledge the many other researchers and students from the Jožef Stefan Institute, the National Institute of Biology, the ETH Zürich and University of Bristol who, over the years, have contributed pieces of the puzzle to the knowledge we now have on fungal protease inhibitors.

4. 1. Funding

This work was supported by the Research Agency of the Republic of Slovenia Grant P4-0127 (to J.K.).

5. References

- C. Lopez-Otin and J. S. Bond, *J Biol Chem* **2008**, *283*, 30433–30437. DOI:10.1074/jbc.R800035200
- M. B. Rao, A. M. Tanksale, M. S. Ghatge and V. V. Deshpande, *Microbiol Mol Biol Rev* **1998**, *62*, 597–635.
- H. Maeda, *Microbiol Immunol* **1996**, *40*, 685–99. DOI:10.1111/j.1348-0421.1996.tb01129.x
- A. Schaller, *Planta* **2004**, *220*, 183–97. DOI:10.1007/s00425-004-1407-2
- I. Yike, *Mycopathologia* **2011**, *171*, 299–323. DOI:10.1007/s11046-010-9386-2
- N. D. Rawlings, D. P. Tolle and A. J. Barrett, *Biochem J* **2004**, *378*, 705–16. DOI:10.1042/bj20031825
- J. Sabotič and J. Kos, *Appl Microbiol Biot* **2012**, *93*, 1351–75. DOI:10.1007/s00253-011-3834-x
- R. Sharma, in: R. Sharma (Ed.): *Enzyme Inhibition and Bio-applications*, InTech, **2012**, pp. 3–36. DOI:10.5772/1963
- N. D. Rawlings, M. Waller, A. J. Barrett and A. Bateman, *Nucleic acids research* **2014**, *42*, D503–9. DOI:10.1093/nar/gkt953
- J. Erjavec, J. Kos, M. Ravnikar, T. Dreo and J. Sabotič, *Trends Biotechnol* **2012**, *30*, 259–73. DOI:10.1016/j.tibtech.2012.01.004
- J. Sabotič, T. Trček, T. Popovič and J. Brzin, *J Biotechnol* **2007**, *128*, 297–307. DOI:10.1016/j.jbiotec.2006.10.006
- G. Salvesen and H. Nagase, in: R. J. Benyou and J. S. Bond (Eds.): *Proteolytic enzymes: A practical approach*, IRL Press, Oxford, **1989**, pp. 83–104.
- N. D. Rawlings, A. J. Barrett, P. D. Thomas, X. Huang, A. Bateman and R. D. Finn, *Nucleic Acids Res* **2018**, *46*, D624–D632. DOI:10.1093/nar/gkx1134
- N. Dohmae, K. Takio, Y. Tsumuraya and Y. Hashimoto, *Arch Biochem Biophys* **1995**, *316*, 498–506. DOI:10.1006/abbi.1995.1066
- S. Kojima, A. Iwahara and H. Yanai, *FEBS Lett* **2005**, *579*, 4430–6. DOI:10.1016/j.febslet.2005.06.083
- J. Brzin, B. Rogelj, T. Popovič, B. Štrukelj and A. Ritonja, *J. Biol. Chem.* **2000**, *275*, 20104–9. DOI:10.1074/jbc.M001392200
- J. Sabotič, T. Popovič, V. Puizdar and J. Brzin, *FEBS J* **2009**, *276*, 4334–45. DOI:10.1111/j.1742-4658.2009.07138.x
- M. Kidrič, H. Fabian, J. Brzin, T. Popovič and R. H. Pain, *Biochem. Biophys. Res. Commun.* **2002**, *297*, 962–7. DOI:10.1016/S0006-291X(02)02328-8
- K. Galeša, R. M. Thomas, M. Kidrič and R. H. Pain, *Biochem Biophys Res Commun* **2004**, *324*, 576–8. DOI:10.1016/j.bbrc.2004.09.092
- J. Sabotič, K. Galeša, T. Popovič, A. Leonardi and J. Brzin, *Protein Expr Purif* **2007**, *53*, 104–11. DOI:10.1016/j.pep.2006.11.015
- S. Žurga, J. Pohleven, J. Kos and J. Sabotič, *J Biochem* **2015**, *158*, 83–90. DOI:10.1093/jb/mvv025
- P. Avanzo, J. Sabotič, S. Anžlovar, T. Popovič, A. Leonardi, R. H. Pain, J. Kos and J. Brzin, *Microbiology* **2009**, *155*, 3971–81. DOI:10.1099/mic.0.032805-0
- J. Sabotič, S. Bleuler-Martinez, M. Renko, P. Avanzo Caglič, S. Kallert, B. Štrukelj, D. Turk, M. Aebi, J. Kos and M. Künzler, *J Biol Chem* **2012**, *287*, 3898–907. DOI:10.1074/jbc.M111.285304
- S. Odani, K. Tominaga, S. Kondou, H. Hori, T. Koide, S. Hara, M. Isemura and S. Tsunasawa, *Eur J Biochem* **1999**, *262*, 915–23. DOI:10.1046/j.1432-1327.1999.00463.x
- J. Sabotič, D. Gaser, B. Rogelj, K. Gruden, B. Štrukelj and J. Brzin, *Biol Chem* **2006**, *387*, 1559–66. DOI:10.1515/BC.2006.194
- J. Sabotič, S. Kilaru, M. Budič, M. B. Gašparič, K. Gruden, A. M. Bailey, G. D. Foster and J. Kos, *Biochimie* **2011**, *93*, 1685–1693. DOI:10.1016/j.biochi.2011.05.034
- J. Sabotič, R. A. Ohm and M. Künzler, *Appl Microbiol Biot* **2015**, submitted.
- A. Deveau, M. Barret, A. G. Diedhiou, J. Leveau, W. de Boer, F. Martin, A. Sarniguet and P. Frey-Klett, *Microbial ecology* **2015**, *69*, 146–59. DOI:10.1007/s00248-014-0445-y
- T. Lukanc, J. Brzin, J. Kos and J. Sabotič, *Acta Biochim Pol* **2017**, *64*, 21–24. DOI:10.18388/abp.2015_1187
- P. Avanzo Caglič, M. Renko, D. Turk, J. Kos and J. Sabotič, *Biochimica et Biophysica Acta* **2014**, *1844*, 1749–56.
- M. Renko, J. Sabotič, M. Mihelič, J. Brzin, J. Kos and D. Turk, *J Biol Chem* **2010**, *285*, 308–16. DOI:10.1074/jbc.M109.043331
- M. Renko, J. Sabotič and D. Turk, *Biological chemistry* **2012**, *393*, 1043–54. DOI:10.1515/hsz-2012-0159

33. J. Pohleven, J. Brzin, L. Vrabec, A. Leonardi, A. Čokl, B. Štrukelj, J. Kos and J. Sabotič, *Appl Microbiol Biotechnol* **2011**, *91*, 1141–8. DOI:10.1007/s00253-011-3236-0
34. J. Pohleven, N. Obermajer, J. Sabotič, S. Anžlovar, K. Sepčić, J. Kos, B. Kralj, B. Štrukelj and J. Brzin, *Biochim Biophys Acta* **2009**, *1790*, 173–81.
35. J. Pohleven, M. Renko, S. Magister, D. F. Smith, M. Künzler, B. Štrukelj, D. Turk, J. Kos and J. Sabotič, *J Biol Chem* **2012**, *287*, 10602–12. DOI:10.1074/jbc.M111.317263
36. S. Žurga, J. Pohleven, M. Renko, S. Bleuler-Martinez, P. Sosnowski, D. Turk, M. Künzler, J. Kos and J. Sabotič, *FEBS J* **2014**, *281*, 3489–506. DOI:10.1111/febs.12875
37. I. Šmid, K. Gruden, M. Buh Gašparič, K. Koruza, M. Petek, J. Pohleven, J. Brzin, J. Kos, J. Žel and J. Sabotič, *J Agr Food Chem* **2013**, *61*, 12499–509. DOI:10.1021/jf403615f
38. I. Šmid, A. Rotter, K. Gruden, J. Brzin, M. Buh Gašparič, J. Kos, J. Žel and J. Sabotič, *Pestic Biochem Physiol* **2015**, *122*, 59–66. DOI:10.1016/j.pestbp.2014.12.022
39. J. Sabotič, K. Koruza, B. Gabor, M. Peterka, M. Barut, J. Kos and J. Brzin, in: S. Magdeldin (Ed.): *Affinity Chromatography*, InTech, Rijeka, **2012**, pp. 307–332.
40. J. Sabotič and J. Kos, in: J.-M. Mérillon and K. G. Ramawat (Eds.): *Fungal Metabolites*, Springer International Publishing, Switzerland, **2016**.

Povzetek

Inhibitorji cisteinskih proteaz, klitocipin in makrocipini iz višjih gliv (mikocipini), skupaj s serinskima proteaznima inhibitorjema, ki sta zelo specifična za tripsin, kospin in knispin iz višjih gliv (mikospini), kažejo številne značilnosti, ki jih razlikujejo od inhibitorjev proteaz iz drugih virov. Visoka genetska raznolikost ima vpliv na funkcionalnost in / ali stabilnost proteinov in privede do številnih proteinskih variant z nekoliko različnimi inhibitorskimi profili, ki vplivajo na vrsto tarčne proteaze in / ali moč inhibicije. Imajo β -triperesno zvitje, ki kaže visoko plastičnost pri uporabi 11 različnih zank za inhibicijo različnih družin proteaz z različnimi mehanizmi inhibicije. Njihova vsestranskost se kaže tudi v regulatorni in obrambni funkciji ter široki potencialni uporabi v biotehnologiji, kmetijstvu in medicini.

Scientific paper

Epitope Mapping of Major Ragweed Allergen Amb a 1

Abida Zahirović,¹ Borut Štrukelj,¹ Peter Korošec² and Mojca Lunder^{1,*}¹ Faculty of Pharmacy, University of Ljubljana, Ljubljana, Slovenia² University Clinic of Respiratory and Allergic Diseases Golnik, Golnik, Slovenia* Corresponding author: E-mail: mojca.lunder@ffa.uni-lj.si
Tel.: +386 1 47 69 570; Fax.: +386 1 42 58 031

Received: 06-01-2018

Dedicated to the memory of Prof. Dr. Igor Kregar

Abstract

Ragweed is a prominent cause of seasonal allergies. Thus far, information on IgE-binding sites of major allergen in ragweed pollen, Amb a 1, is very limited. A powerful experimental method to gain insights on the allergen epitopes is the selection of peptides from biological libraries that bind to anti-allergen antibodies. In this work, we aimed to map IgE epitopes of Amb a 1 using epitope-mimicking short peptides – mimotopes that were affinity-selected from phage-displayed random peptide libraries. The peptides weakly aligned with the Amb a 1 primary sequence, thus suggesting that the epitopes are conformational. When the peptides were mapped onto the surface of Amb a 1 homology model, the EpiSearch analysis predicted the location of four potential epitopic sites on surface patches centred at residues K₁₀₄, S₁₁₀, H₂₁₄, and W₃₁₂. The peptides matching to the predicted epitopes bound selectively to the IgE from pool of ragweed-allergic patients' sera and therefore represent mimetics of Amb a 1 IgE epitopes. The knowledge of IgE epitopes is a prerequisite for the rational design of molecular-based approaches to diagnosis and immunotherapy of allergic diseases.

Keywords: Ragweed allergy; Amb a 1; epitope mapping; phage display; mimotopes

1. Introduction

Short ragweed (*Ambrosia artemisiifolia*) is one of the most important allergen source in North America.¹ Because of its fast spreading, sensitization rates are also increasing in Central and Southeastern Europe, ranging from 15% to ~80%.² Current therapeutic options for ragweed allergy involve symptomatic treatment and allergen-specific immunotherapy. Conventional immunotherapy with crude pollen extracts is the only available curative treatment. However, it may induce undesired IgE-mediated side effects and long-term therapy is required, which often hampers patient compliance.^{3,4} Therefore, new approaches to immunotherapy that include well-defined therapeutic molecules with reduced or abolished IgE binding capacity are being investigated.

Ragweed pollen allergy is especially suited for molecule-based immunotherapeutic strategies due to the dominance of one allergen. Molecule-based vaccines are based on individual allergen proteins, allergen-derived

peptides containing relevant epitopes or epitope-mimicking peptides (mimotopes).⁵ Among 14 allergens described in ragweed pollen, Amb a 1 has been identified as the major disease-causing agent, which reacts with IgE of more than 90% of the ragweed-sensitized patients.^{6,7} It is a non-glycosylated 38 kDa protein that belongs to the family of pectate lyases and accounts for up to 15% of total proteins in the ragweed pollen.^{8,9} It has been demonstrated that Amb a 1 in a form of a conjugate with toll-like receptor agonist can replace the whole pollen extract in immunotherapy.¹⁰ Five different isoforms of Amb a 1 with about 80% sequence identity have been found.¹¹ They display distinct patterns of IgE binding and immunogenicity with limited B- and T-cell cross-reactivity patterns.¹² Amb a 1 is cross-reactive with its homologous allergen in mugwort pollen Art v 6, a pectate lyase with 65% of sequence identity with Amb a 1.^{13–15} The identification of relevant epitopes can reveal the molecular basis of allergenic cross-reactivity. Therefore, detailed studies of T- and B- cell epitopes are necessary for rational de-

sign of molecule-based reagents for diagnosis and immunotherapy.

Investigation of T-cell response to Amb a 1 revealed multiple dominant T-cell epitopes (Amb a 1 176–191, 200–215, 280–295, 304–319, 320–335, and 344–359).^{16,17} However, the data on the conformational B-cell epitopes is still scarce. Screening of random peptide phage libraries against anti-allergen antibodies is a fast and relatively inexpensive alternative compared to other methods for epitope mapping and in combination with computer-based algorithms can lead to the identification of conformational allergen epitopes.^{18,19} Successful application of this technology provides peptide mimotopes that are able to bind IgE antibodies and are not necessarily identical to original epitope, but rather mimic its essential features.^{20,21} Mimotopes are considered to have similar physicochemical characteristics and spatial organization as their corresponding epitopes. As such, they may be employed for the development of safer immunotherapies either based on carrier-bound peptide vaccines or based on hypoallergenic recombinant allergens.^{22,23}

In this study, we screened phage display libraries of random peptides using Amb a 1-specific IgG to define peptides mimicking Amb a 1 epitopes. Best mimotope candidates were tested for their IgE reactivity with sera of ragweed-allergic patients. Using computational epitope mapping tools affinity-selected peptide sequences were analyzed to predict the location of epitopes on Amb a 1.

2. Experimental

2.1. Purification and Evaluation of Target Antibodies

Anti-Amb a 1 IgG were affinity-purified from rabbit antiserum (Indoor Biotechnologies, Cat# PA-AM1, RRID:AB_2728628) using natural allergen Amb a 1 (INDOOR Biotechnologies) immobilized on Dynabeads M-280 Tosylactivated (Thermo Fisher Scientific, Waltham, Massachusetts, USA) following the manufacturer's instructions.

2.2. Biopanning of Phage Display Libraries

Affinity-purified rabbit IgG specific for Amb a 1 were immobilized alternately onto 0.45 mg of protein G or protein A coupled magnetic beads (Dynabeads, Thermo Fisher Scientific) by incubation in PBS/0.05% Tween 20 for 30 min at room temperature and used as a target in biopanning. Three phage display libraries (New England Biolabs, Ipswich, Massachusetts, USA) of linear heptamer, linear dodecamer, and cyclic heptamer random peptides were panned as described in the manufacturer's manual. The libraries contain approximately 10^9 unique peptide sequences fused to the pIII minor coat protein of

the M13 filamentous phage. Bound phages were eluted from the target antibodies either with 0.1 M glycine-HCl (pH 2.2) for 10 min followed by immediate neutralization with 1 M Tris (pH 8.0) or competitively with Amb a 1 at the final concentration of 12 $\mu\text{g}/\text{ml}$. After three rounds of affinity selection, 24 individual clones from each elution method (total 144 clones) were amplified and screened for binding to target antibodies by monoclonal phage ELISA.

2.3. Monoclonal Phage ELISA

MaxiSorp microtiter plates (Thermo Fisher Scientific, Waltham, Massachusetts, USA) were coated with 2 $\mu\text{g}/\text{ml}$ of anti-Amb a 1 IgG (RRID:AB_2728628) in PBS overnight at 4 °C. Plates were blocked with 5% skimmed milk in PBS for 1.5 h at room temperature and washed three times with PBS/0.1% Tween 20. A separate set of wells was covered with blocking buffer only, to determine background binding. The amplified phage clones or control (wild-type phage clone with no peptide displayed on its surface) in LB were then loaded into the wells. After 60 min of incubation, the wells were washed five times with PBS/0.1% Tween 20. For detection, HRP-conjugated anti-M13 monoclonal antibodies (GE Healthcare Cat# 27942101 RRID: AB_2616587) diluted 1:5000 were added to the wells and incubated for 1 h. The colour was developed with TMB Super Tracker substrate (ImmunoO4, Westminster, UK) supplemented with 0.006% H_2O_2 . After terminating the reaction with 2 M H_2SO_4 , absorbance was measured at 450 nm with the microtiter plate reader (Tecan Safire, Tecan Group AG, Männedorf, Switzerland). Phage clones with the highest target to background absorbance ratio were subjected to DNA sequencing (GATC Biotech, Konstanz, Germany).

2.4. Characterization of Phage-displayed Peptides Binding to Target Antibodies

Seventeen phage clones displaying unique peptides were purified by PEG-precipitation, resuspended in PBS and quantified by spectrophotometry. Binding of the phage-displayed peptides to the target antibodies was assessed by semiquantitative ELISA. The suspensions containing 2×10^9 pfu of individual phage clones or control phage in PBS were loaded into the wells. To detect possible binders to antibody constant regions, the wells were coated with control rabbit antiserum raised against procathepsin X (Biogenes, Berlin, Germany) diluted 1:1000 in PBS overnight at 4 °C. For competition ELISA selected clones were added to the wells together with the allergen in three different concentrations (1 $\mu\text{g}/\text{ml}$, 5 $\mu\text{g}/\text{ml}$, 10 $\mu\text{g}/\text{ml}$) and incubated with target antibodies for 1 h at room temperature. The following steps in the assays were as described above for monoclonal phage ELISA. All experiments were carried out in triplicates.

2. 5. Linear Alignment of Peptides with Amb a 1 Sequence and Mapping to the 3D Homology Model of Amb a 1

Obtained amino acid sequences were checked for the presence of target-unrelated peptides using the MIMOdb 2.0 database. Peptides were compared among themselves and aligned with Amb a 1 sequence using multiple sequence alignment program, Clustal Omega, to find a consensus pattern of amino acids.²⁴ The 3D model structure of Amb a 1 was generated using a protein fold recognition server Phyre.^{2,25} The EpiSearch method was used to define the potential epitope sites on the surface of Amb a 1.²⁶

2. 6. Isolation of pIII-Fused Peptides from *E. coli* Periplasm

Six peptides showing the highest specific binding to target antibodies were extracted from the periplasm of *E. coli* ER2738 as fusions with pIII phage coat protein. Host bacteria were infected with individual peptide-displaying phage clone and grown for 2 h at 37 °C with agitation. Bacterial pellets were spun down at 5000 ×g for 10 min and resuspended in 1 ml of an ice-cold solution consisting of 20% sucrose, 200 mM Tris-HCl (pH 8.0) and 1 mM EDTA supplemented with protease inhibitor cocktail (EZBlock™, BioVision, San Francisco, USA) at a dilution of 1:200. Following 1 h incubation on ice with occasional stirring, supernatants were harvested by centrifugation at 12000 ×g for 20 min at 4 °C. The resulting periplasmic extracts were concentrated (4–5 fold) and the extraction buffer was exchanged for PBS by ultrafiltration using 10 kDa cut-off membranes (Microsep Advance Centrifugal Device, Pall Corporation, New York, USA). Extracts of non-infected bacteria and bacteria infected with phage clone carrying unrelated pIII-fused control peptide (linear GTFDHPQ targeting streptavidin) were prepared in the same way and used as negative controls.²⁷

2. 7. Sera of Ragweed-Allergic Patients

Serum samples from ragweed-allergic patients with positive sIgE to Amb a 1 were collected at the University Clinic of Respiratory and Allergic Diseases, Golnik, Slovenia prior to starting immunotherapy. Patients' characteristics are shown in Table 1. The study was approved by National Medical Ethics Committee of Republic of Slovenia (No. 35/06/14). All patients willingly donated their blood for research.

2. 8. Immunodot Assay: Binding of pIII-Fused Peptides to Patients' IgE

Two microliters of each sample of pIII-fused peptides were spotted onto 0.45 µm nitrocellulose membrane (GE Healthcare). The membrane was blocked with 5%

Table 1. Characteristics of ragweed-allergic patients.

	sIgE* Amb a 1 (kU/L)
Patient 1	0.77
Patient 2	41.4
Patient 3	1.51
Patient 4	0.61
Patient 5	0.62
Patient 6	0.5
Patient 7	1.6
Patient 8	1.71

sIgE* – specific immunoglobulin E were measured by using CLIA Immulite (Siemens, Erlangen, Germany).

skimmed milk in Tris-buffered saline/0.05% Tween 20 (0.05% TBST) for 3 h at room temperature and then incubated overnight at 4 °C with a pool of sera from ragweed allergic-patients (patients 1 to 8, Table 1) diluted 1:10 in 0.05% TBST. After triple washing with 0.1% TBST, membranes were incubated with HRP-conjugated goat anti-human IgE antibodies (Thermo Fisher Scientific Cat# A18793 RRID: AB_2535570) diluted 1:2000 in 1% BSA/0.1% TBST for 2 h at room temperature. The reactive dots were visualized with CCD image analysis system (G-Box, Syngene, United Kingdom) using SuperSignal West Dura Extended Duration Substrate (Thermo Fisher Scientific).

3. Results and Discussion

In this study, we sought to map epitopes of major ragweed allergen Amb a 1 by panning phage-displayed random peptide libraries. A thoughtful choice of biopanning conditions is crucial to overcome the limitations of commercially available peptide libraries and to improve the selection success rate.^{28,29} To avoid recovery of target-unrelated binders we used protein A or protein G coupled beads alternately for immobilization of target antibodies. Biopanning of three phage displayed-libraries was carried out with affinity-purified rabbit IgG specific for Amb a 1 using specific and non-specific elution. Given that the antibodies of IgG isotype were used as target, the reactivity of selected peptides with serum IgE was tested in order to evaluate whether a conserved epitope specificity between the IgG and IgE exist and thus to determine whether the identified peptides are also mimetics of IgE epitopes in ragweed-allergic patients. Forty-two phage clones reactive with Amb a 1-specific target antibodies but not with the components of background buffer in preliminary phage ELISA were selected for sequencing. Peptides RVVLMMDWTVLH, CLFSQGNRC, MRTDMVI, and CIMSLVGTC were the most strongly enriched (number of isolated identical sequences is shown in brackets alongside these peptides in Figs. 1 and 2). Overall, sequencing yielded 17 different peptides.

Binding of individual peptides displayed on phage to target antibodies was ranked in semiquantitative ELISA assay (Fig 1, A). In contrast to control phage (with no peptide displayed), six peptide-displaying phage clones demonstrated at least two-fold higher binding to the target antibodies compared to the background. Other 11 peptide-displaying phage clones showed lower binding to target antibodies. Potential non-specific interaction with anti-

body constant region was checked by ELISA with control antibodies that were produced in the same species as target antibody and thus contain identical Fc fragment. Binding to control rabbit antisera was low and comparable between peptide-displaying phage clones and control phage (Fig 1, B). Therefore, the interaction of peptides with antibody constant region was excluded. Six phage-displayed peptides that exhibited the best binding to target antibodies (RV-

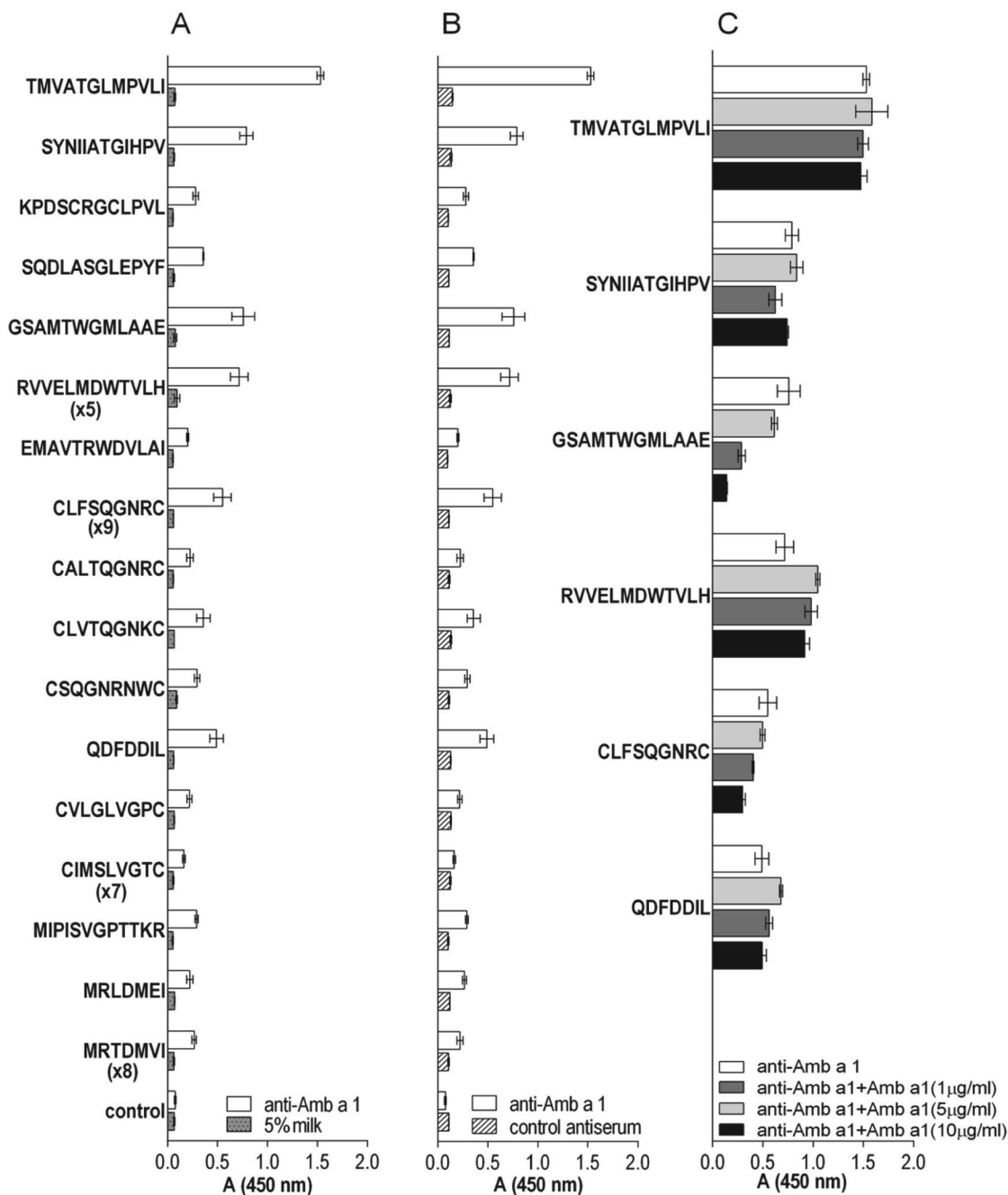


Figure 1: Characterization of the phage-displayed peptides affinity-selected with anti-Amb a 1 rabbit IgG. (A) Binding of phage-displayed peptides to the immobilized target antibodies and background (5% milk). Values in brackets represent the frequency of the selected peptides. (B) Binding of phage-displayed peptides to the immobilized control rabbit antiserum (anti-procathepsin X). Wild-type phage with no displayed peptide served as negative control. The data are presented as the mean \pm standard deviation of three individual experiments. (C) Displacement of six selected phage-displayed peptides from target antibodies with 1 μ g/ml, 5 μ g/ml and 10 μ g/ml of natural Amb a 1.

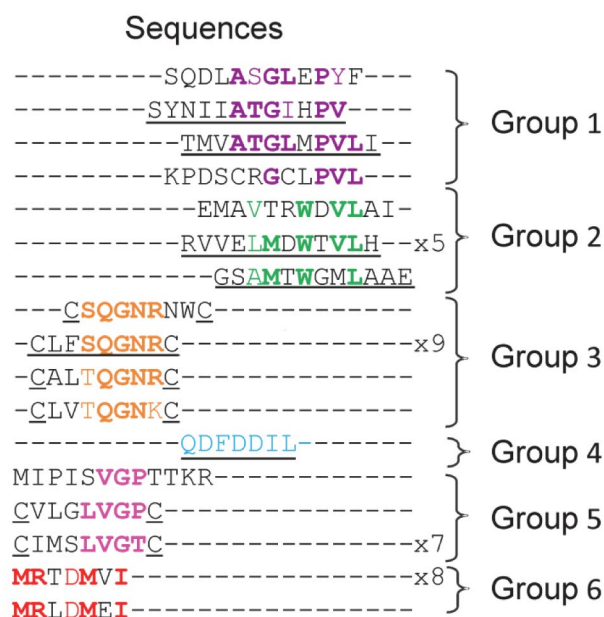


Figure 2: Sequence alignment of isolated peptides obtained using multiple sequence alignment program Clustal Omega. Consensus residues within each group are marked in different colours. Bolded amino acids are exact match; not bolded amino acids have similar physicochemical properties. Underlined peptides from groups 1–4 showed the highest binding to target antibodies.

VELMDWTVLH, GSAMTWGMLAAE, SYNIIATGIHPV, TMVATGLMPVLI, QDFDDIL, and CLFSQGNRC) were further examined for competitive binding to target antibody paratopes in the presence of allergen (Fig 1, C). After addition of 5 or 10 µg/ml of Amb a 1, the signal for phage-displayed peptide GSAMTWGMLAAE substantially decreased. The signal drop, albeit less pronounced, was also observed for Cys constrained phage-displayed peptide CLFSQGNRC. Peptide displacement from the target antibody by allergen indicates that they competed with allergen for the same paratopes on target antibodies i.e. the peptides and allergen share the same binding sites. Interestingly, other tested peptides showed no change or even slight increase in signal after addition of allergen (Fig 1, C). This may imply that they have a higher affinity for target antibodies than the allergen. Enhanced binding of phages to target antibodies occur possibly due to the conformational stabilization of target antibodies upon allergen binding that makes the paratopes more accessible for phages.

Isoforms of Amb a 1 display distinct patterns of IgE binding. In previous study, Amb a 1.01 showed higher IgE-binding activity compared to Amb a 1.02 or 03 isoforms.¹² Therefore, we used Amb a 1.01 isoform for *in silico* linear alignment and conformational epitope mapping. The sequences of 17 different peptides were arranged into six groups according to their degree of similarity (Fig. 2). Despite common amino acid motifs within individual groups, not all peptides exhibited high binding to the target antibodies. For example, motif SQGNR appeared in 12 out of 14 peptides from the cyclic library but only one pep-

tide sequence (CLFSQGNRC) bound significantly to the target antibodies (Fig. 1A). This indicated that other residues outside the motif were important for target antibody binding as well.

Fig. 3 depicts linear alignment of the peptides with Amb a 1.01 sequence. The peptides were either aligned with shorter segments consisting of only a few matching residues within Amb a 1 sequence or not aligned at all (Fig. 3). Matching amino acids were also not the same as those included in common motifs within individual groups. This suggests that the epitopes of Amb a 1 are conformational. Indeed, it has been previously shown that inhalational allergens contain mainly conformational epitopes consisting of amino acids that are distributed over the protein sequence and come into close contact upon protein folding.^{30–32}

For *in silico* mapping of conformational epitopes on Amb a 1, we created the 3D structural model of Amb a 1 since its crystal structure is not yet available. Using a protein fold recognition server Phyre², we generated a high confidence close homology model of Amb a 1 with sequence coverage of 92%.²⁵ The model is based on structural template d1pxza of Jun a 1, the major allergen from cedar pollen, as the closest homolog with known structure that contains a single-stranded right-handed beta-helix fold. Jun a 1 is a member of the pectate lyase family of allergens and provides a reliable homology model since it has a sequence identity of 47% with a FFAS score –93.1 with Amb a 1.³³ EpiSearch method was used to reveal the location of epitopes on surface of Amb a 1 model.²⁶ This approach uses patch analysis and solvent accessible surface area of amino acids to map peptides obtained from phage display experiments onto the 3D structure of a protein. The best match between the amino acid composition of the peptides and surface-exposed areas on the 3D model of allergen is predictive of epitope.

We used six representative peptides from groups 1–4 that showed the highest binding to target antibodies (Fig. 1C, Fig. 2; underlined peptides) as input sequences for EpiSearch. The natural allergen Amb a 1 is composed of two non-covalently associated subchains, the N-terminal β chain (amino acids 26–180) and the C-terminal α chain (amino acids 181–396). Two representatives from group 1 were mapped to the loop on β chain at the N terminus containing residues V₇₂, A₇₃, N₇₄, L₁₀₂, K₁₀₄, V₁₀₇, G₁₂₇, V₁₄₈, N₁₄₉, P₁₅₀, G₁₅₁, G₁₅₂, L₁₅₃, S₁₅₆, A₁₆₁, A₁₆₂, P₁₆₃, A₁₆₅, G₁₆₆, and S₁₆₇ with center residue at K₁₀₄ (score: 1.000) (Fig. 4A). Two representatives from group 2 were mapped to the beta strand on α chain at the C terminus containing residues R₂₅₃, H₂₅₄, A₂₇₆, S₂₇₇, T₂₇₉, L₂₈₁, L₂₉₉, G₃₀₀, R₃₀₁, H₃₀₂, G₃₀₃, E₃₀₄, A₃₀₅, A₃₀₆, E₃₀₈, S₃₀₉, M₃₁₀, W₃₁₂, R₃₁₅, V₃₂₈, A₃₂₉, S₃₃₀, and, G₃₃₁ with center residue at W₃₁₂ (score: 0.950) (Fig. 4B). A representative from group 3 was mapped to the loop on β chain at the N terminus containing residues Q₈₆, N₈₇, R₈₈, L₉₀, N₁₀₉, S₁₁₀, N₁₃₁, G₁₃₂, N₁₃₅, N₁₅₇, G₁₅₉, G₁₇₆, S₁₇₈, and Q₁₇₉ with center residue at S₁₁₀ (score: 1.000)

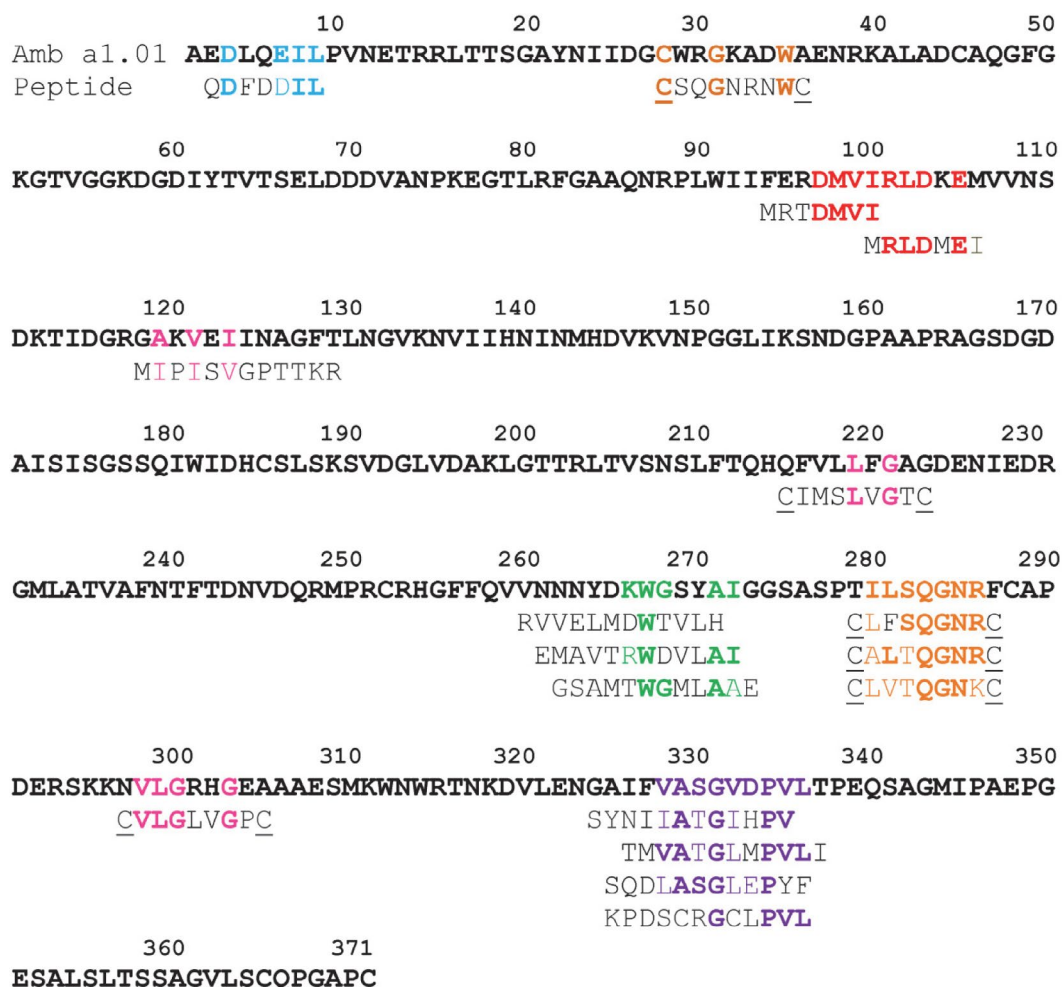


Figure 3: Alignment of isolated peptide sequences to the sequence of Amb a 1.01 isoform (the accession number in the gene bank of NCBI: P27759). Amino acids in individual peptides are coloured corresponding to groups 1–6 (Fig. 2). Bolded amino acids are exact match to residues in Amb a 1; not bolded amino acids have similar physicochemical properties as residues in Amb a 1.01.

(Fig. 4C). A representative from group 4 was mapped to the beta strand on α chain at the C terminus containing residues D₁₄₅, D₁₇₀, D₁₉₂, L₂₁₀, Q₂₁₃, H₂₁₄, Q₂₁₅, F₂₁₆, D₂₄₃, D₂₄₆, Q₂₄₇, and D₂₆₅ with center residue at H₂₁₄ (score: 1.000) (Fig. 4D). β chain was suggested to contain IgE binding sites based on its higher IgE reactivity compared to α subchain in the previous study.³⁴ In this study, Epi-search analysis predicted two epitopes to be located on β chain at the N terminus (mapped by peptides from groups 1 and 3) and also predicted two epitopes on α chain at the C terminus (mapped by peptides from groups 2 and 4). Predicted epitopes are located on the solvent-exposed loops and beta strands of Amb a 1 model structure. These results agree with the known fact that conformational B-cell epitopes are usually associated with turns or loops and exposed regions protruding from protein surfaces and suggest that residues in these areas are involved in antibody binding.^{35,36}

Given that the biopanning was carried out with antibodies of IgG isotype as target, in order to determine the

relevance of deduced epitopes in ragweed-allergic patients we tested the conserved epitope specificity between IgG and IgE by evaluating the reactivity of identified peptides with patient sera. Six representative peptides from groups 1–4 that showed the highest binding to target (Fig. 1C, Fig. 2; underlined peptides) were isolated as fusions with pIII phage coat protein from *E. coli* and tested for binding to IgE from sera pool of ragweed-allergic patients (patients 1–8, Table 1). Extract from noninfected bacteria and an unrelated pIII-fused peptide (linear GTFDHPQ targeting streptavidin) were used as controls.²⁷ Sera pool showed IgE binding to the six pIII-fused peptides (Fig. 5). Protein pIII used as a carrier of peptides ensured the correct conformation of the peptides during the assay and allowed efficient immobilisation on the membrane. Signals were not detected with the control samples (Fig. 5). Therefore, binding was attributed only to the IgE epitope-mimicking peptides (mimotopes). Thus, the mimotopes showed binding with target IgG as well as with patients' IgE. This indicates that the identified epitopes are relevant for both anti-

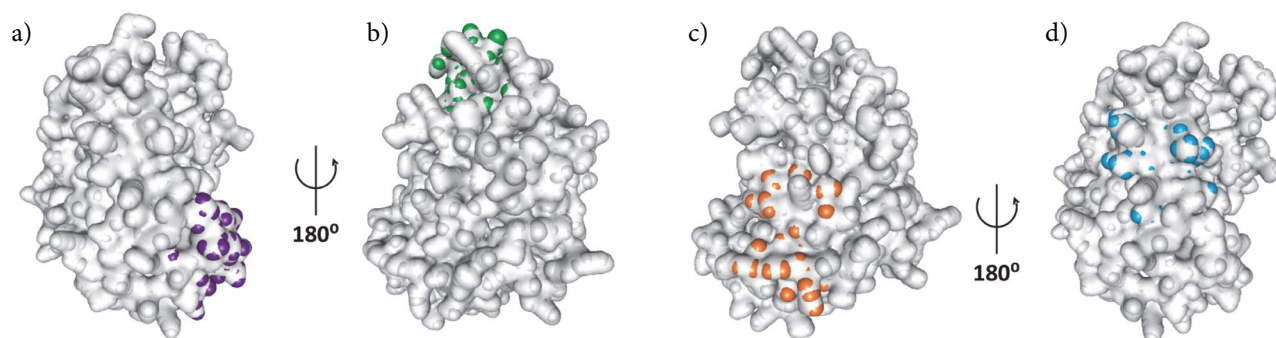


Figure 4: Mapping epitopes on a 3D structure of Amb a 1 homology model. The Amb a 1 model was generated using a protein fold recognition server Phyre². (A) Two representatives from group 1 were mapped to the loop on β chain at the N terminus containing residues V₇₂, A₇₃, N₇₄, L₁₀₂, K₁₀₄, V₁₀₇, G₁₂₇, V₁₄₈, N₁₄₉, P₁₅₀, G₁₅₁, G₁₅₂, L₁₅₃, S₁₅₆, A₁₆₁, A₁₆₂, P₁₆₃, A₁₆₅, G₁₆₆, and S₁₆₇ (violet). (B) Two representatives from group 2 were mapped to the beta strand on a chain at the C terminus containing residues R₂₅₃, H₂₅₄, A₂₇₆, S₂₇₇, T₂₇₉, L₂₈₁, L₂₉₉, G₃₀₀, R₃₀₁, H₃₀₂, G₃₀₃, E₃₀₄, A₃₀₅, A₃₀₆, E₃₀₈, S₃₀₉, M₃₁₀, W₃₁₂, R₃₁₅, V₃₂₈, A₃₂₉, S₃₃₀, and G₃₃₁ (green). (C) A representative from group 3 was mapped to the loop on β chain at the N terminus containing residues Q₈₆, N₈₇, R₈₈, L₉₀, N₁₀₉, S₁₁₀, N₁₃₁, G₁₃₂, N₁₃₅, N₁₅₇, G₁₅₉, G₁₇₆, S₁₇₈, and Q₁₇₉ (orange). (D) A representative from group 4 was mapped to the beta strand on a chain at the C terminus containing residues D₁₄₅, D₁₇₀, D₁₉₂, L₂₁₀, Q₂₁₃, Q₂₁₅, H₂₁₄, F₂₁₆, D₂₄₃, D₂₄₆, Q₂₄₇, and D₂₆₅ (blue).

body isotypes. Since the mimotopes were selected with IgG antibodies, additional IgE epitopes might still be present on Amb a 1.

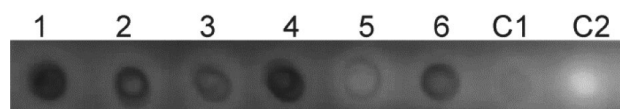


Figure 5. Binding of pIII-fused representative peptides from groups 1–4 to IgE from sera pool of eight ragweed-allergic patients. (1) pIII-RVVELMDWTVLH, (2) pIII-GSAMTWGMLAAE, (3) pIII-SYNIIATGHPV, (4) pIII-TMVTGLMPVLL, (5) pIII-QDFDIL, and (6) pIII-CLFSQGNRC. Controls: (C1) non-infected *E. coli* and (C2) unrelated pIII-fused peptide pIII-GTFDHPQ.

4. Conclusions

In biopanning experiments against the polyclonal Amb a 1-specific rabbit IgG, we enriched peptides and arranged them into six groups according to their degree of similarity. The peptides weakly matched with shorter segments of Amb a 1 sequence, thus suggesting that the epitopes of Amb a 1 are conformational. Conformational mapping of the six representative peptides to the surface of the structural model of Amb a 1 predicted the location of four epitopic sites on surface patches centred at residues K₁₀₄, S₁₁₀, H₂₁₄, and W₃₁₂. The representative peptides bound to IgE from ragweed-allergic patients and are therefore mimetics of Amb a 1 IgE epitopes. These results pave the way towards the identification of conformational epitopes of Amb a 1. The structure and location of each new epitope increase our knowledge and, hence, the probability of identifying common features of cross-reactive allergen-antibody recognition sites, which would ultimately help to reveal the characteristics of the cross-reactive

allergens and their underlying mechanism of action. In the context of immunotherapy, the identification of allergen epitopes and their mimotopes provides the basis for the rational design of immunotherapeutic constructs either based on recombinant allergen derivatives with reduced allergenic activity or mimotope-based carrier-bound vaccine for more defined and safer allergen-specific immunotherapy.

Conflict of interest

Authors declare no conflict of interest.

5. References

1. F. Ihler, M. Canis, *J. Asthma Allergy* **2015**, *8*, 15–24. DOI:10.2147/JAA.S47789
2. M. L. Oswald, G. D. Marshall, *Allergy Asthma Clin. Immunol.* **2008**, *4*, 130–135. DOI:10.1186/1710-1492-4-3-130
3. H. Löwenstein, *Chem. Immunol. Allergy* **2014**, *100*, 323–332. DOI:10.1159/000359989
4. M. Turkalj, I. Banic, S. A. Anzic, *Patient Prefer. Adherence* **2017**, *Volume 11*, 247–257. DOI:10.2147/ppa.s70411
5. B. Linhart, R. Valenta, *Curr. Opin. Immunol.* **2005**, *17*, 646–655. DOI:10.1016/j.coi.2005.09.010
6. M. Wallner, U. Pichler, F. Ferreira, *Immunotherapy* **2013**, *5*, 1323–1338. DOI:10.2217/imt.13.114
7. G. Gadermaier, N. Wopfner, M. Wallner, M. Egger, A. Didierlaurent, G. Regl, F. Aberger, R. Lang, F. Ferreira, T. Hawranek, *Allergy* **2008**, *63*, 1543–1549. DOI:10.1111/j.1398-9995.2008.01780.x
8. V. Bordas-Le Floch, R. Groeme, H. Chabre, V. Baron-Bodo, E. Nony, L. Mascarell, P. Moingeon, *Curr. Allergy Asthma Rep.* **2015**, *15*, DOI:10.1007/s11882-015-0565-6
9. T. Rafnar, I. J. Griffith, M. C. Kuo, J. F. Bond, B. L. Rogers, D. G. Klapper, *J. Biol. Chem.* **1991**, *266*, 1229–1236.
10. P. S. Creticos, J. T. Schroeder, R. G. Hamilton, S. L. Bal-

- cer-Whaley, A. P. Khattignavong, R. Lindblad, H. Li, R. Coffman, V. Seyfert, J. J. Eiden et al., *N. Engl. J. Med.* **2006**, 355, 1445–1455. DOI:10.1056/NEJMoa052916
11. I. J. Griffith, J. Pollock, D. G. Klapper, B. L. Rogers, A. K. Nault, *Int. Arch. Allergy Appl. Immunol.* **1991**, 96, 296–304.
 12. M. Wolf, T. E. Twaroch, S. Huber, M. Reithofer, M. Steiner, L. Aglas, M. Hauser, I. Aloisi, C. Asam, H. Hofer et al., *Allergy* **2017**, 72, 1874–1882. DOI:10.1111/all.13196
 13. N. Wopfner, G. Gadermaier, M. Egger, R. Asero, C. Ebner, B. Jahn-Schmid, F. Ferreira, *Int. Arch. Allergy Immunol.* **2005**, 138, 337–346. DOI:10.1159/000089188
 14. B. Jahn-Schmid, M. Hauser, N. Wopfner, P. Briza, U. E. Berger, R. Asero, C. Ebner, F. Ferreira, B. Bohle, *J. Immunol.* **2011**, 188, 1559–1567. DOI:10.4049/jimmunol.1102445
 15. U. Pichler, M. Hauser, M. Wolf, M. L. Bernardi, G. Gadermaier, R. Weiss, C. Ebner, H. Yokoi, T. Takai, A. Didierlaurent et al., *PLoS One* **2015**, 10, e0120038. DOI:10.1371/journal.pone.0120038
 16. J. Pham, C. Oseroff, D. Hinz, J. Sidney, S. Paul, J. Greenbaum, R. Vita, E. Phillips, S. Mallal, B. Peters et al., *Clin. Exp. Allergy* **2016**, 46, 1194–1205. DOI:10.1111/cea.12772
 17. B. Jahn-Schmid, N. Wopfner, G. Hubinger, R. Asero, C. Ebner, F. Ferreira, B. Bohle, *J. Allergy Clin. Immunol.* **2010**, 126, 1068–1071.e1062. DOI:10.1016/j.jaci.2010.05.038
 18. P. Molek, B. Strukelj, T. Bratkovic, *Molecules* **2011**, 16, 857–887. DOI:10.3390/molecules16010857
 19. T. Bratkovic, *Cell. Mol. Life Sci.* **2010**, 67, 749–767. DOI:10.1007/s00018-009-0192-2
 20. E. Ganglberger, *FASEB J.* **2000**, 14, 2177–2184. DOI:10.1096/fj.99-1000com
 21. J. M. Davies, E. O'Hehir R, C. Suphioglu, *J. Allergy Clin. Immunol.* **2000**, 105, 1085–1092.
 22. E. Jensen-jarolim, A. Leitner, H. Kalchauer, A. Zurcher, E. Ganglberger, B. Bohle, O. Scheiner, G. Boltz-nitulescu, H. Breiteneder, *FASEB J.* **1998**, 12, 1635–1642.
 23. X. Chen, S. C. Dreskin, *Mol. Nutr. Food Res.* **2017**, 61, 1600568. DOI:10.1002/mnfr.201600568
 24. F. Sievers, A. Wilm, D. Dineen, T. J. Gibson, K. Karplus, W. Li, R. Lopez, H. McWilliam, M. Remmert, J. Soding et al., *Mol. Syst. Biol.* **2011**, 7, 539. DOI:10.1038/msb.2011.75
 25. L. A. Kelley, S. Mezulis, C. M. Yates, M. N. Wass, M. J. Sternberg, *Nat. Protoc.* **2015**, 10, 845–858. DOI:10.1038/nprot.2015.053
 26. R. Tiwari, S. S. Negi, B. Braun, W. Braun, A. Pomes, M. D. Chapman, R. M. Goldblum, T. Midoro-Horiuti, *Int. Arch. Allergy Immunol.* **2012**, 157, 323–330. DOI:10.1159/000330108
 27. P. Molek, T. Bratkovic, *Acta Chim. Slov.* **2016**, 63, 914–919. DOI:Molek-2016-4 [pii]
 28. S. S. Sidhu, C. R. Geyer: Phage Display In Biotechnology and Drug Discovery, Second Edition, CRC Press. Boca Raton, **2015**. 584 p.
 29. M. Vodnik, U. Zager, B. Strukelj, M. Lunder, *Molecules* **2011**, 16, 790–817. DOI:10.3390/molecules16010790
 30. A. Pomés, *Int. Arch. Allergy Immunol.* **2010**, 152, 1–11. DOI:10.1159/000260078
 31. S. Padavattan, S. Flicker, T. Schirmer, C. Madritsch, S. Randow, G. Reese, S. Vieths, C. Lupinek, C. Ebner, R. Valenta et al., *J. Immunol.* **2009**, 182, 2141–2151. DOI:10.4049/jimmunol.0803018
 32. M. Lombardero, P. W. Heymann, T. A. Platts-Mills, J. W. Fox, M. D. Chapman, *J. Immunol.* **1990**, 144, 1353–1360.
 33. L. Jaroszewski, L. Rychlewski, Z. Li, W. Li, A. Godzik, *Nucleic Acids Res.* **2005**, 33, W284–288. DOI:10.1093/nar/gki418
 34. N. Wopfner, B. Jahn-Schmid, G. Schmidt, T. Christ, G. Hubinger, P. Briza, C. Radauer, B. Bohle, L. Vogel, C. Ebner et al., *Mol. Immunol.* **2009**, 46, 2090–2097. DOI:10.1016/j.molimm.2009.02.005
 35. A. Pomes, M. Li, J. Glesner, S. Wunschmann, E. M. King, M. D. Chapman, A. Wlodawer, A. Gustchina, *J. Allergy Clin. Immunol.* **2009**, 123, S229–S229. DOI:10.1016/j.jaci.2008.12.881
 36. S. Padavattan, T. Schirmer, M. Schmidt, C. Akdis, R. Valenta, I. Mittermann, L. Soldatova, J. Slater, U. Mueller, Z. Markovic-Housley, *J. Mol. Biol.* **2007**, 368, 742–752. DOI:10.1016/j.jmb.2007.02.036

Povzetek

Ambrozija je pomemben vzrok sezonskih alergij. Do sedaj imamo zelo malo informacij o IgE vezavnih mestih na glavnem alergenu iz cvetnega prahu ambrozije, Amb a 1. Afinitetna selekcija peptidov iz bioloških knjižnic z uporabo specifičnih protiteles proti alergenu je uporabna laboratorijska metoda za določevanje epitopov. V tej raziskavi smo s pomočjo mimotopov, kratkih peptidov, ki posnemajo epitope, izoliranih iz bakteriofagnih knjižnic naključnih peptidov, določali IgE epitope Amb a 1. Izbrani peptidi so se le šibko ujemali s primarnim zaporedjem Amb a 1, kar je nakazovalo, da so epitopi konformacijski. Da bi jih določili, smo izdelali homologni model tridimenzionalne strukture Amb a 1, na katerega smo prilegali izbrane peptide. S pomočjo programa EpiSearch smo identificirali štiri potencialne epitope na površini alergena okoli aminokislinskih ostankov K₁₀₄, S₁₁₀, H₂₁₄ in W₃₁₂. Peptidni mimetiki predvidenih epitopov so se specifično vezali na IgE iz zmesi serumov za ambrozijo alergičnih pacientov in tako predstavljajo mimetike IgE epitopov Amb a 1. Poznavanje IgE epitopov je predpogoj za racionalno načrtovanje molekularnih pristopov v diagnostiki in imunoterapiji alergijskih bolezni.

Scientific paper

The Titre of the Virus in the Inoculum Affects the Titre of the Viral RNA in the Host Plant and the Occurrence of the Disease Symptoms

Maruša Pompe-Novak,* Maja Križnik and Kristina Gruden

National Institute of Biology, Ljubljana, Slovenia

* Corresponding author: E-mail: marusa.pompe.novak@nib.si

Received: 07-04-2018

Dedicated to the memory of Prof. Dr. Igor Kregar

Abstract

Potato virus Y (PVY) is the most economically important potato virus, therefore extensive research is focusing on elucidation of its interaction with the host. To obtain repeatable results, strict standardization of research methods is crucial. Mechanical inoculation by rubbing sap from a PVY infected plant onto the leaf surface together with a fine abrasive powder is the most convenient way of experimental transmission of PVY to host plants. However, factors determining reproducibility of this process need to be determined. In the present study, it was shown that higher titre of the virus in the inoculum resulted in faster increase of PVY^{NTN} RNA titre in the inoculated leaves, as well as in faster translocation of PVY^{NTN} from inoculated leaves into upper non-inoculated leaves. The final titre of PVY^{NTN} RNA in upper non-inoculated leaves was independent of the virus titre in the inoculum. In addition, the occurrence of the disease symptoms was followed and the dependence to the titre of the virus in the inoculum was observed.

Keywords: *Potato virus Y*; PVY; potato; mechanical inoculation; inoculum; virus titre; symptoms

1. Introduction

Potato virus Y (PVY) is the most economically important potato virus affecting potato production worldwide¹ and it was classified as one of ten most important plant viruses overall.² In sensitive potato cultivars, it can cause potato tuber necrosis ring spot disease.³ On the green part of a plant, local lesions, chlorosis, mosaic, crinkling, systemic necrosis, leaf drop and plant death can appear.⁴ The outcome of the interaction depends on genotypes of both, potato host plant and PVY pathogen. In addition, the response of a potato towards PVY infection can vary with various environmental conditions and various developmental and physiological growth stages of a plant.⁵

PVY infected potato plants can exhibit either a compatible or an incompatible response.⁶ Plants exhibiting a compatible interaction are susceptible and the virus can replicate and invade the plants.⁷ Susceptible potato plants can be either sensitive or tolerant to PVY infection. Sensitive potato plants develop disease symptoms, while tolerant plants develop no or very mild symptoms, although they can accumulate high titre of the virus.⁸

In an incompatible interaction, plants resist the virus by restricting cell invasion, virus replication and/or virus spread. Plants can respond to virus infection with an extreme resistance (ER) or a hypersensitive response (HR). In the case of ER, potato plants show no symptoms or very limited necrosis in the form of pinpoint lesions.⁹ Virus titres remain extremely low, below the limit of detection also in the initially infected leaf.^{9,10,11,12} In the case of HR, virus translocation from the initially infected leaf to other parts of the plant is prevented, although the virus replication and initial cell-to-cell movement are not blocked. Later, most of the infected cells die, which result in a localised necrotic lesion at the site of infection.^{12,13}

In the natural environment, PVY is transmitted by sap-feeding aphid vector, or vegetatively through propagated potato tubers. Experimentally, PVY can be transmitted by mechanical means such as grafting or rubbing of a sap from a PVY infected plant onto the leaf surface together with a fine abrasive powder, e.g. carborundum.¹⁴ The latter method is a convenient mean for experimental transmission of the PVY to host plants, although strict standardization of the method is crucial for repeatable re-

sults. The aim of the present study was to investigate the relation between the titre of the virus in the inoculum and the titre of the viral RNA in the host plant, and additionally to determine whether there is the correlation between PVY titre in the inoculum and induction of disease symptom development in inoculated plants.

2. Experimental

96 virus free potato plants (*Solanum tuberosum* L.) of cultivar Désirée and 105 virus free plants of cv. Igor from stem node tissue culture (cultivated for 2 weeks) were planted in soil and kept at 21 ± 2 °C in growth chambers, with illumination at $70 \mu\text{Mm}^{-2}\text{s}^{-1}$ (Osram L36W/77 lamp), a photoperiod of 16 h and relative humidity 70%. After 4 weeks, three bottom leaves of each plant were mechanically inoculated by rubbing the inoculum onto the leaf surface together with a fine abrasive powder of carborundum (0.037 mm). Inoculum was prepared by grinding PVY^{NTN} (NIB-NTN isolate, AJ585342, referred also as NTN-Slo Isolate¹⁵) infected plants of cv. Pentland Squire from node tissue culture in the grinding buffer (0.02 M phosphate buffer, 0.01 M DETC, pH 7.6) in the ratios (w/v) 1:5, 1:10, 1:50 and 1:100. For control mock inoculation, healthy plants of cv. Pentland Squire from node tissue culture were ground in the grinding buffer in the ratio (w/v) 1:5. After 10 min incubation, the inoculum was washed from the leaf surface by tap water.

On potato plants of cv. Igor disease symptom development was monitored at 0, 3, 4, 5, 6, 7, 10 and 14 days post inoculation (dpi). At the same time points, samples from three plants per treatment were collected for the quantification of PVY RNA. For that purpose, the right distal quarter of the second inoculated leaf and the right distal quarter of the second upper non-inoculated leaf were collected and further analysed separately from each plant of cv. Désirée. Collected leaf tissues were frozen immediately in liquid nitrogen and stored at -80 °C for further analysis.

Plant tissue was homogenised by Tissue Lyser (Qiagen, Hilden, Germany). RNA was isolated by MagMAX™ Plant RNA Isolation Kit (Applied Biosystems, Foster City, CA, USA) including DNase treatment. RNA concentration, quality, and purity were assessed using agarose gel electrophoresis and NanoDrop ND-1000 spectrophotometer (Thermo Fisher Scientific, Waltham, Massachusetts, USA). RT-qPCR reactions were performed on 2 μl of extracted RNA in a total volume of 10 μl using the Ag-Path-IDTM One-Step RT-PCR Kit

(Applied Biosystems, Foster City, CA, USA) according to the manufacturer's instructions.

Primer and probe concentrations, together with PCR amplification conditions, were as in Kogovšek *et al.*¹⁶ Two dilutions of RNA were analysed, each in duplicate. Reactions were carried out using the ABI 7900HT Sequence Detection System (Applied Biosystems, Foster

City, CA, USA). RT-qPCR conditions included a reverse transcription step (10 min at 48 °C) followed by 40 amplification cycles (1 min at 60 °C, 15 s at 95 °C). Data were analysed using the SDS v 2.3 software (ABI, Foster City, CA, USA). PVY RNA amount was quantified using a relative standard curve method by normalization to the endogenous control cox mRNA by quantGenius.¹⁷ The significance of differences ($p \leq 0.05$) between mean values was determined by the Student's t-test.

3. Results and Discussion

The titre of PVY^{NTN} RNA was studied in potato host plants of tolerant cv. Désirée after inoculation with the inocula obtained by grinding PVY^{NTN} infected plant tissue in grinding buffer in different ratios (w/v), 1:5, 1:10 and 1:100, and therefore containing different titres of PVY^{NTN}. The amount of PVY^{NTN} RNA detected immediately after inoculation (0 dpi) correlated with the titre of PVY^{NTN} in the inoculum, indicating that the remnants of PVY^{NTN} RNA on the leaf surface after washing the inoculum was detected.

From 0 dpi to 4 dpi the detected amount of PVY^{NTN} RNA decreased (Figure 1) due to degradation of PVY^{NTN} RNA on the leaf surface. It was already demonstrated in previous studies¹⁸ that it is possible to detect the traces of the inoculum on the leaf surface of extremely resistant cv. Santé (in which PVY cannot multiply) even at 14 dpi; and to detect viral RNA in dry inoculum 12 days after its preparation. Double-stranded RNA products shown to arise during viral replication of *Potyviridae*^{19,20} can explain the stability of viral RNA.

It is hypothesised that PVY enters the initial potato cells for further multiplication through broken leaf hairs

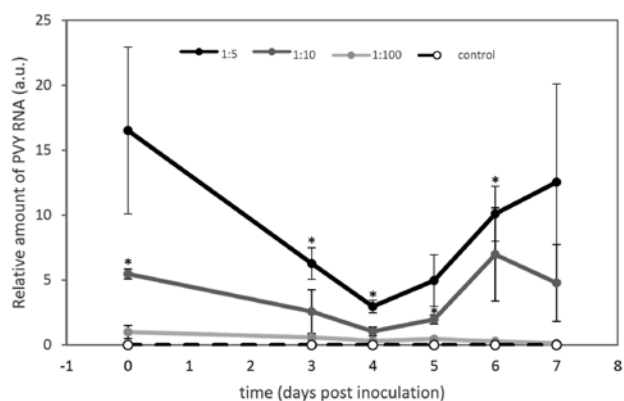


Figure 1. The relative amount of PVY^{NTN} RNA measured by RT-qPCR in the inoculated leaves of cv. Désirée from 0 to 7 dpi. Error bars represent the standard error ($n = 3$). Statistical comparison was made between plants inoculated with the inoculum in which PVY^{NTN} infected potato sap was diluted in buffer in the ratio 1:100 and plants inoculated with the inocula in which PVY^{NTN} infected potato sap was diluted in buffer in the ratios 1:5 or 1:10. Statistically significant differences ($p \leq 0.05$) are indicated with.*

(broken by rubbing at mechanical inoculation). At 5 dpi the amount of newly multiplied PVY^{NTN} RNA exceeded the amount of PVY^{NTN} RNA in the remnants of the inoculum on the leaf surface of the plants inoculated with the inocula in which PVY^{NTN} infected potato sap was diluted in buffer in the ratios 1:5 or 1:10 (Figure 1). From 5 to 7 dpi, higher PVY^{NTN} RNA titres were observed in plants inoculated with more concentrated inoculum (Figure 1). In leaves, inoculated with the inoculum in which PVY^{NTN} infected potato sap was diluted in buffer in the ratio 1:100, the titre of PVY^{NTN} probably increased later than 7 dpi, as also the translocation of PVY^{NTN} from inoculated into upper noninoculated leaves occurred later (Figure 2).

In inoculated leaves of potato the concentric distribution of PVY around the point of infection was shown during HR.¹² In inoculated leaves of tobacco (*Nicotiana tabacum* L.) cv. Xanthi movement of PVY from initially inoculated cells to neighbour cells in concentric circles, loading of PVY into the veins and translocation of PVY into upper non-inoculated leaves was shown in tolerant interaction.²¹ Our results in tolerant potato–PVY interaction showed that the translocation of PVY^{NTN} from inoculated into upper non-inoculated leaves of potato cv. Désirée occurred regardless of the virus titre in the inoculum, while the speed of the process was dependent on the virus titre in the inoculum (Figure 2). Although the multiplication of PVY^{NTN} in inoculated leaves and the translocation of PVY^{NTN} from inoculated into upper non-inoculated leaves was slower in the case of lower viral titre in the inoculum, the final titre of PVY^{NTN} RNA in upper non-inoculated leaves 14 dpi was independent of the virus titre in the inoculum (Figure 2). Even much longer times (a few months) are required for the spread of PVY^{NTN} from nutrient solution containing extremely low titre of PVY^{NTN}, through the roots, to the green parts of the plants as shown in experiments using a hydroponic system.²²

Additionally, the disease symptom development after inoculation with different PVY^{NTN} titre was monitored on potato plants of cv. Igor, which is one of the most susceptible and sensitive potato varieties to PVY^{NTN}. A few days after infection, local lesions appeared on inoculated leaves, followed by leaf chlorosis (yellowing of the leaves) and leaf drop of inoculated leaves. In general, the severity of the disease symptoms correlated with the titre of PVY^{NTN} in the inoculum. The appearance and the development of disease symptoms was slower in the plants inoculated with lower titre of PVY^{NTN} in the inoculum (Figure 3), what is shown also by the correlation between the titre of PVY^{NTN} in the inoculum and the leaf drop (Figure 4). By 14 dpi, all 3 inoculated leaves dropped in plants inoculated with the inocula diluted in the ratios 1:5 or 1:10. At the same time, in plants inoculated with the inocula diluted in the ratios 1:50 or 1:100 only the 1st and the 2nd inoculated leaf dropped, while the 3rd inoculated leaf showed more severe symptoms in plants inoculated with the inoculum diluted in the ratio 1:50 as compared to the plants inoculated with the inoculum diluted in the ratio 1:100 (Figure 3). No symptoms appeared on control potato plants, where also no leaf drop was observed at 14 dpi (Figure 3, right panel).

Besides the high titre of PVY^{NTN} in the inoculum, also too much carborundum or too excessive rubbing at mechanical inoculation promotes the leaf drop on inoculated plants (data not shown). Early leaf drop of inoculated leaves can prevent the spread of the virus to upper non-inoculated leaves and the development of symptoms in upper non-inoculated leaves. In PVY^{NTN} – cv. Igor interaction, the absence of symptoms in upper non-inoculated leaves indicates with a high probability the absence of the virus in upper non-inoculated leaves.

Although the plants are kept in the same growth chamber controlled environment with the same tempera-

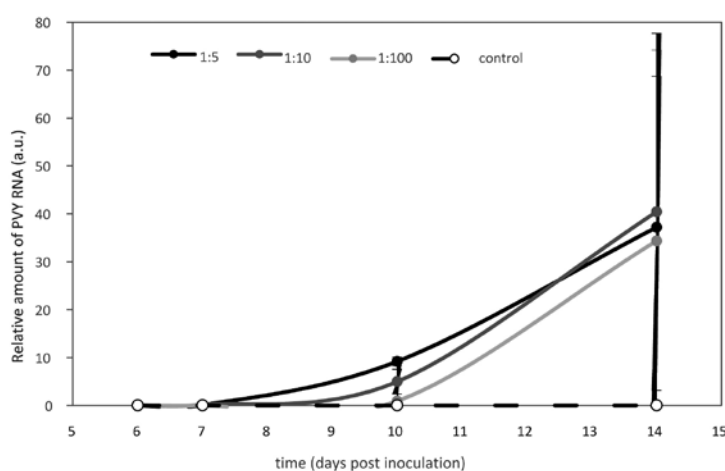


Figure 2. The relative amount of PVY^{NTN} RNA measured by RT-qPCR in upper non-inoculated leaves of cv. Désirée from 6 to 14 dpi. Error bars represent the standard error (n = 3). Statistical comparison was made between plants inoculated with the inoculum in which PVY^{NTN} infected potato sap was diluted in buffer in the ratio 1:100 and plants inoculated with the inocula in which PVY^{NTN} infected potato sap was diluted in buffer in the ratios 1:5 or 1:10. None of the differences was statistically significant ($p \leq 0.05$).



Figure 3. Disease symptoms on potato plants of cv. Igor at 14 days after inoculation with the inocula in which PVY^{NTN} infected potato sap was diluted in buffer in the ratios 1:5 (left), 1:10 (second from the left), 1:50 (middle) or 1:100 (second from the right); and control potato plants (right).

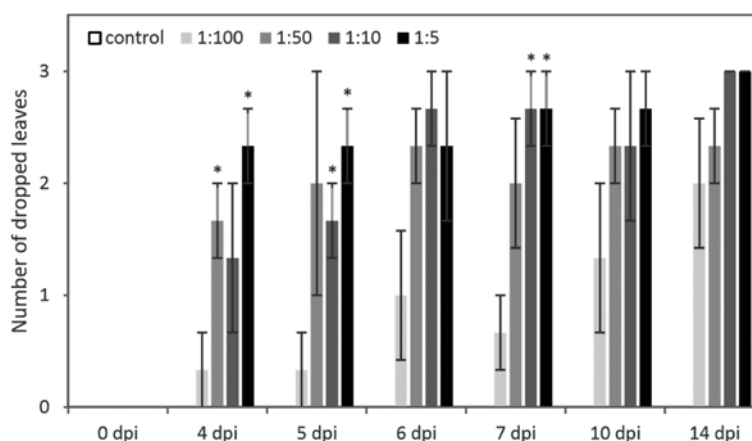


Figure 4. The average number of dropped inoculated leaves per plant in cv. Igor after infection with PVY^{NTN} from 0 dpi to 14 dpi. Error bars represent the standard error ($n = 3$). Statistical comparison was made between plants inoculated with the inoculum in which PVY^{NTN} infected potato sap was diluted in buffer in the ratio 1:100 and plants inoculated with the inocula in which PVY^{NTN} infected potato sap was diluted in buffer in the ratios 1:50, 1:10 or 1:5. Statistically significant differences ($p \leq 0.05$) are indicated with.*

ture, relative humidity, illumination and photoperiod, the plant's response to viral infection (including the development of symptoms) can vary between experiments (biological repetitions) due to yet unknown parameters (e.g. physiological state of the plant, season...).

4. Conclusions

We can conclude that higher titre of PVY^{NTN} in the inoculum resulted in faster increase of PVY^{NTN} RNA titre in the inoculated leaves and in faster translocation of PVY^{NTN} from inoculated leaves into upper non-inoculated leaves. The final amount of PVY^{NTN} RNA in upper noninoculated leaves was independent of PVY^{NTN} titre in the inoculum. In addition, the occurrence of the disease symptoms was slower in the plants inoculated with lower titre of PVY^{NTN} in the inoculum as compared to the plants inoculated with higher titre of PVY^{NTN} in the inoculum. Thus to obtain reproducible results of any biochemical, physiological or molecular study of potato – PVY interaction one should use standardised titre of the virus in the inoculum.

5. Acknowledgment

The research was financially supported by the Slovenian Research Agency (research core funding No. P4-0165). The authors thank Tjaša Cof, Mihaela Leupušček and Živa Marinko, who joined to the research as students; and Neža Turnšek for technical help.

6. References

1. A. V. Karasev, S. M. Gray, *Annu. Rev. Phytopathol.* **2013**, *51*, 571–586. DOI:10.1146/annurev-phyto-082712-102332
2. K. B. Scholthof, S. Adkins, H. Czosnek, P. Palukaitis, E. Jacquot, T. Hohn, B. Hohn, K. Saunders, T. Candresse, P. Ahlquist, C. Hemenway, G.D. Foster. *Mol Plant Pathol.* **2011**, *12*, 938–954. DOI:10.1111/j.1364-3703.2011.00752.x
3. L. Beczner, J. Horvath, I. Romhanyi, H. Forster, *Potato Res.* **1984**, *27*, 339–352. DOI:10.1007/BF02357646
4. M. Kus, in: M. Rečnik, M. Kus (Eds.) Proceedings of the 9th EAPR Virology Section Meeting, Ribno, Bled, Slovenia, **1995**, pp. 135–138.
5. M. Pompe-Novak, C. Lacomme, in: C. Lacomme, L. Glais, D.

- Bellstedt, B. Dupuis, A.V. Karasev, E. Jacquot (Eds.), *Potato virus Y–biodiversity, pathogenicity, epidemiology and management*, Cham, Springer, 2017, pp. 22–42.
6. J. Hinrichs-Berger, M. Harford, S. Berger, H. Buchenauer, *Physiol. Mol. Plant Pathol.* **1999**, 55, 143–150.
DOI:10.1006/pmpp.1999.0216
7. J. I. Cooper, A. T. Jones, *Phytopathology* **1983**, 73, 127–128.
DOI:10.1094/Phyto-73-127
8. M. Ravnikar, in: J. Freitag (Ed.) *ETNA Plant genomics and bioinformatics: expression microarrays and beyond: a course book*, Postdam, 2005, pp. 66–71.
9. J. P. T. Valkonen, R. A. C. Jones, S. A. Slack, K. N. Watanabe, *Plant Breed.* **1996**, 115, 433–438.
DOI:10.1111/j.1439-0523.1996.tb00952.x
10. J.P.T. Valkonen, *Plant Breed.* **1994**, 112, 1–16.
DOI:10.1111/j.1439-0523.1994.tb01270.x
11. R.M. Solomon-Blackburn, H. Barker, *Heredity* **2001**, 86, 17–35. DOI:10.1046/j.1365-2540.2001.00799.x
12. J. P. T. Valkonen, *Breed. Sci.* **2015**, 65, 69–76.
DOI:10.1270/jsbbs.65.69
13. T. Lukan, Š. Baebler, M. Pompe-Novak, K. Guček, M. Zagorščak, A. Coll, K. Gruden, *Front. Plant Sci.* **2018**, 9, 168.
DOI:10.3389/fpls.2018.00168
14. C. Lacomme, J. Pickup, A. Fox, L. Glais, B. Dupuis, T. Steinger, J.-L. Rolot, J. P. T. Valkonen, K. Kruger, X. Nie, S. Modic, N. Mehle, M. Ravnikar, M. Hullé, in: C. Lacomme, L. Glais, D. Bellstedt, B. Dupuis, A.V. Karasev, E. Jacquot (Eds.), *Potato virus Y–biodiversity, pathogenicity, epidemiology and management*, Cham, Springer, 2017, pp. 141–176.
DOI:10.1007/978-3-319-58860-5_6
15. H. Barker, K. McGeachy, N. Toplak, K. Gruden, J. Žel, I. Browning, *Am. J. Potato Res.* **2009**, 86, 227–238.
DOI:10.1007/s12230-009-9076-0
16. P. Kogovšek, L. Gow, M. Pompe-Novak, K. Gruden, G.D. Foster, N. Boonham, M. Ravnikar, *J. Virol. Methods* **2008**, 149, 1–11. DOI:10.1016/j.jviromet.2008.01.025
17. Š. Baebler, M. Svalina, M. Petek, K. Stare, A. Rotter, M. Pompe-Novak, K. Gruden, *BMC Bioinformatics* **2017**, 18, 276.
DOI:10.1186/s12859-017-1688-7
18. N. Mehle, M. Kovač, N. Petrovič, M. Novak Pompe, Š. Baebler, H. Krečič-Stres, K. Gruden, M. Ravnikar, *Physiol. Mol. Plant Pathol.* **2004**, 64, 293–300.
DOI:10.1016/j.pmpp.2004.10.005
19. I.P. Gadh, V. Hari, *Virology* **1986**, 150, 304–307.
DOI:10.1016/0042-6822(86)90292-8
20. V. Hari, in: R.P. Singh, U.S. Singh, K. Kohmoto (Eds.), *Pathogenesis and host specificity in plant diseases. Histopathological, biochemical, genetic and molecular bases. Viruses and viroids*, vol. III. Great Britain, Elsevier, 1995, pp. 1–18.
21. M. Rupar, F. Faurez, M. Tribodet, I. Gutiérrez-Aguirre, A. Delaunay, L. Glais, M. Križnik, D. Dobnik, K. Gruden, E. Jacquot, M. Ravnikar, *Mol. Plant Microbe. Interact.* **2015**, 28, 739–750. DOI:10.1094/MPMI-07-14-0218-TA
22. N. Mehle, I. Gutiérrez-Aguirre, N. Prezelj, D. Delić, U. Vidic, M. Ravnikar, *Applied and environmental microbiology* **2014**, 80, 1455–1462. DOI:10.1128/AEM.03349-13

Povzetek

Virus krompirja Y (*Potato virus Y*, PVY) je ekonomsko najpomembnejši virus krompirja, zato se številne raziskave osredotočajo na študij interakcije PVY z gostiteljsko rastlino. Za zagotavljanje ponovljivosti rezultatov je pomembna standardizacija raziskovalnih metod. Najpogostejši način prenosa PVY na gostiteljsko rastlino v eksperimentalnih pogojih je mehanska inokulacija, pri kateri na površino lista naneseemo abrazivno sredstvo in sok okužene rastline, pri čemer pa je potrebno določiti dejavnike, ki so ključni za ponovljivost tega postopka. V raziskavi smo pokazali, da se je višji titer virusa v inokulumu odražal v hitrejšem dvigu titra RNA PVY^{NTN} v inokuliranih listih ter v hitrejšem širjenju PVY^{NTN} iz inokuliranih listov v zgornje neinokulirane liste. Končni titer RNA PVY^{NTN} v zgornjih neinokuliranih listih pa ni bil odvisen od titra virusa v inokulumu. Poleg tega smo opazili tudi, da je bila hitrost pojava bolezenskih znamenj odvisna od titra virusa v inokulumu.

Scientific paper

Characterization of Legumain Degradome Confirms Narrow Cleavage Specificity

Robert Vidmar,¹ Matej Vizovišek,¹ Dušan Turk,^{1,2} Boris Turk,^{1,3}
and Marko Fonovič^{1,*}

¹ Jožef Stefan Institute, Department of Biochemistry and Molecular and Structural Biology, Jamova 39,
SI-1000 Ljubljana, Slovenia

² Centre of Excellence for Integrated Approaches in Chemistry and Biology of Proteins, Ljubljana, Slovenia, Jamova 39,
SI-1000 Ljubljana, Slovenia

³ Faculty of Chemistry and Chemical Technology, University of Ljubljana, Večna pot 113, SI-1000 Ljubljana, Slovenia

* Corresponding author: E-mail: marko.fonovic@ijs.si
Phone: +386 1 477 3474

Received: 08-02-2018

Dedicated to the memory of Prof. Dr. Igor Kregar

Abstract

Legumain or asparagine endopeptidase is a unique cysteine endopeptidase with a distinctive specificity for the hydrolysis of peptide bonds after asparagine and to a lesser extent after aspartate. It is ubiquitously expressed in various tissues and besides its involvement in immune response and other physiological processes, it was also shown to play a role in pathological states such as inflammation and cancer. In order to improve our understanding of legumain substrate recognition we have performed proteomic profiling of legumain specificity on native proteins derived from MDA-MB-231 cells using two different N-terminal labelling methodologies (FPPS and ISIL). Our data revealed narrow cleavage specificity for P1 position combined with clear cleavage preference for unstructured secondary regions in the substrate proteins. No extended cleavage specificity on native proteins was observed. Moreover, a limited number of identified cleavages on individual substrates suggest its primary role in precision proteolysis and regulatory proteolytic events.

Keywords: Proteolysis; proteases; degradome; cleavage specificity; legumain

1. Introduction

Legumain or asparagine endopeptidase (AEP) is a lysosomal cysteine protease (C13 family, EC number 3.4.22.34) that catalyses the hydrolysis of peptide bonds after asparagines and to a lower extent also after aspartates.^{1–2} The catalytic site of legumain is composed of a catalytic dyad (His148 and Cys189). Consistent with its lysosomal localization, legumain has a pH optimum for substrate hydrolysis at acidic pH (pH = 5.8). In mammals, legumain is expressed in various organs and tissues, most abundantly in kidneys, testis and antigen-presenting cells. In contrast to other lysosomal proteases such as cathepsins with a high degree of functional redundancy, legumain exhibits unique substrate specificity and evolutionary highly conserved primary structure, which suggests that legu-

main may be involved in specific physiological processes. However, the exact physiological role of legumain is still not well understood. Although it was reported to regulate immune response through the activation of TLR receptors and antigen presentation it has not been shown to be crucial in these processes.^{3–5} In pathological conditions legumain is strongly associated with tumorigenesis, where its overexpression was shown in a number of human solid tumours such as carcinomas of the breast, colon and prostate.^{6–7} Recent reports have also shown its possible involvement in atherosclerosis⁸ and ischemic brain injury.⁹ Legumain has been also linked to the development of neuropathology in Alzheimer's disease, where it cleaves amyloid precursor protein and tau protein.^{10–11}

Nevertheless, the pathophysiological functions of legumain, its substrates and its association with disease de-

velopment and progression remain poorly understood. Conservation of legumain between evolutionary divergent plants and animals suggest that there is a biological need for legumain that has yet to be identified. A better understanding of features that govern the legumain substrate recognition is therefore expected to provide a novel insight in its biological role. Processing of legumain substrates *in vitro* was usually performed on peptides or denatured proteins and although these studies revealed its primary amino acid preference, it did not account for the possible influence of secondary and tertiary structure of the substrate.^{12–13} In this work, we studied legumain processing on a complex pool of structurally native proteins. We treated native human proteome with recombinant legumain and used in-gel stable isotope labelling (ISIL) and fast profiling of protease specificity (FPPS) for the identification of substrate cleavages. This enabled identification of primary cleavage specificity of legumain on native proteins as well as determination of secondary structure cleavage preference.

2. Experimental

2. 1. Materials

Antibodies against human prelamina-A/C (ab8984) were purchased from Abcam, United Kingdom. Recombinant human legumain was expressed in the baculovirus expression system as previously described.¹³ Ac(D3)-NHS was synthesized at the Faculty of Pharmacy (University of Ljubljana, Slovenia) according to the established protocol.¹⁴

2. 2. Cells and Cell Lysate Preparation

MDA-MB-231 breast cancer cells were routinely maintained in DMEM medium (Lonza) supplemented with 10% FBS (Sigma-Aldrich), 2 mM glutamine (Gibco) and 1% antibiotic stock solution (10.000 U/ml penicilin and 10 mg/ml streptomycin) (Sigma-Aldrich) at 37 °C and 5% CO₂. Before the harvesting, the cells were grown to confluency and washed with DPBS (Lonza). The cells were detached with enzyme-free dissociation solution (Millipore). After the centrifugation, the cell pellet was lysed on ice for 15 min in 20 mM sodium phosphate buffer pH 6.0, containing 150 mM NaCl, 0.05% NP-40, 1 mM EDTA, 25 μM E-64, 1 mM PMSF. The insoluble material was removed by centrifugation at 14 000 g for 10 min and the cleared cell lysate was used to determine protein concentration with the Bradford assay and portioned into aliquots containing 0.5 mg of total protein.

2. 3. *In vitro* Processing of the Cell Lysate

Recombinant prolegumain was first activated in 50 mM citric buffer pH 4.0, supplemented with 5 mM DTT

for 30 min at 37 °C. The active concentration of legumain was determined to be 16.7 μM.¹² In our degradomic workflow, recombinant human legumain was added to each aliquot of the cell lysate at 0.2 μM and 1.0 μM final concentration and the samples were incubated at 37 °C for 1h before further processing.

Immunological detection of prelamina-A/C was performed under identical conditions except that additional time-points were used for the *in vitro* processing (0, 10, 30 and 60 min). Western blot analysis was performed on nitrocellulose membrane using mouse monoclonal antibodies against prelamina-A/C according to manufacturer's recommendations.

2. 4. N-terminal Labelling with Trideutero-Acetylation

2. 4. 1. In-Gel Stable Isotope Labelling Protocol

After the *in vitro* processing, the samples were labelled with Ac(D3)-NHS according to the ISIL protocol described earlier with some modifications.¹⁵ Briefly, the samples were incubated in 6x SDS-PAGE loading buffer at 95 °C for 5 min and separated on a 12.5% SDS-PAGE gel (Lonza). The gel was stained with Comassie brilliant blue and each of the protein lanes was cut into six bands and destained with 25 mM NH₄HCO₃ in 50% acetonitrile/dH₂O. The proteins were reduced with 10 mM DTT (56 °C, 45 min) and alkylated with 55 mM iodoacetamide in the dark at room temperature for 30 min. In-gel stable isotope labelling was performed with an addition of 1 mg Ac(D3)-NHS per sample (40 mM final concentration). Prior to the labelling step Ac(D3)-NHS was dissolved in 100 mM phosphate buffer, pH 8.5. The reaction was performed at 30 °C for 1h and the labelling step was repeated one more time. To reverse any potential threonine and serine O-acetylation 1 mg hydroxylamine was added to each sample and the samples were incubated at room temperature for 20 min. The excess Ac(D3)-NHS reagent was quenched by adding 1 mg of glycine per sample followed by an incubation at 30 °C for 1h. The gel pieces were washed with acetonitrile and vacuum dried before rehydrating in 80 μl 25 mM NH₄HCO₃ solution containing 1 μg of sequencing-grade modified porcine trypsin per sample, and the trypsinization was then performed over night at 37 °C. The next day the peptides were extracted from the gel using the extraction solution (50% acetonitrile, 5% formic acid). The samples were desalted before LC-MS/MS analysis on C18 tips as described elsewhere.¹²

2. 4. 2. Fast-Profiling of Protease Specificity Protocol

The samples after *in vitro* processing were prepared according to the FPPS protocol described elsewhere.¹⁶ Briefly, the samples were transferred to a 500 μl micro-fil-

ter device with a cut-off of 3000 Da (Millipore) and the buffer was exchanged with 100 mM phosphate buffer pH 8.5. Subsequently, 2 mg of Ac(D3)-NHS reagent was dissolved in the sample followed by 1 hour incubation at 30 °C. Afterwards, the labelling step was repeated. To reverse partial labelling of serines, threonines and tyrosines, hydroxylamine was added to the sample at 1 mM concentration and left at room temperature for 20 min. Afterwards, 8 M urea was added and proteins were reduced with 10 mM DTT for 1 hour at room temperature before addition of iodoacetamide at 50 mM final concentration for 1 hour in the dark at room temperature. After the free cysteines were alkylated, the unreacted iodoacetamide was quenched with 50 mM DTT for 30 min at room temperature before the buffer was exchanged with 25 mM ammonium bicarbonate pH 7.8. The sample volume was set to 250 µl before the overnight trypsinization at a 1:100 (w/w, enzyme/substrate) ratio at 30 °C. The peptide-rich flow-through was collected the next day by spinning the micro-filters in the centrifuge and concentrated to 50 µl. The peptide samples were fractionated using a SAX-C18 stage tip protocol as previously described.^{17–18} Accordingly, the samples were mixed with Britton & Robinson buffer (20 mM acetic acid, 20 mM phosphoric acid and 20 mM boric acid, pH 11) and the pH was set to 11 with 1 M NaOH. The SAX tips were prepared by stacking 6 discs of Empore/Disk Anion Exchange (Varian) in a 200 µl pipet tip (Eppendorf) and the C18 tips were prepared by stacking 4 discs of Empore/C18 (Varian). The samples were applied to the SAX-C18 tip and the peptide fractions were eluted using buffers at pH 11, 10, 9, 8, 7, 6, 5, 4 and 3. The eluting peptides were captured on C18 tips and subjected to LC-MS/MS analysis.

2. 5. Mass Spectrometric Analysis

The LC-MS/MS analysis of the samples was performed using an Orbitrap LTQ Velos mass spectrometer (Thermo Fischer Scientific) coupled to an EASY-nanoLC II HPLC (Thermo Fischer Scientific) operated automatically via XCalibur software (Thermo Fischer Scientific). The samples containing 0.1% FA were loaded onto a C18 trapping column (Proxeon Easy-column, Thermo Fischer Scientific) and separated on a C18 PicoFrit Aquasil analytical column (New Objective). The peptides were eluted using a 5–40% (v/v) 50 min linear gradient of acetonitrile with 0.1% FA at a constant flow rate of 300 nl/min. The full MS mass spectra were acquired with the Orbitrap mass analyzer in the mass range of 300 to 2,000 m/z at resolution of 30,000 in the profile mode. The MS/MS spectra were obtained by HCD fragmentation of the nine most intense MS precursor ions and recorded at a resolution of 7,500 in the centroid mode. Only the precursor ions with assigned charge states (> 1) were chosen for MS/MS fragmentation. The dynamic exclusion was set to repeat count of 1, repeat duration of 30 s, and exclusion duration of 20 s.

2. 6. Database Search and Data Processing

For the identification of peptides we used the MaxQuant proteomic software¹⁹ and performed the database searches against the human proteome deposited in the UniProt/Swiss-Prot database (UniProtKB, *Homo sapiens*, canonical database, 20 336 entries). The settings for the database searches applied trideutero-acetylation of peptide N-termini (+45.029 Da) and methionine oxidation (+15.995 Da) as variable modifications, trideutero-acetylation of lysines (+45.029 Da) and carbamidomethylation of cysteines (+57.021 Da) as fixed modifications, Semi-ArgC/P as the enzyme specificity setting while allowing for one missed cleavage, precursor ion and fragment ion mass tolerances were set to 20 ppm and 0.5 Da, respectively. A reversed database search was performed and the false discovery rate (FDR) was set at 1% for peptide and protein identifications. Raw data and database search files are available via ProteomeXchange with identifier PXD010466.

After the database searches, the identified modification specific peptides were filtered to obtain the true positive hits for the legumain cleavage sites. Peptides with trideutero-acetylated N-termini identified only in the legumain-treated samples were considered to be the result of legumain cleavages. Reverse and contaminant peptides were removed from the peptide list. Additionally, the peptides were filtered for posterior error probability (PEP values above 0.05 were discarded) and score (values below 40 were discarded) as described previously.²⁰ The P1'–P4' positions were determined from the peptide N-terminus, whilst the P4–P1 positions were determined bioinformatically. The iceLogo representations were generated using the frequencies of positional amino acid occurrences normalised to the natural amino acid abundances in the human Swiss-Prot database.²¹

2. 7. Analysis of Structural Determinants of Legumain Substrates

To analyse the structural determinants of legumain substrate recognition we first prepared a list of the most reliable legumain substrates. Accordingly, we analysed the identified cleavages with ISIL and FPPS protocol and constructed Venn diagrams to identify the overlapping substrates and cleavages (identified in both experiments). These substrates were selected for further analysis to assign the identified cleavages to the secondary structure of each substrate using PSIPRED.^{22–24}

3. Results and Discussion

3. 1. Determination of Legumain Cleavage Specificity

For specificity profiling of the native proteome, we prepared protein lysates under mild lysis conditions to

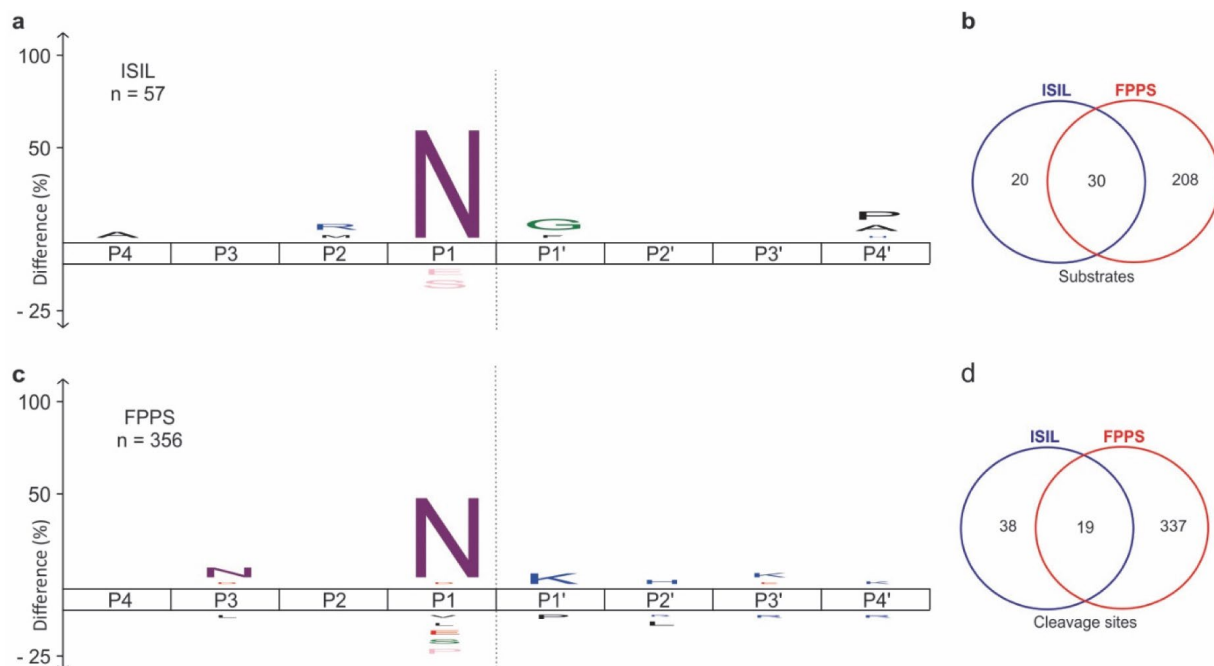


Figure 1. Legumain cleavage specificity profiling. (a) ISIL and (c) FPPS specificity profile of legumain for P4 to P4' positions presented as iceLogo²¹ with the representative number of determined cleavages used for the iceLogo construction (n-value). Venn diagrams of unique and shared legumain (b) substrates and (d) cleavage sites between ISIL and FPPS approaches.

preserve the protein fold. During the lysis, we inhibited proteolytic background with general protease inhibitors in order to minimise potential false positive hits as a result of endogenous proteases. After the treatment of the native proteome with recombinant human legumain we applied two different approaches for chemical labelling of neo-N-terminal peptides in order to identify the corresponding cleavage events (Fig 1). Using ISIL we identified 57 cleavage sites in 50 proteins, FPPS enabled us to identify 356 cleavages in 238 legumain substrates (Fig. 1b, c). This difference can be attributed to a better performance of the in-solution approach and the extensive peptide fractionation using the anion exchange resin.

Our results confirmed that P1 asparagine is the main determinant of legumain substrate specificity and that even cleavages of native protein substrates showed no extended cleavage specificity. Both tested approaches resulted in similar cleavage specificity profiles with a strong preference for asparagine in the P1 position (ISIL 68.4% and FPPS 52.2% of cleavages, respectively) and less prominently for the P1 aspartate (ISIL 8.8% and FPPS 9.0% of cleavages, respectively). These results are consistent with the canonical specificity of legumain reported in the CutDB²⁵ and PMAP²⁶ databases, which is based on 15 proteolytic events deposited in both databases. The cleavage specificity determined is also in a good agreement with previously reported profiling experiments performed on the denatured protein samples, where primary structure was shown to be the leading factor of protease-substrate recognition.¹² In both experimental setups the specificity for P1 asparagine

was highly similar under native (52.2–68.4%) as well as under denaturing conditions (85%). This led us to the conclusion that regardless of the native/denatured state of the substrates, legumain has a relatively stringent requirement for an Asn in the P1 position. Such observations were reported also by studies using combinatorial peptide substrate libraries which concluded that the P1 position is crucial for recognition of legumain substrates, while other positions did not have a significant role.¹³

3. 2. Validation of Substrate Processing in the Case of Prelamin-A/C

Our specificity profiling of legumain showed a considerable overlap of identified cleavages between the ISIL and FPPS approach (Fig. 1d). Among the 19 overlapping cleavage events (33% of the total ISIL-determined cleavage sites) we selected the cleavage after Asn283 in human prelamina-A/C (Uniprot code P02545, gene LMNA) for further validation. Prelamin-A/C is an important constituent of the nuclear lamina that provides framework for nuclear envelope. Maturation of prelamina-A/C involves several steps, including farnesylation of C-terminal – CAAX motif and subsequent proteolytic maturation by zinc metalloprotease ZMPSTE24.²⁷ Failure of prelamina-A/C proteolytic maturation due to protease absence or mutations was shown to result in its accumulation and consequently to development of several diseases.²⁸

We identified prelamina-A/C cleavage after Asn283 using both labelling approaches. The incubation with in-

that investigate sequence and structure specific features of legumain substrates. Further *in vivo* studies are therefore required to determine possible physiological relevance of identified cleavages and since legumain has been shown to be localized in the nucleus²⁹ there is a potential spatial link present in living cells.

3. 3. Structural Preferences for Legumain Cleavages

In addition to the sequence-based substrate specificity interpretation of the legumain substrate repertoire we also investigated the structural features of the cleaved sub-

Table 2. Structural determinants of 19 identified legumain cleavage sites determined using disordered regions and secondary structure prediction algorithms.

Gene name	Uniprot code	neo-N-terminal peptide sequence	Cleavage site	2D structure at cleavage site	3D structure at cleavage site
ACTN4	O43707	GTLEDQLSHLKQYER	N680	unstructured	n.a.
FLNB	O75369	ETSSILVESVTR	N2483	unstructured	2EEC
CSDE1	O75534	IMLLKKKQAR	N175	α -helical	2YTX
PNP	P00491	STVPGHAGR	R58	unstructured	1RSZ
LMNA	P02545	LVGAAHEELQQR	N283	α -helical	n.a.
NPM1	P06748	DENEHQLSLR	N35	unstructured	n.a.
HSP90AB1	P08238	ASDALDKIR	N46	unstructured	3NMQ
HNRNPL	P14866	YDDPHKTPASPVVHIR	N91	unstructured	n.a.
EEF1D	P29692	EEEDKEAAQLR	N164	unstructured	2MVM
RPL12	P30050	EIKVVYLR	N8	unstructured	n.a.
RPL22	P35268	LGGGVVTIER	N55	unstructured	n.a.
RPS16	P62249	GRPLEMIEPR	N35	unstructured	n.a.
RPL7A	P62424	FGIGQDIQPKR	N38	unstructured	n.a.
EIF5A	P63241	GFVVLKGR	N28	unstructured	3CPF
ACTG1	P63261	SYVGDEAQSQR	D51	unstructured	n.a.
TUBA1B	P68363	AAIATIKTKR	N329	α -helical	n.a.
PCBP1	Q15365	STAASRPPVTLR	N89	unstructured	n.a.
CNN3	Q15417	KIASKYDHQAEDLR	N18	unstructured	n.a.
RPL36	Q9Y3U8	KGHKVTKNVSKPR	N12	unstructured	n.a.

n.a. – not available

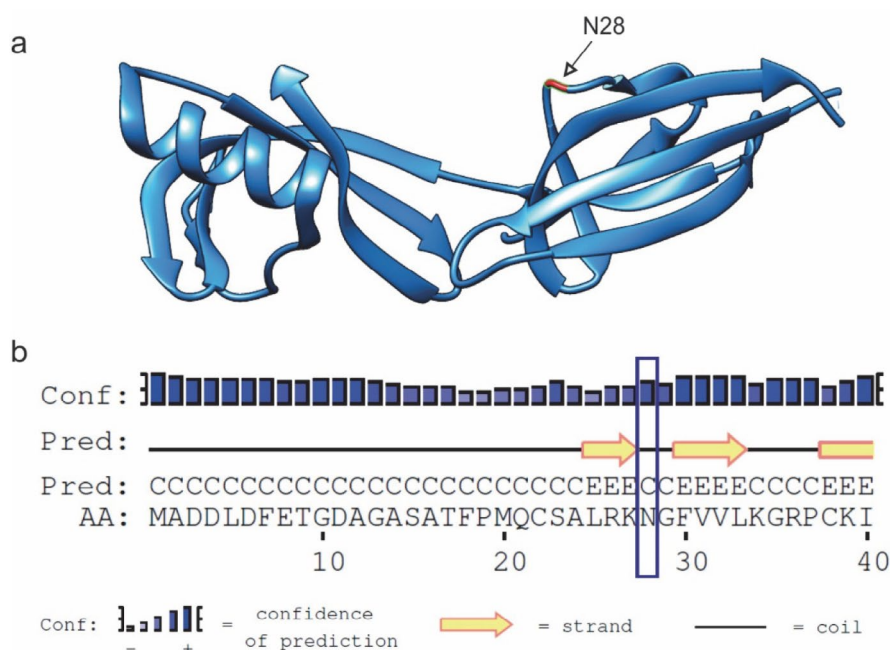


Figure 3. Example of a legumain cleavage site in a 3D protein structure. (a) The structure of eukaryotic translation initiation factor 5A-1 with annotated scissile site at asparagine 28 (For preparing this image the structure with PDB 3CPF was used). (b) An example of secondary structure prediction algorithm output for the region around Asn28 in eukaryotic translation initiation factor 5A-1 (marked in blue).

strates. We performed a detailed structural analysis on 19 substrates identified by both ISIL and FPPS approaches (Table 2, Appendix 1) and combined the exact cleavage site information to the secondary structural characteristics of each substrate using a 2D structure and disordered region prediction tool (i.e. PSIPRED protein sequence analysis workbench).²² The close inspection of individual secondary structure features has shown that the large majority of legumain cleavage sites are not located in the structured regions like alpha-helices or beta-sheets (84%). Since the unstructured elements are devoid of regular secondary structures they often serve as flexible linkers or loops connecting the organized secondary structure elements. Our observation that unstructured elements are more easily accessible to legumain proteolysis is in good agreement with the central proteolytic paradigm stating that most cleavages occur in easily accessible protein regions. Moreover, similar observations were also reported by other studies showing that largest number of proteolytic cleavages occurs in the loops, followed by alpha-helices and beta-sheets.^{30–33}

Among the identified substrates, 6 have known 3D structures of the cleavage site regions and we were able to confirm our observation, that cleavage sites are mainly located on unstructured regions characteristic for loops between protein domains or exposed tails near protein termini (Supplementary Figures 1–5). For example, in the crystal structure of eukaryotic translation initiation factor 5A-1 legumain cleaved the protein after an asparagine located in the unstructured region connecting two neighbouring beta-sheets (Fig 3), consistent with our predictions. For a more precise analysis a larger pool of cleavage sites and 3D structures would be required.

4. Conclusions

Determination of protease specificity provides the most basic information about protease-substrate interactions and helps us to understand why certain proteins are cleaved or processed by proteases. Whether a substrate cleavage will occur depends on several factors: (i) subsite cleavage specificity of a protease that recognizes an amino acid motif in a protein substrate, (ii) structural arrangement of a potential cleavage site(s) in a substrate (iii), presence of potential protease's exosites located outside the active site cleft and (iv), spatiotemporal co-localization of a protease and a corresponding substrate. Our study was focused on the first two factors and it showed that P1 asparagine (or less preferably aspartate) is the most important determinant of legumain specificity even in the processing of native proteins. The identified protein cleavages also revealed that legumain has a high preference for cleavages outside secondary structure elements, since only a minor portion of cleavages was found in the alpha-helical regions and none in the beta-sheets. The low number of

identified cleavage events in individual substrates showed that legumain is a highly selective protease, which promotes limited proteolysis rather than general protein degradation. Within the lysosomes, such limited proteolytic processing could serve as the first step in protein degradation, where legumain cleavage would increase exposure of proteins to other proteases. However, since legumain is also known to be secreted to extracellular space and translocated to the cell nucleus, its limited proteolysis could play an important role in cell signalling and other highly specific cellular processes.

5. Acknowledgments

The work was funded by the Slovenian Research Agency (P1-0140, J1-3602, and N1-0022 to B.T.; J1-0185 and J1-5449 to M.F.; and I0-0048 to D.T.) and the COST Action PROTEOSTASIS BM1307. The mass spectrometry proteomics data have been deposited to the ProteomeXchange Consortium via the PRIDE³⁴ partner repository with the dataset identifier PXD010466.

6. References

- Dall, E.; Brandstetter, H., *Proc Natl Acad Sci* **2013**, *110* (27), 10940–5. DOI:10.1073/pnas.1300686110
- Dall, E.; Brandstetter, H., *Biochimie* **2016**, *122*, 126–50. DOI:10.1016/j.biochi.2015.09.022
- Sepulveda, F. E.; Maschalidi, S.; Colisson, R.; Heslop, L.; Ghirelli, C.; Sakka, E.; Lennon-Dumenil, A. M.; Amigorena, S.; Cabanie, L.; Manoury, B., *Immunity* **2009**, *31* (5), 737–48. DOI:10.1016/j.immuni.2009.09.013
- Maschalidi, S.; Hassler, S.; Blanc, F.; Sepulveda, F. E.; Tohme, M.; Chignard, M.; van Endert, P.; Si-Tahar, M.; Descamps, D.; Manoury, B., *PLoS Pathog* **2012**, *8* (8), e1002841. DOI:10.1371/journal.ppat.1002841
- Descamps, D.; Le Gars, M.; Balloy, V.; Barbier, D.; Maschalidi, S.; Tohme, M.; Chignard, M.; Ramphal, R.; Manoury, B.; Salenave, J. M., *Proc Natl Acad Sci U S A* **2012**, *109* (5), 1619–24. DOI:10.1073/pnas.1108464109
- Liu, C.; Sun, C.; Huang, H.; Janda, K.; Edgington, T., *Cancer Res* **2003**, *63* (11), 2957–64.
- Luo, Y.; Zhou, H.; Krueger, J.; Kaplan, C.; Lee, S. H.; Dolman, C.; Markowitz, D.; Wu, W.; Liu, C.; Reisfeld, R. A.; Xiang, R., *J Clin Invest* **2006**, *116* (8), 2132–2141. DOI:10.1172/JCI27648
- Lunde, N. N.; Holm, S.; Dahl, T. B.; Elyouncha, I.; Sporsheim, B.; Gregersen, I.; Abbas, A.; Skjelland, M.; Espevik, T.; Solberg, R.; Johansen, H. T.; Halvorsen, B., *Atherosclerosis* **2017**, *257*, 216–223. DOI:10.1016/j.atherosclerosis.2016.11.026
- Ishizaki, T.; Erickson, A.; Kuric, E.; Shamloo, M.; Hara-Nishimura, I.; Inacio, A. R.; Wieloch, T.; Ruscher, K., *J Cereb Blood Flow Metab* **2010**, *30* (10), 1756–66. DOI:10.1038/jcbfm.2010.39

10. Zhang, Z.; Song, M.; Liu, X.; Kang, S. S.; Kwon, I. S.; Duong, D. M.; Seyfried, N. T.; Hu, W. T.; Liu, Z.; Wang, J. Z.; Cheng, L.; Sun, Y. E.; Yu, S. P.; Levey, A. L.; Ye, K., *Nat Med* **2014**, *20* (11), 1254–62. DOI:10.1038/nm.3700
11. Zhang, Z.; Song, M.; Liu, X.; Su Kang, S.; Duong, D. M.; Seyfried, N. T.; Cao, X.; Cheng, L.; Sun, Y. E.; Ping Yu, S.; Jia, J.; Levey, A. L.; Ye, K., *Nat Commun* **2015**, *6*, 8762. DOI:10.1038/ncomms9762
12. Vidmar, R.; Vizovisek, M.; Turk, D.; Turk, B.; Fonovic, M., *EMBO J* **2017**, *36* (16), 2455–2465. DOI:10.15252/embj.201796750
13. Poreba, M.; Solberg, R.; Rut, W.; Lunde, N. N.; Kasperkiewicz, P.; Snipas, S. J.; Mihelic, M.; Turk, D.; Turk, B.; Salvesen, G. S.; Drag, M., *Cell Chem Biol* **2016**, *23* (8), 1023–35.
14. Staes, A.; Impens, F.; Van Damme, P.; Ruttens, B.; Goethals, M.; Demol, H.; Timmerman, E.; Vandekerckhove, J.; Gevaert, K., *Nat Protoc* **2011**, *6* (8), 1130–41. DOI:10.1038/nprot.2011.355
15. Asara, J. M.; Zhang, X.; Zheng, B.; Christofk, H. H.; Wu, N.; Cantley, L. C., *J Proteome Res* **2006**, *5* (1), 155–63. DOI:10.1021/pr050334t
16. Vizovisek, M.; Vidmar, R.; Van Quickenberghe, E.; Impens, F.; Andjelkovic, U.; Sobotic, B.; Stoka, V.; Gevaert, K.; Turk, B.; Fonovic, M., *Proteomics* **2015**, *15* (14), 2479–90. DOI:10.1002/pmic.201400460
17. Wisniewski, J. R.; Zougman, A.; Mann, M., *J Proteome Res* **2009**, *8* (12), 5674–8. DOI:10.1021/pr900748n
18. Wisniewski, J. R.; Zougman, A.; Nagaraj, N.; Mann, M., *Nat Methods* **2009**, *6* (5), 359–62. DOI:10.1038/nmeth.1322
19. Cox, J.; Mann, M., *Nat Biotechnol* **2008**, *26* (12), 1367–72. DOI:10.1038/nbt.1511
20. Vizovisek, M.; Vidmar, R.; Fonovic, M., *Methods Mol Biol* **2017**, *1574*, 183–195. DOI:10.1007/978-1-4939-6850-3_13
21. Colaert, N.; Helsens, K.; Martens, L.; Vandekerckhove, J.; Gevaert, K., *Nat Methods* **2009**, *6* (11), 786–7. DOI:10.1038/nmeth1109-786
22. Buchan, D. W.; Minneci, F.; Nugent, T. C.; Bryson, K.; Jones, D. T., *Nucleic Acids Res* **2013**, *41*, W349–57. DOI:10.1093/nar/gkt381
23. McGuffin, L. J.; Bryson, K.; Jones, D. T., *Bioinformatics* **2000**, *16* (4), 404–5. DOI:10.1093/bioinformatics/16.4.404
24. Jones, D. T.; Cozzetto, D., *Bioinformatics* **2015**, *31* (6), 857–63. DOI:10.1093/bioinformatics/btu744
25. Igarashi, Y.; Eroshkin, A.; Gramatikova, S.; Gramatikoff, K.; Zhang, Y.; Smith, J. W.; Osterman, A. L.; Godzik, A., *Nucleic Acids Res* **2007**, *35* (Database issue), D546–9. DOI:10.1093/nar/gkl813
26. Igarashi, Y.; Heureux, E.; Doctor, K. S.; Talwar, P.; Gramatikova, S.; Gramatikoff, K.; Zhang, Y.; Blinov, M.; Ibragimova, S. S.; Boyd, S.; Ratnikov, B.; Cieplak, P.; Godzik, A.; Smith, J. W.; Osterman, A. L.; Eroshkin, A. M., *Nucleic Acids Res* **2009**, *37* (Database issue), D611–8. DOI:10.1093/nar/gkn683
27. Casasola, A.; Scalzo, D.; Nandakumar, V.; Halow, J.; Recillas-Targa, F.; Groudine, M.; Rincon-Arango, H., *Nucleus* **2016**, *7* (1), 84–102. DOI:10.1080/19491034.2016.1150397
28. Rankin, J.; Ellard, S., *Clin Genet* **2006**, *70* (4), 261–74. DOI:10.1111/j.1399-0004.2006.00677.x
29. Haugen, M. H.; Johansen, H. T.; Pettersen, S. J.; Solberg, R.; Brix, K.; Flatmark, K.; Maelandsmo, G. M., *PLoS One* **2013**, *8* (1), e52980. DOI:10.1371/journal.pone.0052980
30. Mahrus, S.; Trinidad, J. C.; Barkan, D. T.; Sali, A.; Burlingame, A. L.; Wells, J. A., *Cell* **2008**, *134* (5), 866–76. DOI:10.1016/j.cell.2008.08.012
31. Timmer, J. C.; Zhu, W.; Pop, C.; Regan, T.; Snipas, S. J.; Eroshkin, A. M.; Riedl, S. J.; Salvesen, G. S., *Nat Struct Mol Biol* **2009**, *16* (10), 1101–8. DOI:10.1038/nsmb.1668
32. Kazanov, M. D.; Igarashi, Y.; Eroshkin, A. M.; Cieplak, P.; Ratnikov, B.; Zhang, Y.; Li, Z.; Godzik, A.; Osterman, A. L.; Smith, J. W., *J Proteome Res* **2011**, *10* (8), 3642–51. DOI:10.1021/pr200271w
33. Ratnikov, B. I.; Cieplak, P.; Gramatikoff, K.; Pierce, J.; Eroshkin, A.; Igarashi, Y.; Kazanov, M.; Sun, Q.; Godzik, A.; Osterman, A.; Stec, B.; Strongin, A.; Smith, J. W., *Proc Natl Acad Sci* **2014**, *111* (40), E4148–55. DOI:10.1073/pnas.1406134111
34. Vizcaino, J. A.; Csordas, A.; Del-Toro, N.; Dianes, J. A.; Griss, J.; Lavidas, I.; Mayer, G.; Perez-Riverol, Y.; Reisinger, F.; Ternent, T.; Xu, Q. W.; Wang, R.; Hermjakob, H., *Nucleic Acids Res* **2016**, *44* (22), 11033. DOI:10.1093/nar/gkw880

Povzetek

Legumain je po svoji specifičnosti edinstvena lizosomalna proteaza, ki cepi C-terminalno od asparagina in v redkih primerih tudi za aspartatom. V eksperimentalnem delu smo izvedli profiliranje specifičnosti legumaina s proteomskim pristopom na osnovi kemijskega označevanja N-koncev z uporabo trideuteroacetilacije. Raziskava predstavlja prvo globalno analizo nativnih legumainskih substratov pri čemer smo potrdili visoko specifičnost legumaina za cepitev peptidne vezi za asparaginom. Na osnovi proteomskih rezultatov smo z bioinformatično analizo podatkov raziskovali tudi povezavo med identificiranimi proteolitičnimi cepitvami ter sekundarno in tridimenzionalno strukturo substratov legumaina.

Short communication

The Carboxypeptidase Activity of Cathepsin X is not Controlled by Endogenous Inhibitors

Urša Pečar Fonovič,^{1,*} Milica Perišić Nanut,² Nace Zidar,¹ Brigita Lenarčič³ and Janko Kos^{1,2}

¹ Faculty of Pharmacy, University of Ljubljana, Aškerčeva 7, 1000 Ljubljana, Slovenia

² Department of Biotechnology, Jožef Stefan Institute, Jamova 39, 1000 Ljubljana, Slovenia

³ Faculty of Chemistry and Chemical Technology, University of Ljubljana, Večna pot 113, 1000 Ljubljana, Slovenia

* Corresponding author: E-mail: ursa.pecarfonovic@ffa.uni-lj.si
Tel.: +386 1 4769 500; Fax: +386 1 4258 031

Received: 04-26-2018

Dedicated to the memory of Prof. Dr. Igor Kregar

Abstract

Cysteine cathepsins are peptidases with housekeeping functions that play different specific roles in different tissues. Endogenous peptidase inhibitors, such as cystatins and thyropins are the ultimate way of controlling their activity. It appears, however, that cathepsin X, a monocarboxypeptidase, whose overexpression is associated with several pathological processes, is not under the control of endogenous inhibitors. Inhibitors belonging to various groups inhibit other cathepsins tested, but none decrease the carboxypeptidase activity of cathepsin X. This absence of inhibitor control is another feature that distinguishes cathepsin X from other members of the cysteine peptidases.

Keywords: Cathepsin X; inhibitor; cystatin; stefin; thyropin

1. Introduction

Lysosomal cysteine cathepsins are expressed in the form of inactive precursors. When activated, their activity is controlled by endogenous inhibitors.¹ These inhibitors are divided into superfamilies of cystatins (which includes stefins, cystatins, kininogens and non-inhibitory fetuins) and thyropins.² Physiologically, endogenous inhibitors can act as emergency inhibitors that usually act on peptidases released from cells or lysosomes, from infecting microorganisms, or as regulatory inhibitors modulating peptidase activity. Regulatory inhibitors are further divided into 1) the threshold inhibitors that act when there is accidental activation of peptidases, 2) buffer type inhibitors that keep peptidases inactive in the absence of substrate or 3) delay type inhibitors that bind slowly to the active enzyme, allowing its action for a certain period of time.²

Cathepsin X is a carboxypeptidase expressed predominantly in immune and neuronal cells.³ It regulates the migration, adhesion, proliferation, and maturation of cells, together with phagocytosis and signal transduction.⁴ Its overexpression, increased activation or mislocalization may trigger pathological processes such as

cancer,^{5–9} neurodegenerative disorders¹⁰ or inflammatory diseases.¹¹

Studies describing the inhibitory action of endogenous peptidase inhibitors towards cathepsin X are rare and contradictory. While some did not report inhibition of cathepsin X by cystatins C and F^{12–15}, others reported its potent inhibition by cystatin C¹⁶ as well as by stefins A and B and chicken cystatin, but not by L-kininogen.

The aim of this study was to evaluate the inhibitory effect of a broader range of endogenous protease inhibitors from the cystatin and thyropin families on cathepsin X in comparison to the related cathepsins B and L. In the assay a recombinant cathepsin X, void of contamination with other cathepsins, and its specific substrate Abz-FEK(Dnp) OH were used.

2. Experimental

Activity assays were performed with recombinant cathepsins X (prepared in *P.pastoris*),¹⁷ B and L (both prepared in *E.coli*).^{18,19} Assay buffers were 100 mM sodium acetate buffer, pH 5.5 (for cathepsins X and L), 60 mM

acetate buffer pH 5.0 (for cathepsin B exopeptidase activity) and 100 mM phosphate buffer pH 6.0 (for cathepsin B endopeptidase activity). All assay buffers contained 5 mM cysteine, 1.5 mM EDTA and 0.1% PEG 8000. Enzymes were activated in the assay buffer at 37 °C for 5 min before assay.¹⁶ Cystatin F was activated for 15 min at 37 °C in the appropriate assay buffer containing 100 mM cysteine.¹⁵ The fluorogenic substrates Abz-FEK(Dnp)-OH,²⁰ Z-FR-AMC, Abz-GIVRAK(Dnp)-OH²¹ and Z-RR-AMC were used for determining cathepsins X, L and B exo- and endopeptidase activities, respectively. Cystatin F (wild type and truncated form $\Delta 15N$) was expressed in FreeStyle 293F cells,²² chicken cystatin was isolated from chicken egg white,²³ recombinant cystatin C and stefins A and B were expressed in *E. coli*,^{24,25} thyropins were from the laboratory of B. Lenarčič. Enzymes, substrates and inhibitor concentrations are summarized in Supplementary Table S1.

90 μ L of activated enzyme (20 nM cathepsin X or 0.5 nM cathepsin L or 0.6 nM/5.5 nM cathepsin B for its exo/ endopeptidase activity) was incubated for 30 min with 5 μ L of the inhibitor (100-fold molar excess over the enzyme) at 37 °C, then added to a black 96-well plate together with 5 μ L of substrate. The reaction was monitored continuously, at 37 °C, at 420 \times 10 nm with excitation at 320 \times 20 nm for Abz substrates and at 460 nm \times 10 nm with excitation at 380 nm \times 20 nm for AMC substrates.

3. Results and Discussion

Various peptidase inhibitors were tested in a standard kinetic assay to determine inhibition of cathepsin X.

Previous reports of their inhibitory activities towards cathepsin X are ambiguous, probably due to the use of native cathepsin X, isolated from human liver, later shown to be contaminated with cathepsin B¹² or of recombinant cathepsin X contaminated with cathepsin L which is needed for the activation of procathepsin X.²⁶ The substrates used, such as FR-AMC, were not specific, being also degraded by other cathepsins. Since most of the cystatins used in these studies (cystatin C, chicken cystatin, stefins A and B)¹⁶ potentially inhibit cathepsins L and B, it is very likely that the measured inhibition was in fact that of contaminating cathepsin B or L. In our study we used recombinant cathepsin X, containing cathepsin L below the detection limit of western blot and ELISA assays,¹⁷ and cathepsin X specific substrate Abz-FEK(Dnp)-OH.²⁶ The tested inhibitors (in 100-fold molar excess) did not significantly inhibit cathepsin X (Figure 1). The irreversible inhibitor of cysteine peptidases, E-64, was used as a control.

Inhibitors from the cystatin and thyropin families were included in the study, namely cystatins C, F (wild type and N-terminally truncated form¹⁵), chicken cystatin, stefins A and B, p41, equistatin, testicans 1 and 2 and thyroglobulin domains of nidogens 1 and 2 (domain 1 from nidogen 1 and domains 1 and 2 from nidogen 2). The results demonstrate the absence of inhibition, even at high inhibitor to enzyme ratios and are in line with studies on cystatins C and F.^{12–15} Inhibitory activity of thyropins has not yet been probed for cathepsin X. Like cystatins, they did not inhibit cathepsin X.

The same set of inhibitors was tested on endo- and exopeptidase (carboxypeptidase) activities of cathepsin B

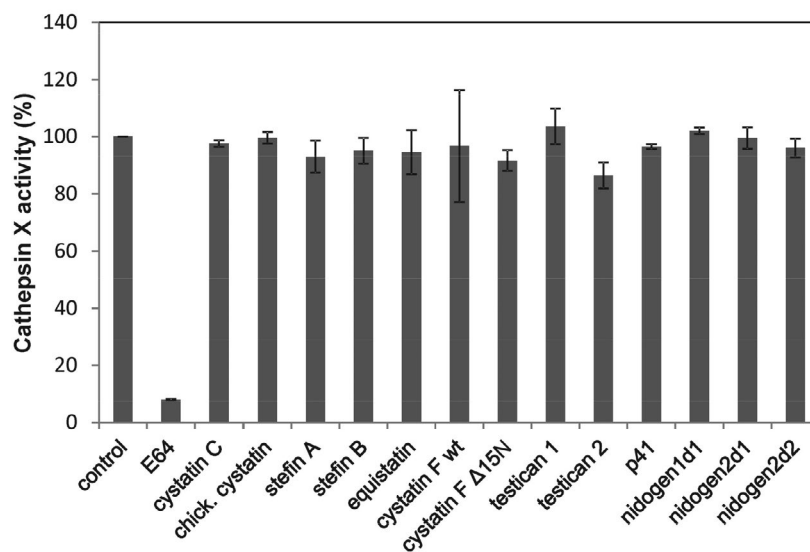


Figure 1: Cathepsin X is not inhibited by endogenous peptidase inhibitors.

Relative inhibition of cathepsin X by various inhibitors was tested in a kinetic assay. Concentrations of endogenous inhibitors were 2 μ M (100-fold higher than that of the enzyme), while E-64 was tested at 10 μ M concentration. Assay buffer was used in a control experiment. Values are the means of two or three independent experiments, each performed in duplicate \pm SEM.

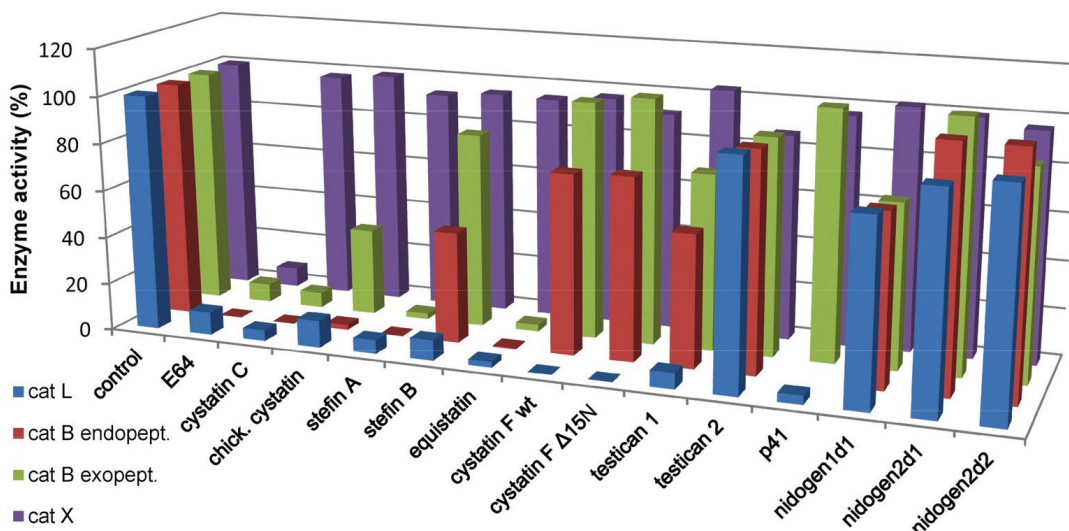


Figure 2: Comparison of the activities of endogenous inhibitors towards cathepsins X, B (exo- and endopeptidase activity) and L.

The relative inhibitory activities of cysteine cathepsins with various inhibitors was tested in a kinetic assay (p41 was not tested on cathepsin B endopeptidase activity). Concentrations of inhibitors were 100-fold higher than those of the enzymes, E-64, used as a positive control, was tested at 10 μ M concentration. Assay buffers were used in control experiments. Values are the means of two or three independent experiments, each performed in duplicate.

(Figure 2). Cystatin C, stefin A and equistatin potently inhibit both, endopeptidase and exopeptidase activities of cathepsin B, whereas stefin B, cystatin F and testican 1 are better inhibitors of endopeptidase activity. We also determined their inhibitory activities towards cathepsin L (Figure 2). As reported, cathepsin L was inhibited by the majority of inhibitors except testican 2 and nidogen 2.^{27,28} Nidogen 1 was not very effective in inhibiting cathepsin L.

4. Conclusions

Our results show that endogenous inhibitors of cysteine peptidases do not inhibit cathepsin X. Thus cathepsin X carboxypeptidase activity escapes this ultimate control. The possible physiological and pathological consequences of this observation have, however, not yet been addressed. The inhibition of other cathepsins, tested in parallel to cathepsin X with the same set of inhibitors, demonstrates a great difference in their potency, contrary to the general opinion that cystatins and thyrpins act in a broad, nonspecific fashion.

5. Acknowledgement

The authors thank prof. Roger Pain for a critical review of the manuscript. This work was supported by the Slovenian Research Agency grant P4-0127 (JK).

6. References

- B. Turk, D. Turk, V. Turk. *EMBO J* **2012**, *31*, 1630–1643. DOI:10.1038/emboj.2012.42
- B. Turk, D. Turk, G. S. Salvesen, *Curr Pharm Des* **2002**, *8*, 1623–1637. DOI:10.2174/1381612023394124
- J. Kos, A. Sekirnik, A. Premzl, V. Zavašnik Bergant, T. Langerholc, B. Turk, B. Werle, R. Golouh, U. Repnik, M. Jeras, V. Turk, *Exp Cell Res* **2005**, *306*, 103–113. DOI:10.1016/j.yexcr.2004.12.006
- J. Kos, Z. Jevnikar, N. Obermajer, *Cell Adh Migr* **2009**, *3*, 164–166. DOI:10.4161/cam.3.2.7403
- G. Rumpler, B. Becker, C. Hafner, M. McClelland, W. Stolz, M. Landthaler, R. Schmitt, A. Bosserhoff, T. Vogt, *Exp Dermatol* **2003**, *12*, 761–771. DOI:10.1111/j.0906-6705.2003.00082.x
- D. K. Nägler, S. Kruger, A. Kellner, E. Ziomek, R. Menard, P. Buhtz, M. Krams, A. Roessner, U. Kellner, *Prostate* **2004**, *60*, 109–119. DOI:10.1002/pros.20046
- S. Krueger, T. Kalinski, T. Hundertmark, T. Wex, D. Kuster, U. Peitz, M. Ebert, D.K. Nagler, U. Kellner, P. Melfertheiner, M. Naumann, C. Rocken, A. Roessner, *J Pathol* **2005**, *207*, 32–42. DOI:10.1002/path.1820
- J. Wang, L. Chen, Y. Li, X. Y. Guan, *PLoS One* **2011**, *6*, e24967. DOI:10.1371/journal.pone.0024967
- T. Vižin, I. J. Christensen, M. Wilhelmsen, H. J. Nielsen, J. Kos, *BMC Cancer* **2014**, *14*, 259. DOI:10.1186/1471-2407-14-259
- A. Pišlar, J. Kos, *Mol Neurobiol* **2014**, *49*, 1017–1030. DOI:10.1007/s12035-013-8576-6
- D. K. Nägler, A. M. Lechner, A. Oettl, K. Kozaczynska, H. P. Scheuber, C. Gippner-Steppert, V. Bogner, P. Biberthaler, M.

- Jochum, *J Immunol Methods* **2006**, *308*, 241–250. DOI:10.1016/j.jim.2005.11.002
- 12 C. Therrien, P. Lachance, T. Sulea, E. O. Purisima, H. Qi, E. Ziomek, A. Alvarez-Hernandez, W. R. Roush, R. Menard, *Biochemistry*, **2001**, *40*, 2702–2711. DOI:10.1021/bi002460a
- 13 D. K. Nägler, R. Zhang, W. Tam, T. Sulea, E. O. Purisima, R. Ménard, *Biochemistry* **1999**, *38*, 12648–12654 (1999). DOI:10.1021/bi991371z
- 14 T. Langerholc, V. Zavasnik-Bergant, B. Turk, V. Turk, M. Abrahamson, J. Kos, *FEBS J* **2005**, *272*, 1535–1545. DOI:10.1111/j.1742-4658.2005.04594.x
- 15 S. Magister, N. Obermajer, B. Mirković, U. Svajger, M. Renko, A. Softić, R. Romih, J. D. Colbert, C. Watts, J. Kos, *Eur J Cell Biol* **2012**, *91*, 391–401. DOI:10.1016/j.ejcb.2012.01.001
- 16 I. Klemencic, A. K. Carmona, M. H. Cezari, M. A. Juliano, L. Juliano, G. Guncar, D. Turk, I. Krizaj, V. Turk, B. Turk, *Eur J Biochem* **2000**, *267*, 5404–5412. DOI:10.1046/j.1432-1327.2000.01592.x
- 17 U. Pečar Fonovič, J. Kos, *Acta Chim. Slov.* **2009**, *56*, 985–988.
- 18 R. Kuhelj, M. Dolinar, J. Pungercar, V. Turk, *Eur J Biochem* **1995**, *229*, 533–539. DOI:10.1111/j.1432-1033.1995.0533k.x
- 19 M. Dolinar, D. B. Maganja, V. Turk, *Biol Chem Hoppe Seyler* **1995**, *376*, 385–388. DOI:10.1515/bchm3.1995.376.6.385
- 20 A. M. Sadaghiani, S. H. Verhelst, V. Gocheva, K. Hill, E. Majerova, S. Stinson, J. A. Joyce, M. Bogyo, *Chem Biol* **2007**, *14*, 499–511. DOI:10.1016/j.chembiol.2007.03.010
- 21 S. S. Cotrin, L. Puzer, W. A. de Souza Judice, L. Juliano, A.K. Carmona, M. A. Juliano. *Anal Biochem* **2004**, *335*, 244–252. DOI:10.1016/j.ab.2004.09.012
- 22 M. Perišič Nanut, J. Sabotič, U. Švajger, A. Jewett, J. Kos, *Front Immunol* **2017**, *8*, 1459. DOI:10.3389/fimmu.2017.01459
- 23 W. Bode, R. Engh, D. Musil, U. Thiele, R. Huber, A. Karshikov, J. Brzin, J. Kos, V. Turk, *EMBO J* **1988**, *7*, 2593–2599.
- 24 N. Cimerman, Preparation of some recombinant human cystatin C mutants and their characterisation, Ph.D. thesis, University of Ljubljana, Slovenia, **1993**.
- 25 R. Jerala, E. Zerovnik, K. Lohner, V. Turk, *Protein Eng* **1988**, *7*, 977–984. DOI:10.1093/protein/7.8.977
- 26 L. Puzer, S. S. Cotrin, M. H. Cezari, I. Y. Hirata, M. A. Juliano, I. Stefe, D. Turk, B. Turk, L. Juliano, A. K. Carmona, *Biol Chem* **2005**, *386*, 1191–1195.
- 27 A. Leonardi, B. Turk, V. Turk, *Biol Chem Hoppe Seyler*. **1996**, *377*, 319–21.
- 28 P. Meh, M. Pavsic, V. Turk, A. Baici, B. Lenarcic, *Biol Chem* **2005** *386*, 75–83. DOI:10.1515/BC.2005.010

Povzetek

Cisteinski katepsini so peptidaze z vzdrževalno vlogo in z različnimi specifičnimi vlogami v različnih tkivih. Endogeni inhibitorji peptidaz, kot so cistatini in tirocini, so bistveni za nadzor njihove aktivnosti, vendar pa rezultati kažejo, da katepsin X, monokarboksipeptidaza, katere prekomerno izražanje je povezano z več patološkimi procesi, ni pod nadzorom endogenih inhibitorjev. Inhibitorji, ki pripadajo različnim skupinam, so zavirali druge preizkušene katepsine, nobeden pa ni zmanjšal karboksipeptidazne aktivnosti katepsina X. Odsotnost takega nadzora z inhibitorji, je še ena značilnost, ki razlikuje katepsin X od drugih članov cisteinskih peptidaz.

Scientific paper

Spectrophotometric Determination of Ru(IV) Using 5-Hydroxyimino-4-imino-1,3-thiazolidin-2-one as a Novel Analytical Reagent

Oleksandr Tymoshuk,¹ Lesia Oleksiv,^{1,*} Liudmyla Khvalbota,² Taras Chaban³ and Ihor Patsay¹

¹ Department of Chemistry, Ivan Franko National University of Lviv, Kyryla and Mefodiya Str., 6, 79005 Lviv, Ukraine;

² Faculty of Chemical and Food Technology, Slovak University of Technology in Bratislava, Radlinského 9, 812 37 Bratislava, Slovakia

³ Faculty of Pharmacy, Danylo Halytsky Lviv National Medical University, Pekarska Str., 69, 79010 Lviv, Ukraine

* Corresponding author: E-mail: l_lozynska@ukr.net

Received: 07-17-2018

Abstract

The interaction of Ru(IV) ions with a novel analytical reagent – 5-hydroxyimino-4-imino-1,3-thiazolidin-2-one, by spectrophotometric method was investigated. The complex is formed at pH 5.0 in acetate buffer medium after heating in the boiling water bath (~371 K) for 25 min. The complex has maximum absorption at 350 nm and is stable for 24 h. Beer's law is valid over the concentration range of 0.5–6.1 $\mu\text{g mL}^{-1}$ for Ru(IV). The molar absorptivity at $\lambda = 350 \text{ nm}$ is $6.21 \times 10^3 \text{ L mol}^{-1} \text{ cm}^{-1}$. The limit of detection of this method is 0.2 $\mu\text{g mL}^{-1}$. The interfering effect of various cations and anions on the spectrophotometric determination of the Ru(IV) were investigated. The proposed method was successfully applied to the determination of Ru(IV) in alloys.

Keywords: Spectrophotometry; ruthenium(IV); 5-hydroxyimino-4-imino-1,3-thiazolidin-2-one.

1. Introduction

Ruthenium and its compounds are widely used in various fields: as a catalyst in chemical, petroleum, and pharmaceutical industries, in electrical contacts, resistors, as electrode materials for supercapacitors, and it improves the corrosion properties of alloys, etc.^{1–3} There is a need to develop sensitive, simple and inexpensive methods for the quantitative determination of ruthenium in different samples. For the determination of ruthenium, different analytical techniques such as: voltammetry, atomic absorption spectrometry, high performance liquid-chromatography, thin-layer chromatography, inductively coupled plasma atomic emission, inductively coupled plasma mass spectroscopy are used.³ But spectrophotometric methods have been widely used thanks to their simplicity, versatility and cheapness.^{3–12}

For spectrophotometric determination of ruthenium, S and N containing organic compounds are widely

used.^{3–6,8–12} Azolidones belong to such compounds. This class of organic compounds was discovered in the middle of the 20th century.¹³ These compounds exhibit different biological activity, in particular hypoglycemic, antimicrobial, fungicidal, antiviral, antiinflammatory, and antitumor.^{14–16}

In our previous studies, the physicochemical properties of the new reagents: 5-hydroxyimino-4-imino-1,3-thiazolidin-2-one (HITO), 4-[N⁷-(4-imino-2-oxo-thiazolidin-5-ylidene)-hydrazino]-benzenesulfonic acid and 1-(5-benzylthiazol-2-yl)azonaphthalen-2-ol, which belong to the class of azolidones, and the interaction of Pd(II), Rh(III), Pt(IV), Ir(IV), Cu(II), Zn(II), Cd(II), Ni(II), and Hg(II) ions with these reagents were investigated^{17–28} and the methods of their determination with good metrological characteristics were proposed.^{18–25,27,28} Therefore in this paper, we investigated the interaction of ruthenium(IV) ions with 5-hydroxyimino-4-imino-1,3-thiazolidin-2-one.

2. Experimental

2.1. Apparatus

A ULAB 108-UV computerized spectrophotometer equipped with 1.0 cm quartz cells was used for absorbance measurements. Absorption spectra were obtained in the wavelength range of 240–600 nm with the step of 2 nm using distilled water as a blank.

The pH measurements and adjustments were performed using pH-meter model pH-150 M equipped with a combination glass electrode.

Voltammetric measurements were carried out using oscillopolarograph CLA-03 and computerized polarographic setup equipped with linear potential scan in three-electrode cell (indicator electrode – dropping mercury electrode, reference electrode – saturated calomel electrode and auxiliary electrode – platinum).

Spectrometer Bruker Avance (400 MHz) was used for registration ^1H NMR spectra of compounds dissolved in DMSO-d_6 , internal reference of TMS.

2.2. Reagents

All chemicals used in the research were analytically pure and all aqueous solutions were prepared using distilled water.

The stock solution of Ru(IV) ($[\text{RuCl}_6]^{2-}$) was prepared by sintering the exact mass of pure metallic ruthenium (99.99%) with the oxidizing mixture of NaOH and NaNO_3 (3:1) in a corundum crucible at 900 K (45–60 min). The obtained fusion was dissolved in 3.0 mol L^{-1} HCl. The form of Ru(IV) in the obtained stock solution was identified by the comparison of its absorption spectra with the ones described in the literature.²⁹ Because of the possible losses during sintering, the obtained solution of Ru(IV) was additionally standardized using iodometric titration.^{3,5} Working solutions of Ru(IV) were prepared by suitable dilution of the stock solution with 1.0 mol L^{-1} hydrochloric acid.

The stock solution of 5-hydroxyimino-4-imino-1,3-thiazolidin-2-one was prepared by the dissolution of an exact mass of the reagent in ethanol (96% v/v). Working solution of HITO was prepared by dilution the stock solution with water. Synthesis of HITO was carried out according to the methodology given in the literature,³⁰ the only difference was the use of 10% HCl instead of 5%, that increased the practical yield of the reagent: 5.8 g (50 mmol) 4-iminothiazolidine-2-one in 10% HCl was placed in a 100 mL round-bottomed flask with a mechanical stirrer and was cooled to 273 K. Then the solution of 10.5 g sodium nitrite in 20 mL of water was added dropwise by stirring for 3 h and the resulting mixture was left for 12 h at room temperature. The precipitate was filtered, washed with water and acetone, and dried at 60 °C. The yield was 70%. The melting point is 477–480 K. After that the HITO was recrystallized from the ethanol. ^1H NMR (400 MHz, DMSO-d_6 ; δ , ppm): 8.98 s (H,

NH), 9.34 s (H, NH), 13.10 s (H, OH). The purity of HITO was determined chromatographically with a mass spectrometric detection and it was 100%.

The solutions of CH_3COONa and NaOH were prepared by dissolving of appropriate amount of CH_3COONa and NaOH in water. The solutions of HCl and CH_3COOH were obtained by dilution of concentrated HCl and CH_3COOH with water. The universal buffer solutions (UBS) were prepared by mixing H_3PO_4 , H_3BO_3 and CH_3COOH .³¹

2.3. Procedure

Spectral and protolytic characteristics of the HITO

In a series of 25.0 mL calibrated flask the volumes of HITO (8.0×10^{-3} mol L^{-1}), NaCl (2.0 mol L^{-1}), UBS (1.5 mol L^{-1}) and distilled water (~15 mL) were added. Then pH was adjusted in the acceptable range of 2.0–12.0 by NaOH (4.0 mol L^{-1}) and distilled water was added up to the mark. For pH 1.0 the solution was prepared in a similar way, but without adding the UBS and pH was adjusted by HCl (6.0 mol L^{-1}). Then the absorption spectra were measured against the distilled water.

Recommended procedure for determination of Ru(IV) by using HITO

An aliquot of the solution that contained 12.5–152.5 μg of Ru(IV) was transferred into a 25.0 mL volumetric flask. To this solution 0.125 mL of 8.0×10^{-3} mol L^{-1} HITO, 1.25 mL of 2.0 mol L^{-1} NaCl, 2.0 mL of 4.0 mol L^{-1} CH_3COONa , and distilled water (~15 mL) were added. Then the pH (pH 5.0) was adjusted by means of CH_3COOH or CH_3COONa solutions and distilled water was added to complete the volume. After that the solutions were heated in the boiling water bath (~371 K) for 25 min and cooled to room temperature (~293–295 K). The absorbance was measured at 350 nm against a reagent blank, prepared in the same way but without the addition of Ru(IV).

Determination of ruthenium in the alloys

The $\text{Ce}_{45}\text{Ru}_{25}\text{Ga}_{20}$ and TbRuGa_5 alloys were prepared by art melting of pure components (not less than 99.9%) under an argon atmosphere. Then the alloys were annealed in evacuated quartz ampoules at 870 K for 720 h.³²

0.05–0.1 g of the sample of alloy were dissolved in 10 mL of HCl + HNO_3 (1:1) mix. The obtained solution was evaporated to wet salts and dissolved in 50.0 mL of 3.0 mol L^{-1} HCl solution. If the alloy dissolved incompletely sintering of the new sample with oxidative mixture of NaOH and NaNO_3 (1:3) was carried out. The obtained solution was dissolved in HCl of 3.0 mol L^{-1} and the content of the beaker was quantitatively transferred into a 250.0 mL volumetric flask and diluted to the mark with distilled water. If necessary, the solution with lower concentration of ruthenium was prepared by dilution of stock solution with 1.0 mol L^{-1} hydrochloric acid. For ruthenium

mium determination, the aliquots of alloys (0.5–1.0 mL) were analyzed as described previously in “Recommended procedure for determination of Ru(IV) by using HITO”. The content of ruthenium was calculated using the method of a normal calibration curve. Voltammetric determination of ruthenium(IV) ions using pyrocatechol violet at pH 4.0 (polarizing range of -0.5 to -1.5 V and the potential sweep rate of 0.5 V s^{-1}) was used as the reference method.³³

3. Results and Discussion

3. 1. Spectral and Protolytic Characteristics of HITO in Water Medium

The new analytical reagent, 5-hydroxyimino-4-imino-1,3-thiazolidin-2-one (Fig. 1), is a sand color powder, which is poorly soluble in water (0.05 g L^{-1}), but soluble in ethanol, methanol, *n*-propanol, isoamyl alcohol, ethylene glycol, glycerol, dimethylformamide and dimethylsulfoxide.

Previous research of the spectral characteristics of HITO^{18–22} has shown that its absorbance spectra depend on pH (Fig. 2). At pH 1.0–6.0 HITO has a maximum at the wavelength of 264 nm, pH 7.0–267 nm and at pH 8.0–12.0 two absorption bands: $\lambda = 278 \text{ nm}$, $\lambda = 330 \text{ nm}$. Beer's law is applicable at 256 nm (pH 5.0) over a wide concentration range (Fig. 3). The molar absorptivity at $\lambda = 256 \text{ nm}$ is $1.60 \times 10^4 \text{ L mol}^{-1} \text{ cm}^{-1}$ and at $\lambda = 278 \text{ nm} - 1.24 \times 10^4 \text{ L mol}^{-1} \text{ cm}^{-1}$, $\lambda = 330 \text{ nm} - 1.02 \times 10^4 \text{ L mol}^{-1} \text{ cm}^{-1}$. The acid dissociation constant of HITO was found ($\text{p}K_a = 7.1$). This indicates that HITO is a weak acid.

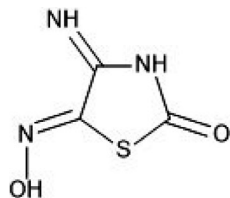


Fig 1. Structural formula of the HITO.

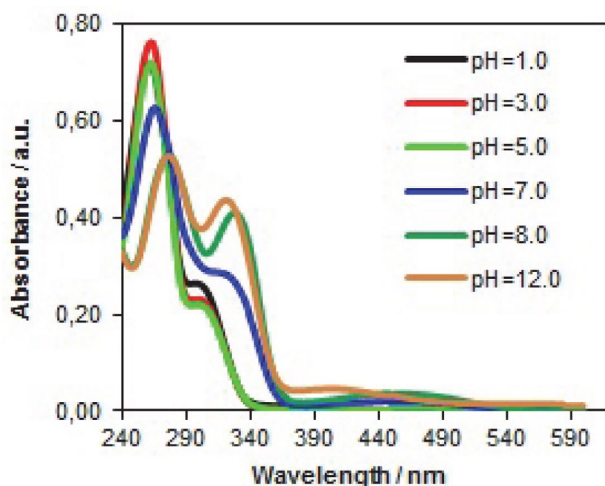


Fig 2. Absorbance spectra of HITO at different pH.

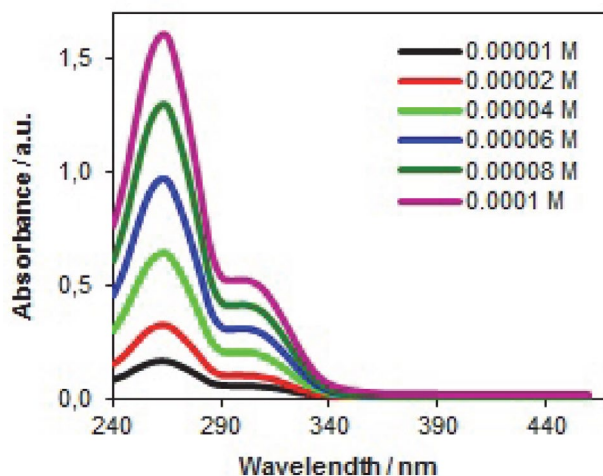
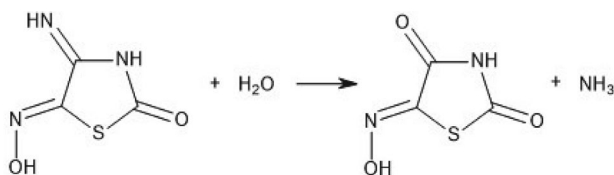


Fig 3. Absorbance spectra of HITO of different molar concentration.

The experimental results show that the absorbance spectra of HITO change over time in the range of pH 6.0–12.0. The influence of oxygen on the shape of absorption spectra of HITO over time at pH 8.0 and pH 9.0 was checked and it was found that oxygen does not affect the shape of absorption spectra. Therefore, we consider that changes in absorbance spectra of a reagent in the range of pH 6.0–12.0 are related to the hydrolysis of the imino group, which lasts for 60 min (Scheme 1). This process is irreversible, since after acidification of solutions to pH 2.0 spectrum of the reagent did not coincide with the spectrum of HITO in acidic media.



Scheme 1. Hydrolysis of 5-hydroxyimino-4-imino-1,3-thiazolidin-2-one.

3. 2. Interaction of Ru(IV) Ions with HITO

HITO forms with Ru(IV) ions a complex compound of sandy color in weakly acidic medium, just like with Pd(II), Pt(IV), Rh(III), and Ir(IV)^{18–22}. The absorbance spectra of the reagent itself and Ru(IV)-HITO complex are shown in Fig. 4. According to Fig. 4, the maximum difference in absorbance of the HITO and complex compound is at 350 nm. Thus all further absorbance measurements were carried out at 350 nm wavelength against reagent blank (where the absorbance of the reagent is negligible).

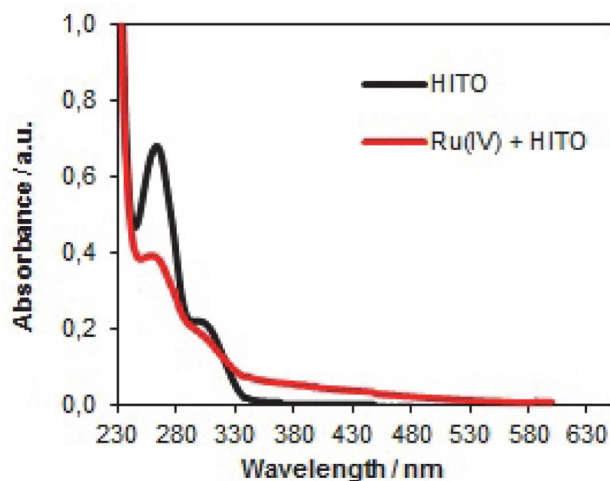


Fig 4. Absorbance spectra of reagent and complex Ru(IV) with HITO.

The effect of pH on the absorbance of Ru(IV)-HITO complex compound was investigated over the range 1.0–7.0 in order to find the optimum conditions (Fig. 5). The optimum pH range for complex formation lies between pH 4.5–5.5. So, further investigations were carried out at pH 5.0.

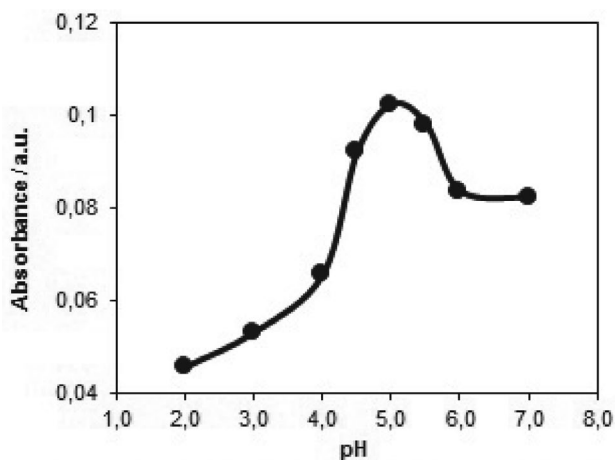


Fig 5. Effect of acidity on the maximum yield of Ru(IV) with HITO colored complex.

The investigation of the influence of ionic strength on the maximum yield of the complex is necessary for the study of optimal conditions for complexation. Therefore, the influence of the concentration and nature of anions of sodium salts (NaCl, NaNO₃, NaClO₄, Na₂SO₄, CH₃COONa) was investigated. The yield of the complex practically does not depend on the nature of anion. The SO₄²⁻ and NO₃⁻ ions practically do not affect the yield of complex, ClO₄⁻ – in large surpluses slightly decreases the yield of the complex. The yield of the complex insignificantly increases in

the presence of Cl⁻ and CH₃COO⁻ ions. Therefore, NaCl and CH₃COONa were chosen as a reaction medium.

The interaction of Ru(IV) ions with HITO at room temperature (~291–296 K) occurs very slowly. So the possibility of accelerating this process by heating the system in the boiling water bath (~371 K) was investigated (Fig. 6). The results show the maximum yield of the complex is observed after heating for 25 min in the boiling water bath (~371 K). The rapid formation of the Ru(IV)-HITO complex during heating can be related to reduction of the kinetic inertness of the [RuCl₆]²⁻ complex. The Ru(IV)-HITO complex is stable for 24 h.

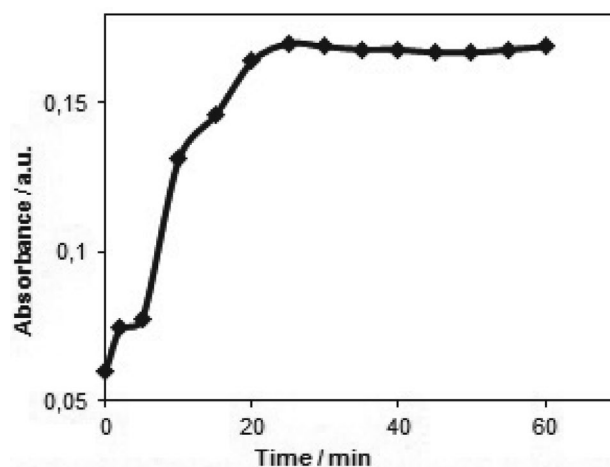


Fig 6. Effect of heating time on the maximum yield of Ru(IV) with HITO colored complex.

The composition of the complex was determined by the mole-ratio method and the method of continuous variations (Fig. 7). The results of both methods agree and show that the molar ratio of Ru(IV) to HITO is 1:1. It was found that a 1.5–2-fold molar excess of the reagent is suffi-

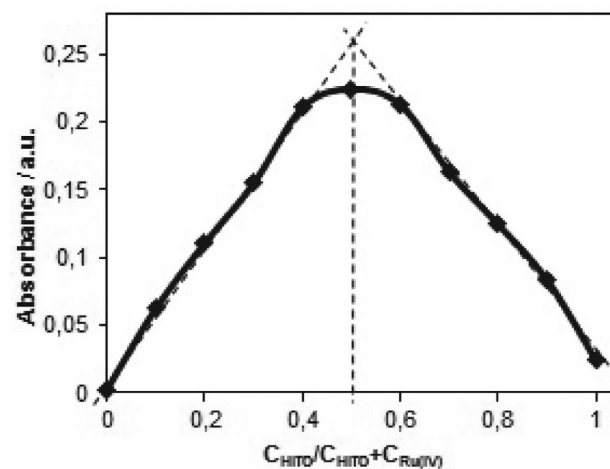
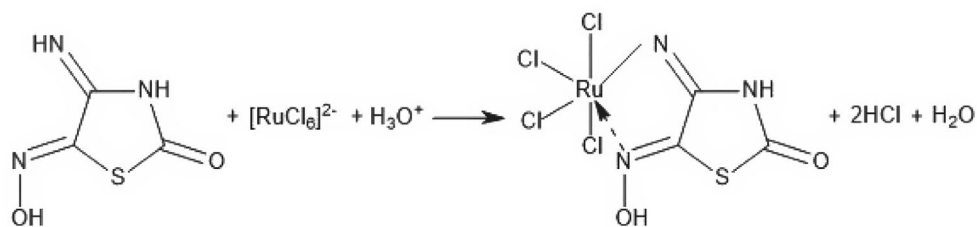


Fig 7. The method of continuous variations.



Scheme 2. The proposed scheme of Ru-HITO complex formation.

cient to obtain maximum absorbances of the Ru(IV)-HITO complex. The formal stability constant is 5.1×10^6 .

Based on the experimental results obtained from the study of the interaction of Ru(IV) ions with HITO and the data given in the literature,^{34,35} it can be assumed that the complex formation most probably takes place as shown in Scheme 2.

Under the optimum conditions a calibration graph for Ru(IV) was obtained. The Beer's law is obeyed in the range from 0.5 to 6.1 $\mu\text{g mL}^{-1}$ for ruthenium(IV). The molar absorptivity is $6.21 \times 10^3 \text{ L mol}^{-1} \text{ cm}^{-1}$. The metrological characteristics of spectrophotometric determination of ruthenium(IV) with HITO are given in Table 1.

Table 1. The metrological characteristics of spectrophotometric determination of the Ru(IV) with HITO ($C(\text{HITO}) = 8.0 \times 10^{-4} \text{ mol L}^{-1}$; $C(\text{CH}_3\text{COOH} + \text{CH}_3\text{COONa}) = 0.32 \text{ mol L}^{-1}$; $C(\text{NaCl}) = 0.1 \text{ mol L}^{-1}$; $\text{pH} = 5.0$; $\lambda = 350 \text{ nm}$; $l = 1.0 \text{ cm}$; $n = 5$; $P = 0.95$)

Characteristic	Value
Limits of Beer's law, $C_{\text{Ru(IV)}}$, $\mu\text{g mL}^{-1}$	0.5–6.1
Calibration equation, $C_{\text{Ru(IV)}}$, $\mu\text{g mL}^{-1}$	$\Delta A = 0.02 + 0.06 \times C$
Limit of detection, $C_{\text{Ru(IV)}}$, $\mu\text{g mL}^{-1}$	0.2
Limit of quantification, $C_{\text{Ru(IV)}}$, $\mu\text{g mL}^{-1}$	0.6
Correlation coefficient, R	0.9993

3. 3. Effect of Foreign Ions on the Determination of Ru(IV)

The effect of some potentially interfering ions on the determination of ruthenium(IV) was investigated (Table

2). According to the obtained results most metals, which often accompany ruthenium, such as Ni(II), Co(II), Zn(II), Cd(II), Pb(II), Mn(II), REE, and other metals, do not interfere on the determination of Ru(IV). Instead, the technique is characterized by low selectivity concerning the noble metals or Cu(II) and Fe(III). Ag(I) interferences significantly, even with tolerance limits up to 0.1, which is due to the influence of chloride ions that are in the solution. The presence of many anions, which were investigated, does not interfere (except EDTA) with the determination of Ru(IV). The selectivity to some cations can be increased using masking agents. For example, Cu(II) and Fe(III) were masked with tartrate ions (the tolerance limits reach 2 for Cu(II) and 4 for Fe(III)), citrate ions (the tolerance limits reach 10 for Cu(II) and 15 for Fe(III)) and phosphate ions (the tolerance limits reach 5 for Cu(II) and 10 for Fe(III)).

3. 4. Application of the Method

In order to verify the possibility of the proposed method usage, initially the determination of ruthenium in synthetic samples was carried out. These solutions were prepared by adding known amount of the Ru(IV). The results of analysis Ru(IV) in synthetic mixture are given in Table 3.

The method was also applied to the determination of Ru(IV) in two samples of three-component alloys (Table 4). When ruthenium is added into alloys, mechanical strength increases significantly, while anticorrosion pro-

Table 2. Tolerance limits of foreign ions in Ru(IV) spectrophotometric determination using HITO ($C(\text{HITO}) = 8.0 \times 10^{-4} \text{ mol L}^{-1}$; $C(\text{Ru(IV)}) = 2.0 \times 10^{-5} \text{ mol L}^{-1}$; $C(\text{NaCl}) = 0.1 \text{ mol L}^{-1}$; $C(\text{CH}_3\text{COOH} + \text{CH}_3\text{COONa}) = 0.32 \text{ mol L}^{-1}$; $\text{pH} = 5.0$; $\lambda = 350 \text{ nm}$; $l = 1.0 \text{ cm}$)

Ion	$C_{\text{ion}}:C_{\text{Ru(IV)}}$	Ion	$C_{\text{ion}}:C_{\text{Ru(IV)}}$	Ion	$C_{\text{ion}}:C_{\text{Ru(IV)}}$
Pd(II)	0.2	Cu(II)	0.4	Al(III)	30
Ir(IV)	0.15	Pb(II)	100	Ba(II)	>200
Rh(III)	0.15	Cd(II)	100	Mg(II), Ca(II)	>200
Pt(IV)	0.14	Zn(II)	100	$\text{C}_2\text{O}_4^{2-}$	100
Au(III)	5	Yb(III)	>200	F^-	>200
Ag(I)	<0.1	Tb(III)	>200	SiO_3^{2-}	>200
Hg(II)	5	Ho(III)	>200	EDTA	5
Co(II)	50	Gd(III)	>200	Sal^-	45
Ni(II)	150	Ga(III)	10	Citr^{3-}	>200
Fe(III)	0.6	Ce(IV)	10	Tart^{2-}	50
Mn(II)	100	Sn(II)	3	PO_4^{3-}	100

Table 3. Determination of Ru(IV) with HITO in synthetic solutions (n = 3; P = 0.95)

Modeling solution	$C_{Ru}:C_{ion}$	Added Ru(IV), μg	Found Ru(IV), $\bar{x} \pm \frac{s \times t_{\alpha}}{\sqrt{n}}$, μg	RSD, %
Ru–Pd–Ni	1:0.1:100	38.0	39.9 \pm 3.8	4.0
Ru–Pt–Co	1:0.1:30	38.0	39.2 \pm 2.9	3.1
Ru–Rh–Zn	1:0.1:50	38.0	39.6 \pm 1.9	2.0

Table 4. Determination of ruthenium(IV) in alloys (n = 3; P = 0.95)

Intermetallides	Spectrophotometry			Voltammetry	
	ω_{Ru}^{calc} , %	$\omega_{Ru}^{pr} \pm \frac{S \times t_{\alpha}}{\sqrt{n}}$, %	RSD, %	$\omega_{Ru}^{pr} \pm \frac{S \times t_{\alpha}}{\sqrt{n}}$, %	RSD, %
Ce ₄₅ Ru ₂₅ Ga ₂₀	23.1	23.0 \pm 0.9	1.6	23.2 \pm 1.2	2.1
TbRuGa ₅	16.6	16.4 \pm 0.8	2.0	16.7 \pm 0.6	1.4

erties, conductivity, etc. are improved. For these reasons, it is necessary to control the content of ruthenium in multicomponent systems.

The results are in perfect agreement with the ones

obtained by voltammetric method. According to the data presented in Table 4 and Table 5, the presented method can be applied to real samples with good reproducibility and accuracy.

Table 5. Comparison of the proposed method with other spectrophotometric methods for the determination of ruthenium(IV)

Reagent	Conditions	λ_{max} , nm	ϵ_{max} , L mol ⁻¹ cm ⁻¹	Linear range, $\mu\text{g mL}^{-1}$	Interfering ions
<i>N,N'</i> -diphenylthiourea ⁴	HCl + C ₂ H ₅ OH, 6 mol L ⁻¹ HCl, 5 min (358 K); CHCl ₃ , 30 min (373 K)	630; 650	–; –	6–18; 1.5–7.5	–; Pt(IV), Fe(II)
	Quercetin ⁷	0.01–0.1 mol L ⁻¹ HCl, CH ₃ OH + H ₂ O (1:1)	291	5.0 \times 10 ³	0.11–30
1,10-Phenanthroline ^{4,8}	pH 6.0, 2 h (373 K)	448	1.9 \times 10 ⁴	0.1–1.5	Platinoids
2-[(5-Bromo-2-pyridylazo)]-5-diethylaminophenol and <i>N</i> -hydroxy- <i>N,N'</i> -diphenylbenzamide ⁹	CH ₂ Cl ₂ , sodium citrate dihydrate, sodium acetate	560	2.99 \times 10 ⁴	0.2–2.8	Pd(II), Mn(II), Pb(II)
1,4-(2,4-Diphenylthiosemicarbazide) ⁴	5.5–6.5 mol L ⁻¹ HCl, CHCl ₃ , 10–15 min (373 K)	565	1.0 \times 10 ⁴	0.5–15.0	Oxidants
<i>p</i> -Nitrosodimethylaniline ⁴	pH 4.0, 50 min (323 K)	610	5.7 \times 10 ⁴	0.3–3.0	Platinoids
Sulphochlorophenolorhodanine ^{5,10,11}	2 mol L ⁻¹ HCl + 10 mol L ⁻¹ CH ₃ COOH, 30 min (353 K)	500	1.6 \times 10 ⁴	0.5–30	Pt(IV), Rh(III)
Sulphobenzolazophenolorodanin ¹⁰	pH 1.0–3.0, surfactants	540	4.0 \times 10 ⁴	–	–
Xylenol orange ¹²	pH 6.0	575	3.23 \times 10 ³	0.2–2.5	Al(III), V(IV), Cd(II), Cu(II), Ni(II), Zr(IV), Fe(III), Hf(IV), Zn(II), Co(II), Pb(II), Pd, Pt, Rh
5-hydroxyimino-4-imino-1,3-thiazolidin-2-one	pH 5.0	350	6.21 \times 10 ³	0.5–6.1	Platinoids, Cu(II), Fe(III), Ag(I)

3. 5. Comparison with other Spectrophotometric Methods

The proposed method has a better selectivity relative to Ni(II), Co(II), Mn(II), Cd(II), Zn(II), Pb(II), REE, etc. in comparison with other spectrophotometric methods for Ru determination mentioned in Table 5. There is no need to use highly acidic media and organic solvents.

4. Conclusions

This work presents the spectral and protolytic characteristics of the new analytical reagent – HITO and a new spectrophotometric method for the ruthenium(IV) ions determination with this reagent. The developed method is simple, reproducible, accurate, sufficiently sensitive and selective. It does not require the separation of the matrix and the use of toxic solvents. This method was successfully used for the determination of Ru(IV) in alloys and synthetic mixtures.

5. References

- Q. Li, S. Zheng, Y. Xu, H. Xue, H. Pang, *Chem. Eng. J.* **2018**, 333, 505–518. DOI:10.1016/j.cej.2017.09.170
- L. Wang, T. Liu, *Chin. J. Catal.* **2018**, 39, 327–333. DOI:10.1016/S1872-2067(17)62994-2
- M. Balcerzak, *Crit. Rev. Anal. Chem.* **2002**, 32, 181–226. DOI:10.1080/10408340290765524
- S. I. Ginzburg, N. A. Yezerskaya, I. V. Prokof'eva, N. V. Fedorenko, V. I. Shlenskaya, N. K. Belsky, *Analiticheskaya Khimiya Platinovykh Metallov*, Nauka, Moscow, Russia, 1972, p. 613.
- Ya. A. Zolotov, G. M. Varshal, V. M. Ivanov, *Analiticheskaya Khimiya Metallov Platinovoi Gruppy*, Editorial URSS, Moscow, Russia, 2003, p. 592.
- T. D. Avtokratova, *Analiticheskaya Khimiya Ruteniya*, IAN SSSR, Moscow, Russia, 1972, p. 264.
- M. Balcerzak, M. Kopacz, A. Kosiorek, E. Swiecicka, S. Kus, *Anal. Sci.* **2004**, 20, 1333–1337. DOI:10.2116/analsci.20.1333
- A. V. Bashilov, N. M. Kuzmin, V. K. Runov, *Zh. Anal. Khim.* **1998**, 53, 738–743.
- P. Ratre, D. Kumar, *Int. J. ChemTech Res.* **2014**, 6, 236–247.
- R. F. Gur'eva, S. B. Savvin, *Usp. Khim.* **1998**, 67, 236–251. DOI:10.1070/RC1998v067n03ABEH000375
- R. F. Gur'eva, S. B. Savvin, *Zh. Anal. Khim.* **1995**, 50, 1150–1157.
- T. Vrublev's'ka, O. Solovey, O. Volyanyk, *Visnyk of the Lviv University. Series Chemistry* **2003**, 43, 126–129.
- R. S. Lebedev, *Russ. Phys. J.* **2002**, 45, 822–830. DOI:10.1023/A:1021928817028
- D. Kaminsky, B. Zimenkovsky, R. Lesyk, *Eur. J. Med. Chem.* **2009**, 44, 3627–3636. DOI:10.1016/j.ejmech.2009.02.023
- R. R. Panchuk, V. V. Chumak, M. R. Fil', D. Ya. Havrylyuk, B. S. Zimenkovsky, R. B. Lesyk, R. S. Stoika, *Biopolym. Cell* **2012**, 28, 121–128. DOI:10.7124/bc.00003D
- T. I. Chaban, O. V. Klenina, B.S. Zimenkovsky, I.G. Chaban, V. V. Ogurtsov, L. S. Shelepeten, *Pharma Chem.* **2016**, 8, 534–542.
- A. Tupys, J. Kalemkiewicz, Y. Ostapiuk, V. Matiichuk, O. Tymoshuk, E. Woźnicka, L. Byczyński, *J. Therm. Anal. Calorim.* **2017**, 127, 2233–2242. DOI:10.1007/s10973-016-5784-0
- L. Lozynska, O. Tymoshuk, *Chem. Chem. Technol.* **2013**, 7, 391–395. DOI:10.23939/chcht07.04.391
- L. Lozynska, O. Tymoshuk, In: O.L. Berezko, *The Interaction of 5-hydroxyimino-4-imino-1,3-thiazolidin-2-one with Platinum(IV) Ions*, 3rd International Conference of Young Scientists CCT-13, Lviv, Ukraine, **2013**, 166.
- L. V. Lozynska, O. S. Tymoshuk, T. I. Chaban, *Metody Ob'ekty Khim. Anal.* **2014**, 9, 50–54. DOI:10.17721/moca.2014.50–54
- L. V. Lozyn's'ka, O. S. Tymoshuk, T. Ya. Vrublev's'ka, *Materials Science* **2015**, 6, 870–876. DOI:10.1007/s11003-015-9795-y
- L. V. Lozynska, O. S. Tymoshuk, *Voprosy Khimii i Khimicheskoi Tekhnologii*, **2014**, 1, 80–85.
- L. Lozynska, O. Tymoshuk, T. Chaban, *Acta Chim Slov.* **2015**, 62, 159–167. DOI:10.17344/acsi.2014.866
- A. Tupys, O. Tymoshuk, P. Rydchuk, *Chem. Chem. Technol.* **2016**, 10, 19–25. DOI:10.23939/chcht10.01.019
- A. Tupys, J. Kalemkiewicz, Y. Bazel, L. Zapala, M. Dranka, Y. Ostapiuk, O. Tymoshuk, E. Woźnicka, *J. Mol. Struct.* **2017**, 1127, 722–733. DOI:10.1016/j.molstruc.2016.07.119
- M. Fizer, V. Sidey, A. Tupys, Y. Ostapiuk, O. Tymoshuk, Y. Bazel, *J. Mol. Struct.* **2017**, 1149, 669–682. DOI:10.1016/j.molstruc.2017.08.037
- Y. Bazel, A. Tupys, Y. Ostapiuk, O. Tymoshuk, V. Matiyuchuk, *J. Mol. Liq.*, **2017**, 242, 471–477. DOI:10.1016/j.molliq.2017.07.047
- Y. Bazel, A. Tupys, Y. Ostapiuk, O. Tymoshuk, J. Imricha, J. Šandrejová, *RSC Adv.*, **2018**, 8, 15940–15950. DOI:10.1039/C8RA02039F
- P. Wehner, J. Hindman, *J. Phys. Chem.* **1952**, 56, 10–15. DOI:10.1021/j150493a003
- I. D. Komaritsa, *Chem. Heterocycl. Compd.* **1968**, 4, 324–325. DOI:10.1007/BF00755270
- Yu. Yu. Lur'e, *Spravochnik po analiticheskoi khimii*, Khimiya, Moscow, Russia, 1971, p. 456.
- O. R. Myakush, A. A. Fedorchuk, A. V. Zelinskii, *Neorganicheskiye materialy*, **1998**, 34, 688–691.
- T. Vrublevska, O. Tymoshuk *Voprosy Khimii i Khimicheskoi Tekhnologii*, **2001**, 2, 9–11.
- R. S. Corrêa, M. M. da Silva, A. E. Graminha, C. S. Meira, J. A. F. dos Santos, D.R.M. Moreira, M. B. P. Soares, G. Von Poelhsitz, E. E. Castellano, C. B. Jr, M. R. Cominetti, A. A. Batista, *J. Inorg. Biochem.* **2016**, 156, 153–163. DOI:10.1016/j.jinorgbio.2015.12.024
- H. Meyer, M. Brenner, S. P. Höfert, T. O. Knedel, P.C. Kunz, A. M. Schmidt, A. Hamacher, M. U. Kassack, C. Janiak, *Dalton Trans.*, **2016**, 45, 7605–7615. DOI:10.1039/C5DT04888E

Povzetek

Raziskali smo interakcijo Ru(IV) ionov z novim analiznim reagentom 5-hydroxyimino-4-imino-1,3-thiazolidin-2-one za uporabo v spektrofotometrični metodi. Kompleks nastane pri pH 5,0 v acetatnem pufru po segrevanju v vreli vodni kopeli (~371 K) 25 min. Kompleks ima maksimum absorpcije pri 350 nm in je stabilen 24 h. Beerov zakon velja v koncentracijskem območju 0,5–6,1 $\mu\text{g mL}^{-1}$ Ru(IV). Molarna absorptivnost pri $\lambda = 350 \text{ nm}$ je $6,21 \times 10^3 \text{ L mol}^{-1} \text{ cm}^{-1}$. Meja zaznave te metode je 0,2 $\mu\text{g mL}^{-1}$. Raziskali smo tudi moteči učinek različnih kationov in anionov na spektrofotometrično določitev Ru(IV). Predlagano metodo smo uspešno uporabili za določitev Ru(IV) v zlitinah.

Scientific paper

Atmospheric Solids Analysis Probe with Mass Spectrometry for Chlorpyrifos and Chlorpyrifos-Oxon Determination in Apples

Mirjana R. Cvijović,^{1,*} Valerio Di Marco,² Srboljub J. Stanković,³ Zoran P. Nedić,⁴ Ljubinka G. Joksović⁵ and Nevena R. Mihailović⁵

¹ Faculty of Medicine, Institute for Microbiology and Immunology, University of Belgrade, Dr Subotića 1, 11000 Belgrade, Serbia

² Dipartimento di Scienze Chimiche, University of Padova, Via Marzolo 1, 35131 Padova, Italy

³ Department of Radiation and Environmental Protection, Vinča Institute of Nuclear Sciences, University of Belgrade, Mike Petrovića 12-14, 11000 Belgrade, Serbia

⁴ Faculty of Physical Chemistry, University of Belgrade, Studentski trg 12-16, 11000 Belgrade, Serbia

⁵ Faculty of Science, Department of Chemistry, University of Kragujevac, Radoja Domanovića 12, 34000 Kragujevac, Serbia

* Corresponding author: E-mail: mirjanacvijovic6@gmail.com;
Phone/fax: +381 11 3643366

Received: 05-15-2018

Abstract

Chlorpyrifos (CPS) is a toxic pesticide present in several pesticide formulations, with low degradability by natural processes. The degradation leads to the toxic metabolite chlorpyrifos-oxon (CPO). The analytical techniques used for the CPS and CPO analysis, like UPLC-PDA and GC-MS, are accurate but also expensive and time consuming, and they need sample pretreatment. In the search of a more rapid and simple analytical procedure, atmospheric solids analysis probe with mass spectrometry (ASAP-MS) was optimized for the determination of CPS and CPO in apples (*Malus domestica* „Idared”). The identification of the analytes was based on protonated ion and isotopic pattern, while the quantification was based on peak intensities. The obtained results were confirmed by re-validated UPLC-PDA and GC-MS techniques. CPS and CPO concentrations determined by ASAP-MS and UPLC-PDA showed moderate discrepancies (on average by 10–20%), thus demonstrating that ASAP-MS can be a semiquantitative tool for the quantification of these compounds. As additional goal of this work, the efficiency of a gamma irradiation treatment to remove CPS and CPO from apples was tested by analyzing their content before and after the irradiation: 89–99% of CPS and CPO were degraded with doses of 3.5–3.8 kGy and 66–72 h of irradiation per sample. Identical degradation results were obtained by UPLC-PDA and ASAP-MS, indicating that the latter technique is well suitable to rapidly check pesticide degradation in apples.

Keywords: GC-MS; UPLC-PDA; ASAP-MS; gamma irradiation

1. Introduction

Chlorpyrifos (*O,O*-diethyl-*O*-3,5,6-trichloro-2-pyridylphosphorothioate, CPS, Figure 1) is an organophosphorous insecticide used in agriculture formulations and in the military field. It is a very persistent (resistant to degradation) and non-volatile compound at room temperature. CPS may be detected in fruit, vegetables, water, soil, and body fluids, even months to years after its application.

This occurs especially after unprofessional application of agricultural formulations, like EC (emulsifiable concentrate) and EW (emulsion in water). EC contains 30–50% of active substance, organic solvents (such as high-boiling mineral oils, 40–60%), and emulsifiers, whereas EW contains active substances (about 30%), emulsifier (15%), antifreeze (10%), antifoam, thickener, biocide, stabilizer, buffer, and water. There are also other formulations based on this pesticide.^{1–3}

The degradation process of CPS leads to the formation of chlorpyrifos-oxon (*O,O*-diethyl-*O*-3,5,6-trichloro-2-pyridylphosphate, CPO) and 3,5,6-trichloro-2-pyridinol (TCP). The formation of CPO (Figure 1) occurs in animal liver, where a phosphorus-sulfur bond of CPS is replaced by a phosphorus-oxygen bond.^{4,5}

TCP is non-toxic, but CPS and CPO are very toxic to humans and cause tens of thousands of deaths per year worldwide because of many reasons: type of pesticide application, short waiting period between treatments, higher doses than allowed, and high toxicity. Both CPS and CPO can cause chemical injury leading to serious damages of human hepatocytes (cells of main liver parenchyma), immune, cognitive, and reproductive systems, in the gastrointestinal tract, and to the hormonal status. The most affected patients are children, elderly, and occupationally exposed people.⁶ K. Choi et al. and J. Choi et al. demonstrated that CPO inhibits the esterase in human liver.^{7,8} In case of highly intoxicated liver, metabolic paths change (due to enzyme inhibition) and carcinoma can appear in humans (colorectal carcinoma, liver, lung).⁹ It is known that hepatocytes in humans with polymorphisms do not have the ability to metabolize, detoxify, and inactivate exogenous compounds such as insecticides and drugs.¹⁰ Thus, both European Commission (EU) and U.S. Environmental Protection Agency (EPA) restricted the use of CPS and are planning to forbid it. The CPS and CPO concentrations in different matrices (food, water, agricultural formulation, blood, urine) should be monitored continuously.¹¹

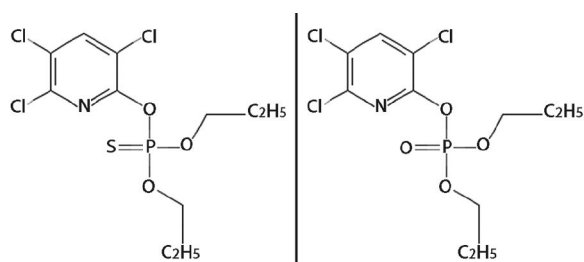


Figure 1. *O,O*-diethyl-*O*-3,5,6-trichloro-2-pyridylphosphorothioate (CPS, left) and *O,O*-diethyl-*O*-3,5,6-trichloro-2-pyridylphosphate (CPO, right).

CPS and CPO concentrations in food and other matrices are most often monitored by chromatographic techniques like high pressure liquid chromatography with photodiode detection (UPLC(HPLC)-PDA), liquid chromatography – mass spectrometry (LC-MS), liquid chromatography – tandem mass spectrometry (LC-MS/MS)¹², gas chromatography with mass spectrometric detector (GC-MS), gas chromatography with nitrogen phosphorus thermoionic detector (GC-NPD), gas chromatography with flame ionization detector (GC-FID),^{13,14} 2D-chromatography with simultaneous analysis by two GC columns (GC×GC-FPD).¹⁵ Other, less used techniques are spectro-

scopic ones like infrared spectroscopy (IR), Fourier transform with infrared spectroscopy (FTIR), and attenuated total reflection – Fourier transform with infrared spectroscopy (ATR-FTIR).¹⁶ Almost all of these techniques are highly expensive, and they require toxic solvents and long time for validation and sample preparation. These techniques are also not suitable to rapidly check the presence or absence of CPS and CPO in food or other matrices.

Atmospheric solids analysis probe with mass spectrometry (ASAP-MS) represents a possible alternative method for the analysis of such analytes.¹⁷ ASAP-MS utilizes heated nitrogen to vaporize the sample and corona discharge to ionize it. This technique is capable of ionizing low polarity compounds, such as CPS and CPO, not amenable to electrospray (ESI), to atmospheric pressure photoionization (APPI), or to atmospheric pressure chemical ionization (APCI), and it is possible to analyze samples via direct introduction at atmospheric pressure, thus shortening the analysis time and simplifying the procedure. In this paper, therefore, an ASAP-MS method was optimized for the rapid and simple determination of CPS and CPO in plant origin food, such as apples. The obtained results were confirmed by values obtained through standard sample preparation methods (extractions) and chromatographic techniques, i.e. gas chromatography with mass spectrometric detection (GC-MS) and reverse-phase ultra-high performance liquid chromatography with photodiode array detector (RP UPLC-PDA), re-validated for these purposes.

Furthermore, as natural processes (sun, air, microbiological) are not effective enough in real time for the removal of CPS from food, forced processes like chemical (acid and base hydrolysis, oxidation by H₂O₂) or physical (gamma irradiation) are necessary for the removal of this pesticide or its conversion into nontoxic compound such as TCP. Therefore, another goal of this work was to evaluate if a gamma irradiation treatment is able to efficiently remove CPS and CPO from apples treated by EC and EW formulations. Analytical measurements were performed with both RP UPLC-PDA and ASAP-MS.

2. Experimental

2.1. Materials

The reference materials for the analysis of CPS (98.0±1.0%) and CPO (98.0±1.0%) were purchased from Dr Ehrenstorfer GmbH (Augsburg, Germany). Multi-residue standard mix with CPS in acetonitrile, Pestanal mix 101 with 20 pesticides and CPS (50 ng/μL, 99.0±0.5%) was purchased from Dr Ehrenstorfer GmbH (Augsburg, Germany). The 30% H₂O₂ solution was purchased from MerckCo (Germany). Radar EC and Radar EW, plant protection formulations (active substance CPS 300 g/L), were purchased from Galenika, Phitopharmacia (Belgrade, Serbia). Apples “Idared” were received from domestic pro-

duction and bought in supermarkets. Methanol, acetonitrile, hexane, petroleum ether, acetone (HPLC grade) were purchased from J. T. Baker (Netherlands). Dichloromethane (HPLC grade) was purchased from Across Organic (New York, USA). Formic acid (98%) was obtained from J. T. Baker (Netherlands). Glacial acetic acid (99.8%, HPLC grade) was a Fisher Chemicals (United Kingdom) product. Deionized water was prepared by Purite Select Fusion System. Multi-walled carbon nanotubes (MWCNT) were a Sigma Aldrich product. QuEChERS kit was composed of two extraction mixtures: a mixture of 1.5 g CH_3COONa and 6 g MgSO_4 , and a PSA sorbent. Cartridges used for analytes separation were Oasis® HLB (hydrophilic-lipophilic balance) from Waters (Milford, MA, USA).

2. 2. Solutions

Standard stock solutions of CPS and CPO were prepared by dissolving 10 mg of CPS and 5 mg of CPO in 1000 μL of methanol (or dichloromethane, depending on the instrumental technique used), and then put in a volumetric Eppendorf tube. The stock solutions were diluted in hexane or in deionized water (pH 6.8) to prepare the desired concentrations for the calibration curves for GC-MS or UPLC-PDA, respectively.

EW and EC formulations stock solutions were prepared by dissolving 100 μL of formulation in a 10 mL volumetric flask with dichloromethane (or in methanol/water mixture 1:3, v/v), at a concentration of 3000 mg/L calculated on active component, and stored at -18°C when not in use.

2. 3. Instrumentations and Methods

2. 3. 1. ASAP-MS

ASAP-MS with triple quadrupole analyzer (TQD, Acquity, Waters, USA) was used for the mass spectrometry analysis of CPS and CPO. The ASAP compartment consists of set probes and removable sample insertions, corona pin, and glass sample capillaries. The capillary glass tubes were sealed at the end and baked at 500°C to remove possible contaminations. The whole assembly (100 mm in length) was inserted in the mass spectrometer. Positive ions were recorded between 50 and 700 Da. The ASAP probe with sample was inserted into the sealed source enclosure and desolvation gas was rapidly heated to 300°C . The heated nitrogen volatilizes the sample from a glass capillary tip, which is then ionized with a corona discharge pin, and MS spectrum is generated. The mass accuracy of the data was based on the instrument internal calibration.

Instrumental parameters were varied to avoid CPS and CPO fragmentation. Values accepted after optimization were: corona voltage 3.8 kV, extraction cone 2.0 V, source temperature 150°C , desolvation gas flow 650 L h^{-1} , sampling cone voltage 35 V, desolvation temperature 300°C . Data were processed by the MassLynx software, version 4.1.

2. 3. 2. GC-MS

The GC-MS QP2010 Ultra instrument (Shimadzu, Kyoto, Japan) was used. A Rtx®-1 (RESTEK, Crossbond® 100% dimethylpolysiloxane, 30 m \times 0.25 mm I.D., 0.25 μm film thickness) column was used. The injector temperature was 290°C . The GC temperature program was held at 50°C for 1 min, then elevated to 140°C at rate of $20^\circ\text{C}/\text{min}$, and to 300°C at rate $10^\circ\text{C}/\text{min}$, with a hold time of 6 min. Helium was used as the carrier gas at approximately 1.0 mL/min pulsed in splitless mode. The mass spectrometric detector was operated in an electron impact ionization mode with an ionizing energy of 70 eV and scanning range from 50 to 500 m/z .

All measurements have been done in triplicate. Quantification of CPS and CPO has been done by external calibration curves. The calibration ranges of CPS and CPO explored in this work were 0.2–5 mg/L and 0.3–3.0 mg/L, respectively; linearity in the signal/concentration ratio was obtained also up to 30 mg/L for CPS and 25 mg/L for CPO. The correlation coefficient R^2 was higher than 0.99. The limit of detection (LOD) for CPS was 0.08 mg/L and it was 0.1 mg/L for CPO, calculated for samples injected three times. The limit of quantification (LOQ) was 0.2 mg/L for CPS and 0.3 mg/L for CPO. Relative standard deviations (RSD) were determined from ten measurements of a CPS standard solution ($C = 2.5\text{ mg/L}$) and a CPO standard solution ($C = 1.5\text{ mg/L}$). The RSD was 4.1% for CPS and 4.8% for CPO.

2. 3. 3. RP-UPLC-PDA

Reversed-phase ultra high performance liquid chromatography (RP UPLC) was performed with an Acquity system with PDA detector (Waters, USA). Samples were injected automatically; the volume of injected sample was 10 μL . Acquity BEH Reverse Phase C18 (1.7 μm \times 100 mm \times 2.1 mm) column was used as a stationary phase for chromatographic separations. Mobile phases contained 0.1% formic acid in water (v/v) (A) and 0.1% formic acid in acetonitrile (v/v) (B). The following gradient elution conditions were used: 0–1.5 min 45% A; 1.5–2 min 40% B; 2–2.5 min 20% B; 2.5–4.5 min 2% B; 4.5–4.8 min 55% B; 4.8–6.0 min 50% B. Flow rate was set at 1 mL/min, and column temperature was 30°C . The chosen absorption wavelengths were 230 and 280 nm. Quantification of CPS and CPO has been done by external calibration curves. All measurements have been done in triplicate.

The calibration ranges of CPS and CPO were 0.1–5 mg/L and 0.03–2.5 mg/L, respectively; linearity in the signal/concentration ratio was obtained also up to 30 mg/L for CPS and 20 mg/L for CPO. The correlation coefficient R^2 was higher than 0.99. The LOD for CPS was 0.03 mg/L and it was 0.01 mg/L for CPO, calculated for samples injected three times. The LOQ was 0.10 mg/L for CPS and 0.03 mg/L for CPO. The accuracy and precision were evaluated by means of the recovery: values obtained by

post-extraction addition of standard to treated apples were 98–108% and 96–104% for the two compounds, respectively. RSD values were determined from ten measurements of CPS standard solution ($C = 0.3$ mg/L) and CPO standard solution ($C = 0.8$ mg/L). The RSD was 2.2% for CPS and 3.3% for CPO.

2. 4. Gamma Irradiation Experiments

Gamma irradiation experiments were carried out in the metrology dosimetry laboratory at the Institute of Nuclear Sciences (Belgrade). The radiation unit IRPIK-B was used as a functional generator with a source of gamma radiation Co-60. The measured value of the absorbed dose in the air at the reference point for the irradiation was 48.27 Gy/h. At the point at which samples were positioned, the absorbed dose in water was 53.51 Gy/h. After each individual campaign irradiation, the total value of the absorbed dose in each sample was 3.5–3.8 kGy, depending on time of irradiation. In general, the relation between the absorbed dose in air and absorbed dose in water as the material that is irradiated with gamma rays is:

$$D_W = D_{air} \cdot \frac{\left(\frac{\mu}{\rho}\right)_{en,air}}{\left(\frac{\mu}{\rho}\right)_{en,W}} \quad (1)$$

where D_W and D_{air} are the absorbed dose in the water and

absorbed dose in the air, respectively, and $\left(\frac{\mu}{\rho}\right)_{en,air}$ and $\left(\frac{\mu}{\rho}\right)_{en,W}$

are the energy absorption coefficients for air and water, respectively. It was assumed that absorption of irradiation in apple samples is equivalent to that in water.

2. 5. Sample Preparation

The plant protection formulations based on CPS were applied to 20 samples of apples “Idared” bought in supermarkets, and to 20 samples of the same variety obtained from orchards. The supermarket samples were sprayed by 2 mL of EC formulation (dissolved in a water methanol mixture, 3:1, v/v) under 100 kPa air pressure from a Potter precision laboratory spray tower (Burkard Scientific, UK). Spraying was performed under controlled conditions of temperature (17 °C) and relative humidity (45%). The treated samples were collected in plastic bags after treatment and stored at –18 °C until further analysis. Some apples were further treated with 30% H₂O₂ solution to cause initial degradation of EC formulation to form CPO.

For ASAP-MS analysis, the samples were brought to room temperature. Apples were peeled, and their skin was cut into small pieces (about 1×1 cm), and the ASAP-MS

probe was dipped into the apple pieces. The skin was weighted before and after dipping the ASAP-MS probe. The sample was then inserted into the ionization source chamber. No particular sample pretreatment was needed for the ASAP-MS analysis, and MS data for each sample were collected in few seconds.

For the chromatographic analysis, apples were homogenized (15 g in 30 mL acetone), vortexed and centrifuged for 10 min at 3500 rpm. The procedure was repeated three times, and acetone extract was collected. The remaining apple homogenate was further mixed with 20 mL of petrol ether and 10 mL of dichloromethane. After centrifugation, the upper organic layer was collected and added to acetone extract by this modified Luke procedure.¹⁸ Combined extracts were evaporated on a water bath at 42–62 °C and reconstituted with methanol for UPLC-PDA analysis or dichloromethane for GC-MS analysis. For some apples, the skin was separated from the mesoderm, and each sample was treated separately.

Three extraction techniques, other than the described Luke procedure, have been tested: liquid phase extraction followed by analytes separation in Oasis® HLB cartridge, extraction with multiwall carbon nanotubes (MWCNT) and extraction with QuEChERS kit. For the liquid phase extraction, 5 g of apples have been homogenized and extracted with 20 mL of acetonitrile; 5 mL of extract were diluted to 100 mL with a 50:50 water/methanol mixture, and eluted through the Oasis® HLB cartridge (previously conditioned with methanol). Eluted solutions were evaporated to dryness at 42–64 °C, and reconstituted with methanol for UPLC-PDA analysis or dichloromethane for GC-MS analysis. For the extraction with MWCNT, 6 mL PTFE tubes (Strata) were filled with 0.035 g MWCNT, sample was added, and pH was then set at 6–7.5 to enhance the analyte extraction. Analytes were eluted with a methanol solution, and then samples were evaporated to dryness and reconstituted as described above for the liquid phase extraction. As regards the QuEChERS kit extraction, 15 g of homogenized sample were loaded into an empty 50 mL tube, and 15 mL of a 1% CH₃COOH in acetonitrile solution were added. The first QuEChERS mixture was then added. After centrifugation at 1500 rpm for 5 min, 3 mL of supernatant solution were transferred into another tube containing the second QuEChERS mixture. After centrifugation at 3000 rpm for 5 min, 100 µL of the final extract were transferred into a vial and diluted with methanol.

The extraction efficiency η (%) was calculated for each method. The combined Luke (Dutch) procedure gave an efficiency of 94% ± 8%, which was the highest among all obtained efficiencies. For the liquid phase extraction it was 84% ± 13%, for the MWCNT it was 88% ± 9%, and for the QuEChERS kit it was 90% ± 8%. Therefore, the combined Luke (Dutch) procedure was chosen for apple preparation for the UPLC-PDA analyses.

3. Results and Discussion

3.1. ASAP-MS

The interpretation of ASAP-MS spectra of CPS and CPO was performed in accordance to m/z values and isotopic pattern. The protonated CPS is at m/z 351.5 ± 0.5 Da, and the protonated CPO is at m/z 335.5 ± 0.5 Da. The non-toxic metabolite TCP can also be observed at m/z 198 with very low abundance. CPS and CPO are chlorinated compounds with three chlorine atoms which are excellently suitable for interpretation by isotope distribution. For example, the isotopic pattern for protonated CPS is 350:351:352:353:354:355:356, and calculated relative ion intensities are 97:11:100:11:36:4:5, respectively. In this pattern the even m/z values (350, 352...) stem mainly from the chlorine isotopes ^{35}Cl (75.8% natural abundance) and ^{37}Cl (24.2% natural abundance), and the uneven values (351, 353...) from the carbon isotopes ^{12}C (98.9% natural abundance) and ^{13}C (1.1% natural abundance). Theoretical ratio is in good agreement with ion ratio detected experimentally from standard and from apple samples (an example of experimental pattern is reported in Figure 1S in the Appendix A – Supporting Information).^{7,19}

The ASAP-MS spectra of a blank apple and of an apple treated by 50 mg/L EC formulation and with H_2O_2 are shown in Figure 2. If the two spectra are compared, the appearance of two new intense signals (10-fold more intense than other m/z signals) due to CPS and CPO can be observed: CPS was added with the EC formulation, whereas CPO was produced by the H_2O_2 addition which simulates CPS degradation.

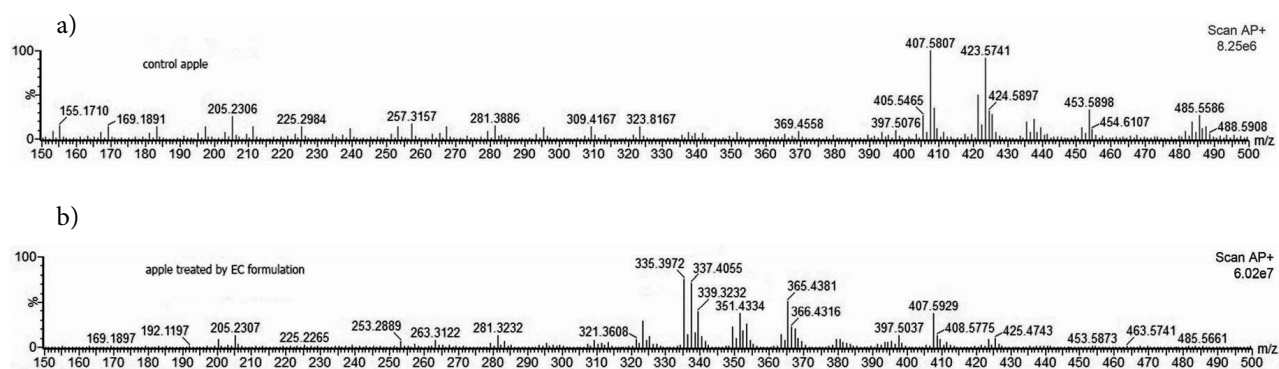


Figure 2. ASAP-MS spectra of a control apple (a) and of an apple treated with 50 mg/L EC formulation and with H_2O_2 (b).

According to literature data,^{20–22} some additional compounds can be likely identified in Figure 2: naringenin pentose (m/z 405), *p*-coumaric pentose (m/z 326), phloridzin (m/z 435), hyperoside (quercetin 3-*O*-galactoside) or isoquercetin (m/z 463), ferulic acid (m/z 368), cyanidin pentosine (m/z 419), cyanidin hexoside (m/z 449), and quercetin pentoside (m/z 435). In principle, therefore,

ASAP-MS might be used also for the detection of these additional compounds.

3.2. Results of Chromatographic Analyses

Chromatographic techniques (GC-MS and UPLC-PDA) were validated and applied for accurate measurements of CPO and CPS in apples, in order to acquire the “true” concentrations of these compounds.

The identity of CPS and CPO in GC-MS has been confirmed from the electron impact (EI) spectra which gave confirmatory product ions, as shown in the Supporting Information (Figures 2S and 3S). The same ions are reported in Wiley database libraries. As well, the retention times of CPS and CPO were identical to those of the standard materials. The identification by UPLC-PDA techniques has been done by the retention time, which was identical to that of the standard material. The retention times were 4.23 min for CPS, 3.08 min for CPO, and 2.01 min for TCP.

From the validation data reported in the Experimental section, UPLC-PDA demonstrated to have slightly better analytical performances (LOD, LOQ, recovery) than GC-MS. For this reason, the subsequent quantitative analyses have been performed using UPLC-PDA. Some quantitative results obtained on apples (blank or treated with pesticide formulations) are shown in Table 1S in the Supporting Information. These results show that CPS residues remained on apple skin, while apple mesoderm did not contain the pesticide. Untreated samples (domestic apple) were also CPS free.

3.3. Comparison Between ASAP-MS and Chromatographic Measurement of CPS and CPO in Apples

The results obtained in the analysis of two samples for both CPS and CPO by using two different techniques, UPLC-PDA and ASAP-MS, are reported in Table 1. The first column reports the concentrations of EC or EW formulations used for apples spraying.

Although results obtained by ASAP-MS method were different than those obtained by UPLC-PDA meth-

od, the order of magnitude of the values given by the two techniques was the same, and relative differences were not very large (around 10–20%). Indeed, ASAP-MS results were obtained in few minutes, whereas UPLC-PDA values required a 10–100-fold longer time. This indicated that ASAP-MS technique can represent a rapid and semiquantitative method for the analysis of CPS and CPO.

The quantitative results for the measure of the degradation efficiency were obtained with UPLC-PDA and are shown in Table 2. The last column reports the removal efficiency of CPS (if applicable also of CPO), as a function of the gamma irradiation doses reported in the previous column and/or of the H₂O₂ pretreatment.

The pretreatment with H₂O₂ caused only a limited

Table 1. Comparison between results from UPLC-PDA and from ASAP-MS in the analysis of two apple samples.

sample	technique	CPS [mg/kg]	CPO [mg/kg]
treated with 50 – EC	UPLC-PDA	0.65±0.02	0.06±0.01
treated with 50 – EC	ASAP-MS	0.58±0.03	0.05±0.01
treated with 50 – EW	UPLC-PDA	0.60±0.03	0.26±0.02
treated with 50 – EW	ASAP-MS	0.54±0.02	0.21±0.02

3. 4. Effect of Gamma Ray Treatment on the Removal of CPS and CPO from Treated Apples

The GC-MS chromatogram (recorded as total ion chromatogram, TIC) obtained in EC formulations (5 mg/L) before gamma irradiation is presented in Figure 4Sa in the Supporting Information. The peak of CPS was observed at $t_R = 18.27$ min. Other minor formulation ingredients can be seen at different t_R values. When the analysis was repeated after gamma irradiation, the CPS peak almost disappeared (Figure 4Sb): CPS peak area is around 10–15% of the same peak in Figure 4Sa. Gamma irradiation caused the appearance of the CPO peak at $t_R = 18.03$ min and of TCP at $t_R = 12.77$ min. Both compounds were produced from the degradation of CPS.

Figure 3 shows the ASAP-MS spectra of a blank apple gamma irradiated (the same sample of Figure 2a), and of an apple treated with 50 mg/L EC formulation, with H₂O₂ and then gamma irradiated (the same sample of Figure 2b). Both apples show an almost identical spectrum, indicating that the degradation was effective, and that the treated apple was almost identical to a blank (i.e. not polluted) apple.

degradation of CPS (around 35–40%), and it caused the production of large amounts of CPO due to chemical oxidation of CPS. The exposure to gamma rays caused the removal of CPS and of CPO depending on the irradiation dose and on the irradiation time. 2.5 kGy for 66 h was not sufficient for pesticide removal, as the removal percentage was below 50%. A good efficiency was achieved for a 3.5 kGy dose and for a 66 h treatment, as the removal percentage of CPS reached 90%. The upper dose of 3.8 kGy for 72 h gave even better results, but the increase with respect to 3.5 kGy for 66 h was not very large. Little amounts of CPO appear as a degradation product of CPS after gamma irradiation. However, if CPO is present on apples in large amounts, it is degraded as well by gamma irradiation, as demonstrated in samples pretreated with H₂O₂. The parameters of gamma irradiation and their effects are in agreement with literature data for interaction of gamma irradiation with water medium.^{23–25}

The removal efficiency of gamma irradiation can be easily checked also by ASAP-MS, by measuring the absolute intensities of the relevant pesticide peaks before and after irradiation. For example, with reference to Figures 2 and 3, in apples treated with 50 – EC the average intensi-

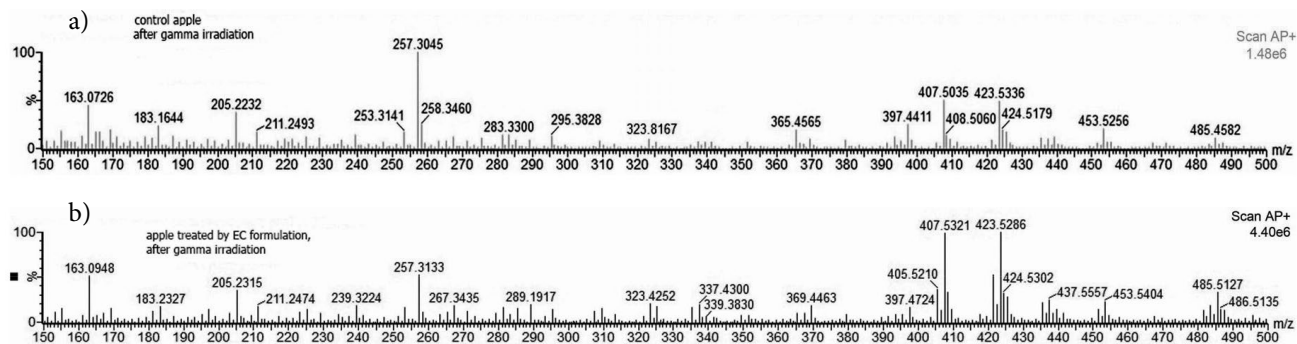


Figure 3. ASAP-MS spectra of a control apple after gamma irradiation (a) and of an apple treated with 50 mg/L EC formulation and with H₂O₂ and then gamma irradiated (b).

Table 2. Removal of CPS and CPO by gamma ray irradiation and, if used, by H₂O₂ pre-treatment. Values were determined by UPLC-PDA.

sample	CPS [mg/kg]	CPO [mg/kg]	H ₂ O ₂ pretr.	Gamma irradi. doses [kGy]/time[h]	Removal of CPS or CPO [%]
Blank apple	≤0.03	≤0.03	no	–	–
treated with 5 – EC	4.93±0.07	–	no	–	–
treated with 5 – EC	2.76±0.04	0.14±0.02	no	2.5/66	44
treated with 5 – EC	0.55±0.02	0.03±0.01	no	3.5/66	89
treated with 5 – EC	0.56±0.02	0.03±0.01	no	3.8/72	88
treated with 5 – EW	4.96±0.05	–	no	–	–
treated with 5 – EW	2.72±0.07	0.13±0.01	no	2.5/66	45
treated with 5 – EW	0.54±0.02	0.03±0.01	no	3.8/72	89
treated with 50 – EC	47.2±1.0	–	no	–	–
treated with 50 – EC	2.7±0.1	0.18±0.02	no	3.8/72	94
treated with 50 – EC	30.2±1.0	14.10±0.08	yes	–	36
treated with 50 – EC	0.65±0.02	0.06±0.01	yes	3.8/72	98 CPS/99 CPO
treated with 50 – EW	48.2±1.1	–	no	–	–
treated with 50 – EW	2.6±0.1	0.16±0.02	no	3.8/72	94
treated with 50 – EW	29.2±1.1	16.2±0.1	yes	–	39
treated with 50 – EW	0.60±0.03	0.26±0.02	yes	3.8/72	98 CPS/98 CPO

ties of the protonated CPS ion, $m/z=351$, before irradiation were $373 \cdot 10^7$. The intensities of the same ion after gamma irradiation were $4.4 \cdot 10^7$. The efficiency of CPS removal can be thus calculated to be 99%, in very good agreement with the value (98%) determined by UPLC-PDA. Also, the average intensities of the protonated CPO ion at $m/z=335$ was $259 \cdot 10^7$ before irradiation and $3.5 \cdot 10^7$ after irradiation, so that the effect of removal of CPO was 99%, identical to what was found by UPLC-PDA. ASAP-MS can therefore represent a rapid tool to accurately check CPS and CPO removal from apples.

4. Conclusions

ASAP-MS was optimized for the determination (identification and semiquantification) of CPS and CPO in raw apples. The technique is simple, rapid and economical, as it enables the analysis without purification and preparation steps. Results are indeed not very accurate if compared with those of validated chromatographic techniques (bias was 10–20%), thus indicating that ASAP-MS represents a semiquantitative tool, but these values can be obtained much more rapidly than with validated chromatographic methods.

In the frame of checking possible degradation treatments of CPS and CPO in apples, gamma irradiation demonstrated to be effective enough with a 3.5 kGy dose for a 66 h treatment. ASAP-MS gave in this case accurate degradation percentages by simply measuring the absolute percentages detected for the CPS and CPO ions before and after irradiation. Degradation percentages obtained from ASAP-MS were in very good agreement with the ones obtained by chromatography. This indicates that ASAP-MS can be very well suitable to rapidly and easily check CPS and CPO removal from apples.

5. Acknowledgements

This work was supported by the Ministry for Science of the Republic of Serbia Grant No. (OI 172019, III 45014, OI 175039, OI 172023 and OI 172016).

Appendix A: Supporting Information

5. References

- S. Gašić, D. Brkić, A. Tomašević, *Pestic. Phytomed.* **2011**, *26*, 409–413. DOI:10.2298/PIF1104409G
- X. Dai, F. Fan, Y. Ye, F. Chen, Z. Wu, X. Lu, Q. Wei, J. Chen, Y. Yan, L. Liao, *J. Forensic Sci. Med.* **2017**, *3*, 22–25. DOI:10.4103/jfsm.jfsm_2_17
- H. Molet, A. Grubeman, *Formulation Technology*, 2nd ed. Wiley-VCH, Weinheim, Germany **2001**, pp. 389–397.
- E. Hodgson, *A Textbook of Modern Toxicology*, 3rd ed, John Wiley & Sons Inc., United States, **2004**, pp. 56–64. DOI:10.1002/0471646776
- D. Tsiipi, H. Botitsi, A. Economou, *Mass Spectrometry for the Analysis of Pesticide Residues and Their Metabolites*, Wiley, USA. **2015**, pp. 187–205, 207–229. DOI:10.1002/9781119070771
- Y. Latif, S. T. H. Sherazi, M. I. Bhangar, S. Nizamani, *Am. J. Analyt. Chem.* **2012**, *3*, 587–595. DOI:10.4236/ajac.2012.38077
- K. Choi, H. Joo, R. L. Rose, E. Hodgson, *J. Biochem. Mol. Toxicol.* **2006**, *20*, 279–291. DOI:10.1002/jbt.20145
- J. Choi, E. Hodgson, R. L. Rose, *Drug Metab. Drug Interact.* **2004**, *20*, 233–245.
- T. Suriyo, P. Tachachartvanich, D. Visitnonthachai, P. Watcharasit, J. Satayavivad, *Toxicol.* **2015**, *2*, 117–129. DOI:10.1016/j.tox.2015.10.009
- R. L. Rose, J. Tang, J. Choi, Y. Cao, A. Usmani, N. Cherring-

- ton, E. Hodgson, *Scand J. Work Environ. Health*. **2005**, *31*, 156–163.
11. J. Hajšlova, J. Zrostlikova, *J. Chromatogr. A*. **2003**, *1000*, 181–197. DOI:10.1016/S0021-9673(03)00539-9
 12. European Norm, BS EN 15662: **2008**, Foods of plant origin: determination of pesticide residues using GC-MS and/or LC-MS/MS following acetonitrile extraction/partitioning and clean up by dispersive SPE – QuEChERS method.
 13. S. Chandra, A. N. Mahindrakar, L. P. Shinde, *Int. J. ChemTech Res.* **2014**, *6*, 124–130.
 14. N. George, P.S. Chauhan, S. Sondhi, S. Saini, N. Puri, N. Gupta, *Int. J. Pure Appl. Sci. Technol.* **2014**, *20*, 79–94.
 15. X. Liu, B. Mitrevski, D. Li, J. Li, P. J. Marriott, *Microchem. J.* **2013**, *111*, 25–31. DOI:10.1016/j.microc.2012.07.013
 16. M. Khanmohammadi, M. A. Karimi, K. Ghasemi, M. Jabbari, A. B. Garmarudi, *Talanta* **2007**, *72*, 620–625. DOI:10.1016/j.talanta.2006.11.029
 17. C. N. McEwen, R. G. McKay, B. S. Larsen, *Anal. Chem.* **2005**, *77*, 7826–7831. DOI:10.1021/ac051470k
 18. M. Cvijović, S. Stanković, B. Tanović in: G. Ristic (ed) *4th Intern. Confer. On Radiation and Application in Various Fields of Research*. Niš, Serbia, **2016**, pp. 452.
 19. S. J. Lenothay, A. de Kok, M. Hiemstra, P. van Bodegraven, *J. AOAC Int.* **2005**, *88*, 595–614.
 20. Scientific Instrument Services [http://www.sisweb.com/mstools/isotope.htm].
 21. L. M. Bystrom, B. A. Lewis, D. L. Brown, E. Rodriguez, R. L. Obendorf, *Food Chem.* **2008**, *111*, 1017–1024. DOI:10.1016/j.foodchem.2008.04.058
 22. F. Sanchez-Rabaneda, O. Jauregui, R. M. Lamuela-Raventos, F. Viladomat, J. Bastida, C. Codina, *Rapid Commun. Mass Spectrom.* **2004**, *18*, 553–563. DOI:10.1002/rcm.1370
 23. A. Balasz, M. Toth, B. Balzics, E. Hethelyi, S. Szarka, E. Fiscor, G. Fizcek, E. Lembercovich, A. Blazovich, *Fitoterapia*. **2012**, *83*, 1356–1363. DOI:10.1016/j.fitote.2012.04.017
 24. M. N. Mori, H. Oikawa, M. H. O. Sampa, C. L. Duarte, *J. Radioanal. Nucl. Chem.* **2006**, *270*, 99–102. DOI:10.1007/s10967-006-0314-3
 25. M. S. Hossain, A. N. M. Fakhruddin, M. A. Z. Chowdhury, M. K. Alam, *J. Environ. Chem. Eng.* **2013**, *1*, 270–274. DOI:10.1016/j.jece.2013.05.006

Povzetek

Klorpirifos (CPS) je strupen pesticid, ki se nahaja v številnih fitofarmaceutskih sredstvih in se pod naravnimi pogoji le malo razgrajuje. Razkroj vodi do nastanka strupenega metabolita klorpirifos-oksona (CPO). Analizne tehnike za določevanje CPS in CPO, kot sta UPLC-PDA in GC-MS, so točne, vendar tudi drage in časovno zamudne ter potrebujejo predpripravo vzorca. Z namenom najti hitrejši in bolj preprost analizni postopek smo za določitev CPS in CPO v jabolkih (*Malus domestica* „Idared”) optimizirali sondo za trdne vzorce pri atmosferskem tlaku v povezavi z masno spektrometrijo (ASAP-MS). Identifikacijo analitov smo izvedli na osnovi protoniranega iona in izotopskega vzorca, medtem ko je bila kvantifikacija osnovana na intenziteti vrhov. Dobljene rezultate smo potrdili z revalidiranimi UPLC-PDA in GC-MS metodama. Koncentracije CPS in CPO, določene z ASAP-MS in UPLC-PDA, so se nekoliko razlikovale (v povprečju za 10–20%), kar je pokazalo, da je ASAP-MS lahko semikvantitativno orodje za kvantifikacijo teh spojin. Dodaten namen te raziskave je bil preizkusiti učinkovitost gama ožarčenja za odstranjevanje CPS in CPO iz jabolk, zato smo jih analizirali pred in po ožarčenju: 89–99% CPS in CPO se je razgradilo pri dozah 3,5–3,8 kGy in času ožarčenja 66–72 h na vzorec. Z UPLC-PDA in ASAP-MS smo dobili identične rezultate razgradnje, kar pomeni, da je slednja tehnika zelo primerna za hitro preverjanje razgradnje pesticidov v jabolkih.

Scientific paper

Solid-Phase Extraction Method by Magnetic Nanoparticles Functionalized with Murexide for Trace U(VI) from Sea Water Prior to Spectrophotometric Determination

Tülay Oymak

Department of Analytical Chemistry, Faculty of Pharmacy, Cumhuriyet University, 58140, Sivas, Turkey

* Corresponding author: E-mail: tulayoymak@cumhuriyet.edu.tr

Tel: +90 346 219 Fax: +90 346 219 16 34

Received: 05-06-2018

Abstract

In this study, magnetic nanoparticles ($\text{Fe}_3\text{O}_4/\text{SiO}_2/\text{APTES}$) functionalized with murexide were used for the determination of uranium(VI) in sea water by spectrophotometric method in perchloric acid medium using Arsenazo-III as chromogenic reagent. The effects of some analytical parameters, such as pH, contact time, and eluent volume, on the recovery of uranium(VI) were examined in synthetic sea water. The optimum conditions were achieved with a 15 min adsorption time and 2 min elution time with 1 mL of 5 mol L⁻¹ HClO₄ at pH of 6.5 and 25 mg of the magnetic sorbent. The linear range, detection limit, and precision (as RSD%) of the method were found to be 0.02–4.0 mg L⁻¹, 0.001 mg L⁻¹ and 3.0%, respectively. The proposed method is simple, rapid, and cost-effective for the determination of U(VI) in sea water, with a total analysis time of approximately 30 min. The adsorption isotherm was well fitted to the Langmuir model, with a correlation coefficient of 0.9997 and Q_{max} value was found to be 77.51 mg g⁻¹. The magnetic sorbent was successfully used for the rapid determination of trace quantities of U(VI) ions in different sea waters, and satisfactory results were obtained.

Keywords: Magnetic nanoparticles; sea water; uranium(VI)

1. Introduction

In recent years, environmental pollution with toxic elements, such as uranium, has increased considerably. Uranium and its associated compounds are carcinogenic, dangerously toxic, and radioactive.^{1–4} Furthermore, it can cause respiratory diseases, such as fibrosis and emphysema, and even cause irreversible effects in some tissues, such as the kidneys. Uranium is found in sea water at 3 µg L⁻¹ and at approximately 0.0004% in the Earth's crust.⁵ In many countries, the uranium concentration in drinking water is determined to be 0.03 mg L⁻¹, according to the United States Environmental Protection Agency.⁶ Currently, the determination of uranium in environmental samples is crucial due to applications of uranium in areas, such as in the products of nuclear energy, catalysis, and nuclear weapons. The determination of trace uranium in complex samples and natural waters is a challenging task. Most instruments are not sensitive enough to allow for its determination at very low concentration levels in complex matrix such as sea water. For example

the heavy salt matrix reduces sensitivity in direct determinations from sea water (ca. 3.5% salt). Therefore, a separation and preconcentration step is commonly applied before instrumental analysis.^{1,6–9} Preconcentration/separation techniques, such as solid phase extraction (SPE),^{3,10–13} liquid-liquid microextraction (LLME),¹⁴ and cloud point extraction (CPE)^{15–17} are used for the determination of uranium in various samples. SPE has commonly been used as a technique for preconcentration/separation due to its higher enrichment factor and practicality. In SPE, Amberlite-XAD, modified silica gels, mesoporous silica, and nanomaterials are commonly used as adsorbents.^{18–21} Most of these sorbents have disadvantage such as low sorption capacities or efficiencies. Recent studies show that nanomaterials exhibit perfect sorption capacity. But the high dispersibility of nanomaterials in aqueous solutions makes it difficult to separate sorbents from aqueous phase after saturated sorption, which limits their real application in large volumes of waters.²² Recently, nanosized iron oxide particles have become an important adsorbent in SPE because they show

magnetic properties, as well as the general properties of nanomaterials. Furthermore, the use of magnetic nanoparticles in SPE has many advantages compared to other adsorbents. For example, magnetic nanoparticles are easily separated from solution with the use of a magnet, low toxicity, and the loss of adsorbent is minimal during the separation.^{23–27} Aside from these advantages, raw Fe_3O_4 nanoparticles have several disadvantages, such as oxidation, aggregation tendencies, and low selectivity. However, magnetic nanoparticles can be modified by special ligands to overcome these problems. Magnetic nanoparticles modified with sulfur and nitrogen-containing ligands are preferred because heavy metals react with these ligands strongly and rapidly.^{28–30} Murexide is one of these ligands.^{18,31}

In this study, for the quantitative determination of uranium in seawater, a simple and rapid method was developed using an Fe_3O_4 nanoparticles modified with murexide. Several experimental parameters, such as pH, contact time, eluent concentration, and sorption capacity, were examined, and the developed method was then applied to real sea water samples.

2. Experimental

2.1. Chemicals and Reagents

All chemicals used were of analytical reagent grade, and ultrapure water was used throughout the study. Tetraethyl orthosilicate (TEOS), 3-triethoxysilylpropylamine (APTES), iron(II) sulfate heptahydrate, methanol and ethanol were provided by Sigma-Aldrich. Ammonium hydroxide (25%), iron(III) chloride, hydrochloric acid, $\text{UO}_2(\text{NO}_3)_2 \cdot 6\text{H}_2\text{O}$, dimethyl sulfoxide (DMSO), and murexide were purchased from Merck. Arsenazo-III was obtained from Fluka.

2.2. Apparatus

The UV–Vis spectra were recorded using a Shimadzu 3600 spectrophotometer. A Selecta brand pH metre was used for all pH measurements. A Biosan multi rotator was employed for the effective mixing of sorbent and solution.

2.3. Synthesis of Murexide Functionalized Magnetic Nanoparticles

Fe_3O_4 nanoparticles (Fe_3O_4 NPs) were synthesized with an eco-friendly method, modified from Gautam et al. Briefly, $\text{FeCl}_3 \cdot 6\text{H}_2\text{O}$ (6.1 g) was dissolved in deionized water (100 mL), followed by the addition of a few drops of concentrated HCl to prevent $\text{Fe}(\text{OH})_3$ precipitation. $\text{FeSO}_4 \cdot 7\text{H}_2\text{O}$ (4.2 g) was then added to the mixture and heated to 90 °C, followed by the rapid addition of NH_4OH (10 mL, 27%), with the solution kept at a pH of 10.0. The mixture

was stirred at 90 °C for 30 min and cooled to room temperature. The resulting solid black substance was collected with a strong magnet and washed several times with ethanol and deionized water. The Fe_3O_4 NPs were then dried under vacuum at 60 °C.

To prepare core–shell nanoparticles ($\text{Fe}_3\text{O}_4/\text{SiO}_2$), the Fe_3O_4 nanoparticles (0.50 g) were dispersed in a solution of ethanol (80 mL) and deionized water (20 mL) by sonicating for 30 min. Then, ammonia solution (5 mL, 27 wt %) and TEOS (4 mL) were added sequentially. The mixture was stirred and allowed to react for 6 h at room temperature. The product, $\text{Fe}_3\text{O}_4/\text{SiO}_2$, was collected by a magnet, washed several times with deionized water, and dried under vacuum at 60 °C for 8 h. $\text{Fe}_3\text{O}_4/\text{SiO}_2$ nanoparticles (1 g) were dispersed in 50 mL of toluene in a flask. After 1 h, APTES (4 mL) was added to the mixture, stirred continuously, and refluxed at 125 °C for 12 h. The magnetic nanoparticles ($\text{Fe}_3\text{O}_4/\text{SiO}_2/\text{APTES}$) were separated with a strong magnet and washed several times with deionized water and ethanol, then dried at 70 °C for 8 h.

In the third step, Mu (0.1 g) was dissolved in DMSO (50 mL), and $\text{Fe}_3\text{O}_4/\text{SiO}_2/\text{APTES}$ (1 g) was added to the reaction mixture and refluxed at 200 °C for 24 h. The resulting product was separated, washed several times with methanol, and dried at room temperature.

2.4. Procedure

The method was tested with synthetic sea solutions prior to its application to real sea samples. For this purpose, the synthetic solutions containing the main components present in synthetic sea water (SSW) were prepared at the following concentrations: $\text{Na}^+ = 10569 \text{ mg L}^{-1}$; $\text{Mg}^{2+} = 1270 \text{ mg L}^{-1}$; $\text{K}^+ = 379 \text{ mg L}^{-1}$; $\text{Ca}^{2+} = 397 \text{ mg L}^{-1}$; $\text{BO}_2^- = 18 \text{ mg L}^{-1}$; $\text{Cl}^- = 18990 \text{ mg L}^{-1}$; $\text{HCO}_3^- = 139 \text{ mg L}^{-1}$; $\text{SO}_4^{2-} = 2648 \text{ mg L}^{-1}$; $\text{Br}^- = 65.5 \text{ mg L}^{-1}$; and $\text{F}^- = 14 \text{ mg L}^{-1}$.¹³ $\text{Fe}_3\text{O}_4/\text{SiO}_2/\text{APTES}$ (25 mg) was transferred to a 50-mL volumetric flask, and synthetic sea water solutions (40 mL) were added ($\text{U(VI)}: 0.05 \text{ mg L}^{-1}$). The pH was adjusted to 6.5 with 0.01 M $\text{CH}_3\text{COOH}/\text{NH}_3$. The solutions were shaken and allowed to stand for 15 min at room temperature. The magnetic sorbent was separated from the suspension using a powerful magnet and supernatant was decanted. 1.0 mL of 5 mol L^{-1} HClO_4 was added to the magnetic sorbent with shaking for 2 min to elute the U(VI) ion. The magnetic sorbent was separated from the eluent using a magnet.

U(VI) ion in eluent was determined spectrophotometrically in perchloric acid medium using Arsenazo-III as chromogenic reagent.¹³ To this end, an Arsenazo-III solution (0.1 mL, 0.1%) was added to eluent solution, and the absorbance of the uranium(VI)–Arsenazo-III complex was measured spectrophotometrically (653 nm). Finally, the magnetic sorbent was washed with deionized water for reuse.

3. Results and Discussion

3. 1. Characterization of Fe₃O₄/SiO₂/APTES Functionalized with Murexide

Scanning electron microscopy (SEM) studies were performed on a Tescan Mira 3XMU with an Oxford EDS analysis system. As shown in Figure 1, the spherical structure of the Fe₃O₄ NPs changed after modification. The surface of Fe₃O₄/SiO₂/APTES functionalized with murexide had a rough morphology compared with Fe₃O₄. SEM images of Fe₃O₄ and Fe₃O₄/SiO₂/APTES functionalized with murexide are shown in Figure 1.

Elemental analysis showed the presence of C, N and Si in the structure of the modified magnetic nanosorbent.

According to the EDS analysis, Fe₃O₄ modified with APTES and Mu contains C: 6.71%, N: 2.90%, Si: 4.06%, O: 49.17%, and Fe: 37.1% (Figure 2b).

Infrared absorption measurements of Fe₃O₄ and Fe₃O₄/SiO₂/APTES were carried out using a Fourier Transform Infrared (FTIR) spectrophotometer (Bruker Optics – Alpha). The FTIR spectra were obtained in the wavenumber range 500–4000 cm⁻¹ using single bounce ATR with selenium crystal. The absorption peaks at 550 cm⁻¹ (Fe-O) in the spectra of Fe₃O₄ NPs confirmed the synthesis of Fe₃O₄ nanoparticles.^{32,33} On the other hand, the peaks observed at 1045 cm⁻¹ (Si-O), 1450 cm⁻¹ (C=N), 1530 cm⁻¹ (C=C) and 1630 cm⁻¹ (C=O) in the spectra of Fe₃O₄/SiO₂/APTES/Mu have shown the successful modification of Fe₃O₄ with silan agents and Mu.³³

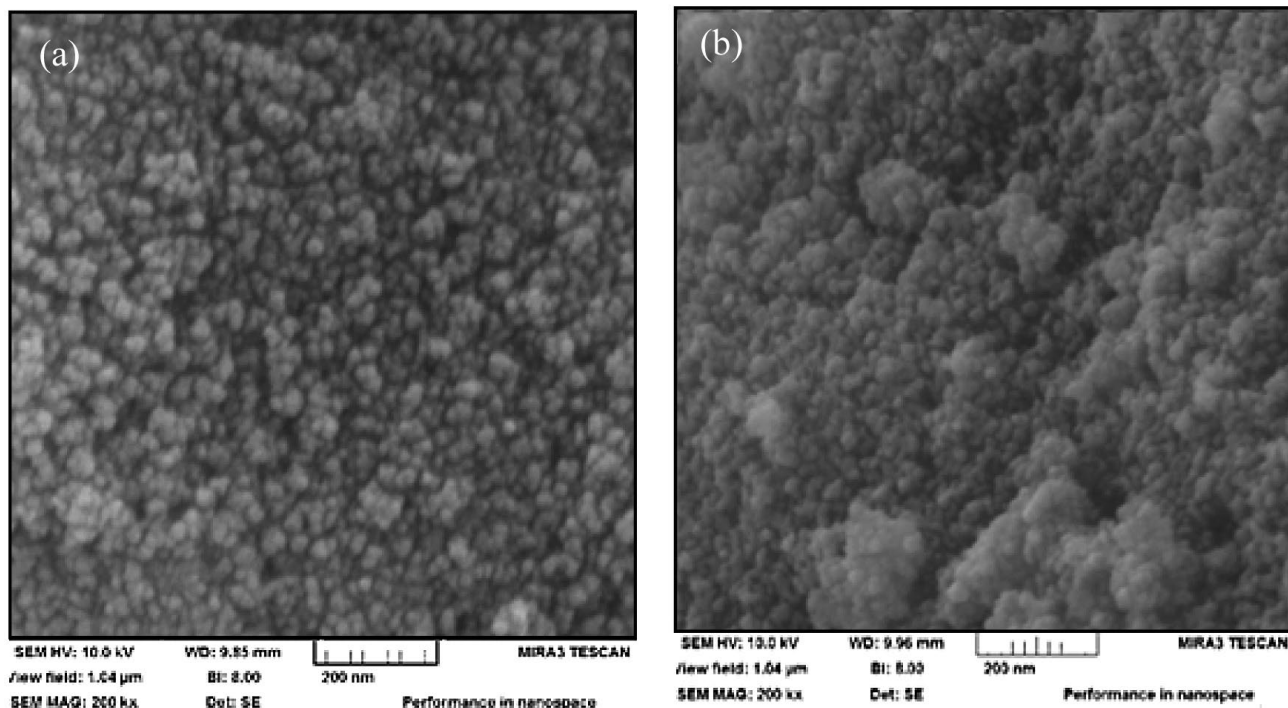


Fig. 1. The Scanning Electron Microscopy images of (a) Fe₃O₄ (b) Fe₃O₄/SiO₂/APTES functionalized with murexide.

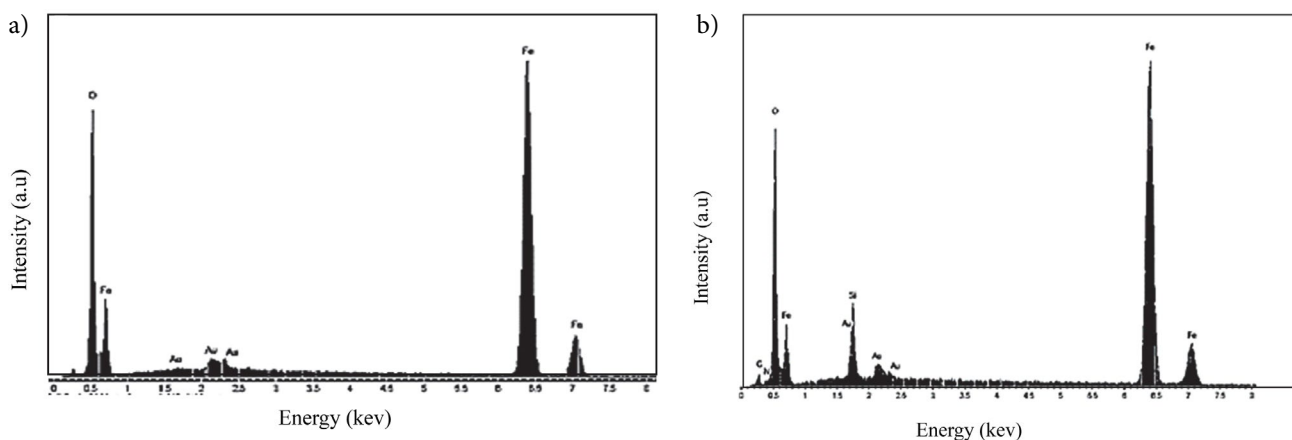


Fig. 2. Energy Dispersive X-Ray Spectroscopy analysis images of (a) Fe₃O₄ (b) Fe₃O₄/SiO₂/APTES functionalized with murexide.

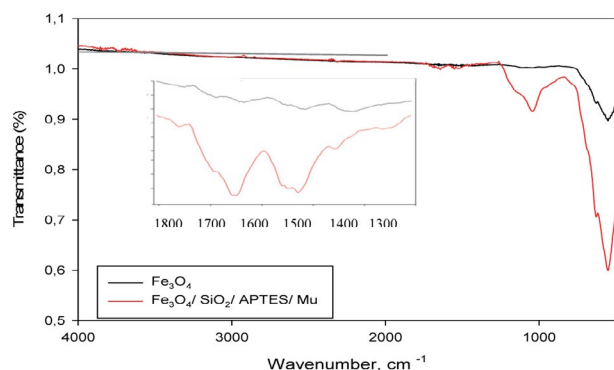


Fig. 3. The FTIR spectra of Fe_3O_4 and $\text{Fe}_3\text{O}_4/\text{SiO}_2/\text{APTES}$ functionalized with murexide (the FTIR spectrum of wavenumber 1300–1800 cm^{-1} is shown in inner figure).

3. 2. Effect of pH

In the SPE, an important parameter for obtaining the quantitative adsorption and recovery of trace elements is pH. For this purpose, the adsorption of uranium ions on Mu-functionalized $\text{Fe}_3\text{O}_4/\text{SiO}_2/\text{APTES}$ sorbent was studied as a function of pH. The pH of the model solutions (40 mL, SSW) containing $50 \mu\text{g L}^{-1}$ of U(VI), was adjusted to a pH range of 4–8 by the use of relevant buffer solutions; the retained uranium ions were eluted by HClO_4 (1 mL, 5 mol L^{-1}). The graph of retention as a function of pH is shown in Fig. 4. The quantitative recovery ($\geq 95\%$) for the uranium ions studied was obtained at a pH of 6–7. Therefore, a pH of 6.5 was chosen as an optimum pH for subsequent experiments.

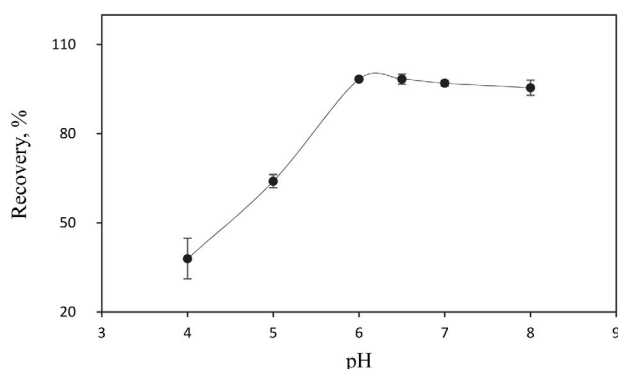


Fig. 4. Effect of pH on recovery % U(VI) with $\text{Fe}_3\text{O}_4/\text{SiO}_2/\text{APTES}/\text{Mu}$.

3. 3. Effect of Eluent Concentration and Volume

In this study the elution of uranium was studied to find the optimum amount of HClO_4 in the range of 2–5 M and volume of 0.5 to 2 mL. 1 mL of 5 M HClO_4 was found to be satisfactory for elution of uranium (recovery $\geq 95\%$).

Therefore, 1 mL of 5 M HClO_4 as eluent was chosen for the following experiments.

3. 4. Effect of Matrix Components

The effects of matrix ions, which are found at high concentrations in real samples, on the recovery of metal ions were studied. Various concentrations of Fe^{3+} , Cd^{2+} , Pb^{2+} , Co^{2+} , Ni^{2+} , Cu^{2+} , Cr^{3+} , Al^{3+} , and Zn^{2+} , as their chloride, nitrate and sulfate salts, were added individually to a model solution of 50 mL containing 0.05 mg L^{-1} U(VI). The described method was applied under optimum conditions. The results are given in Table 1. The most significant interferences were found with 1 mg L^{-1} of Cr^{3+} and Ni^{2+} when determining the presence of uranium. These interferences were prevented by using 0.02 M EDTA. Besides, EDTA can be used as a masking agent for many elements such as Th, Zr, because EDTA forms stable complex with these elements, and unstable complex with U(VI).³⁴

Table 1. Tolerance limits for interference ions on the determination of U(VI) ($n = 3$, 0.05 mg L^{-1} U, 1 mg L^{-1} of metal ions)

Ion	Interference ion to metal ion/ratio	Recovery %, U(VI)
Zn^{2+}	20	101.4 ± 4.2
Cd^{2+}	20	97.5 ± 1.8
Pb^{2+}	20	99.2 ± 0.2
Fe^{3+}	20	100.2 ± 4.3
Al^{3+}	20	96.0 ± 2.3
Cr^{3+}	20	81.1 ± 0.7
$\text{Cr}^{3+} + 0.02 \text{ M EDTA}$	20	96.2 ± 0.4
Ni^{2+}	20	86.8 ± 2.4
$\text{Ni}^{2+} + 0.02 \text{ M EDTA}$	20	97.8 ± 0.5
Cu^{2+}	20	95.4 ± 1.2

3. 5. Effect of Adsorption and Elution Time

The rate of U(VI) adsorption by $\text{Fe}_3\text{O}_4/\text{SiO}_2/\text{APTES}/\text{Mu}$ was studied (50 mL, 0.05 mg L^{-1}) with 25 mg of the sorbent over a series of varying shaking times (5–30 min). The results showed that the extraction percentage of U(VI) at 15 min was higher than 98%. The rate of elution of U(VI) by $\text{Fe}_3\text{O}_4/\text{SiO}_2/\text{APTES}/\text{Mu}$ was studied (50 mL, 0.05 mg L^{-1}) with 25 mg of the sorbent and an adsorption of 15 min over a series of varying shaking times (1–5 min). Therefore, 15 min and 2 min, respectively, were used in all subsequent experiments for quantitative sorption and elution of U(VI).

3. 6. Sorption Capacity

The maximum sorption capacity of $\text{Fe}_3\text{O}_4/\text{SiO}_2/\text{APTES}/\text{Mu}$ was obtained from the batch methods. A total of 25 mg of $\text{Fe}_3\text{O}_4/\text{SiO}_2/\text{APTES}/\text{Mu}$ was added to a 40-mL

solution containing different amounts of U(VI) ions (0.8–8 mg) at pH 6.5. After shaking for 1 h, the mixture was separated with the use of a magnet. The supernatant solutions were then measured by UV-Vis spectrophotometry after dilution. Many isotherm models have been proposed to explain the adsorption equilibrium, such as the Langmuir and Freundlich isotherms, which are the most commonly used for the clarification of adsorption of molecules from the liquid phase. The Langmuir equation is given as follows:

$$\frac{C_e}{Q_e} = \frac{1}{Q_{\max}} C_e + \frac{1}{KQ_m} \quad (1)$$

where Q_{\max} (mg g^{-1}) is the maximum adsorption capacity; Q_e is the amount of solute adsorbed per unit weight of adsorbent (mg g^{-1}) at equilibrium; C_e is the equilibrium solute concentration (mg L^{-1}) in solution and K is the Langmuir constant (L mg^{-1}).

The Freundlich isotherm equation is given below:^{35,36}

$$Q_e = K_f C_e^{1/n} \quad (2)$$

where Q_e is the amount of adsorbed U(VI) per mass of adsorbent, K_f is the Freundlich constant, C_e is the equilibrium U(VI) concentration and $1/n$ is a constant related to the adsorption intensity.³⁷

As shown in Table 2, the adsorption mechanism was well-suited to the Langmuir model, with a correlation coefficient of 0.9997. The Q_{\max} value was found to be 77.51 mg g^{-1} . The n value was 3.87, calculated from the Freundlich isotherm, which is higher than 1. The n value indicated the favourable adsorption of U(VI) on $\text{Fe}_3\text{O}_4/\text{SiO}_2/\text{APTES}/\text{Mu}$. The Langmuir and Freundlich isotherm parameters are shown in Table 2.

3. 7. Analytical Performance and Applications to Real Sea Water Sample

The limit of detection (LOD) study was performed by applying the described method to ten blank solutions of 40 mL. The limit of detection calculated as the ratio of the three standard deviations of the blank to the slope of plot was 0.001 mg L^{-1} with a preconcentration factor of 40. The relative standard deviation was calculated as 3.0% at 0.05 mg L^{-1} of U(VI) ($n = 7$) and the linear range in final eluate was 0.02–4.0 mg L^{-1} of uranium(VI).

The method was successfully applied to sea water. The accuracy of the developed method for sea water was

tested by adding the known amounts of U(VI). After applying the separation/ preconcentration procedure, quantitative recovery ($\geq 95\%$) was found for U(VI). The results of the analysis of sea water samples are shown in Table 3.

Table 3. The results for determination of U(VI) in sea water

Sample	Added ($\mu\text{g L}^{-1}$)	Found ($\mu\text{g L}^{-1}$)	Recovery, %
Sea water from the Aegean Sea	0	2.7±0.1	
	20	22.1±0.4	97.0±2.0
	40	44.2±0.5	104.0±1.2
Sea water from the Mediterranean	0	≤DL	
	20	19.3±1.0	96.7±5.3
	40	40.5±0.8	101.1±2.7

3. 8. Reusability of the Adsorbent

The reusability of the $\text{Fe}_3\text{O}_4/\text{SiO}_2/\text{APTES}/\text{Mu}$ adsorbent was investigated by adsorption and desorption cycling experiments. The results have shown that the sorbent was stable up to 86 cycles without an obvious decrease in the recoveries. The mean recovery ± standard deviation from 86 runs was found to be 97.6 ± 3.6%. This result indicates that the adsorbent possessed a perfect reusability.

4. Conclusions

In this paper, $\text{Fe}_3\text{O}_4/\text{SiO}_2/\text{APTES}/\text{Mu}$ was prepared. Then SPE procedure was developed by using these magnetic nanoparticles. The proposed SPE method is simple, fast, practical, and low-cost. The SPE method has a good potential for the extraction of uranium(VI) from sea water. Significant advantages of this method are a short analysis time and satisfactory results in sea water, which has a high salt concentration. In comparison to other SPE methods, the presented method has a low consumption of time, with a total analysis time of approximately 30 min, including the enrichment/separation procedure and the measurement by spectrophotometry. The adsorbent has considerable reusability. The initially synthesized $\text{Fe}_3\text{O}_4/\text{SiO}_2/\text{APTES}/\text{Mu}$ was used for optimization studies and for a sample application. The adsorbent was reused for 86 cycles. The obtained results show that $\text{Fe}_3\text{O}_4/\text{SiO}_2/\text{APTES}/\text{Mu}$ has a good adsorption capacity (77.51 mg g^{-1}). As a result, $\text{Fe}_3\text{O}_4/\text{SiO}_2/\text{APTES}/\text{Mu}$ is indeed an efficient scav-

Table 2. Langmuir and Freundlich isotherm parameters

	Langmuir Parameters			Freundlich Parameters		
	$Q_{\max}(\text{mg g}^{-1})$	$K(\text{L mg}^{-1})$	R^2	$K_f(\text{L mg}^{-1})$	n	R^2
U(VI)	77.51	0.896	0.9997	26.22	3.87	0.9455

enger for U(VI) in sea water in terms of its fast sorption time, large sorption capacity, selectivity, easy separation and good reusability of the material.

5. Acknowledgement

This work is supported by the Scientific Research Project Fund of Cumhuriyet University under the project number ECZ-040.

6. References

1. M. Rezaee, F. Khalilian, *Journal of Radioanalytical and Nuclear Chemistry* **2015**, *304*, 1193–1200.
DOI:10.1007/s10967-015-3951-6
2. S. Saeed, H. Davarani, H. Reza, A. Reza, M. Hossein, S. Nojavan, *Analytica Chimica Acta* **2013**, *783*, 74–79.
DOI:10.1016/j.aca.2013.04.045
3. M. Tuzen, E. Bagda, B. Hazer, *Journal of Radioanalytical and Nuclear Chemistry* **2016**, *310*, 1255–1263.
DOI:10.1007/s10967-016-4949-4
4. D. Mwalongo, N. K. Mohammed, *Radiation Physics and Chemistry* **2013**, *91*, 15–18.
DOI:10.1016/j.radphyschem.2013.06.002
5. S. R. Tetgure, B. C. Choudhary, D. J. Garole, A. U. Borse, A. D. Sawant, S. Prasad, *Microchemical Journal* **2017**, *130*, 442–451.
DOI:10.1016/j.microc.2016.10.019
6. T. S. Anirudhan, L. Divya, P. S. Suchithra, *Journal of Environmental Management* **2009**, *90*, 549–560.
DOI:10.1016/j.jenvman.2007.12.010
7. J. Kim, C. Tsouris, R. T. Mayes, Y. Oyola, J. Kim, C. Tsouris, R. T. Mayes, et al., *Separation Science and Technology* **2013**, *48*, 367–368.
DOI:10.1080/01496395.2012.712599
8. E. Schneider, D. Sachde, *Science & Global Security* **2017**, *21*, 9882.
9. S. Shahida, A. Ali, M. H. Khan, *Journal of the Iranian Chemical Society* **2014**, *11*, 1–8.
10. A. Nilchi, T. S. Dehaghan, S. R. Garmarodi, *Journal of Radioanalytical and Nuclear Chemistry* **2013**, *295*, 2111–2115. DOI:10.1007/s10967-012-2252-6
11. S. Durani, M. Krishnakumar, K. Satyanarayana, *Journal of Radioanalytical and Nuclear Chemistry* **2012**, *294*, 215–220. DOI:10.1007/s10967-011-1610-0
12. A. Khayambashi, X. Wang, Y. Wei, *Hydrometallurgy* **2016**, *164*, 90–96.
DOI:10.1016/j.hydromet.2016.05.013
13. O. Hazer, S. Kartal, *Talanta* **2010**, *82*, 1974–1979.
DOI:10.1016/j.talanta.2010.08.023
14. R. Rodriguez, J. Avivar, L. Ferrer, L. O. Leal, V. Cerdi, *Talanta* **2015**, *134*, 674–680.
DOI:10.1016/j.talanta.2014.12.007
15. C. Labrecque, S. Potvin, L. Whitty-Léveillé, D. Larivière, *Talanta* **2013**, *107*, 284–291.
DOI:10.1016/j.talanta.2013.01.049
16. S. Gao, T. Sun, Q. Chen, X. Shen, *Journal of Hazardous Materials* **2013**, *263*, 562–568.
DOI:10.1016/j.jhazmat.2013.10.014
17. J. B. Ghasemi, B. Hashemi, M. Shamsipur, *Journal of the Iranian Chemical Society* **2012**, *9*, 257–262.
18. A. Tadjarodi, A. Abbaszadeh, M. Taghizadeh, N. Shekari, A. A. Asgharinezhad, *Materials Science and Engineering C* **2015**, *49*, 416–421.
DOI:10.1016/j.msec.2015.01.013
19. M. Wierucka, M. Biziuk, *TrAC - Trends in Analytical Chemistry*, **2014**, *59*, 50–58.
DOI:10.1016/j.trac.2014.04.007
20. S. Sadeghi, E. Sheikhzadeh, *Journal of Hazardous Materials*, **2009**, *163*, 861–868
DOI:10.1016/j.jhazmat.2008.07.053
21. D. Li, S. Egodawatte, D.I. Kaplan, S.C. Larsen, S. M. Serkiz, J. C. Seamand, *Journal of Hazardous Materials*, **2016**, *317*, 494–502
DOI:10.1016/j.jhazmat.2016.05.093
22. Y. Zhao, J. Li, L. Zhao, S. Zhang, Y. Huang, X. Wua, X. Wang, *Chemical Engineering Journal*, **2014**, *235*, 275–283 DOI:10.1016/j.cej.2013.09.034
23. X. Liu, J. Xing, Y. Guan, G. Shan, H. Liu, *Colloids and Surfaces A: Physicochemical and Engineering Aspects* **2004**, *238*, 127–131.
DOI:10.1016/j.colsurfa.2004.03.004
24. R. K. Gautam, P. K. Gautam, S. Banerjee, S. Soni, S. K. Singh, M. C. Chattopadhyaya, *Journal of Molecular Liquids* **2015**, *204*, 60–69.
DOI:10.1016/j.molliq.2015.01.038
25. C. Hu, J. Deng, Y. Zhao, L. Xia, K. Huang, S. Ju, N. Xiao, *Food Chemistry* **2014**, *158*, 366–373.
DOI:10.1016/j.foodchem.2014.02.143
26. M. Hidarian, S. Hashemian, *Oriental Journal of Chemistry* **2014**, *30*, 1753–1762.
27. X. Qin, A. A. A. Bakheet, X. Zhu, *Journal of the Iranian Chemical Society* **2017**, *14*, 2017–2022.
28. C. Atila Dincer, N. Yildiz, N. Aydogan, A. Calimli, *Applied Surface Science* **2014**, *318*, 297–304.
DOI:10.1016/j.apsusc.2014.06.069
29. Y. Huang, A. A. Keller, *Water Research* **2015**, *80*, 159–168. DOI:10.1016/j.watres.2015.05.011
30. S. Sánchez-Rodríguez, J. Trujillo-Reyes, E. Gutiérrez-Segura, M. Solache-Ríos, A. Colín-Cruz, *Separation Science and Technology* **2015**, *50*, 1602–1610.
DOI:10.1080/01496395.2014.986579
31. Y. Izadmanesh, J. B. Ghasemi, *Talanta* **2014**, *128*, 511–517. DOI:10.1016/j.talanta.2014.06.008
32. R. S. Juang, Yao. C. Yei, C. S. Lia, K. S. Lind, H. C. Lu, S. F. Wang, A. C. Sun, *Journal of the Taiwan Institute of Chemical Engineers* **2018**, *90*, 51–60.
DOI:10.1016/j.jtice.2017.12.005
33. A. A. Asgharinazed, M. Rezvani, H. Ebrahimzadeh, N. Shekari, N. Ahmandinasab, M. Loni, *Analytical Methods*, **2015**, *7*, 10350–10358.
DOI:10.1039/C5AY02362A

34. A. H. Orabi, *Journal of Radiation Research And Applied Sciences*, **2013**, 6, 1–10.
DOI:10.1016/j.jrras.2013.09.001
35. Q. Zhou, F. Chen, W. Wu, R. Bu, W. Li, F. Yang, *Chemical Engineering Journal* **2016**, 285, 198–206.
DOI:10.1016/j.cej.2015.10.004
36. T. Robinson, B. Chandran, P. Nigam, *Water Research* **2002**, 36, 2824–2830.
DOI:10.1016/S0043-1354(01)00521-8
37. C. Kannan, K. Muthuraja, M. R. Devi, *Journal of Hazardous Materials* **2013**, 244–245, 10–20.
DOI:10.1016/j.jhazmat.2012.11.016

Povzetek

V tej raziskavi smo uporabili magnetne nanodelce ($\text{Fe}_3\text{O}_4/\text{SiO}_2/\text{APTES}$), funkcionalizirane z mureksidom, za določanje urana(VI) v morski vodi s spektrofotometrično metodo v perklorno-kislinskem mediju z Arsenazo-III kot kromogenim reagentom. Vpliv nekaterih analiznih parametrov, kot so pH, kontaktni čas in volumen eluenta, na izkoristek ekstrakcije urana(VI) smo raziskovali v sintetski morski vodi. Optimalne pogoje smo dosegli z adsorpcijskim časom 15 min in elucijskim časom 2 min pri eluciji z 1 mL 5 mol L⁻¹ HClO₄ pri pH 6,5 in s 25 mg magnetnega sorbenta. Linearno območje, meja zaznave in natančnost (kot RSD%) metode so bili: 0,02–4,0 mg L⁻¹, 0,001 mg L⁻¹ in 3,0 %. Predlagana metoda je preprosta, hitra in cenovno ugodna za določanje U(VI) v morski vodi s skupnim časom analize približno 30 min. Adsorpcijska izoterma se je dobro prilegala Langmuirjevemu modelu s korelacijskim koeficientom 0,9997 in vrednostjo Q_{max} 77,51 mg g⁻¹. Magnetni sorbent smo uspešno uporabili za hitro določitev U(VI) ionov v sledovih v različnih vzorcih morske vode ter dobili zadovoljive rezultate.

Scientific paper

Dawson-Type Polyoxometalate Incorporated into Nanoporous MIL-101(Cr): Preparation, Characterization and Application for Ultrafast Removal of Organic Dyes

Afsoon Jarrah and Saeed Farhadi*

Department of chemistry, Lorestan University, Khorramabad, 68151-44316, Iran

* Corresponding author: E-mail: sfarhadi1348@yahoo.com

Tel: +986633120611, fax: +986633120618

Received: 06-01-2018

Abstract

In this work, Dawson-type $K_6P_2W_{18}O_{62}$ polyoxometalate salt (abbreviated as P_2W_{18}) was successfully encapsulated into mesoporous MIL-101(Cr) metal organic framework. The as-prepared $P_2W_{18}@MIL-101(Cr)$ nanohybrid was characterized by FT-IR spectroscopy, XRD, Raman spectroscopy, EDX, SEM, zeta potential measurements and BET surface area. The results demonstrated the successful loading of $K_6P_2W_{18}O_{62}$ (~36 wt.%) into porous MIL-101(Cr) framework. Compared with the pristine MIL-101(Cr), the encapsulated sample demonstrated a significant decrease in both surface area and pore volume owing to the insertion of large Dawson-type POM into the cages of MOF. The resulting $P_2W_{18}@MIL-101(Cr)$ was applied as a new adsorbent to remove methylene blue (MB), Rhodamine B (RhB) and methyl orange (MO) organic dyes from aqueous solutions. The effect of effective parameters such as adsorbent dosage, dye concentration, pH, and the temperature was studied on the dye removal process. Furthermore, the selective adsorption of the nanohybrid was investigated towards MB/MO, MB/RhB, MO/RhB and MB/MO/RhB mixed dye solutions. The nanohybrid showed rapid and selective adsorption for cationic MB and RhB dyes from mixed dye solutions. The results indicated that the dye adsorption followed Langmuir isotherm. The thermodynamic data showed that the adsorption is an endothermic process. This nanohybrid can function as a recyclable efficient adsorbent for the rapid removal of various cationic textile dyes from aqueous solutions.

Keywords: Dawson-type polyoxometalate; MIL-101(Cr); Metal organic framework (MOF); Nanohybrid; Dye adsorption.

1. Introduction

Metal organic frameworks (MOFs) are crystalline porous materials whose structures are defined by metal ions or metallic clusters that are connected to bi- or multipodal organic linkers.¹ Nowadays, MOFs have attracted significant research attention in many attractive fields because of their high surface areas, tunable structures and pore sizes, low framework densities, and high pore volumes relative to other porous matrices.^{2,3} These unique and outstanding features of MOFs have resulted in a vast range of promising potential applications such as catalysis,⁴ luminescence,⁵ magnetism,⁶ drug delivery,⁷⁻¹⁰ chemical sensing,¹¹ ion exchange,¹² pollutant removal in aqueous media,¹³⁻¹⁶ and gas storage and separation.^{17,18} Furthermore, owing to their large surface areas and high pore volumes, MOFs can be utilized as hosts for encapsulating large molecules to construct novel multifunctional materials.¹⁹

Polyoxometalates (POMs) are a class of compounds formed by bulky clusters of transition metal oxide anions and have attracted intensive attention due to their earth-abundant source, rich topology and versatility, controllable shape and size, oxo-enriched surfaces, highly electronegative etc, with various applications in many fields, such as catalysis, optics, magnetism, biological medicine as well as dye adsorption.²⁰ The disadvantages of low surface area ($<10 \text{ m}^2 \text{ g}^{-1}$) and high solubility in the reaction system limit their the recovery and reuse on a large scale. To overcome this limitation, permanent heterogenization of these homogeneous catalysts into various host supports such as SBA-15, MCM-41, and ZrO_2 has been reported.^{21,22} However, these systems tend to have limited POM loading and present some leaching, and the supported POMs show a tendency for agglomeration. Therefore, it is of great importance to look for more appro-

appropriate materials to immobilize POMs. MOF is an attractive host matrix for the encapsulation of POM taking into account the benefit of its (i) large mesocages for the encapsulation of POM molecules, (ii) good POM dispersion, (iii) high surface area, (iv) a simple and efficient one-pot synthesis of the formulation and (v) a relatively high framework stability. To date, the encapsulation of Keggin-type POMs in MOFs has been reported, and research on their adsorption performance of the POM@MOFs has been performed.^{23–31}

In this work, a novel nanohybrid material based on Dawson-type polyoxometalate ($K_6P_2W_{18}O_{62}$; P_2W_{18}) encapsulated in metal organic framework MIL-101(Cr) was prepared by a simple hydrothermal method. The resulting P_2W_{18} @MIL-101(Cr) material was characterized by several techniques in detail, and its ability was evaluated in the adsorptive removal of organic dyes under ambient conditions. The results showed that the P_2W_{18} @MIL-101(Cr) hybrid is an effective adsorbent for ultrafast removal of cationic dyes such as methylene blue (MB) and rhodamine B (RhB) from aqueous solutions. The effects of dye concentration, pH, adsorbent dosage, and temperature were investigated on the adsorption process. Moreover, the kinetics, thermodynamic, and isothermal properties of the adsorption process were also studied.

2. Experimental

2.1. Materials

Chromium(III) nitrate ($Cr(NO_3)_3 \cdot 9H_2O$, 99%), terephthalic acid (H_2BDC , 98%), sodium tungstate ($Na_2WO_4 \cdot 2H_2O$, 99%), phosphoric acid (H_3PO_4 , 85%) were provided from Sigma-Aldrich. All organic solvents were purchased from Merck or Aldrich and were utilized without further purification. Potassium chloride (KCl, 98%), hydrochloric acid (HCl, 35%), methyl orange (MO, $C_{14}H_{14}N_3NaO_3S$, 98%), methylene blue (MB, $C_{16}H_{18}ClN_3S$, 98%) and Rhodamine B (RhB, $C_{28}H_{31}ClN_2O_3$, 98%) were purchased from Merck Chemical Co.

2.2. Synthesis of MIL-101(Cr) Metal Organic Framework

MIL-101(Cr) was synthesized by a hydrothermal route in aqueous media and in the absence of hydrofluoric acid.³² $Cr(NO_3)_3 \cdot 9H_2O$ (2.4 g), terephthalic acid (0.98 g) were blended in 29 ml distilled water and mixed at room temperature for time 10–20 min was stirred. The suspension to a 50 ml Teflon-lined autoclave was transferred and in oven was heated for 24 h at 200 °C. After slowly cooling at room temperature, the green solid was filtered and washed with DMF at 60 °C for 3 h and then with ethanol at 70 °C for 2.5 h to remove the unreacted terephthalic acid (H_2BDC). Finally, the green solid was separated by centrifugation and was dried at room temperature.

2.3. Synthesis of Dawson-Type $K_6P_2W_{18}O_{62}$ Polyoxometalate

The Dawson-type $K_6P_2W_{18}O_{62}$ polyoxometalate was prepared according to the reported method.³³ A sample of $Na_2WO_4 \cdot 2H_2O$ (300 g; 0.91 mol) dissolved in 350 mL distilled water was acidified by fractional addition of HCl 4 M (250 mL; 1.00 mol) under vigorous stirring. When the cloudy solution becomes limpid again, H_3PO_4 4 M (250 mL; 1.00 mol) was added slowly. The pale yellow and limpid solution was refluxed for at least 24 h. After this reaction time, the yellow colour of the solution had become more intense. This solution was allowed to cool to room temperature and was then treated with 150 g KCl. The precipitate which appeared was filtered off and air-dried by aspiration. This crude material was dissolved in 650 mL distilled water, and the solution was, eventually, filtered to remove insoluble impurities. The limpid solution was then heated at 80 °C for 72 h. After this period of time, the solution was allowed to cool to room temperature before being placed finally in a refrigerator at 4 °C. After a few days, well-behaved yellow crystals of α - $K_6P_2W_{18}O_{62} \cdot 14H_2O$ were collected (232.5 g; 95%).

2.4. Synthesis of P_2W_{18} @MIL-101 (Cr) Nanohybrid

The P_2W_{18} @MIL-101(Cr) nanohybrid was fabricated as follows: $Cr(NO_3)_3 \cdot 9H_2O$ (2.0 g, 5 mmol), terephthalic acid (0.83 g, 5 mmol), α - $K_6P_2W_{18}O_{62} \cdot 14H_2O$ (2.0 g, 0.7 mmol) in 20 mL of distilled water were dispersed for 15 min by sonicating. The suspension color with a pH of 2.58 became dark blue. The suspension to a 50 ml Teflon-lined autoclave was transferred and heated at 200 °C for 18 h without stirring under autogenous pressure. Then, green powder was separated by centrifugation, washed five times with distilled water, one-time ethanol, and acetone, and then was dried at room temperature. The ICP-AES results indicated that the loading amount of P_2W_{18} in the as-prepared P_2W_{18} /MIL-101 nanocomposite was estimated to be 36 wt%.

2.5. Methods of Characterization

FT-IR was registered using a Shimadzu-8400S (Japan) spectrometer with temperature controlled high sensitivity detector (DLATGS detector) in the wavenumber range of 500–4000 cm^{-1} . Powder X-ray diffraction (XRD) patterns were recorded at room temperature on a Rigaku D-max X-Ray diffractometer using $Cu K\alpha$ radiation ($\lambda = 1.5418 \text{ \AA}$). The morphological properties nanohybrid acquired by scanning electron microscopy (SEM, MIRA3 TESCAN) along with the energy-dispersive X-ray analysis (EDX). Specific surface area of samples was determined by the N_2 adsorption-desorption Brunauer-Emmett-Teller (BET) method at 77 K (Micrometrics PHS-1020). Zeta po-

tential measurements were carried out by using a Nano Zeta sizer system (Malvern, UK) equipped with a standard 628 nm laser. Raman spectrum was recorded on a SENTERRA 2009 system using laser wavelength of 758 nm. The adsorption process of dyes was evaluated on a Varian Cary 100 spectrophotometer. UV-Vis spectrophotometer. The loading amount of HPW in the composite adsorbent and the concentrations of Cr and W metals in the filtrates and solutions after recovering adsorbent were determined was determined by inductively coupled plasma atomic emission spectrometer (Perkinelmer ICP-AES, USA).

2. 6. Dye Adsorption Tests

Experiments were carried out to investigate the adsorption attributes and parameters affecting the adsorption of the dyes. Firstly, stock solutions (200 mg L⁻¹) of RhB, MB, and MO dyes were prepared by dissolving them in distilled water. Then, the stock solution was constructed in the form of dye solutions of MB, MO, and RhB, with consecutive dilutions using distilled water. The adsorbent (30 mg) was added into 30 mL of the aqueous solution of different dyes with an initial concentration of 25 mg L⁻¹ such as MB, RhB, and MO. In order to prevent degradation of the dyes, the containers holding the dye solution were wrapped in dark paper during the adsorption tests to protect the dye from light. The mixture was stirred gently at a speed of 300 rpm at 25 °C for 0.5 to 10 min, and the adsorbent was separated by centrifugation. The residual dye concentrations were determined at the maximum wavelength of 463 nm for MO, 553 nm for RhB and 664 nm for MB by using a UV-Vis spectrophotometer. Similar experiments were performed to study the adsorption of MB with different dosages of the adsorbent; (10, 20, 30, and 40 mg). In addition, different initial concentrations of MB solution (25, 50, 75, 100, 125, 150, 175, and 200 mg L⁻¹) were used for studying the capability of the synthesized nano hybrid. Also, the nano hybrid was poured into mixtures of MO/RhB, MO/MB, RhB/MB, and MB/RhB/MO (v: v 1/1, 30 mL, 25 mg L⁻¹) to study the selective adsorption activity of adsorbent. The effects of initial pH (2–10) and temperature (25–95 °C) of MB dye solution on the adsorption capacity were also investigated. The equilibrium adsorption capacity q_e (mg/g) and the dye removal efficiency (R%) were calculated according to Equations (1) and (2), respectively:

$$q_e(\text{mg/g}) = \frac{V(C_0 - C_t)}{m} \quad (1)$$

$$R\% = \left[\frac{(C_0 - C_t)}{C_0} \right] \times 100 \quad (2)$$

Where C_0 and C_t (mg L⁻¹) are the dye concentrations at initial and t times, respectively. V (in L) is the volume of the dye solution and m (in g) indicates the mass of the ad-

sorbent in the adsorption process. Thermodynamic studies were conducted at different temperatures (25–75 °C) to investigate the dye adsorption. In all aqueous solutions containing dye and P₂W₁₈/MIL-101 adsorbent, the residual concentrations of Cr and W after removing the adsorbent were detected to be less than 0.1 % by the ICP-AES analysis of the reaction mixtures.

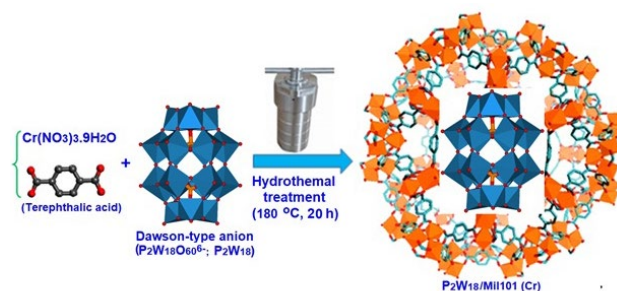
2. 7. Desorption Studies

Nano hybrid after each adsorption test of the MB dye solution using centrifugation was separated and several times with mixed distilled water, NaCl (0.1 M), and ethanol was washed and at room temperature was dried and reused for the next adsorption experiment.

3. Results and Discussion

3. 1. Characterization of Nano hybrid

Among various MOFs, MIL-101(Cr) is one of the most promising porous materials for future energy and environmental applications, owing to its superior physico-chemical properties including high hydrothermal/chemical stability and desirable textural properties. The structure of MIL-101(Cr) was formed of Cr(III) clusters interconnected by terephthalate (BDC) anions. The framework of MIL-101(Cr) was composed of two types of mesoporous cages with diameters of 29 and 34 Å accessible through two types of microporous windows. The smaller cages have pentagonal windows with a free opening of 12 Å, while the larger cages possess both pentagonal and hexagonal windows with a 14.7 Å by 16 Å free aperture.^{34,35} In this work, the Dawson-type POM was encapsulated into the porous MIL-101(Cr) framework by a simple hydrothermally reaction of K₆P₂W₁₈O₆₂ (abbreviate as P₂W₁₈), Cr(NO₃)₃·9H₂O and terephthalic acid (H₂BDC). at 180 °C for 24 h. Scheme 1 shows the general preparation procedure of the P₂W₁₈@MIL-101(Cr) nano hybrid. During the formation of the MIL-101 (Cr) framework, K₆P₂W₁₈O₆₂ molecules are encapsulated into the MIL-101 (Cr) framework to create a new hybrid with the formula of P₂W₁₈@MIL-101(Cr).³⁶ The structure and composition of the



Scheme 1. Schematic illustration for the preparation of P₂W₁₈@MIL101(Cr).

as-obtained hybrid nanomaterial was further characterized by FT-IR, Raman, XRD, EDX, SEM, and BET surface area analyses

FT-IR spectra of MIL-101 (Cr), P_2W_{18} and $P_2W_{18}@MIL-101(Cr)$ samples were recorded in the range of 400–4000 cm^{-1} , as shown in Figure 1. As shown in Figure 1(a), the characteristic absorption peaks of MIL-101(Cr) sample are observed in the region from 1400 to 1600 cm^{-1} , which could mainly originate from the carboxylate groups (-COO) vibrations and are identical to those of reported data in the literatures.³⁷ The two sharp peaks at 1636 and 1396 cm^{-1} are assigned to asymmetric and symmetric vibrations of -COO groups, respectively, confirming the presence of the dicarboxylate linker within the sample. The presence of free terephthalic acid (H_2BDC) impurities in MIL-101 sample was evidenced by absorption bands at 1680 and 1510 cm^{-1} . It should be mentioned that the preparation of MIL-101 with high purity is very difficult due to the presence of trapped H_2BDC residues within the pores of MIL-101. Figure 1(b) shows the characteristic bands of Dawson-type P_2W_{18} at 1091, 960, 912, and 775 cm^{-1} which are related to P-O, W=O_t, W-O_b-W and W-O_c-W bonds, respectively.^{38–40} As displayed in Figure 1(c), the absorption bands of P_2W_{18} at 1090, 963, 912, and 775 cm^{-1} corresponding to the P-O, W=O_t, W-O_b-W and W-O_c-W bonds and the vibrational bands of MIL-101 lo-

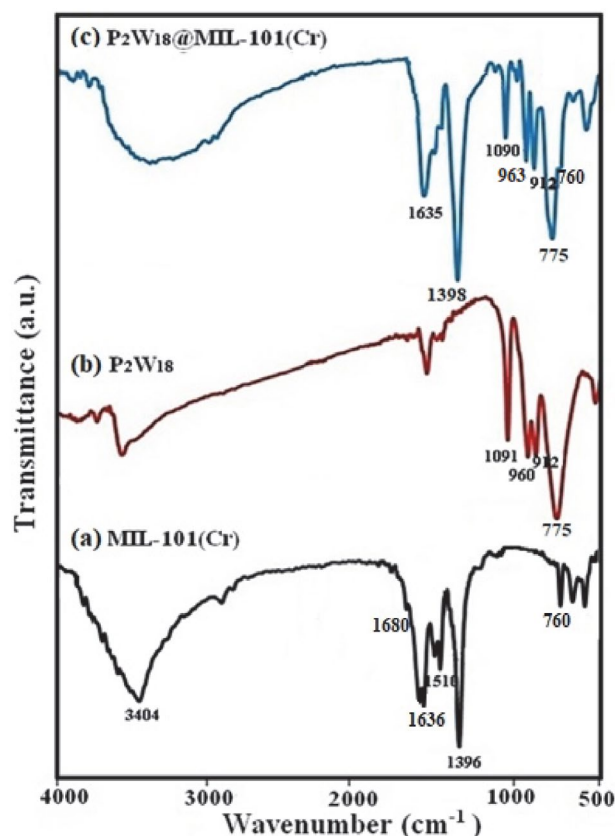


Figure 1. FT-IR spectra of (a) MIL-101 (Cr), (b) P_2W_{18} and (c) $P_2W_{18}@MIL-101(Cr)$ samples.

cated around 1635, 1398, and 760 cm^{-1} were all observed in the FT-IR spectrum of $P_2W_{18}@MIL-101(Cr)$ nanocomposite, which demonstrates the presence of P_2W_{18} and MIL-101 in the $P_2W_{18}@MIL-101$ composite. However, there are slightly shifted peaks compared with the pure P_2W_{18} . These shifts imply that a strong interaction exists between the Dawson-type anion and MIL-101(Cr) MOF.³⁷

XRD patterns of the MIL-101(Cr) and $P_2W_{18}@MIL-10(Cr)$ samples are presented in Figure 2. The XRD pattern of the pristine MIL-101(Cr) is presented in Figure 2(a). The main diffraction peaks corresponding to reflection planes are indexed, which are consistent with the peak positions reported for standard MIL-101(Cr) structure, indicating that the synthesized material has the MIL-101(Cr) phase with good crystallinity.⁴¹ The peak positions of $P_2W_{18}@MIL-10(Cr)$ in Figure 2(b) are matched well with the parent MIL-101(Cr). As can be seen, some diffraction peaks related to P_2W_{18} are observed albeit with very low intensities, confirming the homogeneous distribution of the P_2W_{18} molecules within the porous structure of MIL-101(Cr). Moreover, the XRD and FT-IR data demonstrate that the structure of the MOF does not destruct during the incorporation of P_2W_{18} molecules.

The existence of the Dawson-type polyoxotungstate (P_2W_{18}) in the MIL-101(Cr) framework was further recognized by FT-Raman spectrum of the nanohybrid material in comparison with those of the isolated compounds as shown in Figure 3(a)-(c). It can be seen that the FT-Raman spectrum of the nanohybrid material reveals the typical bands of the porous material MIL-101 and some vibra-

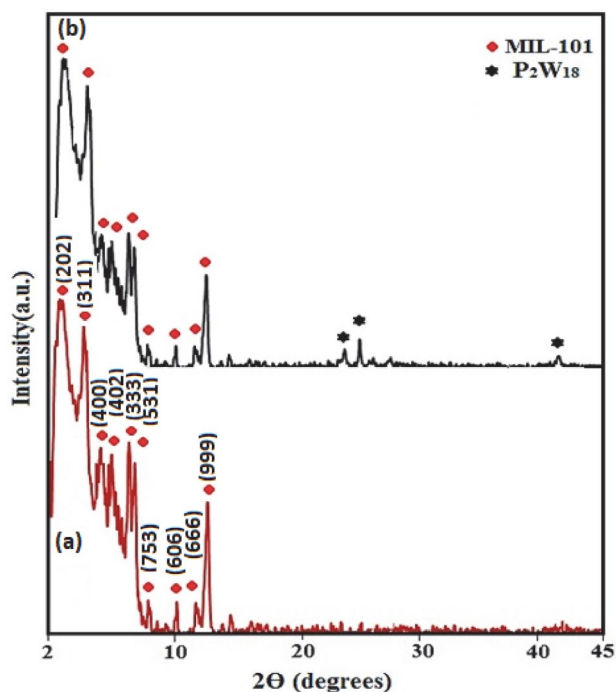


Figure 2. XRD patterns of (a) MIL-101(Cr) and (b) $P_2W_{18}@MIL-101(Cr)$ samples.

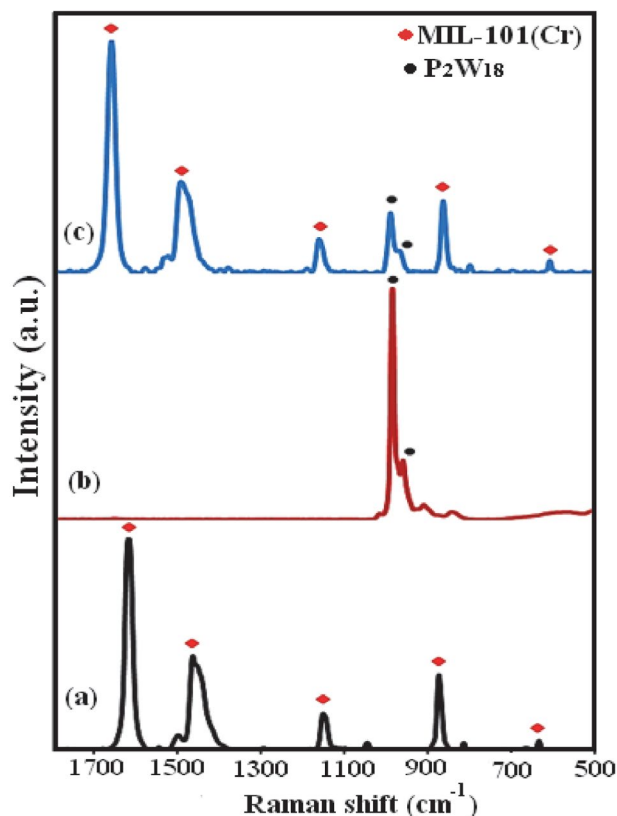


Figure 3. FT-Raman spectra of (a) MIL-101 (Cr), (b) P_2W_{18} , and (c) $P_2W_{18}@MIL101$ (Cr) samples.

tional modes of the P_2W_{18} . In particular, the strong band located at about 965 cm^{-1} assigned to W=O symmetrical stretching mode is clearly evident in the spectrum of the composite material, $P_2W_{18}@MIL-101(Cr)$.⁴² The characteristic bands verify the existence of the both P_2W_{18} and MIL-101 in the $P_2W_{18}@MIL-101(Cr)$ nanocomposite.

The morphology and microstructure of samples were clarified by FE-SEM observations. The SEM images of the samples are indicated in Figure 4. Figure 4(a)–(c) exhibits FE-SEM images of the pristine MIL-101(Cr) particles. It shows that the MIL-101(Cr) particles are irregular polyhedral in shape with high porosity. The sizes of these polyhedral crystals are in the range of $0.5\text{--}2\text{ }\mu\text{m}$. The SEM images of the $P_2W_{18}@MIL-101(Cr)$ composite in Figure 4(d)–(f) clearly show that its shape and morphology are similar with those of the MIL-101(Cr). Confirming that the crystalline structure of MIL-101(Cr) remains unchanged after incorporating P_2W_{18} anions. However, the porosity of MIL-101(Cr) decreased with the incorporation of P_2W_{18} anions.

Figure 5 show the EDX spectrum and a representative SEM image of the hybrid nanomaterial with corresponding EDX elemental mappings. The presence of C, O, P, K, Cr, and W elements in the composite can be proved by the EDX spectrum in Figure 5(a). As presented in Figure 5(b)–(h), the corresponding elemental mapping distribution shows the existence of C, O, P, K, Cr, and W. From the maps, it can be seen that the elements are uniformly distributed over the hybrid nanomaterial, confirming the

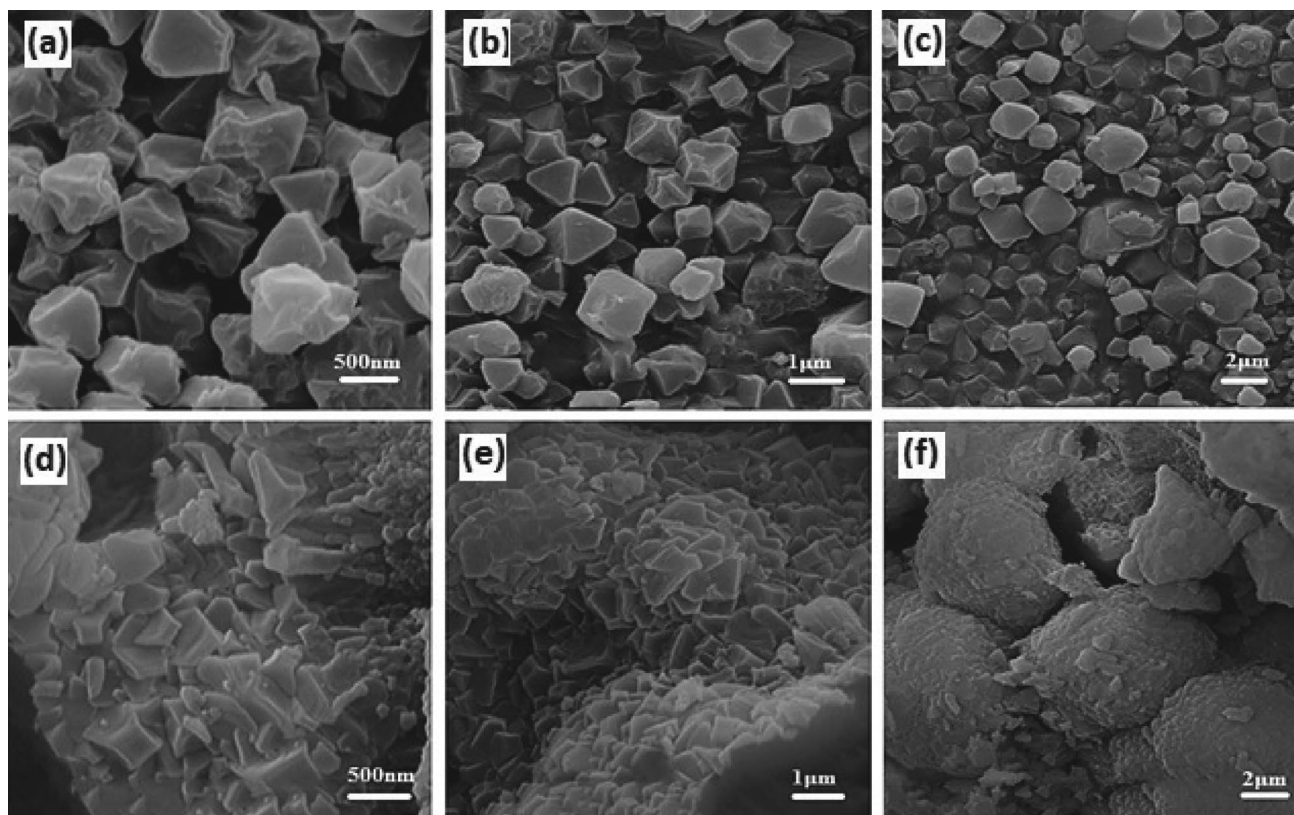


Figure 4. SEM images of (a–c) MIL-101 (Cr) and (d–f) $P_2W_{18}@MIL-10$ (Cr) at different magnifications.

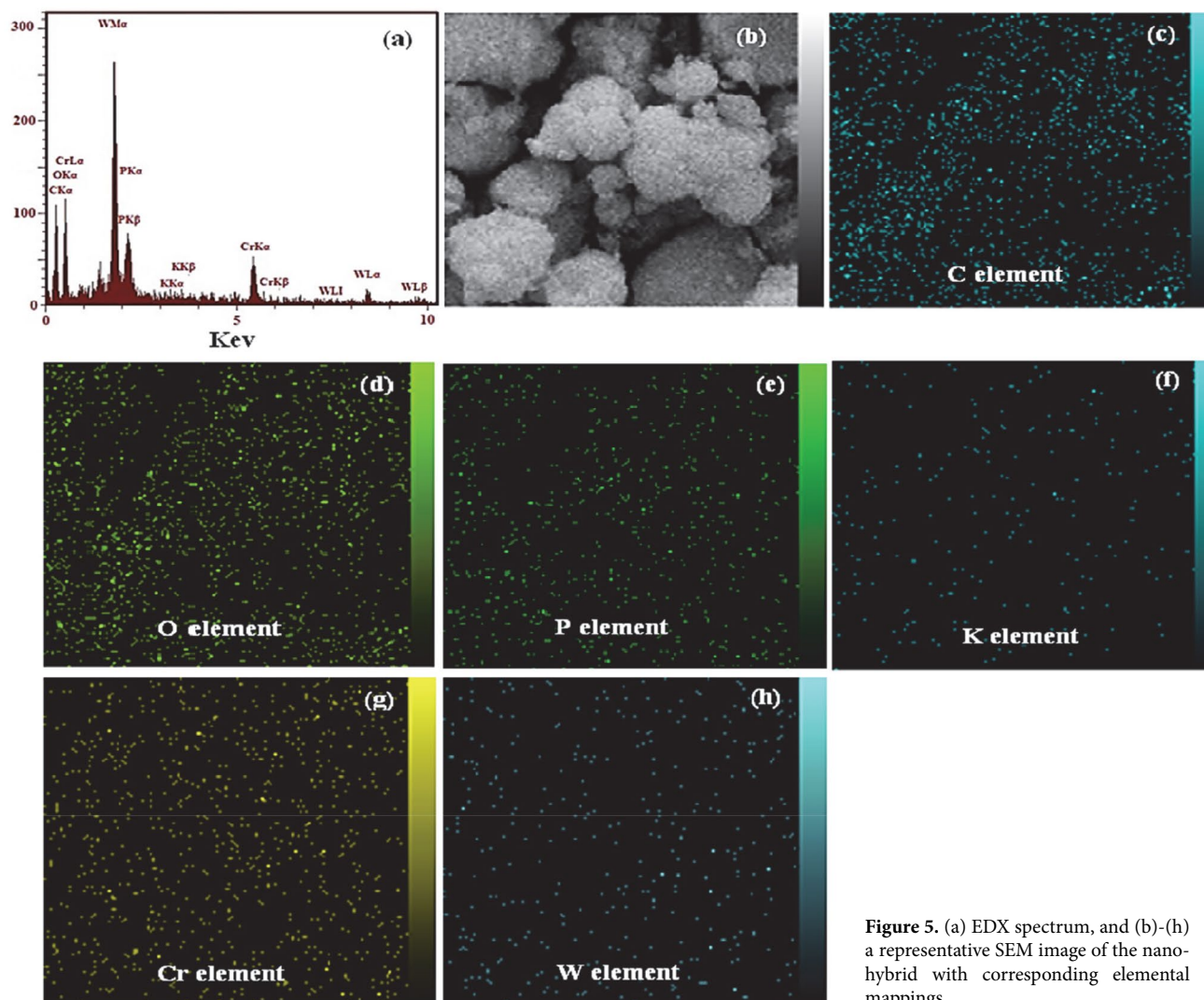


Figure 5. (a) EDX spectrum, and (b)-(h) a representative SEM image of the nano-hybrid with corresponding elemental mappings.

homogeneity of the sample. The K, P and W elements were from P_2W_{18} , thus confirming the uniform incorporation of P_2W_{18} anions into the porous MIL-101(Cr) framework.

The BET surface area and pore volume of the samples were determined by N_2 adsorption-desorption isotherms at 77 K and the results are indicated in Figure 6. On the basis of the IUPAC classification, the N_2 adsorption-desorption isotherms of the samples in Figure 6(a) reveal mixed type I/IV isotherms with H4-type hysteresis loop, which is characteristic of solids with mesoporous and microporous cages.³⁶ The textural properties of these materials were summarized in Table 1. Compared with the pris-

tine MIL-101, the encapsulated sample demonstrated a significant decrease in surface area, pore volume, and pore diameter owing to the insertion of P_2W_{18} polyanion into the cages of the MOF.⁴³ The pores of $P_2W_{18}@MIL-101(Cr)$ were further occupied by the P_2W_{18} polyanion which resulted in a further decrease in pore volume and surface area. The Barrett-Joyner-Halenda (BJH) pore size distributions in Fig. 6(b) also confirmed the mesoporous cages of MIL-101 and reflected the volume changes during the encapsulation process. These findings confirm that the P_2W_{18} polyanion had been encapsulated within the channels of MIL-101(Cr) rather than outside the surfaces.

Table 1. The textural properties of MIL-101(Cr) and $P_2W_{18}@MIL-101(Cr)$ samples.

Sample	BET surface area (m ² /g)	Langmuir surface area (m ² /g)	Total pore volume (cm ³ /g)	V _{micro}	V _{meso}	Average pore diameter (nm)
MIL-101 Cr	2692.403	3455	2.481	0.045	2.436	0.768
$P_2W_{18}@MIL-101(Cr)$	1167.413	1671	1.108	0.029	1.079	0.504

V_{micro}: Micropore volume calculated using t-plot method. V_{meso}: Mesopore volume calculated using BJH method.

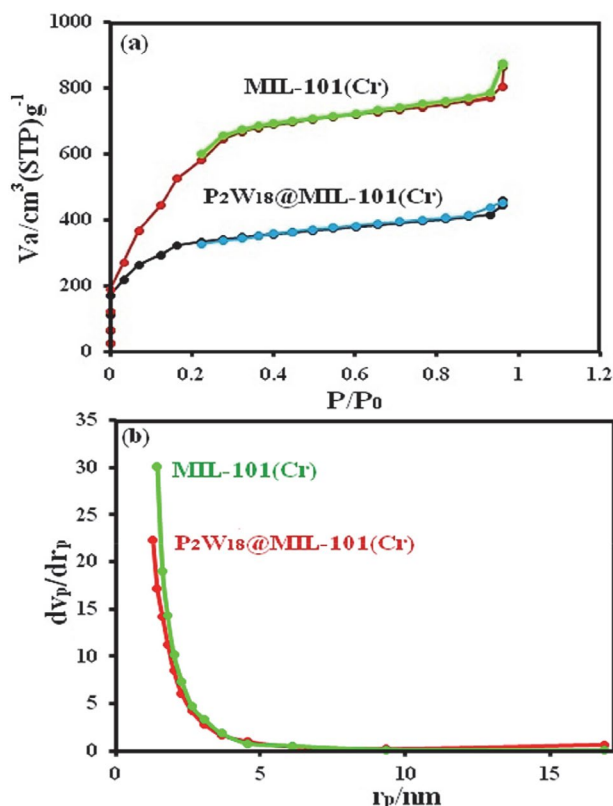


Figure 6. (a) Nitrogen adsorption-desorption isotherms curve at 77 K and (b) pore size distributions obtained by the BJH method for nanohybrid.

Zeta potential of materials is another key factor to influence their adsorption capacity, and thus was tested to understand further why $P_2W_{18}/MIL-101(Cr)$ sample can remove cationic dyes MB and RhB more effectively than for anionic MO dye. As shown in Figure 7, zeta potential of MIL-101 (Cr) and $P_2W_{18}/MIL-101(Cr)$ samples are about -2.7 and -12.8 mV, respectively. This illustrates that the higher efficiency removal of cationic dye is attributed to the electrostatic attraction interactions between the adsorbents and cationic dye. After modification with P_2W_{18} , the obtained $P_2W_{18}/MIL-101$ (Cr) showed higher negative zeta potential than that of pristine MIL-101 (Cr), thus capable of adsorbing more cationic dye MB, whereas it is unfavorable for $P_2W_{18}/MIL-101$ (Cr) to adsorb anionic dye MO. The obtained results on the selective adsorption of cationic dyes as well as studies on the Zeta potential of adsorbents clearly suggest that the adsorption of MB dye on the $P_2W_{18}/MIL-101$ (Cr) nanohybrid has been associated with electrostatic interaction between cationic dye molecules and the highly negative charged $P_2W_{18}/MIL-101$ (Cr) nanohybrid.

3. 2. Adsorption Capability of Nanohybrid Toward Organic Dyes

In this work, the removal of dyes from contaminated aqueous solutions by using $P_2W_{18}@MIL-101(Cr)$ nanohy-

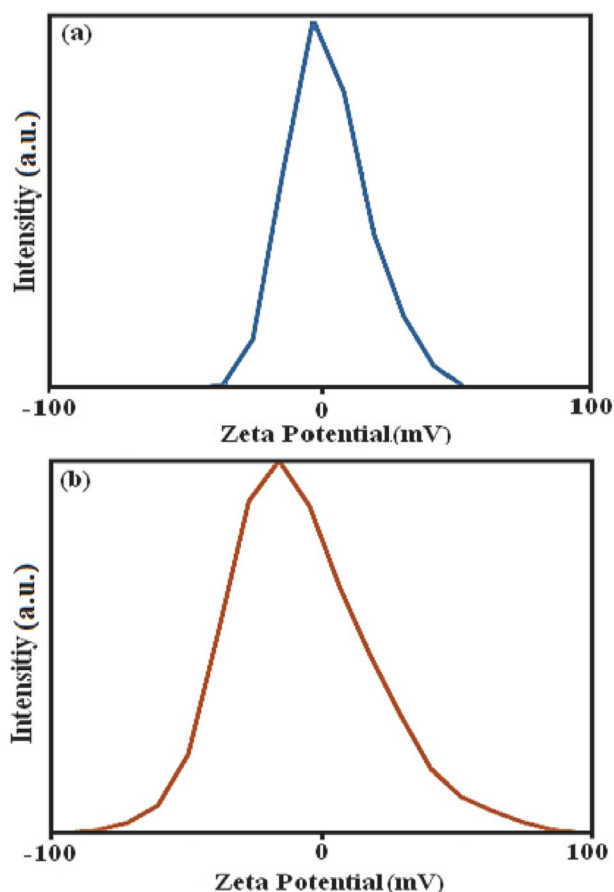


Figure 7. Zeta potential distribution curves of (a) pristine MIL-101 and (b) $P_5W_{30}/MIL-101$ (Cr) hybrid in aqueous solutions.

brid as a novel adsorbent was investigated. Three organic dyes were used herein: MB and RhB as cationic dyes and MO as an anionic dye. From contaminated water, three organic pollutants (MB, RhB, and MO) with different sizes and charges were selected for experiments. The adsorption was monitored using the characteristic absorption peak, which is 664, 553 and 463 nm for MB, RhB, and MO, respectively. The process of adsorption was specified with the fading of the blue, red and orange colors of MB, RhB, and MO, respectively. The time dependent UV-Vis absorption spectra of dyes in the presence of $P_2W_{18}@MIL-101(Cr)$ are shown in Figure 8(a)–(c). As shown in Figure 8(a) and (b), the digital images and UV-Vis spectroscopic results show that the characteristic absorption peaks of cationic MB and RhB dyes at 664 and 553 nm almost completely disappeared within 0.5 and 2 min, respectively. The result in Figure 8(c) confirms that the nanohybrid is a poor absorbent for anionic MO dye from aqueous solution even after 30 min.

To further demonstrate the role of anionic P_2W_{18} POM in the composite material, a set of control experiments was designed using pristine MIL-101(Cr) MOF and pure P_2W_{18} POM samples as adsorbents in removing the different types of organic dyes involving cationic dye MB,

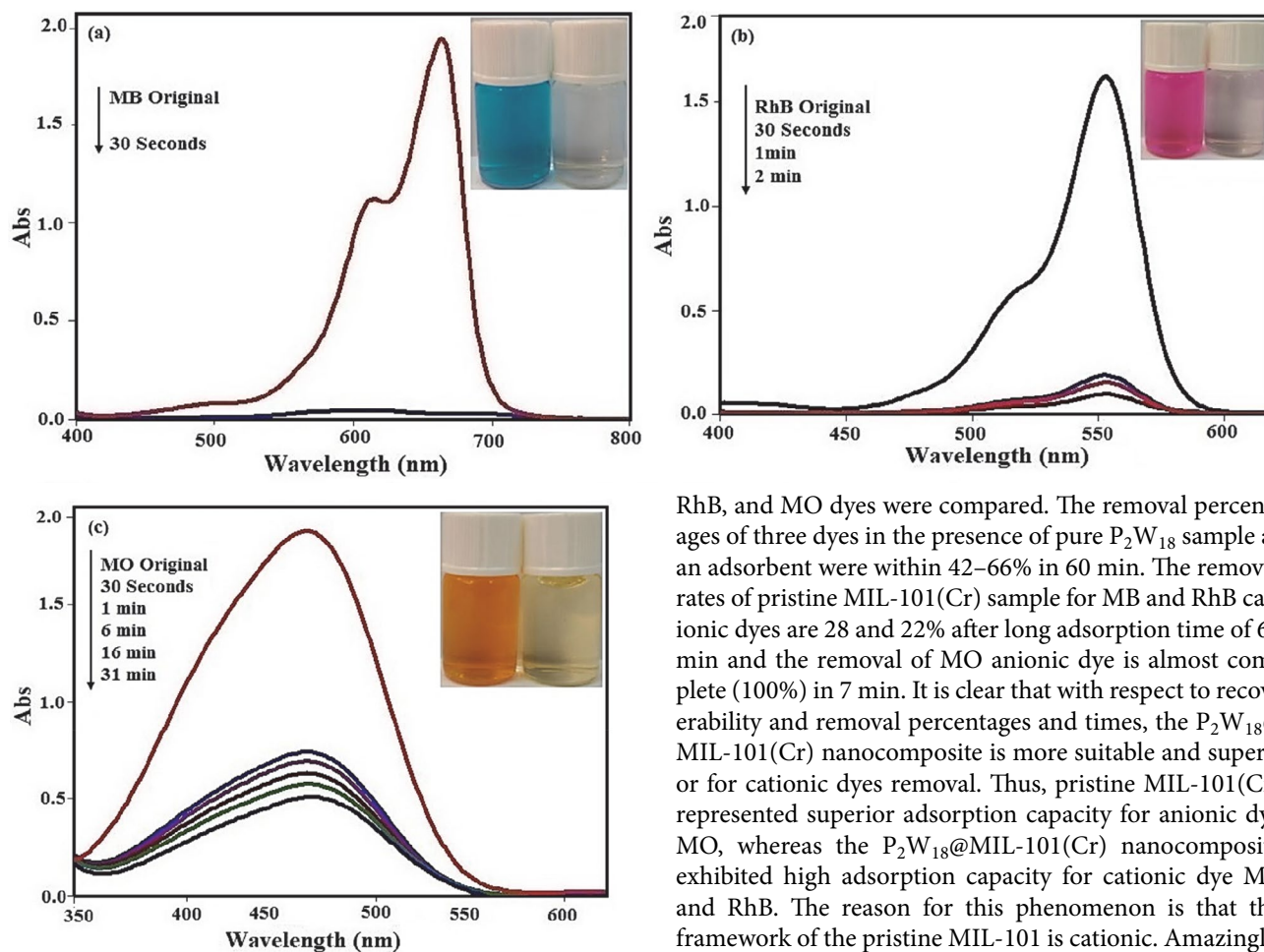


Figure 8. Time dependent UV-Vis spectra during adsorption of dyes over $P_2W_{18}@MIL-101$: (a) MB, (b) RhB, (c) MO. $[dye]_0 = 25 \text{ mgL}^{-1}$; 30 mL, adsorbent amount = 30 mg, temp. = 25 °C.

RhB and anionic dye MO. Figure 9 shows the adsorption abilities of Pristine MIL-101(Cr) MOF and pure P_2W_{18} POM samples toward MB, RhB, and MO dyes under our reaction conditions. By using Pristine MIL-101(Cr) adsorbent, it is clear from Figure 9(a) and (b) the decrease in intensities of characteristic UV-Vis absorption bands of cationic MB and RhB dyes is almost negligible within 60 min, indicating that it has no considerable ability to adsorb cationic dyes even after long contact times whereas it adsorbs completely anionic MO dye within a very short time of 7 min. Figure 9(d)–(f) shows that the pure P_2W_{18} sample has different adsorption ability towards the dyes. It can be seen that the intensity of the absorption bands of MB and RhB decreases with increasing contact time. The adsorption efficiencies of the pure P_2W_{18} sample toward these two dyes are moderate, albeit after long adsorption times of 40–60, (Figure 9(d) and (e)). On the other hand, as can be seen in Figure 9(f), the noticeable decrease in intensity of characteristic absorption band of MO dye was not observed after a long time of 60 min. In Figure 9(g) the adsorption abilities of pure P_2W_{18} and pristine MIL-101(Cr) and $P_2W_{18}@MIL-101(Cr)$ samples toward MB,

RhB, and MO dyes were compared. The removal percentages of three dyes in the presence of pure P_2W_{18} sample as an adsorbent were within 42–66% in 60 min. The removal rates of pristine MIL-101(Cr) sample for MB and RhB cationic dyes are 28 and 22% after long adsorption time of 60 min and the removal of MO anionic dye is almost complete (100%) in 7 min. It is clear that with respect to recoverability and removal percentages and times, the $P_2W_{18}@MIL-101(Cr)$ nanocomposite is more suitable and superior for cationic dyes removal. Thus, pristine MIL-101(Cr) represented superior adsorption capacity for anionic dye MO, whereas the $P_2W_{18}@MIL-101(Cr)$ nanocomposite exhibited high adsorption capacity for cationic dye MB and RhB. The reason for this phenomenon is that the framework of the pristine MIL-101 is cationic. Amazingly, after the introduction of P_2W_{18} polyoxoanions into the cavity of MIL-101, the adsorption capacity of $P_2W_{18}@MIL-101$ has changed a lot comparing with that of the isolated MIL-101 (Figures 8 and 9). This is because that P_2W_{18} polyanions encapsulated in MIL-101 MOF can quickly and effectively adsorb MB and RhB cationic molecules, whereas strongly reject MO anions.

3. 2. 1. Effect of pH

One of the important parameters affecting the adsorption of dyes is the pH of solution. The effect of pH on dye elimination by $P_2W_{18}@MIL-101$ (Cr) is shown in Figure 10(a). The results showed that the pH dependency specifications represent adsorption independent of the entire pH range because nanohybrids have a high negative charge, which allows them to interact with the positive charges of the dyes in all ranges of pHs.

3. 2. 2. Effect of Initial Dye Concentration

As shown in Figure 10(b), with an increment in the initial dye concentration, the dye removal decreases. With the increment of the initial MB concentration in the solution more dye was adsorbed onto $P_2W_{18}@MIL-101$ (Cr), in the event that the dosage of adsorbent remained unchanged.

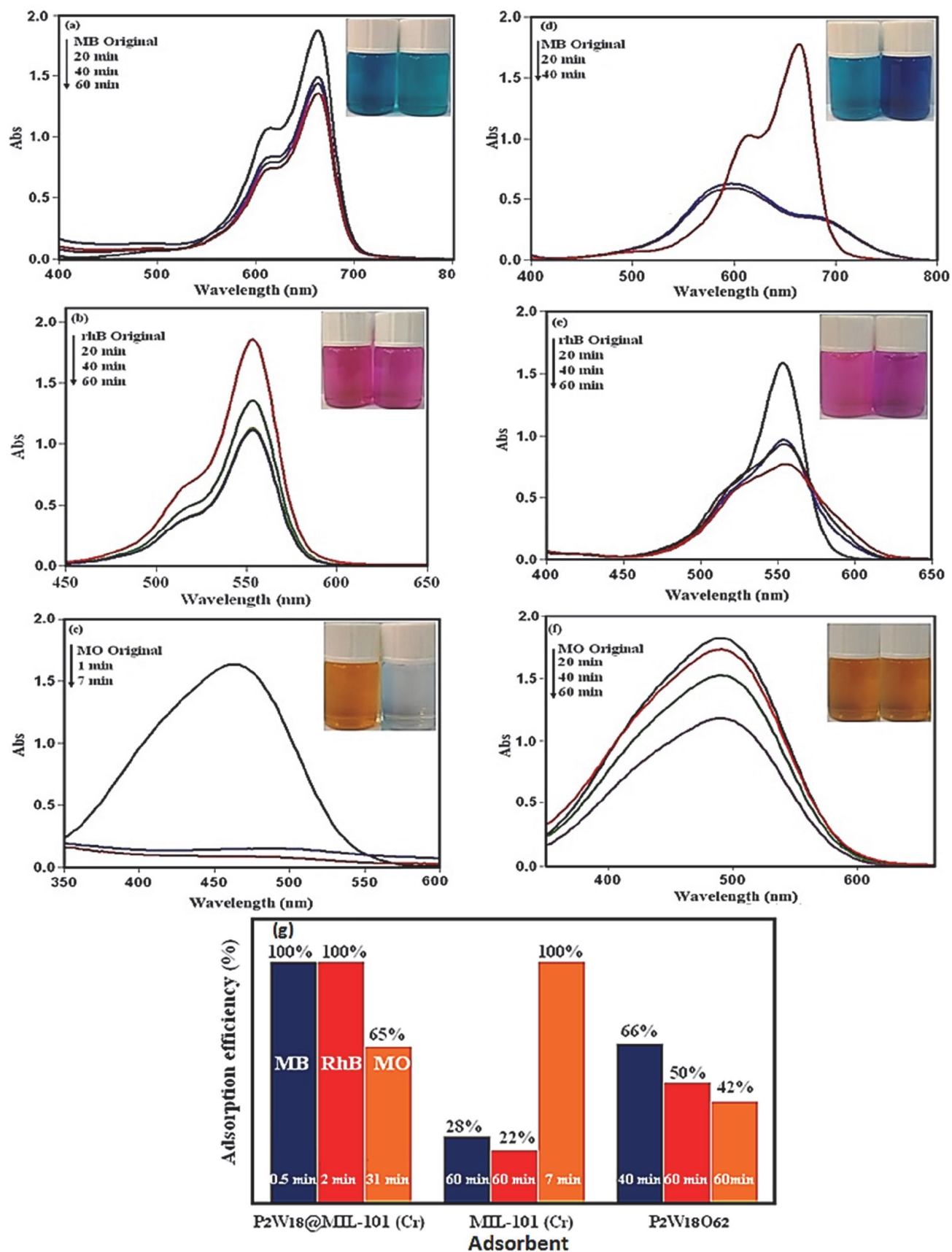


Figure 9. The adsorption capabilities of (a)–(c) pristine MIL-101(Cr) and (d)–(f) pure P₂W₁₈ toward MB, RhB, and MO dyes. (g) Adsorption efficiency (%) of the dyes in the presence of different adsorbent samples.

The reason for this is that with the increased initial dye concentration, an increment occurs in the driving force of the concentration gradient. The adsorption of dye by $P_2W_{18}@MIL-101(Cr)$ in a low initial concentration is very intense and a balance is reached quickly. In fact, for the initial concentration of MB in 25 mg L^{-1} , the nano hybrid has a removal efficiency of 100%, in 30 seconds. This demonstrates that P_2W_{18} was probably distributed homogeneously and uniformly within the porosities of the MIL-101 (Cr). At a constant adsorbent dosage, with an increasing concentration of the solution, the amount of adsorbed dye increased while the adsorption efficiency of the nano hybrid decreased.

3. 2. 3. Effect of Temperature

The effect of temperature is another significant physicochemical process parameter because the temperature can change the adsorption capacity of the adsorbent.⁴⁴ The adsorption investigations were carried out at different temperatures (25, 35, 45, 55, 65, 75, 85 and 95 °C) (Figure 10(c)). Decreasing the adsorption time with the increase of temperature shows that the adsorption is a spontaneous

and endothermic process. With an increase in the temperature, the mobility of the dyes molecules increase and more molecules will be able to penetrate the inner structure of the nano hybrid.⁴⁵

3. 2. 4. Effect of Adsorbent Dosage

For the purpose of wastewater purification, determining a suitable adsorbent dosage is very important.⁴⁶ The influence of POM@MOF dosage on dye elimination was investigated with fixed conditions such as dye solution volume of 30 mL, dye concentration of 100 mg L^{-1} , pH = 6, and temperature of 25 °C for MB. The adsorbent dosage was applied in different amounts within a range of 10 to 40 mg. Following this, the dye solution was centrifuged and samples were investigated by a spectrophotometer, as Figure 10(d) shows. With increasing adsorbent dosage, the removal of MB dye increases which could be related to the more adsorption sites. In the result, the suitable adsorbent dosage was found to be 30 mg.

To show the advantages of the present adsorbent, we have compared the obtained results in the removal of MB

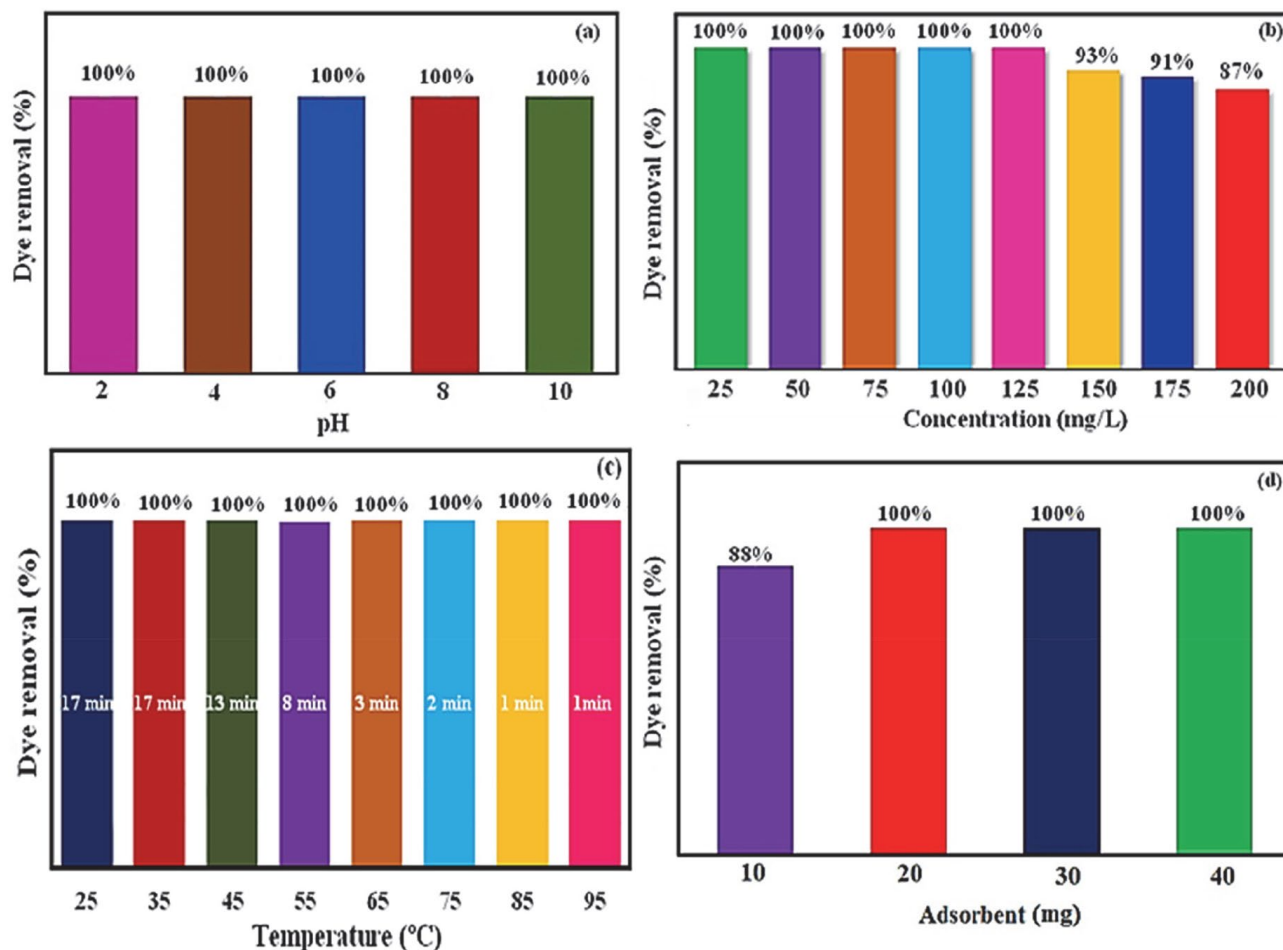
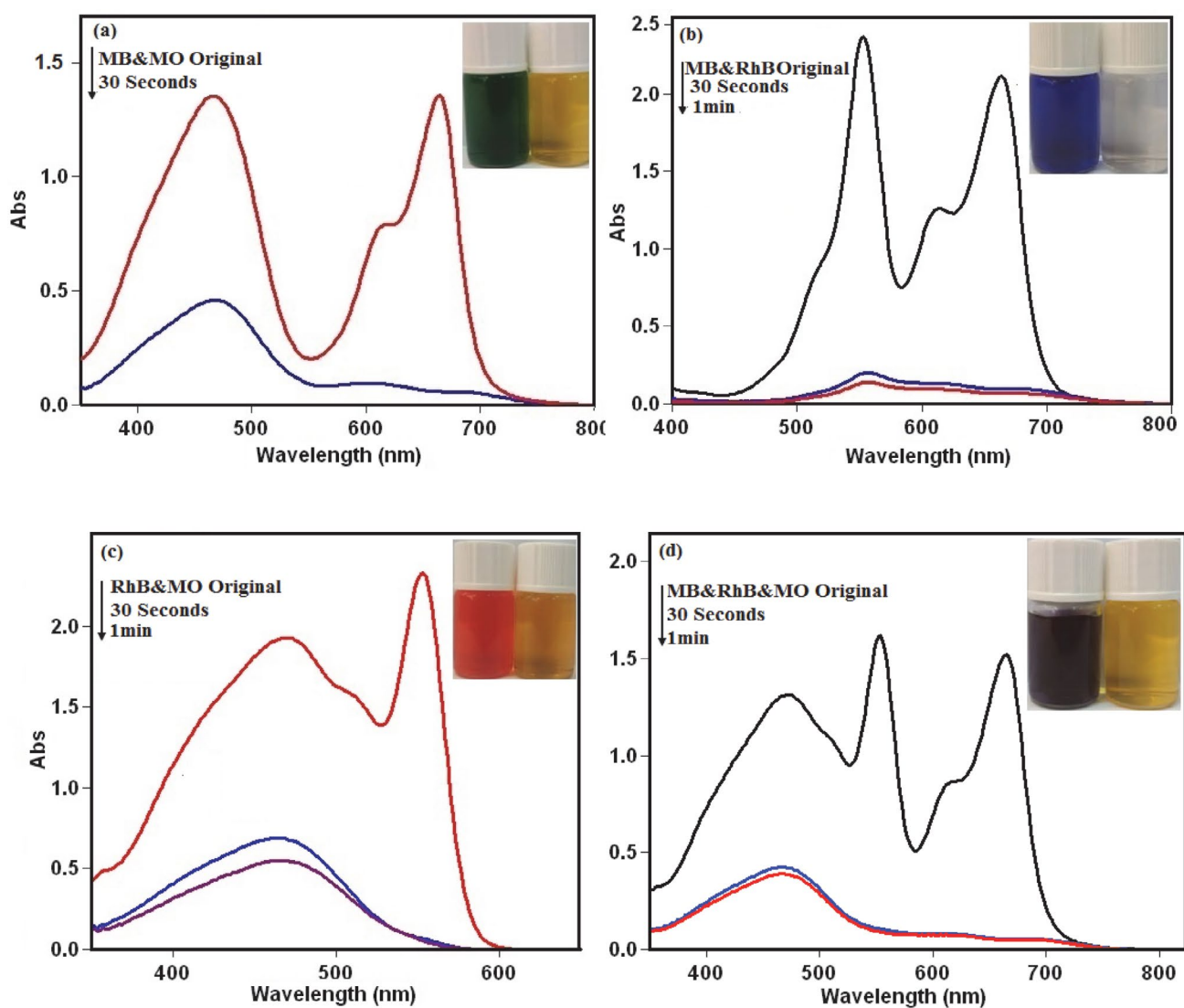


Figure 10. Effects of (a) pH, (b) dye concentration, (c) different temperatures and (d) adsorbent dosage on dyes removal by the $P_2W_{18}@MIL-101(Cr)$ sample. Conditions: C_0 (MB) = 100 mg/L in 30 mL dye solution at 25 °C.

Table 2. Comparison of the results of the newly synthesized nanohybrid with some reported adsorbents for the removal of dye pollutants.

Adsorbent	Dye pollutant	Concentration of dye (mg/L)	Removal efficiency (%)	Time (min)	Ref
H ₆ P ₂ W ₁₈ O ₆₂ @Cu ₃ (BTC) ₂	MB	20	80	60	[12]
PV ₂ Mo ₁₀ /M (membrane)	MB	20	100	48h	[47]
H ₃ PW ₁₂ O ₄₀ / ZIF-8	MB	60	100	30	[48]
LaMnO ₃ @SiO ₂ /PW ₁₂	MB	25	98	30	[49]
PW ₁₁ V@ MIL-101(Cr)	MB	10	98	60	[26]
PW ₁₁ V@ MIL-101(Cr)	RhB	10	60	60	[26]
MoS ₂ @ MIL-101 (Cr)	RhB	20	90	10	[52]
Fe ₃ O ₄ /reduced graphene oxide	RhB	5	91	120	[50]
PW ₁₂ @MIL-101(Fe)	MB	100	100	30	[37]
Fe ₃ O ₄ /MIL-101(Cr)	MO	25	25	150	[51]
P ₂ W ₁₈ @MIL-101 (Cr)	MB	25	100	0.5	This work
P ₂ W ₁₈ @MIL-101 (Cr)	RhB	25	100	2	This work
P ₂ W ₁₈ @MIL-101 (Cr)	MO	25	31	73	This work

**Figure 11.** The selective adsorption ability of P₂W₁₈@MIL-101 (Cr) toward the mixed dyes of (a) MB/MO, (b) MB/RhB, (c) RhB/MO and (d) MB/MO/RhB. Conditions: C₀ (MB) = C₀ (RhB) = C₀ (MO) = 25 mg/L; adsorbent dose = 25 mg in 30 mL mixed dye solution at 25 °C.

from aqueous solution by the $P_2W_{18}@MIL-101(Cr)$ nano-hybrid with some reported similar adsorbents in the literature.^{12,20,37,47–52} From Table 2, it is clear that with respect to the adsorption conditions (adsorption time, initial dye concentration and adsorption efficiency), the present method is more suitable and/or superior. We can see that the adsorption process in the presence of most reported adsorbents required longer reaction time compared to the $P_2W_{18}@MIL-101(Cr)$ nano-hybrid. The P_2W_{18} polyanions with a large number of negative charges incorporated in the hybrid have a stronger attraction force with the positive charges of cationic dyes (e.g. MB). In fact, higher adsorption efficiency of the $P_2W_{18}@MIL-101(Cr)$ is due to synergistic effect between MIL-101(Cr) and P_2W_{18} polyanions.

3. 2. 5. Selective Adsorption Ability of the Nano-hybrid for the Mixed Organic Dyes

The selective adsorption of dyes from their mixture is more attractive and challenging. To verify the selective adsorption property of the $P_2W_{18}@MIL-101(Cr)$ nano-hybrid adsorbent, the dye molecules with different sizes and charges were selected for the experiments, considering that the charge and size of organic dyes are the two major factors controlling the adsorption process. In this work, cationic MB (molecule size 1.38 nm × 0.64 nm × 0.21 nm), cationic RhB (molecule size 1.56 nm × 1.35 nm × 0.42 nm) and anionic MO (molecule size 1.54 nm × 0.48 nm × 0.28 nm) were selected, considering that they possess different sizes and different charges. As shown in Figure 10(a)-(c), the selective uptake of dyes was tested using the MB/MO mixture (30 mL, $C_{0MB} = C_{0MO} = 25$ mg/L), MB/RhB mixture (30 mL, $C_{0MB} = C_{0RhB} = 25$ mg/L) and MO/RhB mixture (30 mL, $C_{0MO} = C_{0RhB} = 25$ mg/L) with 25 mg of the $P_2W_{18}@MIL-101(Cr)$ adsorbent, and then the process was monitored by UV-vis spectroscopy. As MB and MO are similar in molecule size, the preferable uptake of MB from MB/MO mixture may be assigned to the anionic nature of $P_2W_{18}@MIL-101(Cr)$, as shown in Figure 11(a). For comparison, cationic RhB was selected to mix with cationic MB, and the results revealed that MB was also preferably adsorbed on $P_2W_{18}@MIL-101(Cr)$ from the MB/RhB mixture as illustrated in Figure 11(b), which may imply that the uptake of dyes is heavily influenced by molecule size along

with charges. Also, for the binary MO/RhB mixture, cationic RhB dye was preferably adsorbed (Figure 11(c)). It can be anticipated that the composite material may also have an outstanding adsorption and separation behavior in treatment of a ternary mixture of MB, RhB and MO. As exhibited in Figure 11(d), the representative peaks of MB and RhB all disappeared quickly in mixed dye, only the characteristic absorption peaks of MO left, suggesting that the $P_2W_{18}@MIL-101(Cr)$ could selectively capture cationic dyes when is utilized in the corresponding ternary mixture.

3. 2. 6. Adsorption Kinetics

According to the adsorption kinetics, several models for a mechanism of solution adsorption onto an adsorbent can be expressed. To investigate the controlling mechanisms and the rate controlling steps in the overall adsorption process, such as diffusion control, chemical reaction, and mass transfer, different kinetic models (intraparticle diffusion, pseudo-first-order, and pseudo-second-order) are utilized. To study the empirical data and investigate the probability of intraparticle diffusion that can influence the adsorption process, the equation below is used:⁵³

$$q_t = k_p t^{\frac{1}{2}} + I \quad (3)$$

The values I and k_p demonstrate the intraparticle dissemination rate constant and intercept, respectively. The parameters I, k_p and R^2 were computed for several dye concentrations and listed in Table 4. The parameter I indicates the thickness of the frontier layer. The results show that the surface adsorption can be performed by the dissemination of the particles. Generally, a pseudo-first-order equation is illustrated as follows:⁵⁴

$$\log(q_e - q_t) = \log(q_e) - \left(\frac{k_1}{2.303} \right) t \quad (4)$$

The parameters q_e and k_1 indicate the value of dye adsorbed at equilibrium (mg/g) and the equilibrium rate constant of the pseudo-first-order kinetic (1/min), respectively.

The pseudo-second-order kinetic equation is expressed as follows:^{55,56}

$$\frac{t}{q_t} = \frac{1}{k_2 q_e^2} + \left(\frac{1}{q_e} \right) t \quad (5)$$

Table 3. Kinetic models parameters for MB dye adsorption at 150, 175 and 200 mg/L dye concentrations.

C_0 (mg/L)	$q_{e,exp}$ (mg/g)	Pseudo-first-order kinetic			Pseudo-second-order kinetic			Intraparticle diffusion model		
		k_1 (min^{-1})	$q_{e,cal}$ (mg/g)	R_1^2	k_2 (g/mg min)	$q_{e,cal}$ (mg/g)	R_2^2	k_p	I	R_3^2
150	146.1	0.07	7.4	0.9892	0.003	151.5	0.9992	12.1	66.7	0.6937
175	169.47	0.07	12.2	0.9891	0.003	175.4	0.9993	13.8	59.8	0.6819
200	192	0.04	18.1	0.9849	0.002	200	0.9989	15.8	50.9	0.6937

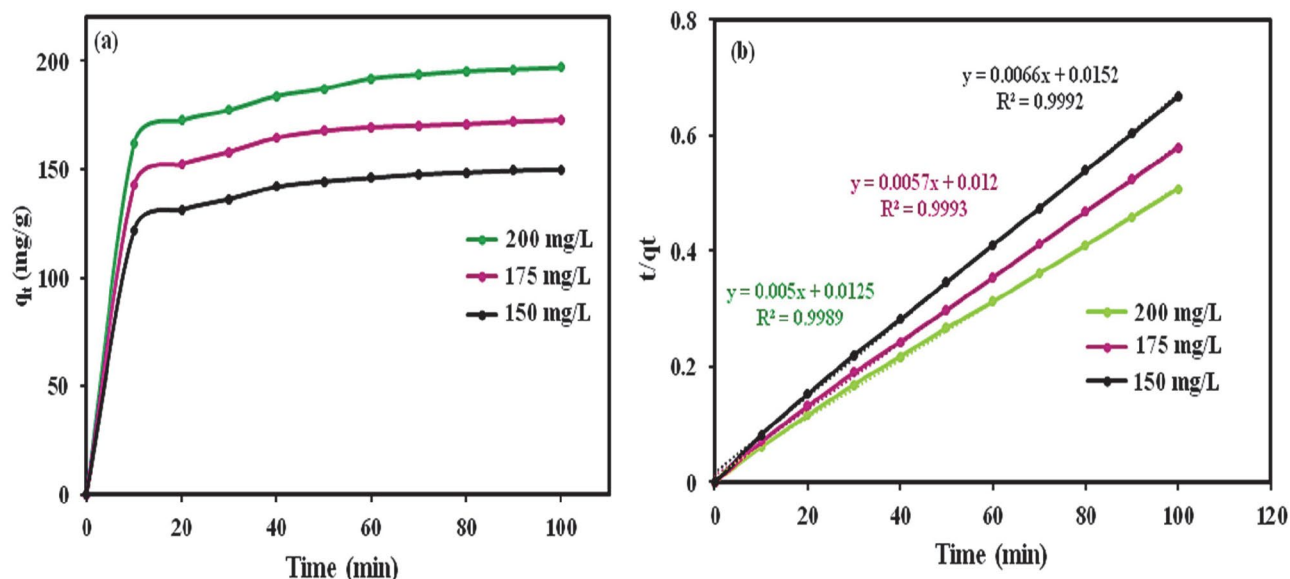


Figure 12. Kinetic adsorption data plots for MB: (a) plot of removal rate q_t vs. t and (b) pseudo-second-order adsorption kinetics on nanomaterial.

To adsorb dyes onto $P_2W_{18}@MIL-101(Cr)$ at the different dye concentration amounts (150, 175, and 200 mg/L) linear plots of t/q_t versus t are indicated in Figure 12. The parameters of K_1 , K_2 , R_1^2 (correlation coefficient for pseudo-first-order adsorption kinetics), R_2^2 (correlation coefficient for pseudo-second-order adsorption kinetics) K_p , I , and R_3^2 (correlation coefficient for intra-particle diffusion model) were calculated and have been presented in Table 3. As it can be seen in Table 3, the values of the $q_{e(\text{exp})}$ (mg/g) are lower than the calculated $q_{e(\text{cal})}$ (mg/g) according to pseudo-second-order equation, which further supports that the pseudo-second-order equation can be utilized to describe the adsorption of dye onto the $P_2W_{18}@MIL-101(Cr)$.

3. 2. 7 Adsorption Isotherm

The design of an adsorption system for an adsorbent provides the most suitable correlation for the equilibrium curves. Different adsorption isotherms were investigated such as the Freundlich, Langmuir, and Temkin isotherms. The basic supposition in the Langmuir theory is that the adsorption in the adsorbent sample occurs at particular homogeneous sites. This equation can be expressed linearly as follows:⁵⁷

$$\frac{C_e}{q_e} = \frac{1}{K_L Q_m} + \frac{C_e}{Q_m} \quad (6)$$

The parameters C_e , K_L , and q_m are the equilibrium concentration of the dye solution (mg/L), the Langmuir constant (L/mg), and the maximum adsorption capacity (mg/g), respectively.

By assuming a non-homogenous surface with a non-uniform diffusion of heat of adsorption over the surface the Freundlich equation is derivative. The Freundlich

equation can be represented linearly as follows:⁵⁸

$$\log q_e = \log K_F + \left(\frac{1}{n}\right) \log C_e \quad (7)$$

Where K_F and $1/n$ indicate the adsorption capacity at unit concentration and the adsorption severity as Freundlich constants, respectively. The isotherm type is determined according to the values of $1/n$, that is, unfavorable ($1/n > 1$), favorable ($0 < 1/n < 1$), and irreversible ($1/n = 0$).⁵⁹ Some indirect adsorbate/adsorbate interactions studied by Temkin in relation to adsorption isotherms were examined, and it was suggested that for all the molecules, the heat of adsorption increases linearly with coverage. The Temkin equation can be expressed linearly as follows:⁶⁰

$$q_e = B_1 \ln K_T + B_1 \ln C_e \rightarrow B_1 = \frac{RT}{b} \quad (8)$$

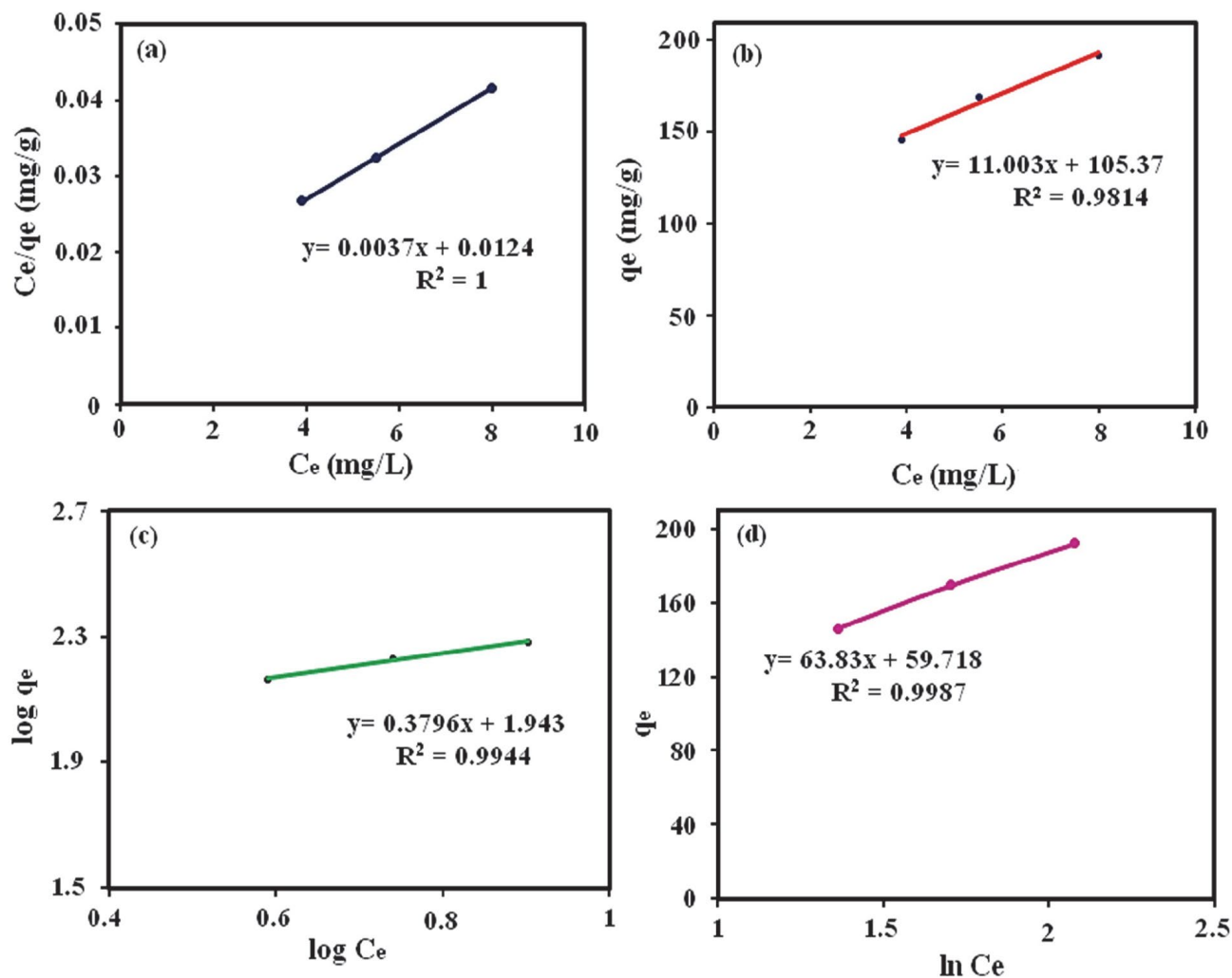
The Temkin isotherm expresses that pending some maximum binding energy, the adsorption is characterized by a uniform distribution of binding energies. The isotherm constants B_1 and K_T were determined using the values q_e and $\ln C_e$, which represent the slope and the intercept, respectively. The constant B_1 represents the heat of adsorption and the constant K_T indicates the maximum binding energy. The correlation coefficients for the Langmuir, Freundlich and Temkin isotherms were obtained from Figures 13(a)-(b) are listed in Table 4. Based on the results obtained, the Langmuir isotherm is most suitable for studying MB dye.

3. 2. 8. Adsorption Thermodynamics

In the adsorption process, energy and entropy are very significant. The value of MB adsorbed at equilibrium

Table 4. Isotherm constants for MB dye adsorption at 150, 175 and 200 mg/L dye concentrations

Dye	Langmuir isotherm model			Freundlich isotherm model			Temkin isotherm model		
	R ²	K _L (L mg ⁻¹)	Q _m (mg g ⁻¹)	R ²	K _F (mg g ⁻¹)	n (mgL ⁻¹)	R ²	K _T	B ₁
MB	1	0.3	270	0.9944	7	2.6	0.9987	2.6	63.83

Figure 13. (a) Isotherm plot of dye elimination, (b) Langmuir isotherm, (c) Freundlich isotherm, (d) Temkin isotherm of dye removal by P₂W₁₈@MIL-101 (Cr).

for determining the thermodynamic parameters at the different temperatures was examined. The enthalpy (ΔH° : kJ/mol), entropy (ΔS° : kJ/mol K), and change in Gibbs energy (ΔG° : kJ/mol) were obtained using the following equations:⁶¹

$$\ln K_c = \left(\frac{\Delta S^\circ}{R} \right) - \left(\frac{\Delta H^\circ}{RT} \right) \quad (9)$$

$$\Delta G^\circ = \Delta H^\circ - T\Delta S^\circ \quad (10)$$

The parameters K_c (L/g), T , and R (8.314 J/mol K) are the standard thermodynamic equilibrium constant,

the equilibrium concentration of the dye in the solution (C_e), the value of dye adsorbed on the adsorbent of the solution at equilibrium (q_e), the absolute temperature, and the gas constant, respectively. The values ΔH° and ΔS° can be determined by drawing curves of $\ln K_c$ versus $1/T$ from the slopes and intercepts, respectively (Figure 14). Table 5 indicates the negative values of ΔG° and positive ΔH° . The data demonstrate that the MB adsorption process is an endothermic and spontaneous process. The increase randomly at the solid/solution interface based on the positive amount of ΔS° occurs in the internal structure of the adsorption of MB dye onto P₂W₁₈@MIL-101 (Cr). Also, the positive amount of ΔH° indicates the presence of an ener-

gy impediment in the adsorption process and the endothermic process.^{62,63}

According to the negative amounts of ΔG° , the adsorption process is a spontaneous process. Moreover, the increase in temperature which leads to a decrease in the amounts of ΔG° indicates that the adsorption process is endothermic. Given the values obtained from ΔG° , of between 20 and 0 kJ/mol, the dominating mechanism in this study is the physisorption mechanism (Table 5).⁶⁴

Table 5. Thermodynamic parameters of dye adsorption on $P_2W_{18}@MIL-101$ (Cr).

Temperature °C MB	Thermodynamic parameters		
	ΔG° (kJ/mol)	ΔH° (kJ/mol)	ΔS° (J/mol K)
25	-9.63	30.52	133.02
35	-10.44		
45	-11.78		
55	-13.1		
65	-14.43		
75	-15.76		

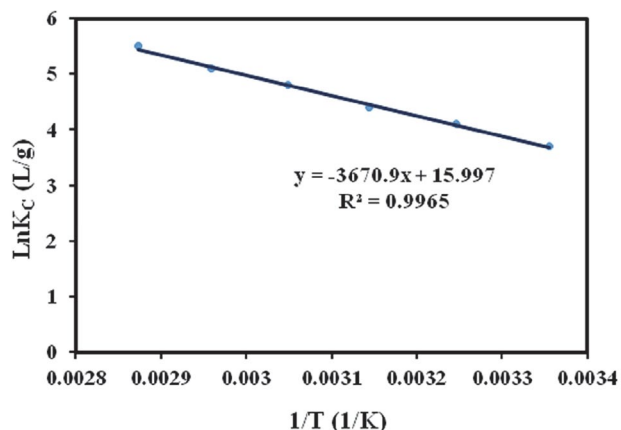


Figure 14. Plots $\ln K_C$ versus $1/T$ for adsorption of dyes.

3. 2. 9. Stability and Recyclability of Hybrid Nanomaterial

The stability and reusability of $P_2W_{18}@MIL-101$ (Cr) are important aspects of the practical removal of dye pol-

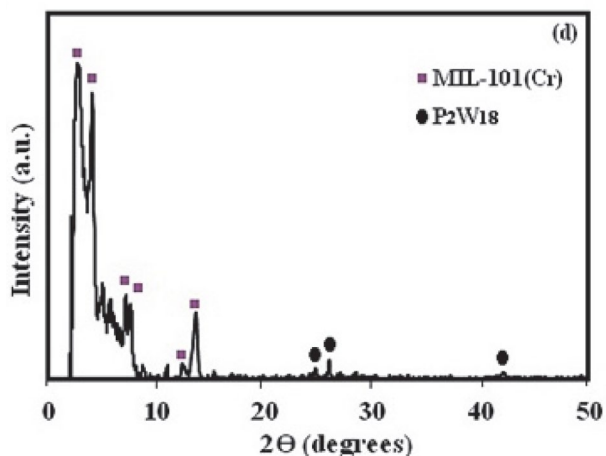
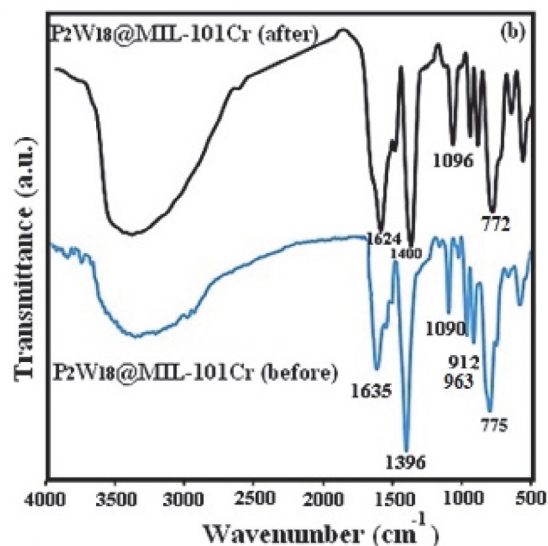
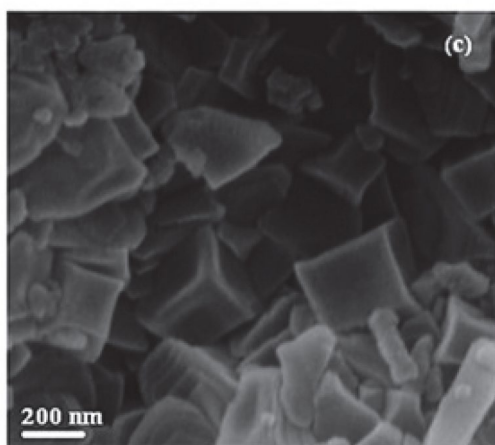
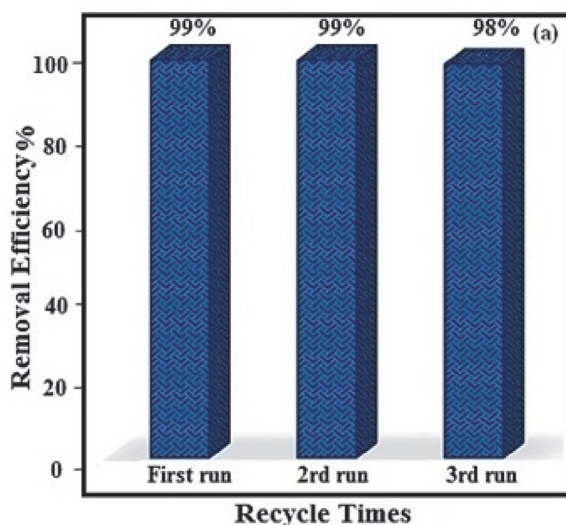


Figure 15. (a) Recycling tests of the nanohybrid toward MB adsorption. (b) FT-IR spectrum before and after adsorption (c) SEM image and (d) XRD pattern of the recovered nanohybrid after 3rd cycle.

lutants. By using cycle tests, the removing of MB was studied. The adsorbent was separated by centrifugation was completely separated by simple centrifugation due to its insoluble property in water. Following, the fast release process of the adsorbed MB was achieved by thoroughly washing the adsorbent with ethanol, water, and NaCl mixture several times and dried overnight at 60 °C and reused for adsorption again under the same condition. As can be seen in Figure 15(a), a slight drop was happened in the removal efficiency after three cycles. This property is significant as it can reduce the cost of the adsorption without the collapse or loss of the structure of the material. Moreover, the Cr and W contents in aqueous phase after the separation of adsorbent were analyzed by ICP-AES. No observable leaching of Cr and W (≤ 0.1 wt%) was observed in the 1st as well as the 3rd run of the adsorption. As shown in Figure 15(b)-(d), FT-IR, SEM and XRD pattern of the recycled $P_2W_{18}@MIL-101$ (Cr) adsorbent did not show significantly more changes after the third run compared to the fresh adsorbent. Therefore, these observations confirm that the as-prepared $P_2W_{18}@MIL-101$ (Cr) adsorbent can work as an effective adsorbent for cationic dyes removal with good stability and recyclability.

4. Conclusions

In summary, the Dowson-type polyoxometalate@MIL-101(Cr) metal-organic framework ($P_2W_{18}@MIL-101$ (Cr)) nanohybrid with a high BET specific surface area of $1167.4 \text{ m}^2 \text{ g}^{-1}$ were successfully prepared by a simple one-pot hydrothermal route. The FT-IR, XRD, and EDX analyses confirmed the successful incorporation of the P_2W_{18} in MIL-101 (Cr) framework. This nanohybrid could selectively adsorb cationic dyes because of the presence of P_2W_{18} polyanions in its structure and strong interaction with cationic dyes. The results revealed that the adsorption process was followed pseudo-second-order kinetic. Furthermore, the $P_2W_{18}@MIL-101$ (Cr) nanohybrid could be recycled and reused several times without losing the adsorption capacity. Thus, this material is a promising adsorbent for the treatment of toxic organic pollutants in the colored wastewater.

5. Acknowledgements

The authors gratefully acknowledge the Lorestan University for financial support.

6. References

- J. Juan-Alcañiz, E. V. Ramos-Fernandez, U. Lafont, J. Gascon and F. Kapteijn, *J. Catal.*, **2010**, 269, 229–241. DOI:10.1016/j.jcat.2009.11.011
- K. Ariga, Y. Yamauchi, G. Rydzek, Q. Ji, Y. Yonamine, K. C.-W. Wu and J. P. Hill, *Chem. Lett.*, **2013**, 43, 36–68. DOI:10.1246/cl.130987
- K. Ariga, H. Ito, J. P. Hill and H. Tsukube, *Chem. Soc. Rev.*, **2012**, 41, 5800–5835. DOI:10.1039/c2cs35162e
- R. Q. Zou, H. Sakurai and Q. Xu, *Angew. Chem. Int. Ed.*, **2006**, 118, 2604–2608. DOI:10.1002/ange.200503923
- M. Allendorf, C. Bauer, R. Bhakta and R. Houk, *Chem. Soc. Rev.*, **2009**, 38, 1330–1352. DOI:10.1039/b802352m
- M. Kurmoo, *Chem. Soc. Rev.*, **2009**, 38, 1353–1379. DOI:10.1039/b804757j
- M. Li, D. Li, M. O’Keeffe and O. M. Yaghi, *Chem. Rev.*, **2013**, 114, 1343–1370. DOI:10.1021/cr400392k
- A. Aijaz, T. Akita, N. Tsumori and Q. Xu, *J. Am. Chem. Soc.*, **2013**, 135, 16356–16359. DOI:10.1021/ja4093055
- L. Wang, M. Zheng and Z. Xie, *J. Mater. Chem. B*, **2018**, 6, 707–717. DOI:10.1039/C7TB02970E
- D. Tian, Q. Chen, Y. Li, Y. H. Zhang, Z. Chang and X. H. Bu, *Angew. Chem. Int. Ed.*, **2014**, 53, 837–841. DOI:10.1002/anie.201307681
- S. Pramanik, C. Zheng, X. Zhang, T. J. Emge and J. Li, *J. Am. Chem. Soc.*, **2011**, 133, 4153. DOI:10.1021/ja106851d
- X. Liu, J. Luo, Y. Zhu, Y. Yang and S. Yang, *J. Alloys Compd.*, **2015**, 648, 986–993. DOI:10.1016/j.jallcom.2015.07.065
- Z.-P. Qi, Y.-S. Kang, F. Guo and W.-Y. Sun, *Microporous Mesoporous Mater.*, **2019**, 273, 60–66. DOI:10.1016/j.micromeso.2018.06.051
- J. Abdi, N. M. Mahmoodi, M. Vossoughi and I. Alemzadeh, *Microporous Mesoporous Mater.*, **2019**, 273, 177–188. DOI:10.1016/j.micromeso.2018.06.040
- J. Li, J.-L. Gong, G.-M. Zeng, P. Zhang, B. Song, W.-C. Cao, H.-Y. Liu and S.-Y. Huan, *J. Colloid Interface Sci.*, **2018**, 527, 267–279. DOI:10.1016/j.jcis.2018.05.028
- S.-N. Zhao, C. Krishnaraj, H. S. Jena, D. Poelman and P. Van Der Voort, *Dyes Pigments*, **2018**, 156, 332–337. DOI:10.1016/j.dyepig.2018.04.023
- S. Qiu, M. Xue and G. Zhu, *Chem. Soc. Rev.*, **2014**, 43, 6116–6140. DOI:10.1039/C4CS00159A
- E. D. Bloch, W. L. Queen, R. Krishna, J. M. Zadrozny, C. M. Brown, J. R. Long, *Science*, **2012**, 335, 1606–1610. DOI:10.1126/science.1217544
- F.-J. Ma, S.-X. Liu, C.-Y. Sun, D.-D. Liang, G.-J. Ren, F. Wei, Y.-G. Chen and Z.-M. Su, *J. Am. Chem. Soc.*, **2011**, 133, 4178–4181. DOI:10.1021/ja109659k
- H. N. Miras, J. Yan, D.-L. Long and L. Cronin, *Chem. Soc. Rev.*, **2012**, 41, 7403–7430. DOI:10.1039/c2cs35190k
- A. Sakthivel, K. Komura, Y. Sugi, *Ind. Eng. Chem. Res.* **2008**, 47, 2538–2544. DOI:10.1021/ie071314z
- A. E. R. S. Khder, H. Hassan, M. S. El-Shall, *Appl. Catal. A* **2012**, 411, 77–86. DOI:10.1016/j.apcata.2011.10.024
- H. N. Miras, J. Yan, D.-L. Long and L. Cronin, *Chem. Soc. Rev.*, **2012**, 41, 7403–7430. DOI:10.1039/c2cs35190k
- X. L. Hao, Y. Y. Ma, H. Y. Zang, Y. H. Wang, Y. G. Li and E. B. Wang, *Chem. Eur. J.*, **2015**, 21, 3778–3784. DOI:10.1002/chem.201405825

25. X.-B. Han, Z.-M. Zhang, T. Zhang, Y.-G. Li, W. Lin, W. You, Z.-M. Su and E.-B. Wang, *J. Am. Chem. Soc.*, **2014**, *136*, 5359–5366. DOI:10.1021/ja412886e
26. A. X. Yan, S. Yao, Y. G. Li, Z. M. Zhang, Y. Lu, W. L. Chen and E. B. Wang, *Chem. Eur. J.*, **2014**, *20*, 6927–6933. DOI:10.1002/chem.201400175
27. X. L. Hao, Y. Y. Ma, H. Y. Zang, Y. H. Wang, Y. G. Li and E. B. Wang, *Chem. Eur. J.*, **2015**, *21*, 3778–3784. DOI:10.1002/chem.201405825
28. F.-Y. Yi, W. Zhu, S. Dang, J.-P. Li, D. Wu, Y.-H. Li and Z.-M. Sun, *Chem. Commun.*, **2015**, *51*, 3336–3339. DOI:10.1039/C4CC09569C
29. C. T. Buru, P. Li, B. L. Mehdi, A. Dohnalkova, A. E. Plate-ro-Prats, N. D. Browning, K. W. Chapman, J. T. Hupp and O. K. Farha, *Chem. Mater.*, **2017**, *29*, 5174–5181. DOI:10.1021/acs.chemmater.7b00750
30. I. Ahmed and S. H. Jhung, *Mater. Today*, **2014**, *17*, 136–146. DOI:10.1016/j.mattod.2014.03.002
31. X.-L. Hao, Y.-Y. Ma, C. Zhang, Q. Wang, X. Cheng, Y.-H. Wang, Y.-G. Li and E.-B. Wang, *CrystEngComm*, **2012**, *14*, 6573–6580. DOI:10.1039/c2ce25747e
32. L. Bromberg, Y. Diau, H. Wu, S. A. Speakman and T. A. Hat-ton, *Chem. Mater.*, **2012**, *24*, 1664–1675. DOI:10.1021/cm2034382
33. I.-M. Mbomekalle, Y. W. Lu, B. Keita and L. Nadjo, *Inorg. Chem. Commun.*, **2004**, *7*, 86–90. DOI:10.1016/j.inoche.2003.10.011
34. X. Hu, Y. Lu, F. Dai, C. Liu and Y. Liu, *Microporous Mesoporous Mater.*, **2013**, *170*, 36–44. DOI:10.1016/j.micromeso.2012.11.021
35. N. V. Maksimchuk, O. A. Kholdeeva, K. A. Kovalenko and V. P. Fedin, *Isr. J. Chem.*, **2011**, *51*, 281–289. DOI:10.1002/ijch.201000082
36. C. Roch-Marchal, T. Hidalgo, H. Banh, R. A. Fischer and P. Horcajada, *Eur. J. Inorg. Chem.*, **2016**, *2016*, 4387–4394.
37. T.-T. Zhu, Z.-M. Zhang, W.-L. Chen, Z.-J. Liu and E. B. Wang, *RSC Adv.*, **2016**, *6*, 81622–81630.
38. B. Hong, L. Liu, S.-M. Wang and Z.-B. Han, *J. Clust. Sci.*, **2016**, *27*, 563–571.
39. L. Zhang, B. Shan, H. Yang, D. Wu, R. Zhu, J. Nie and R. Cao, *RSC Adv.*, **2015**, *5*, 23556–23562
40. Y. Zhang, V. Degirmenci, C. Li and E. J. Hensen, *ChemSus-Chem.*, **2011**, *4*, 59–64. DOI:10.1002/cssc.201000284
41. N. M. Mahmoodi, *J. Taiwan. Inst. Chem. Eng.*, **2013**, *44*, 322–330. DOI:10.1016/j.jtice.2012.11.014
42. N. M. Mahmoodi, U. Sadeghi, A. Maleki, B. Hayati and F. Najafi, *J. Ind. Eng. Chem.*, **2014**, *20*, 2745–2753. DOI:10.1016/j.jiec.2013.11.002
43. J. Lee, O. K. Farha, J. Roberts, K. A. Scheidt, S. T. Nguyen and J. T. Hupp, *Chem. Soc. Rev.*, **2009**, *38*, 1450–1459. DOI:10.1039/b807080f
44. J.-R. Li, R. J. Kuppler and H.-C. Zhou, *Chem. Soc. Rev.*, **2009**, *38*, 1477–1504. DOI:10.1039/b802426j
45. T. K. Trung, P. Trens, N. Tanchoux, S. Bourrelly, P. L. Llewellyn, S. Loera-Serna, C. Serre, T. Loiseau, F. Fajula and G. Férey, *J. Am. Chem. Soc.*, **2008**, *130*, 16926–16932. DOI:10.1021/ja8039579
46. S.-I. Noro, R. Kitaura, M. Kondo, S. Kitagawa, T. Ishii, H. Matsuzaka and M. Yamashita, *J. Am. Chem. Soc.*, **2002**, *124*, 2568–2583. DOI:10.1021/ja0113192
47. L. Yao, L. Zhang, R. Wang, S. Chou and Z. Dong, *J. Hazard. Mater.*, **2016**, *301*, 462–470. DOI:10.1016/j.jhazmat.2015.09.027
48. R. Li, X. Q. Ren, J. S. Zhao, X. Feng, X. Jiang, X. X. Fan, Z. G. Lin, X. G. Li, C. G. Hu, and B. Wang, *J. Mater. Chem. A*, **2014**, *2*, 2168–2173. DOI:10.1039/C3TA14267A
49. S. Farhadi, F. Mahmoudi, M. M. Amini, M. Dusek and M. Jarosova, *Dalton Trans.*, **2017**, *46*, 3252–3264. DOI:10.1039/C6DT04866H
50. H. Sun, L. Cao and L. Lu, *Nano Res.*, **2011**, *4*, 550–562. DOI:10.1007/s12274-011-0111-3
51. Z. Jiang and Y. Li, *J. Taiwan. Inst. Chem. Eng.*, **2016**, *59*, 373–379. DOI:10.1016/j.jtice.2015.09.002
52. C. Yang, J. Cheng, Y. Chen and Y. Hu, *J. Colloid Interface Sci.*, **2017**, *504*, 39–47. DOI:10.1016/j.jcis.2017.05.020
53. S. M. Humphrey and P. T. Wood, *J. Am. Chem. Soc.*, **2004**, *126*, 13236–13237. DOI:10.1021/ja046351l
54. N. M. Mahmoodi, B. Hayati and M. Arami, *Ind Crop Prod.*, **2012**, *35*, 295–301. DOI:10.1016/j.indcrop.2011.07.015
55. N. M. Mahmoodi, B. Hayati, M. Arami and C. Lan, *Desalination*, **2011**, *268*, 117–125. DOI:10.1016/j.desal.2010.10.007
56. J. An, S. J. Geib and N. L. Rosi, *J. Am. Chem. Soc.*, **2009**, *131*, 8376–8377. DOI:10.1021/ja902972w
57. G. Férey, *Chem. Soc. Rev.*, **2008**, *37*, 191–214. DOI:10.1039/B618320B
58. J. D. Joshi, N. B. Patel and S. D. Patel, *Iran Polym J.*, **2006**, *15*, 219.
59. K. A. Cychosz, A. G. Wong-Foy and A. J. Matzger, *J. Am. Chem. Soc.*, **2008**, *130*, 6938–6939. DOI:10.1021/ja802121u
60. Y. Kim, C. Kim, I. Choi, S. Rengaraj and J. Yi, *Environ. Sci. Technol.*, **2004**, *38*, 924–931. DOI:10.1021/es0346431
61. Z. A. Lethbridge, J. J. Williams, R. I. Walton, K. E. Evans and C. W. Smith, *Microporous Mesoporous Mater.*, **2005**, *79*, 339–352. DOI:10.1016/j.micromeso.2004.12.022
62. F. Di Renzo, *Catal. Today*, **1998**, *41*, 37–40. DOI:10.1016/S0920-5861(98)00036-4
63. T. O. Drews and M. Tsapatsis, *Curr. Opin. Colloid Interface Sci.*, **2005**, *10*, 233–238. DOI:10.1016/j.cocis.2005.09.013
64. W. J. Rieter, K. M. Taylor and W. Lin, *J. Am. Chem. Soc.*, **2007**, *129*, 9852–9853. DOI:10.1021/ja073506r

Povzetek

V ogrodje kovinsko-organskega poroznega materiala (MOF, MIL-101(Cr)) smo uspešno vgradili sol $K_6P_2W_{18}O_{62}$ (skrajšano P_2W_{18}). Nano-hibrid $P_2W_{18}@MIL-101(Cr)$ smo karakterizirali z infrardečo spektroskopijo, rentgensko difrakcijo (XRD), ramansko spektroskopijo, energijsko disperzijsko spektroskopijo rentgenskih žarkov EDX, vrstično elektronsko mikroskopijo (SEM), meritvami zeta potenciala in meritvami površine (BET). Glede na rezultate lahko ocenimo, da se je $K_6P_2W_{18}O_{62}$ (~ 36 ut.%) vgradil v porozni okvir MIL-101(Cr). V primerjavi s čistim MIL-101(Cr) sta v vzorcu $P_2W_{18}@MIL-101(Cr)$ znatno zmanjšana površina in volumen por zaradi vgraditve velike soli $K_6P_2W_{18}O_{62}$ v kletke MOF. $P_2W_{18}@MIL-101(Cr)$ smo uporabili kot nov adsorbent za odstranjevanje barvil metilen modro (MB), rodamine B (RhB) in metiloranž (MO) iz vodnih raztopin. V tem delu študije smo preučevali učinek parametrov, kot so odmerjanje adsorbenta, koncentracija barvila, pH in temperatura, na postopek odstranjevanja barvil. Poleg tega smo učinkovitost in selektivnost adsorpcije preučevali tudi v raztopinah mešanice barvil MB/MO, MB/RhB, MO/RhB in MB/MO/RhB. $P_2W_{18}@MIL-101(Cr)$ je hitro in selektivno adsorbiral kationski barvili MB in RhB iz mešanice raztopin barvil. Glede na termodinamske podatke je adsorpcija barvila endotermni proces. $P_2W_{18}@MIL-101(Cr)$ je lahko učinkovit adsorbent, ki ga je mogoče reciklirati in je uporaben za hitro odstranjevanje različnih kationskih tekstilnih barvil iz vodnih raztopin.

Scientific paper

Synthesis, Anti-Inflammatory and Antioxidant Activities of Novel 3*H*-Thiazolo[4,5-*b*]Pyridines

Taras I. Chaban,^{1,*} Volodymyr V. Ogurtsov,¹ Vasyl S. Matyichuk,²
Ihor G. Chaban,³ Inna L. Demchuk⁴ and Ihor A. Nektegayev⁵

¹ Department of General, Bioinorganic, Physical and Colloidal Chemistry, Danylo Halytsky Lviv National Medical University, 69 Pekarska, Lviv, 79010, Ukraine

² Department of Organic Chemistry, Ivan Franko National University of Lviv, 6 Kyryla i Mefodia, Lviv, 79005, Ukraine

³ Department of Pharmaceutical Chemistry FPGE, Danylo Halytsky Lviv National Medical University, 69 Pekarska, Lviv, 79010, Ukraine

⁴ Department of Pharmaceutical, Organic and Bioorganic Chemistry Danylo Halytsky Lviv National Medical University, Lviv, 79010, Ukraine

⁵ Department of Pharmacology, Danylo Halytsky Lviv National Medical University, 69 Pekarska, Lviv, 79010, Ukraine

* Corresponding author: E-mail: chabantaras@ukr.net
Tel. +38 098 942-79-56; Fax. +38 0322 75-77-34

Received: 06-07-2018

Abstract

5-Hydroxy-7-methyl-3*H*-thiazolo[4,5-*b*]pyridin-2-one was obtained by the reaction of 4-iminothiazolidin-2-one with acetoacetic ester. Further structural modifications include the introduction of diversity at the C⁵ and C⁶ positions. The anti-inflammatory action of novel thiazolo[4,5-*b*]pyridine-2-one derivatives was evaluated *in vivo* employing the carrageenan-induced rat paw edema method. The antioxidant activity of the synthesized compounds was evaluated *in vitro* by the method of scavenging effect on 2,2-diphenyl-1-picrylhydrazyl (DPPH) radicals.

Keywords: Thiazolo[4,5-*b*]pyridines; synthesis; anti-inflammatory activity; antioxidant activity

1. Introduction

In modern theoretical and clinical medicine the inflammation problem remains one of the main research focuses.¹⁻⁴ Inflammation occurs as a defensive response which induces physiological adaptations to limit the tissue damage and remove the pathogenic infections. Deregulation of inflammatory processes leads to specific pathologies including psoriasis, rheumatoid arthritis, periodontal disease, asthma and atherosclerosis. It has also been shown that inflammation can be a fundamental contributor to other degenerative conditions, such as diabetes, cancer and cardiovascular diseases.⁵⁻⁶ Furthermore, the inflammatory response can be identified as the major cause of damage related to autoimmune diseases.⁵ Consequently, the regulation of inflammatory processes is an essential avenue in

the treatment of various pathologies. Even if many efforts have been made in this direction in the past years,⁷⁻¹¹ the search for new anti-inflammatory compounds is still an important area of research, as traditional therapies involving steroidal or non-steroidal agents are often associated with a lack of efficiency and undesirable side effects. Of no lesser interest is the search for new antioxidants. There is an increasing evidence of the implication of free radicals in a variety of diseases. Free radicals are being formed during normal cellular metabolism and they are known to contribute to healthy functions in human health and development when they are not present in excessive amounts. At high concentrations free radicals can cause damage to cell structures, nucleic acids, lipids and proteins,¹² leading to age-related degenerative diseases, cancer and a wide range of different human diseases.¹³ The major action of antiox-

idants in human diseases is to prevent damage caused by the action of reactive oxygen species. The development of new potent antioxidant agents is a major goal for pharmaceutical and medicinal chemistry, as a way of removing the excess of free radicals, and thus, to ameliorate their hazardous effects on human beings.

4-Azolidone core is considered to be an efficient scaffold for drug-like molecules design as the integral part of modern medicinal chemistry. Pyridine derivatives have always been among the most important research areas in the field of drug design. The thiazolidine-based heterocycles and their analogs fused to the pyridine ring were shown to possess a wide range of biological actions. The incorporation of these heterocyclic systems into a bicyclic scaffold commonly provides much more interesting analogs with the enhanced activity profile in comparison with their parent monocyclic constituents.^{14–15} Thiazolo[4,5-*b*]pyridine derivatives are characterized by diverse biological activities, among which antioxidant,^{16–18} tuberculostatic,¹⁹ anticancer,²⁰ anti-inflammatory,^{21–22} and antifungal²³ effects have been reported in the past decade.

The objective of the present work was to synthesize a series of 3*H*-thiazolo[4,5-*b*]pyridine-2-ones by the structural modification of the core heterocycle at its C⁵ and C⁶ positions for further pharmacological screening *in vivo* as anti-inflammatory and *in vitro* as antioxidants activities.

2. Experimental Section

2.1. Materials

All chemicals were of analytical grade and are commercially available. All reagents and solvents were used without further purification and drying.

2.2. Chemistry

All the melting points were determined in an open capillary and are uncorrected. ¹H NMR spectra of newly synthesized compounds in DMSO-*d*₆ solutions were recorded on a spectrometer Varian Mercury VX-400 (400 MHz) at 298 K. Chemical shifts are reported as δ (ppm) relative to TMS as the internal standard, coupling constant *J* are expressed in Hz. The elemental analysis experimental data on contents of sulfur and nitrogen were within ±0.4% of the theoretical values.

5-Hydroxy-7-methyl-3*H*-thiazolo[4,5-*b*]pyridin-2-one (2a)

Sodium (109 mmol) was dissolved in anhydrous methanol (125 mL) and to the solution obtained 4-iminothiazolidin-2-one (50 mmol) and acetoacetic ester (8 mL) were added at 20 °C. The mixture was left standing for 5 days with the intermittent stirring, then it was acidified with acetic acid to pH ~5, five-fold diluted with water, the precipitate was filtered off, washed with water, and dried.

Compound **2a** was obtained as a white crystalline powdered solid, well soluble in DMF, DMSO, solutions of alkali and mineral acids, sparingly soluble in the other organic solvents. White solid; yield: 75%; mp > 300 °C with dec.; ¹H NMR: δ 2.33 (s, 3H, CH₃), 6.31 (s, 1H, Py), 10.84 (s, 1H, OH), 12.18 (s, 1H, NH); ¹³C NMR: δ 19.85, 104.73, 107.84, 144.59, 147.91, 162.91, 169.55; ESI-MS: *m/z* 183 [M+H]⁺; anal. calcd. for C₇H₇N₂O₂S: C 46.15, H 3.32, N 15.37; found: C 46.24, H 3.38, N 15.44.

General Procedure for the Synthesis of 6-Alkyl-5-hydroxy-7-methyl-3*H*-thiazolo[4,5-*b*]pyridin-2-ones 2*b*–*c*

Metallic sodium (200 mmol) was dissolved in anhydrous methanol (100 mL), and to the solution obtained 4-iminothiazolidin-2-one (50 mmol) and alkyl derivatives acetoacetic ester (50 mmol) were added at 20 °C. The mixture was left standing for 7 days with the intermittent stirring, then it was acidified with acetic acid to pH ~5, five-fold diluted with water. The precipitate was filtered off, washed with water, and dried at 100–110 °C. The obtained compounds were re-crystallized from acetic acid.

5-Hydroxy-7-methyl-6-propyl-3*H*-thiazolo[4,5-*b*]pyridin-2-one (2b)

White solid; yield: 60%; mp 249–250 °C; ¹H NMR: δ 0.90 (t, *J* = 5.1 Hz, *J* = 7.2 Hz, 3H, CH₂-CH₂-CH₃), 1.43 (d, *J* = 7.3 Hz, 2H, CH₂-CH₂-CH₃), 2.19 (s, 3H, CH₃), 2.48 (d, *J* = 7.4 Hz, 2H, CH₂-CH₂-CH₃), 11.48 (s, 1H, OH); ¹³C NMR: δ 14.42, 17.63, 22.39, 28.02, 108.56, 116.20, 141.73, 144.83, 160.88, 169.48; ESI-MS: *m/z* 225 [M+H]⁺; anal. calcd. for C₁₀H₁₂N₂O₂S: C 53.55, H 5.39, N 12.49; found: C 53.30, H 5.44, N 12.56.

6-Benzyl-5-hydroxy-7-methyl-3*H*-thiazolo[4,5-*b*]pyridin-2-one (2c)

White solid; yield: 75%; mp 277 °C; ¹H NMR: δ 2.18 (s, 3H, CH₃), 3.93 (s, 2H, CH₂-C₆H₅), 7.15–7.19 (m, 3H, C₆H₅), 7.25 (t, *J* = 7.4 Hz, 2H, C₆H₅), 10.96 (s, 1H, OH), 12.18 (s, 1H, NH); ¹³C NMR: δ 18.02, 31.46, 108.87, 114.86, 126.27, 128.44, 128.77, 140.73, 142.60, 145.62, 161.16, 169.48; ESI-MS: *m/z* 273 [M+H]⁺; anal. calcd. for C₁₄H₁₂N₂O₂S: C 61.75, H 4.44, N 10.29; found: C 62.02, H 4.38, N 10.36.

General Procedure for the Synthesis Sodium Salts 5-Hydroxy-7-methyl-3*H*-thiazolo[4,5-*b*]pyridin-2-one and 6-Benzyl-5-hydroxy-7-methyl-3*H*-thiazolo[4,5-*b*]pyridin-2-one 3*a*–*b*

To 20 mL of water and (10 mmol) of potassium hydroxide was added (10 mmol) of compounds **2a** or **2b**, and the mixture was heated to complete dissolution. The solution obtained was evaporated to dryness. The residue was dried at 100 °C.

5-Hydroxy-7-methyl-3*H*-thiazolo[4,5-*b*]pyridin-2-one sodium salt (3a)

White solid; yield: 60%; mp 280 °C; ¹H NMR: δ 1.99 (s, 3H, CH₃), 5.41 (s, 1H, Py), 11.07 (s, 1H, NH); ¹³C NMR:

δ 21.47, 104.13, 104.18, 144.71, 154.52, 162.27, 162.31; ESI-MS: m/z 205 [M+H]⁺; anal. calcd. for C₇H₅N₂NaO₂S: C 41.18, H 2.47, N 13.72; found: C 41.25, H 2.52, N 13.66.

6-Benzyl-5-hydroxy-7-methyl-3H-thiazolo[4,5-b]pyridin-2-one sodium salt (3b)

White solid; yield: 86%; mp 298 °C; ¹H NMR: δ 2.00 (s, 3H, CH₃), 3.79 (s, 2H, CH₂), 7.11 (t, $J = 7.0$ Hz, 1H, C₆H₅), 7.17–7.23 (m, 4H, C₆H₅), 11.07 (s, 1H, NH); ¹³C NMR: δ 18.06, 31.45, 108.87, 114.86, 126.27, 128.43, 128.78, 140.72, 142.61, 145.61, 161.15, 169.49; ESI-MS: m/z 295 [M+H]⁺; anal. calcd. for C₁₄H₁₁N₂NaO₂S: C 57.14, H 3.77, N 9.52; found: C 57.30, H 3.74, N 9.48.

General Procedure for the Synthesis 5-yl Esters Aliphatic Derivatives 7-Methyl-3H-thiazolo[4,5-b]pyridin-2-ones 4a–d

Compounds **2a** or **2b** or **2c** (5 mmol), an appropriate aliphatic chloroanhydride (5 mmol), and triethylamine (5 mmol) were added to dioxane (20 mL). The reaction mixture was refluxed 15 min. On cooling the crystalline precipitate was filtered off, washed with methanol and dried. The obtained compounds were re-crystallized from methanol.

Acetic acid 7-methyl-2-oxo-2,3-dihydro-thiazolo[4,5-b]pyridin-5-yl ester (4a)

White solid; yield: 92%; mp 240–241 °C; ¹H NMR: δ 2.30 (s, 3H, CH₃), 2.36 (s, 3H, CH₃-CO), 6.88 (s, 1H, Py), 12.69 (s, 1H, NH); ¹³C NMR: δ 12.13, 18.45, 117.33, 118.36, 143.89, 146.07, 154.01, 168.76, 169.30; ESI-MS: m/z 225 [M+H]⁺; anal. calcd. for C₉H₈N₂O₃S: C 48.21, H 3.60, N 12.49; found: C 48.66, H 3.55, N 12.51.

Butyric acid 7-methyl-2-oxo-2,3-dihydro-thiazolo[4,5-b]pyridin-5-yl ester (4b)

White solid; yield: 56%; mp 164 °C; ¹H NMR: δ 0.99 (t, $J = 7.3$ Hz, 3H, CH₃-CH₂-CH₂-CO), 1.64–1.69 (m, 2H, CH₃-CH₂-CH₂-CO), 2.36 (s, 3H, CH₃), 2.59 (t, $J = 7.1$ Hz, 3H, CH₃-CH₂-CH₂-CO), 6.87 (s, 1H, Py), 12.69 (s, 1H, NH); ¹³C NMR: δ 14.81, 19.81, 22.08, 28.15, 116.84, 118.37, 144.52, 148.15, 154.07, 166.14, 169.23; ESI-MS: m/z 253 [M+H]⁺; anal. calcd. for C₁₁H₁₂N₂O₃S: C 52.37, H 4.79, N 11.10; found: C 52.50, H 4.74, N 11.25.

Acetic acid 7-methyl-2-oxo-6-propyl-2,3-dihydro-thiazolo[4,5-b]pyridin-5-yl ester (4c)

White solid; yield: 91%; mp 212 °C; ¹H NMR: δ 1.21 (t, $J = 7.3$ Hz, 3H, CH₃-CH₂-CH₂), 1.41–1.45 (m, 2H, CH₃-CH₂-CH₂), 2.32–2.36 (m, 2H, CH₃-CH₂-CH₂), 2.34 (s, 3H, CH₃), 2.47–2.49 (m, 3H, CH₃-CO), 12.56 (s, 1H, NH); ¹³C NMR: δ 14.39, 17.99, 21.06, 22.74, 28.37, 117.61, 122.45, 143.69, 146.20, 154.23, 168.79, 169.64; ESI-MS: m/z 267 [M+H]⁺; anal. calcd. for C₁₂H₁₄N₂O₃S: C 54.12, H 5.30, N 10.52; found: C 54.18, H 5.10, N 10.46.

Acetic acid 6-benzyl-7-methyl-2-oxo-2,3-dihydro-thiazolo[4,5-b]pyridin-5-yl ester (4d)

White solid; yield: 90%; mp 216 °C; ¹H NMR: δ 2.26 (s, 3H, CH₃), 2.28 (s, 3H, CH₃-CO), 3.95 (s, 2H, CH₂-C₆H₅), 7.12 (d, $J = 7.1$ Hz, 2H, C₆H₅), 7.18 (t, $J = 6.2$ Hz, $J = 7.0$ Hz, 1H, C₆H₅), 7.27 (t, $J = 7.3$ Hz, $J = 7.1$ Hz, 2H, C₆H₅), 12.65 (s, 1H, NH); ¹³C NMR: δ 18.45, 21.06, 31.84, 117.80, 121.08, 126.62, 128.49, 128.91, 139.38, 144.22, 146.77, 154.54, 168.72, 169.31; ESI-MS: m/z 315 [M+H]⁺; anal. calcd. for C₁₆H₁₄N₂O₃S: C 61.13, H 4.49, N 8.91; found: C 61.10, H 4.45, N 8.88.

General Procedure for the Synthesis 5-yl Esters Aromatic Derivatives 7-Methyl-3H-thiazolo[4,5-b]pyridin-2-ones 4e–f

To a solution of pyridine (20 mL) and an appropriate aromatic chloroanhydride (5 mmol) was added compound **IIa** or **IIb** (5 mmol). The reaction mixture was refluxed 30 min. On cooling, the crystalline precipitate was filtered off, washed with acetic acid and dried. The obtained compounds were re-crystallized from acetic acid.

4-Nitrobenzoic acid 7-methyl-2-oxo-2,3-dihydro-thiazolo[4,5-b]pyridin-5-yl ester (4e)

White solid; yield: 72%; mp 207 °C; ¹H NMR: δ 2.41 (s, 3H, CH₃), 7.12 (s, 1H, Py), 8.38 (d, $J = 8.7$ Hz, 2H, C₆H₄), 8.44 (d, $J = 8.7$ Hz, 2H, C₆H₄), 12.78 (s, 1H, NH); ¹³C NMR: δ 19.98, 111.78, 116.85, 127.67, 129.85, 132.20, 139.94, 145.60, 148.69, 155.86, 164.04, 168.88; ESI-MS: m/z 332 [M+H]⁺; anal. calcd. for C₁₄H₉N₃O₅S: C 50.76, H 2.74, N 12.68; found: C 51.00, H 2.69, N 12.85.

Benzoic acid 7-methyl-2-oxo-6-propyl-2,3-dihydro-thiazolo[4,5-b]pyridin-5-yl ester (4f)

White solid; yield: 74%; mp 203 °C; ¹H NMR: δ 0.86 (t, $J = 5.1$ Hz, $J = 7.2$ Hz, 3H, CH₂-CH₂-CH₃), 1.46–1.51 (m, 2H, CH₂-CH₂-CH₃), 2.38 (s, 3H, CH₃), 2.54 (d, $J = 7.0$ Hz, 2H, CH₂-CH₂-CH₃), 7.66 (t, $J = 6.4$ Hz, $J = 7.3$ Hz, 2H, C₆H₅), 7.81 (t, $J = 7.0$ Hz, $J = 6.5$ Hz, 1H, C₆H₅), 8.16 (d, $J = 7.5$ Hz, 2H, C₆H₅), 12.65 (s, 1H, NH); ¹³C NMR: δ 14.44, 18.08, 21.21, 22.74, 117.33, 118.31, 126.25, 128.34, 131.15, 138.75, 144.05, 146.18, 154.25, 167.71, 168.11; ESI-MS: m/z 329 [M+H]⁺; anal. calcd. for C₁₇H₁₆N₂O₃S: C 62.18, H 4.91, N 8.53; found: C 62.22, H 4.84, N 8.50.

General Procedure for the Synthesis 6-Arylazo-5-hydroxy-7-methyl-3H-thiazolo[4,5-b]pyridin-2-ones 5a–i

Metallic sodium (0.2 mol) was dissolved in anhydrous methanol (100 mL), and to the solution obtained 4-iminothiazolidin-2-one (50 mmol) and α -arylazo derivatives acetoacetic ester (50 mmol) were added at 20 °C. The mixture was left standing for 7 days with the intermittent stirring, then it was acidified with acetic acid to pH ~5, five-fold diluted with water. The precipitate was filtered off, washed with water, and dried at 100–110 °C. The obtained compounds were re-crystallized from acetic acid.

5-Hydroxy-7-methyl-6-phenylazo-3H-thiazolo[4,5-b]pyridin-2-one (5a)

Red solid; yield: 97%; mp 265 °C; ¹H NMR: δ 2.40 (s, 3H, CH₃), 7.27 (t, *J* = 7.4 Hz, 1H, Ph), 7.48 (t, *J* = 7.9 Hz, *J* = 7.4 Hz, 2H, Ph), 7.67 (d, *J* = 7.5 Hz, 2H, Ph), 13.30 (s, 1H, OH), 14.56 (s, 1H, NH); ¹³C NMR: δ 19.96, 112.44, 118.33, 128.87, 129.96, 133.44, 138.95, 143.98, 147.07, 163.11, 168.25; ESI-MS: *m/z* 287 [M+H]⁺; anal. calcd. for C₁₃H₁₀N₄O₂S: C 54.54, H 3.52, N 19.57; found: C 54.61, H 3.49, N 19.66.

5-Hydroxy-7-methyl-6-*p*-tolylazo-3H-thiazolo[4,5-b]pyridin-2-one (5b)

Red solid; yield: 73%; mp 255 °C with dec.; ¹H NMR: δ 2.33 (s, 3H, C₆H₄-CH₃), 2.40 (s, 3H, CH₃), 7.28 (d, *J* = 7.0 Hz, 2H, C₆H₄), 7.54 (d, *J* = 7.0 Hz, 2H, C₆H₄), 13.26 (s, 1H, OH), 14.52 (s, 1H, NH); ¹³C NMR: δ 14.44, 19.98, 112.23, 117.84, 128.15, 129.42, 132.15, 138.77, 144.32, 147.11, 163.07, 168.66; ESI-MS: *m/z* 301 [M+H]⁺; anal. calcd. for C₁₄H₁₂N₄O₂S: C 55.99, H 4.03, N 18.65; found: C 55.84, H 4.00, N 18.59.

5-Hydroxy-7-methyl-6-*m*-tolylazo-3H-thiazolo[4,5-b]pyridin-2-one (5c)

Red solid; yield: 97%; mp 233 °C; ¹H NMR: δ 2.35 (s, 3H, C₆H₄-CH₃), 2.38 (s, 3H, CH₃), 7.07 (d, *J* = 7.6 Hz, 1H, C₆H₄), 7.35 (t, *J* = 7.8 Hz, *J* = 7.6 Hz, 1H, C₆H₄), 7.44 (d, *J* = 10.0 Hz, 2H, C₆H₄), 13.28 (s, 1H, OH), 14.58 (s, 1H, NH); ¹³C NMR: δ 19.89, 21.54, 104.71, 107.70, 112.56, 114.58, 117.66, 119.61, 122.67, 130.06, 144.61, 148.11, 162.89, 169.8; ESI-MS: *m/z* 301 [M+H]⁺; anal. calcd. for C₁₄H₁₂N₄O₂S: C 55.99, H 4.03, N 18.65; found: C 55.87, H 4.08, N 18.68.

6-(2,4-Dimethyl-phenylazo)-5-hydroxy-7-methyl-3H-thiazolo[4,5-b]pyridin-2-one (5d)

Yellow solid; yield: 97%; mp 282 °C; ¹H NMR: δ 2.32 (s, 3H, C₆H₃-CH₃), 2.38 (s, 3H, CH₃), 2.42 (s, 3H, C₆H₃-CH₃), 7.18–7.20 (m, 2H, C₆H₃), 7.69–7.71 (m, 1H, C₆H₃), 13.37 (s, 1H, OH), 15.10 (s, 1H, NH); ¹³C NMR: δ 13.15, 16.23, 18.21, 102.08, 106.75, 112.12, 115.07, 118.71, 120.96, 125.12, 130.42, 144.77, 148.05, 162.44, 169.55; ESI-MS: *m/z* 315 [M+H]⁺; anal. calcd. for C₁₅H₁₄N₄O₂S: C 57.31, H 4.49, N 17.82; found: C 57.45, H 4.44, N 17.77.

5-Hydroxy-6-(2-hydroxy-phenylazo)-7-methyl-3H-thiazolo[4,5-b]pyridin-2-one (5e)

Orange solid; yield: 99%; mp > 280 °C with dec.; ¹H NMR: δ 2.40 (s, 3H, CH₃), 6.95–6.98 (m, 2H, C₆H₄), 7.12 (t, *J* = 7.3 Hz, 1H, C₆H₄), 7.71 (d, *J* = 7.7 Hz, 1H, C₆H₄), 10.75 (s, 1H, C₆H₄-OH), 13.28 (s, 1H, OH), 14.89 (s, 1H, NH); ¹³C NMR: δ 19.44, 103.12, 107.07, 113.44, 115.35, 119.33, 121.25, 124.71, 130.33, 145.12, 148.11, 163.08, 169.79; ESI-MS: *m/z* 303 [M+H]⁺; anal. calcd. for C₁₃H₁₀N₄O₃S: C 51.65, H 3.33, N 18.53; found: C 51.59, H 3.40, N 18.58.

3-(5-Hydroxy-7-methyl-2-oxo-2,3-dihydro-thiazolo[4,5-b]pyridin-6-ylazo)-benzenesulfonic acid (5f)

Yellow solid; yield: 99%; mp > 280 °C with dec.; ¹H NMR: δ 2.41 (s, 3H, CH₃), 7.44–7.51 (m, 2H, C₆H₄), 7.60 (d, *J* = 7.0 Hz, 1H, C₆H₄), 7.86 (s, 1H, C₆H₄), 13.31 (s, 1H, OH), 14.61 (s, 1H, NH); ¹³C NMR: δ 17.35, 114.27, 117.95, 124.07, 125.74, 129.79, 137.54, 141.28, 141.58, 150.24, 160.62; ESI-MS: *m/z* 367 [M+H]⁺; anal. calcd. for C₁₃H₁₀N₄O₅S₂: C 42.62, H 2.75, N 15.29; found: C 42.33, H 2.65, N 15.38.

5-Hydroxy-6-(4-methoxy-phenylazo)-7-methyl-3H-thiazolo[4,5-b]pyridin-2-one (5g)

Red solid; yield: 99%; mp > 258 °C with dec.; ¹H NMR: δ 2.41 (s, 3H, CH₃), 3.80 (s, 3H, O-CH₃), 7.05 (d, *J* = 9.0 Hz, 2H, C₆H₄), 7.67 (d, *J* = 8.0 Hz, 2H, C₆H₄), 13.14 (s, 1H, OH), 14.78 (s, 1H, NH); ¹³C NMR: δ 16.44, 19.15, 111.97, 117.75, 128.17, 129.23, 132.42, 138.92, 143.98, 146.88, 162.65, 168.07; ESI-MS: *m/z* 317 [M+H]⁺; anal. calcd. for C₁₄H₁₂N₄O₃S: C 53.16, H 3.82, N 17.71; found: C 53.25, H 3.88, N 17.64.

4-(5-Hydroxy-7-methyl-2-oxo-2,3-dihydro-thiazolo[4,5-b]pyridin-6-ylazo)-benzenesulfonamide (5h)

Orange solid; yield: 100%; mp > 280 °C with dec.; ¹H NMR: δ 2.36 (s, 3H, CH₃), 7.38 (s, 2H, NH₂), 7.76 (d, *J* = 8.5 Hz, 2H, C₆H₄), 7.86 (d, *J* = 8.5 Hz, 2H, C₆H₄), 13.32 (s, 1H, OH), 14.32 (s, 1H, NH); ¹³C NMR: δ 17.44, 116.88, 123.19, 125.82, 127.62, 141.33, 142.11, 146.10, 160.55, 166.84, 177.99; ESI-MS: *m/z* 366 [M+H]⁺; anal. calcd. for C₁₃H₁₁N₅O₄S₂: C 42.73, H 3.03, N 19.17; found: C 42.82, H 3.14, N 19.25.

***N*-(5-Ethyl-[1,3,4]thiadiazol-2-yl)-4-(5-hydroxy-7-methyl-2-oxo-2,3-dihydro-thiazolo[4,5-b]pyridin-6-ylazo)-benzenesulfonamide (5i)**

Orange solid; yield: 100%; mp 276–278 °C; ¹H NMR: δ 1.21 (t, *J* = 7.5 Hz, 3H, CH₃-CH₂-thiadiazole), 2.36 (s, 3H, CH₃), 2.80–2.85 (m, 2H, CH₃-CH₂-thiadiazole), 7.76 (d, *J* = 8.7 Hz, 2H, C₆H₄), 7.83 (d, *J* = 8.7 Hz, 2H, C₆H₄), 13.67 (s, 1H, OH), 14.32 (s, 1H, NH); ¹³C NMR: δ 12.78, 17.43, 24.17, 117.44, 126.79, 128.03, 138.78, 140.71, 144.96, 145.01, 160.55, 168.03, 168.06; ESI-MS: *m/z* 478 [M+H]⁺; anal. calcd. for C₁₇H₁₅N₇O₄S₃: C 42.76, H 3.17, N 20.53; found: C 42.79, H 3.33, N 20.46.

2. 3. Anti-Inflammatory Activity Evaluation Assays

Anti-inflammatory activity²⁴ was evaluated using carrageenan induced rat paw edema method in rats. Outbred (male/female) white rats weighing 180–220 g were used for the edema test. Animals were divided into 13 groups comprising five rats per group. One group was kept as the control and remaining 12 groups (test groups) were used to determine the anti-inflammatory activity

elicited by the 10 drug candidates, respectively. Rats were kept in the animal house under standard conditions of light and temperature on the general diet prior to the experiment. The standard drug, Ibuprofen (50 mg/kg body weight) and the test drugs (50 mg/kg body weight) were dissolved in DMSO and administered through intraperitoneal route. DMSO was injected to the control group; 30 minutes later, 0.1 mL of 2% carrageenan solution in saline was injected in the sub-plantar region of the right hind paw of each rat. After 4 h of the carrageenan injection, the volume of paw edema (in mL) was measured using water plethysmometer and paw edema decreasing was compared between control group and drug-tested groups. Danylo Halysky Lviv National Medical University ethics committee, constituted by the Ministry of Health of Ukraine, approved the experimental protocol. The inflammatory reaction inhibition was expressed as percent of paw volume reduction and it was calculated using the following formula:

$$\% \text{ Inhibition} = \frac{V_{\text{control}} - V}{V_{\text{control}}} \cdot 100 \% \quad (1)$$

where V_{control} is the increase in paw volume in control group animals; V is the increase in paw volume in animals injected with the test substances.

2. 4. Free Radical Scavenging Assays

The antioxidant activity was determined on the basis of free radical scavenging activity of stable 2,2-diphenyl-1-picrylhydrazyl radical (DPPH). The effect of the studied compounds on DPPH radicals were estimated according to the method of Blois^{25–26} with minor modifications. The solution of DPPH in ethanol with the concentration of 150 $\mu\text{mol/L}$ (4 mL) was mixed with the compound or control solution in ethanol, its concentration being 250 $\mu\text{mol/L}$ (0.2 mL). The reaction mixture was vortex mixed thoroughly and incubated at room temperature in the dark for 60 min. Simultaneously, a control was prepared as ascorbic acid solution in ethanol (0.2 mL) mixed with DPPH solution in ethanol (4 mL) without sample fraction. Reduction in the absorbance of the mixture was measured at 517 nm using ethanol as blank. Ascorbic acid was used as the standard. Also the absorbance of DPPH solution was measured. Percentage of free-radical-scavenging activity was expressed as percent inhibition and it was calculated using the following formula:

$$\% \text{ Inhibition} = \frac{A_{\text{DPPH}} - A_s}{A_{\text{DPPH}}} \cdot 100 \% ; \quad (2)$$

where A_{DPPH} is the absorbance of DPPH free radicals solution, A_s is the absorbance of the sample. Each experiment was performed in triplicate and average values were recorded. Results are expressed as the means \pm S.D.

3. Results and Discussion

3. 1. Chemistry

One of the efficient synthetic approaches for thiazolo[4,5-*b*]pyridine system construction used in modern medical chemistry is the protocol based on [3+3] cyclocondensation of 4-iminothiazolidin-2-one²⁷ (**1**) on account of its N,C-binucleophilic properties when reacting with dielectrophilic reagents.²⁸

We used 4-iminothiazolidin-2-one (**1**) as the initial compound that was reacted with acetoacetic ester. We optimized the conditions of this reaction that made it possible to obtain 5-hydroxy-7-methyl-3*H*-thiazolo[4,5-*b*]pyridin-2-one (**2a**) in good yield (Scheme 1). The best results were observed in the case keeping when methanol was used and the reagents mixture was kept in the presence of sodium methylate over 7 days.

The next stage of our strategy includes the core heterocycle structural modification at its C⁶ position. The direct functionalization procedure has been shown to be of a small synthetic utility owing to the low nucleophilic activity of the compound **1** at the C⁶ position. We studied the behavior in reaction of [3+3] cyclocondensation of 4-iminothiazolidin-2-one with alkylated acetoacetic ester derivatives. Under the chosen reaction conditions the corresponding 6-alkyl-5-hydroxy-7-methyl-3*H*-thiazolo[4,5-*b*]pyridin-2-ones **2b–c** were isolated in good yields (Scheme 1).

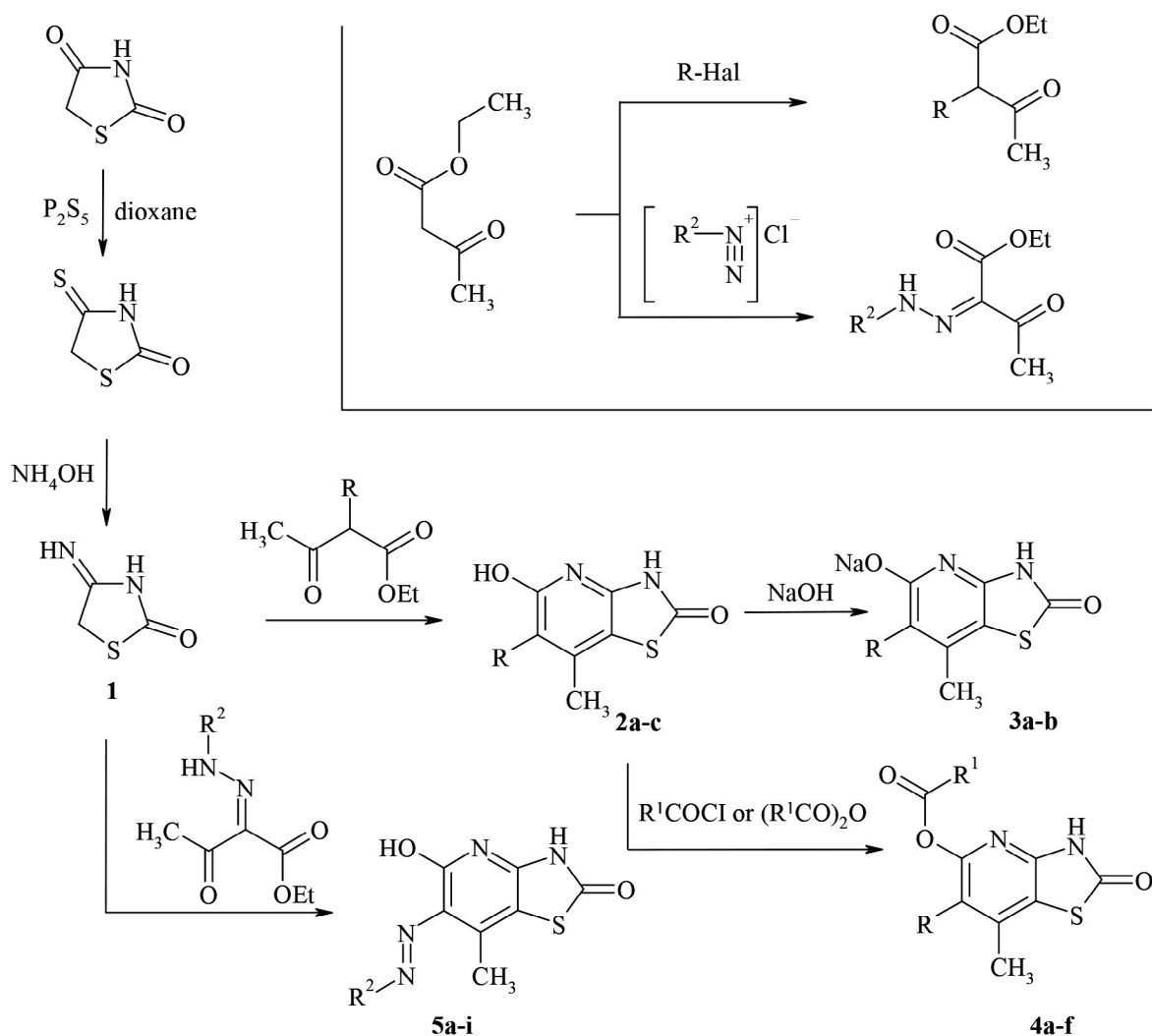
Some properties of the obtained compounds were investigated. The proton at the position 5 retained the acidic properties and the reaction with sodium hydroxide furnished the corresponding salts **3a–b** (Scheme 1).

Chloroacetamides are highly reactive chemicals which are being involved in alkylation reactions forming the basis for creating building blocks of wide utility for combinatorial chemistry, including biologically active substances, to design combinatorial libraries on their basis.

The hydroxy group present at C⁵ position in compounds **2a–c** provides an entry to 5-yl ester derivatives **4a–f**. Anhydride was found to be the most suitable medium for the reaction of compounds **2a–c** with aliphatic chloroanhydrides **4a–d**. Reaction of compounds **2a–b** with chloroanhydrides of aromatic acids readily took place in pyridine medium and enabled the preparation of compounds **4e,f** (Scheme 1).

Literature survey revealed that some antimicrobial drugs like sulfasalazine, salazopyridazine *etc.* contain arylazo group.²⁹ In its turn, arylazo moiety introduction into thiazolidine ring system led to antimicrobial activity enhancement possessed by the respective thiazolidine arylazo derivatives.

In view of the results mentioned above, 5-hydroxy-7-methyl-6-aryloxy-3*H*-thiazolo[4,5-*b*]pyridin-2-ones **5a–i** were synthesized following the same protocol as for α -aryloxy derivatives of acetoacetic esters, by treatment with 4-iminothiazolidin-2-one (Scheme 1). Powders of these



2a-c: R = H (a), C₆H₅-CH₂ (b), C₃H₇ (c); **3a-b:** R = H (a), C₆H₅-CH₂ (b); **4a-f:** R = H, R¹ = CH₃ (a), R = H, R¹ = C₃H₇ (b), R = C₃H₇, R¹ = CH₃ (c), R = C₆H₅-CH₂, R¹ = CH₃ (d), R = H, R¹ = 4-NO₂-C₆H₄ (e), R = C₃H₇, R¹ = C₆H₅ (f), **5a-i** R² = C₆H₅ (a), 4-CH₃-C₆H₄ (b), 3-CH₃-C₆H₄ (c), 2,4-(CH₃)₂C₆H₃ (d), 2-OH-C₆H₄ (e), 3-SO₃H-C₆H₄ (f), 4-OCH₃-C₆H₄ (g), 4-SO₂NH₂C₆H₄ (h), 4-(N-(5-ethyl-[1,3,4]thiadiazol-2-yl)-benzenesulfonamide) (i).

Scheme 1. Synthesis of novel 3H-thiazolo[4,5-b]pyridines

substances are well soluble in DMF and DMSO, sparingly soluble in water and in other organic solvents.

The structures of the obtained compounds were confirmed by ¹H and ¹³C NMR spectroscopy and elemental analysis. All these new compounds gave spectroscopic data in accordance with the proposed structures. The ¹H NMR spectra of all compounds show the protons signals of methyl group in pyridine ring as singlets in the 1.99–2.41 ppm.

Endocyclic NH groups of basic scaffold are apparent in the region of weak magnetic field at 11.07–15.10 ppm. Proton signals of pyridine cycle for compounds are evident at 5.41–7.12 ppm and are represented by correspondent singlets. Absence of given signals confirms the origin of reaction [3+3]cyclocondensation with corresponding

alkyl as well as with arylazo derivatives of acetoacetic ester.

OH group of basic scaffold is represented by relatively broad singlets at 10.84–13.67 ppm. The corresponding salts obtained are characterized by the absence of OH group signals. Conducting acylation reaction is characterized by the absence of OH group signal at position C⁵ as well as by the presence of a set of singlets, doublets and multiplets at 0.99–8.44 ppm that confirm the formation of the corresponding 5-acyl derivatives.

3. 2. Anti-inflammatory Activity *in vivo* Evaluation

Carrageenan-induced paw edema is the most widely used animal model of acute inflammation. *In vivo* studies

of novel thiazolo[4,5-*b*]pyridine-2-one derivatives were carried out for anti-inflammatory activity employing the carrageenan-induced rat paw edema method. Marked paw edema was produced in rats with sub-planter injection of 0.1 mL of 2% carrageenan. The test compounds were dissolved in DMSO and injected intraperitoneally in the dose of 50 mg/kg body weight 0.5 h prior to carrageenan injection. The NSAID drug Ibuprofen in its effective therapeutic dose was tested in parallel as an activity reference. Anti-inflammatory activity was defined by measuring the paw edema volume 4 h after the carrageenan injection. Results of paw edema decreasing are expressed as the mean \pm standard deviation and compared statistically with the control group using Student's *t*-test. A level of $p < 0.05$ was adopted as the test of significance (Table 1). The percentage protection against inflammation was calculated as % inhibition by comparison between DMSO injected control group and drugs-tested groups.

Table 1. Anti-inflammatory effect of thiazolo[4,5-*b*]pyridine-2-ones on carrageenan-induced rat paw edema (mL) *in vivo* evaluation, % protection from inflammation

Compound	Paw edema volume (mL) \pm SEM*	% Inhibition	Compound	Paw edema volume (mL) \pm SEM*	% Inhibition
Control	2.20 \pm 0.050	–	4f	1.29 \pm 0.025	41.2
2a	1.41 \pm 0.040	36.2	5a	1.54 \pm 0.040	30.1
2c	1.64 \pm 0.035	25.3	5g	1.60 \pm 0.035	27.2
3a	1.44 \pm 0.040	34.5	5h	1.25 \pm 0.020	43.1
4a	1.57 \pm 0.035	28.5	5i	1.09 \pm 0.025	50.5
4c	1.22 \pm 0.020	44.5	ibuprofen	1.32 \pm 0.035	40.2

Evaluation of anti-inflammatory activity indicated that six compounds (*i.e.* 2a, 2c, 3a, 4a, 5a and 5g) showed no significant decrease in edema, the inhibition rate for them was observed at the level of 25.3–36.2% as compared to control group. The compounds 4c, 4f and 5h possessed the anti-inflammatory activity in the range of 41.2–44.5% which is comparable to the effect of Ibuprofen. The anti-inflammatory evaluation test for compound 5i gave the result as 50.5% inhibition indicating the compound was more potent than Ibuprofen.

The results of the pharmacological tests were analyzed with respect to the compounds structure. For C⁶-substituted 5-hydroxy-7-methyl-3*H*-thiazolo[4,5-*b*]pyridin-2-one derivatives prepared by [3+3] cyclocondensation of 4-iminothiazolidin-2-one with arylazo derivatives of acetoacetic ester comparison of the substituents nature on the C⁶ position indicated that *N*-(5-ethyl-[1,3,4]thiazol-2-yl)-methanesulfonamide presence in the phenyl ring contributed to the inflammation inhibition efficiency. The presence of the acetyl or phenyl groups at the C⁵ position of the basic scaffold and a propyl group at the C⁶ position caused the anti-inflammatory activity which is comparable to the effect of Ibuprofen. Among the remaining test compounds no active compounds were evaluated in-

dicating the nature and position of the substituted groups did not influence notably their anti-inflammatory activity.

3.3. *In vitro* Antioxidant Assay

The antioxidant activity was determined on the basis of free radical scavenging activity of 2,2-diphenyl-1-picrylhydrazyl (DPPH) free radical. DPPH radical has found many applications due to its high stability in the methanolic solutions and its intense purple color. In its oxidized form, the DPPH radical has an absorbance maximum centered at a wavelength about 540 nm. The absorbance decreases when the radical is reduced by antioxidants. Its reduction affords 2,2-diphenyl-1-picrylhydrazine (DPPH-H), or the corresponding anion (DPPH⁻) in basic medium. The DPPH radical acts as a scavenger for other odd-electron species which afford *para*-substitution products at phenyl rings.

The DPPH method is described as a simple, rapid and convenient method for screening of many samples for radical scavenging activity. These advantages make the DPPH method interesting for testing newly synthesized compounds to scavenge radicals and to find out promising antioxidant drug candidates.

In the present paper we demonstrate a modified spectrophotometric method that makes use of the DPPH radical and its specific absorbance properties. The free radical scavenging activities of each compound were assayed using a stable DPPH and were quantified by decolorization of the solution being mixed with DHHP as observed at the wavelength of 540 nm. The absorbance of DPPH solution in ethanol (150 μ mol/L) was measured as 0.770. The absorbances and free-radical-scavenging activities % inhibitions of standard (ascorbic acid) and each compound are listed in Table 2.

The antioxidant activity evaluation results showed that, in general, most of the tested compounds showed that their free radical scavenging effect was insignificant being in the range of 5.50–21.10%. The pharmacological screening allowed identification of only one lead compound, namely 5i, whose free radical scavenging activity (65.80%) exceeded that of ascorbic acid. Thus, the presence of *N*-(5-

Table 2: Values of Absorbance and % Inhibition of 3H-thiazolo[4,5-b]pyridine-2-ones

Compound or Standard	Absorbance of a Sample, A _s	% Inhibition	Compound or Standard	Absorbance of a Sample, A _s	% Inhibition
ascorbic acid	0.406 ± 0.015	47.30	4f	0.654 ± 0.025	15.10
2a	0.682 ± 0.025	11.50	5a	0.670 ± 0.025	13.00
2b	0.654 ± 0.020	15.10	5b	0.725 ± 0.030	5.80
2c	0.608 ± 0.020	21.10	5c	0.715 ± 0.030	7.10
3a	0.704 ± 0.030	8.50	5d	0.728 ± 0.030	5.50
3b	0.672 ± 0.025	12.70	5e	0.662 ± 0.020	14.00
4a	0.697 ± 0.025	9.50	5f	0.700 ± 0.025	9.10
4b	0.697 ± 0.025	9.50	5g	0.711 ± 0.020	7.70
4c	0.706 ± 0.030	8.30	5h	0.691 ± 0.025	10.30
4d	0.704 ± 0.030	8.50	5i	0.263 ± 0.010	65.80
4e	0.684 ± 0.025	11.20			

ethyl-[1,3,4]thiadiazol-2-yl)-methanesulfonamide in the phenyl ring of the core scaffold at C⁶ position was essential to the antioxidant activity of these compounds.

4. Conclusions

A series of 5-hydroxy-7-methyl-3H-thiazolo[4,5-b]pyridin-2-one derivatives possessing anti-inflammatory and antioxidant activities were prepared by the structural modification of the core heterocycle at C⁵ and C⁶ positions. Therefore, we have shown that the proposed approaches and developed synthetic protocols provided the possibility to synthesize diverse 5-hydroxy-7-methyl-3H-thiazolo[4,5-b]pyridin-2-ones with a considerable chemical novelty involving alkylation, Japp–Klingemann condensation, [3+3] cyclocondensation and acylation reactions. Anti-inflammatory activity evaluated *in vivo* and free radicals scavenging effect determined *in vitro* allowed to identify some lead compounds causing significant decrease in edema formation or considerable antioxidant effect. The present results suggest that the core fused heterocycle can be developed as a promising scaffold for anti-inflammatory and antioxidant drug candidates.

5. References

- I. S. Shin, J. W. Park, N. R. Shin, C. M. Jeon, O. K. Kwon, J. S. Kim, J. C. Kim, S. R. Kyung-Seop Ahn, *Immunobiology* **2014**, *219*, 901–908. DOI: 10.1016/j.imbio.2014.08.004
- M. J. Killeen, M. Linder, P. Pontoniere, R. Crea, *Drug Discov. Today* **2014**, *19*, 373–378. DOI: 10.1016/j.drudis.2013.11.002
- P. Batchelor, *Br Dent J.* **2014**, *217*, 405–409. DOI: 10.1038/sj.bdj.2014.912
- M. M. Bosma-den Boer, M. L. Van Wetten, L. Pruijboom, *Nutr. Metab.* **2012**, *9*, 32–45. DOI: 10.1186/1743-7075-9-32
- S. M. Lucas, N. J. Rothwell, R. M. Gibson, *Br. J. Pharmacol.* **2006**, *147*, S232–S240. DOI: 10.1038/sj.bjp.0706400
- K. A. Lebedev, I. D. Ponyakina, N. V. Kozachenko, *Hum. Physiol.* **2005**, *31*, 86–97. DOI: 10.1007/s10747-005-0012-5M
- S. S. Fatahala, M. A. Khedr, M. S. Mohamed, *Acta Chim. Slov.* **2017**, *64*, 865–876. DOI: 10.17344/acsi.2017.3481
- S. Cardinal, P. A. Paquet-Cote, J. Azelmat, C. Bouchard, D. Grenier, N. Voyer, *Bioorg. Med. Chem.* **2017**, *25*, 2043–2056. DOI: 10.1016/j.bmc.2017.01.050. Epub 2017 Feb 16
- O. Kolomoets, O. Voskoboynik, O. Antypenko, G. Berest, I. Nosulenko, V. Palchikov, O. Karpenko, S. Kovalenko, *Acta Chim. Slov.* **2017**, *64*, 902–910. DOI: 10.17344/acsi.2017.3575
- R. Paprocka, M. Wiese, A. Eljaszewicz, A. Helmin-Basa, A. Gzella, B. Modzelewska-Banachiewicz, J. Michalkiewicz, *Bioorg. Med. Chem. Lett.* **2015**, *25*, 2664–2667. DOI: 10.1016/j.bmcl.2015.04.079. Epub 2015 Apr 30
- R. M. Mohareb, F. Al-Omran, M. A. Abdelaziz, R. A. Ibrahim, *Acta Chim. Slov.* **2017**, *64*, 349–364. DOI: 10.17344/acsi.2017.3200
- M. Valko, C. J. Rhodes, J. Monocol, M. Izakovic, M. Mazur, *Chem. Biol. Interact.* **2006**, *160*, 1–40. DOI: 10.1016/j.cbi.2005.12.009
- R. Amarowicz, I. Estrella, T. Hernandez, S. Robredo, A. Troczynska, A. Kosinska, R. Pegg, *Food Chem.* **2010**, *121*, 705–711. DOI: 10.1016/j.foodchem.2010.01.009
- Z. Chaban, S. Harkov, T. Chaban O. Klenina, V. Ogurtsov, I. Chaban, *Pharmacia* **2017**, *64*(3), 52–66.
- T. Chaban, O. Klenina, I. Chaban, V. Ogurtsov, S. Harkov, M. Lelyukh, *Pharmacia* **2018**, *65*(2), 54–70.
- T. I. Chaban, V. V. Ogurtsov, I. G. Chaban, O. V. Klenina, J. D. Komarytsia, *Phosphorus, Sulfur Silicon Relat. Elem.* **2013**, *188*, 1611–1620. DOI: 10.1080/10426507.2013.777723.
- O. Klenina, I. Drapak, T. Chaban, V. Ogurtsov, I. Chaban, I. Golos, *Chem. & Chem. Techn.* **2013**, *7*, 397–404.
- O. Klenina, T. Chaban, B. Zimenkovsky, S. Harkov, V. Ogurtsov, I. Chaban, I. Myrko, *Pharmacia* **2017**, *64*(4), 49–71.
- T. Chaban, O. Klenina, I. Drapak, V. Ogurtsov, I. Chaban, V. Novikov, *Chem. & Chem. Techn.* **2014**, *89*, 287–292.
- T. I. Chaban, R. R. Panchuk, O. V. Klenina, N. R. Skorokhyd, V. V. Ogurtsov, I. G. Chaban, *Biopolym. Cell* **2012**, *28*, 389–396. DOI: 10.7124/bc.000075
- T. Chaban, O. Klenina, B. Zimenkovsky, I. Chaban, V.

- Ogurtsov, L. Shelepeten, *Der Pharma Chemica*. **2016**, *8*, 534–542.
22. T. Chaban, O. Klenina, S. Harkov, V. Ogurtsov, I. Chaban, I. Nekttegaev, *Pharmacia* **2017**, *64(4)*, 16–30.
23. S. Marzoog, Al-Thebeiti, *Il Farmaco* **2000**, *55*, 109–118.
DOI: 10.1016/S0014-827X(99)00130-5
24. A. D. Pillai, P. D. Rathod, P. X. Franklin, H. Padh, K. K. Vasu, V. Sudarsanam, *Biochem. Biophys. Res. Commun.* **2004**, *317*, 1067–1074. DOI: 10.1016/j.bbrc.2004.03.148
25. M. S. Blois, *Nature* **1958**, *181*, 1199–1200.
DOI:10.1038/1811199a0
26. P. Molyneux, *J. Sci. Technol.* **2004**, *26*, 211–219.
27. I. D. Komaritsa, *Chem. Heterocycl. Compd.* **1970**, *4*, 324–325.
DOI: 10.1007/BF00755270
28. T. I. Chaban, B. S. Zimenkovskii, J. D. Komaritsa, I. G. Chaban, *Rus. J. Org. Chem.* **2012**, *48*, 268–272.
DOI:10.1134/S1070428012020170
29. B. Combe, C. Codreanu, U. Fiocco, M. Gaubitz, P. P. Geusens, T. K. Kvien, K. Pavelka, P. N. Sambrook, J. S. Smolen, J. Wajdula, S. Fatenejad, *Ann. Rheum. Dis.* **2006**, *65*, 1357–1362.
DOI:10.1136/ard.2005.049650

Povzetek

5-Hidroksi-7-metil-3*H*-tiazolo[4,5-*b*]piridin-2-on smo pripravili z reakcijo med 4-iminotiazolidin-2-onom in acetoacetatnim estrom. Nadaljnje strukturne modifikacije so vključevale uvedbo diverzitete na položajih C⁵ in C⁶. Anti-inflamatorno učinkovanje novih tiazolo[4,5-*b*]piridin-2-onskih derivatov smo ugotovili z *in vivo* metodo s pomočjo s karagenanom inducirane edema na podganjih tacah. Antioksidantno aktivnost sintetiziranih spojin smo določili z *in vitro* metodo s pomočjo radikalskega lovilca 2,2-difenil-1-pikrilhidrazilnega radikala (DPPH).

Scientific paper

A Novel Environmentally Friendly Synergistic Mixture for Steel Corrosion Inhibition in 0.51 M NaCl

Stojan Božović,^{1,*} Sanja Martinez² and Veselinka Grudić¹¹ University of Montenegro, Faculty of Metallurgy and Technology, Cetinjski put, 81000 Podgorica, Montenegro² University of Zagreb, Faculty of Chemical Engineering and Technology, Department of Electrochemistry, ReCorr Laboratory, Savska cesta 16, HR-1000 Zagreb, Croatia* Corresponding author: E-mail: stojan.bozovic90@yahoo.com,
Telephone: +38267499528

Received: 09-02-2018

Abstract

The ubiquitous use of plain and low-alloy steels in neutral, chloride bearing environments presents an everyday challenge for corrosion protection professionals. This paper explores the possibility of developing a non-toxic and environmentally friendly synergistic inhibitor mixture made of propolis, tannin, sodium benzoate, PEG400 and starch that could be applied into the solution to induce the formation of a persistent protective layer on steel. Components of the mixture were chosen based on the references giving their characteristics relevant to their possible action in the solution and/or at the surface of the steel. The efficiency of the protective layer formed under the influence of the inhibitor mixture, and then measured by the LPR probe in the inhibitor-free solution, was the lowest under quiescent conditions (75%) and the highest (95%) under flow conditions. Both, LPR and EIS data indicate that the inhibitor modified layer presents a barrier for diffusion of oxygen that acts as a primary corrosion reaction depolarizer in the investigated neutral chloride solution. The demonstrated persistence of the inhibitor modified layer is of primary interest as it gives possibility batch application.

Keywords: Synergistic inhibitor mixture; steel; corrosion inhibition

1. Introduction

Steel is the most widely used metallic material thanks to its good mechanical properties and low price. However, when it comes into contact with aerated neutral electrolyte, especially in the presence of chloride ions, steel is subject to rapid corrosion degradation.

Neutral saline aqueous environments of various origins are frequently simulated in laboratory by the use of 0.35–0.85 M NaCl solutions.¹ Corrosion rates recorded on plain steel by polarization and weight loss techniques are fairly consistent and range between 0.1 and 0.5 mm per year.^{2,3} These rates are generally not acceptable and protective measures have to be applied. Due to the inherent characteristics of corroding systems (e.g. complex geometry or need for good thermal conductance) corrosion inhibitors frequently stand out as the most practical or the only solution. Unfortunately, protection of steel in neutral chloride media is challenging from theoretical and practical viewpoint. It can readily be observed that considerably more literature is found on inhibition of steel corrosion in acidic

media than in neutral media and that the inhibitor effectiveness is generally higher. From the theoretical aspect, the reason is that in near-neutral, neutral and alkaline media, inhibitor action is complicated by formation of iron oxides and hydroxides at the surface of metal.⁴

In acidic media, bare iron (or steel) surface is positively charged and behaves as a soft Lewis acid, hence, soft Lewis base compounds with heteroatoms O, N, S, P and/or π electrons in their structure, are good inhibitor candidates due to the possibility of soft acid-soft base adsorption bond formation.^{5,6} On the other hand, when oxide is present, surface acidity and basicity depends on oxide's isoelectric point, which e.g. for Fe_2O_3 , equals pH 8.6.⁷ Below this pH it may be assumed that the surface oxide is protonated, positively charged and acting as a hard Lewis acid. Hard Lewis bases would therefore be good inhibitor candidates capable of hard acid-hard base adsorptive bond formation.

In the present study, tannin, sodium benzoate, propolis, starch and polyethylene glycol (PEG400) were chosen as components of the investigated inhibitor mixture. When

such a mixture rich in OH groups is used for inhibiting corrosion, in near neutral and neutral pH, part of the OH groups will be deprotonated forming anions that have electronegativity practically equal to their ionization potential, and therefore act as almost pure electron donors or hard Lewis bases.⁵ Adsorptive hard acid-hard base bond which is of predominantly ionic character would therefore be possible between compounds of the mixture and the oxidized steel surface. Additionally, metal cations in high oxidation state, such as ferric ions dissolved from the steel surface into the electrolyte, are hard Lewis bases, so that formation of protective deposits of hardly soluble complexes and/or chelates of ferric ions with anionic organic ligands is possible.⁸

Components of the inhibitor mixture investigated in the present study were chosen after careful consideration of their environmental friendliness and previously published characteristics relevant to corrosion inhibition. E.g., ethanolic propolis extract applied to mild steel forms a very effective anticorrosion coating in neutral and near neutral aqueous 3.5% w/v NaCl solution.⁹ Propolis was also proven to be effective on copper in neutral chloride solution,¹⁰ but copper is more favourable for adsorption of organic compounds under such conditions.¹ Adsorption of effective propolis layer on steel from the solution is probably hindered by its insufficient concentration due to the limited solubility of propolis in water. Dispersion of propolis in neutral chloride medium produces a yellowish emulsion.⁹ Based on literature data, PEG is used as an alternative solvent for non-ethanolic propolis extraction,¹¹ and when used together with propolis, could beneficially influence propolis dispersibility in a water solution.¹² Furthermore, it has been shown that a compact layer, with barrier effect for the diffusion of oxygen in 0.1 NaCl solution, has been deposited on mild steel from the solutions containing 1000, 2500 and 5000 g ppm of PEG after 30 min of immersion time, showing that PEG itself can act as a corrosion inhibitor.¹³ Formation of the protective ferric “tannate film” deposited from solution of tannin is also possible, and it was shown to begin at pH = 3, but relevant efficiencies are attained only at concentrations ~1000 ppm.¹⁴ Recent investigation of low carbon steel inhibition by 1–5% tannic acid solution in 3.5% NaCl shows that efficiencies up to 51% can be obtained.¹⁵ Concentrations of the same order are needed for efficient steel corrosion inhibition in chloride media by starch¹⁶ and sodium benzoate.¹⁷ In the present study, minimal quantities of individual components that would be effective, based on the above literature references, were chosen for the inhibitor mixture composition.

In general, extra costs are incurred in neutral chloride media because the enhancement of inhibitor effectiveness is frequently attained through the increase in concentration up to a few thousands of ppm.¹⁸ The most explored strategy for lowering inhibitor concentration, while retaining good efficiency is application of synergistic inhibiting mixtures.^{1,18–22} In the present case, different chemical nature of components of the mixture used was

expected to yield a combination of mechanisms of action, which is usually argued to be the basis for synergism.²³

Propolis was chosen as a starting component of the mixture. It is generally accepted that propolis is composed of approximately 50% resin (polyphenolic fraction), 30% wax, 10% essential oils, 5% pollen and 5% other organic and inorganic compounds.⁹ Main propolis phenolic esters and flavonoids are of amphiphilic nature,²⁴ and are expected not only to inhibit corrosion but also to increase the hydrophobicity of steel or corrosion products due to adsorption with the hydrophilic part of the molecule oriented to the surface and the hydrophobic part oriented towards the liquid phase.²⁵ Chestnut tannin extract⁶ was chosen as a second component in order to increase the water-soluble inhibiting fraction of the mixture. Since polyphenols are weak organic acids known to decrease pH of neutral solutions,¹⁴ along with the inhibitive effect of the tannate layer, iron dissolution enhancing effect may be expected.¹⁵ Increased release of iron ions from steel, on the other hand, is favourable for ferric tannate formation. Hence, sodium benzoate¹⁷ has been added to the mixture for controlled iron release, until the protective surface layer is fully formed.

The last two components added to the mixture were polymeric substances, PEG and starch. Besides with the intention of increasing propolis solubility, PEG was added alongside with starch, with the intention of strengthening surface layer through interaction with tannin. Tannins have an abundance of hydroxyl groups in close proximity capable of strong and specific interaction with carbohydrate polymers via hydrogen bonding and hydrophobic interactions.²⁶ When phenolic components and PEG and starch are mixed, the hydroxyl groups of phenolic chemicals can interact with PEG oxygens²⁷ and side chains of starch amylopectin,²⁸ respectively.

In this paper we extend the synergistic approach by hypothesising that a carefully chosen mixture of non-toxic and environmentally benign inhibitive compounds could modify the rust layer on steel. This layer would form in neutral chloride solutions, as to produce a persistent film which would lower corrosion rate considerably. The inherent advantage of the novel mixture would be environmental friendliness as well as the retention and resiliency of the inhibitor modified rust layer even in the inhibitor free solution. High concentration requirement would be counteracted by a long inhibitor free period, following batch application, during which the protective surface film would ensure acceptable corrosion rates.

2. Experimental

2.1. Solutions

Tests were performed on 0.51 M NaCl, obtained by dissolving analytical grade NaCl (Lachner, p.a.) in redistilled water.

Natural propolis (Naturwaren-niederrhein, GmbH, Propolis Pulver) was used at a concentration of 100 ppm in 0.51 M NaCl. 100 mg of propolis was first dissolved in 5 ml of 70% ethanol before preparing 1 dm³ of solution. Chestnut Tannin (Tanin Sevnica) and sodium benzoate (AGZ, food additive) were both used at a concentration of 2000 ppm.

PEG400 (Sigma Aldrich) and corn starch (Sigma Aldrich) were used in concentrations of 200 and 400 ppm, respectively.

The inhibitive mixture of 2000 ppm of tannin (T), 2000 ppm of benzoate (B) and 100 ppm of propolis (P), 200 ppm of PEG400 (PEG) and 400 ppm of starch (S) in 0.51 M NaCl is in further text denoted by abbreviation T+B+P+PEG+S, and the other combinations of single components are denoted accordingly.

All the measurements were done in aerated solutions under ambient conditions.

2. 2. LPR Probe

The measurements of corrosion rate were performed on the LPR (Linear Polarization Resistance) probe manufactured by RCSL with the data collector MS1500L. The corrosion rate was determined by software of the MS1500L instrument.

Corrosion monitoring LPR pins made of C1010 steel had composition declared by the producer (Metal Samples) as: C (0.02–0.08), Mn (0.3–0.6), P (0–0.04), S (0.05) and Fe (bal.).

LPR electrodes were, prior to immersion, treated mechanically by abrasive paper of grit 240, followed by degreasing with ethanol in an ultrasound bath and rinsing in redistilled water. Measurements were made by immersion of the electrodes in the solution of 0.51 M NaCl, as well as in solutions with the chosen concentrations of inhibitors. A protective layer at the electrode surface was formed for 24 h in quiescent solutions. In one experiment, the layer was deposited from the inhibited solution mixed at 80m RPM, in order to rate the influence of solution mixing on layer formation and its protective properties. In the non-inhibited solutions, the rust layer was formed, while in the inhibited solutions, the rust layer modified by the action of corrosion inhibitors was obtained. The layer formed without inhibitor is in the rest of the text referred to as the "rust layer", and the layer formed under the influence of the inhibitors in 0.5 M NaCl or the layer-forming solution, is in the rest of the text referred to as the "inhibitor-modified rust layer". The corrosion rate was measured after the probe was transferred into a fresh 0.51 M NaCl solution and left to stand for 24 h. The LPR measurement was then performed in a quiescent solution as well as in a solution stirred by magnetic stirrer at 90 to 150 RPM. Long-term measurements with the layer formed in the most effective inhibitor mixture as well as the pure rust layer were performed continuously for 10 days. In this way, the persistence

of the protective layer is tested by LPR probe, which was previously found to be particularly suitable technique for that laboratory testing of inhibitor persistence.²⁹

2. 3. Electrochemical Impedance Spectroscopy (EIS)

For EIS, the PalmSens3 device with PC Trace 5.3 software has been used. A cylindrical steel sample made of API X52 5L steel embedded in epoxy resin and having circular cross section exposed to the electrolyte, was used as a working electrode.

Typical chemical composition of commercial grade API 5L used is C (0.26 max.), MN (1.40 max.), Si (0.4 max.), P (0.03 max.), S (0.03 max), Fe (bal.).³⁰

A saturated calomel electrode was used as reference electrode and a graphite electrode was used as an auxiliary electrode. The working electrode surface was 0.2826 cm². Prior to electrochemical testing, the surface of the working electrode was mechanically treated by abrasive paper of various grits, namely: 240, 600 and 800. Subsequently, the surface was degreased in an ultrasonic bath with ethanol and washed with redistilled water.

EIS measurements were performed in quiescent solution, at the open circuit potential, at frequencies from 10 kHz to 1 mHz, with the amplitude of 10 mV. The electrodes on which a protective layer (of rust or inhibitor-modified rust) has been forming for 24 h, as in the experiment with LPR probe, were left to freely corrode for another 24 h in a fresh 0.51 M NaCl solution, in order to simulate a situation 24 h after batch inhibitor treatment. Additionally, EIS measurement has been done in the inhibited solution prior to transfer into the fresh NaCl in order to compare inhibitive effect in inhibitor bearing and inhibitor free solutions.

2. 4. Fourier Transform Infrared Spectroscopy (FTIR)

FTIR spectra were recorded using a PerkinElmer spectrometer Spectrum One. Spectra were obtained in the range from 400 to 4000 cm⁻¹, each spectrum being an average of ten scans with a resolution of 4 cm⁻¹. Coupons used as substrate were made of previously mentioned API X52 5L material and were cut to size 30 × 40 × 3 mm, polished with abrasive paper of grit 240, 600 and 800 and degreased before exposure to inhibitor mixture solution. Inhibitor-modified rust layer has been formed for 24 hours, identically as for the EIS measurements, and then the coupons were left in 0.51 M NaCl for 10 days. 350 mg of KBr was rubbed onto the surface of steel coupons after ending the experiment and drying of the coupons. Samples bearing KBr were then hydraulically pressed into a 13 mm stainless steel die and the resulting pellets further subjected to FTIR measurement. Preparation of pellets was in conformance with the standard ASTM E1252:2007.

2. 5. Scanning Electron Microscopy (SEM) and Energy-Dispersive X-ray (EDX) Analysis

SEM and EDX analysis was recorded using Tescan Vega III, SBU EasyProbe scanning electron microscope with 15 kV accelerating voltage of the electron beam at various magnifications. Measurements were done on surface of the coupons prior to FTIR experiments.

3. Results and Discussion

Cathodic reaction takes place on iron or steel through two possible processes. At lower pH values of the solution, hydrogen evolution is controlled by the rate of charge transfer reaction, and at higher pH of the solution, oxygen reduction is controlled by the rate of oxygen diffusion. Lorbeer and Lorentz,³¹ state pH of 4.2 as critical, above which the dominant cathodic process is oxygen reduction and anodic iron dissolution is inhibited by time-dependent formation of a three-dimensional porous oxide layer on the electrode surface. In the present study, the pH of uninhibited solution was 6, while the pH of inhibited solutions was between 4.6 and 4.7 so the primary conjugate cathodic reaction of metal dissolution was reduction of oxygen. This reaction is known to be under diffusion control and satisfactory degree of corrosion inhibition requires dense blocking of the surface.²³ Oxygen reduction generates OH⁻ ions which react with the dissolved Fe²⁺ ions yielding Fe(OH)₂ that is considered to be a precursor of other rust forming compounds.¹⁶ Formation of particular rust component depends on pH, temperature and oxygen content. The rust layer partially protects metal surface from dissolution.² It has been found that increasing the immersion time of iron and steel in the solution enables thickening of the corrosion product layer resulting in the decrease of the corrosion rate. The decrease of the weight loss has been observed for carbon steel during the first 10 days of immersion in 3.5% NaCl, followed by a period of 20 days in which the weight lost remained low, while in the following 30 days the weight loss became more noticeable and higher.³ This observation indicates that dissolution of rust itself also occurs under the attack of chloride ions. The experiments in the present study were focused on modification of the rust layer by the inhibitors in order to obtain a persistent protective layer that lowers the corrosion rate to acceptable values.

3. 1. Measurements at the LPR Probe

Figure 1 a) shows LPR corrosion rates on electrodes with the rust layer or with the inhibitor-modified rust layer formed under the influence of various inhibitors and inhibitors mixtures. The rates were measured after 24 h in layer-forming solutions, 24 h after transfer to quiescent

0.51 M NaCl solution and in in the same solution at the magnetic stirrer rate of 150 rpm. Except for tannin, single components show <30% inhibitive action both in the inhibitor solutions and quiescent 0.51 M NaCl with a formed layer. As expected,¹⁵ the solution of tannin as a chelating agent significantly increases corrosion rate of steel to 1.6 mmpy, but at the same time forms the most protective modified rust layer suppressing the corrosion rate in 0.51 M NaCl to 0.06 mmpy. Addition of benzoate to tannin solution decreases the corrosion rate to 0.11 mmpy but at the same time hinders the formation of protective tannin modified rust layer, increasing the corrosion rate in 0.51 M NaCl to 0.2 mmpy. Further addition of propolis and PEG decreased the corrosion rates in quiescent 0.51 M NaCl, while the addition of starch decreased the corrosion rate in quiescent and mixed 0.51 M NaCl. For the final inhibitor mixture, all corrosion rates were below 0.1 mmpy.

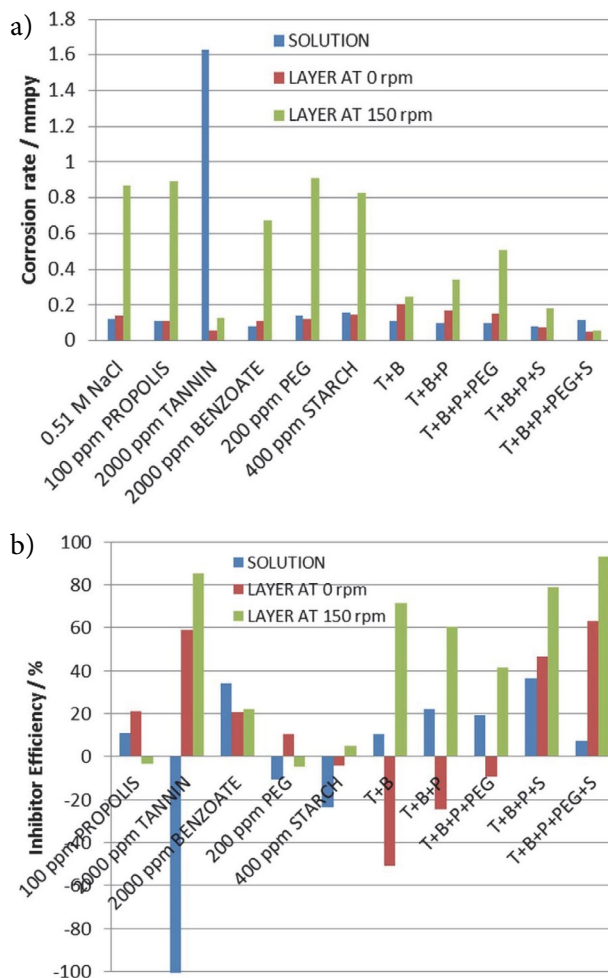


Figure 1. a) corrosion rates and b) the appending inhibitor efficiencies obtained from the LPR measurements after 24h in the layer-forming solution and after subsequent 24h in 0.51 NaCl at 0 and 150 rpm.

Measurements for each system, has been done in triplicate and the expanded measurement uncertainty

equal to $U = (0,051 \times \text{corrosion rate} + 0.005)$ mmpy has been calculated from these data.³²

The efficiency of the inhibitor containing solution, or the inhibitor-modified rust surface layer can be calculated by the equation:

$$IE / \% = \frac{CR_0 - CR}{CR_0} \quad (1)$$

where CR_0 denotes corrosion rate for the system without inhibitor or with only the rust layer and CR denotes corrosion rate for the system with the inhibitor or the inhibitor-modified rust layer.

In parallel to the corrosion rates, the inhibitor/layer efficiencies are presented in Figure 1 b). Tannin shows a highly negative efficiency of -1200% when present in the solution, while at the same time forming a protective modified rust layer that shows the efficiency of $\approx 60\%$ in quiescent and $\approx 84\%$ in mixed 0.51 M NaCl. Benzoate counteracts the facilitation of iron dissolution by tannin but decreases the efficiency of the inhibitor-modified layer below the efficiency of the pure rust layer. Addition of propolis, PEG and starch, gradually “repairs” the layer, at the same time still successfully counteracting the iron dissolution by tannin. Although interpretation is complicated by the mixed mechanism of action of various components, by comparison of single inhibitor component action with their mixed effect, it is revealed that starch acts in synergy with T+B+P mixture in the layer-forming solution as well as in quiescent and mixed 0.51 M NaCl. Starch also shows synergy with T+B+P+PEG mixture in quiescent and mixed 0.51 M NaCl.

Figure 2. shows LPR inhibitor efficiencies with the inhibitor-modified rust layer formed under the influence of T+B+P+PEG+S inhibitor mixture, measured in quiescent 0.51 M NaCl solution and in the same solution mixed

at various magnetic stirrer rotation rates. Identical measurements were repeated for 10 days in order to assess inhibitor-modified rust layer persistence.

The increase in the inhibitor efficiency is observed with the increase in magnetic stirrer rotation rate. The increase is most remarkable between the quiescent system and the system with the lowest mixing rate of 80 RPM. This observation may be explained by the increase of oxygen transport to the electrode by stirring causing higher increase in corrosion rate^{33,34} for rust covered electrodes than for the inhibitor-modified rust covered electrodes. However, the inhibitor efficiency levels off with further increase in the electrolyte mixing rate. It is reasonable to assume that as the oxygen supply through mixing completely counteracts the diffusional influence the efficiency becomes almost constant with stirring rate.

The data also show gradual loss of efficiency with time. After 10 days of immersion, with the inhibitor-modified rust layer, the efficiency at 150 rpm is $\approx 70\%$ and the corrosion rate is still below 0.2 mmpy as opposed to inhibitor free system in which the corrosion rate at 150 rpm roughly equals 0.875 mmpy. The concept of improving corrosion resistance of steel by the formation of a surface layer that efficiently blocks corrosive components from surrounding medium, is self-explanatory, and has also previously been proposed in for steel corrosion in hot tap-water.^{35,36}

The brown-orange colour of rust in the system without inhibitor indicates that its main component is lepidocrocite (γ -FeOOH).³⁷ On the inhibitor protected electrode, a dark violet layer is visible, proving formation of ferric tannate.¹⁴ Significantly smaller amount of corrosion products is observed in the solution with electrodes having inhibitor-modified rust layer indicating better protection offered by that layer compared to the protection provided by the pure rust layer.

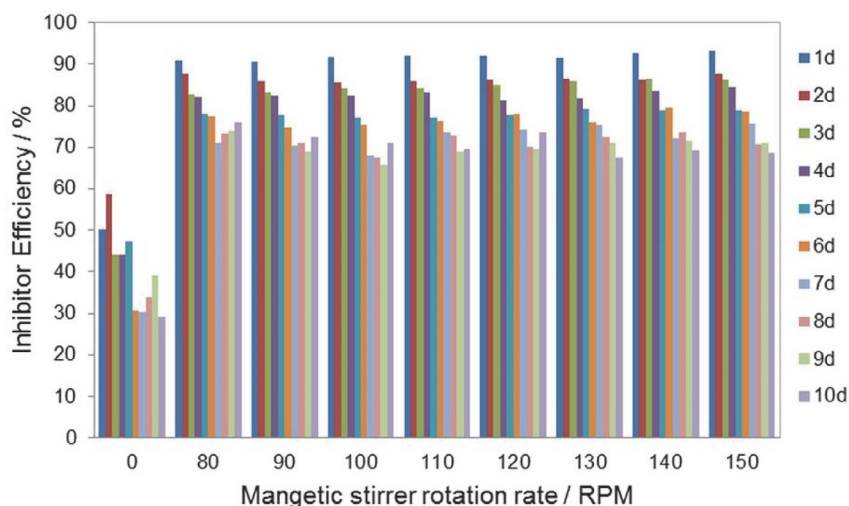


Figure 2. LPR inhibitor efficiencies with the inhibitor-modified rust layer formed under the influence of T+B+P+PEG+S inhibitor mixture, measured in quiescent 0.51 M NaCl solution and in the same solution mixed at various magnetic stirrer rotation rates

3. 2. Electrochemical Impedance Spectroscopy (EIS)

Figure 3 shows the EIS results for the electrodes with layers formed without and with T+B+P+PEG+S inhibitor

mixture. To compare protective effect of the presence of the inhibitors in solution, the measurement was also done in the layer-forming solution immediately before transfer of the electrode with the formed protective layer into fresh 0.51 M NaCl solution. Figure 4 shows the equivalent cir-

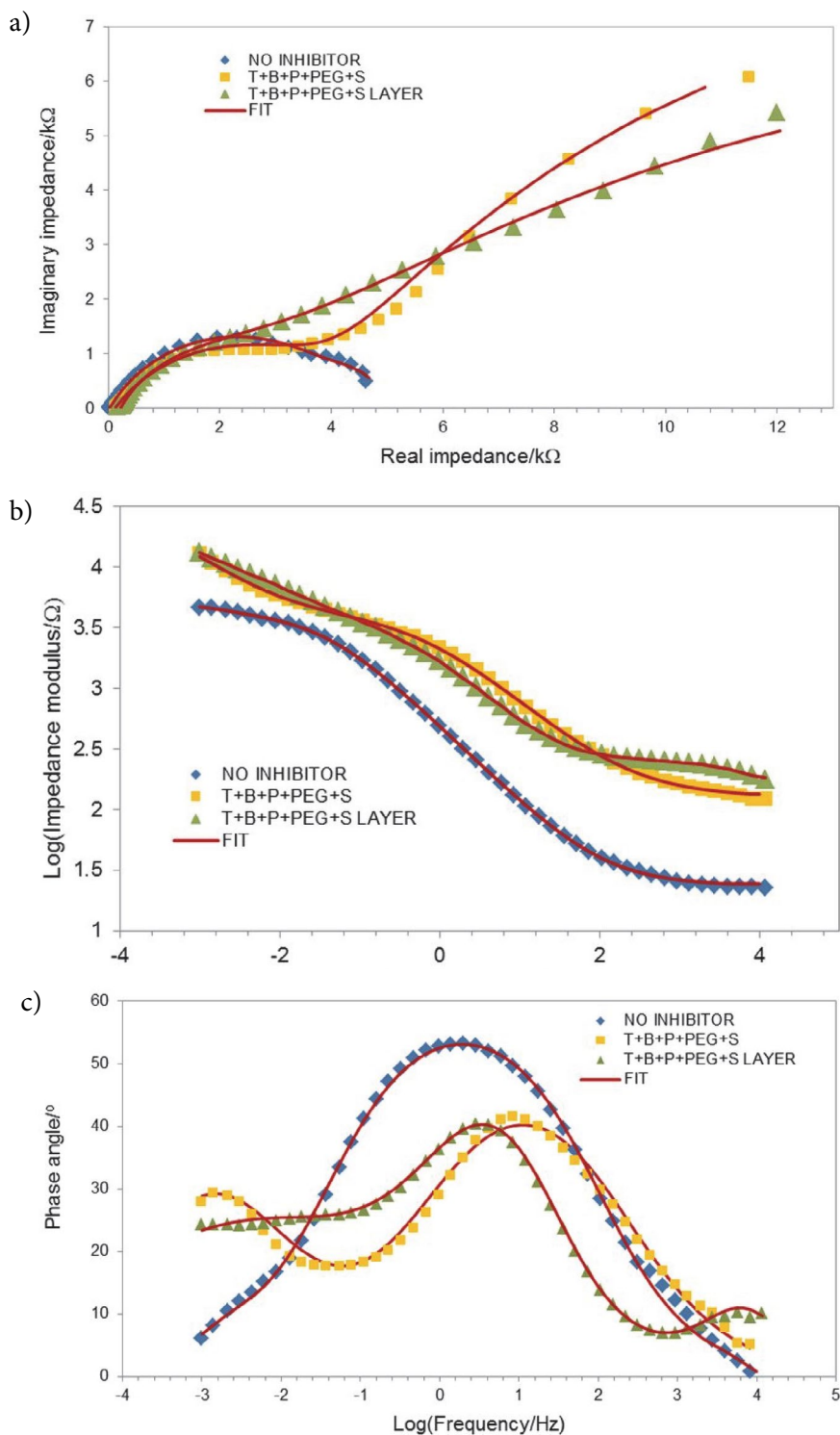
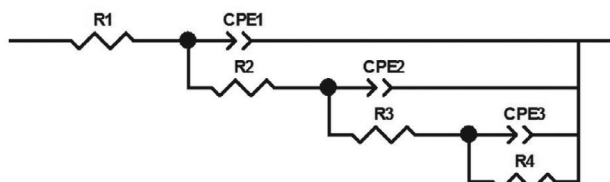


Figure 3. a) Nyquist and b) and c) Bode EIS results on steel electrode after 24 h of immersion in 0.51 M NaCl, in the layer-forming T+B+P+PEG+S solution after 24 h of immersion and after further 24 h of immersion in 0.51 M NaCl with the inhibitor-modified rust layer at the steel surface.

Table 1. Results of EIS data fitting to the equivalent circuit shown in Figure 4.

	R1	C2/ μ F	n1	R2/ Ω	C2/ μ F	n2	R3/ Ω	C3/mF	n3	R4/ Ω	IE _{AVG} /%
NO I NHIBITOR	23.5 ± 2.1	-	-	-	951.7 ± 47.5	0.66 ± 0.04	4526 ± 227	145.51 ± 6.59	1 ± 0.00	514 ± 27	-
T+B+P+PEG+S SOLUTION	126.6 ± 2.3	-	-	-	60.9 ± 3.0	0.61 ± 0.04	4197 ± 211	20.57 ± 0.80	0.632 ± 0.03	26333 ± 1358	83.5
T+B+P+PEG+S LAYER	160 ± 5.6	0.345 ± 0.07	0.89 ± 0.05	91.6 ± 7.3	79.6 ± 4.6	0.74 ± 0.05	2268 ± 135	27.69 ± 0.19	0.407 ± 0.03	39370 ± 2134	87.9

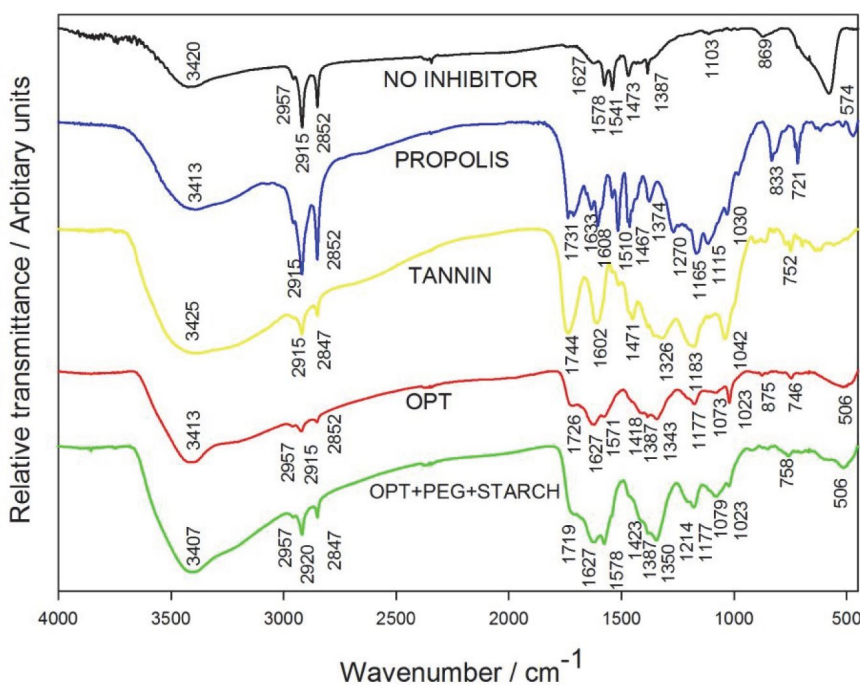
**Figure 4.** Equivalent circuit used for modelling the EIS data.

circuit used for modelling the EIS data. Table 1 shows EIS fitting results. Two parallel nested RC circuits were used to model the EIS spectrum of the electrode with the rust layer and EIS spectrum of the electrode in the inhibitor solution. Three parallel nested RC circuits were used to model the EIS spectrum of the electrode with an inhibitor-modified rust layer.

The efficiency of the rust and inhibitor-modified rust layer can be calculated by the equation:

$$IE / \% = \frac{R - R_0}{R} \quad (2)$$

where R denotes $R_2 + R_3 + R_4$ from Table 1, calculated for the system without inhibitor (R), and system with the inhibitor or the inhibitor-modified rust layer (R_0). High efficiency is obtained irrespective of the inhibitor presence or absence in the solution. High frequency resistance R_1 of the unprotected electrode is probably due to the solution resistance while the R_1 of the protected electrodes may be interpreted as a sum of the solution resistance and resistance due to the partial barrier properties introduced by the surface layers.³⁸ The R_1 resistance is disregarded in the effectiveness calculation due to its value being insignificantly small with respect to the inhibitor-modified rust layer resistance. The inhibitor-modified rust layer protected electrode shows the decrease of n_2 parameter close to

**Figure 5.** FTIR spectra of propolis and tannin and of the layers formed on X52 5L steel electrodes in pure 0.51 M NaCl, T+B+P and T+B+P+PEG+S solution.

0.5, as well as the typical shape of Nyquist plots³⁹ that indicate that the inhibitor-modified rust layer presents a barrier for oxygen diffusion, as previously concluded from LPR measurements.

3. 3. Fourier Infrared Spectroscopy (FTIR)

Figure 5 shows FTIR spectra of propolis and tannin and of the layers formed on steel electrodes in uninhibited, T+B+P and T+B+P+PEG+S solutions. Spectrum of the rust layer from the uninhibited solution indicates a mixture of FeCl₃ (spectrum ID = 8ns2iWUHtq7,⁴⁰), Fe₃O₄ (spectrum ID = 8ns2iWUHtq7,⁴¹) and Fe₂O₃ (Spectrum ID = AVGw5xAY59X,⁴²). In particular, the band at 574 cm⁻¹ corresponds to the Fe-O vibrations of magnetite,⁴³ the bands around 750 and 870 cm⁻¹ show presence of goethite and the bands at 1023 and 1177 cm⁻¹ indicate presence of lepidocrocite. Fingerprint region of FTIR spectra between 400 and 1800 cm⁻¹ of tannin, propolis and T+B+P layer, is similar between the three samples and is also similar to the reference tannin spectrum (Spectrum ID = KPLVhGIArJg,⁴⁴). Dark purple coloration of the electrode surface layer that fully develops over the period of 24 hours, confirms presence of tannin in the form of ferric tannate.¹³ In particular, the band at 1326 cm⁻¹ in tannin spectrum is characteristic of bending vibration of O–C in a phenolic hydroxyl group.⁴⁵ The interaction between ferric ions and the phenolic hydroxyl group shifts the O–C bond stretching vibration to higher wavenumbers, in the present case from 1343 and 1350 cm⁻¹ in T+B+P and T+B+P+PEG+S layers, respectively. The tannin band at 1744 cm⁻¹ that corresponds to C=O stretching of the polyphenol shifts to shorter wavenumbers,⁴⁵ i.e. 1726 cm⁻¹ in the case of T+B+P layer and to 1719 cm⁻¹ in the case of T+B+P+PEG+S layer. The peaks at 1417 cm⁻¹ and 1423 cm⁻¹, in T+B+P and T+B+P+PEG+S layers, respectively, can be ascribed to the adsorption peak of a polyphenol C=O vibration.⁴⁶

The most remarkable difference in FTIR spectra of rust and inhibitor-modified rust layers is the loss of intensity and shift of magnetite peak at 574 cm⁻¹ of the rust layer to 506 cm⁻¹ in the case of the inhibitor-modified rust layer, probably due to the conversion process to ferric tannate.⁴⁵ FTIR spectra show a dominant role of flavonoid species, present both in tannin and propolis, on the formation of the inhibitor-modified rust layer.

3. 4. Scanning Electron Microscopy (SEM) and Energy Dispersive X-ray (EDX) Analysis

Before the electron microscope scanning, the loosely held part of the layer has been blown off in the nitrogen gas stream so that only the firmly held parts of the layer remained. Figures 6 a), c) and e) show the surface of metal with the rust layer and Figures 6 b) and d) and f) with the inhibitor-modified rust layer from T+B+P+PEG+S solution.

EDX results for measurement positions #1 to #9 are shown in Table 2.

Oxygen and carbon in the rust layer, found in excess with respect to the substrate, probably originate from surface oxides and carbonates that may form in neutral solutions in contact with the air.⁴⁷ Fine grained structure observed in both cases is also probably due to surface oxides and carbonates. The inhibitor-modified rust layer is significantly denser and uniform in micrograph shown in Figure 6 b) than the rust layer shown in Figure 6 a). Corrosion defects in the form of shallow pits are visible only in the case of the rust layer. The morphology of the tannate layer is close to the one recently reported for tannic acid on Q235 carbon steel in 3.5% NaCl.¹⁵ Similarly, due to inhibitor presence, the carbon content of the layer is much higher in the inhibitor-modified rust layer at locations #2, #4, #5 and #8 (16–25 %wt) than in the rust layer at locations #1, #3 and #7 (<6 %wt). Low carbon content is also observed at the location of the crack in the inhibitor layer protruding to the metal surface at position #6, and in the area of the damaged layer where the substrate is clearly visible at position #9.

4. Conclusion

Rust layer obtained by exposing steel surface to 0.51 M NaCl solution containing a mixture of non-toxic, environmentally friendly compounds (propolis, tannin, benzoate, PEG400 and starch) has shown better protective characteristics than the rust layer formed in the inhibitor free solution. From LPR probe measurements in quiescent and mixed solution and from the values of EIS parameters in quiescent solution, it may be concluded that the inhibitor-modified rust layer primarily presents a barrier for oxygen diffusion. A synergy effect has been demonstrated for

Table 2. EDX elemental analysis results in %wt for measurement positions in Figure 6.

Element	#1	#2	#3	#4	#5	#6	#7	#8	#9
Fe	68.7	46.9	57.4	40.6	40.4	66.5	79.0	41.7	66.5
O	25.9	31.7	34.8	29.1	33.2	26.2	19.2	27.8	26.2
C	4.2	16.5	4.6	25.9	21.4	5.6	1.8	25.7	5.6
Na	1.2	3.6	3.2	3.9	3.1	1.7	–	4.8	1.7
Cl	–	1.3	–	0.5	1.8	–	–	–	–

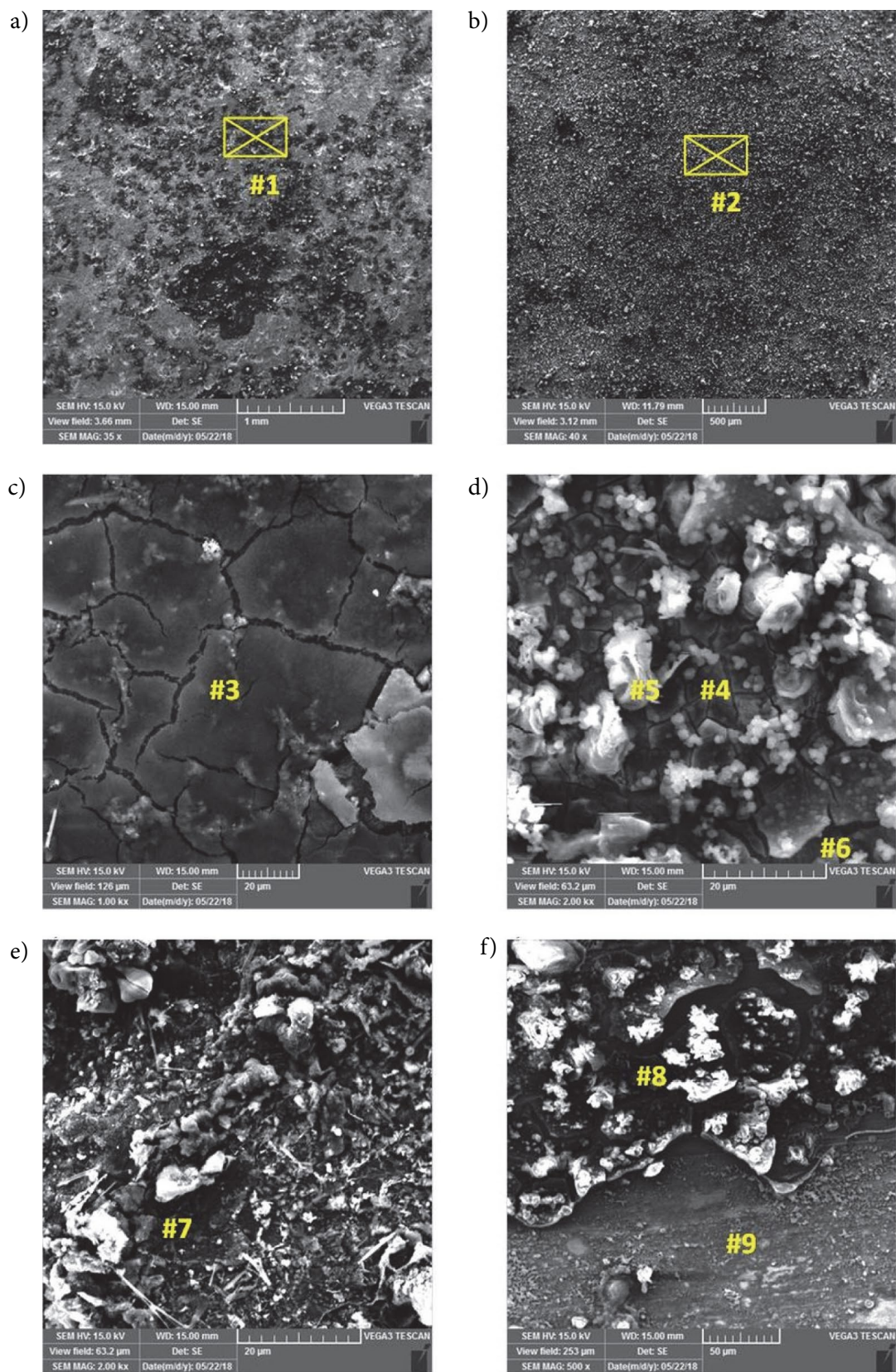


Figure 6. Surface of metal with the rust layer a) magnified 35 \times , c) magnified 1000 \times and e) magnified 2000 \times , and with the inhibitor-modified rust layer from T+B+P+PEG+S solution, b) magnified 40 \times , d) magnified 2000 \times and f) magnified 500 \times .

starch as the mixture component, from LPR data. The inhibitor-modified rust layer shows persistence in a mixed solution. The efficiency of inhibitor-modified rust layer measured by LPR after 24 h of exposure to 0.51 M NaCl is the lowest in quiescent solution 75% and the highest, equalling 95% in mixed solution. Visual observation and FTIR data confirm the formation of ferric tannate in the inhibitor-modified rust layer while the SEM/EDX data show increased carbon content of the inhibitor-modified rust layer having a fine grain structure that is more uniform and denser than the one of the rust layer.

The persistence of the inhibitor-modified rust layer is of great technological interest as it allows batch application, increases flow corrosion resistance and offers prolonged protection at acceptable corrosion rates. The suggested concept of attaining these beneficial effects through rust modification by inhibitors of various action mechanisms is not fully exploited in scientific reports and is worthy of further investigation.

5. References

1. T. Huiwen, L. Weihua, A. Liua, X. Gaoa, P. Hana, R. Dinga, C. Yanga, D. Wang, *Corros. Sci.* **2017**, *131*, 1–16.
2. M. El-S. Sherif, *Int. J. Mol. Sci.* **2014**, *19*, 9962–9974.
3. H. Hassan, A. Ismaila, S. Ahmada, C. F. Soonb, *IOP Conf. Mater. Sci. Eng.* **2017**, *215*, 012–023.
4. M. Ramezanzadeha, Z. Sanaeia, G. Bahlakehb, B. Ramezanzadeha, *J. Mol. Liq.* **2017**, *256*, 67–83.
DOI:10.1016/j.molliq.2018.02.021
5. S. Martinez, L. Valek, I. Stipanović, *J. Electrochem. Soc.* **2007**, *154*, 11; 671–677. DOI:10.1149/1.2777882
6. S. Martinez, I. Štagljar, *J. Mol. Struct.* **2003**, *640*, 1–3; 167–174.
DOI:10.1016/S0166-1280(02)00610-3
7. P. Kern, D. Landolt, *Electrochim. Acta* **2001**, *47*, 589–598.
DOI:10.1016/S0013-4686(01)00781-2
8. O. D. Alessandro, G. J. Selmi, C. Deya', A. D. Sarli, R. Romagnoli, *J. Mater. Eng. Perform.* **2018**, *27*, 687–704.
DOI:10.1007/s11665-017-3103-y
9. L. M. P. Dolabella, J. G. Oliveira, *J. Coat. Technol. Res.* **2016**, *13*, 543–555. DOI:10.1007/s11998-015-9765-1
10. L. Vrsalović, S. Gudić, D. Gracić, I. Smoljko, I. Ivanić, M. Klišković, E. E. Oguzie, *Int. J. Electrochem. Sci.* **2018**, *13*, 1; 2102–2117. DOI:10.20964/2018.02.71
11. L. Kubiliene, V. Laugaliene, A. Pavilionis, A. Maruska, D. Majiene, K. Barcauskaitė, R. Kubilius, G. Kasparaviciene, A. Savickas, *BMC Compl. Altern. Med.* **2015**, *15*, 156.
12. W. Yang, Z. Wu, ZY. Huang, X. Miao, *J. Food Sci. Technol.* **2017**, *54*, 3375–3383. DOI:10.1007/s13197-017-2754-x
13. H. M. Boudelloua, Y. Hamlaoui, L. Tifouti, F. Pedraza, *J. Mater. Eng. Perform.* **2017**, *26*, 4402.
DOI:10.1007/s11665-017-2867-4
14. S. Martinez, I. Štern, *Chem. Biochem. Eng. Q.* **1999**, *13*, 191–199.
15. W. Xua, E. H. Hana, Z. Wang, *J. Mater. Sci. Technol.* **2019**, *35*, 64–75. DOI:10.1016/j.jmst.2018.09.001
16. The 2015 UKM FST Postgraduate Colloquium, Faculty of Science and Technology, **2015**, Postgraduate Colloquium, Conference Paper, Malaysia.
17. F. Wormwell, A. D. Mercer, *J. Chem. Technol. Biotechnol.* **1952**, *2*, 150–160.
18. A. Shaban, I. Felhosi, J. Telegdi, *Int. J. Corros. Scale Inhib.* **2017**, *6*, 262–275.
19. J. Jin, M. L. Shenzhen, Y. Guan, *Desalin. Water Treat. J.* **2016**, *57*, 23556–23570. DOI:10.1080/19443994.2015.1137789
20. A.P.I. Popoola, O. Sanni, C.A. Lotoa, O.M. Popoolac, *Port. Electrochim. Acta* **2015**, *33*, 353–370.
DOI:10.4152/pea.201506353
21. E. Asghari, H. A. Sorkhabi, M. Ahangari, R. Bagheri, *J. Mater. Eng. Perform.* **2016**, *25*, 1416–1425.
DOI:10.1007/s11665-015-1865-7
22. R. T. Loto, C. A. Loto, *Orient. J. Chem.* **2018**, *34*(4).
23. V. M. Ledov'skykh, Y. P. Vyshnev'ska, I. V. Brazhnyk, S. V. Levchenko, *Mater. Sci.* **2017**, *52*, 634–642.
24. E. Mascheroni, A. Figoli, A. Musatti S. Limbo, E. Drioli, R. Suevo, S. Talarico, M. Rollini, *Int. J. Food. Sci. Tech.* **2014**, *49*, 1401–1407. DOI:10.1111/ijfs.12442
25. M. Ali, A. Ali, A Thesis Submitted to the University of Manchester, 2016.
26. D. Amoako, J. M. Awika, *Curr. Opin. Food. Sci.* **2016**, *8*, 14–18.
27. H. Liang, Y. Pei, J. Li, W. Xiong, Y. He, S. Liu, Y. Liac, B. Li, *Rsc. Adv.* **2016**, *6*, 31374–31385. DOI:10.1039/C6RA02527G
28. R. Marino, S. Giovando, D. Gabriele, *Appl. Rheol.* **2014**, *24*, 1–10.
29. C. W. Hahn, P. R. Petersen, *Nace Corros. Paper* **2001**, 01526.
30. M. J. H. Gayosso, G. Z. Olivares, S. B. Frago, G. E. B. D. Valle, D. M. G. Oidor, V. Á. R. Gómez, *Mater. Sci. Appl.* **2016**, *7*, 623–643.
31. P. Lorbeer, W. J. Lorenz, *Electrochim. Acta* **1980**, *25*, 375–381.
DOI:10.1016/0013-4686(80)87026-5
32. B. Magnusson, T. Näykki, H. Hovind, M. E. Krysell, Nordtest, Handbook for calculation of measurement uncertainty in environmental laboratories, 2nd edition, Nordtest, 2004.
33. J. M. Q. Slaimana, B. O. Hasan, *Can. J. Chem. Eng.* **2010**, *88*, 114–1120. DOI:10.1002/cjce.20383
34. P. V. Seheers, *J. S. Afr. Inst. Min. Metall.* **1992**, *92*, 275–281.
35. G. S. Vasyliov, *Corros. Sci.* **2015**, *98*, 33–39.
DOI:10.1016/j.corsci.2015.05.007
36. S. E. Kaskah, M. Pfeiffer, H. Klock, H. Bergen, G. Ehrenhaft, P. Ferreira, J. Gollnick, C. B. Fischer, *Surf. and Interfac.* **2017**, *9*, 70–78. DOI:10.1016/j.surf.2017.08.002
37. J. Argo, *Stud. Conserv.* **1981**, *26*, 140–142.
38. A. A. Razin, B. Ramezanzadeh, H. Yari, *Prog. Org. Coat.* **2016**, *92*, 95–109. DOI:10.1016/j.porgcoat.2015.11.023
39. S. Y. Cai, L. Wen, Y. Jin, *Int. J. Min. Met. Mater.* **2017**, *24*, 1112–1124. DOI:10.1007/s12613-017-1502-6
40. Bio-Rad Laboratories, Inc. SpectraBase; SpectraBase Compound ID=BvsSOr0JLoz SpectraBase Spectrum ID=ESQ-8z2iupzm. (accessed Aug 18, 2018).
41. Bio-Rad Laboratories, Inc. SpectraBase Compound ID=6sX-m4f3qGO3, SpectraBase Spectrum ID=8ns2iWUHtq7. (accessed Aug 18, 2018).

42. Bio-Rad Laboratories, Inc. SpectraBase Compound ID=Sah-b89o6Tw, Spectrum ID=AVGw5xAY59X. (accessed Aug 18, 2018).
43. S. F. Merino, J. J. Caprari, L. V. Torres, L. F. Ramos, A. H. Girola, *Anti-Corros. Method M.* **2017**, *64*, 136-147.
44. Bio-Rad Laboratories, Inc. SpectraBase Compound ID=B-T7y97K1oFp, SpectraBase Spectrum ID=KPLVhGlarJg. (accessed Aug 18, 2018).
45. R. Zhang, L. Li, J. Liu, *Rsc. Adv.* **2015**, *5*, 40785–40791.
DOI:10.1039/C5RA02035B
46. F. M. A. Santos, J. A. L. Macedo, H. M. Chaves, M. Espinoza-Castañeda, A. Merkoçi, F. D. C. A. Lima, W. Cantanhêde, *J. Braz. Chem. Soc.* **2016**, *27* (4) 727–734.
DOI:10.1590/S0103-50532005000500008
47. H. Möller, E.T. Boshoff, H. Fronema, *J. South Afr. Inst. Min. Metall.* **2006**, *106*, 585–592.

Povzetek

Vseprisotna uporaba navadnih in nizko legiranih jekel v nevtralnih okoljih s kloridnimi anioni predstavlja vsakodnevni izziv strokovnjakom za zaščito pred korozijo. V prispevku preučujemo možnosti razvoja netoksične in okolju prijazne sinergijske mešanice inhibitorjev iz propolisa, tanina, natrijevega benzoata, PEG400 in škroba, ki jih lahko uporabimo v raztopini, z namenom nanosa trajnega zaščitnega sloja na jeklu. Sestavine zmesi so bile izbrane na podlagi njihovih lastnosti, ki so pomembne za njihovo možno delovanje v raztopini in/ali na površini jekla. Učinkovitost zaščitne plasti, ki je nastala pod vplivom zmesi inhibitorja in nato izmerjena z meritvami linearne polarizacijske upornosti (LPR) v raztopini brez inhibitorja, je bila najnižja v primeru konstantnih pogojev (75 %) in najvišja (95 %) pri pretočnih pogojih. Podatki LPR in elektrokemijske impedančne spektroskopije (EIS) kažejo, da modificirana plast inhibitorja predstavlja bariero za difuzijo kisika, ki deluje kot depolarizator primarne korozijske reakcije v preučevani nevtralni raztopini klorida. Dokazana obstojnost inhibitorjsko modificiranega sloja ima velik pomen, saj omogoča uporabo tudi v industrijskem merilu.

Scientific paper

Adsorptive Removal of Fluoride from Aqueous Solution by Biogenic Iron Permeated Activated Carbon Derived from Sweet Lime Waste

Mohd. Ibrahim,¹ Adil Siddique,¹ Lata Verma,¹ Jiwansingh^{1,*}
and Janardhan Reddy Koduru^{2,*}

¹ Department of Environmental Science, Babasaheb Bhimrao Ambedkar University, Lucknow-226025, India

² Department of Environmental Engineering, Kwangwoon University, Seoul 139-701, Republic of Korea

* Corresponding author: E-mail: jiwansingh95@gmail.com
reddyjchem@gmail.com

Received: 09-14-2018

Abstract

In this study, biogenic activated carbon were successfully synthesized from *Citrus limetta* pulp residue, and applied to remove fluoride from an aqueous solution. For the synthesis activated carbon of biosorbents, raw materials were heated in muffle furnace at two different temperatures i.e. (250 °C and 500 °C) and were noted as ACP-250 and ACP-500. The prepared biosorbents were characterized through scanning electron microscopy (SEM), Fourier transform infrared (FTIR), and X-ray diffraction (XRD). Batch adsorption studies were performed with varying temperature, dosage, pH, and various initial concentrations. Adsorption isotherms and the reaction kinetics were also analyzed in order to understand the adsorption mechanism. The results of this study shows that the maximum removal achieved was approximately (86 and 82) % of ACP-500 and ACP-250, respectively. The isotherm results show that the Langmuir isotherm model fitted better, with monolayer adsorption capacity of 12.6 mg/g of fluoride. However, for kinetic study, the pseudo-second-order kinetics fitted well. The synthesized materials at different temperature were highly effective for the removal of fluoride from water, with reusability of three to four times.

Keywords: Sweet lime waste; adsorption; fluoride; isotherm; thermodynamic; cost analysis.

1. Introduction

The presence of fluoride in drinking water offerings a severe complication worldwide¹. In India, more than 95% of rural and (30–40) % of the urban population are dependent on groundwater.² The higher amount of fluoride in groundwater is dangerous for drinking purposes. Normally, fluoride is released in groundwater through the slow leaching of fluorine-containing rock,³ and of several minerals viz., topaz, biotite, fluorite, and their corresponding host rock, such as basalt, syenite, granite, etc.⁴ Moreover, while the natural geological source contributes fluoride to groundwater, several industries also contribute to fluoride contamination.⁵ According to Shen et al.⁶ some industries generate fluoride in the environment, and discharge higher fluoride concentration than natural geological dissolution, ranging (10–1,000) mg/L.⁷ More than 200 million people worldwide are affected by higher fluoride concentration

that exceeds the WHO guideline of 1.5 mg/L.⁸ Contamination of fluoride occurs in different parts of India, including Andhra Pradesh, Assam, Gujarat, Haryana, Rajasthan, and Uttar Pradesh.⁹ The amount of fluoride in groundwater in some parts of India is above 30 mg/L.¹⁰ The impact of fluoride in drinking water depends on the concentration and duration of continuous uptake, and can be useful or harmful to humankind. Even a small concentration of fluoride in water has a significant effect on dental caries, mainly among children.¹¹ An excessive amount of fluoride causes various diseases, such as osteoporosis, arthritis, brittle bones, cancer, infertility, brain damage, Alzheimer syndrome, and thyroid disorder.¹² Among these diseases, fluorosis is one of the most common diseases in human who are consuming fluoride regularly, also causing mottling of the teeth, and embrittlement of the bones of human.¹³ Hence, there is necessity to treat of water contaminated with fluoride before drink or release to environment.

Many technologies, such as chemical precipitation, coagulation, ion exchange, electrocoagulation, nanofiltration, catalytic ozonation, and electrochemical oxidation^{14–18} and Donnan dialysis¹⁹ have been used for the fluoridation of water. However those methods have limitations in terms of high operational and maintenance cost, and generation of waste. The adsorptive removal of fluoride has been considered one of the most facile, cost-effective, and eco-friendly techniques among the various defluoridation technologies.^{14–20} Several adsorbents, including various conventional and non-convention sorbents/biosorbents, such as red mud, bone char, rare earth oxides, zeolite, citrus lemon leaves, rice husk ash, peepal leaf, musambi peel, banana peel, and laterite soils, have been reported for the defluoridation of water.²¹ However, most biosorbents have low fluoride removal abilities to treat fluoride-contaminated groundwater. Therefore, the development of better bioadsorbents with superior adsorption capacities for fluoride is still needed. Given the higher cost of production, presented agriculture solid waste is being intensively studied for the production of low-cost activated carbons. Waste materials that are converted into activated carbon improve economic value, reduce the cost of waste disposal, and potentially offer a cheap alternative to the current viable sample.²²

However, functionalizing iron-oxide nanoparticles with parent biosorbent, improving adsorption capacity, selectivity and stability levels of tested materials.²³ So, these functionalized activated carbons with iron oxide are great interest for removing pollutants from water. Moreover, the modification of biogenic activated carbon with iron oxide that can enhances its adsorption ability and selectivity of parent material.²⁴

In the present study, *Citrus limetta* pulp was used for the synthesis of biogenic activated carbon permeated with iron. It is valuable waste material that is thrown away from the juice industry, and engenders land space occupation and pollution with phenolic compounds, due to the dumping of wastes. Natural biomaterial waste *citrus limetta* pulp was used as a template, and $\text{FeCl}_3 \cdot 6\text{H}_2\text{O}$ was used for the iron precursor source to develop magnetic properties in both the adsorbents for the removal of fluoride from an aqueous solution. Two adsorbents were prepared at two different temperatures of (250 and 500) °C for the potential application for fluoride removal.

2. Materials and Methods

2.1. Chemicals

For the purpose of the research work, analytical grade chemicals were used. These chemicals were anhydrous sodium fluoride (NaF), iron chloride hexahydrate ($\text{FeCl}_3 \cdot 6\text{H}_2\text{O}$), sodium hydroxide (NaOH), hydrochloric acid (HCl), and Ionic Strength Adjustment (ISA) Solution, purchased from Fisher Scientific (a part of Thermos Fisher Scientific).

2.2. Preparation of Pulp powder

Citrus limetta (sweet lime) pulp waste was collected from a local juice seller nearby the area of BBAU, Lucknow, India. Plenty of water was required for the washing of raw material so firstly the tap water was used for washing of collected pulp material to eliminate the dust particles and other adherence from the surface of collected material, af-

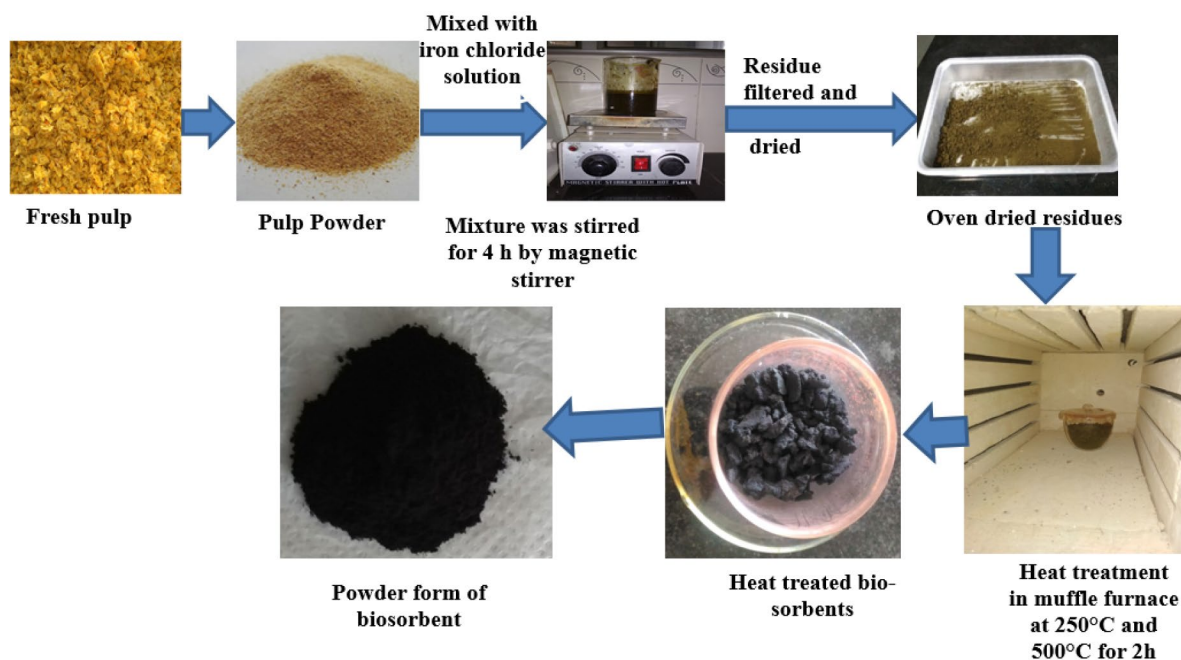


Figure 1. A flowchart for the synthesis of biogenic iron permeated activated carbon (ACP-250 and ACP-500).

ter that the material was washed with distilled water at least three times. The study area is not affected by fluoride. Pulp waste was chopped in small pieces, and then air-dried. The dried pulp was crushed and ground with the help of grinder, and finally, powder forms were obtained by sieving with 250 μm sieve. The sieved powder was used for the preparation of activated carbon (bio-sorbents).

2. 3. Synthesis of Biogenic Iron Permeated Activated Carbon

Bioadsorbents were prepared according to the method given by Lunge.²⁵ The details of synthesis are that 15 g of Iron chloride hexahydrate ($\text{FeCl}_3 \cdot 6\text{H}_2\text{O}$) was dissolved in 150 mL of distilled water, and 30 g of fine pulp powder was added and stirred for 4 h, and kept overnight, then, the solid materials were separated by vacuum pump filtration, followed by oven drying at 105 $^\circ\text{C}$ for 4 h. The iron-treated material was heated in a muffle furnace (Model No.11C 106B; ICOAN Instruments Company, India) at two different temperatures *i.e.* (250 and 500) $^\circ\text{C}$ for 2 h.

Iron chloride hexahydrate was used for the preparation of ACP to develop magnetic properties and acidic nature to the ACP. Moreover, the addition of FeCl_3 can be improve positive surface which is favorable for adsorption negative charge fluoride. The heated material was washed with double distilled water, and then dried. A black color final product was obtained named as activated carbon of pulp, denoted as ACP-250 and ACP-500. These materials were ground and made uniform using mortar and pestle, and applied for the fluoride removal. Fig. 1 shows the different steps in the synthesis of bioadsorbents.

2. 4. Preparation of Standard Solution of Fluoride and its Determination

For the purpose of batch experiment, different concentrations of fluoride solution were prepared by diluting the stock solution of 1,000 mg/L concentration of F^- (a stock solution prepared by NaF salt). The concentration of fluoride and pH of the solution was determined by digital Ion-pH meter (EUTECH Handheld Meter Kit; Thermo Scientific).

2. 5. Spectroscopy and Microscopy Identification of Adsorbents

The XRD configuration of the biosorbent was attained by X-ray Diffractometer (PW 30 40/60, PANalytical, Netherlands), which was used to analyze the phase and structure of both biosorbents. Surface morphology, structure, and elemental composition of the biosorbents were obtained with SEM equipped with EDX (JSM 6490-LV, JEOL, Japan). Various functional groups analysis of the adsorbents were analyzed by using FTIR Spectrophotometry (NICOLETMM 6700, Thermo Scientific, USA) with

KBr at a ratio of 1:200, and the mixture was pressed, as reference material and spectra were detailed in the region of (400 to 4,000) cm^{-1} . The synthesized bioadsorbents were analyzed for surface charge *i.e.* zero point charge (pHzpc), by the method reported by Sharma.¹⁰

2. 6. Procedure for Adsorptive Removal of Fluoride

A 50 mL of fluoride solution (10 mg/L) was mixed with 1 g/L dose of **biogenic activated carbon** material, and kept in horizontal water bath shaker (LI-WBIS-20; Labard Instruchem. Pvt. Ltd) at 25 $^\circ\text{C}$ for 5 h for shaking at 100 rpm. Samples were collected at different time intervals. The optimum conditions for maximum removal of fluoride using bioadsorbents have been estimated by observing the effect of contact time of (30–300) min, initial pH of (4–10), adsorbent dose of (0.5–3.0) g/L, temperature of (25–55 $^\circ\text{C}$), and initial fluoride concentrations of (5–30) mg/L at 100 rpm; then the flasks were taken at different time intervals from the water bath shaker, followed by filtration through Whatman 42 filter paper. The filtrate was used for the determination of the remaining fluoride ions using ion selective electrode contain digital Ion-pH meter. The batch study was carried out in duplicate, and average values were calculated, and taken as the final value.

The fluoride removal efficiency using biosorbents (ACP-250 and ACP-500) during adsorption was calculated as follows:

$$\text{Removal efficiency (\%)} = ((C_0 - C_1) / C_0) \times 100 \quad (1)$$

The amount of adsorbed F^- per unit mass of adsorbent was obtained using the formula:

$$q_e = (C_0 - C_e)V/W \quad (2)$$

Where, q_e is the adsorption capacity of F^- (mg/g); C_0 is the initial F^- concentration (mg/L); C_e is the F^- concentration at equilibrium (mg/L); W is the adsorbent mass (g), and V is the volume of F^- solution (L).

3. Results and Discussion

3. 1. Characterization of Biosorbent

3. 1. 1. Zero Point Charge (pH_{zpc})

The pH_{zpc} of an adsorbing material is a significant parameter that regulates the pH at which the adsorbent surface has net electrical charge neutral. In the case pH of solution < pH_{zpc}, the adsorbent surface charge is positive to attract negative ions; however, when pH of solution > pH_{zpc}, then the surface charge of adsorbent is negative to attract positive ions.²⁶ The pH_{zpc} of the prepared materials, ACP-250 and ACP-500 have been found to be 2.66

and 3.06, respectively. From the results, both biosorbents may have more acidic functional groups such as carboxylic, phenolic groups etc., on their surfaces. It is fact that the biosorbents show different pH_{Zpc} values may be due to the presence or absences of acidic groups. These groups decrease with increasing carbonization temperature. However, during the burning of adsorbent, acidic metal oxides formed on the adsorbent surface. The pH_{Zpc} value of an aqueous solution plays an important role in the surface charge of the biosorbent.

3. 1. 2. SEM Analysis

Fig. 2 (a)–(d) show the SEM images of ACP-250 and ACP-500, and reveal a rough surface with porous and crystalline structure for both biosorbents, which may be favorable for fluoride adsorption. The morphology of the two biosorbents was different, because of the thermal treatment at different temperatures. Furthermore, the adsorption of fluoride ion onto ACP-250 and ACP-500 was established by EDX analysis. Fig. 2 (e) and (f) show the EDX spectra of ACP-250 and ACP-500, which indicate

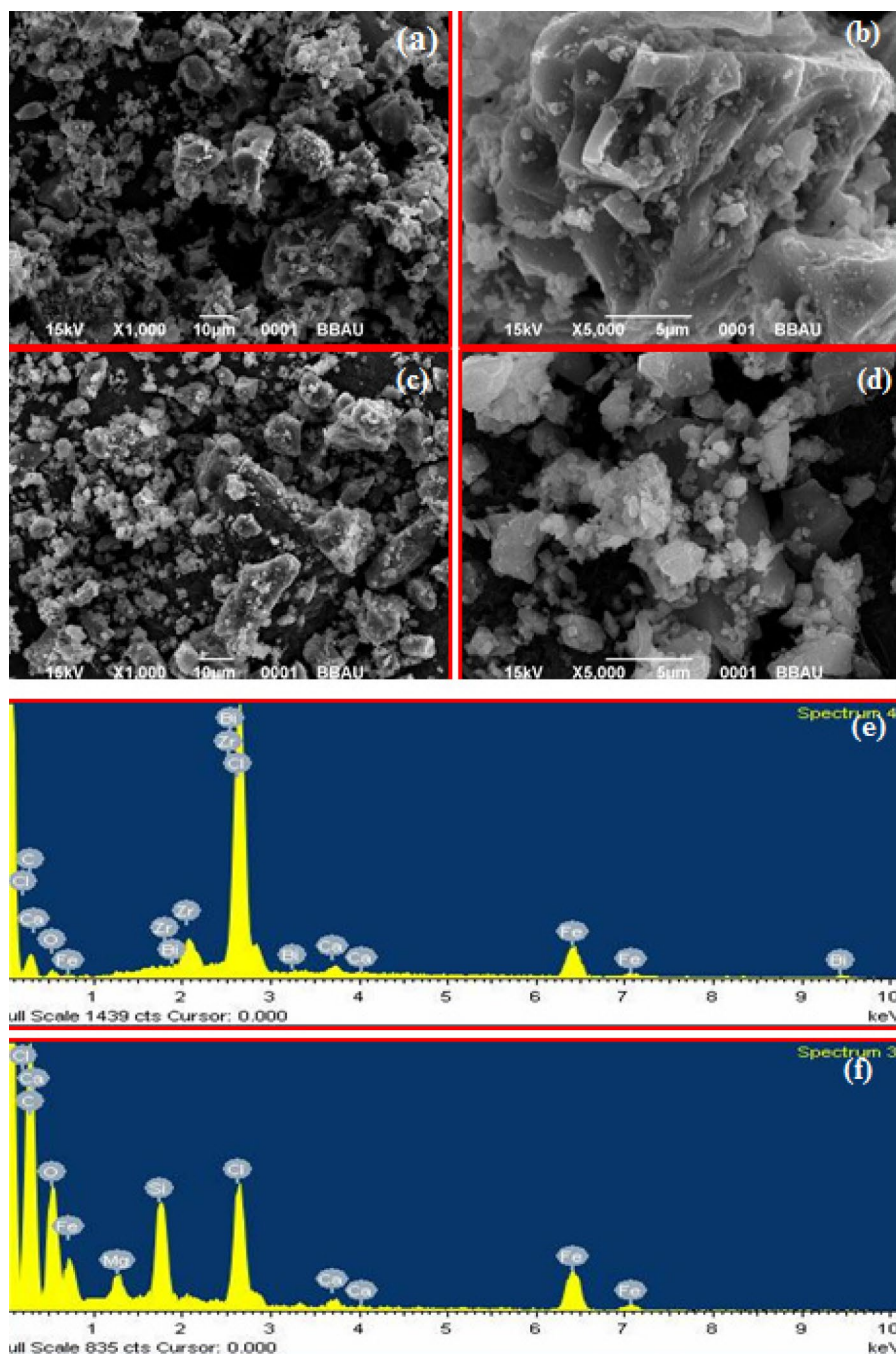


Figure 2. SEM images of (a) and (b) ACP-250, (c) and (d) ACP-500; and EDX spectra of (e) ACP-250, and (f) ACP-500.

Consequently, the removal of fluoride from water by applying ACP-500 was found to be higher than that by ACP-250. The XRD pattern of ACP-500 reveals peaks at $2\theta = (24.55, 33.52, 36.04, 41.23, \text{ and } 62.77^\circ)$ that were assignable by their indices (220), (311), (400), (422), and (440), respectively.^{32–33} All these peaks are in accord with the database in JCPDS file (82-1533), and represent the iron oxides (for example Fe_3O_4). The diffraction peaks at (49.88 and 54.29) corresponding to the (131) and (230) planes, respectively, represent Fe_3C . Carbides of iron may be classified into two categories on the basis of the location of carbon atoms present either in trigonal-prismatic interstices (Fe_3C and Fe_5C_2), or octahedral interstices (e.g., Fe_2C , $\text{Fe}_{2.2}\text{C}$). The formation of the carbides may increase the mechanical strength of the synthesized nano/micro size material.³⁴

3. 2. Fluoride Adsorption Study

3. 2. 1. Effect of Contact Time

Figures S1 (a)–(d) show the removal percentage of ACP-250 and ACP-500 toward fluoride ion with time. It was observed that in the first 30 minute of contact time, about (35 and 58.5)% fluoride adsorption was observed by ACP-250 and ACP-500, respectively; and afterward, the adsorption rate slowed down with contact time. During the early stage of the adsorption experiment, many vacant sites are available on the surface of the adsorbent for the removal of fluoride. After a certain period of time, fluoride ion is difficult to attach to the surface of the adsorbent, because of the repulsive force between the adsorbed fluoride ion on the surface, and fluoride ion in the aqueous solution. The removal of fluoride increased along with time, and then progressively reached equilibrium at 180 min. Therefore, 180 min is considered the minimum contact time to maximum removal of fluoride from the water. A similar result was also reported by Dwivedi³⁵ and Singh and Majumder.³⁶

3. 2. 2. Effect of the Amount of Biosorbents

The removal of fluoride ions by ACP-250 and ACP-500 was performed at different adsorbent doses i.e. (0.5, 1.0, 2.0, and 3.0) g/L, while keeping all other parameters constant, such as pH (6.6±0.5), initial fluoride concentration 10 mg/L, temperature 25 °C, with different time intervals i.e. 30, 60, 120, 180, 240, and 300 min. Figures S1 (c) and (d) indicates the removal percentage of fluoride of both of the adsorbents. The adsorption of fluoride by adsorbent was observed to be increases from 32.5 to 47% for 0.5 g/L, and the maximum removal was observed 70% in case of 1.0 g/L. While in the case of 2.0 and 3.0 g/L, the adsorption removal gradually decrease from 41 to 29.5% and 49.2 to 39%, respectively for both the bioadsorbents. The highest removal percentage was shown for both bioadsorbents at 1.0 g/L dosage. The increase of the percentage of fluoride removal with increasing biosorbent dose might be due to the avail-

ability of more active site on the adsorbents surface for the binding of fluoride ions with the increased surface area,³⁷ While further increase of the biosorbent dose, the removal percentage was not increased, because of the partial aggregation of biomass, which resulted in decrease in the active surface area of both biosorbents for the adsorption.³⁸

3. 2. 3. The Effect of pH Values

The pH of a solution is a critical aspect that affects the adsorption process, due to its close relationship with the surface charge of the biosorbents, and the ionization potential of fluoride ion; therefore fluoride adsorption on adsorbent was performed at different pH values ranging (4–10), while keeping all other parameters constant. The required pH was adjusted by adding 0.1 N NaOH or 0.1 N HCl. Fig. S1 (b) shows the effect of pH on the removal of fluoride. The result shows that the adsorption of fluoride on ACP-250 and ACP-500 observed a maximum of 76.5 and 74% respectively, at pH 4. It was perceived that the removal of fluoride is extremely sensitive to the change in pH of the solution. It was also observed that fluoride adsorption decreased approximately (44 and 26.4) % for ACP-250 and ACP-500, respectively, with increasing pH of the solution from (4 to 10). Fluoride adsorption decreases may be due to the following facts: (i) the negative charge increased on the surface of adsorbent as increased pH (> pH_{zpc} is around 3.0 for both adsorbents) of solution, which reduces adsorption of the fluoride ions due to electrostatic repulsion; and (ii) enhancement of OH^- ions reduces the adsorption of fluoride ions, as it increases the competition for adsorption sites.³⁹

3. 2. 4. Effect of Various Fluoride Concentrations on the Adsorption Process

The effects of various fluoride concentrations on its removal were studied at different concentrations in the range (1–30) mg/L with keeping all the other parameters constant, such as pH (6.6±1), temperature (25±1) °C, with different time intervals i.e. 30, 60, 120, 180, 240, and 300 min, and shaking speed 100 rpm. Fig. 4 (a) and (b) show the removal percentage of fluoride. The results show that when an initial concentration of fluoride increased from (1 to 30) mg/L, the removal percentage decreased from (80 to 24) % for ACP-250, and (86 to 38.33) % for ACP-500. This might have happened because of the fixed number of active sites of the adsorbent, which might be saturated at a certain concentration.

3. 2. 5. Effect of Temperature

Temperature is an essential parameter for the adsorption mechanism. Temperature determines the type of relations between the biosorbent and fluoride ions. If the removal percentage decreases with enhancing the tempera-

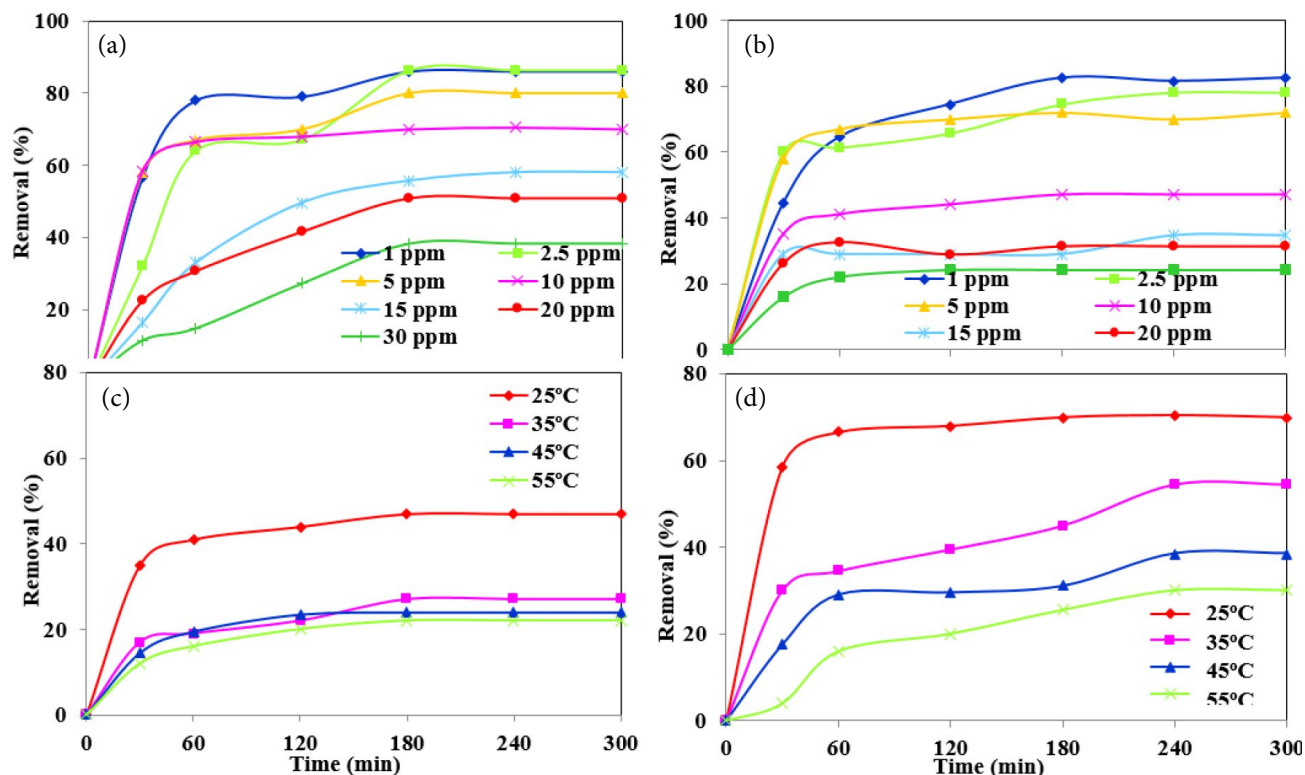


Figure 4. Effect of various parameters (a) and (b) initial fluoride concentration, (c) and (d) temperature of ACP-250 and ACP-500 for the removal of fluoride.

ture, this may represent physical adsorption or exothermic process². In the present study, the impact of temperature on fluoride adsorption by ACP-250 and ACP-500 was studied at four different temperatures of (25, 35, 45, and 55) °C, while keeping all the other parameters constant. Fig. 4 (c) and (d) show the removal percentage of fluoride. The removal percentage of fluoride was observed to decrease with increase of the temperature of the solution. This represents that the fluoride removal from aqueous solution by both biosorbents is an exothermic process.⁴⁰ Further it is proved by thermodynamic studies at section 3.5.

3. 3. Adsorption Isotherm Studies

An adsorption isotherm defines the interaction between pollutant and adsorbent with adsorption properties and equilibrium information at equilibrium, a point where no further adsorption take place. To understand the nature of the interaction between the adsorbent and amount of adsorbate at a constant temperature, the adsorption isotherm is applied.²¹ In the present work, to understand the adsorption behavior, the Langmuir and Freundlich isotherm model were applied.^{41–42}

3. 3. 1. Langmuir Isotherm Model

The Langmuir adsorption isotherm model describes a monolayer with homogeneous adsorption, in which all

sites of the adsorbent hold an equal affinity for the pollutant.⁴³ This model also describes an equilibrium saturation point, where no further adsorption can take place.^{44–45} The monolayer adsorption model is given as Eq. (3).

$$\frac{C_e}{q_e} = \frac{1}{Q_0} + \frac{1}{bQ_0C_e} \quad (3)$$

where, q_e is the amount of F^- adsorbed per unit mass of adsorbent ($mg\ g^{-1}$); Q_0 and b are the Langmuir constant concerning the adsorption capacity (mg/g) and the binding energy constant (L/ mg), respectively. The values of Q_0 and b can be obtained using linear plot between C_e/q_e and $1/C_e$ at different fluoride concentrations (Figs. 5a and b). The Langmuir isotherm is stated as a dimensionless constant (R_L), and also denoted as a separation factor that can be calculated by applying the following equation.

$$R_L = \frac{1}{1 + bC_0} \quad (4)$$

Where, C_0 is the initial fluoride concentration ($mg\ L^{-1}$), and the value of R_L indicates the adsorption process i.e. if the value of R_L lies between 0 and 1, then the adsorption process is favorable, $R_L=1$ signifies linear adsorption; if $R_L=0$, the adsorption process is irreversible; and $R_L > 1$ represents uncomplimentary adsorption, while favorable ($0 < R_L < 1$). Table 1 shows the R_L values ($0 < R_L < 1$) for both materials.

3. 3. 2. Freundlich Isotherm Model

The Freundlich adsorption isotherm describes the reversible, as well as non-ideal, adsorption. This model has been used only for multilayer adsorption with different binding energy spectra. The linear form of the Freundlich isotherm equation is given below:

$$\log q_e = \log K_F + \frac{1}{n} \log C_e \quad (5)$$

Where, K_f and n are the Freundlich isotherm constants that represent the adsorption capacity and adsorption intensity of the fluoride ions on the biosorbents. These values can be obtained from the linear plot of $\ln q_e$ vs. $\ln C_e$. The values of the Freundlich constants

3. 4. 1. Kinetics Studies

Adsorption kinetics studies describe the adsorption rate and mechanism of fluoride adsorption on biosorbents. Two different types of kinetics model viz, the Lagergren first-order kinetics model and the pseudo second kinetics model were applied to understand the kinetics of fluoride adsorption. The Lagergren pseudo- first-order by Ho and McKay⁴⁶ and pseudo second kinetics model⁴⁷ are expressed as Eqs. (6) and (7), respectively.

$$\log (q_e - q_t) = \log q_e - \frac{k_1 t}{2.303} \quad (6)$$

$$\frac{t}{q_t} = \frac{1}{k_2 q_e^2} + \frac{t}{q_e} \quad (7)$$

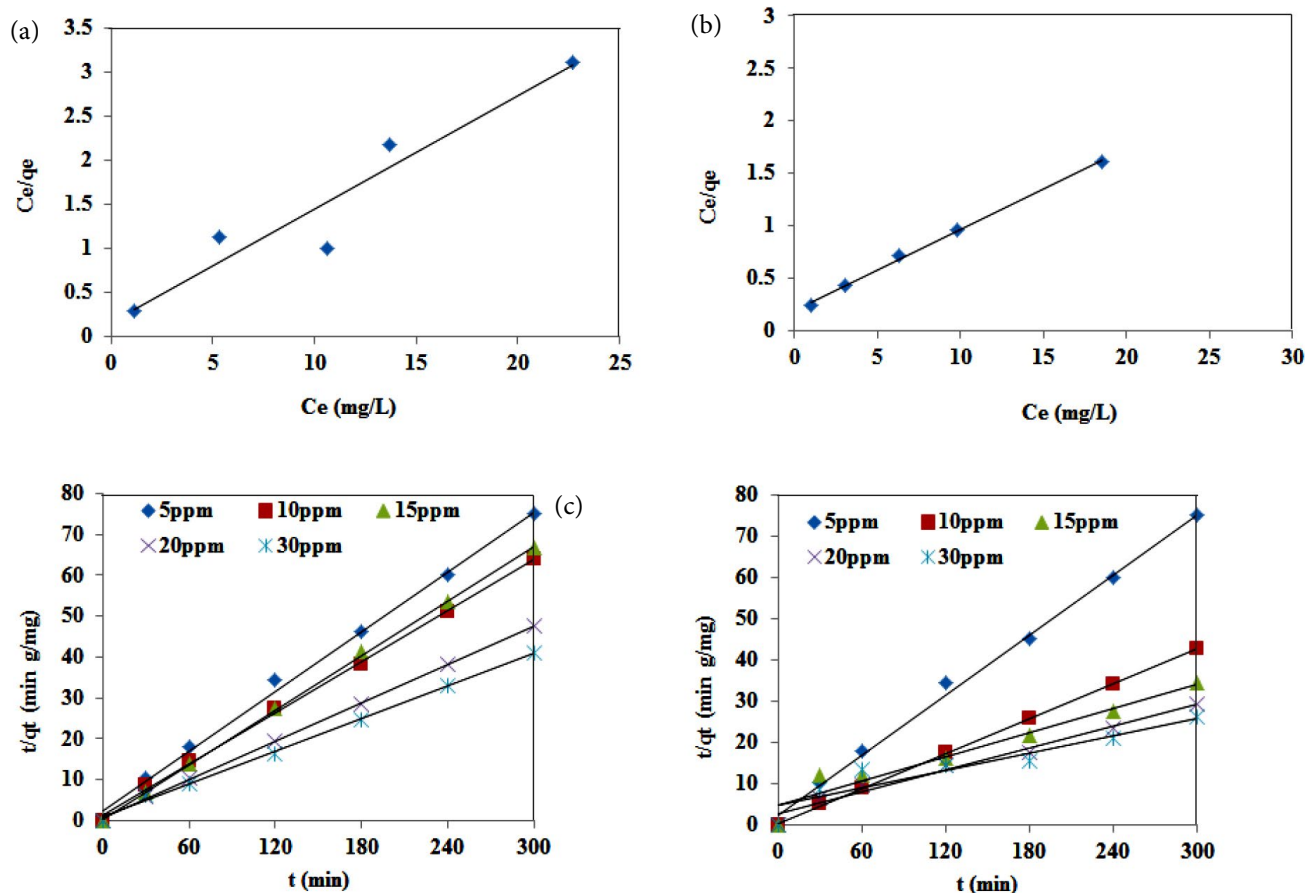


Figure 5. Adsorption isotherm and kinetics of fluoride onto ACP-250 and ACP-500 for (a) and (b) the Langmuir isotherm, and (c) and (d) second order kinetics.

K_f are (3.5886 and 4.2833) for ACP-250 and ACP-500, respectively. Table 1 shows that the values of $1/n$ are (5.4347 and 2.7593) for ACP-250 and ACP-500, respectively. The results show that fluoride adsorption follows the monolayer Langmuir isotherms ($R^2 = 0.9772$ for ACP-250, and 0.9963 for ACP-500).

where, k_1 and k_2 are the rate constants of the pseudo first order and pseudo second order kinetics, respectively; q_e (mg g^{-1}) is the adsorption capacity of the biosorbent at equilibrium, and q_t (mg g^{-1}) is the amount of fluoride adsorbed on the adsorbent surface at time t (min^{-1}). The values of k_1 , k_2 , and q_e were obtained from the linear plot of $\log (q_e - q_t)$ vs. t and t/q_t vs. t .

Table 1: Isotherms Parameters for adsorption of fluoride on the ACP-250 and ACP-500

Isotherms	Parameters	Values	
		ACP-250	ACP-500
Langmuir	Q_0 (mg/g)	7.5757	12.6262
	b (L/mg)	0.4404	0.4634
	R_L	0.6942	0.6833
Freundlich	R^2	0.9772	0.9963
	k_f (mg/g)	2.2344	3.2433
	N	2.4324	1.9531
	R^2	0.9353	0.9513

Table 2 lists the results of the Lagergren first-order kinetics and pseudo second kinetics model (Figures 5 (c and d)) and their regression coefficient (R^2). Pseudo-First-order theoretical adsorption capacity (mg/g) of fluoride was

increased from 0.83 mg/g to 7.3 mg/g for ACP-250 and from 0.57 mg/g to 11.6 mg/g for ACP-500 with increasing concentration of fluoride from 1 mg/L to 30 mg/L. However, pseudo-second-order theoretical adsorption capacity (mg/g) of fluoride was also increased for both adsorbents ACP-250 and ACP-500, adsorption capacity for ACP-250 was almost similar to pseudo-first-order theoretical adsorption capacity. However, it was increased from 0.89 mg/g to 14.3 mg/g for ACP-500 with increasing concentration of fluoride from 1 mg/L to 30 mg/L. In comparison of the two models, the pseudo-second-order kinetics model fitted well with the adsorption data, as compared to the pseudo-first order kinetics model.

3. 4. 2 Intra-Particle Diffusion Model (IPDM)

IPDM represents the three steps for the adsorption of contaminant on to the surface of adsorbent,⁴⁸ in the

Table 2: Kinetics parameters of Pseudo first, Pseudo second and Intraparticle diffusion model for fluoride adsorption on ACP-250 and ACP-500

Pseudo First Order						
ACP-250				ACP-500		
Co(mg/L)	Qe (mg g ⁻¹)	$k_{1 ads}$ (min ⁻¹)	R ²	Qe (mg g ⁻¹)	$k_{1 ads}$ (min ⁻¹)	R ²
1	0.825	-0.00326	0.9091	0.5757	-0.0039	0.8007
2.5	0.825	-0.00287	0.6926	1.8513	-0.0024	0.8405
5	3.6	-0.00243	0.6608	2.5153	-0.003	0.7729
10	4.7	-0.00408	0.8914	3.8010	-0.0053	0.8425
15	5.2	-0.00126	0.3642	10.0855	-0.0034	0.9923
20	6.3	-0.00343	0.7567	9.4566	-0.0026	0.9901
30	7.3	-0.0076	0.9957	11.6064	-0.0019	0.9787
Pseudo Second Order						
ACP-250				ACP-500		
Co(mg/L)	Qe (mg g ⁻¹)	$K_{2 ads}$ (min ⁻¹)	R ²	Qe (mg g ⁻¹)	$K_{2 ads}$ (min ⁻¹)	R ²
1	0.825	0.3755	0.9452	0.8858	0.1288	0.9974
2.5	1.865	0.04817	0.9941	2.3889	0.0135	0.9699
5	3.6	0.07282	0.9992	4.1220	0.00473	0.9963
10	4.7	0.03008	0.9986	7.1022	0.04044	0.9996
15	5.2	0.01738	0.9952	10.2040	0.00204	0.9391
20	6.3	0.05227	0.9984	11.2612	0.00293	0.9765
30	7.3	0.02057	0.9978	14.3061	0.00095	0.8763
Intraparticle Diffusion						
ACP-250				ACP-500		
Co(mg/L)	Kid(mg g ¹ min ⁻¹)	C(mg ⁻¹)	R ²	Kid(mg g ¹ min ⁻¹)	C(mg ⁻¹)	R ²
1	0.0478	0.076	0.9302	0.0456	0.2146	0.7769
2.5	0.0998	0.4898	0.7837	0.1299	0.2019	0.9157
5	0.1774	1.1369	0.6774	0.2088	1.0068	0.7863
10	0.2429	1.2854	0.7534	0.3452	2.2925	0.6642
15	0.2459	1.4985	0.6932	0.5522	0.2456	0.9445
20	0.3027	2.1699	0.6187	0.6149	0.9012	0.6645
30	0.3894	1.8909	0.7581	0.7478	0.2924	0.9547

first step, adsorbate is adsorb onto the surface of adsorbent through the external surface or prompt adsorption process; in the second step steady adsorption step which shows the controlled intraparticle diffusion, and in the third step, adsorbate transfers from larger pore to micropores consequently decrease in adsorption rate and finally attaining equilibrium step. Another kinetics model including IPDM has also described the mechanism of fluoride adsorption by the adsorbent. The IPDM was proposed by Weber and Morris⁴⁹ by Eq. (8):

$$q_t = K_{id} t^{1/2} + C \quad (8)$$

Where, K_{id} ($\text{mg g}^{-1} \text{min}^{-1}$) is the Intraparticle diffusion rate constant, C (mg g^{-1}) is the thickness of the boundary layer, and the values of K_{id} and C are calculated from the slope and intercept of q_t vs. $t^{1/2}$ plots (Figs. S2 (a) and (b)), respectively. Table 2 shows the obtained value. According to IPDM, if the adsorption of a solute is controlled by the intra-particle diffusion process, a plot of q_t versus $t^{1/2}$ passes through the origin. Therefore, it was concluded that intraparticle diffusion are involved in the adsorption of Fluoride onto ACP-250 and ACP-500.

3. 5. Study of Adsorption Thermodynamics

The thermodynamics parameters could be responsible for comprehensive information about the essential energy and structural change after adsorption. The thermodynamics parameters were calculated as Eqs. (9)–(10): the change in Gibbs free energy (ΔG°) (KJ mol^{-1}),

where ΔH is the change in enthalpy and ΔS° is the change in entropy.

$$K_c = \frac{q_e}{C_e} \quad (9)$$

$$\Delta G = -RT \ln K \quad (10)$$

$$\ln K_c = \frac{\Delta S}{R} - \frac{\Delta H}{RT} \quad (11)$$

where, K_c is the equilibrium constant, q_e is the quantity (mg/g) of fluoride adsorbed on the surface of biosorbent at equilibrium, C_e represents the equilibrium concentration of fluoride in a solution (mg/L), and R denotes the universal gas constant (8.314 J/mol K), while T is the absolute temperature (K) respectively. Fluoride adsorption experiments were completed at different temperatures of (25, 35, 45, and 55) $^\circ\text{C}$, and showed that the removal percentage of fluoride decreased with increased absolute temperature. The changes in enthalpy and entropy were calculated from the plot of $\ln K_c$ vs. $1/T$, which are shown in Fig. S2 (c) and (d), and Table S2 gives the obtained values. The results show that the adsorption of fluoride depends on temperature. The negative value of ΔG° for ACP-250 represents a non-spontaneous process; however, the value of ΔG° for ACP-500 specifies that the adsorption process favorable at (25 and 35) $^\circ\text{C}$ temperature.⁵⁰ The process of thermodynamics was exothermic which was confirmed by the negative value of ΔH° and ΔS° means the adsorption decreases with increase in temperature. The opportunity for favorable adsorption can be represented by the negative value of ΔS° for both the bioadsorbents.⁵¹

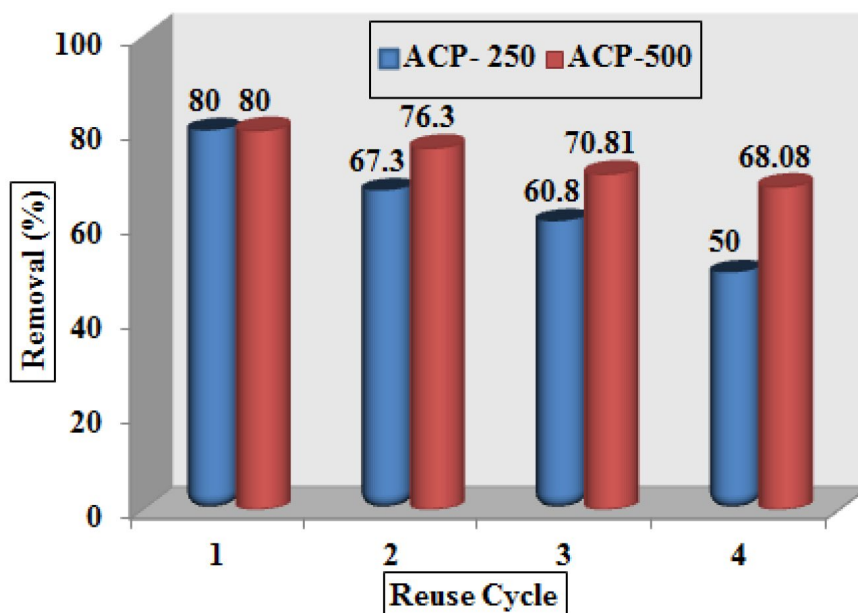


Figure 6. Reusability potential of the synthesized biosorbents (ACP-250 and ACP-500).

4. Regeneration Stability Test

The adsorption and desorption efficiency are the significant characteristics of an adsorbent. The reproducibility of an adsorbent decreases its overall cost, hence increases its value in the continuous batch experiment. The desorption of fluoride from ACP-250 and ACP-500 for the regeneration of active site was performance in 0.1 M sodium hydroxide (NaOH) solution as a desorbing agent for two hours; the adsorbent was then washed with distilled water, until the solution pH became neutral. The regenerated adsorbents (ACP-250 and ACP-500) were tested for fluoride removal from aqueous solution. The regeneration experiment was conducted with a concentration of 5.0 mg L⁻¹ of aqueous fluoride solution during the beginning of every cycle. Fig. 6 shows the results of reusability. For the (1st, 2nd, 3rd, and 4th) cycle, the removal efficiencies of ACP-500 were (80, 76.3, 70.81, and 68.08)%; however for ACP-250, they were (80, 67.3, 60.8, and 50)% , respectively. The results clearly show that both biosorbents can be reused effectively to remove fluoride ion from water. However, ACP-500 has higher regeneration efficiency, as compared to ACP-250.

6. Comparison of the Fluoride Adsorption Capacity of ACP and other Biomass-Based Adsorbents

Comparisons of the maximum fluoride adsorption capacity of ACP-250 and ACP-500 with a wide variety of adsorbent have been reported. Table 3 shows that the Langmuir adsorption capacity of fluoride was (7.58 and 12.63) mg/g using ACP-250 and ACP-500, respectively, which values are higher than those of activated alumina, wheat straw raw, original tea, *Moringa indica* based activated carbon, activated bagasse carbon, biomass carbon at

Table 3: Comparison of the defluoridation capacities of different biomass based sorbents

Adsorbent	Adsorption capacity (mg/g)	References
Activated alumina	7.6	(Ku and Chiou, 2002) ⁵²
Wheat straw raw	1.9	(Yadav <i>et al.</i> , 2013) ⁵⁴
Original tea	3.83	(Caia <i>et al.</i> , 2015) ⁵⁵
Tea-Fe	10.47	(Caia <i>et al.</i> , 2015) ⁵⁵
<i>Moringa indica</i> based activated carbon	0.23	(Karthikeyan <i>et al.</i> , 2007) ⁵⁶
Wheat straw raw	1.93	(Yadav <i>et al.</i> , 2013) ⁵⁴
Activated bagasse carbon	1.15	(Yadav <i>et al.</i> , 2013) ⁵⁴
Biomass carbon at 300 °C	0.52	(Sinha <i>et al.</i> , 2003) ⁵⁷
Biomass carbon at 600 °C	1.54	(Sinha <i>et al.</i> , 2003) ⁵⁷
Pine wood biochar	7.66	(Mohan <i>et al.</i> , 2012) ⁵⁸
ACP-250	7.8247	This study
ACP-500	13.0039	This study

300 °C, and biomass carbon at 600 °C based adsorbents. It requires less time (equilibrium-3hrs) to remove almost all amount of fluoride in comparison with some other studies.^{52,53} Removal of fluoride was not much affected by pH of the aqueous solution so it can be applied for the removal of fluoride from ground water as well as from wastewater of any pH. For ACP-500 maximum 80.5% removal was observed at pH 4 and at alkaline medium i.e. pH 8, about 56% removal was obtained. While ACP-250 shows good results at pH 4. As shown in the Table 3, it was observed that the adsorbents of present study having higher adsorption capacity than other adsorbent.

7. Cost Analysis for Fluoride Removal

The cost of the fluoride treatment by applying biosorbents is dependent on various factors, such as the adsorption efficiency of the adsorbent, reuse capability scale of the application, etc. The present study showed some important efforts of the regeneration and reuse of ACPs in successive cycles, which indicate that ACP-250 and ACP-500 were used to remove fluoride up to four cycles. Table S3 summarizes the cost of some of the material that is used for the removal of fluoride. As the present adsorbent is cost effective and yet it is non-commercial but can be commercialized. *Citrus limetta* pulp alone could not be used directly as an adsorbent for fluoride removal because it leaches in the solution as well as shows negligible adsorption. Hence, modification is done to increase the removal efficiency of the material. Material developed after modification makes adsorbent magnetic and it becomes very easy to separate the adsorbent through magnet and can be recycled many times. The cost of activated carbon prepared from pulp was calculated on the basis of raw material cost and process cost.

8. Conclusion

Low-cost highly efficient magnetic or iron pre-treated activated carbon (ACP-250 and ACP-500) were synthesized from *Citrus limetta* pulp waste, and applied for the removal of fluoride ions from aqueous solution. FTIR analysis of ACP-250 and ACP-500 confirmed that fluoride-adsorbing groups were present on the surface of biosorbents. EDX results show that carbon was the dominant element in both biosorbents (Carbon content of 58% in ACP-500 and 50.3% in ACP-250). XRD results show that iron was present in the form of oxides and carbide. Slightly acidic pH and 25 °C temperature were favorable for the removal of fluoride from an aqueous solution using magnetically active resource materials. Adsorption of fluoride followed the monolayer Langmuir isotherm model and pseudo-second-order kinetics. This study confirmed that ACP-500 showed higher removal efficiency of fluo-

ride than ACP-250. It was observed that the synthesized bioadsorbent can be used up to four cycles with effective removal of fluoride and the cost analysis proved that the synthesized biogenic iron permeated activated carbon was cost effective. Therefore, waste biomass of *Citrus limetta* could be applied as highly proficient material for the removal of fluoride from the water.

9. Acknowledgment

The authors are grateful to the Science and Engineering Research Board, for providing financial support for this work (Department of Science and Technology (SERB-DST) Sponsored Project No. ECR/2016/001924). Special thanks to the University Sophisticated Instrumentation Center (USIC) BBAU, Lucknow, for their kind support in the characterization of adsorbents. In addition this was partially supported by research grant-2019 of Kwangwoon University, Seoul and Republic of Korea.

10. References

- M. Amini, K. Mueller, K. C. Abbaspour, T. Rosenberg, M. Afyuni, K. N. Moller, M. Sarr, C. A. Johnson, *Environ. Sci. Technol.* 2008, 42, 3662–3668. DOI:10.1021/es071958y
- A. L. Srivastav, P. K. Singh, V. Srivastava, Y. C. Sharma, *J. Hazard. Mater.* 2013, 263, 342–352. DOI: 10.1016/j.jhazmat.
- D. Banks, C. Reimann, O. Røyset, H. Skarphagen, O. M. Saether, *Appl. Geochem.* 1995, 10, 1–16. DOI:10.1016/0883-2927(94)00046-9
- M. Edmunds, P. Smedley, *Elsevier Academic Press Environ. Sci. Technol.* 2005, 34, 3247–3253.
- E. J. Reardon, Y. Wang, *Environ. Sci. Technol.* 2000, 34, 3247–3253. DOI: 10.1021/es990542k
- F. Shen, X. Chen, P. Gao, G. Chen, *Chem. Eng. Sci.* 2003, 58, 987–993. DOI:10.1016/S0009-2509(02)00639-5
- G. Puente, J. J. Pis, J. A. Menéndez, P. J. Grange, *Anal. Appl. Pyrolysis.* 1997, 43, 125–138. DOI:10.1016/S0165-2370 (97)00060-0.
- W.H.O. Guidelines for Drinking Water Quality. Geneva. 2004.
- S. Ayooob, A. K. Gupta, *Environ. Sci. Technol.* 2006, 36, 433–487. DOI:10.1080/10643380600678112
- B. S. Sharma, J. Agrawal, A. K. Gupta, *Asian J. Environ. Biol.* 2011, 2, 131–134. DOI:10.1021/ie202189
- M. Mahramanlioglu, I. Kizilcikli, I. O. Bicer, *J. Fluorine Chem.* 2002, 115, 41–47. DOI:10.1016/S0022-1139(02)00003-9
- P. T. C. Harrison, *J. Fluorine Chem.* 2005, 126, 1448–1456. DOI:10.1016/j.jfluchem.2005.09.009
- X. Fan, D. J. Parker, M. D. Smith, *Water Res.* 2003, 37, 4929–4937. DOI:10.1016/j.watres.2003.08.014
- M. G. Sujana, G. Soma, N. Vasumathi, S. Anand, *J. Fluorine Chem.* 2009, 130, 749–754. DOI:10.1016/j.jfluchem.2009.06.005
- X. Wu, Y. Zhang, X. Dou, M. Yang, *Chemosphere.* 2007, 69, 1758–1764. DOI:10.1016/j.chemosphere.2007.05.075
- K. Biswas, K. Gupta, A. Goswami, U. C. Ghosh, *Desalination.* 2010, 255, 44–51. 10.1016/j.desal.2010.01.019. DOI:10.1016/j.desal.2010.01.019
- N. Viswanathan, S. Meenakshi, *Appl. Clay Sci.* 2010, 48, 607–611. DOI:10.1016/j.clay.2010.03.012
- R. C. Meenakshi, Maheshwari, *J. Hazard. Mater.* 2006, B137, 456–463. DOI:10.1016/j.jhazmat.2006.02.024
- J. Wioeniewski, A. Rozanska, *Desalination.* 2007, 212, 251–260. DOI:10.1016/j.desal.2006.11.008
- S. Deng, H. Liu, W. Zhou, J. Huang, G. Yu, *J. Hazard. Mater.* 2011, 186, 1360–1366. DOI:10.1016/j.jhazmat.2010.12.024
- A. Bhatnagar, E. Kumar, M. Sillanpaa, *Chem. Eng. J.* 2011, 171, 811–840. DOI:10.1016/j.cej.2011.05.028
- M. Rafatullah, O. Sulaiman, R. Hashim, A. Ahmad, *J. Hazard. Mater.* 2010, 177(1–3), 70–80. DOI:10.1016/j.jhazmat.2009.12.047
- J. R. Koduru, L. P. Lingamdinne, J. Singh, K. H. Choo, *Process Saf. Environ. Prot.* 2016, 103, 87–96. DOI:10.1016/j.psep.2016.06.038
- Y. Li, N. Li, D. Chen, X. Wang, Z. Xu, D. Dong, 2009, *Water, air, and soil pollut.* 196(1–4), 41–49. DOI:10.1007/s11270-008-9756-2
- J. Singh, N. S. Mishra, S. Uma Banerjee, Y. C. Sharma, *Bio. Resour.* 2011, 6(3), 2732–2743.
- H. Paudyala, B. Pangenja, K. Inouea, H. Kawakitaa, K. Ohtoa, H. Haradaa, S. Alam, *J. Hazard. Mater.* 2011, 192, 676–682. DOI:10.1016/j.jhazmat.2011.06.068.
- H. Li, Z. Li, T. Liu, X. Xiao, Z. Peng, L. Deng, *Bioresour. Technol.* 2008, 99, 6271–6279. DOI:10.1016/j.biortech.2007.12.002
- S. Srivastava, S. B. Agrawala, M. K. Mondalb, *Ecol. Eng.* 2015, 85, 56–66. DOI:10.1016/j.ecoleng.2015.10.011
- Lambert, J. B (1987). Macmillan, New York
- L. H. V. Jimenez, R. H. Hurt, J. Matos, J. R. R. Mendez, *Environ. Sci. Technol.* 2014, 48, 1166–1174. DOI: 0.1021/es403929b
- L. Batistella, L. D. Venquiaruto, M. D. Luccio, J. V. Oliveira, S. B. C. Pergher, M. A. Mazutti, D. de Oliveira, A. J. Mossi, H. Treichel, R. Dallago, *Ind. Eng. Chem. Res.* 2011, 50, 6871–6876. DOI: 10.1021/ie101020r
- J. Sun, S. Zhou, P. Hou, Y. Yang, J. Weng, X. Li, M. Li, *J. Biomed. Mater. Res.* 2006, 80A, 333–341. DOI: 10.1002/jbm.a.30909
- S. Shukla, V. Arora, A. Jadaun, J. Kumar, N. Singh, V. K. Jain, *Int J. Nanomedicine. J.* 2015, 10, 4901–17. DOI:10.2147/IJN.S77675
- C. Gai, F. Zhang, Q. Lang, T. Liu, N. Peng, Z. Liu, *Appl. Catal. B: Environ.* 2017, 204, 566–576. DOI:10.1016/j.apcatb.2016.12.005
- S. Dwivedi, P. Mondal, C. Balomajumder, *Res. J. Chem. Sci.* 2014, 4(1), 50–58.
- T. P. Singh, C. B. Majumder, *Int. J. Pharm. Pharm. Sci.* 2016, 8, 8–7. DOI:10.22159/ijpps.2016v8i10.12253
- S. Karthikeyan, R. Balasubramanian, C. S. P. Iyer, *Bioresour. Technol.* 2007, 98, 452–455. DOI:10.1016/j.biortech.2006.01.010

38. M. D. Meitei, M. N. V. Prasad, *Ecol. Eng.* 2014, 71, 308–317. DOI:10.1016/j.ecoleng.2014.07.036
39. D. Tang, G. Zhang, *Chem. Eng. J.* 2016, 283, 721–729. DOI:10.1016/j.cej.2015.08.019
40. D. P. Das, J. Das, K. Parida, *J. Colloid Interface Sci.* 2003, 261, 213–220. DOI:10.1016/S0021-9797(03)00082-1
41. I. J. Langmuir, *Am. Chem. Soc.* 1916, 38, 2221–2295. DOI: 10.1021/ja02268a002
42. H. Freundlich, 1906, 57, 385–470. DOI: 10.4236/ojn.2015.56057
43. S. Kundu, A. K. Gupta, *Chem. Eng. J.* 2006, 122(1–2), 93–106. DOI:10.1016/j.cej.2006.06.002
44. E. Bulut, M. Ozacar, I. A. Sengil, *J. Hazard. Mater.* 2008, 154, 613–622. DOI:10.1016/j.jhazmat.2007.10.071
45. E. Demirbas, M. Kobya, A. E. S. Konukman, *J. Hazard. Mater.* 2008, 154, 787–794. DOI:10.1016/j.jhazmat.2007.10.094
46. Y. S. Ho, G. McKay, *Process Saf. Environ. Prot.* 1998, 76, 332–340. DOI: 10.1205/095758298529696
47. Y. S. Ho, D. A. J. Wase, C. F. Forster, *Water Res.* 1995, 29, 1327–1332. DOI:10.1016/0043-1354(94)00236-Z
48. F. C. Wu, R. L. Tseng, R. S. Juang, *Chem. Eng. J.* 2009, 153, 1–8. DOI:10.1016/j.cej.2009.04.042
49. J. W. J. Weber, J. C. Morris, *J. Sanit. Eng. Div. ASCE.* 1963; 89(SA2), 31–59.
50. J. Singh, K. J. Reddy, Y. Y. Chang, S. H. Kang, J. K. Yang, *Process Saf. Environ. Prot.* 2016, 99, 88–97. DOI:10.1016/j.psep.2015.10.011
51. M. E. Mahmoud, G. M. Nabil, N. M. El-Mallah, H. I. Basiouny, S. Kumar, T. M. Abdel-Fattah, *J. Ind. Eng. Chem.* 2016, 37, 156–167. DOI:10.1016/j.jiec.2016.03.020
52. Y. Ku, H. Chiou, *Water Air Soil Pollut.* 2002, 133, 349–361. DOI:10.1023/A:1012929900113
53. H. Huang, J. Liu, P. Zhang, D. Zhang, F. Gao, *Chem. Eng. J.* 2017, 307, 696–706. DOI: 10.1016/j.cej.2016.08.134
54. A. K. Yadav, R. Abbassi, A. Gupta, M. Dadashzadeh, *Ecol. Eng.* 2013, 52, 211–218. DOI: 10.1016/j.ecoleng.2012.12.069
55. H. M. Caia, G. J. Chena, C. Y. Penga, Z. Z. Zhanga, Y. Y. Donga, G. Z. Shanga, X. H. Zhua, H. J. Gaob, X. C. Wana, *Appl. Surf. Sci.* 2015, 328, 34–44. DOI: 10.1016/j.apsusc.2014.11.164
56. G. Karthikeyan, S. S. Llango, *Iran. J. Environ. Healt. Sci. Eng.* 2007, 4, 21–28.
57. S. Sinha, K. P. Pandey, D. Mohan, K. P. Singh, *Ind. Eng. Chem. Res.* 2003, 42, 6911–6918. DOI: 10.1021/ie030544k
58. D. Mohan, R. Sharma, V. K. Singh, P. Steele, C. U. Pittman, *Ind. Eng. Chem. Res.* 2012, 51, 900–914. DOI: 10.1021/ie202189

Povzetek

Tekom študije smo uspešno sintetizirali biogeni aktivni ogljik iz ostankov pulpe limete (*Citrus limetta*) in ga uporabili za odstranjevanje fluoridnih ionov iz vodne raztopine. Za sintezo aktivnega oglja smo surovino segreli v pečici pri dveh različnih temperaturah (250 °C in 500 °C) in vzorca označili kot ACP-250 in ACP-500. Pripravljen biosorbent smo karakterizirali z vrstično elektronsko mikroskopijo (SEM), infrardečo spektroskopijo s Fourierjevo transformacijo (FTIR) in rentgensko difrakcijo (XRD). Šaržne študije adsorpcije smo izvedli pri različnih temperaturah, količini, pH vrednostih in začetnih pogojih. Za razumevanje adsorpcijskega mehanizma smo določili adsorpcijske izoterme in reakcijsko kinetiko. Rezultati študije so pokazali, da je bila maksimalna odstranjena količina ionov znašala za ACP-500 86 % in za ACP-250 82 %. Izoterme najbolje opišemo z Langmuirjevo izotermo, z enoslojno adsorpcijsko kapaciteto fluoridnih ionov 12.6 mg/g. Vendar pa kinetiko vezave dobro opišemo kot reakcijo psevdodrugerega reda. Sintetizirani material je bil učinkovit za odstranjevanje fluoridnih ionov iz vode pri različnih temperaturah in bil uporaben tri do štirikrat.

Scientific paper

Fabrication of Silver-Modified Halloysite Nanotubes and their Catalytic Performance in Rhodamine 6G and Methyl Orange Reduction

Maryam Akhondi and Effat Jamalizadeh*

Department of Chemistry, Shahid Bahonar University of Kerman, Kerman, Iran.

* Corresponding author: E-mail: jamalizadeh@uk.ac.ir, jamalizadeheffat@yahoo.com.
Tel./fax: +98 34 33257433

Received: 09-12-2018

Abstract

Halloysite nanotube supported Ag nanoparticles (Ag/HNT) as catalyst for reduction of Rhodamine 6G (Rh6G) and Methyl orange (MO) have been synthesized and tested. 3-glycidyloxypropyltrimethoxysilane and Triethylene tetramine were successfully utilized to modify the HNTs surface, then Ag⁺ ions were reduced to AgNPs on this functionalized HNT surface. The structure of AgNPs-impregnated HNT wall was characterized by FTIR, XRD, TEM, FE-SEM and EDX showing the AgNPs to be 10–15 nm in size. The catalytic activity of Ag/HNTs for Rh6G and MO reduction was investigated by UV-vis spectroscopy so as catalyzed and uncatalyzed reaction rate constants could be compared. The rate constant (k) of Rh6G and MO reduction was calculated for catalyzed reactions as 0.224 min⁻¹ and 0.222 min⁻¹, and for un-catalyzed reactions as 0.049 min⁻¹ and 0.014 min⁻¹, respectively. The Ag/HNT catalyzer was effectively recycled six times without appreciable loss of activity. Results indicate that supporting AgNPs on HNT surface functionalized with other compounds with superior performance in reducing Rh6G and MO dyes exist.

Keywords: Catalyst; Ag nanoparticles; Functionalized halloysite; GPTMS; TETA

1. Introduction

In recent years, great strides have been taken in use of metal nanomaterials as heterogeneous catalysts.^{1–3} Nanomaterials have special properties such as the surface and interface effect which arise from the alteration of boundary between material and its surrounding, small size effect due to decrease in atom density of amorphous nanoparticles near the surface layer, quantum size effect arising from confinement of electrons to small regions of space in one, two, or three dimensions and also macroscopic quantum tunneling effect, leading to some new and potential applications such as catalysis, bio-engineering, medicine.^{4–6} Industrial dye production and use apart from forming toxic by-products and non-biodegradable wastes that affect plants, animals and fish, are suspect as potential carcinogens.^{7,8} Therefore, depending on the local laws and bylaws, to prevent environmental pollution, industrial wastewaters retaining organic dyes need treatment to remove the residual compounds. Various techniques for removal of dye molecules exist such as membrane filtration, ion exchange, biological treatment, coagulation-flocculation, ozone flashing, Fentons reagent.^{9–13} The coagulation-floc-

ulation process is widely used, due to its simplicity and cost-effectiveness,⁹ however, it just transfers the dye molecules from liquid to solid form.¹⁴ Catalysis as an efficient method to treat wastewater bearing colorants has attracted much interest.¹⁵

Among different type of metal nanoparticles, noble metal nanoparticles have attracted extensive attention as chemical catalyst.^{16–18} Among these, Ag is particularly striking due to its remarkable catalytic activity and low cost. A significant number of studies on the catalytic reactions of Ag nanoparticles (AgNPs) have been reported, such as alcohol dehydrogenation,¹⁹ oxidation of phenylsilanes,²⁰ reduction of aromatic compounds,²¹ and Diels-Alder cycloadditions.²² Since during a chemical reaction, the active surface atoms dislodge the AgNPs,^{22–27} various supports such as polymeric^{28,29} and inorganic materials, including silica,^{30,31} zeolite,^{32,33} alumina,^{34,35} ceria,³⁶ titania,^{37,38} zirconia,³⁹ activated carbon,^{40,41} carbon nanotubes (CNTs),^{42,43} and halloysite nanotubes (HNTs),^{44–46} have been used to immobilize AgNPs. Halloysite silicate nanotubes of about 15 nm lumen, 50 nm external diameter and 1000–2000 nm length are abundant in nature. Furthermore, HNTs are biocom-

patibile,^{47,48} chemically stable,⁴⁹ with high absorption capability⁷ and potential to settle down quickly. HNTs ($\text{Al}_2\text{Si}_2\text{O}_5(\text{OH})_4 \cdot n\text{H}_2\text{O}$) have two-layered (1:1) aluminosilicate with aluminol (Al–OH) group in the internal and Si–OH group on the external surfaces. Presence of hydroxyl groups allows easy surface functionalization.^{50–53} Existence of halloysite significantly improves the size control of Ag nanoparticles as Ag nanoparticles without halloysite get to larger size and also aggregate heavily.⁵⁴ Nanotube supported Ag nanoparticles (Ag/HNT), are used with various precursors and for different applications such as biosensor,^{55–56} polymerization catalyst,⁴⁴ photocatalyst,^{45,46} enzyme immobilization,⁵⁵ dielectric material⁵⁷ and antibacterial usage.^{58,59} In addition, the Ag/HNTs show high catalytic activity even at minute amounts towards reduction and degradation of some industrial dyes, 4-nitrophenol^{60–62} or methylene blue.⁶²

The purpose of this paper is to enhance the catalytic effect of Ag nanoparticles as a heterogeneous catalyst to reduce 6G Rh6G and MO dyes by supporting them on the walls of halloysite nanotubes modified with new compounds. Such modification of the external surface of HNTs was achieved, and then in situ reduction of Ag^+ to Ag nanoparticles on the functionalized HNTs surface resulted in synthesized Ag/HNTs which was then utilized as a heterogeneous catalyst in the degradation of Methyl orange and Rhodamine 6G in aqueous solution (Fig. 1). The recyclability of the Ag/HNTs catalyst was tested by carrying out repeated runs of the same reaction system.

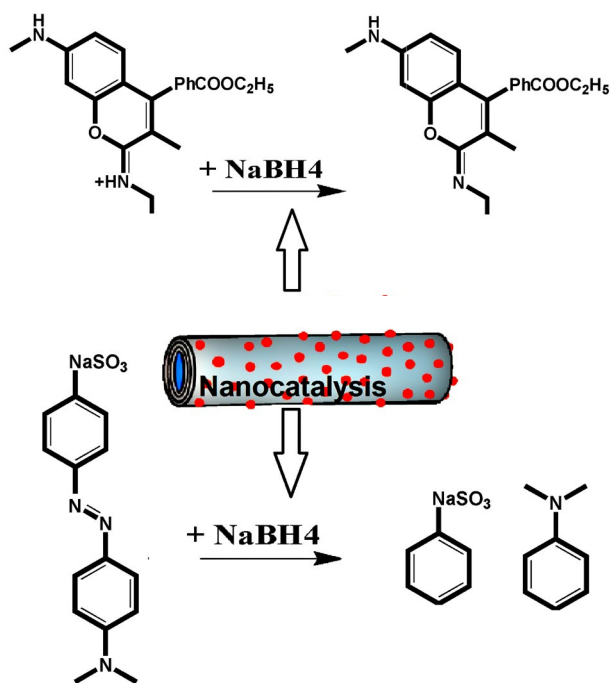


Fig 1. Reduction of Rh6G and MO by NaBH_4 catalyzed by the Ag/HNT.

2. Methods

2. 1. Materials

The halloysite nanotube powder was provided by New Zealand China Clays Ltd., Auckland, New Zealand. The Sodium borohydride ($\text{NaBH}_4 \geq 99.99\%$), Sodium hydroxide ($\text{NaOH} \geq 97.00\%$) and hydrochloric acid ($\text{HCl} \geq 37.00\%$) were acquired from the Sigma Aldrich. The silver nitrate ($\text{AgNO}_3 \geq 99\%$), 3-glycidyloxypropyltrimethoxysilane (GPTMS $\geq 98\%$), Triethylene tetramine (TETA), Ethanol, MO and Rh6G were purchased from Merck.

2. 2. Instruments

UV-vis spectra were recorded on a spectrophotometer (Varian, Cary50), with a quartz cuvette (1.0 cm path length, and 4 mL volume). Scanning electron microscope images were obtained with a field-emission scanning electron microscope (FE-SEM) KYKT, EM-3200. Transmission Electron Microscope (TEM) images were recorded from JEOL 2100F TEM. XRD patterns were obtained in reflection mode using a powder X-ray diffractometer (X'Pert Pro MPD Philips X-ray diffractometer (Ni-filtered Cu-K α radiation, $\lambda = 0.154$ nm). FT-IR spectra of samples as KBr discs were recorded on a FT-IR 8400-Shimadzu in the range 400–4000 cm^{-1} . The pH measurements were performed using a pH-meter (METROHM, Model 713).

2. 3. Functionalization of HNTs

As shown in Fig 2, for functionalization of HNTs by grafting the GPTMS containing epoxy groups on the surface of HNTs via silanization; 1 mL of GPTMS was added to 0.5g of HNTs dispersed in 7 mL of ethanol and was stirred at 65 °C for 24 h and then centrifuged to collect the suspension. The precipitate (GPTMS/HNT) was washed five times with pure ethanol and dried at 60 °C for 10 h. Following that, TETA was grafted on tubes via ring opening reaction of epoxy groups by adding 6mL of pure ethanol containing TETA (0.1 mg L^{-1}) to 0.5 g of GPTMS/HNTs, stirred and refluxed for 24 h at 70 °C. This mixture was then centrifuged and the precipitate (TETA/HNT) was again washed with ethanol five times, dried at 70 °C for 10 h.

2. 4. Synthesis of Ag/HNTs Nanocomposite

The Ag/HNT composite was prepared using AgNO_3 as silver precursor, so that silver ions get reduced to silver nanoparticles on TETA/HNT's surface amine functional groups. In a typical synthesis process, 0.5 g of TETA/HNTs was added to 10 mL of deionized water under stirring for 1 h and then, 1 mL of 0.2 M AgNO_3 solution was added dropwise to the mixture and left stirring for 30 min. The solution was reduced by addition of 2 mL of freshly pre-

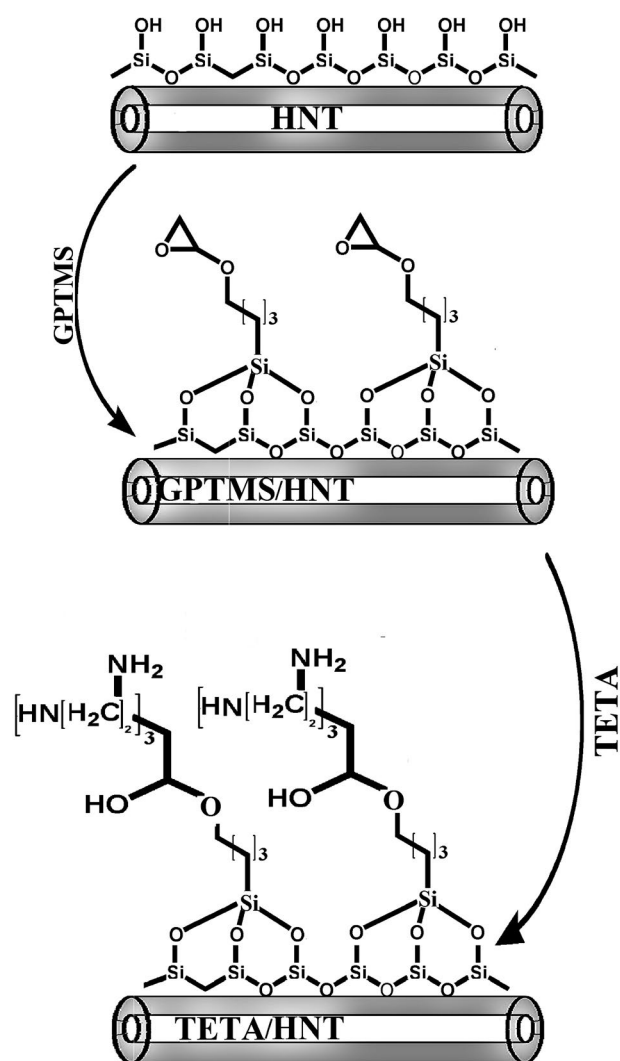


Fig 2. Schematic Illustration of the role of GPTMS and TETA in the formation of the TETA/HNTs.

pared 0.1 M aqueous NaBH_4 solution. The color of the reaction mixture turns from white to dark green, indicating formation of Ag NPs on the surface of HNTs (Ag/HNTs). The final product was washed several times with de-ionized distilled water to remove unreacted Ag^+ ions and any byproducts. All experiments were performed at room temperature.

2. 5. Catalytic Reduction of Dyes by Ag/HNTs Nanocomposite

Catalytic activity of Ag/HNTs nanocomposite, on decomposing Rh6G and MO dyes was investigated by comparing the rate they reacted with NaBH_4 in the presence and absence of nanocomposite. The reduction of dyes was carried out in the quartz cell by admixing 1.0 mL of 1mM NaBH_4 as reducing agent to a mixture of 2 mL of aqueous dye solution and 1 mg of Ag/HNTs nanocompos-

ite. The process was continuously monitored by a UV-vis spectroscopy at room temperature. In order to determine its reusability after the reaction was over, the Ag/HNT catalyst was centrifuged and washed with deionized water for two times, and dried in vacuum for 24 h at 50 °C, to be used again in dye decomposition processes.

The reduction of Rh6G and MO with an excess amount of NaBH_4 has been used as a model reaction to examine the catalytic performance of the Ag/HNTs.

The reaction kinetics can be described as Eq. (1):⁴⁰

$$\ln(C/C_0) = -kt \quad (1)$$

where C_0 is the initial concentration of dye, C is the concentration of dye at time t , k is the apparent first-order rate constant (min^{-1}), and t is the time. Since the concentration of a solution is proportional to its adsorption, Eq. (1) can be written as follow:

$$\ln(A/A_0) = -kt \quad (2)$$

A_0 and A are respectively, the initial and time t dye adsorption.

Degradation efficiency (%D) of Ag/HNT is calculated according to the following Eq. (3):

$$\%D = \frac{A_0 - A}{A_0} \times 100 \quad (3)$$

Rh6G and MO reduction was investigated under various solution pH values of 3, 5, 7, 9 and 11 using sodium hydroxide and hydrochloric acid were also performed.

3. Results and Discussion

3. 1. FTIR Spectra

The FTIR spectra were used to determine the chemical structure of the HNTs during the functionalization process. As shown in Fig 3, the characteristic peaks of HNTs occurs at 3698 cm^{-1} and 3623 cm^{-1} ; attributable to O–H stretching of hydroxyl groups.⁶³ Peaks observed at 1109 cm^{-1} and 1034 cm^{-1} are ascribed to in-plane stretching of Si–O bond.⁶³ FTIR of the modified halloysite with GPTMS (GPTMS/HNT) shows new peaks at 2925 and 2854 cm^{-1} , which is assigned to the asymmetric and symmetric stretching vibration of aliphatic $-\text{CH}_2$ groups. This can also confirm the existence of GPTMS grafted on the HNTs.⁶⁴ For GPTM/halloysite grafted by TETA (TETA/HNT), in addition to the presence of CH_2 bands at 2946 cm^{-1} and 2871 cm^{-1} , there are also two new peaks at 1200 and 1600 cm^{-1} , belonging to the C–N and NH_2 groups, respectively.⁶⁵ These results can also show the interaction between TETA and epoxide ring of GPTMS grafted on the HNTs indicating that nanotubes have been successfully functionalized with amine groups. In comparing these results with the FTIR spectra of pure HNTs, the positions of

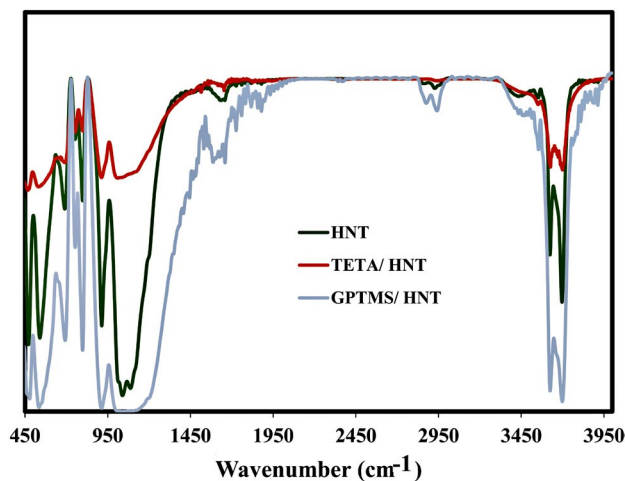


Fig 3. FT-IR spectra of HNTs, GPTMS/HNTs and TETA/HNTs.

most HNT peaks do not show any change, demonstrating preservation of main structure of HNT following GPTMS and TETA grafting.

3. 2. UV-vis Spectra

Fig 4 shows the UV-vis optical absorption spectra of the HNTs and Ag/HNTs in the 200–800 nm spectral range. The UV-vis spectra of HNTs dispersed in water revealed no absorption band, while the Ag/HNTs sample revealed an absorption band in 427 nm, corresponding to the surface plasmon resonance (SPR) of Ag nanoparticles.

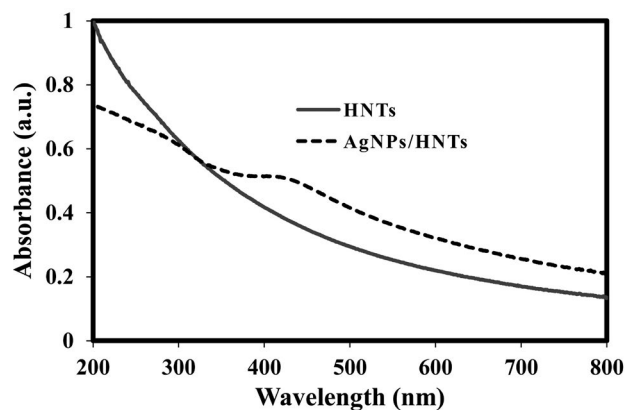


Fig 4. UV-vis spectra of HNTs and Ag/HNTs.

3. 3. FE-SEM and EDX Analysis

The FE-SEM image of HNTs and Ag/HNTs are shown in Figs 5(a) and 5(b). The diameter of the HNTs particles are about 123 nm with random length. Fig 5 shows the halloysite nanotubes along with some non-tubular structures. The particles of halloysite can adopt a multifariousness of morphologies, the most common of which is the elongated tube. However, short tubular, spher-

oidal and plate shapes have all been widely reported.^{66–68} The Ag nanoparticles are almost unobservable in Fig 5(b) but EDX analysis confirms the existence of Ag element on the surface of halloysites.

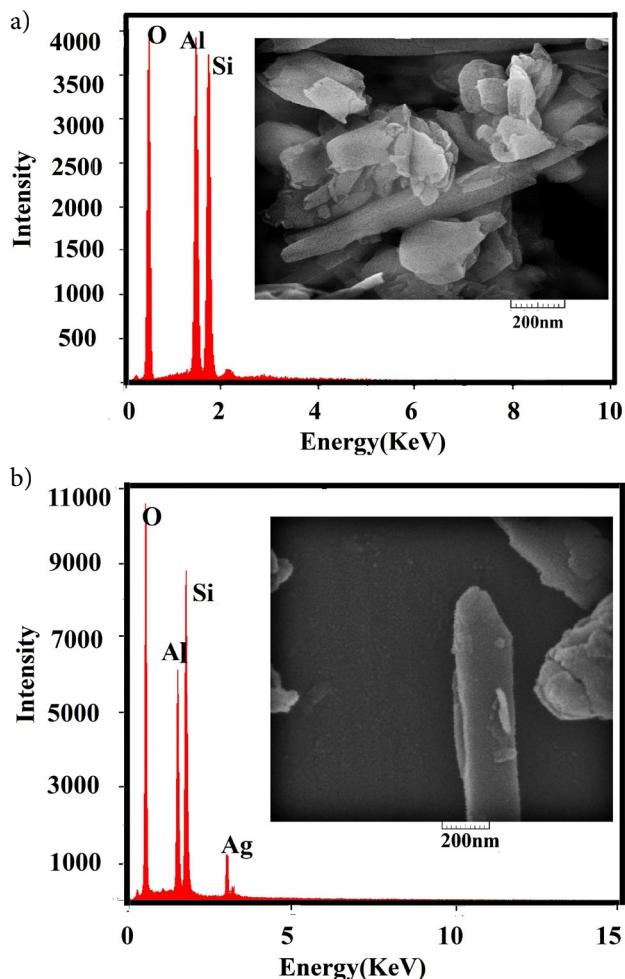


Fig 5. EDX spectra and FE-SEM images of (a) HNTs and (b) Ag/HNTs.

3. 4. TEM Analysis

TEM image of structure and morphology of Ag/HNTs is shown in Fig 6. This reveals the hollow open ended tubular morphology of HNTs with the inner and outer

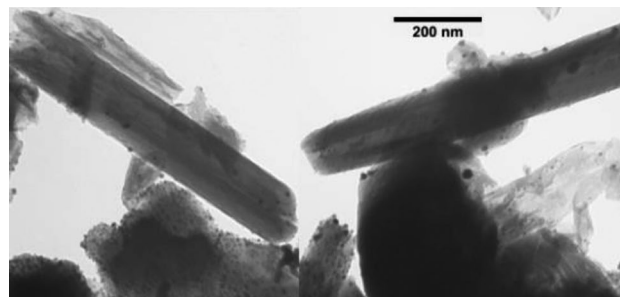


Fig 6. TEM image of Ag/HNTs.

diameters of about 15–40 nm and 50–140 nm, respectively. It also shows spherical single nanoparticles with average size of 10 nm dispersed evenly, indicating that amine terminated groups had adsorbed Ag^+ ions from solution.

3. 5. X-ray Diffraction Analysis

The X-ray diffraction (XRD) pattern of HNTs and Ag/HNTs are shown in Fig 7. The XRD patterns of the functionalized HNT reveal well defined diffraction peaks all corresponding to the HNT, confirming that modification with GPTMS and TETA does not affect the structure of the HNT. However, in the XRD pattern of the Ag/HNTs nanocomposite, four new peaks at 2θ value of 37.7° , 43.5° , 64.2° and 77.4° emerge which are ascribed to (1 1 1), (2 0 0), (2 2 0) and (3 1 1) reflections of FCC structure of silver;^{46,69} so this further affirming successful attachment of AgNPs to the surface of the nanotubes.

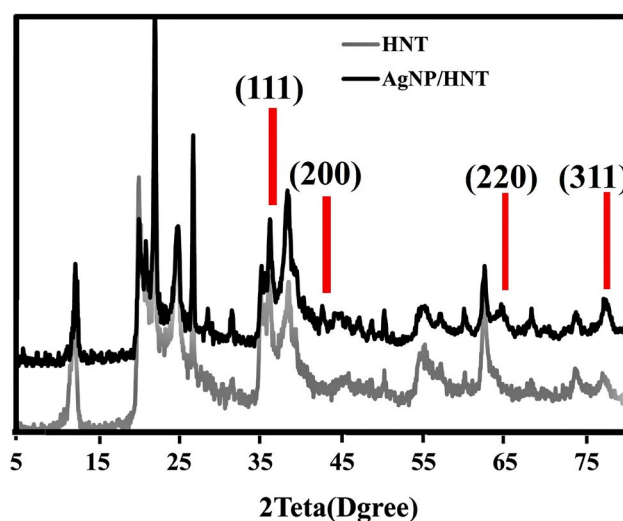


Fig 7. XRD pattern of HNTs and Ag/HNTs.

3. 6. Catalytic Reduction of Rh6G and MO

The results of catalytic activity of synthesized Ag/HNTs in reduction of Rhodamine 6G and methyl orange studied by UV-visible spectrophotometry are shown in Figs 8 and 9. Time dependent reduction of Rh6G and MO with NaBH_4 in presence and absence of Ag/HNTs was observed by the successive decrease in the absorbance value at 516 and 467 nm, respectively. Results indicate that the reduction of Rh6G and MO in absence of catalyst at room temperature occurs which is greatly enhanced by addition of Ag/HNTs. Fig 8, exhibits a rapid Rh6G concentration decay in presence of Ag/HNTs in 12 min ($\Delta\text{OD}_{12 \text{ min}} = 0.4$), compared to sluggish 30 min un-catalyzed reaction ($\Delta\text{OD}_{30 \text{ min}} = 0.4$). Similarly, Fig 9, demonstrates rapid decay of MO in presence of Ag/HNTs in just 12 min ($\Delta\text{OD}_{12 \text{ min}} = 0.8$), compared to its slow degradation needing 30 min when relying on un-catalyzed reaction ($\Delta\text{OD}_{30 \text{ min}}$

$= 0.34$). It is observed that degradation of methyl orange is classically enhanced in presence of silver nanoparticles due to electron relay effect.^{25, 26}

As presented in Table 1, the rate constant (k) of Rh6G and MO degradation has been calculated for catalyzed reactions as 0.224 min^{-1} and 0.222 min^{-1} , and for un-catalyzed reactions as 0.049 min^{-1} and 0.014 min^{-1} , respectively.

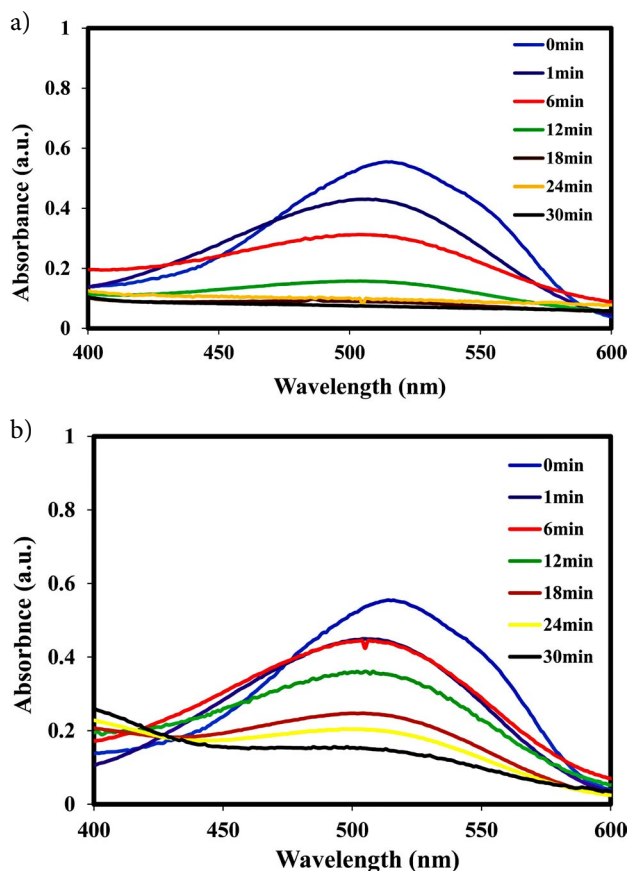


Fig 8. Time-dependent UV-vis absorption spectra for the reduction of Rh6G with NaBH_4 (a) in the presence and (b) absence of Ag/HNTs at room temperature.

3. 7. Effect of Amount of Catalyst

The amount of catalysts is an important factor affecting suitability of a catalyst for chemical reactions. Tables 2 and 3 present the optimization of degradation conditions for Rh6G and MO in early times. The Ag/HNTs catalyst amount was varied in 0.0002 g L^{-1} to 0.0025 g L^{-1} range at constant NaBH_4 concentration of 4 mg L^{-1} and dye concentration of 10 mg L^{-1} . According to the results, the rate of catalytic degradation of both dyes increased with increase in the amount of catalyst. This is due to the increase in the number of surface active sites and increased dye molecules adsorption on the catalyst surface.²⁵

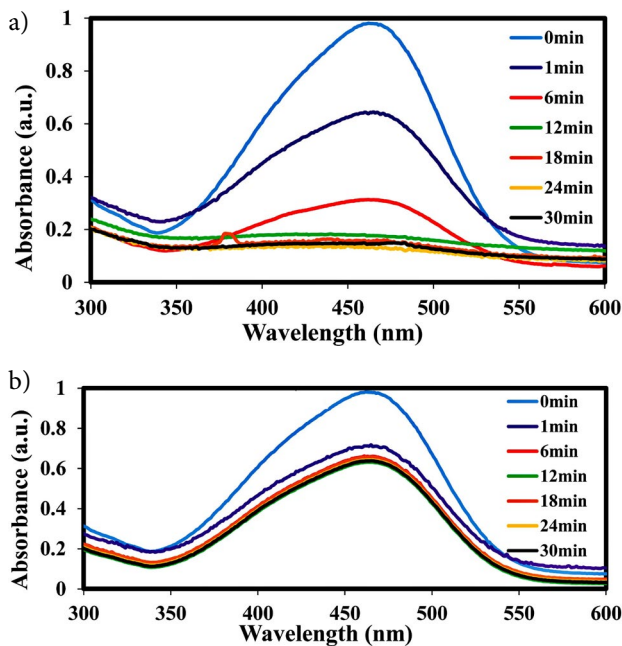


Fig 9. Time-dependent UV-vis absorption spectra for the reduction of MO with NaBH_4 (a) in presence and (b) absence of Ag/HNTs at room temperature.

3. 8. Effect of Amount of NaBH_4

In order to evaluate the effect of NaBH_4 concentration on degradation of dyes, this was varied in the range of 1.5 to 16 g L^{-1} , while keeping dye concentration at 10 mg L^{-1} and Ag/HNT concentration at 0.001 g L^{-1} . Tables 2 and 3 show that with one exception, the increase in NaBH_4 concentration, increases degradation of both dyes, due to higher number of electrons which promotes the simultaneous reduction of the Ag particles from its oxide and the reduction of dyes.²⁵ However, as mentioned, the rate constant for the 8 g L^{-1} concentration of NaBH_4 is observed to decrease. This is caused by excessive production of electrons from the ion leading to the saturation of electrons⁷⁰ leaving AgNPs incapable of relaying the electrons.

The catalytic reduction of dyes in the presence of NaBH_4 on the surface of noble metal nanoparticles is considered to follow Langmuir–Hinshelwood mechanistic pathway,^{62,71} as Fig 10 demonstrates, these dyes are electrophilic with respect to Ag NPs and nucleophilic toward BH_4^- . Thus both dyes and BH_4^- are adsorbed on the surface of AgNPs attached to the surface of HNTs. The fast nature of adsorption on the surface of nanoparticles and its reversibility has been reported.^{62,71,72} When NaBH_4 is added to the reaction solution, the hydride from NaBH_4 may be trapped by AgNPs and get adsorbed on the surface transferring its electron to the AgNPs. Following this electron exchange, a hydrogen atom is formed from BH_4^- that subsequently attacks any nearby dye molecule, and a spontaneous electron transfer-induced hydrogenation of the dye occurs. In fact, a negatively charged AgNP may be re-

garded as a nano-electrode at a negative potential which is trying to release its extra electrons which are finally released to dye molecule as an electron acceptor producing its reduced form.^{71,73} AgNPs on the surface of HNTs significantly increases the rate of catalytic reduction due to lower work function of Ag (4.26 eV) and its tendency to release electron more easily even compared to the other noble metals.^{62,74} Both nanoparticle's surface area and heterogeneous organic–inorganic hybrid structure supporting for AgNPs may contribute to reduction rate by increasing adsorption ability of reactant.⁶²

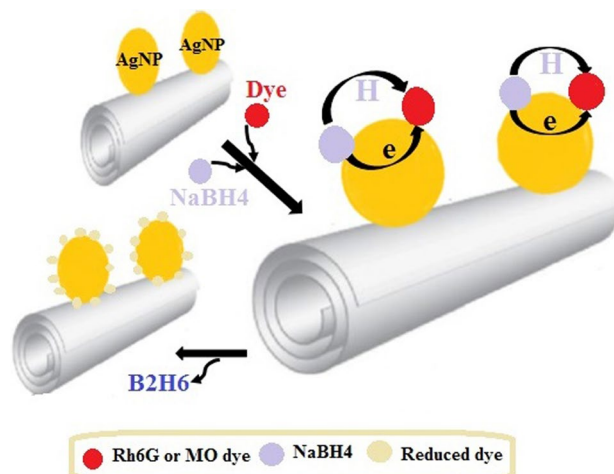


Fig 10. Proposed mechanism of reduction of dyes by catalytic sample.

3. 9. Effect of pH

The solution pH has significant effect on degradation of organic dyes. Fig 11 shows the reduction of MO and Rh6G at pH 3, 5, 7, 9, and 11 after 20 min. It was observed that the percentage of degradation of both dyes increased with decreasing pH from 7 to 3, and conversely, degradation falls at pH 9 and 11. The results show decreasing Rh6G solution pH from 7 to 3, increases the degradation efficiency from 78.0% to 79.7% while, pushing pH towards 11 decrease it to 73.6%. Similarly, decomposition of MO goes up from 73.9% to 77.1% by reducing pH from 7 to 3 and solution pH of 11, cuts it to 70.6%. In acidic media the MO molecules ($\text{pK}_a = 3.4$) undergo protonation^{74,75} and the resulted protonated molecules are adsorbed better on negatively charged AgNPs, enhancing MO degradation. Similarly, the lower degradation rate observed for Rh6G at higher pH may attributed to the deprotonation of the Rh6G in alkaline solution since Rhodamine 6G ($\text{pK}_a = 7.5$) is a weak base and can easily lose proton under the effect of a strong base, which leads to partial neutralization of its positive charge.⁷⁶ As a result, electrostatic interaction with negatively charged Ag/HNT decreases decreasing the overall Rh6G degradation.

Table 4 summaries the dye reduction studies reported in literature. The synthesized Ag/HNTs while perform-

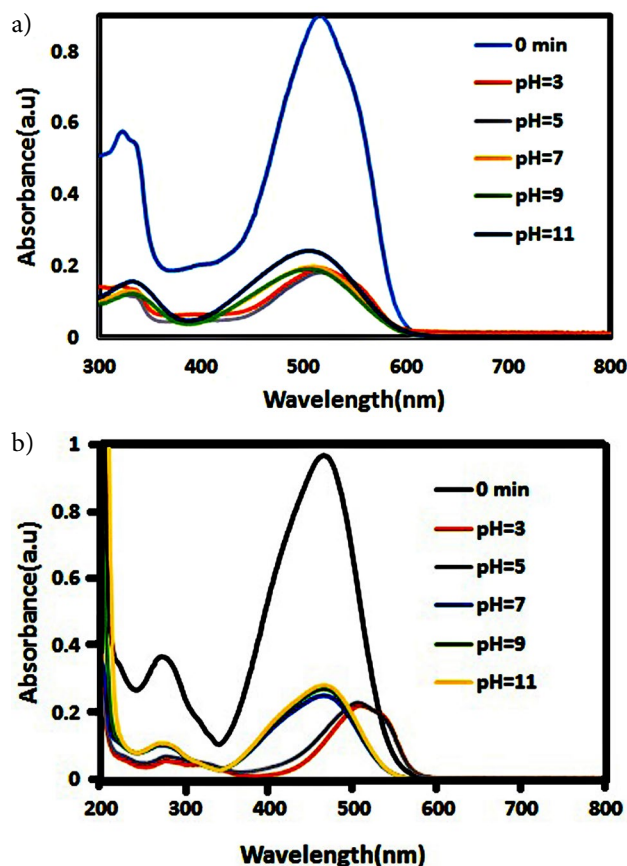


Fig 11. Time-dependent UV-vis absorption spectra for the reduction (a) Rh6G and (b) MO with NaBH_4 in presence of Ag/HNTs at different pH values.

ing on par with other Ag catalysts for the degradation of MO and Rh6G.^{25,77–79} although, the K value in this work is 0.21 min^{-1} which is slightly lower compared to the Ag supported on zeolite (0.30 min^{-1}),⁷⁷ it has the advantage of using much smaller amounts of Ag. In the present work, amount of used Ag/HNTs as catalyst is 2.4 times less than the AgNPs/Zeolite X, hence, the Ag/HNT catalysis would be more economical compared to the other catalysts reported in Table 4.^{25,78} not only because of low concentrations used but also due to the easy recovery and reusability. The halloysite as a natural mineral with high stability as support material for Ag nanoparticles, while Zeolite X⁷⁷ is not natural and its preparation is costly. Also, although the Ag/tannic acid membrane⁷⁹ has inner shell as natural substrate but this substrate is unstable.

3. 10. Reusability of the Synthesized Catalysts

The environment impact by catalysts such as heavy metals which should include recovery and recycling is an important factor in choosing a catalyst.⁸⁰ Due to the one-dimensional nature of Ag/HNTs its use as a recyclable and reusable catalysts which is easily recovered from the reaction mixture by simple filtration is very advanta-

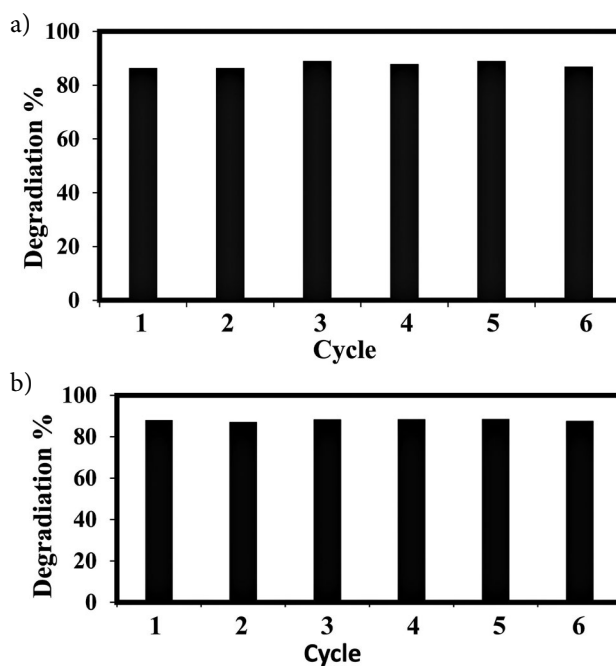


Fig 12. Recyclability and reusability of the synthesized Ag/HNTs for the reduction of Rh6G and MO.

geous. The recycling experiments involving synthesized Ag/HNTs for reduction of MO and Rh6G are shown in Fig 12. The data show that the Ag/HNT catalyst could be repeatedly used for at least six times and still maintained degradation potency of over 85. Overall, Ag/HNT as a dye decomposing catalyst has a high operational stability with no appreciable loss in catalytic activity and good reusability.

4. Conclusion

Halloysite nanotube supported Ag nanoparticles synthesized in situ by reduction of silver ions on the amine functional groups on the surface of TETA/HNTs greatly improves dispersion and stability of the Ag nanoparticles on HNT surfaces. The Ag/HNTs exhibit good catalytic activity in decomposition of MO and Rh6G by NaBH_4 as the reducing agent. The catalytic efficiency was enhanced with the increasing amount of Ag/HNTs. Notably, the Ag/HNTs could be easily recycled due to the one-dimensional nanostructural property. These results signify that Ag nanoparticles strongly attached and immobilized on the surface of halloysite modified with GPTMS and TETA increase silver performance as Rh6G and MO dyes decomposer.

5. References

1. D. Kumar Dutta, B. Jyoti Borah and P. Pollov Sarmah, *Catal Rev.* 2015, 57, 257–305.

- DOI:10.1080/01614940.2014.1003504
2. T. Yasukawa, A. Suzuki, H. Miyamura, K. Nishino and S. Kobayashi, *J. Am. Chem. Soc.* **2015**, *137*, 6616–6623. DOI:10.1021/jacs.5b02213
 3. S. Zhang, X. Shen, Z. Zheng, Y. Ma and Y. Qu, *J. Mater. Chem. A.* **2015**, *3*, 10504–10511. DOI:10.1039/C5TA00409H
 4. J. Wang and H. Gu, *Molecules.* **2015**, *20*, 17070–17092. DOI:10.3390/molecules200917070
 5. V. Pareek, A. Bhargava, R. Gupta, N. Jain and J. Panwar, *Adv. Sci. Eng. Med.* **2017**, *9*, 527–544. DOI:10.1166/asem.2017.2027
 6. K. W. Choi, D. Y. Kim, S. J. Ye and O. O. Park, *Adv. Mater. Res.* **2014**, *3*, 199–216. DOI:10.12989/amr.2014.3.4.199
 7. P. Velusamy, S. Pitchaimuthu, S. Rajalakshmi and N. Kannan, *J. Adv. Res.* **2014**, *5*, 19–25. DOI:10.1016/j.jare.2012.10.001
 8. H. R. Pouretedal, H. Eskandari, M. H. Keshavarz and A. Semnani, *Acta Chim. Slov.* **2009**, *56*. **2007**, *2*, 14–18.
 9. A. K. Verma, R. R. Dash and P. Bhunia, *J. Environ. Manage.* **2012**, *93*, 154–168. S. Mostafa, F. Behafarid, J. R. Croy, L. K. Ono, L. Li, J. C. Yang, A. I. Frenkel and B. R. Cuenya, *J. Am. Chem. Soc.* **2010**, *132*, 15714–15719.
 10. T. Poznyak, P. Colindres and I. Chairez, *J. Mex. Chem. Soc.* **2007**, *51*, 81–86.
 11. C. Thamaraiselvan and M. Noel, *Crit Rev Env Sci Tec.* **2015**, *45*, 1007–1040. DOI:10.1080/10643389.2014.900242
 12. P. Palaniandy and S. F. AHBA, *Int. j. innov. eng.* **2014**, *2*.
 13. S. Karcher, A. Kornmüller and M. Jekel, *Water Res.* **2002**, *36*, 4717–4724. DOI:10.1016/S0043-1354(02)00195-1
 14. S. Rajalakshmi, S. Pitchaimuthu, N. Kannan and P. Velusamy, *Appl Water Sci.* **2017**, *7*, 115–127. DOI:10.1007/s13201-014-0223-5
 15. B. K. Ghosh and N. N. Ghosh, *J. Nanosci. Nanotechnol.* **2018**, *18*, 3735–3758. DOI:10.1166/jnn.2018.15345
 16. B. Hvolbæk, T. V. Janssens, B. S. Clausen, H. Falsig, C. H. Christensen and J. K. Nørskov, *Nano Today.* **2007**, *2*, 14–18. DOI:10.1016/S1748-0132(07)70113-5
 17. F. P. da Silva, J. L. Fiorio and L. M. Rossi, *ACS Omega.* **2017**, *2*, 6014–6022.
 18. S. Mostafa, F. Behafarid, J. R. Croy, L. K. Ono, L. Li, J. C. Yang, A. I. Frenkel and B. R. Cuenya, *J. Am. Chem. Soc.* **2010**, *132*, 15714–15719. DOI:10.1021/ja106679z
 19. T. Mitsudome, Y. Mikami, H. Funai, T. Mizugaki, K. Jitsukawa and K. Kaneda, *Angew. Chem. Int. Ed.* **2008**, *120*, 144–147. DOI:10.1002/ange.200703161
 20. T. Mitsudome, S. Arita, H. Mori, T. Mizugaki, K. Jitsukawa and K. Kaneda, *Angew. Chem. Int. Ed.* **2008**, *120*, 8056–8058. DOI:10.1002/ange.200802761
 21. P. Zhang, C. Shao, Z. Zhang, M. Zhang, J. Mu, Z. Guo and Y. Liu, *Nanoscale.* **2011**, *3*, 3357–3363. DOI:10.1039/c1nr10405e
 22. N. Pradhan, A. Pal and T. Pal, *Colloids Surf. A: Physicochem. Eng. Asp.* **2002**, *196*, 247–257. DOI:10.1016/S0927-7757(01)01040-8
 23. L.-Q. Zheng, X.-D. Yu, J.-J. Xu and H.-Y. Chen, *Chem. Commun.* **2015**, *51*, 1050–1053. DOI:10.1039/C4CC07711C
 24. V. Vidhu and D. Philip, *Spectrochim. Acta A.* **2014**, *117*, 102–108. DOI:10.1016/j.saa.2013.08.015
 25. B. Vellaichamy and P. Periakaruppan, *RSC Adv.* **2016**, *6*, 31653–31660.
 26. N. Isa, S. H. Sarijo, A. Aziz and Z. Lockman: AIP Conference Proceedings, AIP Publishing, **2017**, pp. 070001.
 27. A. Rajan, V. Vilas and D. Philip, *J. Mol. Liq.* **2015**, *207*, 231–236. DOI:10.1016/j.molliq.2015.03.023
 28. S. Patra, A. N. Naik, A. K. Pandey, D. Sen, S. Mazumder and A. Goswami, *Appl Catal A-Gen.* **2016**, *524*, 214–222. DOI:10.1016/j.apcata.2016.07.001
 29. N. P. B. Tan, C. H. Lee and P. Li, *J. Polym.* **2016**, *8*, 105.
 30. Z.-J. Jiang, C.-Y. Liu and L.-W. Sun, *J. PHYS. CHEM. B.* **2005**, *109*, 1730–1735. DOI:10.1021/jp046032g
 31. Z. Qu, W. Huang, M. Cheng and X. Bao, *J. PHYS. CHEM. B.* **2005**, *109*, 15842–15848. DOI:10.1021/jp050152m
 32. Y. Wu, C. Li, J. Bai and J. Wang, *Results in physics.* **2017**, *7*, 1616–1622.
 33. M. Choi, Z. Wu and E. Iglesia, *J. Am. Chem. Soc.* **2010**, *132*, 9129–9137. DOI:10.1021/ja102778e
 34. R. Poredy, E. J. García-Suárez, A. Riisager and S. Kegnæs, *Dalton Trans.* **2014**, *43*, 4255–4259. DOI:10.1039/C3DT52499J
 35. B. Naik, V. S. Prasad and N. N. Ghosh, *Powder Technol.* **2012**, *232*, 1–6. DOI:10.1016/j.powtec.2012.07.052
 36. M. J. Beier, T. W. Hansen and J.-D. Grunwaldt, *J. Catal.* **2009**, *266*, 320–330. DOI:10.1016/j.jcat.2009.06.022
 37. S. Deshmukh, R. Dhokale, H. Yadav, S. Achary and S. Delekar, *Appl Surf Sci.* **2013**, *273*, 676–683. DOI:10.1016/j.apsusc.2013.02.110
 38. H. Sakai, T. Kanda, H. Shibata, T. Ohkubo and M. Abe, *J. Am. Chem. Soc.* **2006**, *128*, 4944–4945. DOI:10.1021/ja058083c
 39. L. Kundakovic and M. Flytzani-Stephanopoulos, *Appl Catal A-Gen.* **1999**, *183*, 35–51. DOI:10.1016/S0926-860X(99)00043-5
 40. L. Ai and J. Jiang, *Bioresour Technol.* **2013**, *132*, 374–377. DOI:10.1016/j.biortech.2012.10.161
 41. H. Le Pape, F. Solano-Serena, P. Contini, C. Devillers, A. Maftah and P. Leprat, *Carbon.* **2002**, *40*, 2947–2954. DOI:10.1016/S0008-6223(02)00246-4
 42. S. Ma, R. Luo, J. I. Gold, Z. Y. Aaron, B. Kim and P. J. Kenis, *J. Mater. Chem. A.* **2016**, *4*, 8573–8578. DOI:10.1039/C6TA00427J
 43. Y. Liu, G. Wu and Y. Cui, *Appl. Organomet. Chem.* **2013**, *27*, 206–208. DOI:10.1002/aoc.2950
 44. C. Li, X. Li, X. Duan, G. Li and J. Wang, *Journal of Colloid and Interface Science.* **2014**, *436*, 70–76. DOI:10.1016/j.jcis.2014.08.051
 45. I. Fatimah and R. Herianto, *Oriental Journal of Chemistry.* **2018**, *34*, 857–862.
 46. M. Zou, M. Du, H. Zhu, C. Xu and Y. Fu, *Journal of Physics D: Applied Physics.* **2012**, *45*, 325302. DOI:10.1088/0022-3727/45/32/325302
 47. V. Vergaro, E. Abdullayev, A. Zeitoun, G. Giovinazzo, A. Santino, R. Cingolani, Y. M. Lvov and S. Leporatti, *J. Microencapsul.* **2008**, *25*, 376.
 48. D. Mills, *Faseb J.* **2014**, *28*, 87.4.

49. R. D. White, D. V. Bavykin and F. C. Walsh, *Nanotech.* **2012**, 23, 065705. DOI:10.1088/0957-4484/23/6/065705
50. P. Sudhakar and H. Soni, *J Environ Chem Eng.* **2018**, 6, 28–36.
51. E. Abdullayev and Y. Lvov, *J. Nanosci. Nanotechnol.* **2011**, 11, 10007–10026. DOI:10.1166/jnn.2011.5724
52. P. Sun, G. Liu, D. Lv, X. Dong, J. Wu and D. Wang, *J. Appl Polym Sci.* **2016**, 133.
53. J. Zhang, Y. Zhang, Y. Chen, L. Du, B. Zhang, H. Zhang, J. Liu and K. Wang, *Ind Eng Chem Res.* **2012**, 51, 3081–3090. DOI:10.1021/ie202473u
54. S. Li, F. Tang, H. Wang, J. Feng and Z. Jin, *RSC Advances.* **2018**, 8, 10237–10245. DOI:10.1039/C8RA00423D
55. S. Kumar-Krishnan, A. Hernandez-Rangel, U. Pal, O. Ceballos-Sanchez, F. Flores-Ruiz, E. Prokhorov, O. A. de Fuentes, R. Esparza and M. Meyyappan, *Journal of Materials Chemistry B.* **2016**, 4, 2553–2560. DOI:10.1039/C6TB00051G
56. D. Rawtani, Y. Agrawal and P. Prajapati, *BioNanoScience.* **2013**, 3, 73–78. DOI:10.1007/s12668-012-0071-4
57. Y. Ren, S. Zhang, X. Wan, Y. Zhan, J. Zhang and Y. He, *Polymer Engineering & Science.* **2018**, 58, 2227–2236. DOI:10.1002/pen.24840
58. S. Jana, A. V. Kondakova, S. N. Shevchenko, E. V. Sheval, K. A. Gonchar, V. Y. Timoshenko and A. N. Vasiliev, *Colloids and Surfaces B: Biointerfaces.* **2017**, 151, 249–254. DOI:10.1016/j.colsurfb.2016.12.017
59. Y. Zhang, Y. Chen, H. Zhang, B. Zhang and J. Liu, *Journal of inorganic biochemistry.* **2013**, 118, 59–64. DOI:10.1016/j.jinorgbio.2012.07.025
60. X. Zeng, Q. Wang, H. Wang and Y. Yang, *Journal of Materials Science.* **2017**, 52, 8391–8400. DOI:10.1007/s10853-017-1073-y
61. P. Liu and M. Zhao, *Applied Surface Science.* **2009**, 255, 3989–3993. DOI:10.1016/j.apsusc.2008.10.094
62. T. K. Das, S. Ganguly, P. Bhawal, S. Remanan, S. Mondal and N. Das, *Applied Nanoscience.* **2018**, 8, 173–186. DOI:10.1007/s13204-018-0658-3
63. H. Zhu, M. Du, M. Zou, C. Xu and Y. Fu, *Dalton Trans.* **2012**, 41, 10465–10471. DOI:10.1039/c2dt30998j
64. E. K. Kim, J. Won, J.-y. Do, S. D. Kim and Y. S. Kang, *J. Cult Herit.* **2009**, 10, 214–221. DOI:10.1016/j.culher.2008.07.008
65. H.-T. Lu, *Colloid J.* **2013**, 75, 311–318. DOI:10.1134/S1061933X13030125
66. E. Joussein, S. Petit, J. Churchman, B. Theng, D. Righi and B. Delvaux, De Gruyter, **2005**.
67. S. Levis and P. Deasy, *Int J Pharm.* **2002**, 243, 125–134. DOI:10.1016/S0378-5173(02)00274-0
68. B. Theng, M. Russell, G. Churchman and R. Parfitt, *Clays Clay Miner.* **1982**, 30, 143–149. DOI:10.1346/CCMN.1982.0300209
69. J. Ellison, G. Wykoff, A. Paul, R. Mohseni and A. Vasiliev, *Colloid Surface A.* **2014**, 447, 67–70.
70. A. A. J. Ranchani, V. Parthasarathy, A. A. Devi, B. Meenarathi and R. Anbarasan, *Appl Nanosci.* **2017**, 7, 577–588. DOI:10.1007/s13204-017-0595-6
71. S. Lijuan, H. Jiang, A. Songsong, J. ZHANG, J. ZHENG and R. Dong, *Chinese Journal of Catalysis.* **2013**, 34, 1378–1385.
72. S. Wunder, F. Polzer, Y. Lu, Y. Mei and M. Ballauff, *The Journal of Physical Chemistry C.* **2010**, 114, 8814–8820. DOI:10.1021/jp101125j
73. S. Cazaux, P. Caselli, A. Tielens, J. Le Bourlot and M. Walmsley: *Journal of Physics: Conference Series, IOP Publishing.* **2005**, pp. 155.
74. H. Hilal, G. Y. M. Nour and A. Zyoud, Book Photodegradation of Methyl orange and phenazo- pyridine HCl with direct solar light using ZnO and activated carbon supported ZnO, 2009.
75. H. Hilal, L. Majjad, N. Zaatar and A. El-Hamouz, *Solid State Sciences.* **2007**, 9, 9–15. DOI:10.1016/j.solidstatesciences.2006.10.001
76. Y. Zhao, E. Abdullayev and Y. Lvov, *IOP Conference Series: Materials Science and Engineering, IOP Publishing.* **2014**, pp. 012043.
77. A. Zainal Abidin, N. H. H. Abu Bakar, E. P. Ng and W. L. Tan, *Journal of Taibah University for Science.* **2017**, 11, 1070–1079. DOI:10.1016/j.jtusci.2017.06.004
78. S. Joseph and B. Mathew, *Journal of Molecular Liquids* **2015**, 204, 184–191. DOI:10.1016/j.molliq.2015.01.027
79. X. Liu, M. Liang, M. Liu, R. Su, M. Wang, W. Qi and Z. He, *Nanoscale Res Lett.* **2016**, 11, 440. DOI:10.1186/s11671-016-1647-7
80. N. Basavegowda, K. Mishra and Y. R. Lee, *J. Alloy Compd.* **2017**, 701, 456–464. DOI:10.1016/j.jallcom.2017.01.122

Povzetek

Sintetizirali in okarakterizirali smo nanodelce srebra z vključenimi haloizitnimi nanocevkami (Ag/HNT) in jih uporabili kot katalizator za redukcijo rodamina 6G (Rh6G) in metiloranža (MO). 3-glicidilokipoiltrimetoksisilan in trietil-tetraamin smo uspešno uporabili za kemijsko modifikacijo površine HNT na katero reducirani Ag⁺ ioni vezali v obliki nanodelcev (AgNP). Strukturo HNT prekritih z AgNP smo karakterizirali s FTIR, XRD, TEM, FE-SEM ter EDM in pokazali, da so nanodelci srebra veliki 10–15 nm. Katalitsko sposobnost reduciranja Rh6G in MO z Ag/HNT smo spremljali z UV-vis spektroskopijo, s čimer smo lahko primerjali hitrost katalizirane in nekatalizirane reakcije. Konstanta reakcijske hitrosti katalizirane reakcije je znašala za redukcijo Rh6G 0.224 min⁻¹, za redukcijo MO pa 0.222 min⁻¹, medtem ko je bila hitrost nekatalizirane reakcije le 0.049 min⁻¹ oziroma 0.014 min⁻¹. Ag/HNT katalizator smo uporabili 6 krat, ne da bi zaznali upad katalitske aktivnosti. Rezultati kažejo možnost obstoja Ag/HNT z izboljšanimi redukcijskimi sposobnostmi, v primeru njihove funkcionalizacije.

Scientific paper

Directed Search of Biologically Active Compounds among Hydrogenated Isoindolylalkyl(alkylaryl-,aryl-)carboxylic Acids with Quinazoline Fragment that Modify the Carbohydrate Metabolism: Design, Synthesis and Modification

Yulya Victorivna Martynenko,¹ Oleksii Mykolayovich Antypenko,¹
Oleksandr Anatolievich Brazhko,² Irina Borisivna Labenska²
and Sergii Ivanovich Kovalenko^{1,*}

¹Organic and Bioorganic Chemistry Department, Zaporizhzhya State Medical University, 26, Mayakovsky Ave., Zaporizhzhya, 69035, Ukraine

²Chemistry Department, Zaporizhzhia National University, 62, Gogol st., Zaporizhzhia, 69095, Ukraine

* Corresponding author: E-mail: kovalenkoserhiy@gmail.com

Received: 10-01-2018

Abstract

An effective synthesis of (3H-quinazoline-4-ylidene)hydrazides of *N*-carboxyalkyl-(arylalkyl-,aryl-)isoindoline-1,3-diones, using activated *N*-protected aminoacids and 4-hydrazinoquinazoline was proposed in the framework methodology of directed search of hypoglycemic agents (fragment-oriented design, molecular docking). These hydrazides prepared *via* cyclocondensation under acid catalysis were converted to the corresponding 2-([1,2,4]triazolo[1,5-*c*]quinazoline-2-yl)-alkyl-(alkylaryl-,aryl)-hydroisoindole-1,3(2*H*)-diones. The structure of synthesized compounds was established using IR, ¹H and ¹³C NMR spectroscopy and LC-MS and the features of spectral pattern were discussed. The results of pharmacological screening revealed a series of compounds, that are short-acting hypoglycemic agents like prandial regulators of glucose (Mitiglinide). The SAR analysis showed, that the introduction of a hydrogenated 1,3-dioxoisoindole moiety bonded through linker groups with 4-hydrazinoquinazoline and triazolo[1,5-*c*]quinazoline cycles is reasonable in the context of searching for short-acting hypoglycemic agents and requires further research.

Keywords: (3H-quinazoline-4-ylidene)hydrazides of *N*-carboxyalkyl-(arylalkyl-,aryl-)isoindoline-1,3-diones; 2-([1,2,4]triazolo[1,5-*c*]quinazoline-2-yl)-alkyl-(alkylaryl-,aryl)-hydroisoindole-1,3(2*H*)-diones; directed search; physico-chemical properties; spectral features; hypoglycemic activity

1. Introduction

Quinazoline derivatives and their condensed analogues have always attracted the attention of medicinal chemists as objects of advanced research, aimed at the elaboration of new drugs. This fact is explained by the high biological activity of natural,^{1–3} as well as synthetic quinazolines^{4–19} and, undoubtedly, their wide ability to chemical modification.^{10–13,18} In recent years, the interest for this heterocyclic system has increased greatly since the introduction of *in silico* approaches to the drug search strategy, combinatorial chemistry and high-throughput screening.

These approaches have led to the discovery and creation of a number of lead-compounds and original drugs with antitumor, antihypertensive, diuretic, hypoglycemic and other biological activities.^{4,6,7,17} It should be noted, that information about the biological targets and fragment-oriented design based on them^{20,21} has played a key role in the creation of therapeutic molecule data. Using the above-mentioned search strategy we performed an attempt to one of the fragments-oriented design approaches based on the available results of hypoglycemic activity of *N*-carboxyalkyl-(arylalkyl-,aryl-) substituted hydrogenated isoindoline-1,3-diones,²² known hypoglycemic agents

(Mitiglinide^{23,24} and Apabetalone²⁵) and virtual screening. To enhance the pharmacological activity a combination in the same molecule of these compounds with a suitable pharmacophore quinazoline fragment was used (Figure 1).

Thus, the aim of this work is a directed search for biologically active compounds, that modify the carbohydrate metabolism, based on unknown (3*H*-quinazoline-4-ylidene)hydrazides of hydrogenated isoindolylalkyl(alkylaryl-,aryl-)carboxylic acids, their further modification toward triazoloquinazolines, the study of their structural peculiarities and establishment of the structure-activity relationship (SAR) for further optimization of their structure.

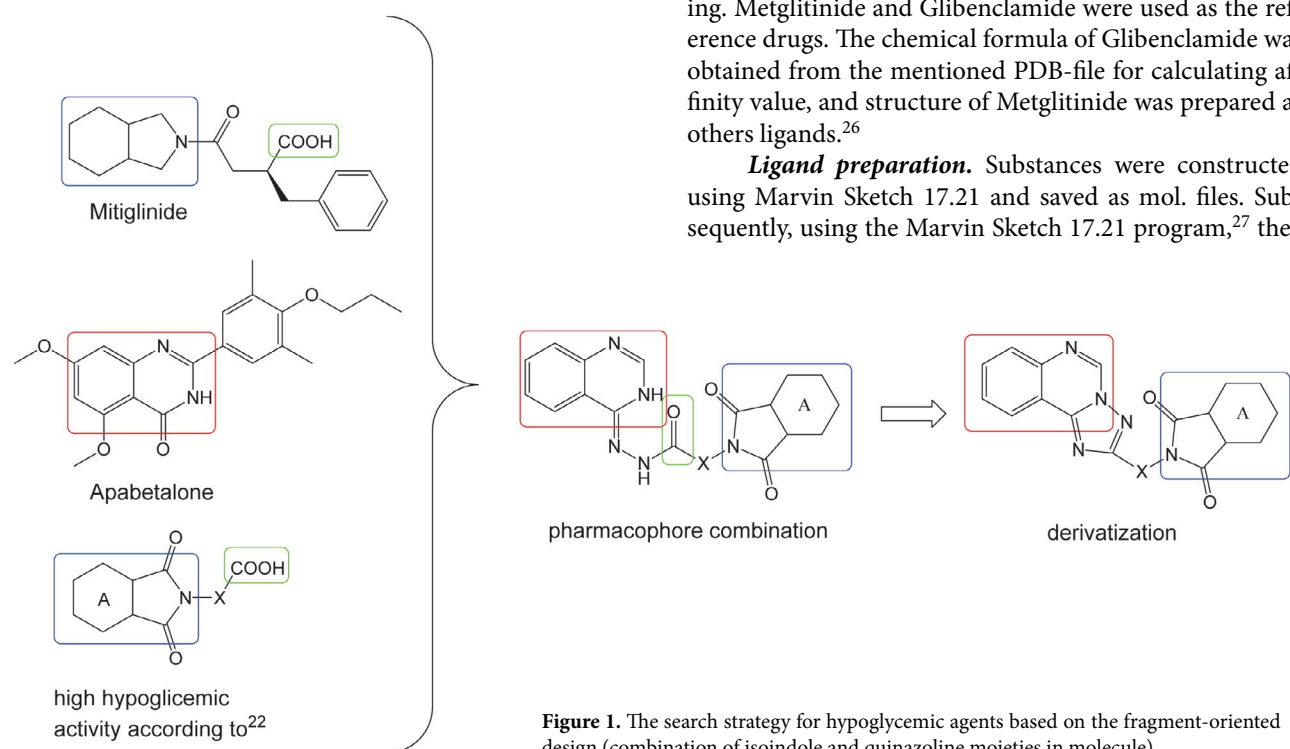


Figure 1. The search strategy for hypoglycemic agents based on the fragment-oriented design (combination of isoindole and quinazoline moieties in molecule).

2. Experimental Section

2.1. Chemistry

General Methods

Melting points were determined in open capillary tubes in a Stuart SMP30 apparatus and are uncorrected. The elemental analyses (C, H, N) were performed using the ELEMENTAR vario EL cube analyzer. IR spectra (4000–600 cm^{-1}) were recorded on a Bruker ALPHA FT-IR spectrometer using a module ATR eco ZnSe. ^1H NMR spectra (400 MHz) were recorded on Varian-Mercury 400 spectrometer with SiMe_4 as the internal standard in $\text{DM-SO}-d_6$ solution. LC-MS spectra were recorded using chromatography/mass spectrometric system, which consists of a high-performance liquid chromatograph Agilent 1100 Series equipped with diode-matrix and a mass-selective

detector Agilent LC/MSD SL (atmospheric pressure chemical ionization – APCI). Ionization mode was a concurrent scanning of positive and negative ions in the mass range 80–1000 m/z .

Substances **1a–i** were synthesized according to the reported procedures.²² Other starting materials and solvents were obtained from commercially available sources and used without additional purification.

2.2. Molecular Docking

Pancreatic beta-cell KATP channel (PDB ID - 6BAA) was used as the target protein to carry out molecular docking. Metglitinide and Glibenclamide were used as the reference drugs. The chemical formula of Glibenclamide was obtained from the mentioned PDB-file for calculating affinity value, and structure of Metglitinide was prepared as others ligands.²⁶

Ligand preparation. Substances were constructed using Marvin Sketch 17.21 and saved as mol. files. Subsequently, using the Marvin Sketch 17.21 program,²⁷ they

were optimized with the help of the molecular-mechanical MM+ algorithm in conjunction with the semiempirical PM3 method of molecular modeling with the maximum number of cycles and the Polak–Ribiere algorithm. Molecular mechanics is used to obtain more realistic geometric values for most organic molecules, since it has a large number of parameters. The next step was to re-optimize MM+-optimized structures with using semiempirical PM3 molecular modeling method and the preservation of molecules in PDB files. Using Auto Dock Tools-1.5.6 these PDB files were converted to PDBQT while the rotational number of link options was typical.

Protein preparation. PDB files have been downloaded from a data bank of proteins.²⁶ Discovery Studio v17.2.0.16349 was used to remove water molecules and ligands from the file. After that, the protein was saved as PDB

file. Polar hydrogen atoms were added and the protein was saved as PDBQT into Auto Dock Tools-1.5.6. The search grid for docking the protein was set as following: center_x = 113, center_y = 191, center_z = 128, size_x = 22, size_y = 22, size_z = 22. Vina was used for proper docking. Discovery Studio v17.2.0.16349 was used for visualization.²⁸

2. 3. Pharmacology

2. 3. 1. Hypoglycemia Activity Test

Study of hypoglycemic activity was conducted on 150 Wistar white rats (male, weight 100–180 g, age 3.5 month) which were obtained from nursery of PE Biomodelservice (Kiev, Ukraine). Experiments on animals were done according to the bioethics principles.²³ Selected after quarantine animals by random sampling were divided in groups of 6 male rats on the assumption of absence of external signs of diseases and homogeneity by weight ($\pm 15\%$). Experimental animals were not fed during 12 hours before injection of studied compounds. The weight of all animals was measured before experiment. Intra-gastric injection of studied compounds was conducted using atraumatic probe as water solution or finely dispersed suspension stabilized by Tween-80 in a dose of 10 mg/kg. Intact and control groups received equivalent volume of water by the same way. Hypoglycemic activity of the synthesized compounds was evaluated *via* changes of glucose level before and after injection of the studied substances. Measurements of glucose level were carried out 2, 4 and 6 hours after injection. Metformine (50 mg/kg) was used as a reference drug.

Before the experiment the compounds were injected as an aqueous solution or 3–5% micronized water suspension, stabilized by Tween-80 in a dose of 10 mg/kg using atraumatic probe in order to identify prandial hypoglycemic agents. Subsequently, after 60 minutes, 40% glucose solution was injected to rats at a dose of 3000 mg/kg. Hypoglycemic activity of the synthesized compounds was evaluated *via* changes of glucose level before and after injection of substances. Measurements of glucose level were carried out in 15, 30, 60 and 120 minutes after injection.

Statistical analysis was done using standard software complex, namely Microsoft Office Excel 2003 and STATISTICA® for Windows 6.0 (StatSoft Inc., № AXXR712D-833214FAN5). For each estimated value arithmetic mean (M), and standard error of the mean ($\pm m$) were defined. During verification of statistical hypothesis, null hypothesis were declined if statistical criterion $p < 0.05$.

General Procedure for the Synthesis of (3*H*-Quinazoline-4-ylidene)hydrazides *N*-Carboxyalkyl-(arylalkyl-, aryl-)isoindoline-1,3-diones (3*a*-*i*)

1.62 g (0.01 mol) of *N,N'*-carbonyldiimidazole was added to a suspension of 0.01 mol of the corresponding 2-(isoindoline-1,3-dione)alkyl-(alkyl-, arylalkyl-, aryl-) carboxylic acids (1*a*-*i*) in 30 mL of dioxane. The mixture

was kept at temperature 60–70 °C for 50–60 minutes until the carbon dioxide was completely released. After addition of 1.6 g (0.01 mol) 4-hydrazinoquinazoline (2*a*) the mixture was kept at a room temperature overnight or at 80 °C for 1.5 hour. Dioxane was distilled off. The water was added and the mixture was neutralized by 0.1 M aqueous hydrochloric acid to pH 6–7. The solid product was filtered in the case of residue formation. If it was necessary, compounds were crystallized.

2-(1,3-Dioxooctahydro-2*H*-isoindole-2-yl)-*N'*-(quinazoline-4(3*H*)-ylidene)propanehydrazide (3*a*). Yield 61.9%; m.p. 100–102 °C; IR (cm⁻¹): 3297, 2917, 2849, 2693, 2353, 1704, 1615, 1550, 1472, 1386, 1194, 1130, 984, 759, 689; ¹H NMR δ (ppm): 11.46 (s, 1H, 3-NH), 10.16/10.03 (s, 1H, NHCO), 7.80–7.61 (m, 2H, H-2,5), 7.37 (t, *J* = 7.9 Hz, 1H, H-7), 7.19 (t, *J* = 7.9 Hz, 1H, H-6), 7.10 (d, *J* = 8.0 Hz, 1H, H-8), 5.15/4.75 (q, *J* = 7.0 Hz, 1H, CHCH₃), 2.82–2.65 (m, 2H, isoindole H-3*a*,7*a*), 1.85–1.64 (m, 4H, isoindole H-4,4',7,7'), 1.58/1.51 (d, *J* = 7.1 Hz, 3H, CHCH₃), 1.47–1.25 (m, 4H, isoindole H-5,5',6,6'); LC-MS: *m/z* = 367 [M]⁺; Anal. Calcd. for C₁₉H₂₁N₅O₃: C, 62.11; H, 5.76; N, 19.06. Found: C, 62.16; H, 5.82; N, 19.13.

4-((1,3-Dioxooctahydro-2*H*-isoindole-2-yl)methyl)-*N'*-(quinazoline-4(3*H*)-ylidene)benzohydrazide (3*b*). Yield: 72.6%; m.p. 263–265 °C; IR (cm⁻¹): 3309, 3180, 3130, 2918, 2953, 2854, 2779, 2714, 1698, 1612, 1525, 1471, 1374, 1341, 1310, 1164, 1093, 906, 762, 690, 662, 646; ¹H NMR δ (ppm): 11.51 (s, 1H, 3-NH), 10.52 (s, 1H, NHCO), 9.01–6.44 (m, 9H, H-2,5,6,7,8, Ar H-2,3,5,6), 4.62 (s, 2H, -CH₂-), 2.98–2.89 (m, 2H, isoindole H-3*a*,7*a*), 1.90–1.58 (m, 4H, isoindole H-4,4',7,7'), 1.50–1.29 (m, 4H, isoindole H-5,5',6,6'); LC-MS: *m/z* = 430 [M+1], 431 [M+2]; Anal. Calcd. for C₂₄H₂₃N₅O₃: C, 67.12; H, 5.40; N, 16.31. Found: C, 67.19; H, 5.48; N, 16.38.

4-(1,3-Dioxooctahydro-2*H*-isoindole-2-yl)-*N'*-(quinazoline-4(3*H*)-ylidene)benzohydrazide (3*c*). Yield: 84.3%; m.p. 187–190 °C; IR (cm⁻¹): 3421, 3280, 2993, 2913, 2855, 1698, 1626, 1537, 1493, 1475, 1385, 1167, 1129, 759, 687, 615; ¹H NMR δ (ppm): 11.60 (s, 1H, 3-NH), 10.65 (s, 1H, NHCO), 8.58–6.95 (m, 9H, H-2,5,6,7,8, Ar H-2,3,5,6), 3.15–3.08 (m, 2H, isoindole H-3*a*,7*a*), 1.97–1.70 (m, 4H, isoindole H-4,4',7,7'), 1.57–1.35 (m, 4H, isoindole H-5,5',6,6'); LC-MS: *m/z* = 416 [M+1], 417 [M+2]; Anal. Calcd. for C₂₃H₂₁N₅O₃: C, 66.49; H, 5.10; N, 16.86. Found: C, 66.54; H, 5.16; N, 16.93.

2-(1,3-Dioxo-1,3,3*a*,4,7,7*a*-hexahydro-2*H*-isoindole-2-yl)-*N'*-(quinazoline-4(3*H*)-ylidene)propanehydrazide (3*d*). Yield: 71.8%; m.p. 201–203 °C, IR (cm⁻¹): 3289, 3214, 3069, 3012, 2960, 2910, 2886, 2850, 2780, 2683, 2410, 1702, 1603, 1566, 1466, 1420, 1383, 1325, 1198, 1117, 927, 776, 755, 685, 661; ¹H NMR δ (ppm): 11.49 (s, 1H, 3-NH), 10.09/10.00 (s, 1H, NHCO), 7.81–7.65 (m, 2H,

H-2,5), 7.49 (t, $J = 7.8$ Hz, 1H, H-7), 7.20 (t, $J = 7.8$ Hz, 1H, H-6), 7.11 (d, $J = 8.4$ Hz, 1H, H-8), 5.89 (m, 2H, isoindole H-5,6), 5.13/4.71 (q, $J = 7.9, 7.2$ Hz, 1H, CHCH₃), 3.05–2.90 (m, 2H, isoindole H-3a,7a), 2.46–2.01 (m, 4H, isoindole H-4,4',7,7'), 1.44 (d, $J = 7.1$ Hz, 3H, CHCH₃); LC-MS: $m/z = 368$ [M+3]; Anal. Calcd. for C₁₉H₁₉N₅O₃: C, 62.46; H, 5.24; N, 19.17. Found: C, 62.49; H, 5.28; N, 19.23.

3-(1,3-Dioxo-1,3,3a,4,7,7a-hexahydro-2H-isoindole-2-yl)-N²-(quinazoline-4(3H)-ylidene)propanehydrazide (3e). Yield: 68.4%; m.p. 135–137 °C, IR (cm⁻¹): 3489, 3409, 3343, 3230, 3128, 3106, 3078, 3010, 2988, 2939, 2859, 2699, 1693, 1611, 1527, 1471, 1440, 1379, 1106, 755, 687; ¹H NMR δ (ppm): 11.53 (s, 1H, 3-NH), 10.03/9.52 (s, 1H, NHCO), 7.88 (d, $J = 7.2$ Hz, 1H, H-5), 7.74 (s, 1H, H-2), 7.37 (t, $J = 7.3$ Hz, 1H, H-7), 7.20 (t, $J = 7.5$ Hz, 1H, H-6), 7.13 (d, $J = 7.8$ Hz, 1H, H-5), 5.95–5.76 (m, 2H, isoindole H-5,6), 3.67 (m, 2H, CH₂CH₂N), 3.24–3.08 (m, 2H, isoindole 3a,7a), 2.82 (t, $J = 7.5$ Hz, 2H, CH₂CH₂N), 2.48–2.11 (m, 4H, isoindole H-4,4',7,7'); LC-MS: $m/z = 366$ [M+1], 367 [M+2]; Anal. Calcd. for C₁₉H₁₉N₅O₃: C, 62.46; H, 5.24; N, 19.17. Found: C, 62.43; H, 5.18; N, 19.13.

4-(1,3-Dioxo-1,3,3a,4,7,7a-hexahydro-2H-isoindole-2-yl)-N²-(quinazoline-4(3H)-ylidene)benzohydrazide (3f). Yield: 94.3%; m.p. 261–263 °C, IR (cm⁻¹): 3418, 3311, 3205, 3168, 3120, 3089, 3056, 3023, 2979, 2915, 2850, 1704, 1612, 1536, 1495, 1474, 1445, 1386, 1177, 845, 759, 687, 625; ¹H NMR δ (ppm): 11.58 (s, 1H, 3-NH), 10.65/9.99 (s, 1H, NHCO), 8.55–7.03 (m, 9H, H-2,5,6,7,8, Ar H-2,3,5,6), 6.15–5.81 (m, 2H, isoindole H-5,6), 3.39–3.19 (m, 2H, isoindole H-3a,7a), 2.69–2.20 (m, 4H, isoindole H-4,4',7,7'); LC-MS: $m/z = 414$ [M+1], 415 [M+2]; Anal. Calcd. for C₂₃H₁₉N₅O₃: C, 66.82; H, 4.63; N, 16.94. Found: C, 66.89; H, 4.70; N, 17.01.

2-(1,3-Dioxo-1,3,3a,4,7,7a-hexahydro-2H-4,7-methanoisoindole-2-yl)-N²-(quinazoline-4(3H)-ylidene)acetohydrazide (3g). Yield: 71.6%; m.p. 168–170 °C, IR (cm⁻¹): 3462, 3292, 3208, 3168, 3133, 3089, 3054, 3029, 2994, 2904, 2858, 2783, 1728, 1632, 1539, 1489, 1477, 1439, 1391, 1173, 845, 761, 683, 629; ¹H NMR δ (ppm): 11.51 (s, 1H, 3-NH), 10.27/9.66 (s, 1H, -NHCO-), 7.90 (d, $J = 7.2$ Hz, 1H, H-5), 7.80 (s, 1H, H-2), 7.40 (t, $J = 7.3$ Hz, 1H, H-7), 7.19 (t, $J = 7.4$ Hz, 1H, H-6), 7.13 (d, $J = 8.0$ Hz, 1H, H-8), 6.18–6.07 (m, 2H, isoindole H-5,6), 4.73/4.37 (s, 2H, CH₂), 3.50–3.38 (m, 2H, isoindole H-3a,7a), 3.39–3.27 (m, 2H, isoindole H-4,7), 1.76–1.55 (m, 2H, isoindole H-8,8'); LC-MS: $m/z = 364$ [M+1], 365 [M+2]; Anal. Calcd. for C₁₉H₁₇N₅O₃: C, 62.80; H, 4.72; N, 19.27. Found: C, 62.87; H, 4.77; N, 19.34.

4-(1,3-Dioxo-1,3,3a,4,7,7a-hexahydro-2H-4,7-methanoisoindole-2-yl)methyl)-N²-(quinazoline-4-yl)benzohydrazide (3h). Yield: 88.1%; m.p. 265–267 °C; IR (cm⁻¹): 3376, 3060, 2990, 2962, 2914, 2849, 2690, 1695, 1611, 1525,

1471, 1375, 1339, 1167, 1093, 907, 763, 722, 690, 659, 644; ¹H NMR δ (ppm): 11.43 (s, 1H, 3-NH), 10.55 (s, 1H, s, 1H, -NHCO), 8.18 (d, $J = 7.4$ Hz, 1H, H-5), 7.94–7.72 (m, 3H, H-2, Ph H-2,6), 7.55 (t, $J = 7.3$ Hz, 1H, H-7), 7.44–7.16 (m, 4H, H-6,8, Ph H-3,5), 6.04–5.86 (m, 2H, isoindole H-5,6), 4.46 (s, 2H, -CH₂-), 3.42–3.34 (m, 2H, isoindole H-3a,7a), 3.34–3.29 (m, 2H, isoindole H-4,7), 1.74–1.48 (m, 2H, isoindole H-8,8'); LC-MS: $m/z = 440$ [M+1], 441 [M+2]; Anal. Calcd. for C₂₅H₂₁N₅O₅: C, 68.33; H, 4.82; N, 15.94. Found: C, 68.41; H, 4.88; N, 16.01.

4-(1,3-Dioxo-1,3,3a,4,7,7a-hexahydro-2H-4,7-methanoisoindole-2-yl)-N²-(quinazoline-4-yl)benzohydrazide (3i). Yield: 99.9%; m.p. 187–189 °C; IR (cm⁻¹): 3476, 3310, 3284, 3028, 2982, 2929, 2856, 2780, 1693, 1614, 1548, 1495, 1474, 1389, 1185, 760, 744, 721, 688, 615; ¹H NMR δ (ppm): 10.63 (s, -NHCO-), 8.21 (d, $J = 7.2$ Hz, 1H, H-5), 8.03–7.89 (m, 3H, H-2, Ph H-2,6), 7.59 (t, $J = 7.4$ Hz, 1H, H-7), 7.50–7.34 (m, 2H, H-6,8), 7.26 (d, $J = 7.9$ Hz, 2H, Ph H-3,5), 6.31–6.19 (m, 2H, isoindole H-5,6), 3.60–3.48 (m, 2H, isoindole H-7a,3a), 3.46–3.28 (m, 2H, isoindole H-4,7), 1.82–1.54 (m, 2H, isoindole H-8,8'); LC-MS: $m/z = 426$ [M+1], 428 [M+3]; Anal. Calcd. for C₂₄H₁₉N₅O₃: C, 67.76; H, 4.50; N, 16.46. Found: C, 67.83; H, 4.58; N, 16.53.

The synthesized compounds are yellow, soluble in DMF, DMSO, dioxane, slightly soluble in alcohol, insoluble in water.

General Procedure for the Synthesis of 2-([1,2,4]Triazolo[1,5-*c*]quinazoline-2-yl)alkyl-(alkylaryl-,aryl-)hydroisoindole-1,3(2H)-diones 4a-i

0.01 mol of the corresponding hydrazides **3a-i** was dissolved in 25 mL of glacial acetic acid and was refluxed for 6 hours. The mixture was cooled. In the case of the residue formation it was filtered off. In the case of a solution, acetic acid was removed by distillation under vacuum. The resulting residue was stirred with a mixture of methanol and water and the precipitate was filtered. If necessary, the crude product can be crystallized.

(2-(1-([1,2,4]Triazolo[1,5-*c*]quinazoline-2-yl)ethyl)hexahydro-1H-isoindole-1,3(2H)-dione (4a). Yield: 62.9%; m.p. 200–203 °C; IR (cm⁻¹): 2922, 2843, 2690, 2359, 1705, 1381, 1342, 1195, 899, 770; ¹H NMR δ (ppm): 9.40 (s, 1H, H-5), 8.39 (d, $J = 7.6$ Hz, 1H, H-10), 8.03 (d, $J = 7.9$ Hz, 1H, H-7), 7.88 (t, $J = 8.1$ Hz, 1H, H-8), 7.76 (t, $J = 7.3$ Hz, 1H, H-9), 5.49 (q, $J = 6.7$ Hz, 1H, CHCH₃), 3.01–2.86 (m, 2H, isoindole 3a,7a), 1.89 (d, $J = 7.0$ Hz, 3H, CHCH₃), 1.86–1.69 (m, 4H, isoindole H-4,4',7,7'), 1.59–1.23 (m, 4H, isoindole H-5,5',6,6'); ¹³C NMR δ (ppm): 179.41/179.29 (C-1,3 isoindole), 166.16 (C-2l), 150.74 (C-5), 142.69 (C-10b), 139.27 (C-6a), 132.80 (C-8), 129.63 (C-7), 128.99 (C-9), 123.46 (C-10), 117.76 (C-10a), 44.28 (-CHCH₃), 40.35 (C-3a,7a isoindole), 23.44/23.36 (C-4,7 isoindole), 21.53/21.48 (C-5,6 isoindole), 15.82 (CH₃); LC-MS: $m/z = 350$ [M+1], 352 [M+2]; Anal. Calcd. for

C₁₉H₁₉N₅O₂: C, 65.32; H, 5.48; N, 20.04. Found: C, 65.39; H, 5.52; N, 20.11.

2-(4-([1,2,4]Triazolo[1,5-*c*]quinazoline-2-yl)benzyl)hexahydro-1H-isoindole-1,3(2H)-dione (4b). Yield: 55.6%; m.p. 248–250 °C; IR (cm⁻¹): 2957, 2929, 2854, 2456, 1689, 1479, 1423, 1397, 1334, 1165, 899, 775, 742; ¹H NMR δ (ppm): 9.48 (s, 1H, H-5), 8.55 (d, *J* = 7.7 Hz, 1H, H-10), 8.26 (d, *J* = 8.1 Hz, 2H, Ar H-2,6), 8.06 (d, *J* = 8.4 Hz, 1H, H-7), 7.90 (t, *J* = 7.9 Hz, 1H, H-8), 7.81 (t, *J* = 7.6 Hz, 1H, H-9), 7.45 (d, *J* = 7.9 Hz, 2H, Ar H-3,5), 4.64 (s, 2H, CH₂), 2.98–2.93 (m, 2H, isoindole 3a,7a), 1.87–1.57 (m, 4H, isoindole H-4,4',7,7'), 1.54–1.26 (m, 4H, isoindole H-5,5',6,6'); LC-MS: *m/z* = 412 [M+1], 413 [M+2]; Anal. Calcd. for C₂₄H₂₁N₅O₂: C, 70.06; H, 5.14; N, 17.02. Found: C, 70.12; H, 5.18; N, 17.11.

2-(4-([1,2,4]Triazolo[1,5-*c*]quinazoline-2-yl)phenyl)hexahydro-1H-isoindole-1,3(2H)-dione (4c). Yield: 74.6%; m.p. > 300 °C; IR (cm⁻¹): 2989, 2924, 2863, 1701, 1514, 1477, 1445, 1357, 1164, 1122, 899, 769, 749, 713, 628; ¹H NMR δ (ppm): 9.50 (s, 1H, H-5), 8.57 (d, *J* = 7.9 Hz, 1H, H-10), 8.41 (d, *J* = 8.4 Hz, 2H, Ar H-2,6), 8.07 (d, *J* = 8.2 Hz, 1H, H-7), 7.96 (t, *J* = 7.6 Hz, 1H, H-8), 7.82 (t, *J* = 7.5 Hz, 1H, H-9), 7.49 (d, *J* = 8.4 Hz, 2H, Ar H-3,5), 3.13 (m, 2H, isoindole 3a,7a), 1.97–1.72 (m, 4H, isoindole H-4,4',7,7'), 1.57–1.39 (m, 4H, isoindole H-5,5',6,6'); LC-MS: *m/z* = 398 [M+1], 400 [M+2]; Anal. Calcd. for C₂₃H₁₉N₅O₂: C, 69.51; H, 4.82; N, 17.62. Found: C, 69.58; H, 4.91; N, 17.71.

2-(1-([1,2,4]Triazolo[1,5-*c*]quinazoline-2-yl)ethyl)-3a,4,7,7a-tetrahydro-1H-isoindole-1,3(2H)-dione (4d). Yield: 71.2%; m.p. 180–184 °C; IR (cm⁻¹): 2954, 2899, 1701, 1493, 1387, 1360, 1214, 900, 773, 706; ¹H NMR δ (ppm): 9.39 (s, 1H, H-5), 8.41 (d, *J* = 7.8 Hz, 1H, H-10), 8.02 (d, *J* = 8.3 Hz, 1H, H-7), 7.87 (t, *J* = 7.6 Hz, 1H, H-8), 7.76 (t, *J* = 7.5 Hz, 1H, H-9), 5.93 (m, 2H, isoindole H-5,6), 5.47 (q, *J* = 7.1 Hz, 1H, CHCH₃), 3.38–3.09 (m, 2H, isoindole 3a,7a), 2.58–2.49 (m, 2H, isoindole H-4,7), 2.37–2.15 (m, 2H, isoindole H-4',7'), 1.83 (d, *J* = 7.1 Hz, 3H, CHCH₃); LC-MS: *m/z* = 348 [M+1], 349 [M+2]; Anal. Calcd. for C₁₉H₁₇N₅O₂: C, 65.69; H, 4.93; N, 20.16. Found: C, 65.66; H, 4.98; N, 20.13.

2-(2-([1,2,4]Triazolo[1,5-*c*]quinazoline-2-yl)ethyl)-3a,4,7,7a-tetrahydro-1H-isoindole-1,3(2H)-dione (4e). Yield: 40.0%; m.p. 165–167 °C; IR (cm⁻¹): 2982, 2843, 2828, 2712, 1693, 1399, 1362, 1325, 1211, 1157, 1010, 929, 904, 770, 698; ¹H NMR δ (ppm): 9.37 (s, 1H, H-5), 8.43 (d, *J* = 7.6 Hz, 1H, H-10), 8.03 (d, *J* = 8.3 Hz, 1H, H-7), 7.88 (t, *J* = 7.9 Hz, 1H, H-8), 7.77 (t, *J* = 7.5 Hz, 1H, H-9), 5.94–5.66 (m, 2H, isoindole H-5,6), 3.85 (t, *J* = 7.3 Hz, 2H, CH₂CH₂N), 3.20–2.97 (m, 4H, CH₂CH₂N, isoindole 3a,7a), 2.50–2.40 (m, 2H, isoindole H-4,7), 2.32–2.06 (m, 2H, isoindole H-4',7'); LC-MS: *m/z* = 348 [M+1], 349

[M+2]; Anal. Calcd. for C₁₉H₁₇N₅O₂: C, 65.69; H, 4.93; N, 20.16. Found: C, 65.74; H, 5.02; N, 20.23.

2-(4-([1,2,4]Triazolo[1,5-*c*]quinazoline-2-yl)phenyl)-3a,4,7,7a-tetrahydro-1H-isoindole-1,3(2H)-dione (4f). Yield: 82.25%; m.p. 250–253 °C; IR (cm⁻¹): 1703, 1514, 1478, 1446, 1360, 1315, 1177, 899, 842, 751, 717, 672; ¹H NMR δ (ppm): 9.50 (s, 1H, H-5), 8.56 (d, *J* = 8.3 Hz, 1H, H-10), 8.39 (d, *J* = 8.3 Hz, 2H, Ar H-2,6), 8.20 (d, *J* = 8.5 Hz, 1H, H-7), 8.06 (t, *J* = 8.6 Hz, 1H, H-8), 7.86 (t, *J* = 8.6 Hz, 1H, H-9), 7.44 (d, *J* = 8.4 Hz, 2H, Ar H-3,5), 6.05–5.92 (m, 2H, isoindole H-5,6), 3.12–2.85 (m, 2H, isoindole 3a,7a), 2.66–2.56 (m, 2H, isoindole H-4,7), 2.37–2.23 (m, 2H, isoindole H-4',7'); LC-MS: *m/z* = 396 [M+1], 397 [M+2]; Anal. Calcd. for C₂₃H₁₇N₅O₂: C, 69.86; H, 4.33; N, 17.71. Found: C, 69.94; H, 4.41; N, 17.80.

2-([1,2,4]Triazolo[1,5-*c*]quinazoline-2-ylmethyl)-3a,4,7,7a-tetrahydro-1H-4,7-methanoisoindole-1,3(2H)-dione (4g). Yield: 85.8%; m.p. 215–217 °C; IR (cm⁻¹): 2994, 2863, 2812, 1721, 1514, 1475, 1446, 1368, 1323, 1183, 899, 846, 751, 721, 682; ¹H NMR δ (ppm): 9.40 (s, 1H, H-5), 8.43 (d, *J* = 7.6 Hz, 1H, H-10), 8.03 (d, *J* = 7.6 Hz, 1H, H-7), 7.89 (t, *J* = 7.5 Hz, 1H, H-8), 7.78 (t, *J* = 7.5 Hz, 1H, H-9), 6.15 (s, 2H, isoindole H-5,6), 4.73 (s, 2H, NCH₂), 3.46 (s, 2H, isoindole H-4,7), 3.37 (s, 2H, isoindole H-3a,7a), 1.67 (dd, *J* = 20.6, 8.0 Hz, 2H, isoindole H-8,8'); LC-MS: *m/z* = 346 [M+1], 348 [M+3]; Anal. Calcd. for C₁₉H₁₅N₅O₂: C, 66.08; H, 4.38; N, 20.28. Found: C, 66.17; H, 4.46; N, 20.32.

2-(4-([1,2,4]Triazolo[1,5-*c*]quinazoline-2-yl)benzyl)-3a,4,7,7a-tetrahydro-1H-4,7-methanoisoindole-1,3(2H)-dione (4h). Yield: 33.06%; m.p. 219–221 °C; IR (cm⁻¹): 2996, 2974, 2918, 1695, 1515, 1476, 1420, 1386, 1334, 1160, 1118, 899, 769, 756, 727, 714; ¹H NMR δ (ppm): 9.48 (s, 1H, H-5), 8.56 (d, *J* = 8.2 Hz, 1H, H-10), 8.24 (d, *J* = 7.1 Hz, 2H, 1,4-phenylene H-2,6), 8.06 (d, *J* = 8.2 Hz, 1H, H-7), 7.91 (t, *J* = 8.2 Hz, 1H, H-8), 7.81 (t, *J* = 8.2 Hz, 1H, H-7, H-9), 7.40 (d, *J* = 7.2 Hz, 1H, 1,4-phenylene H-3,4), 5.95 (s, isoindole H-5,6), 4.48 (s, 2H, -NCH₂-), 3.37 (s, 2H, isoindole H-4,7), 3.32 (s, 2H, isoindole H-3a,7a), 1.63 (dd, *J* = 22.0, 8.5 Hz, 2H, isoindole H-8,8'); ¹³C NMR δ (ppm): 177.75 (C-1,3; isoindole), 169.81 (C-2), 153.47 (C-5), 143.95 (C-10b), 137.96 (C-6a), 135.40 (C-4; Ar), 134.92 (C-5,6; isoindole), 132.76 (C-8), 131.69 (C-1a; Ar), 129.55 (C-7), 129.01 (C-9), 128.90 (C-2,6; Ar), 127.51 (C-3,5; Ar), 123.81 (C-10), 114.13 (C-10a), 52.36 (C-8; isoindole), 45.87 (C-4,7; isoindole), 44.87 (C-3a,7a; isoindole), 41.49 (-NCH₂-); LC-MS: *m/z* = 422 [M+1], 424 [M+3]; Anal. Calcd. for C₂₅H₁₉N₅O₂: C, 71.25; H, 4.54; N, 16.62. Found: C, 71.31; H, 4.58; N, 16.68.

2-(4-([1,2,4]Triazolo[1,5-*c*]quinazoline-2-yl)phenyl)-3a,4,7,7a-tetrahydro-1H-4,7-methanoisoindole-1,3(2H)-dione (4i). Yield: 86.87%; m.p. 269–271 °C;

IR (cm⁻¹): 2982, 2932, 2861, 2812, 1703, 1477, 1447, 1357, 1186, 899, 838, 778, 744, 708, 669, 608; ¹H NMR δ (ppm): 9.50 (s, 1H, H-5), 8.57 (d, *J* = 7.7 Hz, 1H, H-10), 8.36 (d, *J* = 7.8 Hz, 2H, 1,4-phenylene H-2,6), 8.07 (d, *J* = 7.7 Hz, 1H, H-7), 7.91 (t, *J* = 7.7 Hz, 1H, H-8), 7.82 (t, *J* = 7.7 Hz, 1H, H-9), 7.32 (d, *J* = 7.7 Hz, 2H, 1,4-phenylene H-3,5), 6.27 (s, 2H, isoindole H-5,6), 3.52 (s, 2H, isoindole H-4,7), 3.43 (s, 2H, isoindole H-3a,7a), 1.59 (dd, *J* = 20.7, 7.9 Hz, 2H, isoindole H-8,8'); LC-MS: *m/z* = 408 [M+1], 409 [M+2]; Anal. Calcd. for C₂₄H₁₇N₅O₂: C, 70.75; H, 4.21; N, 17.19. Found: C, 70.82; H, 4.28; N, 17.23.

The synthesized compounds are yellow, soluble in DMF, DMSO, dioxane, slightly soluble in alcohol, insoluble in water.

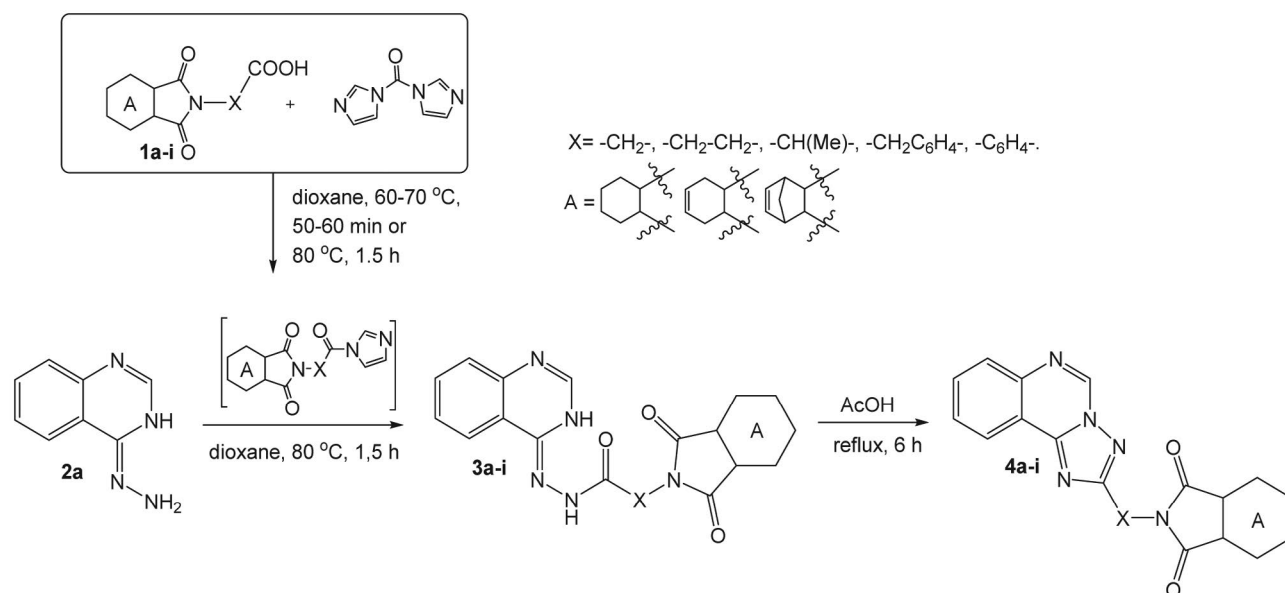
3. Results and Discussion

3.1. Chemistry

As it has been mentioned above, the combination in one molecule of more pharmacophore fragments, which are responsible for hypoglycemic effect, is interesting as well as offering further structural modifications and prospects to study such compounds in pharmacological screenings. Thus, following the search strategy, *N*-carboxyalkyl-(arylalkyl-,aryl-)isoindoline-1,3-diones **1a-i** were utilized in the reaction with *N,N'*-carbonyldiimidazole for obtaining corresponding imidazolides, in the first stage of the study (Scheme 1). The last ones formed previously unknown hydrazides **3a-i** in the reaction with 4-hydrazinoquinazoline (**2a**). The presence of anhydrous dioxane and the temperature control (not above 80 °C) is obligatory for the regioselectivity of the reaction. Reaction products **3a-i** are formed with high yields and in most cas-

es they do not require additional purification. The appearance in the ¹H NMR spectrum of low-field broad singlet of exocyclic *NH*-group proton of the quinazoline ring at the range of 11.60–11.46 ppm and *NH*-protons signal of the hydrazide fragment at the 10.65–9.52 ppm indicates the **3a-i** compounds formation. It is important to note, that some hydrazides, like **3a**, **3d–3g** are characterized by doubling of *NH*-protons signals of the hydrazide fragment due to the prototropic tautomerism in DMSO, resulting in the appearance of aromatic and aliphatic protons in the form of multiplets or double signals. Besides, the IR spectra of hydrazides **3a-i** are characterized by -C=O groups band valence vibrations of isoindole fragments at the 1728–1693 cm⁻¹ and -C(O)NH-groups (amide-I) at the 1632–1603 cm⁻¹, valence-deformation vibrations of the N-H and C-N (amide-II) bonds at the 1566–1525 cm⁻¹ as well as the band of *NH*-groups valence vibrations at the range of the 3489–3168 and 3180–2993 cm⁻¹.

The formed hydrazides **3a-i** were subjected to cyclocondensation by known methods.²⁹ As we expected, intermediate [1,2,4]triazolo[4,3-*c*]quinazolines are subjected to the recyclic isomerization by the Dimroth rearrangement under acidic catalysis conditions with 2-(2-([1,2,4]triazolo[1,5-*c*]quinazoline-2-yl)-alkyl-(arylalkyl-,aryl-)-1*H*-isoindole-1,3(2*H*)-dione formation (**4a-i**, Scheme 1).^{29,30} Signals of triazine[1,5-*c*]quinazoline ring protons, namely the low-field singlet of H-5 nucleus at the 9.50–9.37 ppm, doublet signals of ABCD-system at the 8.57–8.39 ppm (H-10) and 8.20–8.03 ppm (H-7) and triplets at the 8.06–7.87 ppm (H-8) and 7.86–7.76 ppm (H-9) are typical for the ¹H NMR spectra of compounds **4a-i**. It is important, that the aromatic proton signals of compounds **4a-i**, in comparison with compounds **3a-i**, undergo a significant paramagnetic shift that indicated the formation of an elec-



Scheme 1. The synthesis of *N*-carboxyalkyl-(arylalkyl-,aryl-)isoindoline-1,3-diones (3*H*-quinazoline-4-ylidene)hydrazides and hydrogenated 2-([1,2,4]triazolo[1,5-*c*]quinazoline-2-yl)-alkyl-(alkaryl-,aryl-)isoindole-1,3(2*H*)-diones.

tron-deficient tricyclic system. In favor of compounds **4a** and **4h** formation is also indicative the appearance of the characteristic signals of sp^2 -hybridized C-2 atoms at the 169.81–166.16 ppm and C-5 at the 153.47–150.74 ppm of triazino[1,5-*c*]quinazoline ring in the ^{13}C NMR spectra.²⁹

In addition, the ^1H NMR spectra of compounds **3a–i**, **4a–i** are characterized by signals of the corresponding hydrogenated isoindoline moieties. Thus, a totally hydrogenated isoindole moiety of compounds **3a–3c** and **4a–4c** in the ^1H NMR spectra is observed as a set of multiplet signals of axial and equatorial protons at the 3.15–2.65 ppm (H-3a, H-7a), at the 1.97–1.58 ppm (H-4,4',7,7') and at the 1.59–1.23 ppm (H-5,5',6,6'). The hexahydroisoindole moiety (compounds **3d–3f**, **4d–4f**) is in the ^1H NMR spectra characterized by multiplet signals of H-5,6 at the 6.15–5.66 ppm and a set of multiplets of axial and equatorial protons at the 3.24–2.90 ppm (H-3a, H-7a) and 2.69–2.01 ppm (H-4,4',7,7'). Whereas, the hexahydro-4,7-methanoisoindole moiety (compounds **3g–3i**) is in the ^1H NMR spectra characterized by multiplet signal of H-5,6 at the 6.31–5.86 ppm and a set of multiplet signals at the 3.60–3.34 ppm (H-3a, H-7a), 3.46–3.27 ppm (H-4,7) and 1.82–1.48 ppm (H-8,8'). The chemical shifts and multiplicity of the indicated signals in the compounds **4g–4i** differs slightly: the H-5,6 signals are recorded at the 6.27–5.95 ppm, H-4,7 at the 3.52–3.37 ppm, H-3a, H-7a at the 3.43–3.32 ppm and a doublet of doublets for H-8,8' appears at the 1.67–1.59 ppm. In addition, there are signals of linker alkyl and aryl groups for which the corresponding multiplicity and chemical shift of protons are typical for the ^1H NMR spectra.³¹

In the IR spectra of compounds **4a–i** there are no bands of vibrations of exchangeable protons differing from compounds **3a–i**, whereas the bands of C=O

groups of isoindole fragments at the 1721–1689 cm^{-1} and $\nu_{\text{C}=\text{C}}$, aromatic rings bonds at the 1515–1381 cm^{-1} , non-flat deformation vibrations of $\gamma_{\text{C-H}}$, bond at the 899–608 cm^{-1} and intensive bands of symmetric and antisymmetric valence vibrations of $-\text{CH}_2$ groups at the 2989–2359 cm^{-1} are present.

3. 2. Hypoglycemic Assay for Preliminary *in vivo* Testing

The screening results of hypoglycemic activity (Table 1) showed that synthesized compounds have different effects on glucose level in the blood of experimental animals. Thus, the compounds **3a**, **3f**, **3h**, **4a**, **4c** and **4f** decreased the glucose level on the second hour of the experiment on 13.99%, 4.09%, 11.86%, 18.47%, 3.18% and 8.61% respectively, substantially yielded to the action of «Metformine». It is important that only compounds **3a**, **3h**, **4f** keep this activity on the fourth hour of the experiment (reduced glucose level on 27.87%, 10.51% and 2.65% respectively). While the compounds **3b**, **3c**, **3e**, **3i**, **4b**, **4e** and **4i** under the given experimental conditions, on the contrary, increased glucose level on the second hour of the experiment from 4.89 to 15.79% (Table 1).

The insulinotropic effect of prandial glucose regulators comes very quickly unlike other oral hypoglycemic agents. Insulin secretion stimulation from β -cells of the pancreas islands is formed in 5–7 minutes (Mitiglinide, Nateglinide) or in 10–30 minutes after using (Repaglinide) these drugs in response to food intake. This is achieved by closing ATP-dependent potassium channels in the membrane of β -cells due to their depolarization. Molecular docking to KATP channel, PDB ID-6BAA was conducted, for a number of synthesized compounds (**3a**, **3f**, **3h**, **4a**,

Table 1 The synthesized compounds' influence on glucose level in blood of experimental animals (%)

Comp.	Initial glucose level	Glucose level in 2 h	%	Glucose level in 4 h	%	Glucose level in 6 h	%
Intact group	6.12±0.12	6.60±0.08	+7.84	5.62±0.14	–8.17	5.85±0.13	–4.41
3a	7.93±0.83	6.82±0.69	–13.99	5.72±0.49	–27.87	8.46±0.79	+6.68
3b	6.46±0.12 ^a	6.94±0.34	+7.43	8.08±0.79	+25.08	8.28±0.95	+28.17
3c	6.12±0.17 ^a	6.80±0.29	+11.11	7.30±0.74	+19.28	7.02±0.65	+14.70
3e	6.68±0.96	7.62±0.17 ^a	+14.07	8.14±0.27	+21.86	8.04±0.15 ^a	+20.36
3f	5.38±0.35	5.16±0.17 ^a	–4.09	5.80±0.29	+7.81	5.42±0.29	+0.74
3h	5.90±0.23 ^a	5.20±0.19	–11.86	5.28±0.21	–10.51	5.20±0.19 ^a	–11.86
3i	6.56±0.05 ^a	7.20±0.17 ^a	+9.75	7.72±0.07 ^a	+17.68	7.72±0.20	+17.68
4a	6.82±0.22	5.56±0.27	–18.47	7.34±0.45	+7.62	6.88±0.17 ^a	+0.88
4b	6.12±0.23	6.94±0.39	+13.39	7.08±0.47	+15.68	6.78±0.35	+10.78
4c	6.28±0.34	6.08±0.26	–3.18	6.56±0.33	+4.46	6.30±0.13 ^a	+0.32
4e	6.28±0.06 ^a	7.10±0.13 ^a	+13.06	7.58±0.33	+20.70	8.36±0.41	+33.12
4f	6.04±0.20	5.52±0.33	–8.61	5.88±0.17 ^a	–2.65	5.34±0.21	–11.59
4h	5.72±0.41	6.00±0.28	+4.89	5.16±0.35	–9.79	4.98±0.37	–12.94
4i	6.46±0.07 ^a	7.48±0.08 ^a	+15.79	8.50±0.43	+31.58	8.20±0.26	+26.93
Metformine	5.50±0.20 ^a	3.71±0.08 ^a	–67.60	3.42±0.06 ^a	–62.30	3.64±0.06 ^a	–66.10

^a differences reliable ($p \leq 0.05$) comparison to intact group of rats.

Table 2 Types of investigated compounds' interactions with amino acid residues of the target active center according to the docking studies

Investigated protein and types of interactions with amino acid residues		
Comp.	Affinity, kcal/mol	KATP channel, PDB ID-6BAA
3a	-8.2	ARG1246 ^a , ARG1300 ^b , TYR377 ^a , LEU434 ^c , TYR377 ^c , LEU592 ^c .
3f	-8.2	ARG1300 ^a , ASP1304 ^b , ILE381 ^c , TRP430 ^c , PHE433 ^c , ARG1300 ^c , ALA1303 ^c .
3h	-8.2	SER1238 ^a , ARG1246 ^a , HASN1245 ^a , TRP430 ^c , ILE381 ^c .
4a	-8.5	ASN1245 ^a , ILE381 ^c , ILE385 ^c , MET429 ^c , PHE433 ^c , ILE381 ^c .
4c	-9.5	THR588 ^a , LEU592 ^c , PHE591 ^c , TYR377 ^c , TYR377 ^c , LEU592 ^c .
4f	-9.5	THR588 ^a , LEU592 ^c , TYR377 ^c , TYR377 ^c , PHE591 ^c .
4h	-10.1	THR1242 ^a , SER1238 ^a , TRP430 ^c , LEU434 ^c , TYR377 ^c , TRP430 ^c , MET429 ^c , TRP430 ^c , TRP430 ^c , ILE381 ^c , LEU434 ^c .
4i	-9.0	ARG1145 ^a , ARG1300 ^{a,b} , TRP1297 ^c , PHE591 ^c , TRP430 ^c , PHE433 ^c , LEU592 ^c .
Mitiglinide	-7.5	THR1242 ^a , LEU434 ^c , TYR377 ^c , TRP430 ^c , TRP430 ^c , PHE433 ^c .
Glibenclamide*	-8.4	ARG306 ^a , ASN437 ^a , THR1242 ^a , ARG1246 ^a , ASN1245 ^a , TYR377 ^a , ASN437 ^a , TYR377 ^a , MET441 ^c , MET429 ^c , LEU592 ^c .

^a hydrogen; ^b electrostatic; ^c hydrophobic * data according to X-ray structure of protein.³²

4c, **4f** and **4i**), taking into account the search strategy. It allowed to identify the main interaction types of the synthesized compounds, Mitiglinide and Glibenclamide with the amino acid residues with active channel centers and select compounds for further studies (Table 2).³²

The visualization of the interaction of the structures with the active site of KATP channel (Figure 2) showed that compounds **3a** and **4a** revealed similar interaction to Glibenclamide. Such common interactions for compound **3a** were: two hydrogen bonds with the amino acid residues ARG1246 (3.12Å), TYR377 (3.96Å) and two hydrophobic interactions with the residues LEU592 (5.44Å), TYR377 (5.17Å). And common interactions for compound **4a** were as following: hydrogen bond with the amino acid residue ASN1245 (3.76Å) and hydrophobic interaction with the residue MET429 (4.74Å). This may indicate that the stated class of compounds might have ability to act in the same way as Glibenclamide does.

Hypoglycemic activity studies in the shorter of the experimental periods with a previous glucose loading allowed to establish that compounds **3a**, **3f**, **3h**, **4a**, **4f** reduced glucose level on 19.34%, 17.54%, 18.85%, 25.09% and 9.51%, respectively on the 15 minute of the experiment, compared to control group (Table 3). It is important that the hypoglycemic effect of these compounds is maintained throughout the experiment from 30 to 120 minutes. While compounds **4c**, **4h** and **4i** did not affect glucose level and in some cases even increased it throughout the experiment.

SAR analysis showed that the compounds with (3H-quinazoline-4-ylidene)hydrazides (**3a**, **3f**, **3h**) or [1,2,4]triazolo[1,5-c]quinazoline (**4a**, **4f**) moieties bonded through the ethyl (**3a**, **4a**) or phenyl (**3f**, **3h**, **4f**) linker groups with a hydrogenated isoindoline ring have hypoglycemic effect in the short term of the experiment. Modification of compounds and their further studies on hypoglycemic activity are going to be continued.

Table 3 Influence of synthesized compounds on glucose level in blood of experimental animals in the short term of the experiment

Comp.	Initial glucose level	Glucose level in 15 min	Glucose level in 30 min	Glucose level in 60 min	Glucose level in 120 min
Control group	5.84±0.05	6.10±0.21	6.60±0.08	5.62±0.14	5.85±0.13
3a	4.34±0.12 ^a	4.92±0.59	4.68±0.54	4.93±1.14	3.84±0.51
3f	5.12±0.15 ^a	5.03±0.14 ^a	4.87±0.19 ^a	5.23±0.12 ^a	5.12±0.34
3h	4.48±0.23	4.95±0.21	4.92±0.19 ^a	5.41±0.24	5.32±0.16 ^a
4a	3.98±0.13 ^a	4.63±0.31	4.52±0.22	4.49±0.14 ^a	5.54±0.11 ^a
4c	5.83±0.27	6.23±0.17 ^a	6.93±0.26	6.08±0.19 ^a	6.12±0.20
4f	5.34±0.22	5.52±0.23	5.48±0.22	5.52±0.15 ^a	5.32±0.17 ^a
4h	5.87±0.25	6.13±0.31	6.54±0.27	5.89±0.24	5.93±0.21
4i	6.10±0.21	8.50±0.58	6.78±0.85	6.34±0.49	5.98±0.38

^a differences reliable (p ≤ 0.05) comparison to control group of rats.

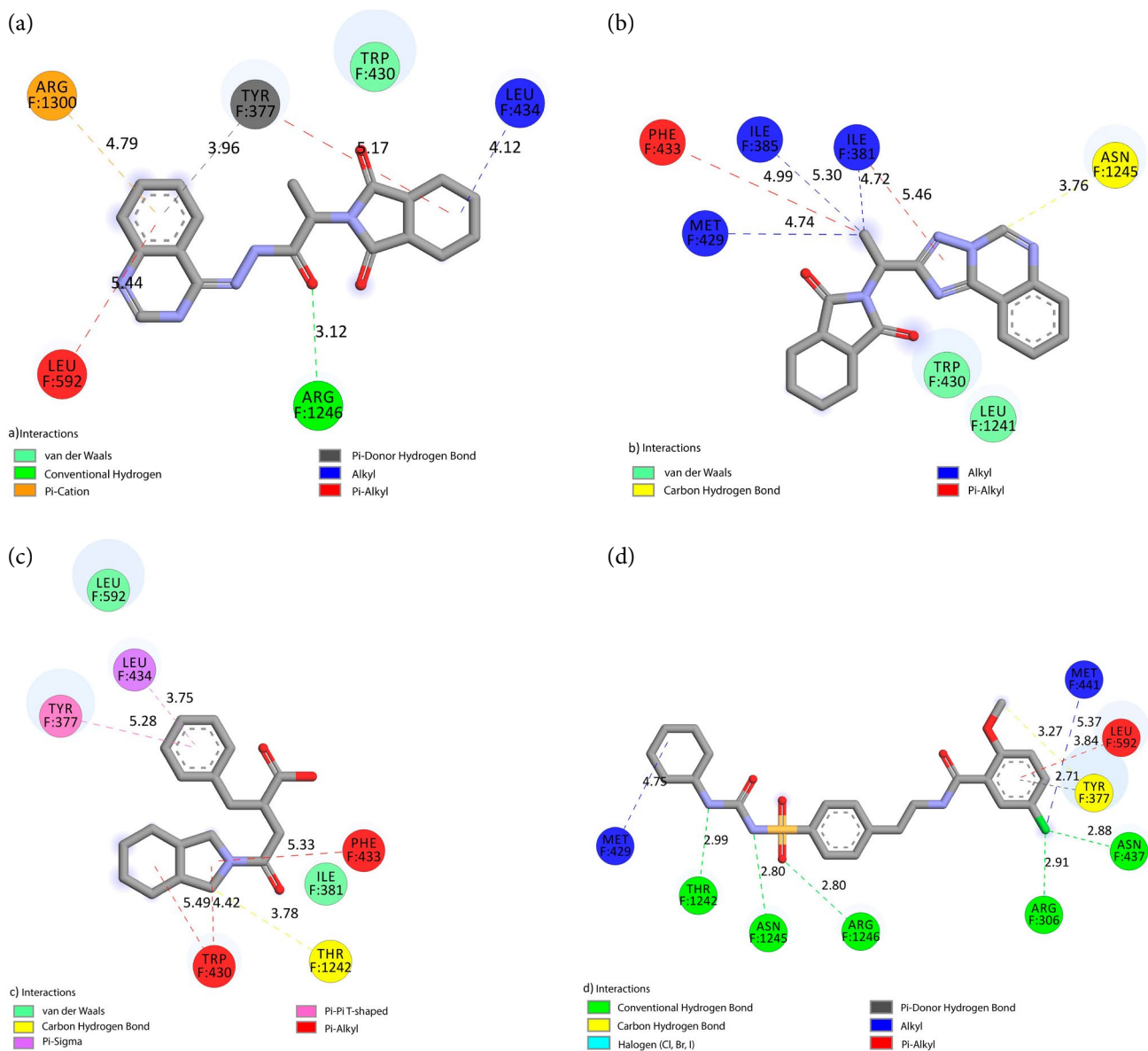


Figure 2. Visualization of affinity according to the docking (a) compound **3a** with KATP channel; (b) compound **4a** with KATP channel; (c) Mitiglinide with KATP channel; (d) Glibenclamide with KATP channel.

4. Conclusions

The synthesis of *N*-carboxyalkyl-(arylalkyl-,aryl-)isoindoline-1,3-dione (*3H*-quinazoline-4-ylidene) hydrazides was carried out using activated *N*-protected aminoacids and 4-hydrazinoquinazoline. The synthesized hydrazides were converted into the corresponding hydrogenated 2-([1,2,4]triazolo[1,5-*c*]quinazoline-2-yl)-alkyl-(alkylaryl-,aryl-)isoindole-1,3(*2H*)-diones by cyclocondensation under the conditions of acidic catalysis. The structures of the synthesized compounds were established using IR, ¹H and ¹³C NMR spectroscopy and LC-MS and the features of spectral pattern were discussed. Search strategy of hypoglycemic drugs based

on the fragment-oriented design revealed a number of perspective compounds, which are short-acting drugs, like prandial glucose regulators. Conducted SAR analysis showed that the introduction of hydrogenated 1,3-dioxoisoindole moiety bonded *via* a linker group with 4-hydrazinoquinazoline and triazolo[1,5-*c*]quinazoline cycle is reasonable in the context of searching for short-acting hypoglycemic agents and requires further research.

5. Acknowledgments

The work was performed with the financial support of «Enamine Ltd» (Kyiv, Ukraine).

6. References

- B. M. Santosh, P. A. Narshinha, *Tetrahedron* **2006**, *62*, 9787–9826. DOI:10.1016/j.tet.2006.07.098
- J. P. Michael, *Nat. Prod. Rep.* **2007**, *24*, 223–246. DOI:10.1039/B509528J
- U. A. Kshirsagar, *Org. Biomol. Chem.* **2015**, *13*(36), 9336–9352. DOI:10.1039/c5ob01379h
- A. N. Parvez, R. Arpana, M. Imran, *Int. J. Pharm. Biol. Arch.* **2011**, *2*(6), 1651–1657.
- P. S. Theivendren, V. K. Palanirajan, *Res. In Pharm.* **2011**, *1*(1), 1–21.
- G. Marzaro, A. Guiotto, A. Chilin, *Expert Opin. Ther. Pat.* **2012**, *22*(3), 223–252. DOI:10.1517/13543776.2012.665876
- S. Ravez, O. Castillo-Aguilera, P. Depreux, L. Goossens *Expert Opin. Ther. Pat.* **2015**, *25*(7), 1–16. DOI:10.1517/13543776.2015.1039512
- A. O. Olayinka, Y. A. Oluwatosin, D. V. Aderohunmu, F. E. Owolabi, A. O. Olomiejia. *Am. J. Drug Discov. Dev.* **2017**, *7*, 1–24. DOI:10.3923/ajdd.2017.1.24
- S. Srivastava, S. Srivastava, *Int. J. Pharm. Sci. Res.* **2015**, *6*(9), 1206–1213. <http://www.ijpsr.info/docs/IJPSR15-06-09-102.pdf>.
- D. Wang, F. Gao, *Chem. Cent. J.* **2013**, *7*(95), 1–15. DOI:10.1186/1752-153X-7-95
- I. Khan, A. Ibrar, N. Abbas, A. Saeed, *Eur. J. Med. Chem.* **2014**, *76*, 193–244. DOI:10.1016/j.ejmech.2014.02.005
- A. Mohammad, *Int. J. Med. Chem.* **2014**, *27*, 1–27. DOI:10.1155/2014/395637
- V. G. Ugale, S. B. Bari, *Eur. J. Med. Chem.* **2014**, *80*, 447–501. DOI:10.1014/j.ejmech.2014.04.072
- O. Voskoboynik, S. Kolomoetsch, G. Berest, I. Nosulenko, Yu. Martunenko, S. Kovalenko, *Chem. Heterocycl. Compd.* **2017**, *53*(3), 256–272. DOI:10.1007/s10593-017-2048-2
- A. G. Reddy, V. H. Babu, Y. J. Prakash Rao, *JCPS* **2017**, *10*(3), 1492–1504.
- Z. Chaban, St. Harkov, T. Chaban, O. Klenina, V. Ogurtsov, I. Chaban, *Pharmacia* **2017**, *64*(3), 52–66. <https://www.researchgate.net/publication/322731545>.
- A. Hameed, M. al-Rashida, M. Uroos, S. A. Arshia, M. Ishtiaq, K. M. Khan, *Expert Opin. Ther. Pat.* **2018**, *28*(4), 281–297. DOI:10.1080/13543776.2018.1432596
- O. Antypenko, S. Kholodnyak, K. Schabelnyk, L. Antypenko, S. Kovalenko, *Chem. Heterocycl. Compd.* **2017**, *53*(3), 292–309. DOI:10.1007/s10593-017-2051-7
- O. Kolomoets, O. Voskoboynik, O. Antypenko, G. Berest, I. Nosulenko, V. Palchikov, O. Karpenko, S. Kovalenko, *Acta Chim. Slov.* **2017**, *64*, 902–910. DOI: 10.17344/acsi.2017.3575
- P. J. Hajduk, J. Greer, *Nat. Rev. Drug Discov.* **2007**, *6*(3), 211–219. DOI:10.1038/nrd2220
- D. A. Erlanson: Introduction to Fragment-Based Drug Discovery, In: *Fragment-Based Drug Discovery and X-Ray Crystallography*, T. G. Davies, M. Hyvönen Eds., Berlin Heidelberg: Springer Verlag, **2012**, 1–32. DOI:10.1007/978-3-642-27540-1
- Yu. Martunenko, M. Kazunin, O. Antypenko, Ye. Selivanova, S. Kovalenko, S. Trzhetsynskiy, *Current issues in pharmacy and medicine: science and practice*, **2018**, *11*(1), 4–11. DOI:10.14739/2409-2932
- H. Ohnota, T. Koizumi, N. Tsutsumi, M. Kobayashi, S. Inoue, F. Sato, *J. Pharmacol. Exp. Ther.* **1994**, *269*(3), 489–495.
- W. J. Malaisse, *Expert. Opin. Pharm.* **2008**, *9*(15), 2691–2698. DOI:10.1517/14656566.9.15.2691
- https://www.drugbank.ca/uneearth/q?c=_score&d=down&query=quinazolines&searcher=drugs.
- Protein Data Bank, pdb. Retrieved from <http://www.pdb.org>.
- MarvinSketch version: 17.21.0, ChemAxon (<http://www.chemaxon.com>).
- O. Trott, A. J. Olson, *J. Comput. Chem.* **2010**, *31*, 455–461. DOI:10.1002/jcc.21334
- S. Kovalenko, L. Antypenko, A. Bilyi, S. Kholodnyak, O. Karpenko, O. Antypenko, N. Mykhaylova, T. Los', O. Kolomoets', *Sci. Pharm.* **2013**, *81*(2), 359–392. DOI:10.3797/scipharm.1211-08
- El H. Sayed, El Ashrya, S. Nadeem, M. R. Shah, Ye. El Kilany, *Adv. Heterocycl. Chem.* **2010**, *101*, 161–228.
- E. Breitmaier, *Structure Elucidation By NMR In Organic Chemistry: A Practical Guide*, John Wiley & Sons, Ltd. **2002**, 258.
- M. M. Gregory, B. Kandasamy, F. DiMaio, C. Yoshioka, S. Show-Ling, *eLife* **2017**, *6*. DOI:10.7554/elife.31054

Povzetek

Opisujemo učinkovito sintezo (3*H*-kinazolin-4-iliden)hidrazidov *N*-karboksialkil-(arilalkil-,aril-)izoindolin-1,3-dionov iz aktiviranih *N*-zaščiteneh amino kislin in 4-hidrazinokinazolinov. Predlagana metoda temelji na neposrednem iskanju hipoglikemičnih agentov s pomočjo načrtovanja, orientiranega na fragmentih, in z molekulskim sidranjem. Željene hidrazide smo pripravili s pomočjo ciklokondenzacij pod kislimi pogoji in jih nadalje pretvorili v ustrezne 2-([1,2,4]triazolo[1,5-*c*]kinazolin-2-il-)alkil-(alkilaril-,aril-)hidroizoindol-1,3(2*H*)-dione. Strukture pripravljenih spojin smo določili s pomočjo IR, ¹H in ¹³C NMR spektroskopije ter LC-MS analize ter s primerjavo spektralnih vzorcev (kar je opisano v diskusiji). Rezultati farmakološkega testiranja so razkrili serijo spojin, ki delujejo kot hitri hipoglikemični agenti, podobno kot prandial regulira glukozo (Mitiglinid). SAR analiza je dodatno pokazala, da je vpeljava hidrogeniranega 1,3-dioksindolnega fragmenta, ki je preko distančnikov vezan na 4-hidrazinokinazolinski ter triazolo[1,5-*c*]kinazolin-ski obroč, primerna za iskanje novih hitro delujočih hipoglikemičnih agentov ter da si zasluži nadaljnje raziskave.

Scientific paper

Investigation of the Electrochemical Reduction Process of the Molybdate Ions in the Tartaric Electrolytes

Vusala Asim Majidzade,^{1,*} Akif Shikhan Aliyev,¹ Dunya Mahammad Babanly,^{1,3} Mahmoud Elrouby² and Dilgam Babir Tagiyev¹

¹ Institute of Catalysis and Inorganic Chemistry named after acad.M.Nagiyev, Azerbaijan National Academy of Sciences, H. Javid ave., 113, AZ 1143, Baku, Azerbaijan

² Chemistry Department, Faculty of Science, Sohag University, 82524 Sohag, Egypt

³ Azerbaijan State Oil and Industry University (Ufaz), Baku, Azerbaijan

* Corresponding author: E-mail: vuska_80@mail.ru

Received: 12-27-2018

Abstract

The electrochemical reduction of molybdate ions in tartaric electrolyte has been investigated in this work. Kinetics and mechanism of the electrochemical process have been studied by cyclic and linear voltammetric polarization methods. The effect of the temperature, the rate of potential-scanning and the concentration of the molybdate ions on the electrochemical process has been also studied. By estimating the effective activation energy, it was revealed that the electroreduction process is accompanied by mixing kinetics control.

Keywords: Molybdate ions; electroreduction; tartaric acid; polarization curves; chronoamperometry

1. Introduction

As known, semiconductors are one of the most important materials that differ from each other by their great manifold of the physical and electrical properties, also of the chemical composition.^{1–4} The need for the chalcogenide semiconductor films increases with the development of the application of the new generation of solar cells.⁵ Today, the using of ecologically waste free solar energy is very actual connecting with the decreasing of the natural resources of the energy. Thin films of chalcogenide can be used as photo-anodes for obtaining of the electrical energy in the solar cells. One of such photosensitive semiconductor materials is molybdenum chalcogenides.

The obtaining of these films can be carried out using various methods.^{1,6} The most suitable method of obtaining molybdenum alloys is the electrochemical method. There are a lot of works dedicated to the electrochemical deposition of thin films of these alloys. To study well the simultaneous electrodeposition process of these compounds, at first, these components should be deposited individually.

In our previous studies, we have investigated the electroreduction and co-electrodeposition of various

metals together with chalcogenides.^{7–11} Many works were dedicated to the electrochemical reduction of molybdate ions. Some researchers¹² have investigated the electrochemical reduction of the hexavalent molybdenum ions in a solution containing tartaric acid. The formed complexes of Mo-tartrate ions were examined by spectroscopic and electrochemical methods. The resulted electrochemical peak was found to be under kinetic control at relatively high pH values or at a relatively low concentration of the tartaric ions. But, the electrochemical reaction occurred by protonation reaction. Moreover, some researchers¹³ studied the reduction of molybdenum (VI) on a pre-hydrogenated platinum electrode in acidic solutions. Reduction of molybdenum (VI) in a solution of 0.8–1.6 M H₂SO₄ occurs via two main steps. The first step is a relatively high cathodic wave attributes to the reduction of Mo (V) to Mo (III), which is accompanied with the decomposition of the solvent. The second step is a relatively low cathodic wave and attributes to the reduction of Mo (VI) to Mo (V), which takes place at +0.07 V. The second peak seems to be controlled by a diffusion and can be used for the determination of molybdenum up to 4×10^{-5} M or 6×10^{-5} M. An incomplete reduction of molybdate

ions from weak acidic and alkaline solutions within the pH interval from 3.0 to 9.0 has been recorded.¹⁴ A film of the hydrated oxides of molybdenum in lower oxidation states forms on the cathode surface. Products of the incomplete reduction adsorbed at the cathode and blocked its working surface.

The following up of the electroreduction process of the molybdate ions in an aqueous medium under different conditions was achieved to obtain the metallic molybdenum.¹⁵ The kinetics and the mechanism of the electroreduction process were studied by the cathodic polarization. It was observed that the rate of the electrochemical process depends on the scan rate of potential, and the temperature of the electrolyte. On the other hand, it can be concluded that the electrochemical reduction occurs in two stages. It was indicated that, during the electrochemical reduction process, the electroreduction process of the molybdate ions is accompanied by releasing of hydrogen after the potential value -0.7 V.

The effect of hydrogen fluoride on the cathodic reduction of molybdate ions has been investigated.¹⁶ It was indicated that the mechanism of the process is controlled by its concentration. It was found that at concentration values less than 25 g/L, the products of the electroreduction process of the molybdate ions are black or colorful precipitations. These precipitates were formed on the cathode, and the average valent of molybdenum was determined to be 3.6–4.0. In the concentration, more than 50 g/L molybdate ions are completely reduced forming on the cathode a dense light metallic coating of thickness 3–5 μm with a great adhesion to the substrate. It was concluded that the addition of hydrogen fluoric acid prevents the polymerization and aggregation of the molybdate ions.

The bright, smooth metallic coating of molybdenum with 25 μm thickness is successfully deposited from aqueous electrolyte consisting high concentration of acetate.^{17–19} The optimal conditions for the electrodeposition of metallic molybdenum have been detected to be as follow: the current density 200–450 mA/cm^2 and temperature $30\text{ }^\circ\text{C} \pm 2$. The obtained coatings are amorphous, but after vacuum annealing at high temperature, they converted into crystalline films. It was concluded that the current density is the major effective factor for the precipitation of a refractory metal.¹⁹ From the published results, it has been indicated that the metallic molybdenum can be deposited through two stages through electroreduction with obtaining intermediate coating from molybdenum oxide. According to the previous studies, kinetics and mechanism of the electrochemical reduction have been investigated differently. Therefore, the main aim of our work is to study of the nature, kinetics and mechanism of the electrochemical reduction process of the molybdate ions in presence of tartaric acid as a complexing agent at different conditions, to obtain the optimal condition of obtaining a considerable coating of high quality.

2. Experimental Part

The preparation of the electrolyte for the electrochemical reduction of molybdate ions was carried out as follows. The desired concentration (0.1–0.5 M) of sodium molybdate ($\text{Na}_2\text{MoO}_4 \cdot 2\text{H}_2\text{O}$) was dissolved in an aqueous electrolyte of 0.007 M tartaric acid. It is observed that, the pH value depends on the concentration of $\text{Na}_2\text{MoO}_4 \cdot 2\text{H}_2\text{O}$. The pH of the electrolyte changed in the intervals of 1.69–2.1. It is found that at the selected optimal electrolyte composition, the pH value is 2.1. The polarization experiments were performed by potentiostat of IVIUM-STAT Electrochemical Interface. A three-electrode electrochemical cell of 100 mL volume was used. Pt and Ni sheets with an area of $2.2 \times 10^{-3} \text{ dm}^2$ were used as working electrodes. Silver-silver chloride electrode was used as a reference electrode. Whereas, a platinum sheet with an area of 4 cm^2 was used as counter electrode. The universal ultra-thermostate UTU – 4 was utilized for regulation of the temperature of the electrochemical reaction inside the cell.

The detection of the nucleation mechanism of the electrodeposited Mo was carried out by taking the chronoamperometric method (current-time), using IVIUM-STAT potentiostat.

The morphology and the chemical composition of electrodeposits were studied by using scanning electron microscope (SEM) and energy-dispersive X-ray analysis (EDAX) of mark “Carl Zeiss Sigma”, respectively. SEM images of the electrodeposited films of Mo on Ni substrate was captured using a JEOL T330A SEM from Japan. The prepared sample was captured at fixed temperature of 20 $^\circ\text{C}$ at working distance of 10 mm, at power of 20 KeV and at magnification factor of 3000 times from the real sample.

3. Results and Discussion

As known, to obtain semiconductive thin films from two or more components, the first required step was to study the electrochemical reduction processes of these components individually. Hence, the electrochemical reduction behavior of molybdate ions was investigated as shown in Fig. 1.

In the presented work, full data about the electroreduction of the molybdate ions in tartaric electrolyte were given. The cyclic polarization curves were recorded by the potentiodynamic method for finding out the kinetics and the mechanism of the electroreduction process of the molybdate ions. As seen from Fig. 1, the electrochemical reduction of the molybdate ions on the cathode occurs through two stages within the potential range of 0.47 – (-0.25) V. It can be expected that within interval of potential values 0.47–0.27 V the process occurs with respect to reaction (1), whereas within 0.27–0.00 V with respect to reaction (2) (Fig.1). This also corresponds to the literature data.²⁰

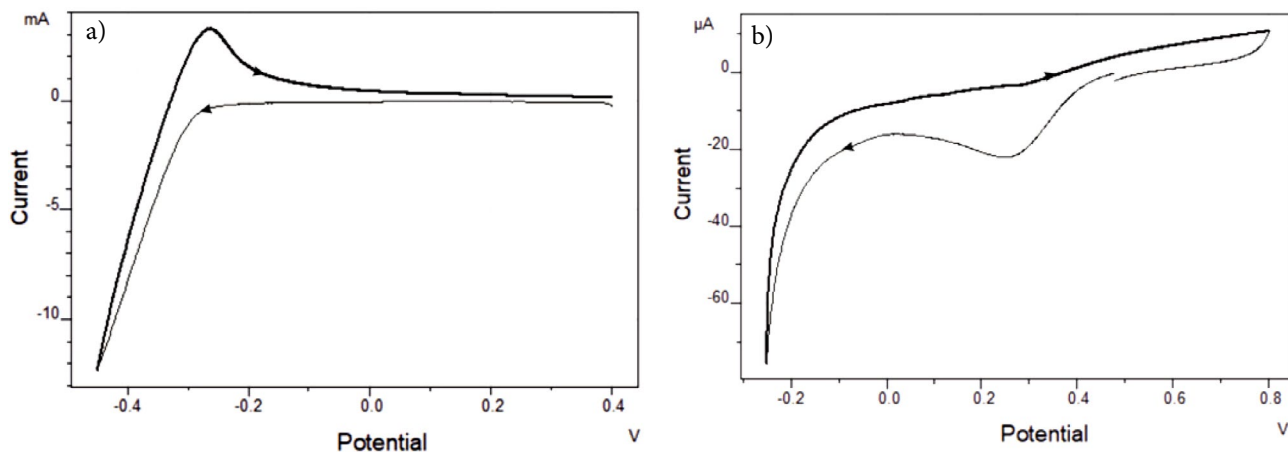
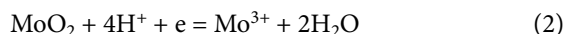


Fig. 1. Cyclic voltamperometric curves of the electroreduction process of the molybdate ions in the presence of tartaric acid on the Pt electrode. The electrolyte consists of: 0.1 M $\text{Na}_2\text{MoO}_4 \cdot 2\text{H}_2\text{O}$ + 0.007 M $\text{C}_4\text{H}_6\text{O}_6$. $T = 293$ K, $E_V = 0.02$ V/s. a – the general process, b – the initial stage.



After that, starting from 0.0 V potential value the reduction process of Mo^{3+} ions to metallic Mo as (3) reaction occurred:



Then, starting from the potential value of -0.45 V along with electroreduction of the molybdate ions the releasing of hydrogen also occurs. Consequently, the electroreduction process was carried out up to this potential (as shown in Fig. 1 a).

The linear polarization experiments were performed as a function of temperature for determination of the kinetics of the process. The effect of temperature was investigated within a temperature range of 293–353°C. As ob-

served from Fig. 2, with increasing of temperature, the current increases due to the acceleration of the process (the peak on the polarization curve obtained near $E = 0.3$ V, which is shown in Fig. 1b, due to an increase in the scale of the current becomes imperceptible in both Fig. 1a and Fig. 2).

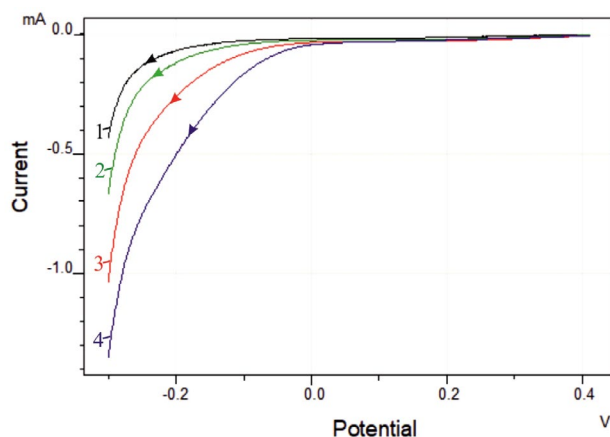


Fig. 2. The effect of temperature on the electroreduction process of the molybdate ions on the Pt electrode. Electrolyte composition in (M): 0.1 $\text{Na}_2\text{MoO}_4 \cdot 2\text{H}_2\text{O}$ + 0.007 $\text{C}_4\text{H}_6\text{O}_6$. T (K): 1- 293; 2- 313; 3- 333; 4- 353. At a scan rate of $E_V = 0.02$ V/s

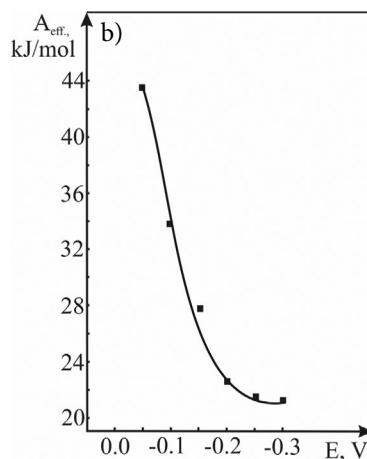
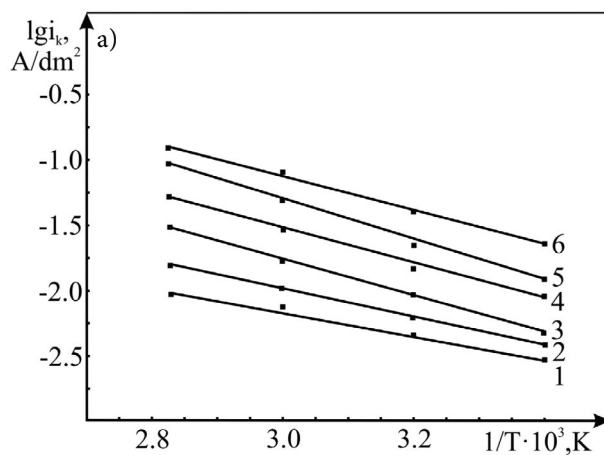


Fig. 3. (a) $\lg i_k$ as a function of $1/T$, (b) Activation energy as a function of potential. Potential (V): 1- (-0.05); 2- (-0.1); 3- (-0.15); 4- (-0.2); 5- (-0.25); 6- (-0.3).

At a temperature of 293 K the reduction occurs at -0.094 V, but at 353 K it occurs at a potential of 0.0 V. The $\lg i_c - 1/T$ relation was plotted within $0.0 - (-0.3)$ V potential range taken from the polarization curves of Fig. 2, shown in Fig. 3 (a). The value of effective activation energy obtained by the aid of equation $A_{\text{app}} = -2.3 Rtg\alpha$, which indicates that the electrochemical reduction of the molybdate ions in tartaric electrolytes is accompanied by mixed kinetics mechanism. In other words, as shown in Fig. 3, at the potential values are $-0.05 - (-0.2)$ B, the kinetics of the electroreduction process is accompanied the electrochemical, and at $-0.2 - (0.3)$ B the concentration polarization (Fig.3 (b)).

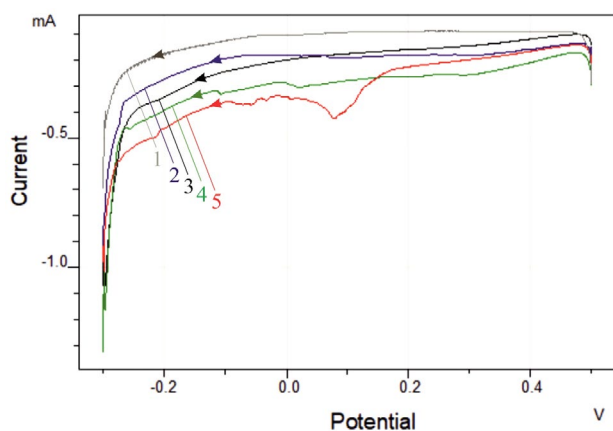


Fig. 4. The effect of concentration of the molybdate ions to electroreduction process on the Pt electrode. The electrolyte consists of $0.007 \text{ C}_4\text{H}_6\text{O}_6 + (\text{M}) \text{Na}_2\text{MoO}_4 \cdot 2\text{H}_2\text{O}$. M= 1- 0.1; 2- 0.2; 3- 0.3; 4- 0.4; 5- 0.5, at $T = 293$ K, and $E_V = 0.02$ V/s.

The effect of concentration of the molybdate ions on the electroreduction process has been studied within the $0.1\text{--}0.5$ mol/L interval (Fig. 4). At concentrations range of

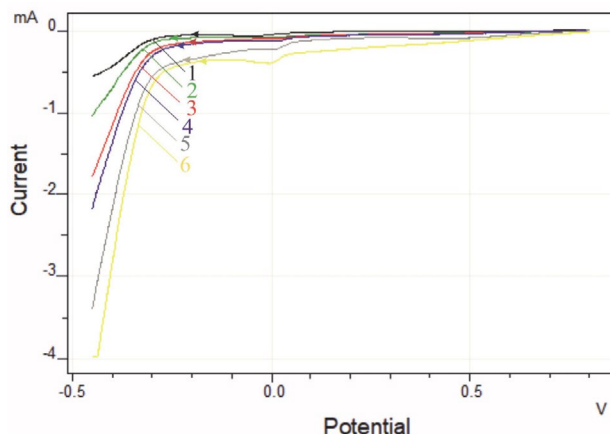


Fig. 5. The effect of potential-scanning to the electroreduction process of the molybdate ions on the Pt electrode. Electrolyte (M): $0.1 \text{ Na}_2\text{MoO}_4 \cdot 2\text{H}_2\text{O} + 0.007 \text{ C}_4\text{H}_6\text{O}_6$. Potential-scanning (V/s): 1- 0.005; 2- 0.01; 3- 0.03; 4- 0.06; 5- 0.09; 6- 0.12. $T = 293$ K.

$0.1\text{--}0.3$ M, the effect is regular. In more precisely, with increasing of the concentration of the ions the electrochemical reduction takes place at more positive potentials. Within these intervals ($0.3\text{--}0.5$ M) the displacement of reduction potential to the negative side is observed. It can be interpreted as, with increasing of the concentration of the molybdate ions their mobilities in the electrolyte decrease, and then the electroreduction process becomes hard. Furthermore, at the high concentration, the molybdate ions form a stable complex with tartaric acid.

Therefore, their subsequent dissociation becomes difficult. As a result of the investigation, the optimal conditions have been detected, then we selected the optimal concentration of the molybdate ions up to 0.2 mol/L.

The effect of potential scanning onto the electroreduction process of the molybdate ions has been studied in the potential range of $-0.27 - (-0.32)$ V as shown in Fig. 5. As seen from Fig. 5, with increasing of potential scanning, the consumed current for the electroreduction process of the molybdate ions is increased. Where, current at 0.005 V/sec is 5.53×10^{-4} A, whereas at 0.12 V/sec is 3.97×10^{-3} A.

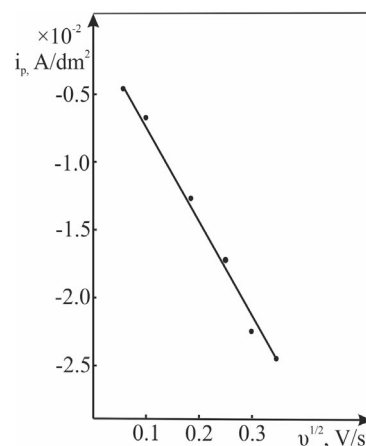


Fig. 6. i_p as a function of $v^{1/2}$ for electroreduction of the molybdate ions. Electrolyte (M): $0.1 \text{ Na}_2\text{MoO}_4 \cdot 2\text{H}_2\text{O} + 0.007 \text{ C}_4\text{H}_6\text{O}_6$, $T = 293$ K.

Fig. 6 indicates that the relationship between i_p and $v^{1/2}$ is linear. It also demonstrates that the electroreduction process of the molybdate ions occurs under the control of concentration polarization overpotential.

The chronoamperometric (CA) method can be easily used for giving more precise information about the electrochemical deposition process, at which the potential can be stopped at the deposition potential (from CV). Via CA method, the mechanisms of the nucleation and growth of the electrodeposited particles can be studied. Current-time curves were carried out at different applied potentials of 0.047 ; 0.03 ; -0.06 ; -0.09 ; and -0.1 V at room temperature as shown in Fig. 7. It seems from the shown figure that the initial regime of the current-time curve is characterized by a sudden decrease in the current under application of the

deposition potential. This can be attributed to the presence of the double-layer between the surface of the substrate and the ions of the solution, which lead to the formation of an immediate nucleation of molybdenum in all cases as shown in Fig. 7.

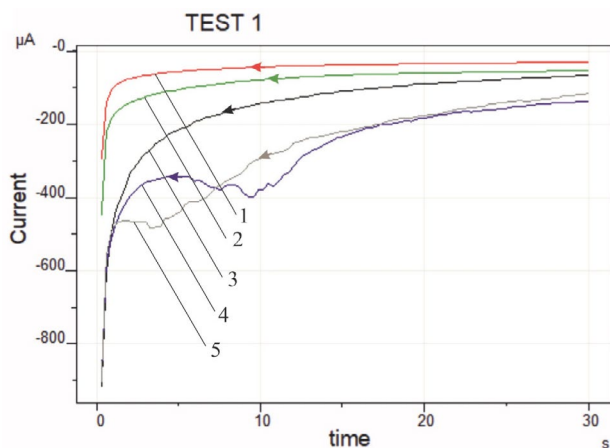


Fig. 7. Current-time curves of the electrodeposition of molybdenum on Pt in electrolyte consists of 0.1 M $\text{Na}_2\text{MoO}_4 \cdot 2\text{H}_2\text{O}$ + 0.007 M $\text{C}_4\text{H}_6\text{O}_6$ at $T = 295$ K at room temperature and at different deposition potentials; 0.047; 0.03; -0.06; -0.09; and -0.1 V vs. Ag/AgCl.

This sudden decrease is followed by a little increase in the resultant current. This due to an increase in the electroactive surface area associated with the crystal growth. Moreover, it can be noted that the current density during the electrodeposition increases in all cases by increasing the deposition potential. The mechanism of crystal nucleation and growth can be determined by the analysis of the resulted current-time curves. The analysis of these curves can be achieved by applying the two equations of Scharifker-Hills,²¹ comparing with the experimental calculated data as shown in Fig. 8 (a-e). The models of the theoretical transients for the instantaneous and the progressive 3D nucleation are given by equations (4) and (5), respectively as follows:

$$\frac{I(t)^2}{I_{\max}^2} = \frac{1.9542}{t/t_{\max}} \left\{ 1 - \exp \left[-1.2564 \left[\frac{t}{t_{\max}} \right] \right] \right\}^2 \quad (4)$$

$$\frac{I(t)^2}{I_{\max}^2} = \frac{1.2254}{t/t_{\max}} \left\{ 1 - \exp \left[-2.3367 \left[\frac{t}{t_{\max}} \right]^2 \right] \right\}^2 \quad (5)$$

Fig. 8 (a-e) shows the nondimensional $I^2 \cdot I_{\max}^2$ vs. t/t_{\max} plots of the CA data at the different condition as in Fig. 7. The solid lines of black and red color are the theoretical transients of the instantaneous and the progressive nucleation, respectively as shown in the figure, and dotted lines for the experimental data. The nucleation and growth processes of molybdenum at these conditions can be predicted from Fig. 8 (a-e). At the early stage, the experimental curve well fits the curve of the progressive nucleation

model by which the molybdenum nucleation occurred on many active sites of Pt surface substrates. Subsequently, the deposition deviates from the instantaneous nucleation as shown in Fig. 8 (a, b, c, and d). The deviation from the ideal assumption of the Scharifker model may be attributed to that the nuclei grow under diffusion control at these conditions.

In fact, through time the nuclei growth and the electrodeposition of molybdenum will be under mixed control (diffusion and charge transfer). The deviation can be also interpreted as due to the hydrogen reduction during the formation of nuclei which cause morphology change of the nucleus. But, the experimental data for Fig. 8 e are in a good agreement with the theoretical model of the progressive nucleation and growth where the deposition potential of 0.1 V. Further information for the growth mechanism can be obtained by calculating the density number of actives sites for nucleation (N_0);

$$N_0 = 0.065 \left(\frac{8\pi C M}{\rho} \right)^{-1/2} \left(\frac{z f C}{t_{\max} i_{\max}} \right)^2 \quad (6)$$

where, C the bulk concentration in mol cm^{-3} , $z f$ the molar charge of electrodepositing species, M and ρ in g cm^{-3} are the molecular weight and the density of the deposited material, respectively. The diffusion coefficient D of the active species in the electrolyte can be calculated via the chronoamperometric method. According to the theoretical nucleation model, the D is related to the i_{\max} and the t_{\max} ^{21, 22} by the following equation;

$$D = \frac{i_{\max}^2 t_{\max}}{0.1629 (z f C)} \quad (7)$$

The values of i_{\max} , t_{\max} , D, and N_0 at different deposition potentials and temperatures are shown in Table 1. From these values, it is clear that by increasing the deposition potential, the i_{\max} t_{\max} value slightly increases. This character is typical for 3D electrochemical nucleation and growth of a new phase under the mixed diffusion and adsorption control.

Moreover, the D values at these conditions of the electroactive species are very small due to the high relative density of the electrolyte and the high relative diameter of molybdate ions. It is also observed that the D value is affected by the polarization potential as seen in Table 1.

Table 1. The experimental data of the CA electrodeposition of Mo onto Pt substrate

E_d , V vs. Ag/AgCl	D, $\text{cm}^2 \text{s}^{-1}$	N_0 , cm^{-2}
0.047	1.89×10^{-9}	25.10×10^6
0.030	3.54×10^{-9}	8.51×10^6
-0.06	5.61×10^{-9}	5.38×10^6
-0.09	8.24×10^{-9}	1.26×10^6
-0.10	10.17×10^{-9}	1.07×10^6

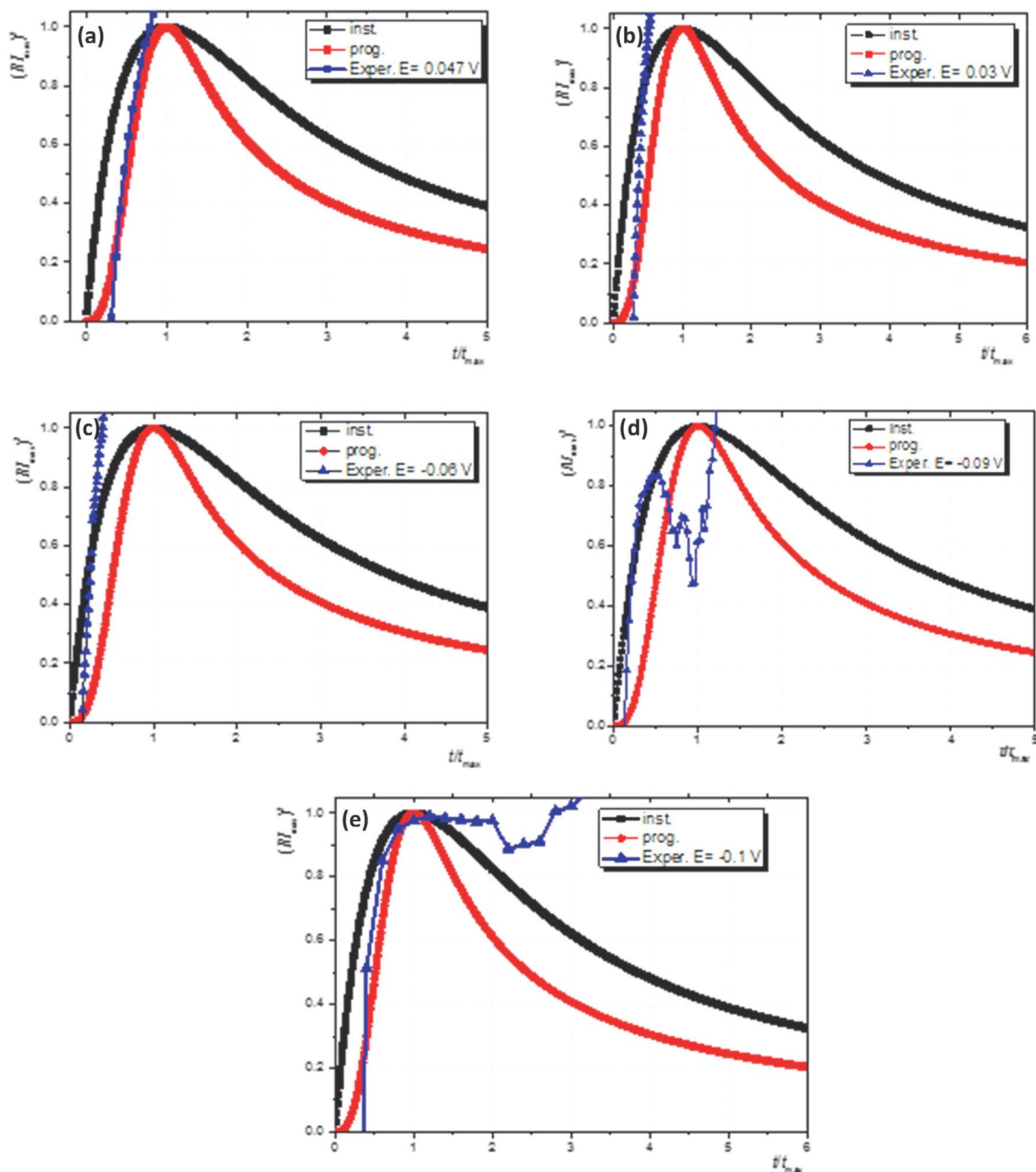


Fig. 8. Comparison of theoretical non-dimensional plots of $(I/I_{\max})^2$ vs (t/t_{\max}) , for instantaneous and progressive nucleation with the experimental data derived from Fig. 7.

It is noted from the table that nuclei densities N_0 decrease significantly with the increase of the deposition potential. This decrease with the applied deposition potential is generally understood as the decreased of the activation of the nucleation sites at higher potentials, which deviates from the classical nucleation models as confirmed by Fig. 7. This deviation may be also explained as, by increasing

the deposition potential the polarization of the working electrodes increases but the diffusion of the active species is still slow because of the high density of surrounding media which hinder the diffusion of the active species.

Fig. 9. shows the morphology and chemical composition of electrodeposits of the metallic Mo films investigated by SEM and EDX. Mapping SEM images and EDX

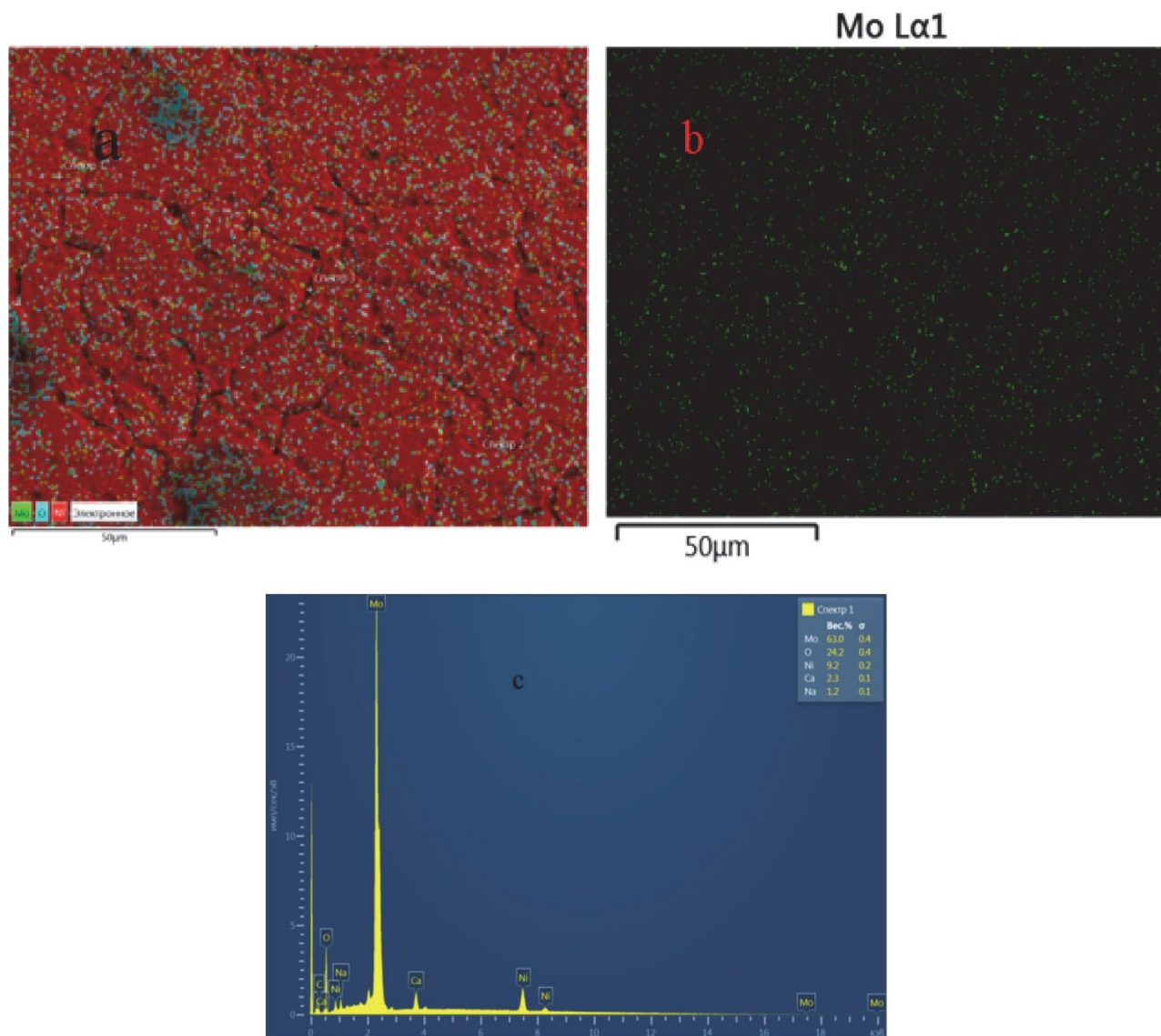


Fig. 9. SEM (a, b) and EDAX (c) of the electrodeposited Mo from a solution consists of 0,1 M $\text{Na}_2\text{MoO}_4 \cdot 2\text{H}_2\text{O}$ + 0.007M $\text{C}_4\text{H}_6\text{O}_6$ at the potential of $E = -0.4$ V, at scan rate = 0.02 Vs^{-1} on Ni electrode at $T = 295$ K

analysis show that the quantity of metallic molybdenum is more than that of oxygen. The presence of oxygen may be returned to that there are some adsorbed molybdate ions on the electrode surface come from the electrolyte.

Both Fig. 9a and 9b refer to the molybdenum sample deposited at $E = -0.4$ V potential. Figure 9a presents the general SEM description including nickel electrode, molybdenum and oxygen components. That is, the area marked with red indicates the Ni electrode, blue colored dots show the oxygen in the sample, and the green dots are molybdenum. Fig. 9b represents only the molybdenum film, in order to demonstrate its deposition more noticeably.

As a result of the conducted experiments, the electroreduction of the molybdate ions has been implemented from an electrolyte consists of 0.1 M $\text{Na}_2\text{MoO}_4 \cdot 2\text{H}_2\text{O}$ and

0.007 M $\text{C}_4\text{H}_6\text{O}_6$, at a potential scan rate of 0.02 Vs^{-1} and temperature of 295 K. EDX analysis shows a good quality of the electrodeposited film from the chemical composition Mo and other elements.

4. Conclusions

The electroreduction process of the molybdate ions from tartaric acid solutions has been investigated on the Pt electrode. Kinetics and mechanism of the process have been studied, using the data of cyclic and linear polarization curves. The nature of polarization process in this case is accompanied by mixing kinetics. The results of all performed experiments indicate that the concentration of the molybdate ions, temperature and potential scanning have

a great effect on the electroreduction process of the molybdate ions in the tartaric acid electrolytes. The optimal conditions and the composition of electrodeposition bath for electroreduction process of the molybdate ions was precisely detected. The electrolyte composition consists of 0.1 M $\text{Na}_2\text{MoO}_4 \cdot 2\text{H}_2\text{O}$ + 0.007 M $\text{C}_4\text{H}_6\text{O}_6$. The electrolysis conditions are detected to be as follow: temperature 295 K, scan-rate 0.02 Vs^{-1} , electrode Pt and Ni, pH = 2.1. In addition, using galvanostatic deposition technique, where thin films of molybdenum were obtained at a current density of 2–4 mA/cm^2 , at electrolysis time of 360–470 minutes. The results of the EDX analysis show that 63% of metallic molybdenum in the deposited thin films.

5. Reference

1. A. Sh. Aliyev, Sh. O. Eminov, B. Sh. Sultanova, V. A. Mejidzadeh, D. A. Kuliyeu, D. Jalilova, D. B. Tagiyev, *Chemical Problems*. **2016**, 2, 139–145.
2. M. Duda, R. Kowalik, K. Mech, P. R. Zabinski, *Rudy Met. Niezel.* **2012**, 9, 586–591. DOI:10.1016/j.mssp.2015.01.006
3. A. Sh. Aliyev, M. Elrouby, S. F. Cafarova, *Mat. Sci. Semicon. Proc.* **2015**, 32, 31–39.
4. F. Golgovici, T. Visan, M. Buda, *Chalcogenide Lett.* **2013**, 6, 197–207.
5. M. R. Palacin, P. Simon, J. M. Tarascon, *Acta Chim. Slov.* **2016**, 63, 417–423. DOI:10.17344/acsi.2016.2314
6. G. M. Huseynov, N. A. Mammadova, H. A. Imanov, *Chemical Problems*. **2017**, 3, 329–334. DOI:10.32737/2221-8688-2017-3-329-334
7. V. A. Majidzade, P. H. Guliyev, A. Sh. Aliyev, M. Elrouby, D. B. Tagiyev, *J. Mol. Struct.* **2017**, 1136, 7–13. DOI:10.1016/j.molstruc.2017.01.082
8. V. A. Majidzade, Sh. E. Alizade, A. Sh. Aliyev, *Nakhchivan State University Scientific works*. **2018**, 92, 3, 176–179.
9. A. Sh. Aliyev, V. A. Majidzade, N. Sh. Soltanova, D. B. Tagiyev, V. N. Fateev, *Chemical Problems*. **2018**, 2, 178–185. DOI:10.32737/2221-8688-2018-2-178-185
10. V. A. Majidzade, *Chemical Problems*. **2018**, 3, 331–336. DOI:10.32737/2221-8688-2018-3-331-336
11. V. A. Majidzade, S. F. Cafarova, A. Sh. Aliyev, D. B. Tagiyev, *Azerbaijan Chemical Journal*. **2018**, 3, 6–10. DOI:10.32737/0005-2531-2018-3-6-10
12. K. Ogura, Y. Enaka, T. Yosino, *Electrochim. Acta.* **1977**, 5, 509–512. DOI:10.1016/0013-4686(77)85113-X
13. P. Zanello, G. Raspi, A. Cinquantini, *Talanta*. **1977**, 1, 25–30.
14. V. V. Kuznetsov, D. I. Zimakov, S. A. Chepeleva, V. N. Kudryavtsev, *Russ. J. Electrochem.* **2004**, 40, 7, 711–715. DOI:10.1023/B:RUEL.0000035253.18329.98
15. S. F. Cafarova, A. Sh. Aliyev, M. Elrouby, N. Sh. Soltanova, D. B. Tagiyev, *J. Electrochem. Sci. Eng.* **2015**, 4, 231–235.
16. N. D. Ivanova, S. V. Ivanov, E. I. Boldyrev, O. A. Stadnik, *Prot. Met. Phys. Chem.* **2006**, 4, 388–392.
17. S. Rajak, S. K. Ghosh, P. U. Sastry, G. Sharma, R. C. Hubli, J. K. Chakravartty, *Surf. Coat. Tech.* **2015**, 261, 15–20. DOI:10.1016/j.surfcoat.2014.11.073
18. S. M. Deambrosis, E. Miorin, F. Montagner, V. Zin, M. Fabrizio, M. Sebastiani, F. Massimi, E. Bemporad, *Surf. Coat. Tech.* **2015**, 266, 14–21. DOI:10.1016/j.surfcoat.2015.02.006
19. T. J. Morley, L. Penner, P. Schaffer, T. J. Ruth, F. Bénard, E. Asselin, *Electrochem. Commun.* **2012**, 1, 78–80. DOI:10.1016/j.elecom.2011.11.026
20. A. A. Sukhotin (Ed): *Handbook of Electrochemistry*, Chemistry, Leningrad, Russian, **1981**, p. 488.
21. B. Scharifker, G. Hills, *Electrochim. Acta.* **1983**, 28, 7, 879–889. DOI:10.1016/0013-4686(83)85163-9
22. M. R. Khelladi, L. Mentar, A. Azizi, A. Sahari, A. Kahoul, *Mater. Chem. Phys.* **2009**, 115, 385–390. DOI:10.1016/j.matchemphys.2008.12.017

Povzetek

V tem delu smo raziskovali redukcijski potencial molibdatnih ionov v tartarski kislini kot elektrolitu. Študirali smo kinetiko in mehanizem elektrokemijskega procesa s ciklično in linearno voltametrično polarizacijsko metodo. Študirali smo vpliv temperature, hitrosti spreminjanja potenciala in koncentracije molibdatnih ionov na elektrokemijski proces. Ocena učinkovite aktivacijske energije je pokazala, da je elektrokemijski proces kontroliran s kinetiko mešanja.

Scientific paper

Kinetic-Spectrophotometric Determination of Thiocyanate in Human Saliva Based on Landolt Effect in Presence of Astrafloxine FF

Alexander Chebotarev,¹ Vitaliy Dubovyi,¹ Dmytro Barbalat,¹
Elena Guzenko,¹ Kateryna Bevziuk¹ and Denys Snigur^{1,*}

¹ Department of Analytical Chemistry, Odessa I. I. Mechnikov National University, Dvoryanskaya 2,
UA-65082 Odessa, Ukraine

* Corresponding author: E-mail: 270892denis@gmail.com

Received: 09-26-2018

Abstract

In the present study a kinetic-spectrophotometric method for thiocyanate determination is described. The suggested method for the determination of thiocyanate is based on its “Landolt effect” on the reaction of bromate with hydrobromic acid, which leads to the formation of only one halogen bromine. The reaction was monitored spectrophotometrically at the maximum wavelength of astrafloxine FF light absorption at 535 nm. The absorbance of reactants mixture decreased with an increase of the reaction time. The calibration curve for thiocyanate determination was obtained in the concentration range of 0.03–2.0 $\mu\text{g mL}^{-1}$ under the optimal conditions (pH 1.5; $C_{\text{BrO}_3^-} = 7.6 \times 10^{-4} \text{ mol L}^{-1}$; $C_{\text{astrafloxine FF}} = 1 \times 10^{-5} \text{ mol L}^{-1}$). The limit of detection was 0.01 $\mu\text{g mL}^{-1}$. The method was successfully applied to the determination of thiocyanate in human saliva samples with satisfactory results.

Keywords: Thiocyanate; human saliva; Landolt effect; spectrophotometry; astrafloxine FF.

1. Introduction

The toxicity of thiocyanates attracts the attention of specialists in various fields, such as medicine, ecology, food technology, etc., to the problem of developing new and improving existing methods for their determination.¹ In the human body, thiocyanates are formed during the metabolism of sulfur-containing tobacco substances and some vegetables of the *Brassica* species or fed with drinking water and food. In biological fluids thiocyanates are also formed as a result of detoxification of cyanides in the liver.² The most common source of inorganic cyanide in the human body is tobacco smoke. Since the content of thiocyanate in body fluids, especially saliva, increases with a constant source of cyanide, which is tobacco smoke, the concentration of thiocyanate in saliva, urine and serum is used as a biomarker to detect smokers.^{3,4}

Various analytical methods have been proposed for the determination of thiocyanates. These include the potentiometry with ion-selective electrodes,⁵ electrophoresis,⁶ gas chromatography, and sequential-injection analysis or extraction-spectrophotometric methods.^{7–10}

The property of thiocyanates to inhibit the oxidation reaction of dyes (Landolt effect) is the basis of a number of kinetic methods. Landolt reactions have frequently been used for analytical purposes because of their operational and instrumental simplicity and high sensitivity.^{11–16} The spectrophotometric methods for the determination of thiocyanates based on the inhibition of the oxidation of Methyl Orange,¹² Methyl Red,¹³ Methylene Blue,¹⁴ Crystalline Violet,¹⁵ and Janus Green have been proposed.¹⁶

The main disadvantage of the existing kinetic methods for the determination of thiocyanates based on the Landolt effect is the formation of a mixture of halogens in the interaction of bromate and hydrochloric acid. In this case, the oxidative destruction or halogenation of the dyes occurs at different rates with formation of several products, which leads to poor reproducibility of the measurement results.

To avoid overlapping absorption spectra of the dye and its oxidation/halogenation products, a symmetric dye astrafloxine FF was chosen. The reaction was monitored spectrophotometrically at the maximum wavelength of astrafloxine FF (535 nm) while measuring the change in the absorbance over time.

In this paper, we describe the development of a new method for the determination of thiocyanate, based on its “Landolt effect” on the reaction of bromate with hydrobromic acid, which leads to the formation of bromine. Bromination of astraflorine FF leads to the formation of only one colorless product.

2. Experimental

2.1. Chemicals and Reagents

The analytically pure reagents were used, and all solutions were prepared using distilled water. A 0.1 mol L⁻¹ stock solution of thiocyanate was prepared by dissolving potassium thiocyanate in water. A 0.01 mol L⁻¹ potassium bromate solution was prepared by dissolving KBrO₃ in water. A 1 × 10⁻³ mol L⁻¹ solution of astraflorine FF was prepared by dissolving dye in 5 mL of ethanol and diluting to 100 mL with water. A 2.8 mol L⁻¹ hydrobromic acid solution was prepared by dilution of concentrated acid. Solutions with lower concentrations were prepared by the appropriate dilution of more concentrated ones.

2.2. Instrumentation

The absorbance measurements were performed using a SF-56 spectrophotometer equipped with thermostat at 25 °C in 1 cm quartz cells. The pH measurements were made using I-160M potentiometer with a combined glass electrode. The digital weight balance Axis ANG50C was used for weighing. Centrifuge type MPW-340 was used.

2.3. General Procedure

An aliquot of the solution containing thiocyanate was transferred to a 25 ml volumetric flask with the expectation that after dilution its concentration would be in the range 0.03–2.0 µg mL⁻¹. Then 1.9 mL of 0.01 mol L⁻¹ potassium bromate solution, 0.3 mL of 2.8 mol L⁻¹ hydrobromic acid solution, and 2.5 mL of 1 × 10⁻⁴ mol L⁻¹ astraflorine FF solution were added. The obtained solution was diluted to 25 mL, mixed and transferred into a quartz cell. The absorbance was recorded as a function of time at 535 nm.

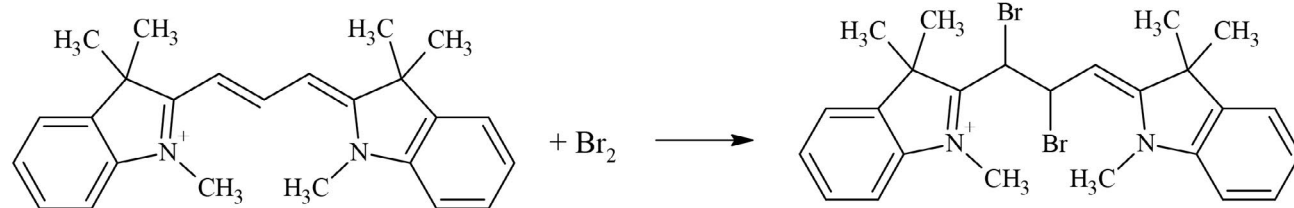


Fig. 1. A probable scheme of astraflorine FF interaction with bromine in aqueous solution.

2.4. Sampling and Sample Preparation

The saliva samples were collected from a smoking and a non-smoking person. These samples were centrifuged for 5 min at 3000 rpm and analyzed according to proposed method after appropriate dilution.

3. Results and Discussion

3.1. Reaction Chemistry

In Landolt processes, a slow reaction is linked to a fast one by the reaction product of the former.¹¹ The Landolt effect may be shown as follows:



Since the second reaction is faster than the first, its product (P) can only be detected once L (the “Landolt reagent”) has disappeared completely as a result of the second reaction.

The reaction of bromate with the hydrobromic acid produces only bromine:



A strong oxidative agents such as Br₂, Cu(III), Ce(VI), and others can cause the decolorization of the astraflorine FF,¹⁷ and the bromination reaction mechanism probably can be described by the scheme shown in Fig. 1. Thiocyanate is a Landolt reagent in the reaction with bromate because the presence of thiocyanate in the solution causes the consumption of the produced Br₂, and its reaction with thiocyanate is much faster than dye bromination.

The absorption spectra of astraflorine FF dye and a product of its decolorisation are shown in Fig. 2.

As can be seen from Fig. 2, the astraflorine FF dye has an absorbance maximum at 535 nm and its bromination reaction product is colorless and has absorbance only in UV region.

3.2. Effects of Variables

To obtain the maximum sensitivity in the determination of thiocyanate, the effects of the media acidity, bromate

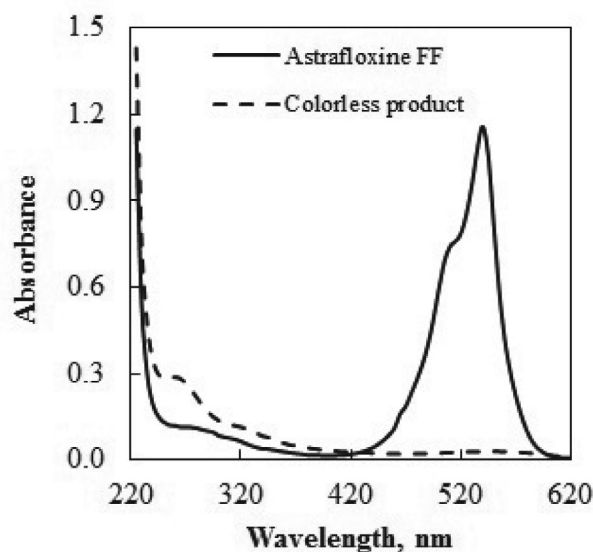


Fig. 2. The absorption spectra of astrafloxine FF dye and a product of its decolorisation, $C_{\text{astrafloxine FF}} = 1 \times 10^{-5} \text{ mol L}^{-1}$; $C_{\text{CNS}^-} = 2 \times 10^{-5} \text{ mol L}^{-1}$; $C_{\text{BrO}_3^-} = 7.6 \times 10^{-4} \text{ mol L}^{-1}$; $l = 1 \text{ cm}$.

and astrafloxine FF concentrations were studied. The effect of media acidity was studied in the interval pH 1.0–3.0 (hydrobromic acid concentration interval was 0.0112 – 0.112 mol L⁻¹). When the concentration of hydrobromic acid was more than 0.112 mol L⁻¹ hydrobromic acid (pH < 1), the decolorization of astrafloxine FF was coupled almost immediately. At pH higher than 2, the reaction takes more than 1 h. Thus, the optimum media acidity was chosen as a compromise. In the case when pH is 1.5, the reaction time

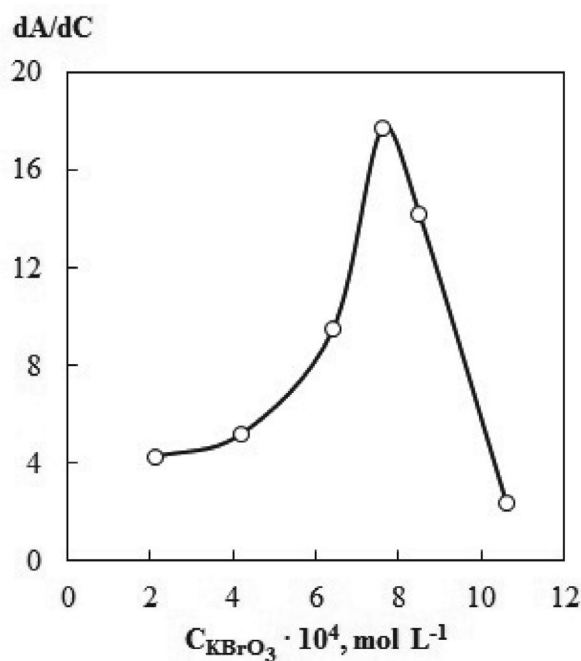


Fig. 3. The differential dependence of absorbance on bromate concentration, $C_{\text{astrafloxine FF}} = 1 \times 10^{-5} \text{ mol L}^{-1}$; pH 1.5; $C_{\text{CNS}^-} = 2 \times 10^{-5} \text{ mol L}^{-1}$; $l = 1 \text{ cm}$.

is about 3 min, which is sufficient for correct registration of the change in absorbance.

The effect of astrafloxine FF concentration on reaction was studied in the range of 5×10^{-6} – $5 \times 10^{-4} \text{ mol L}^{-1}$. The results showed that astrafloxine FF concentration does not influence the reaction. Therefore, the astrafloxine FF concentration of $1 \times 10^{-5} \text{ mol L}^{-1}$ was selected as optimal.

The effect of bromate concentration was also studied. Fig. 3 shows the differential dependence of absorbance on bromate concentration ($dA/dC = f(C)$).

As can be seen from Fig. 3, a bromate concentration equal to $7.6 \cdot 10^{-4} \text{ mol L}^{-1}$ on the differential curve is the maximum. Thus, this concentration was used in further work.

The effect of ionic strength on the kinetics of the oxidation of thiocyanate was not studied in this work, because a number of studies point to the lack of or very weak influence.^{12–14} Despite the fact that the temperature can significantly affect the reaction rate in this study, a temperature of 25 °C was a priori chosen as the most convenient for routine work.

3. 3. Analytical Figures of Merit and Interference Study

The slope method was used to construct the calibration plot for kinetic-spectrophotometric determination of thiocyanate (Fig. 4).

In the concentration range 0.03–2.0 $\mu\text{g mL}^{-1}$ of thiocyanate, a regression equation: $-\text{tg}\alpha = -5.11 \times 10^{-3} C_{\text{CNS}^-} + 1.14 \times 10^{-2}$ with correlation coefficient of 0.99 was ob-

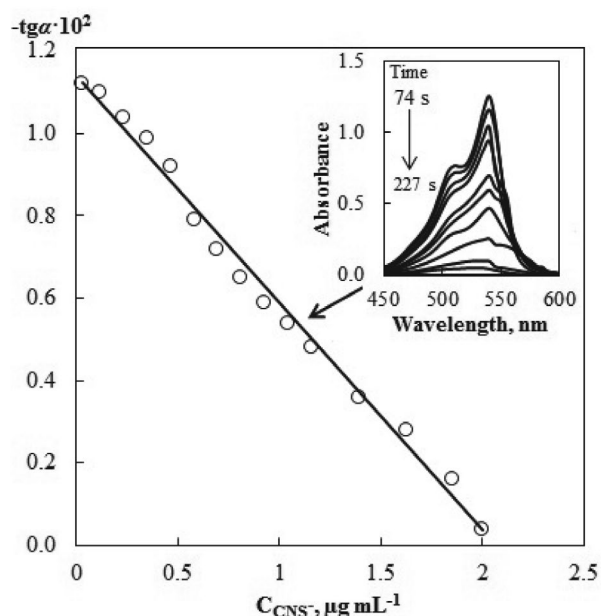


Fig. 4. The calibration plot for kinetic-spectrophotometric determination of thiocyanate by slope method, $C_{\text{astrafloxine FF}} = 1 \times 10^{-5} \text{ mol L}^{-1}$; pH 1.5; $C_{\text{BrO}_3^-} = 7.6 \times 10^{-4} \text{ mol L}^{-1}$; $l = 1 \text{ cm}$.

tained. Also, limit of detection LOD (3σ) $0.01 \mu\text{g mL}^{-1}$ was calculated. The reproducibility of the proposed method was determined on the basis of 5 parallel determinations of thiocyanate with a concentration of $1 \mu\text{g mL}^{-1}$, and the obtained relative standard deviation RSD value was 2.9%.

The effect of some interfering ions on the determination of the $2 \times 10^{-5} \text{ mol L}^{-1} \text{ CNS}^-$ by the suggested method was studied and it was established that ions of alkaline metals, alkaline earth metals and a number of other ions did not interfere at the following molar ratios: 1:1500 (Na^+ , K^+ , Ca^{2+} , Cl^-); 1:1000 (CO_3^{2-} , F^- , PO_4^{3-} , Cu^{2+} , Mg^{2+} , Al^{3+}); 1:500 (Co^{2+} , Fe^{2+} , Fe^{3+}); 1:100 (SO_3^{2-} , NO_2^- , $\text{C}_2\text{O}_4^{2-}$).

3. 4. The Analytical Applications of the Method

To demonstrate the analytical applications of the proposed method, the non-smoker and smoker human saliva samples were analyzed according to the suggested procedure. The received results are summarized in Table 1. The accuracy and reliability of the proposed method were investigated by applying it to determination of thiocyanate using the standard addition method. High (98.8–99.6%)

recoveries (R) indicated that the suggested kinetic-spectrophotometric procedure was accurate, reliable and can be used for the thiocyanate quantification.

3. 4. Comparison with Literature Studies

A comparison of the proposed kinetic-spectrophotometric method with other spectrophotometric methods which were reported in literature for thiocyanate determination is given in Table 2. The spectrophotometric method based on formation of Fe(III)-thiocyanate complex is poorly sensitive.¹⁸ The increased sensitivity of the determination of thiocyanate by kinetic-spectrophotometric methods should be noted.^{12–16,19,20} Methods for the determination of thiocyanate based on the formation and extraction of its ion pair with astraflaxine FF are also of low sensitivity.^{9,10} Zaruba with coauthors have proposed an original two-in-one device for online monitoring of direct immersion single-drop microextraction for preconcentration and determination of thiocyanate.²¹ This is the first time an optical probe was proposed as the microdrop holder and measuring cell. However, with the simplicity and convenience of this approach, its disadvantages are

Table 1. Determination of thiocyanate in human saliva by the proposed method ($n = 5$, $P = 0.95$)

range ¹²	Sample	Spiked, $\mu\text{g mL}^{-1}$	Found, $\mu\text{g mL}^{-1}$	RSD, %	R, %	*Thiocyanate concentration
Non-smoker saliva	**M	–	86.25±2.46	2.3	–	51.98–155
		20.0	105.8±3.28	2.5	99.6	
	***F	–	78.54±3.02	3.1	–	
		20.0	99.12±3.57	2.9	100.6	
Smoker saliva	M	–	251.4±8.74	2.8	–	170.23–265
		20.0	268.2±8.99	2.7	98.8	
	F	–	235.7±8.49	2.9	–	
		20.0	254.1±9.47	3.0	99.4	

*The interval of thiocyanate concentration ($\mu\text{g mL}^{-1}$) in human saliva according to the literature data; **Male; ***Female; R – recovery.

Table 2. Comparison of the developed method with some other methods of thiocyanate determination with spectrophotometric detection

Method	Reagent (λ , nm)	Linearity, $\mu\text{g mL}^{-1}$	LOD, $\mu\text{g mL}^{-1}$	Ref.
Spectrophotometry	$\text{Fe}(\text{NO}_3)_3$ (447)	2–100	–	18
Kinetic-spectrophotometry	Methyl Orange (525)	$2 \times 10^{-7} - 4 \times 10^{-5}^*$	$7 \times 10^{-8}^*$	12
Kinetic-spectrophotometry	Methyl Red (520)	0.05–1.1	0.0025	11
Kinetic-spectrophotometry	Ferroine/ IO_4^- (510)	0.02–0.2	0.016	19
Kinetic-spectrophotometry	4-amino- <i>N,N</i> -diethylanilinesulphate/ Fe^{3+} (515)	0.05–0.5	20	
DLLME [†]	Astrafloxine FF (555)	3.1–28.2	0.11	9
SIA ^{**}	Astrafloxine FF (555)	2.9–29	1.16	10
DI-SDME ^{**}	Astrafloxine FF (555)	0.29–4.35	0.12	21
Kinetic-spectrophotometry ^{***}	Astrafloxine FF (535)	0.03 – 2.0	0.01	This work

DI-SDME – direct immersion single drop microextraction; DLLME – dispersive liquid-liquid microextraction; SIA – sequential injection analysis; * concentration given in mol L^{-1} ; **ion pair formation between thiocyanate and astraflaxine FF and its extraction; ***decolorization of astraflaxine FF

low sensitivity and the need for optical probe with a special design. Also, the micropumping multicommutation flow system was successfully applied to determine thiocyanate in human saliva samples.²² In general, the proposed kinetic-spectrophotometric method for the determination of thiocyanate based on the decolorization of astraflavine FF can be attributed among the most sensitive methods. At the same time, the proposed method lacks the disadvantages of other kinetic methods, namely, poor reproducibility.

4. Conclusions

In this study, a novel, accurate and sensitive kinetic-spectrophotometric procedure for determination of thiocyanate trace concentrations has been reported. The method for the determination of thiocyanate is based on its “Landolt effect” on the reaction of bromate with hydrobromic acid, which leads to the formation of only one halogen bromine and promotes decolorization of astraflavine FF. The reaction was monitored spectrophotometrically at the maximum wavelength of astraflavine FF at 535 nm. The limit of detection was 0.01 $\mu\text{g mL}^{-1}$. The method was successfully applied to the determination of thiocyanate in human saliva samples with satisfactory results.

5. References

- Z. Glatz, P. Bouchal, O. Janiczek, M. Mandl, P. Ceskova, *J. Chromat. A.* **1999**, 838, 139–148.
- Z. Glatz, S. Novakova, H. Sterbova, *J. Chromat. A.* **2001**, 916, 273–277.
- G. F. Wang, M. G. Li, Y. C. Gao, B. Fang, *Sensors*, **2004**, 4, 147–155. DOI:10.3390/s40900147
- S. Narkowicz, E. Jaszczak, Ź. Polkowska, B. Kielbratowska, A. Kotłowska, J. Namieśnik, *Biomed. Chromatogr.* **2018**, 32, e4111. DOI:10.1002/bmc.4111
- N. Giorgio, *Anal. Chem.* **1975**, 47, 763–764. DOI:10.1021/ac60354a002
- C. Bjerregaard, P. Muller, H. Sorensen, *J. Chromat. A.* **1995**, 717, 409–414.
- Y. Tanaka, N. Naruishi, H. Fukuya, J. Sakata, K. Saito, S. Wakida, *J. Chromatogr. A.* **2004**, 1051, 193–197. DOI:10.1016/S0021-9673(04)00979-3
- S. Kage, T. Nagata, K. Kudo, *J. Chromatogr. B.* **1996**, 675, 27–32. DOI:10.1016/0378-4347(95)00344-4
- V. Andruch, C. C. Acebal, J. Škrliková, H. Sklenářová, P. Solich, I. S. Balogh, F. Billes and L. Kočurová, *Microchem J.* **2012**, 100, 77–82. DOI:10.1016/j.microc.2011.09.006
- C. C. Acebal, H. Sklenářová, J. Škrliková, I. Šramková, V. Andruch, I. S. Balogh and P. Solich, *Talanta*, **2012**, 96, 107–112. DOI:10.1016/j.talanta.2012.01.021
- D. Perez-Bendito and M. Silva, *Kinetic Methods in Analytical Chemistry*, 1st ed. Ellis Horwood, Chichester, **1988**, 330.
- T. Madrakian, A. Esmaeili, A. Abdolmaleki, *J. Anal. Chem.* **2004**, 59, 28–32. DOI:10.1023/B:JANC.0000011664.22353.e3
- J. Ghasemi, R. Amini, A. Afkhami, *Anal. Sci.* **2001**, 17, 435–437. DOI:10.2116/analsci.17.435
- M. R. Shishehbore, N. Nasirizadeh, A. A. Kerdegari, *Anal. Sci.* **2005**, 21, 1213–1216. DOI:10.2116/analsci.21.1213
- G. Bagherian, M. A. Chamjangali, Z. Berenji, *Eurasian J. Anal. Chem.* **2008**, 3, 307–317.
- M. Keyvanfard, K. Alizad, P. Elahian, *J. Chem.* **2013**, 2013, 1–5.
- I. S. Balogh, M. Ruschak, V. Andruch, Y. Bazel, *Talanta*. **2008**, 76, 111–115. DOI:10.1016/j.talanta.2008.02.011
- J. Hovinen, M. Lahti, J. Vilpo, *J. Chem. Educ.* **1999**, 76, 1281–1282. DOI:10.1021/ed076p1281
- A. Afkhami, H. Bahrami, *Anal. Letters*. **1995**, 28, 1785–1791.
- V. R. Igov, R. M. Simonovic, R. P. Igov, *Facta Univ. Ser. Phys., Chem. Technol. Univ. Nis.* **2002**, 2, 209–213. DOI:10.1080/00032719508000356
- S. Zaruba, A. Vishnikin, J. Škrliková, A. Diuzheva, I. Ozimaničová, K. Gavazov, V. Andruch, *RSC Advances*. **2017**, 7, 29421–29427. DOI:10.1039/C7RA02326J
- J. J. Silva Júnior, M. A. Farias, V. L. Silva, M. C. B. S. M. Montenegro, A. N. Araújo, A. F. Lavorante, A. P. S. Paim, *Spectrosc. Lett.* **2010**, 43, 213–219. DOI:10.1080/00387010903287094

Povzetek

V predstavljeni študiji opisujemo kinetično spektrofotometrično metodo za določanje tiocianata. Predlagana metoda za določanje tiocianata je osnovana na njegovem “Landoltovem učinku” na reakcijo med bromatom in bromovodikovo kislino, ki vodi do nastanka ene molekule broma. Reakcijo spremljamo spektrofotometrično pri absorpcijskem maksimumu astraflavina FF pri 535 nm. Absorbanca reakcijske mešanice se zmanjšuje z naraščanjem reakcijskega časa. Umeritveno krivuljo za določitev tiocianata smo pridobili v koncentracijskem območju 0,03–2,0 $\mu\text{g mL}^{-1}$ pod optimalnimi pogoji (pH 1,5; $C_{\text{BrO}_3^-} = 7,6 \times 10^{-4} \text{ mol L}^{-1}$; $C_{\text{astraflavsin FF}} = 1 \times 10^{-5} \text{ mol L}^{-1}$). Meja zaznave je bila 0,01 $\mu\text{g mL}^{-1}$. Metodo smo uspešno uporabili za določitev tiocianata v vzorcih človeške sline z zadovoljivimi rezultati.

Scientific paper

Synthesis and Crystal Structure of a Polymeric Copper(II) Complex Derived from 2-Hydroxy-5-methylbenzaldehyde Oxime with Antibacterial Activities

Ya-Li Sang* and Xue-Song Lin

Department of Chemistry and Chemical Engineering, Chifeng University, Chifeng 024001, P. R. China

* Corresponding author: E-mail: sangyali0814@126.com

Received: 09-28-2018

Abstract

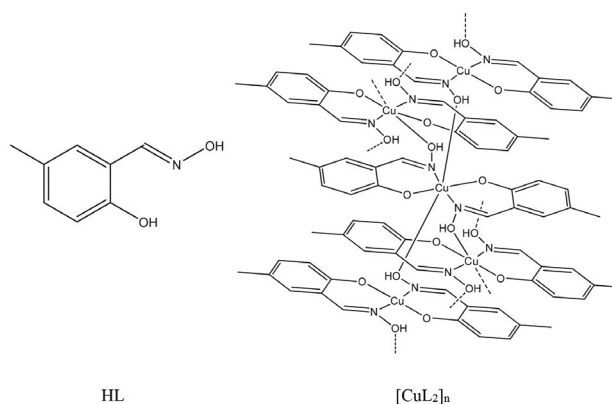
A centrosymmetric O-bridged polynuclear copper(II) complex, $[\text{CuL}_2]_n$, where L is the deprotonated form of the Schiff base ligand 2-hydroxy-5-methylbenzaldehyde oxime, has been prepared and characterized by IR, UV and single-crystal X-ray determination. There is a crystallographic inversion center in the complex. The Cu atom in the complex is coordinated by the phenolate oxygen, imino nitrogen and hydroxyl oxygen atoms from two Schiff base ligands, forming octahedral geometry. The complex was tested *in vitro* for its antibacterial activity.

Keywords: Schiff base; copper complex; synthesis; crystal structure; antibacterial activity

1. Introduction

Schiff bases are readily synthesized by the condensation reaction of carbonyl compounds with primary amines.¹ Schiff bases have been widely investigated for their biological activities, such as antibacterial and antitumor activities,² biomimetic catalytic properties, *etc.*³ Metal complexes of Schiff bases have also been received much attention. These complexes not only play an important role in the development of coordination chemistry related to catalysis and enzymatic reactions, magnetism and molecular architectures,⁴ but also exhibit interesting biological activities.⁵

In recent years, a number of Schiff bases derived from salicylaldehyde and its derivatives with various amines, and their complexes have been reported.⁶ Most of the compounds show versatile biological properties especially antibacterial activities.⁷ In addition, copper complexes show effective biological activities.⁸ In the present work, we choose 2-hydroxy-5-methylbenzaldehyde oxime (HL) as ligand, to prepare a novel polymeric copper complex $[\text{CuL}_2]_n$. To our knowledge, there have been no complexes derived from HL reported so far. The antibacterial activities against *Bacillus subtilis*, *Staphylococcus aureus*, *Escherichia coli*, and *Pseudomonas fluorescens*, were evaluated for the Schiff base and the copper complex.



Scheme 1. The Schiff base HL and the copper complex

2. Experimental

2.1. Materials and Measurements

2-Hydroxy-5-methylbenzaldehyde, hydroxylamine hydrochloride, and copper perchlorate hexahydrate with AR grade were obtained from Aldrich and were used as received. Elemental analyses were performed using a Perkin-Elmer 240C analytical instrument. Infrared spectra were recorded on a Nicolet 5DX FT-IR spectrophotometer

with KBr pellets. ^1H NMR spectrum was recorded on a Bruker instrument at 300 MHz. UV-Vis spectra were recorded on a JASCO V-570 spectrophotometer. Molar conductance was measured with a Shanghai DDS-11A conductometer.

Caution! Although no problems were encountered in our work, perchlorate salts are potentially explosive. Therefore, only a small amount of copper perchlorate should be used at a time and handled with proper care.

2. 2. Synthesis of HL

Hydroxylamine hydrochloride (0.70 g, 0.010 mol) and NaOH (0.40 g, 0.010 mol) were reacted in absolute ethanol (30 mL). The solid was removed by filtration. To the filtrate an ethanol solution of 2-hydroxy-5-methylbenzaldehyde (1.36 g, 0.01 mol) was added with stirring. The mixture was stirred at room temperature for 30 min to give yellow solution. The solution was evaporated to give yellow powder, which was recrystallized from methanol and dried in air. Yield: 87%. Anal. Calcd. for $\text{C}_8\text{H}_9\text{NO}_2$ (%): C, 63.56; H, 6.00; N, 9.27. Found (%): C, 63.45; H, 6.12; N, 9.15. ^1H NMR (d^6 -DMSO): δ : 2.32 (s, 6H, CH_3), 6.87 (d, 1H, ArH), 7.14 (d, 1H, ArH), 7.53 (s, 1H, ArH), 8.28 (s, 1H, $\text{CH}=\text{N}$), 11.71 (s, 1H, OH), 12.23 (s, 1H, OH). ^{13}C NMR (d^6 -DMSO): δ : 21.2, 116.7, 118.1, 130.5, 131.3, 133.0, 146.7, 157.2.

2. 3. Synthesis of $[\text{CuL}_2]_n$

To an ethanolic solution (15 mL) of HL (15.1 mg, 0.10 mmol) an ethanolic solution (10 mL) of copper perchlorate hexahydrate (37.1 mg, 0.10 mmol) was added with stirring. The mixture was stirred for half an hour and filtered. The filtrate was kept undisturbed at room temperature to slowly evaporate for a few days, generating blue crystals suitable for X-ray diffraction. Crystals were isolated by filtration and dried in air. Yield 37% with respect to HL. Anal. Calcd. for $\text{C}_{16}\text{H}_{16}\text{CuN}_2\text{O}_4$ (%): C, 52.82; H, 4.43; N, 7.70. Found (%): C, 52.63; H, 4.55; N, 7.81.

2. 4. X-ray Crystallography

A suitable single crystal with high quality of the complex was selected and mounted on a Bruker Smart 1000 CCD area-detector diffractometer with graphite monochromatized Mo-K α radiation ($\lambda = 0.71073 \text{ \AA}$). Diffraction data for the complex were collected by ω scan mode at 298(2) K. Data reduction and cell refinement were performed by the SMART and SAINT programs.⁹ Empirical absorption correction was applied by using SADABS.¹⁰ The structure was solved by direct methods and refined with the full-matrix least-squares technique using the SHELXL97 package.¹¹ The non-H atoms in the structure were subjected to refined anisotropic refinement. Hydrogen atoms were located in geometrically and treated with

the riding mode. Crystallographic data and experimental details for the complex are summarized in Table 1. Selected bond lengths and angles for the complex are listed in Table 2.

Table 1. Crystallographic and experimental data for the copper complex

Parameter	Value
Chemical formula	$\text{C}_{16}\text{H}_{16}\text{CuN}_2\text{O}_4$
Formula weight	363.85
T (K)	298(2)
Crystal system	orthorhombic
Space group	$Pbca$
a (\AA)	7.5170(5)
b (\AA)	6.4796(4)
c (\AA)	32.076(2)
V (\AA^3)	1562.3(2)
Z	4
ρ (g/cm^3)	1.547
μ (Mo-K α) (mm^{-1})	1.419
$F(000)$	748
No. of measured reflections	12412
No. of unique reflections	1440
No. of observed reflections	1269
Parameters/restraints	107/0
R_{int}	0.0234
Goodness of fit on F^2	1.300
R_1, wR_2 [$I \geq 2\sigma(I)$] ^a	0.0397, 0.0859
R_1, wR_2 (all data) ^a	0.0450, 0.0884
$\Delta\rho_{\text{max}}/\Delta\rho_{\text{min}}$, e \AA^{-3}	0.269, -0.254

$$^a R_1 = \frac{\sum |F_o| - |F_c|}{\sum |F_o|}, wR_2 = \left[\frac{\sum w(F_o^2 - F_c^2)^2}{\sum w(F_o^2)^2} \right]^{1/2}$$

Table 2. Selected bond lengths (\AA) and angles ($^\circ$) for the copper complex

Bond	$d, \text{\AA}$	Bond	$d, \text{\AA}$
Cu(1)–O(1)	1.921(2)	Cu(1)–N(1)	1.934(2)
Cu(1)–O(2A)	2.571(3)		
Angle	$\omega, ^\circ$	Angle	$\omega, ^\circ$
O(1)–Cu(1)–O(1A)	180	O(1)–Cu(1)–N(1A)	88.36(9)
O(1)–Cu(1)–N(1)	91.64(9)	N(1)–Cu(1)–N(1A)	180
O(1)–Cu(1)–O(2A)	98.85(9)	N(1)–Cu(1)–O(2A)	84.28(9)
O(1)–Cu(1)–O(2B)	81.15(9)	N(1)–Cu(1)–O(2B)	95.72(9)

Symmetry codes: A: $1 - x, 1 - y, -z$; B: $\frac{1}{2} + x, \frac{1}{2} - y, -z$.

2. 5. Antibacterial test

Antibacterial activities of the Schiff base and the complex were tested *in vitro* against *Bacillus subtilis*, *Staphylococcus aureus*, *Escherichia coli*, and *Pseudomonas fluorescens* using MH medium (Mueller–Hinton medium: casein hydrolysate 17.5 g, soluble starch 1.5 g, beef extract 1000 mL). The minimum inhibitory concentrations (MIC)

of the test compounds were determined by a colorimetric method using the dye MTT (3-(4,5-dimethylthiazol-2-yl)-2,5-diphenyltetrazolium bromide).¹² A solution of the compounds ($50 \mu\text{g mL}^{-1}$) in DMSO were prepared and graded quantities of the test compounds were incorporated in specified quantity of sterilized liquid MH medium. A specified quantity of the medium containing the compound was poured into microtitration plates. Suspension of the microorganism was prepared to contain about 10^5 colony forming units cfu mL^{-1} and applied to microtitration plates with serially diluted compounds in DMSO to be tested and incubated at 37°C for 24 h. After the MICs were visually determined on each of the microtitration plates, $50 \mu\text{L}$ of PBS (Phosphate Buffered Saline $0.01 \text{ mol}\cdot\text{L}^{-1}$, pH 7.4: $\text{Na}_2\text{HPO}_4\cdot 12\text{H}_2\text{O}$ 2.9 g, KH_2PO_4 0.2 g, NaCl 8.0 g, KCl 0.2 g, distilled water 1000 mL) containing 2 mg of MTT was added to each well. Incubation was continued at room temperature for 4–5 h. The content of each well was removed, and $100 \mu\text{L}$ of isopropyl alcohol containing 5% 1.0 mol L^{-1} HCl was added to extract the dye. After 12 h of incubation at room temperature, the optical density (OD) was measured with a microplate reader at 550 nm. The observed MICs are presented in Table 3.

Table 3. Antibacterial activities of the compounds

	MIC ($\mu\text{g mL}^{-1}$)			
	<i>Bacillus subtilis</i>	<i>Escherichia coli</i>	<i>Pseudomonas fluorescens</i>	<i>Staphylococcus aureus</i>
HL	> 100	12.5	> 100	25
$[\text{CuL}_2]_n$	3.12	1.56	12.5	1.56
Penicillin B	1.3	> 100	> 100	2.1
Kanamycin G	0.78	3.12	3.12	0.78

3. Results and Discussion

The Schiff base HL was readily prepared by the reaction of 2-hydroxy-5-methylbenzaldehyde with hydroxylamine in ethanol. The copper complex was prepared by reaction of equimolar quantities of the Schiff base ligand and copper perchlorate hexahydrate in ethanol. The molar conductivities of the copper complex measured in acetonitrile at concentration of 10^{-3} and 10^{-4} M are 25 and $7.0 \Omega^{-1} \text{ cm}^2 \text{ mol}^{-1}$, indicating the dissociation of the polymeric complex to form single $[\text{CuL}_2]$ units in such solution.¹³

3. 1. Crystal structure Description

Figure 1 gives the perspective view of the copper complex. The molecule of the complex possesses crystallographic inversion center symmetry, with the inversion center located at the Cu atom. The smallest repeat unit of the complex contains $[\text{CuL}_2]$ unit. The adjacent $[\text{CuL}_2]$

units are bridged by hydroxyl groups, with Cu...Cu separation of $4.962(2) \text{ \AA}$. The Schiff base ligand forms one six-membered chelate ring with bite angle of $91.64(9)^\circ$. The Cu atom is in an octahedral coordination, with the two phenolate oxygen and two imino nitrogen donor atoms from two Schiff base ligands defining the equatorial plane, and with two hydroxyl oxygen donor atoms from symmetry related Schiff base ligands occupying the axial positions. The axial coordinate bonds are much longer than those in the equatorial plane, which is caused by the Jahn-Teller distortion. The *cis* bond angles are in the range $88.36(9)$ – $91.64(9)^\circ$. The Cu–O and Cu–N bond lengths in the complex are comparable to the values observed in Schiff base copper(II) complexes.¹⁴ The molecules are linked by hydroxyl groups to form two-dimensional network (Figure 2).

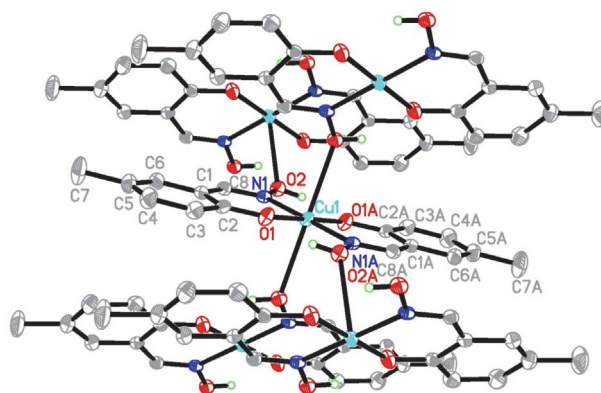


Figure 1. Molecular structure of the copper complex. Displacement is drawn at the 30% probability level. Atoms labeled with the suffix A are at the symmetry position $1 - x, 1 - y, -z$. Hydrogen atoms of the carbon atoms were omitted for clarity.

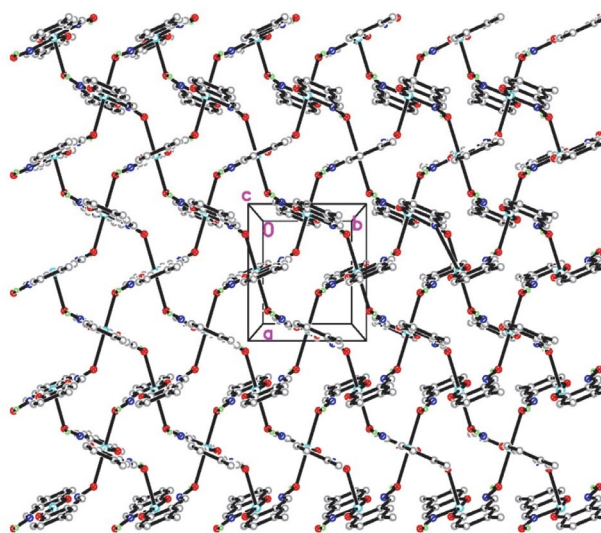


Figure 2. Molecular packing diagram of the copper complex, viewed along the *c* axis. Hydrogen atoms of the carbon atoms were omitted for clarity.

3. 2. IR and UV-Vis Spectra

The IR spectra of the free Schiff base and the copper complex provide information about the metal-ligand bonding. The weak and broad absorptions at 3350–3500 cm^{-1} are assigned to the stretching vibrations of the phenolic O–H group of the compounds. Several bands in the range of 2900–3150 cm^{-1} are assigned to the characteristic absorption of CH groups. The phenolic $\nu(\text{C}-\text{O})$ in the spectrum of the Schiff base is observed as a medium band at 1278 cm^{-1} . However, in the spectrum of the complex, the absorption appears at 1287 cm^{-1} . The strong band at 1639 cm^{-1} of the free Schiff base is assigned to the azomethine group, $\nu_{\text{C}=\text{N}}$,¹⁵ which is observed at low wave number of 1627 cm^{-1} for the complex, indicating the coordination of the imino nitrogen atom to the Cu atom. The newly observed bands in the region 450–650 cm^{-1} can be assigned to the Cu–O and Cu–N bonds.

The electronic spectra of the compounds in acetonitrile were recorded in the range of 200–800 nm. The intense absorption band at 270 nm may be assigned to intra-ligand $\pi-\pi$ transitions in the complex. The weak absorptions centered at 350 nm may be assigned to the phenolate of Schiff base ligand to Cu center charge transfer band (LMCT). Unlike the spectrum of the free ligand, much weaker and less well-defined broad band found in the spectrum of the complex at 605 nm which is assigned to the $d-d$ transition. The transition is typical for square-planar copper(II) complexes,¹⁶ which indicates that the complex dissociated to form $[\text{CuL}_2]$ units with square planar geometry in such solution.

3. 3. Antibacterial Activity

The Schiff base HL and the complex were screened *in vitro* for antibacterial activities against *Bacillus subtilis*, *Staphylococcus aureus*, *Escherichia coli*, and *Pseudomonas fluorescens* by the MTT method. The MICs of the compounds against the bacteria are presented in Table 3. Penicillin B was used as a reference.

The Schiff base HL shows medium antibacterial activities against *Escherichia coli* and *Staphylococcus aureus*, and no activity against *Bacillus subtilis* and *Pseudomonas fluorescens*. In general, the copper complex has stronger activities against the bacteria than the free Schiff base. The complex has strong activity against *Bacillus subtilis*, *Escherichia coli* and *Staphylococcus aureus*, and medium activity against *Pseudomonas fluorescens*. The present complex has stronger activities against *Bacillus subtilis* and *Escherichia coli* than the copper complex we reported recently.¹⁷ It is quite interesting that the complex has better activity against *Staphylococcus aureus* than Penicillin B, and better activity against *Escherichia coli* than Kanamycin G, which deserve further study and to explore new antibacterial drugs.

4. Conclusion

A new centrosymmetric O-bridged polynuclear copper(II) complex derived from 2-hydroxy-5-methylbenzaldehyde oxime has been prepared and characterized. The Cu atom in the complex is in octahedral coordination. The antibacterial activities of the Schiff base and the complex were assayed. The results indicated that the complex is a potential antibacterial material.

5. Supplementary Material

CCDC reference number 1445981 for the copper complex contain the supplementary crystallographic data for this paper. These data can be obtained free of charge at www.ccdc.cam.ac.uk, or from Cambridge Crystallographic Data Center, 12, Union Road, Cambridge CB2 1EZ, UK; Fax: +44 1223 336 033; e-mail: deposit@ccdc.cam.ac.uk.

Acknowledgements

The authors gratefully acknowledge the financial support by the Research Program of Universities of Inner Mongolia Autonomous Region (NJ10245).

6. References

- (a) J. Valentova, S. Varenýi, P. Herich, P. Baran, A. Bilkova, J. Kozisek, L. Habala, *Inorg. Chim. Acta* **2018**, *480*, 16–26; DOI:10.1016/j.ica.2018.04.058
(b) P. Nithya, R. Rajamanikandan, J. Simpson, M. Ilanchelian, S. Govindarajan, *Polyhedron* **2018**, *145*, 200–217. DOI:10.1016/j.poly.2018.02.008
- (a) V. P. Radha, S. J. Kirubavathy, S. Chitra, *J. Mol. Struct.* **2018**, *1165*, 246–258; DOI:10.1016/j.molstruc.2018.03.109
(b) A. Carreno, C. Zuniga, D. Paez-Hernandez, M. Gacitua, R. Polanco, C. Otero, R. Arratia-Perez, J. A. Fuentes, *New J. Chem.* **2018**, *42*, 8851–8863. DOI:10.1039/C8NJ00390D
- G. Kumaravel, P. P. Utthra, N. Raman, *Bioorg. Chem.* **2018**, *77*, 269–279. DOI:10.1016/j.bioorg.2018.01.024
- (a) Y. Soberanes, K. A. Lopez-Gastelum, J. Moreno-Urbalejo, A. J. Salazar-Medina, M. C. Estrada-Montoya, R. Sugich-Miranda, J. Hernandez-Paredes, A. F. Gonzalez-Cordova, B. Vallejo-Cordoba, R. R. Sotelo-Mundo, E. F. Velazquez-Contreras, F. Rocha-Alonzo, *Inorg. Chem. Commun.* **2018**, *94*, 139–141; DOI:10.1016/j.inoche.2018.06.010
(b) V. A. Neacsu, C. Maxim, A. M. Madalan, M. Hillebrand, C. Gonzalez-Arellano, S. Soriano, E. Rentschler, M. Andruh, *Polyhedron* **2018**, *150*, 77–82; DOI:10.1016/j.poly.2018.05.007
(c) J. Mayans, M. Font-Bardia, A. Escuer, *Dalton Trans.* **2018**, *47*, 8392–8401. DOI:10.1039/C8DT01684D
- (a) M. T. Kaczmarek, M. Zabiszak, M. Nowak, R. Jastrzab, *Coord. Chem. Rev.* **2018**, *370*, 42–54;

- DOI:10.1016/j.ccr.2018.05.012
- (b) N. A. Illan-Cabeza, S. B. Jimenez-Pulido, F. Hueso-Urena, M. J. Ramirez-Exposito, P. Sanchez-Sanchez, J. M. Martinez-Martos, M. N. Moreno-Carretero, *J. Inorg. Biochem.* **2018**, *185*, 52–62; DOI:10.1016/j.jinorgbio.2018.04.022
- (c) J. Valentova, S. Varenyi, P. Herich, P. Baran, A. Bilkova, J. Kozisek, L. Habala, *Inorg. Chim. Acta* **2018**, *480*, 16–26. DOI:10.1016/j.ica.2018.04.058
6. (a) Y.-T. Li, J.-W. Dong, Y. Lu, Y.-T. Gu, C.-N. Shang, F.-Y. Liu, Y. Xin, C.-L. Jing, Z.-L. You, *Chinese J. Inorg. Chem.* **2018**, *34*, 1192–1198;
- (b) W. H. Sun, K. H. Li, H. Liu, Y. T. Gu, Y. Zhang, Z. L. You, W. Li, *Russ. J. Coord. Chem.* **2017**, *43*, 693–699; DOI:10.1134/S1070328417100104
- (c) M. Galini, M. Salehi, M. Kubicki, A. Amiri, A. Khaleghian, *Inorg. Chim. Acta* **2017**, *461*, 167–173. DOI:10.1016/j.ica.2017.02.001
7. (a) R. M. Ramadan, A. K. Abu Al-Nasr, O. A. M. Ali, *J. Mol. Struct.* **2018**, *1161*, 100–107; DOI:10.1016/j.molstruc.2018.01.071
- (b) H. Keypour, M. Mahmoudabadi, A. Shooshtari, L. Hosseinzadeh, F. Mohsenzadeh, R. W. Gable, *Polyhedron* **2017**, *127*, 345–354; DOI:10.1016/j.poly.2017.02.008
- (c) A. Ahlawat, P. Khatkar, V. Singh, S. Asija, *Res. Chem. Intermediat.* **2018**, *44*, 4415–4435. DOI:10.1007/s11164-018-3395-z
8. (a) Z. Asadi, M. Golchin, V. Eigner, M. Dusek, Z. Amirghofran, *J. Photochem. Photobiol. A: Chem.* **2018**, *361*, 93–104; DOI:10.1016/j.jphotochem.2018.05.016
- (b) K. Venkateswarlu, M. P. Kumar, A. Rambabu, N. Vamsikrishna, S. Daravath, K. Rangan, Shivaraj, *J. Mol. Struct.* **2018**, *1160*, 198–207; DOI:10.1016/j.molstruc.2018.02.004
- (c) H. Keypour, M. Mahmoudabadi, A. Shooshtari, M. Bayat, M. Ghassemzadeh, L. Hosseinzadeh, F. Mohsenzadeh, K. Harms, *Polyhedron* **2017**, *129*, 189–198. DOI:10.1016/j.poly.2017.03.035
9. SMART and SAINT. Area Detector Control and Integration Software, Siemens Analytical X-Ray Systems, Inc., Madison, Wisconsin, USA, 1996.
10. G. M. Sheldrick. SADABS. Program for Empirical Absorption Correction of Area Detector Data, University of Göttingen, Germany, 1996.
11. G. M. Sheldrick. SHELXTL V5.1 Software Reference Manual, Bruker AXS, Inc., Madison, Wisconsin, USA, 1997.
12. J. Meletiadis, J.F. Meis, J.W. Mouton, J.P. Donnelly, P.E. Verweij, *J. Clin. Microbiol.* **2000**, *38*, 2949–2955.
13. J. W. Geary, *Coord. Chem. Rev.* **1971**, *7*, 81–122. DOI:10.1016/S0010-8545(00)80009-0
14. (a) F. Niu, K.-X. Yan, L.-H. Pang, D. Qu, X. Zhao, Z. You, *Inorg. Chim. Acta* **2015**, *435*, 299–304; DOI:10.1016/j.ica.2015.07.014
- (b) Z. You, M. Liu, C. Wang, G. Sheng, X. Zhao, D. Qu, F. Niu, *RSC Advances* **2016**, *6*, 16679–16690. DOI:10.1039/C6RA00500D
15. R. Golbedaghi, M. Rezaeivala, M. Khalili, B. Notash, J. Karimi, *J. Mol. Struct.* **2016**, *1125*, 144–148. DOI:10.1016/j.molstruc.2016.05.096
16. A. B. P. Lever. *Inorganic Electronic Spectroscopy*, 2nd ed., Elsevier, Amsterdam, 1984, p. 553.
17. Y.-L. Sang, X.-S. Lin, W.-D. Sun, *Acta Chim. Slov.* **2016**, *63*, 856–863. DOI:10.17344/acsi.2016.2795

Povzetek

Sintetizirali smo centrosimetrični O-premosteni polimerni bakrov(II) kompleks, $[\text{CuL}_2]_n$, kjer je L deprotonirana oblika Schiffove baze 2-hidroksi-5-metilbenzaldehyd oksim, ter ga okarakterizirali z IR, UV in monokristalno rentgensko difrakcijo. Kompleks vsebuje kristalografski center inverzije. V kompleksu je Cu atom koordiniran s fenolatih kisikovim atomom, imino dušikovim atomom in hidroksilnim kisikovim atomom dveh ligandov Schiffove baze in ima oktaedrično geometrijo. Kompleks smo testirali *in vitro* za antibakterijsko aktivnost.

Scientific paper

Density Functional Approach: To Study Copper Sulfide Nanoalloy Clusters

Prabhat Ranjan¹ and Tanmoy Chakraborty^{2,*}¹ Department of Mechatronics Engineering, Manipal University Jaipur, Dehmi-Kalan, Jaipur-303007, India² Department of Chemistry, Manipal University Jaipur, Dehmi-Kalan, Jaipur-303007, India* Corresponding author: E-mail: tanmoychem@gmail.com;
tanmoy.chakraborty@jaipur.manipal.edu

Received: 10-20-2018

Abstract

Nano clusters of Copper sulfides (CuS) have paramount importance due to its significant adsorption property and non-toxic behaviour. In this report, nanoalloy clusters of $(\text{CuS})_n$; ($n = 1-8$) have been theoretically analyzed in terms of Conceptual Density Functional Theory (CDFT) based descriptors, aiming to explore its electronic and other properties. Global DFT based descriptors have been computed for ground state configurations and low-lying isomers of $(\text{CuS})_n$ clusters. Computed HOMO-LUMO gaps, lying in the range of 1.25–3.53 eV, indicate that $(\text{CuS})_n$ clusters may be utilized as renewable energy sources specially in photocatalysis and solar cell applications. A statistical correlation has been established between electronic and photo-catalytic properties of copper-sulfide clusters with their computational counterparts. The close agreement between experimental and computed data supports our analytical approach.

Keywords: Density Functional Theory; Copper-Sulfide Cluster; Descriptors; Optoelectronic Property; Regression Analysis

1. Introduction

A search of alternative energy resources is one of the most popular topics of the scientific research. Recently, transition metal chalcogenide clusters have gained considerable importance due to their potential applications in the field of energy conversion, storage and optoelectronics.¹⁻⁶ Among them, the compound formed between Cu and S is well known semiconducting material that has been extensively used in technological and strategic industries, including thermoelectric cooling materials, solar cells, clean-energy sectors, nonlinear optical materials, lithium ion batteries, gas sensors, nanoscale switches, photocatalysts, supercapacitors, petrochemicals, pharmaceuticals etc.⁷⁻²¹ In addition, transition metal clusters particularly Cu, Ag and Au have huge applications in diverse technological domains due to its superior catalytic, magnetic, electronic and optical properties.^{16,22-24} In similar line, advancement of methodologies and characterization techniques have a strong dependence on utilization of different compositions of nanoalloys.^{16,25-26} A deep insight of core-shell structure of nano compounds has paramount importance since its properties may be regulated through proper control of other structural and chemical parameters.

In view of regulating power of band gap on electronic properties of any materials, analysis of band gap of semiconductor materials has emerged as a major research domain in science and engineering. Band gap signifies energy difference between the top of the valence band and bottom of the conduction band. The highest occupied energy band represents the valence band and the lowest unoccupied energy band is known as conduction band.²⁷ The nature of interaction of light absorbed by semiconducting material can be explained in terms of atomic structure of material. This complex interaction generates the free charge carriers i.e. electrons and holes, which are responsible factors for energy transformation. In order to free an electron from a covalent bond, the light particles, photons, must have to carry at least the energy equal or greater than the band gap of a semiconductor material.²⁸ Band gap of semiconductor electrode in the range of 1.63–3.27 eV (760–380 nm), facilitates generation of free charge carriers in the visible light. It is already reported that zero consumption of energy (no external voltage) for hydrogen production with the use of UV solar light can be achieved utilizing TiO₂ electrodes in Photo Electro Chemical (PEC) cells sunlight-absorbing semiconductor.²⁹ A large number of theoretical

and experimental studies based on catalytic materials for water splitting reaction have also been reported, which generate the new results on bulk semiconductor photocatalysts.³⁰ Recently, heterogeneous nanomaterials have also confirmed their highest catalytic performance to be developed as novel semiconductor electrodes in PEC cells.³¹

Copper Sulfides (CuS) have become popular in view of their three major properties namely high adsorption, non-toxic behaviour and the most importantly abundance in nature (i.e. cheap material).³² By customizing the structure and concentration ratio of copper or sulfide, their respective energy band gap can be regulated. A number of reported data reveals the band gap of stoichiometric composition of copper sulfides, chalcocite (Cu₂S), djurleite (Cu_{1.97}S), digenite (Cu_{1.8}S) and covellite (CuS) as 1.22, 1.40, 1.55 and 2.0 eV respectively.^{33–36} Keeping in view the data, it can be assumed that there is inverse relationship energy between band gap and the number of copper atoms in the clusters. The energy band gap for copper sulfide clusters, ranging from 1.2 eV to 2.5 eV, supports behavior of cluster as a leading p-type semiconducting material and suitable candidate for solar cells, nonvolatile memory devices, optoelectronics and non-linear optical devices.^{1,8,11–13,37–38} Recently, Li et al. have reported copper and sulfur doped copper clusters, describing the growth pattern of the Cu_{n-1}S clusters.³⁹ In this work, authors have computed the optimized geometry, HOMO-LUMO gap, molecular orbital energy and density of states of Cu_{n-1}S clusters. The computed HOMO-LUMO gaps are in the range of 1.42–2.96 eV, which make Cu_nS clusters suitable for renewable energy sources. The cluster Cu₂S (Planar structure, C_{2v}) has been identified as the most stable geometry with the highest HOMO-LUMO gap (2.96 eV). Sánchez et al. have also reported the structure and electronic properties of (CuS)_N clusters (N = 1–6) in terms of DFT calculations.¹⁵ The authors also claimed the renewable energy property of the clusters on basis of computed HOMO-LUMO gaps, ranging between 1.3–3.3 eV. Due to high theoretical capacity, flat discharge curve and very good specific charge capacities, copper sulfide has been proven an excellent cathode material for lithium ion batteries.^{40–42} The inclusion of copper nanocrystals into sulfur electrode helps to intensify the cyclability of Li-S battery by alteration of sulfur to more electrochemically stable CuS.^{43,44} All these properties make copper sulfide a suitable candidate for capacity-contributing conductive filler for the sulfur electrode.⁴⁵ Xie et al. have studied the compositional transformations of CuS nanocrystals when exposed to divalent cations, as Cd²⁺ and Hg²⁺ at room temperature in organic solvents.⁴⁶ The authors claimed that the feature and mechanism of this analysis may be helpful in study of nanoscale chemical transformations. Karikalan et al. have studied the sonochemical route to synthesis of sulfur doped reduced graphene oxide and CuS nanocomposite.⁴⁷ The authors have validated the practicability of the developed glucose sensor in real biological samples.

Selvi et al. have synthesized CuS and CdS nanoparticles capped with CTAB using hydrothermal technique.⁴⁸ The result obtained from this study indicate that CuS and CdS with band gap of 1.8 eV and 2.3 eV respectively can be suitable for optoelectronic devices and photovoltaic applications. However, it is felt that deep insight in terms of experimental and theoretical analysis is required to further explore the intrinsic properties of these clusters.^{49–50}

Density Functional Theory has gained importance due its computational friendly behavior. DFT is a widely accepted method to study the electronic structure of many-body systems. In the domain of material science research, particularly in super conductivity of metal based alloys,⁵¹ magnetic properties of nano-alloy clusters,⁵² quantum fluid dynamics, molecular dynamics,⁵³ nuclear physics,⁵⁴ DFT has become popular technique. The study of density functional theory spreads over three major areas viz. theoretical, conceptual, and computational.^{55–57} Conceptual density functional theory is recognized as an important tool to study the chemical reactivity of materials.^{58–60} The conceptual density functional theory is highlighted following Parr's dictum "Accurate calculation is not synonymous with useful interpretation. To calculate a molecule is not to understand it".⁶¹ We have been extensively applying conceptual density functional based global and local descriptors to study physico-chemical properties of nano-engineering materials and drug designing processes.^{62–68}

Computational study invoking DFT on CuS clusters is very limited. In this venture, we have analyzed electronic and photo-catalytic properties of (CuS)_n nanoalloy clusters as a function of their size; n = 1–8. Conceptual DFT based descriptors namely electronegativity, hardness, HOMO-LUMO gap, softness, electrophilicity index and dipole moment have been computed to correlate physico-chemical properties of the compounds. It also helps to analyze the stability and the semiconducting behavior of the clusters. A comparative analysis has been done between available experimental reports with our computed data. Considering paucity of DFT based study on these compounds, it is assumed that our analysis may help to bring a new insight in the domain of renewable energy sources.

2. Computational Details

In this report, we have done computational analysis of the nanoalloy clusters of (CuS)_n (n = 1–8) in terms of Density Functional Theory based global descriptors. 3d modeling and structural optimization of all the compounds have been performed using Gaussian 03⁶⁹ within Density Functional Theory framework. Hybrid functional Becke, three parameter, Lee-Yang-Parr (B3LYP) exchange correlation with basis set LanL2dz has been adopted for geometry optimization. No restriction is imposed on mo-

lecular spin during energy minimization process. Z-axis is considered as spin polarization axis. In order to ensure orthogonalization on the (frozen) Core Orbitals (COs), Symmetrized Fragment Orbitals (SFOs) have been combined with auxiliary Core Functions (CFs).

Invoking Koopmans' approximation,⁵⁸ we have computed Ionization Energy (I) and Electron Affinity (A) for all the nano alloys using the following ansatz-

$$I = -\epsilon_{\text{HOMO}} \quad (1)$$

$$A = -\epsilon_{\text{LUMO}} \quad (2)$$

Thereafter, using I and A, the conceptual DFT based global molecular descriptors viz. electronegativity (χ), global hardness (η), molecular softness (S) and electrophilicity index (ω) have been computed. The equations used for such calculations are as follows-

$$\chi = -\mu = \frac{I + A}{2} \quad (3)$$

Where, μ represents the chemical potential of the system.

$$\eta = \frac{I - A}{2} \quad (4)$$

$$S = \frac{1}{2\eta} \quad (5)$$

$$\omega = \frac{\mu^2}{2\eta} \quad (6)$$

3. Results and Discussion

3.1. Equilibrium Geometries

In this section the structural aspects of low lying isomers of $(\text{CuS})_n$ ($n = 1-8$), which were obtained during the search of ground state geometries, are discussed. The results for the most stable structure and low-lying structures of CuS clusters are presented in Figure-1. The linear structure is obtained for diatomic CuS cluster. The structure with $C_{\infty v}$ symmetry has a bond length of 2.18 Å, which is nicely correlated with the data reported by Sánchez et al.¹⁵

We have listed five low-lying isomers for $n = 2$. It is observed that the optimized ground state geometry of $(\text{CuS})_2$, 2-a, with D_{2h} symmetry is energetically more favorable than the other isomers, because rhombus structure of this cluster forces Cu-Cu bond distances to be shorter. In the lowest energy structure of $(\text{CuS})_2$, the bond length of Cu-Cu and CuS is 2.30 and 2.12 Å respectively. The structure 2-b and 2-c with symmetry of C_2 and C_1 respectively, have an angle of 109.47°. The structure 2-b is energetically higher than the lowest energy structure of 2-a by 0.3 eV but at the same time it is lower in energy than

structure 2-c. Magnitude of energy difference between the structures 2-d and 2-e is very small.

Six low lying isomers of $(\text{CuS})_3$ clusters are identified. The cluster 3-a, having a 3D geometry and symmetry C_1 , is more stable than the planar structures. The 3-a cluster arises from the coordination of one copper and one sulfur atom from top and bottom of rectangular cluster. The bond lengths of Cu-Cu, Cu-S and S-S in 3-a cluster are 2.31, 2.19 and 2.06 Å respectively. The second most low lying isomer is 3-b which is 0.82 eV lower than the most stable structure of 3-a. Four more low-lying isomers, namely 3-c, 3-d, 3-e and 3-f, are also found in the range of 2.77 eV. A close agreement of energy value is observed for the structures 3-c and 3-d. Cluster 3-d is energetically higher than 3-c by 0.16 eV.

A number of low-lying isomers are found out for the $(\text{CuS})_4$ cluster. Our computed result indicates that first three low-lying three dimensional structures (4-a, 4-b and 4-c) are lower in energy than the planar structure. The most stable structure 4-a has a triangle in between the cluster, surrounded by sulfur atoms, forming triangle with copper. The bond lengths of Cu-Cu, Cu-S and S-S in cluster 4-a are 2.35, 2.27 and 1.94 Å respectively. The clusters 4-d and 4-e are found to be very close in energy and 4-e is only 0.08 eV higher than 4-d. The most stable structure (4-a), with C_1 symmetry and 3D geometry, is energetically lower than the planar structure (4-d) by 1.00 eV. The planar structures of three isomers (4-d, 4-f and 4-g), formed by placing Cu atoms on all sites of structures, are within an energy range of 2.72 eV.

It is observed that for cluster $(\text{CuS})_5$, structure 5-a, having symmetry group C_1 , is the most stable isomer. The structure corresponds to an interaction of two four atoms cluster of Cu_2S_2 connected back to back, while one sulfur and copper atom are coordinated to an edge of the same Cu_2S_2 cluster. In the structure 5-a, the bond lengths between Cu-Cu, Cu-S and S-S are 2.25, 2.17 and 1.89 Å respectively. The second most stable isomer, 5-b is found to be 1.02 eV higher in energy than 5-a. Four more low-lying structures are found in the range of 4.61 eV. The structure 5-e is also formed through the interaction of two Cu_2S_2 clusters connected back to back, though Cu and S atoms arranged in a different way compared to structure 5-a. The isomer 5-e is 4.61 eV higher in energy than the most stable structure 5-a.

Five low-lying isomers are identified for $(\text{CuS})_6$ cluster. The cluster 6-a with symmetry C_1 is found to be the most stable structure. It arises from the coordination of four sulfur atoms on the edge forming triangles with six copper atoms, while remaining two sulfur atoms interacting with the face of the cluster. The bond lengths between Cu-Cu, Cu-S and S-S in the lowest energy structure of $(\text{CuS})_6$ are 2.28, 2.19 and 2.13 Å respectively. The second most stable structure 6-b is a star like structure with interaction of two six atoms double layered cluster. The second and third most stable structures, 6-b and 6-c are energetically

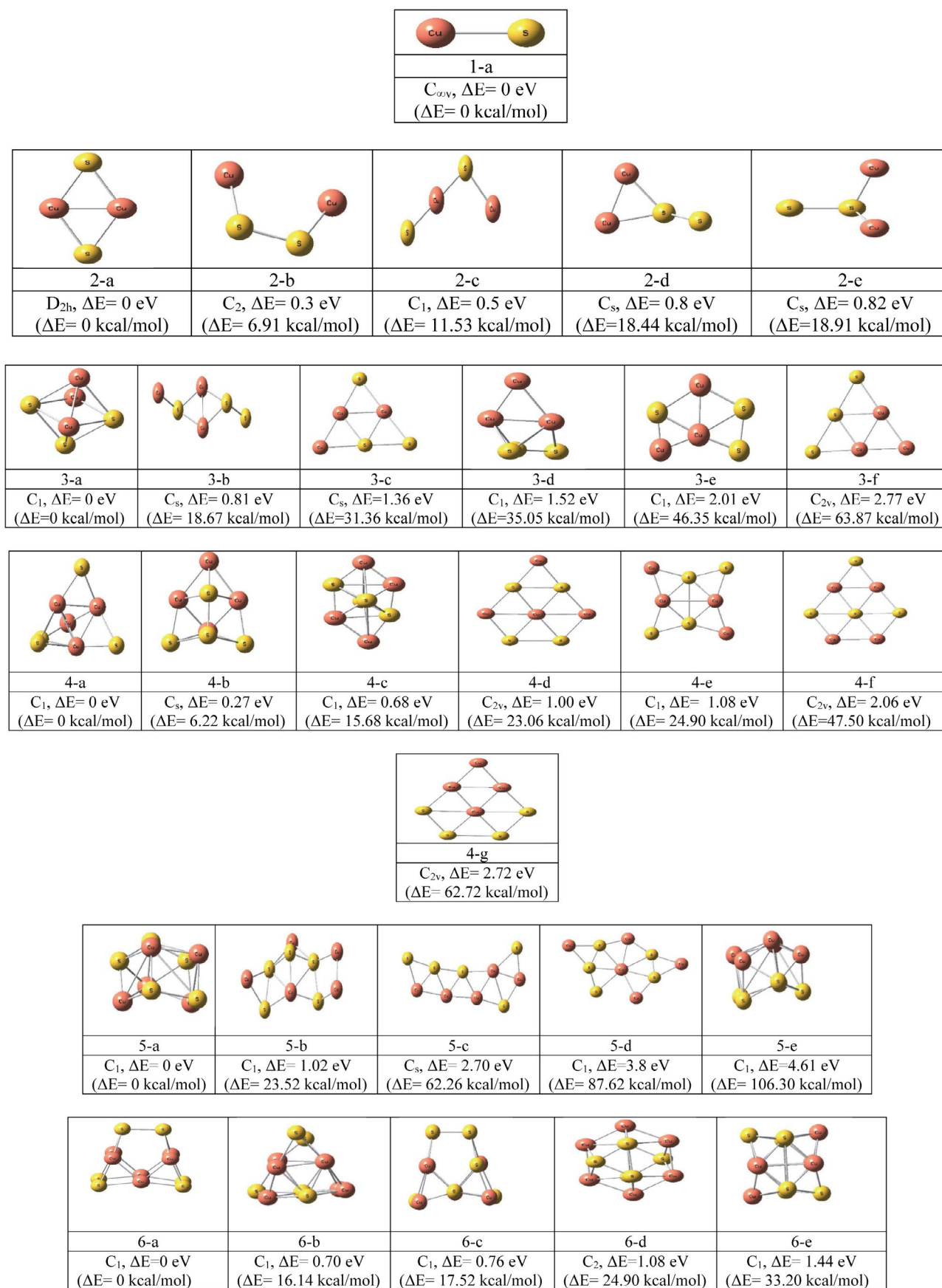


Figure 1.

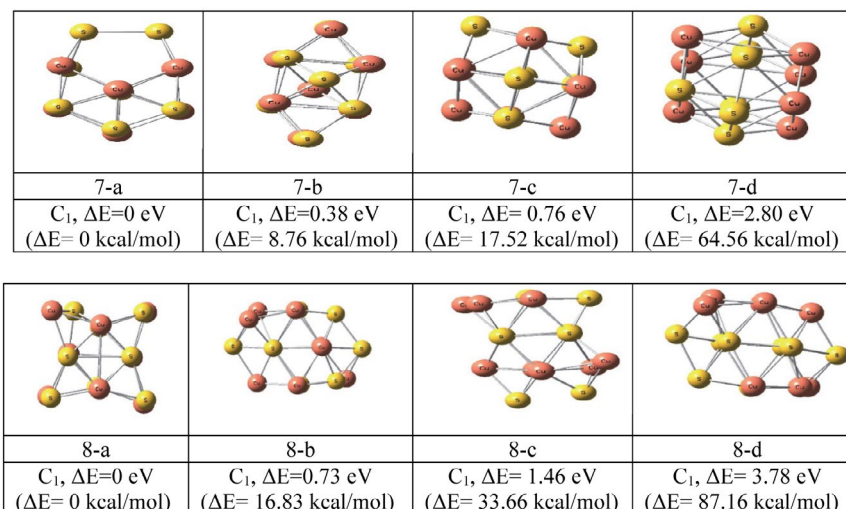


Figure 1. Structures of low-energy isomers for $(CuS)_n$ clusters ($n = 1-8$). Relative energies and symmetry group are given at B3LYP/ LanL2dz level. Red spheres represent Cu atoms and yellow ones represent S atoms.

cally less stable than 6-a by 0.70 and 0.76 eV respectively.

Among four low-lying isomers of $(CuS)_7$ cluster, the structure 7-a, having symmetry group C_1 , is the most stable cluster. In the structure 7-a, the bond lengths between Cu-Cu, Cu-S and S-S are 2.24, 2.14 and 2.13 Å respectively. The second most stable cluster is energetically higher than 7-a by 0.38 eV. Two more low-lying isomers are found to be within 2.80 eV energy range.

Four low-lying isomers, within the range of 3.78 eV, are identified for $(CuS)_8$ cluster. The 8-a structure arises from the coordination of double layer Cu_4S_4 , C_1 cluster. The bond lengths between Cu-Cu, Cu-S and S-S in the lowest energy structure of $(CuS)_8$ are 2.32, 2.29 and 2.15 Å respectively. The second and third most stable isomers, 8-b and 8-c are 0.73 and 1.46 eV less stable than 8-a, respectively. Other isomers are also found but they are of high energy. The computed bond lengths between Cu-Cu, Cu-S and S-S of lowest energy structure reveals that the bond lengths in $(CuS)_n$ clusters follow the order Cu-Cu > Cu-S > S-S. The calculated bond lengths are consistent with the results obtained by Sanchez et al. [15].

3. 2. The HOMO-LUMO Gaps and DFT Based Global Descriptors

In this paper, we have reported computational analysis invoking electronic structure theory of copper sulfide nanoalloy clusters. The orbital energies as HOMO (Highest Occupied Molecular Orbital)-LUMO (Lowest Unoccupied Molecular Orbital) gap along with computed DFT based global descriptors for copper sulfide nanoalloy clusters have been presented in the Table-1. The molecular dipole moment of the compounds in Debye unit is also reported in the Table-1. Our computed HOMO-LUMO gap for the copper sulfide clusters $(CuS)_n$, $n = 1-8$ has range

from 1.25 to 3.53 eV. This is in close agreement with the desirable band gap of semiconducting nano materials, suitable for photo-catalytic processes and renewable energy application.^{15,32,39} The HOMO-LUMO gap of these clusters is running parallel with the reported data.¹⁵ From Table-1, a direct relationship is revealed between HOMO-LUMO gaps of the nano-clusters and their evaluated global hardness. Frontier orbital energy gap and computed global hardness run hand in hand. This trend is expected considering experimental analysis. The molecule possessing the highest HOMO-LUMO gap will be the least prone to response against any external perturbation. It validates that clusters, having larger HOMO-LUMO gap, require significant amount of energy to promote electrons from the occupied to the unoccupied molecular orbitals. Our computed data reveals that $(CuS)_3$ restricts itself to exhibit any response against the external perturbation whereas $(CuS)_4$ exhibits the maximum reactivity under similar condition. In absence of quantitative benchmark pertaining to optical properties of aforesaid clusters, it is tacitly assumed that there must be a direct qualitative relationship between optical properties (specifically photo-catalytic) of CuS nano-clusters with their computed HOMO-LUMO gap. The assumption has the basis that optical properties of materials are governed by flow of electrons within the systems, which in turn depends on the energy difference between valence and conduction band. A linear relationship between HOMO-LUMO gap with the difference in the energy of valence-conduction band is already reported.⁷⁰ In view of that, it can be concluded that optical properties of the nano-clusters will be enhanced with an increase in their hardness values. Similarly, the softness data exhibits an inverse relationship towards the experimental optical properties. Table-1 also signifies that computed electronegativity and electrophilicity index have an

inverse relationship with HOMO-LUMO gap of CuS nano-clusters. Parr et al. have already reported that electrophilicity index measures the energy lowering of a ligand due to maximal electron flow between donor and acceptor and it depends on conjoint action of ionization potential and electron affinity.⁷¹ The linear correlation between HOMO-LUMO gap along with their evaluated electrophilicity index is depicted in the Figure 2. The high value of regression coefficient ($R^2 = 0.902$) supports our prediction.

The shell model of metal clusters arises on the concept of full delocalization of molecular orbitals for the cluster electrons, in which the valence electrons of the cluster atoms are placed in shells of s, p and d character of the overall system.⁷²⁻⁷⁵ The analysis of the $(\text{CuS})_3$ clusters in terms of orbitals i.e., HOMO, HOMO-1, LUMO and LUMO+1, exhibiting the highest HOMO-LUMO gap among the mentioned nano-clusters, is plotted in the Figure 3.

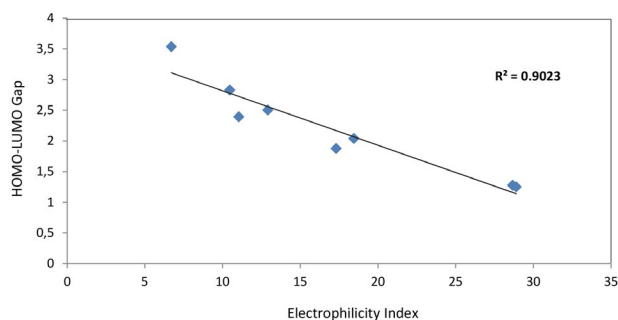


Figure 2. A Correlation Plot between Electrophilicity Index (eV) Vs HOMO-LUMO Gap (eV)

Table 1. Computed DFT Based Global Descriptors of $(\text{CuS})_n$ nanoalloy clusters ($n = 1-8$)

Species	HOMO-LUMO Gap (eV)	Electronegativity (eV)	Global Hardness (eV)	Global Softness (eV)	Electrophilicity Index (eV)	Dipole Moment (Debye)
CuS	2.394	5.142	1.197	0.417	11.045	4.440
$(\text{CuS})_2$	1.278	6.054	0.639	0.781	28.661	0.658
$(\text{CuS})_3$	3.537	4.870	1.768	0.282	6.706	0.817
$(\text{CuS})_4$	1.251	6.013	0.625	0.798	28.890	3.986
$(\text{CuS})_5$	2.041	6.135	1.020	0.490	18.448	1.533
$(\text{CuS})_6$	1.877	5.701	0.938	0.532	17.308	4.814
$(\text{CuS})_7$	2.829	5.442	1.414	0.353	10.465	2.142
$(\text{CuS})_8$	2.503	5.686	1.251	0.399	12.910	1.744

Table 2. A comparative analysis between computed bond lengths (Å) and frequency (cm^{-1}) with their experimental counterparts for the species Cu_2 , S_2 and CuS.⁷⁶⁻⁷⁹

Species	Computed bond length	Experimental bond length	Computed Frequency	Experimental Frequency
Cu_2	2.25	2.21	257	265
S_2	2.07	1.89	662	726
CuS	2.18	2.05	372	415

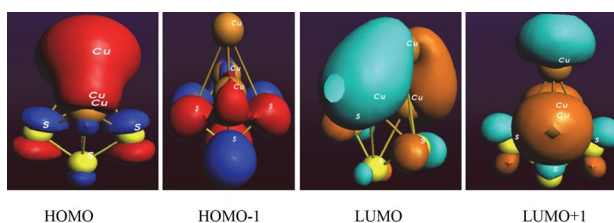


Figure 3. Orbitals of $(\text{CuS})_3$ Nanoalloy Cluster

A comparative analysis has also been done in the Table-2, between experimental bond length and frequency with our computed data of the species namely Cu_2 , S_2 and CuS. The result reveals that bond lengths follow the order as- $\text{Cu-Cu} > \text{Cu-S} > \text{S-S}$, which is in same line as previously reported.¹⁵ The close agreement between the experiment data and our computed data signifies the theoretical analysis.

4. Conclusion

Study on copper-sulfide nanoalloy clusters has become important considering its wide field applications. In this paper, computational analysis of the structure, electronic and optical/ photo-catalytic properties of $(\text{CuS})_n$, [$n = 1-8$] nanoalloy clusters in terms of conceptual DFT based descriptors, are reported. The ground state configurations and low-lying isomers of $(\text{CuS})_n$ clusters have been analyzed invoking electronic structure theory. The result exhibits an appearance of 3D structure of $(\text{CuS})_3$ with C_1

symmetry, which is more stable than the planar structure. The computed HOMO-LUMO gap, ranging from 1.25 to 3.53 eV, makes these clusters as potential candidates for renewable energy sources. Our computational data identifies the most reactive and least reactive species. The computed data describes that optical property of the instant clusters and global hardness run hand in hand, which is very much expected considering experimental facts. The high value of regression coefficient between electrophilicity

ty index and HOMO-LUMO gap supports our predicted model. Observed close agreement between experimental bond length and frequency with our computed data encourages further possibility of analysis in this domain.

5. References

- J. Kundu, D. Pradhan, *New J. Chem.* **2013**, *37*, 1470–1478. DOI:10.1039/c3nj41142g
- M. Antoniadou, V. M. Daskalaki, N. Balis, D. I. Kondarides, C. Kordulis, P. Lianos, *Appl. Catal. B* **2011**, *107*, 188–196. DOI:10.1016/j.apcatb.2011.07.013
- C. H. Lai, M. Y. Lu, L. J. Chen, *J. Mater. Chem.* **2012**, *22*, 19–30. DOI:10.7312/li--16274-023
- M. G. Panthani, V. Akhavan, B. Goodfellow, J. P. Schmidtke, L. Dunn, A. Dodabalapur, P. F. Barbara, B. A. Korgel, *J. Am. Chem. Soc.* **2008**, *130*, 16770–16777. DOI:10.1021/ja805845q
- J. S. Steckel, J. P. Zimmoler, S. C.-Sullivan, N. E. Stott, V. Bulovic, M. G. Bawendi, *Angew. Chem., Int. Ed.* **2004**, *43*, 2154–2158. DOI:10.1002/anie.200453728
- Y. Justo, B. Goris, J. S. kamal, P. Geiregat, S. Bals, Z. Hens, *J. Am. Chem. Soc.* **2012**, *134*, 5484–5487. DOI:10.1021/ja300337d
- Y. Zhao, C. Burda, *Energy Environ. Sci.* **2012**, *5*, 5564–5576. DOI:10.1039/C1EE02734D
- A. A. Sagade, R. Sharma, I. Sulaniya, *J. Appl. Phys.* **2009**, *105*, 043701-1-8. DOI:10.1063/1.3053350
- T. Sakamoto, H. Sunamura, H. Kawuara, T. Hasegawa, T. Nakayama, M. Aono, *Appl. Phys. Lett.* **2003**, *82*, 3032–3034. DOI:10.1063/1.1572964
- E. Ramli, T. B. Rauchfuss, C. L. Stern, *J. Am. Chem. Soc.* **1990**, *112*, 4043–4044. DOI:10.1021/ja00166a054
- L. Reijnen, B. Meester, A. Goossens, J. Schoonman, *Chem. Vap. Deposition* **2003**, *9*, 15–20. DOI:10.1002/cvde.200290001
- M. C. Lin, M. W. Lee, *Electrochem. Commun.* **2011**, *13*, 1376–1378. DOI:10.1016/j.elecom.2011.08.013
- Y. Wu, C. Wadia, W. Ma, B. Sadtler, A. P. Alivisatos, *Nano Lett.* **2008**, *8*, 2551–2555. DOI:10.1021/nl801817d
- T. Rasmussen, B. C. Berks, J. S. Loehr, D. M. Dooley, W. G. Zumft, A. J. Thomson, *Biochemistry* **2000**, *39*, 12753–12756. DOI:10.1021/bi001811i
- O. J. J.-Sanchez, N. P. -Peralta, R. H. - Urbina, M. Sanchez, A. P. -Amarillas *Chem. Phys. Lett.* **2013**, *570*, 132–135.
- R. Ferrando, J. Jellinek, R. L. Johnston, *Chem. Rev.* **2008**, *108*, 845–910. DOI:10.1021/cr040090g
- N. Sounderya, Y. Zhang, *Recent Pat. Biomed. Eng.* **2008**, *1*, 34–42. DOI:10.2174/1874764710801010034
- O. V. J. Salata, *Nanobiotechnology* **2004**, *2*, 3–10. DOI:10.1186/1477-3155-2-3
- W. He, X. Wu, J. Liu, X. Hu, K. Zhang, S. Hou, W. Zhou, S. Xie, *Chem. Mater.* **2010**, *22*, 2988–2994. DOI:10.1021/cm100393v
- H. -J. Freund, *Surf. Sci.* **2002**, *500*, 271–299. DOI:10.1016/S0039-6028(01)01543-6
- J. K. Norskov, T. Bligaard, J. Rossmaisi, C. H. Christensen, *Nat. Chem.* **2009**, *1*, 37–46. DOI:10.1038/nchem.121
- A. Henglein, *J. Phys. Chem.* **1993**, *97*, 5457–5471. DOI:10.1021/j100123a004
- S. C. Davis, K. J. Klabunde, *Chem. Rev.* **1982**, *82*, 153–208. DOI:10.1021/cr00048a002
- L. N. Lewis, *Chem. Rev.* **1993**, *93*, 2693–2730. DOI:10.1021/cr00024a006
- H. Y. Oderji, H. Ding, *Chem. Phys.* **2011**, *388*, 23–30. DOI:10.1016/j.chemphys.2011.07.011
- F. Baletto, R. Ferrando, *Rev. Mod. Phys.* **2005**, *77*, 371–423. DOI:10.1103/RevModPhys.77.371
- R. Koole, E. Groeneveld, D. Vanmaekelbergh, A. Meijerink, C. D. M. Dongea, in: C. D. M. Dongea (Ed.): *Nanoparticles: Workhorses of Nanoscience*, Springer-Verlag Berlin Heidelberg, **2014**, pp. 13–51.
- K. Hashimoto, H. Irie, A. Fujishima, *Jpn. J. Appl. Phys.* **2005**, *44*, 8269–8285. DOI:10.1143/JJAP.44.8269
- A. Fujishima, K. Honda, *Nature* **1972**, *238*, 37–38. DOI:10.1038/238037a0
- A. Kudo, *Pure Appl. Chem.* **2007**, *79*, 1917–1927. DOI:10.1351/pac200779111917
- N. V. Long, T. D. Hien, T. Asaka, M. Ohtaki, M. Nogami, *Int. J. Hydrogen Energy* **2011**, *36*, 8478–8491. DOI:10.1016/j.ijhydene.2011.03.140
- M. Page, O. Niitsoo, Y. Itzhaik, D. Cahen and G. Hodes, *Energy Environ. Sci.* **2009**, *2*, 220–223. DOI:10.1039/B813740D
- Y. Zhao, H. Pan, Y. Lou, X. Qiu, J. Zhu, C. Burda, *J. Am. Chem. Soc.* **2009**, *131*, 4253–4261. DOI:10.1021/ja805655b
- P. V. Q.-Ramirez, M. C. A. Arrocena, J. S. Cruz, M. V. Gonzalez, O. M. Alvarez, V. M. C. Meneses, L. S. A. Torres, *Beilstein J. Nanotechnol.* **2014**, *5*, 1542–1552.
- P. Leidinger, R. Popescu, D. Gerthsen, H. Lunsdorf, C. Feldmann, *Nanoscale* **2011**, *3*, 2544–2551. DOI:10.1039/c1nr10076a
- M. T. S. Nair, L. Guerrero, P. K. Nair, *Semicond. Sci. Technol.* **1998**, *13*, 1164–1169. DOI:10.1088/0268-1242/13/10/019
- I. Grozdanov, M. Najdoski, *Solid State Chem.* **1995**, *114*, 469–475. DOI:10.1006/jssc.1995.1070
- L. Chen, Y. D. Xia, X. F. Liang, K. B. Yin, J. Yin, Z. G. Liu, Y. Chen, *Appl. Phys. Lett.* **2007**, *91*, 073511–073513. DOI:10.1063/1.2771064
- C. -G. Li, Y. -Q. Yuan, Y. -F. Hu, J. Zhang, Y. -N. Tang, B. -Z. Ren, *Comput. Theor. Chem.* **2016**, *1080*, 47–55. DOI:10.1016/j.comptc.2016.01.018
- K. Sun, D. Su, Q. Zhang, D. C. Bock, A. C. Marschilok, K. J. Takeuchi, E. S. Takeuchi, H. Gan, *J. Electrochem. Soc.* **2015**, *162*, A2834–A2839. DOI:10.1149/2.1021514jes
- G. Chen, Z. Wei, B. Jin, X. Zhong, H. Wang, W. Zhang, J. Liang, Q. Jiang, *Appl. Surf. Sci.* **2013**, *277*, 268–271. DOI:10.1016/j.apsusc.2013.04.041
- M. Nagarathinam, K. Saravanan, W. L. Leong, P. Balaya, J. J. Vittal, *Cryst. Growth Des.* **2009**, *9*, 4461–4470.

- DOI:10.1021/cg9004938
43. Y. Wang, X. Zhang, P. Chen, H. Liao, S. Cheng, *Electrochim. Acta.* **2012**, *80*, 264–268.
DOI:10.1016/j.electacta.2012.07.004
44. Y. Du, Z. Yin, J. Zhu, X. Huang, X. J. Wu, Z. Zeng, Q. Yan, H. Zhang, *Nat. Commun.* **2012**, *3*, 1177–1183.
DOI:10.1038/ncomms2181
45. S. Zheng, Y. Feng, Z. Li, Y. Zhu, Y. Xu, C. Luo, J. Yang, C. Wang, *Adv. Funct. Mater.* **2014**, *24*, 4156–4263.
DOI:10.1002/adfm.201304156
46. Y. Xie, G. Bertoni, A. Riedinger, A. Sathya, M. Prato, S. Marras, R. Tu, T. Pellegrino, L. Manna, *Chem. Mater.* **2015**, *27*, 7531–7537. DOI:10.1021/acs.chemmater.5b03892
47. N. Karikalan, R. Karthik, S. M. Chen, C. Karuppiah, A. Elan-govan, *Sci. Rep.* **2017**, *7*, 2494–2504.
DOI:10.1038/s41598-017-02479-5
48. S. S. T. Selvi, J. M. Linet, S. Sagadevan, *J. Exp. Nanosci.* **2018**, *13*, 130–143. DOI:10.1080/17458080.2018.1445306
49. C. Ratanatawanate, A. Bui, K. Vu, K. J. Balkus, *J. Phys. Chem. C* **2011**, *115*, 6175–6180. DOI:10.1021/jp109716q
50. J. Zhang, J. Yu, Y. Zhang, Q. Li, J. R. Gong, *Nano Lett.* **2011**, *11*, 4774–4779. DOI:10.1021/nl202587b
51. O. J. Wacker, R. Kummel, E. K. U. Gross, *Phys. Rev. Lett.* **1994**, *73*, 2915–2918. DOI:10.1103/PhysRevLett.73.2915
52. B. Gyorffy, J. Staunton, G. Stocks in: E. Gross, R. Dreizler (Eds.), *Fluctuations in density functional theory: random metallic alloys and itinerant paramagnets*, Plenum, NY, **1995**, pp. 461–484. DOI:10.1007/978-1-4757-9975-0_18
53. R. Car, M. Parrinello, *Phys. Rev. Lett.* **1985**, *55*, 2471–2474.
DOI:10.1103/PhysRevLett.55.2471
54. M. Koskinen, P. Lipas, M. Manninen, *Nucl. Phys. A* **1995**, *591*, 421–434. DOI:10.1016/0375-9474(95)00209-J
55. R. G. Parr, W. Yang, *Annu. Rev. Phys. Chem.* **1995**, *46*, 701–728.
DOI:10.1146/annurev.pc.46.100195.003413
56. W. Kohn, A. D. Becke, R. G. Parr, *J. Phys. Chem.* **1996**, *100*, 12974–12980. DOI:10.1021/jp960669l
57. T. Ziegler, *Chem. Rev.* **1991**, *91*, 651–667.
DOI:10.1021/cr00005a001
58. R. G. Parr, W. Yang, *Density functional theory of atoms and molecules*, Oxford, University Press, Oxford, 1989.
59. H. Chermette, *J. Comput. Chem.* **1999**, *20*, 129–154.
DOI:10.1002/(SICI)1096-987X(19990115)20:1<129::AID-JCC13>3.0.CO;2-A
60. P. Geerlings, F. D. Proft, W. Langenaeker, *Chem. Rev. Wash- ington, D.C.* **2003**, *103*, 1793–1874.
61. P. Geerlings, F. D. Proft, *Int. J. Mol. Sci.* **2002**, *3*, 276–309.
DOI:10.3390/i3040276
62. P. Ranjan, A. Kumar, T. Chakraborty, in: G. M. Mishra (Ed.), *Environmental Sustainability: Concepts, Principles, Evidences and Innovations*, Excellent Publishing House, New Delhi, , **2014**, pp. 239–242.
63. P. Ranjan, S. Venigalla, A. Kumar, T. Chakraborty, in: T. Chakraborty, L. Ledwani (Eds.), *Research Methodology in Chemical Sciences: Experimental and Theoretical Approaches*, Apple Academic Press, USA, 2016, pp. 337–346.
DOI:10.1201/b19855-19
64. P. Ranjan, S. Dhail, S. Venigalla, A. Kumar, L. Ledwani, T. Chakraborty, *Mat. Sci. - Pol.* **2015**, *33*, 719–724.
DOI:10.1515/msp-2015-0121
65. P. Ranjan, S. Venigalla, A. Kumar, T. Chakraborty, *New Front. Chem.* **2014**, *23*, 111–122.
66. S. Venigalla, S. Dhail, P. Ranjan, S. Jain, T. Chakraborty, *New Front. Chem.* **2014**, *23*, 123–130.
67. P. Ranjan, A. Kumar, T. Chakraborty, *AIP Conf. Proc.* **2016**, *1724*, 020072.
68. P. Ranjan, A. Kumar, T. Chakraborty, *Mat. Today Proc.* **2016**, *3*, 1563–1568. DOI:10.1016/j.matpr.2016.04.043
69. Gaussian 03, Revision C.02, M. J. Frisch, G. W. Trucks, H. B. Schlegel, G. E. Scuseria, M. A. Robb, J. R. Cheeseman, J. A. Montgomery, Jr., T. Vreven, K. N. Kudin, J. C. Burant, J. M. Millam, S. S. Iyengar, J. Tomasi, V. Barone, B. Mennucci, M. Cossi, G. Scalmani, N. Rega, G. A. Petersson, H. Nakatsuji, M. Hada, M. Ehara, K. Toyota, R. Fukuda, J. Hasegawa, M. Ishida, T. Nakajima, Y. Honda, O. Kitao, H. Nakai, M. Klene, X. Li, J. E. Knox, H. P. Hratchian, J. B. Cross, V. Bakken, C. Adamo, J. Jaramillo, R. Gomperts, R. E. Stratmann, O. Yazyev, A. J. Austin, R. Cammi, C. Pomelli, J. W. Ochterski, P. Y. Ayala, K. Morokuma, G. A. Voth, P. Salvador, J. J. Dannenberg, V. G. Zakrzewski, S. Dapprich, A. D. Daniels, M. C. Strain, O. Farkas, D. K. Malick, A. D. Rabuck, K. Raghavachari, J. B. Foresman, J. V. Ortiz, Q. Cui, A. G. Baboul, S. Clifford, J. Ci-oslowski, B. B. Stefanov, G. Liu, A. Liashenko, P. Piskorz, I. Komaromi, R. L. Martin, D. J. Fox, T. Keith, M. A. Al-Laham, C. Y. Peng, A. Nanayakkara, M. Challacombe, P. M. W. Gill, B. Johnson, W. Chen, M. W. Wong, C. Gonzalez, and J. A. Pople, Gaussian, Inc., Wallingford CT, **2004**.
70. H. Xiao, J. T. Kheli, W. A. Goddard III, *J. Phys. Chem. Lett.* **2011**, *2*, 212–217. DOI:10.1021/jz101565j
71. R. G. Parr, L. V. Szentpaly, S. Liu, *J. Am. Chem. Soc.* **1999**, *121*, 1922–1924. DOI:10.1021/ja983494x
72. W. A. deHeer, *Rev. Mod. Phys.* **1993**, *65*, 611–676.
DOI:10.1103/RevModPhys.65.611
73. W. D. Knight, K. Clemenger, W. A. deHeer, M. Y. Chou, M. L. Cohen, *Phys. Rev. Lett.* **1984**, *52*, 2141–2143.
DOI:10.1103/PhysRevLett.52.2141
74. W. Ekardt, Z. Penzar, *Phys. Rev. B.* **1998**, *38*, 4273–4276.
DOI:10.1103/PhysRevB.38.4273
75. M. L. Cohen, W. D. Knight, *Phys. Today.* **1990**, *43*, 42–50.
DOI:10.1063/1.881220
76. R. P. Amerigo, M. Merchan, I. N. Gil, P. A. Malmqvist, B. O. Roos, *J. Chem. Phys.* **1994**, *101*, 4893–4902.
DOI:10.1063/1.467411
77. H. E. King Jr., C. T. Prewitt, *Am. Mineral.* **1979**, *64*, 1265–1271.
78. H. W. Evans Jr., *Am. Mineral.* **1981**, *66*, 807–810.
79. D. Hohl, R. O. Jones, R. Car, M. Parrinello, *J. Chem. Phys.* **1988**, *89*, 6823–6835. DOI:10.1063/1.455356

Povzetek

Nanoklastri bakrovih sulfidov (CuS) so zaradi njihovih adsorpcijskih lastnosti in netoksičnosti izjemnega pomena. V prispevku smo nanoklastre (CuS)_n (n = 1–8) analizirali s pomočjo računske kemije na podlagi teorije gostotnega potenciala (conceptual DFT (CDFT)), z namenom dobiti vpogled v njihove elektronske in druge lastnosti. S pomočjo DFT kalkulacij smo izračunali nekatere parametre (»global descriptors«) za konfiguracije osnovnega stanja in nizko ležeče izomere (CuS)_n klastrov. Izračunane HOMO-LUMO vrzeli, ki ležijo v območju od 1,25 do 3,53 eV kažejo, da bi lahko (CuS)_n klastre uporabljali v procesu pridobivanja energije iz obnovljivih virov, zlasti pri fotokatalizi in kot material v sončnih celicah. Prikazali smo statistično korelacijo med elektronskimi in fotokatalitičnimi lastnostmi nanoklastrov na osnovi bakrovih sulfidov. Takšen pristop računske kemije podpira tudi ujemanje med eksperimentalnimi in izračunanimi podatki.

Scientific paper

Voltammetric Investigation of Inclusion Complexes of the Selected Succinimides with β -Cyclodextrin and (2-Hydroxypropyl)- β -Cyclodextrin

Jelena Lović,^{1,*} Milka Avramov Ivić,¹ Bojan Božić,² Jelena Lađarević³
and Dušan Mijin³

¹ Institute of Electrochemistry, University of Belgrade, Belgrade, Serbia

² Faculty of Biology, University of Belgrade, Belgrade, Serbia

³ Department of Organic Chemistry, Faculty of Technology and Metallurgy, University of Belgrade, Belgrade, Serbia

* Corresponding author: E-mail: jlovic@tmf.bg.ac.rs, jelena.lovic@ihtm.bg.ac.rs

Received: 12-08-2018

Abstract

The inclusion complexes of the selected, potentially biologically active, succinimides with β -cyclodextrin (β CD) and (2-hydroxypropyl)- β -cyclodextrin (HP β CD) were prepared. The formation of the inclusion complexes of the investigated monophenyl and diphenyl succinimide derivatives was confirmed using attenuated total reflection (ATR) study. Their electrochemical behavior was examined by cyclic voltammetry (CV) and square wave voltammetry (SWV) in 0.05 M NaHCO₃ on a gold electrode. The stability constants for compound **1** were determined by cyclic voltammetry and calculated as $K_{\beta\text{CD}} = 350.87 \text{ M}^{-1}$ and $K_{\text{HP}\beta\text{CD}} = 250.67 \text{ M}^{-1}$. The SWV measurements reveal well defined peak at potential $E_p = \sim 60 \text{ mV}$ and the higher currents at E_p for both inclusion complex of the succinimides compared to the free compounds. The impact of chlorine atom in the phenyl moiety of succinimide derivatives on the activity in electrooxidation reaction is presented. Among the studied succinimides, according to SWV measurements, the most active is the monophenyl succinimide derivative (compound **1**) in complex with β CD. The difference of peak current of compound **1** + β CD compared to compound **1** + HP β CD and free compound is 6.3 and 35.2 $\mu\text{A cm}^{-2}$, respectively.

Keywords: Diphenylsuccinimide; threphenylsuccinimide; ATR analysis; inclusion complexes; voltammetry.

1. Introduction

Succinimides are derivatives of pyrrolidine-2,5-dione which can be modified by the introduction of various alkyl and/or aryl groups on nitrogen or carbon atoms. Some of the modifications can be illustrated by the structures presented in Fig. 1. Succinimide ring represents a renowned pharmacophore in the drug discovery since its derivatives possess anticonvulsant activity.^{1–3} Substituted succinimides show anticholinesterase and antioxidant potentials,⁴ possess antimicrobial,^{5,6} antitumor,⁷ analgesic⁸ and antispasmodic⁹ activity. Apart from their biological importance, they also find application in liquid crystal displays (LCD)¹⁰ and in the production of water soluble reactive copolymers and polymers.^{11,12} They are appropriate scaffolds for organic synthesis,¹³ and in some cases, they are used as effective and recyclable catalysts.¹⁴ Evaluation of pharmacokinetic properties and in vitro cytotoxic activ-

ity of *N*-phenyl substituted succinimides showed that all compounds were predicted for good permeability and solubility, oral absorption rate and moderate volume of distribution even for blood brain permeation, followed by acceptable observed toxicity.^{15,16} Furthermore, quantum mechanical and experimental studies of *N*-phenyl succinimides were performed and detailed interpretation of spectral data were reported.^{17,18} For 1-aryl-3-methylsuccinimides, it is shown that interactions with hydrogen bond donor solvents and non-specific interactions with solvents play an important role in the solvatochromic behavior of these compounds. Moreover, MEP (Molecular electrostatic potential) data revealed regions of possible intermolecular interactions of *N*-phenyl succinimides and according to the analysis, oxygen atoms are suitable sites for electrophilic attack as well as for hydrogen bonding interactions with environment.

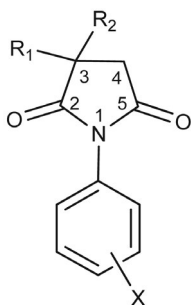


Figure 1. The structure of the investigated succinimides: (1) $R_1=H$, $R_2=Ph$, $X=H$; (2) $R_1=Ph$, $R_2=Ph$, $X=H$; (3) $R_1=H$, $R_2=Ph$, $X=4-Cl$; (4) $R_1=Ph$, $R_2=Ph$, $X=4-Cl$; (5) $R_1=H$, $R_2=Ph$, $X=3-Cl$; (6) $R_1=Ph$, $R_2=Ph$, $X=3-Cl$.

The synthesis and physico-chemical properties of the succinimides given in Fig. 1, classify as monophenyl succinimide derivatives (1, 3, 5) and 3,3-diphenyl succinimide derivatives (2, 4, 6) have been reported earlier.^{19,20} Recently, the results obtained from cyclic and square wave voltammetry, on the gold electrode, combined with computational studies, revealed that these compounds are electrochemically active and oxidized by the mechanism involving the conversion of COCHPh or $-CH_2-$ group in free radical by the loss of one proton in one electron process.²¹

Succinimide electrochemistry has received modest attention so far. Previous electrochemical studies involve the electrochemical reduction of succinimides.^{22,23} Voltammetric studies on Pt cathode in aqueous media reveal that the *N*-bromosuccinimide is a two-electron reduction process and succinimide anion is an intermediate in this reaction while succinimide and *N*-alkylated succinimide are the observed products.²² The electrochemical reduction of succinimide examined on Pt cathode by cyclic voltammetry in aprotic media (acetonitrile) shows a single irreversible reduction peak. The product of these reaction is the succinimide anion in good yield and it was shown that this anion is stable in electrolysis medium.²³

The aim of this work is to compare the already observed electrochemical activity of six selected succinimides with their activity in the form of inclusion complexes with cyclodextrins. Cyclodextrins (CD) are widely applied as non toxic encapsulated materials for a variety of guest molecules in order to improve their physico-chemical properties, such as aqueous solubility, physical chemical stability, and bioavailability of drug.^{24–29} Due to the fact that the investigated succinimides are slightly soluble in water, their inclusion complexes are prepared in order to enhance their water solubility. Among the host molecules, β -cyclodextrins (β -cyclodextrin (β CD) and (2-hydroxypropyl)- β -cyclodextrin (HP β CD)), built up from seven glucopyranose units, are chosen since they are suitable for complexing molecules bearing phenyl groups such as investigated succinimides.

A number of nitrogen containing compounds have been electrochemically investigated, but to the best of our knowledge, the activity of succinimides (heterocyclic “pyrrolidine-2,5-dione” derivatives) in the form of inclusion complexes with cyclodextrins have not been subjected to the electrochemical studies. Since the impact of certain functional groups on the activity has been neglected in the literature, in this manuscript we provide the explanation about the influence of hydroxypropyl groups, chlorine atom or phenyl ring on the reactivity of investigated complexed compounds.

2. Experimental

2.1. Material and Methods

All investigated compounds have been previously synthesized.²⁰ All used chemicals were p.a. grade (sodium hydrogen carbonate and sulphuric acid) obtained commercially from Sigma. 18 M Ω cm deionised water was obtained from a Milipore Waters Milli-Q purification unit.

ATR spectra of the investigated succinimides were collected on a Nicolet™ iS™ 10 FT-IR Spectrometer (Thermo Fisher SCIENTIFIC) with Smart iTR™ attenuated total reflectance sampling accessories.

2.2. Preparation of Inclusion Complexes

The inclusion complexes of the investigated succinimides were prepared by mixing of the succinimides solution (0.15 mmol in 1 cm³ of methanol and then added to 100 cm³ of 0.05 M NaHCO₃) with cyclodextrins solution (0.15 mmol in 50 cm³ of 0.05 M NaHCO₃) to obtain 150 cm³ of 1:1 succinimide:cyclodextrine complex in 0.05 M NaHCO₃. The resulting mixture was shaken thoroughly and allowed to equilibrate at room temperature for 30 min before the addition to the electrochemical cell for electrochemical analysis.

2.3. CV and SWV Measurements

Electrochemical studies were performed using three-electrode cell with an Au working electrode (surface area 7 mm²), an Au wire auxiliary electrode and a calomel reference electrode. The Au working electrode was polished with diamond paste, cleaned with a mixture of 18 M Ω water and sulfuric acid and further cleaned with 18 M Ω deionized water in an ultrasonic bath. Prior to each experiment working electrode was checked by cycling the potential scan between -0.40 and 1.1 V in basic solution (0.05 M NaHCO₃; pH = 8.4) at the scan rate of 50 mV s⁻¹ until the unchanged CV characteristics for Au electrode were obtained. After that the electrode was transfer to the electrochemical cell containing succinimides or complexed succinimides and CVs were performed.

For SWV measurements the accumulation of the succinimides and their inclusion complexes at the Au elec-

trode was carried out for 0.2 s at -0.45 V. After that a square-wave voltammetric stripping initiated in the positive potential direction was performed. The following instrumental parameters were used to record the square-wave voltammograms: step size 5 mV, pulse size 75 mV, frequency 10 Hz, scan rate 50 mV s $^{-1}$. CV and SWV was carried out using PGZ 402 Volta Lab (Radiometer Analytical, Lyon, France).

3. Results and Discussion

In the first part of the work, inclusion complexes were prepared by dissolving corresponding succinimide and CD in 0.05 M NaHCO $_3$. The solutions were shaken for 15 min, and then evaporated under vacuum and dried. In order to study the formation of inclusion complexes, ATR analysis was performed. For illustration, Fig. 2A depicts ATR spectra of the relevant samples for the study of the inclusion complex of the compound **1** with HP β CD. The spectrum of HP β CD (b) displays characteristic bands at 3280 and 2926 cm $^{-1}$ originating from O–H and C–H stretching vibrations, respectively and 1659 cm $^{-1}$ as a result of H–O–H bending vibrations. The most prominent peaks at 1080 and 1021 cm $^{-1}$ are ascribed to composition of the valence vibrations C–O–C, C–C–O and C–C–C. ATR spectra of **1** (c) show characteristic vibrations of carbonyl groups at 1775 and 1701 cm $^{-1}$. The spectrum of the physical mixture (d) represents the simple sum of the spectra of the succinimide molecule and HP β CD implying that this mixture do not provide inclusion of the guest molecule into the host molecule cavity. On the other hand, spectrum of inclusion complex (e) significantly differ from

all of the spectra (a-d). Bands at 1425 and 878 cm $^{-1}$ of the inclusion complex appear from NaHCO $_3$, since the complexes are prepared in bicarbonate solution. The disappearance of the some corresponding peaks originating from succinimide ring and HP β CD is observed in this spectrum due to the restricted vibrations of the groups after the insertion of succinimide into HP β CD cavity. The decrease of the intensity and the shift from 1701 to 1685 cm $^{-1}$ of the vibrations of the carbonyl group is observed in the spectrum of the inclusion complex as a result of the intermolecular hydrogen bonds between host and guest molecules. Furthermore, a broad band at 3280 cm $^{-1}$ of HP β CD significantly decreased intensity and moved to 3458 cm $^{-1}$ in complex clearly indicating the formation of inclusion complex. The same conclusions are derived for the inclusion complex of **1** with β CD (Fig. 2B).

In order to confirm the stoichiometry of the complex 1:1, CVs were recorded for different concentrations of succinimide **1** while the HP β CD concentration remains unchanged, as it was proposed by³⁰. From Fig. 3 it is clear that the oxidation peak corresponding to the succinimides is growing proportional to the amount added suggesting that the molar ratio is 1:1. In inset of Fig. 3 it is presented linearity of current density vs. concentration dependency recorded at 0.7 V with excellent regression coefficient $R = 0.998$.

For compound **1**, with the most pronounced electrochemical activity²¹, the stability constants were determined by cyclic voltammetry and calculated by “electrochemical current method” for both inclusion complexes.^{30,31} With the constant concentration of compound **1** and with different concentrations of both complexes the CVs were recorded as is presented in Fig. 4 and using

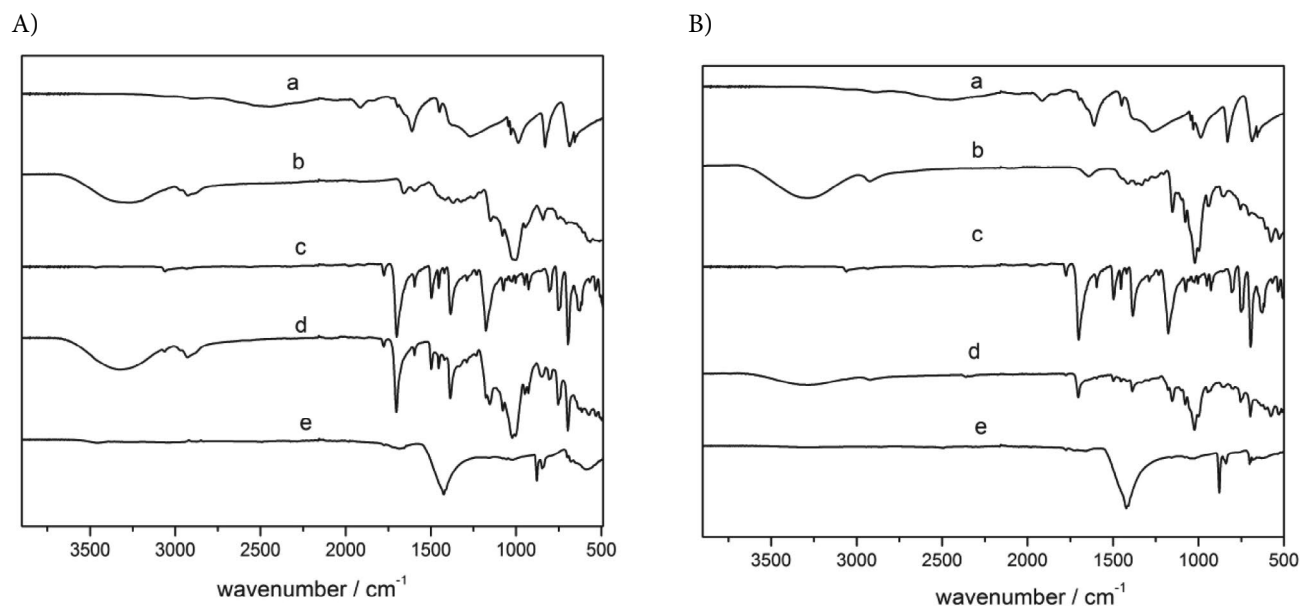


Figure 2. ATR spectra of the corresponding compounds in the formation of inclusion complex of **1** with HP β CD (A) and β CD (B): (a) NaHCO $_3$; (b) corresponding CD; (c) compound **1**; (d) physical mixture of the compound **1** and corresponding CD and (e) the inclusion complex of **1** with corresponding CD.

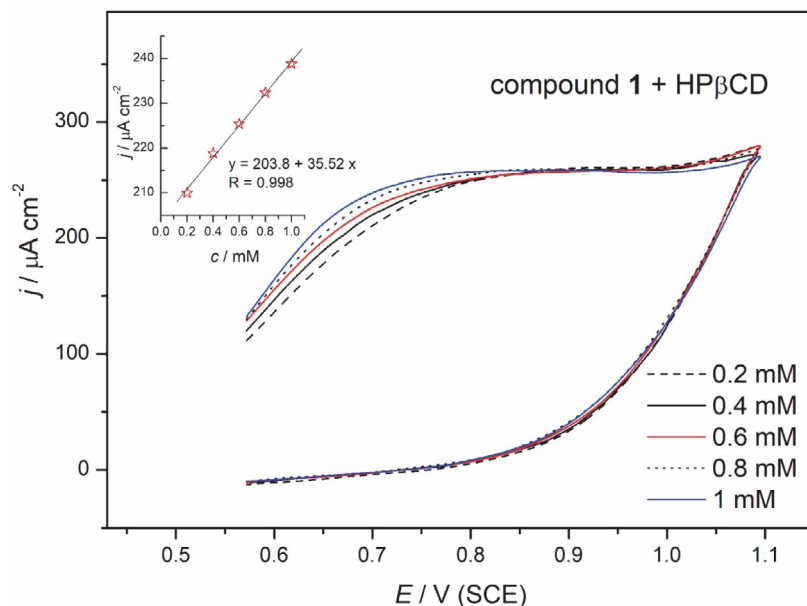


Figure 3. CVs of Au electrode in 0.05 M NaHCO₃ in the presence of compound **1** complexed with HPβCD ($c = 1$ mM). Concentrations of compound **1** are 0.2; 0.4; 0.6; 0.8 and 1 mM. $\nu = 100$ mV s⁻¹. Inset: current density vs. concentration dependency at 0.7 V.

equation from ^{30,31}, the obtained stability constants are: $K_{\beta\text{CD}} = 350.87$ M⁻¹ and $K_{\text{HP}\beta\text{CD}} = 250.67$ M⁻¹. Those calculated values are in accordance with the determined constants of cyclodextrin inclusion complexes for aromatic carbonyl compounds ³¹ and inclusion complexes with ascorbic acid, uric acid, acetaminophen and some xantine alkaloids.³⁰

The electrochemical investigation consisted of voltammetric and kinetic studies of selected succinimides

performed by cyclic voltammetry is already published.²¹ The cyclic voltammetry of the all examined inclusion complexes of succinimides show the same response as free compounds, with the higher current in the region of the oxide formation. In ²¹ is shown and pointed out that the anodic currents of investigated succinimides, appeared only in the region of the oxide formation at gold electrode, are more pronounced when SWV technique is applied. With the same succinimides inclusion complexes with

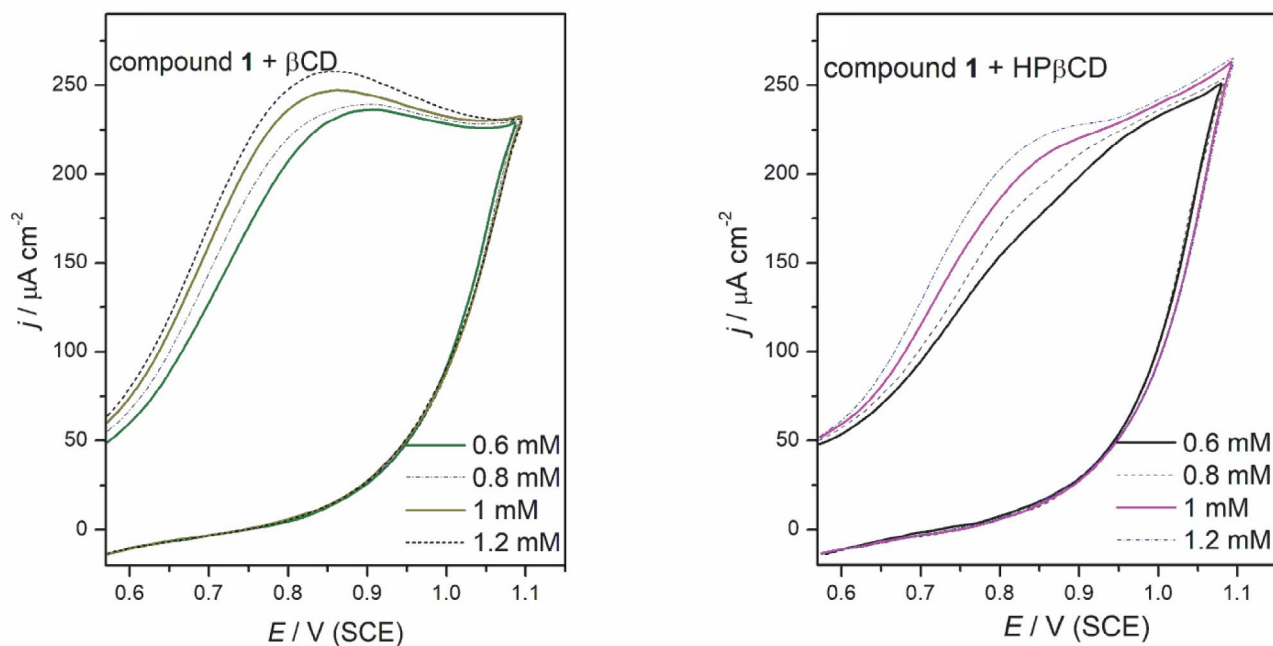


Figure 4. CVs of Au electrode in 0.05 M NaHCO₃ in the presence of compound **1** ($c = 1$ mM) complexed with βCD (A) and complexed with HPβCD (B). Concentrations of CDs are 0.6, 0.8, 1 and 1.2 mM. $\nu = 100$ mV s⁻¹.

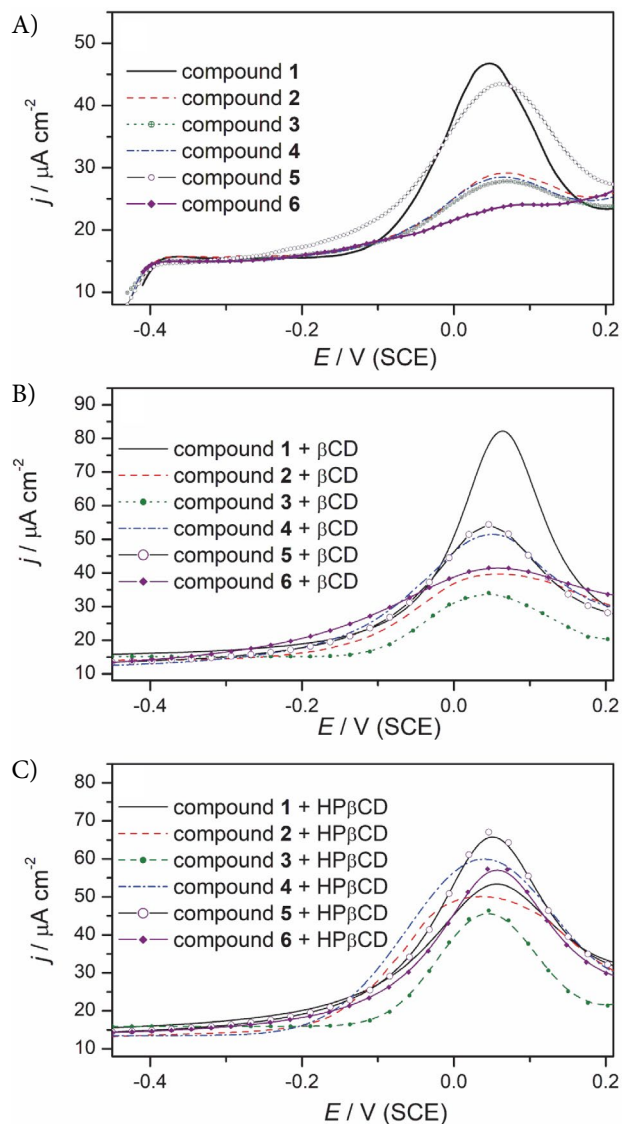


Figure 5. SWVs of investigated compounds (A); of the inclusion complexes of the investigated compounds with β CD (1:1) (B) and of the inclusion complexes of the investigated compounds with HP β CD (1:1) (C), obtained on Au electrode using 0.05 M NaHCO₃. Accumulation time: 0.2 s at $E = -0.45$ V; step size 5 mV, pulse size 75 mV, frequency 10 Hz, scan rate 50 mV s⁻¹.

β -cyclodextrin and (2-hydroxypropyl)- β -cyclodextrin are prepared and examined in this work by SWV.

Figure 5A shows the SWVs of the selected succinimides recorded at the Au electrode in 0.05 M NaHCO₃. Their 1:1 inclusion complexes with β -cyclodextrin are presented in Fig. 5B and their 1:1 inclusion complexes with (2-hydroxypropyl)- β -cyclodextrin are presented in Fig. 5C.

The SWV measurements reveal well defined peak at potential $E_p = \sim 60$ mV (Fig. 5) and the higher currents at E_p for both inclusion complex of the succinimides (Fig. 5B and 5C) comparing to succinimides presented in Fig. 5A. It indicates that the complexation of succinimides improves their electrooxidation ability.

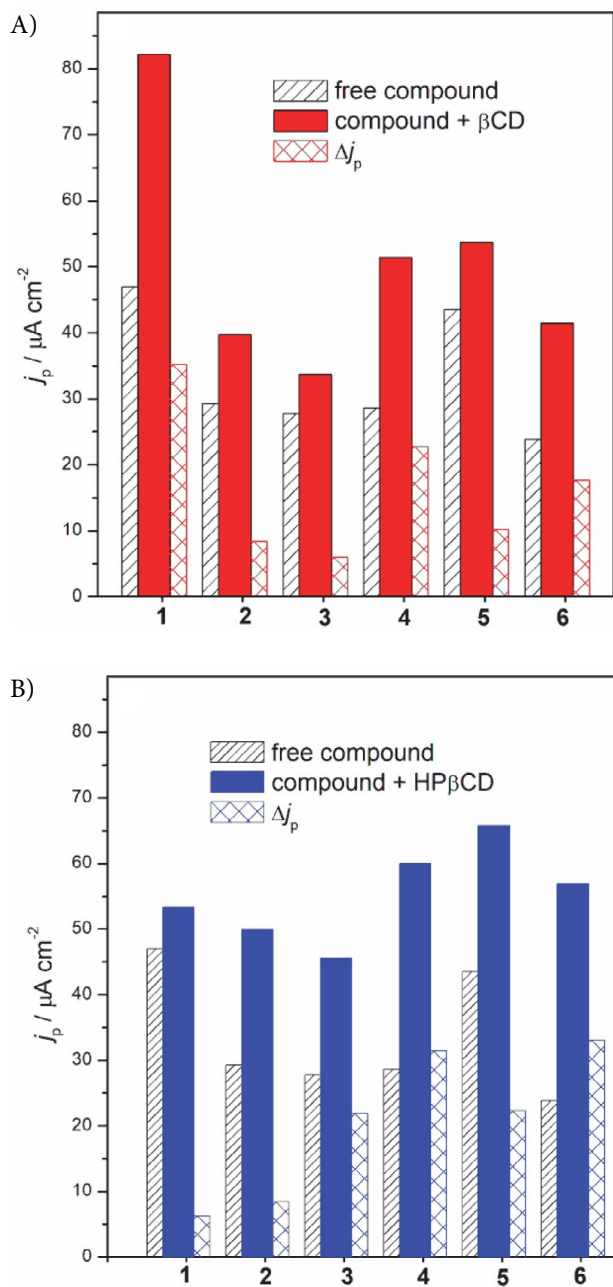


Figure 6. Bar plots of the peak current densities obtained by the oxidation of the free succinimides and their inclusion complexes with β CD (A) and HP β CD (B) derived from Fig. 5 and their difference (network grid bar).

According to Fig. 5A higher currents of the SWV signal for the compounds 1 and 5 in the region of E_p are observed. The highest peak current is observed for compound 1 complexated with β CD as is presented in Fig. 5B. Concerning the inclusion complexes with HP β CD, the highest peak current is observed for compound 5 according to Fig. 5C.

The difference between the peak current of free compound and inclusion complex (Δj_p), presented in Fig. 6 is a characteristic of improved electrooxidation ability. Re-

garding the inclusion complexes of succinimides with β CD, the highest Dj_p is noticed for compound **1**, while for the inclusion complexes of succinimides with HP β CD the highest Dj_p is observed for compound **6**. According to the computational analysis for the free compounds reported earlier,²¹ the obtained improved electrooxidation ability of the investigated succinimides was ascribed to the influence of the structural parameters. Namely, the monophenyl succinimide derivatives (**1**, **3**, **5**) were characterized by the formation of radical and anion at position C3, while 3,3-diphenyl succinimide derivatives (**2**, **4**, **6**) can form only one species of radical and anion as consequences of deprotonation at position C4.²¹

The complexing pattern likely involves hydrophobic *N*-phenyl ring bound in the hydrophobic cavity by van der Waals interactions. The structure is additionally stabilized through the formation of hydrogen bonds between carbonyl groups of succinimide and hydroxyl groups outside the cavity (Fig. 7). Thusly, the part of the molecule responsible for electrochemical activity is preserved and available for oxidation process in the complex. The stabilization of the formed anion/radical through the hydrogen bonds and non specific interactions in CD:succinimide complex may be the reason for improved electrochemical activity with regard to corresponding succinimide. Proposed complexing mode is in accordance with complex formed between cyclodextrin and maleimides reported earlier.³²

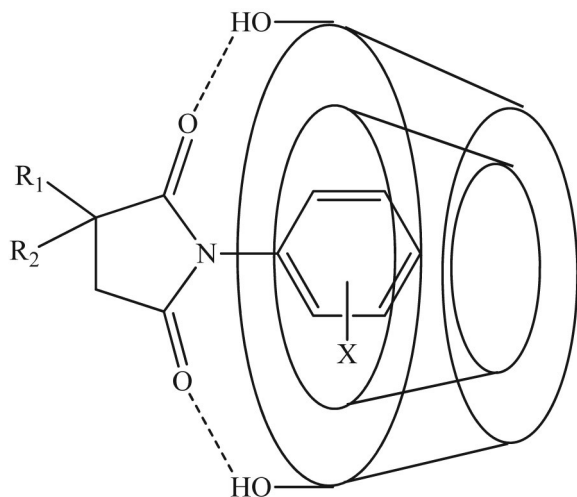


Figure 7. Schematic illustration of the succinimide:cyclodextrin complex.

For consideration of complex activity, three structural factors should be taken into account: structure of the employed CD, electronic nature of substituent at *N*-phenyl ring and the presence/absence of phenyl group at the position 3 of succinimide ring.

As can be seen from the data given in Fig. 6, except for compound **1**, where inclusion complex with β CD

showed higher electrochemical activity, inclusion complexes with HP β CD were more electrochemically active. The presence of hydroxypropyl groups additionally stabilize complex since this cyclodextrin provides more hydrophobic microenvironment convenient for *N*-phenyl ring and thus interactions in greater extent than in the case of β CD. The prominent activity of **1** with β CD is observed, while with HP β CD the highest activity is observed for **5**.

From Fig. 6, it can be observed that introduction of phenyl ring in the position 3 of the succinimide ring has a different impact on the electrochemical activity depending on the nature of the substituent in *N*-phenyl ring. Namely, unsubstituted (**1**) and *meta*-Cl substituted (**5**) diphenylsuccinimide: CD complexes show higher activity than corresponding threphenylsuccinimides:CD complexes (**2** and **6**, respectively), while for **3** and **4**, the opposite trend is observed. For both CD, the lowest electrochemical activity is observed for compound **3** which could be attributed to the weak mesomeric effect of chlorine atom affecting accumulation of electron density and hindering the formation of radicals and anions during the electrooxidation of molecule. On the basis of the obtained electrochemical activity, it can be concluded that introduction of phenyl ring in **3**, noticeable increases the current of complexes of **4** indicating that phenyl group contributes in stabilization of this particular anion/radical forms. For other compounds (**1** and **5**), by insertion of phenyl ring (**2** and **6**) the lower electrochemical activity is observed due to destabilization of complex caused both by conformational changes of the molecule and weakening of the interactions between host and guest molecules. Different behavior of different positioned chlorine atoms is related to diverse electronic effect in *meta*- and *para*- positions. As mentioned before, chlorine in *para*- position (**3**, **4**) exerts weak mesomeric positive effect, while *meta*-chlorine (**5**, **6**) exhibit strong negative inductive effect causing withdrawal of electron density and stabilization of the obtained anion/radical.

The overall conclusion is that the effects of different groups and different cyclodextrins on the electrochemical activity of the complexes is complicated and involves synergistic interplay of each effect both through the electronic nature of the substituents and the strength of the interactions between guest and host molecules.

4. Conclusions

The complex formation between selected succinimides and β -cyclodextrin and (2-hydroxypropyl)- β -cyclodextrin was confirmed with ATR spectral analysis. The stability constants for compound **1** were determined by cyclic voltammetry and calculated as $K_{\beta\text{CD}} = 350.87 \text{ M}^{-1}$ and $K_{\text{HP}\beta\text{CD}} = 250.67 \text{ M}^{-1}$. The SWV measurements reveal well defined peak at potential $E_p = \sim 60 \text{ mV}$ and the higher currents at E_p for both inclusion complex of the succinimides comparing to the free compounds. It indicates that the

complexation of succinimides improves their electrooxidation ability. The highest peak current in this study is observed for compound **1** complexed with β CD. Inclusion complexes with HP β CD of succinimide derivatives (**2**, **3**, **4**, **5**, **6**) were more electrochemically active in regard to the inclusion complexes with β CD since the presence of hydroxypropyl groups additionally stabilize complex through interaction with the succinimide molecule. The complexing mode is suggested and involves entering of hydrophobic *N*-phenyl ring into the hydrophobic cavity of cyclodextrins which is additionally strengthened by hydrogen bonds between carbonyl groups of succinimide and hydroxyl groups outside the cavity. Different electrochemical activity of the complexes is caused by synergetic interplay of the substituent effects at *N*-phenyl ring, absence/presence of the phenyl group at the position 3 of succinimide ring and the structure of the employed CD on the stability of the formed radical/anion and its interactions with corresponding CD.

Acknowledgment

The work was supported by the Ministry of Education, Science and Technological Development of the Republic of Serbia under the research projects: ON172013 and ON172060.

5. References

- M. K. Hargreaves, J. G. Pritchard, H. R. Dave, *Chem. Rev.* **1970**, *70*, 439–469. DOI:10.1021/cr60266a001
- K. Kamiński, J. Obniska, *Bioorg. Med. Chem.* **2008**, *16*, 4921–4931. DOI:10.1016/j.bmc.2008.03.037
- K. Kamiński, S. Rzepka, J. Obniska, *Bioorg. Med. Chem. Lett.* **2011**, *21*, 5800–5803. DOI:10.1016/j.bmcl.2011.07.118
- A. Sadiq, F. Mahmood, F. Ullah, M. Ayaz, S. Ahmad, F. U. Haq, G. Khan, M. S. Jan, *Chem. Cent. J.* **2015**, *9*, 31–39. DOI:10.1186/s13065-015-0107-2
- N. P. Shetgiri, B. K. Nayak, *Indian J. Chem. B* **2005**, *44B*, 1933–1936.
- T. N. Bansode, J. V. Shelke, V. G. Dongre, *Eur. J. Med. Chem.* **2009**, *44*, 5094–5098. DOI:10.1016/j.ejmech.2009.07.006
- S. H. Han, S. Kim, U. De, N. K. Mishra, J. Park, S. Sharma, J. H. Kwak, S. Han, H. S. Kim, I. S. Kim, *J. Org. Chem.* **2016**, *81*, 12416–12425. DOI:10.1021/acs.joc.6b02577
- O. N. R. Fhid, T. H. Zeglam, S. E. A. Saad, M. S. Shlaka, M. A. Dao, *World Pharm. Pharm. Sci.* **2015**, *4*, 24–34.
- V. C. Filho, R. J. Nunes, J. B. Calixto, R. A. Yunes, *Pharm. Pharmacol. Comm.* **1995**, *1*, 399–401.
- K. Kishikawa, Y. Furukawa, T. Watanabe, M. Kohri, T. Taniguchi, S. Kohmoto, *Liq. Cryst.* **2017**, *44*, 1332–1339. DOI:10.1080/02678292.2017.1295477
- H. Peng, M. Kather, K. Rübsum, F. Jakob, U. Schwaneberg, A. Pich, *Macromolecules* **2015**, *48*, 4256–4268.
- K. M. Doll, R. L. Shogrent, R. A. Holser, J. L. Willett, G. Swift, *Lett. Org. Chem.* **2005**, *2*, 687–689. DOI:10.2174/157017805774717553
- P. Chauhan, J. Kaur, S.S. Chimni, *Chem. Asian. J.* **2013**, *8*, 328–346. DOI:10.1002/asia.201200684
- F. Shirini, N.G. Khaligh, *Dyes Pigm.* **2012**, *95*, 789–794. DOI:10.1016/j.dyepig.2012.06.022
- N. U. Perisic-Janjic, R. Kaliszsan, N. P. Milosevic, G.S. Uscumlic, N.R. Banjac, *J. Pharm. Biomed. Anal.* **2013**, *72*, 65–73. DOI:10.1016/j.jpba.2012.09.006
- N. P. Milosevic, V. Kojic, J. Curcic, D. Jakimov, N. Milic, N. Banjac, G. Uscumlic, R. Kaliszsan, *J. Pharmaceut. Biomed.* **2017**, *137*, 252–257. DOI:10.1016/j.jpba.2017.01.042
- V. D. Vitnik, Ž. J. Vitnik, N. R. Banjac, N. V. Valentić, G. S. Ušćumlić, I. O. Juranić, *Spectrochim. Acta A* **2014**, *117*, 42–53. DOI:10.1016/j.saa.2013.07.099
- N. R. Banjac, B. Đ. Božić, J. M. Mirković, V. D. Vitnik, Ž. J. Vitnik, N. V. Valentić, G. S. Ušćumlić, *J. Mol. Struct.* **2017**, *1129*, 271–282. DOI:10.1016/j.molstruc.2016.09.086
- N. U. Perisic-Janjic, R. Kaliszsan, P. Wiczling, N. P. Milosevic, G. S. Uscumlic, N. R. Banjac, *Mol. Pharm.* **2011**, *8*, 555–583. DOI:10.1021/mp100373d
- N. Banjac, N. Trisovic, Z. Vitnik, V. Vitnik, N. Valentic, G. Uscumlic, I. Juranic, *Monatsh. Chem.* **2013**, *144*, 1525–1535. DOI:10.1007/s00706-013-1052-1
- B. Božić, J. Lović, N. Banjac, Ž. Vitnik, V. Vitnik, D. Mijin, G. Ušćumlić, M. Avramov Ivić, *Int. J. Electrochem. Sci.* **2018**, *13*, 4285–4297. DOI:10.20964/2018.05.54
- J. E. Barry, M. Finkelstein, W. M. Moore, S. D. Ross, *J. Org. Chem.* **1982**, *47*, 1292–1298. DOI:10.1021/jo00346a026
- W. M. Moore, M. Finkelstein, S. D. Ross, *Tetrahedron* **1980**, *36*, 727–730. DOI:10.1016/S0040-4020(01)93685-3
- Z. Z. Stoiljković, V. M. Jovanović, D. Ž. Mijin, V. Nikolić, Lj. Nikolić, S. D. Petrović, M. L. Avramov Ivić, *Int. J. Electrochem. Sci.* **2013**, *8*, 9543–9557.
- I. V. Terekhova, N. A. Obukhova, *Mendeleev Commun.* **2005**, *15*, 38–40. DOI:10.1070/MC2005v015n01ABEH001901
- I. V. Terekhova, T. V. Volkova, G. L. Perlovich, *Mendeleev Commun.* **2007**, *17*, 244–246. DOI:10.1016/j.mencom.2007.06.022
- I. V. Terekhova, *Mendeleev Commun.* **2009**, *19*, 110–112. DOI:10.1016/j.mencom.2009.03.021
- A. Yu. Ziganshina, S. V. Kharlamov, E. Kh. Kazakova, S. K. Latypov, A. I. Konovalov, *Mendeleev Commun.* **2007**, *17*, 145–147. DOI:10.1016/j.mencom.2007.05.004
- S. S. Jambhekar, P. Breen, *Drug Discov. Today* **2016**, *21*, 363–368. DOI:10.1016/j.drudis.2015.11.016
- L. Fritea, M. Tertis, T. L. Topala, R. Sandulescu, *Farmacia* **2013**, *61*, 1054–1068.
- M. Vilar, M. Navarro, *Electrochim. Acta* **2010**, *56*, 305–313. DOI:10.1016/j.electacta.2010.08.079
- S. Chaudhuri, T. Phelan, M. Levine, *Tetrahedron Lett.* **2015**, *56*, 1619–1623. DOI:10.1016/j.tetlet.2015.01.185

Povzetek

Z ATR spektralno analizo smo potrdili tvorbo kompleksa med izbranimi sukcinimidi in β -ciklodekstrinom ter (2-hidroksipropil)- β -ciklodekstrinom. S ciklično voltometrijo smo določili stabilnostne konstante za spojino **1** in izračunali vrednosti konstant $K_{\beta\text{CD}}$ in $K_{\text{HP}\beta\text{CD}}$ kot $K_{\beta\text{CD}} = 350.87 \text{ M}^{-1}$ in $K_{\text{HP}\beta\text{CD}} = 250.67 \text{ M}^{-1}$. SWV meritve so pokazale dva dobro definirana vrhova pri potencialu $E_p = \sim 60 \text{ mV}$ in, v primerjavi s prostimi spojinami, višje tokove pri E_p za oba vključitvena kompleksa s sukcinimidom. To kaže, da vključevanje sukcinimidov v ciklodekstrine izboljša njihovo elektrooksidativno sposobnost. Najvišji tok pri vrhu smo v tej študiji opazili za spojino **1** kompleksirano z βCD . Vključitveni kompleks derivatov (**2**, **3**, **4**, **5**, **6**) sukcinimida z $\text{HP}\beta\text{CD}$ so bili bolj elektrokemijsko aktivni v primerjavi z vključitvenim kompleksom z βCD , ker prisotnost hidroksipropilnih skupin dodatno stabilizira kompleks preko interakcij z molekulo sukcinimida. Predlagali smo način tvorbe kompleksa, ki vključuje vstop hidrofobnih *N*-fenilnih obroče v hidrofobno votlino ciklodekstrina, kar je dodatno okrepljeno še z vodikovimi vezmi med karbonilnimi skupinami sukcinimida in hidroksilnimi skupinami izven votline. Različno elektrokemijsko aktivnost kompleksov povzroči sinergistična interakcija med substituentami na *N*-fenilnem obroču, odsotnost/prisotnost fenilnih skupin na položaju 3 v sukcinimidnem obroču in struktura uporabljenega CD s svojim vplivom na stabilnost nastalega radikala/aniona ter njegove interakcije z ustreznim CD.

Synthesis, Crystal Structures, and Antimicrobial Activity of Zinc(II) and Manganese(II) Complexes Derived from *N*'-(1-(Pyridin-2-yl)ethylidene)isonicotinohydrazide

Ling-Wei Xue,* Hui-Jie Zhang and Pan-Pan Wang

College of Chemistry and Chemical Engineering, Pingdingshan University, Pingdingshan Henan 467000, P.R. China

* Corresponding author: E-mail: pdsuchemistry@163.com

Received: 10-08-2018

Abstract

Two mononuclear zinc(II) and manganese(II) compounds, $[ZnL_2]$ (1) and $[MnL(HL)]ClO_4$ (2), where L is the mono-anionic form of *N*'-(1-(pyridin-2-yl)ethylidene)isonicotinohydrazide (HL), and HL is the zwitterionic form of HL, have been prepared and characterized by elemental analyses, IR and UV-Vis spectroscopy, and single-crystal X-ray crystallographic determination. Compound 1 contains a neutral $[ZnL_2]$ complex molecule. Compound 2 contains a $[MnL(HL)]^+$ complex cation and one perchlorate anion. The metal atoms in the complexes are in octahedral coordination. The hydrazone ligands coordinate to the metal atoms through the pyridine N, imine N, and enolate O atoms. The compounds were investigated for their antimicrobial activity against *Staphylococcus aureus*, *Escherichia coli*, and *Candida albicans*.

Keywords: Hydrazone, Zinc complex, Manganese complex, Crystal structure, Antimicrobial activity

1. Introduction

Schiff bases bearing characteristic C=N bonds are a kind of versatile ligands in coordination chemistry.¹ In recent years, metal complexes of Schiff bases have attracted considerable attention due to their interesting biological activity, such as antifungal, antibacterial and antitumor.² Schiff base complexes derived from salicylaldehyde and its derivatives with primary amines, bearing the N_2O , N_2S , NO_2 or NSO donor sets, have particular biological activities.³ Hydrazone is a kind of special Schiff base compound, which possess interesting biological activities.⁴ Metal complexes usually show stronger biological activities than the hydrazone ligands.⁵ Chang and coworkers have reported that some transition metal complexes derived from *N*'-(1-(pyridin-2-yl)ethylidene)isonicotinohydrazide (HL; Scheme 1) have interesting antitumor and antioxidant activities.⁶ However, no report on the antimicrobial activity of complexes derived from HL has been reported so far. As an extension of our work on Schiff base complexes,⁷ a new

zinc(II) compound, $[ZnL_2]$ (1), and a new manganese(II) compound, $[MnL(HL)]ClO_4$ (2), are reported.

2. Experimental

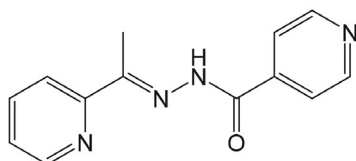
2.1. Material and Methods

2-Acetylpyridine and pyridine-4-carbohydrazide were purchased from Fluka. Other reagents and solvents were analytical grade and used without further purification. Elemental (C, H, and N) analyses were made on a Perkin-Elmer Model 240B automatic analyzer. Infrared (IR) spectra were recorded on an IR-408 Shimadzu 568 spectrophotometer. UV-Vis spectra were recorded on a Lambda 35 spectrometer. X-ray diffraction was carried out on a Bruker SMART 1000 CCD area diffractometer. The ligand HL was prepared according to the literature method.⁸

Caution! Perchlorate salts are potentially explosive. Only a small amount of material should be prepared, and they should be handled with great care.

2.2. Synthesis of Compound 1

The hydrazone (48.0 mg, 0.20 mmol) was dissolved by methanol (10 mL) and then a methanol solution (10 mL) of $Zn(ClO_4) \cdot 6H_2O$ (37.2 mg, 0.10 mmol) was added with stir-



Scheme 1. The ligand HL

ring. The mixture was stirred for 1 h at ambient temperature to give a colorless solution. Colorless block-shaped single crystals suitable for X-ray diffraction were formed by slow evaporation of the solution in air for several days. The yield is 45% (based on Zn). IR data (KBr, cm^{-1}): 1595 (C=N),

1498, 1451, 1363, 1160, 1072, 947, 854, 543, 522. UV-vis data in methanol [λ_{max} (nm), ϵ ($\text{L mol}^{-1} \text{cm}^{-1}$): 277, 6450; 362, 15510. Anal. Calcd. (%) for $\text{C}_{26}\text{H}_{22}\text{N}_8\text{O}_2\text{Zn}$: C, 57.42; H, 4.08; N, 20.60. Found (%): C, 57.61; H, 4.17; N, 20.45.

Table 1. Crystallographic data and refinement parameters for complexes **1** and **2**

Parameters	1	2
Habit, color	Block, colorless	Block, brown
Molecular formula	$\text{C}_{26}\text{H}_{22}\text{N}_8\text{O}_2\text{Zn}$	$\text{C}_{26}\text{H}_{23}\text{ClMnN}_8\text{O}_6$
Formula weight	543.89	633.91
Crystal system	Orthorhombic	Monoclinic
Space group	<i>Aba2</i>	<i>P2₁/n</i>
Unit cell dimensions:		
<i>a</i> , Å	12.363(2)	11.755(2)
<i>b</i> , Å	20.251(2)	9.437(2)
<i>c</i> , Å	9.595(2)	26.198(2)
α , °	90	90
β , °	90	98.197(2)
γ , °	90	90
<i>V</i> , Å ³	2402.2(7)	2876.5(8)
<i>Z</i>	4	4
ρ_{calcd} , g cm^{-3}	1.504	1.464
<i>F</i> (000)	1120	1300
Absorption coefficient, mm^{-1}	1.065	0.607
Reflections collected	6959	16410
Independent reflections	1732	5322
Data/parameters	1353/169	3869/381
Restraints	1	0
R_1 , wR_2 [$I > 2\sigma(I)$]	0.0333, 0.0634	0.0879, 0.2408
R_1 , wR_2 (all data)	0.0538, 0.0718	0.1133, 0.2583
Goodness-of-fit on F^2	1.020	1.070

2. 3. Synthesis of Compound 2

The hydrazone (48.0 mg, 0.20 mmol) was dissolved by methanol (10 mL) and then a methanol solution (10 mL) of $\text{Mn}(\text{ClO}_4)_2 \cdot 6\text{H}_2\text{O}$ (36.2 mg, 0.10 mmol) was added with stirring. The mixture was stirred for 1 h at ambient temperature to give a brown solution. Brown block-shaped single crystals suitable for X-ray diffraction were formed by slow evaporation of the solution in air for several days. The yield is 33% (based on Mn). IR data (KBr, cm^{-1}): 1596 (C=N), 1499, 1450, 1365, 1160, 1079 (ClO_4), 945, 855, 756, 696, 622, 546, 518. UV-vis data in methanol [λ_{max} (nm), ϵ ($\text{L mol}^{-1} \text{cm}^{-1}$): 271, 7270; 366, 16480. Anal. Calcd. (%) for $\text{C}_{26}\text{H}_{22}\text{ClMnN}_8\text{O}_6$: C, 49.34; H, 3.50; N, 17.70. Found (%): C, 49.16; H, 3.62; N, 17.83.

2. 4. X-ray Structure Determination

Data were collected from selected crystals mounted on glass fibres. The data were collected with MoK_α radiation (0.71073 Å) at 298(2) K with a Bruker SMART 1000 CCD area diffractometer. The data for the two complexes were processed with SAINT⁹ and corrected for absorption using SADABS.¹⁰ Multi-scan absorption corrections were applied with ψ -scans.¹¹ The structures were solved by direct methods using the program SHELXS-97 and were refined by full-matrix least-squares techniques on F^2 using anisotropic displacement parameters.¹² All hydrogen atoms were placed at the calculated positions. Idealized H atoms

Table 2. Selected bond lengths (Å) and bond angles (°) for complexes **1** and **2**

1			
Zn(1)–N(3)	2.069(3)	Zn(1)–O(1)	2.149(3)
Zn(1)–N(4)	2.193(4)		
N(3)–Zn(1)–N(3A)	173.3(3)	N(3)–Zn(1)–O(1A)	101.34(13)
N(3)–Zn(1)–O(1)	74.22(13)	O(1)–Zn(1)–O(1A)	100.30(17)
N(3)–Zn(1)–N(4)	75.14(14)	N(3)–Zn(1)–N(4A)	109.70(15)
O(1)–Zn(1)–N(4A)	91.47(13)	O(1)–Zn(1)–N(4)	148.77(11)
N(4)–Zn(1)–N(4A)	93.19(19)		
2			
Mn(1)–O(1)	2.144(4)	Mn(1)–O(2)	2.151(4)
Mn(1)–N(7)	2.191(4)	Mn(1)–N(3)	2.193(4)
Mn(1)–N(4)	2.314(5)	Mn(1)–N(8)	2.326(4)
O(1)–Mn(1)–O(2)	107.34(16)	O(1)–Mn(1)–N(7)	122.05(15)
O(2)–Mn(1)–N(7)	72.27(15)	O(1)–Mn(1)–N(3)	72.01(14)
O(2)–Mn(1)–N(3)	125.51(15)	N(7)–Mn(1)–N(3)	155.58(17)
O(1)–Mn(1)–N(4)	142.00(15)	O(2)–Mn(1)–N(4)	90.07(16)
N(7)–Mn(1)–N(4)	95.15(16)	N(3)–Mn(1)–N(4)	70.41(15)
O(1)–Mn(1)–N(8)	90.69(16)	O(2)–Mn(1)–N(8)	142.58(14)
N(7)–Mn(1)–N(8)	70.38(15)	N(3)–Mn(1)–N(8)	90.90(15)
N(4)–Mn(1)–N(8)	95.35(16)		

Symmetry code for A: $-x, -y, z$.

were refined with isotropic displacement parameters set to 1.2 (1.5 for methyl groups) times the equivalent isotropic U values of the parent atoms. The large average U_{eq} of residue including Cl1 (0.335) in complex is caused by the disorder of the perchlorate anion. The crystallographic data for the complexes are listed in Table 1, selected bond lengths and bond angles for compounds **1** and **2** are given in Table 2.

2. 5. Antimicrobial Assay

Qualitative determination of antimicrobial activity was done using the disk diffusion method as described in the literature.¹³ Suspensions in sterile peptone water from 24-h cultures of microorganisms were adjusted to 0.5 McFarland. Muller–Hinton Petri dishes of 90 mm were inoculated using these suspensions. Paper disks (6 mm in diameter) containing 10 μ L of the substance to be tested (at a concentration of 2048 μ g/mL in DMSO) were placed in a circular pattern in each inoculated plate. Incubation of the plates was done at 37 °C for 18–24 h. Reading of the results was done by measuring the diameters of the inhibition zones generated by the test substance. Tetracycline was used as a reference substance. Determination of MIC was done using the serial dilutions in liquid broth method. The materials used were 96-well plates, suspensions of microorganism (0.5 McFarland), Muller-Hinton broth (Merck) and stock solutions of each substance to be tested (2048 μ g/mL in DMSO). The following concentrations of the substances to be tested were obtained in the 96-well plates: 1024, 512, 256, 128, 64, 32, 16, 8, 4 and 2 μ g/mL. After incubation at 37 °C for 18–24 h, the MIC for each tested substance was determined by microscopic observation of microbial growth. It corresponds to the well with the lowest concentration of the tested substance where microbial growth was clearly inhibited.

3. Results and Discussion

3. 1. Chemistry

The hydrazone compound HL was prepared by the condensation of equimolar quantities of 2-acetylpyridine

with pyridine-4-carbohydrazone in methanol at ambient temperature. The hydrazone compound prepared in this way was formed in nearly quantitative yield and of high purity. The compounds **1** and **2** were readily synthesized by reaction of the hydrazone compound HL with zinc perchlorate and manganese perchlorate in methanol at ambient temperature. All the compounds are very stable at room temperature in the solid state, and soluble in common organic solvents, such as methanol, ethanol, and acetonitrile. The results of the elemental analyses are in accord with the composition suggested for the hydrazone and the complexes.

3. 2. IR and UV-Vis Spectra

The typical band indicative of the azomethine group in the ligand of the complexes was observed at 1595 cm^{-1} for compound **1** and 1596 cm^{-1} for compound **2**. The strong absorption at 1079 cm^{-1} in the spectrum of compound **2** is assigned to the stretching vibration of the perchlorate anion. UV-visible spectra of HL and the complexes were carried out in methanol. In the hydrazone, the band at 345 nm is attributed to the azomethine chromophore π - π^* transition. The band at higher energy (265 nm) is associated with the benzene π - π^* transition. In the spectra of the complexes, however, the azomethine chromophore π - π^* transition is shifted to 362–366 nm, indicating that the imino nitrogen is involved in coordination to the metal ion. The absorption frequencies ascribed to the benzene π - π^* transition (271–277 nm) are slightly changed.

3. 3. Structure Description of Compound 1

The molecular structure of compound **1** is shown in Fig. 1. Selected bond distances and angles are listed in Table 2. The Zn atom is coordinated by two pyridine N, two imine N, and two enolate O atoms from two deprotonated forms of hydrazone ligands, forming an octahedral geometry. The hydrazone acts as a tridentate ligand, forming two five-membered chelate rings with the Zn atom. The bond distances subtended at the Zn atom are comparable to those observed in the similar zinc(II) complexes with Schiff bases.¹⁴ The *cis* and *trans* coordinate bond angles are

Table 3 Distances (Å) and angles (°) involving hydrogen bonding of the complexes

$D-H\cdots A$	$d(D-H)$	$d(H\cdots A)$	$d(D\cdots A)$	Angle($D-H\cdots A$)
1				
C(9)–H(9)···O(1) ^{#1}	0.93	2.36(5)	3.180(5)	148(6)
C(10)–H(10)···N(1) ^{#2}	0.93	2.54(5)	3.455(5)	170(6)
C(13)–H(13A)···N(2)	0.96	2.43(5)	2.811(5)	103(6)
2				
N(1)–H(1)···N(5) ^{#3}	0.93	2.39(3)	3.284(4)	161(7)
C(10)–H(10)···O(5) ^{#4}	0.93	2.39(3)	3.284(4)	161(7)
C(13)–H(13C)···N(2)	0.96	2.40(3)	2.778(4)	103(5)
C(23)–H(23)···O(6) ^{#5}	0.93	2.48(4)	3.258(5)	142(6)
C(26)–H(26A)···N(6)	0.96	2.37(3)	2.788(4)	106(5)

Symmetry codes: #1: $\frac{1}{2} + x, -y, -\frac{1}{2} + z$; #2: $\frac{1}{2} - x, -\frac{1}{2} + y, -1 + z$; #3: $\frac{1}{2} + x, -\frac{1}{2} - y, -\frac{1}{2} + z$; #4: $\frac{1}{2} - x, \frac{1}{2} + y, \frac{1}{2} - z$; #5: $-x, 1 - y, -z$.

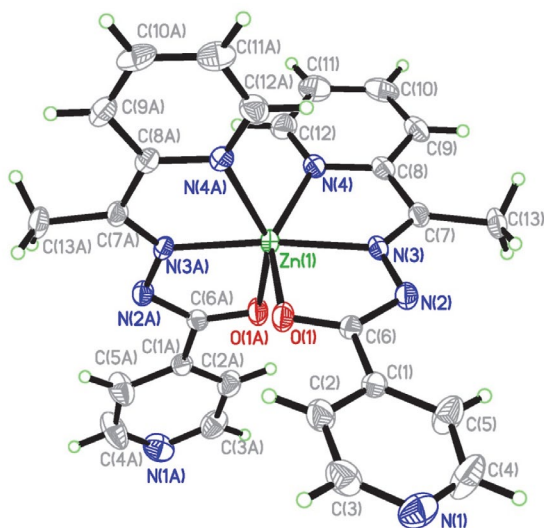


Fig. 1. Perspective view of complex 1 with 30% probability thermal ellipsoids. Atoms labeled with the suffix A are related to the symmetry operation $-x, -y, z$.

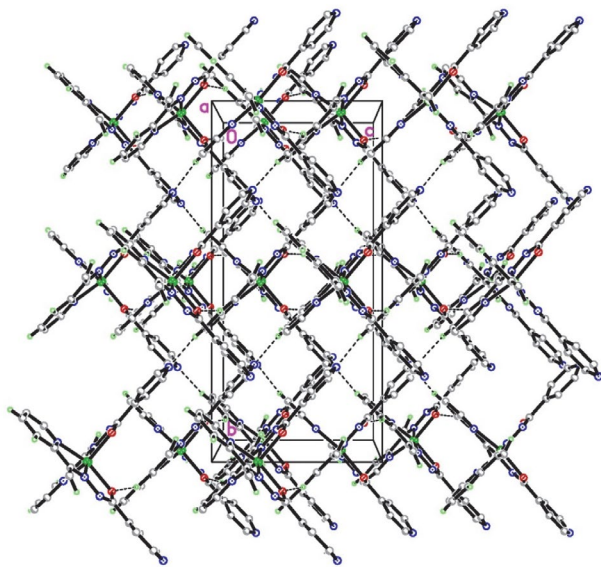


Fig. 2. Molecular packing structure of complex 1, with hydrogen bonds drawn as dashed lines.

range from $74.22(13)$ to $109.70(15)^\circ$ and from $148.77(11)$ to $173.3(3)^\circ$, respectively, indicating the distortion of the octahedral coordination from ideal geometry. In the crystal structure of the compound, the complex molecules are linked through hydrogen bonds (Table 3), to form a three-dimensional network (Fig. 2).

3. 4. Structure Description of Compound 2

The molecular structure of compound 2 is shown in Fig. 3. Selected bond distances and angles are listed in Table 2. The compound contains a $[\text{MnL}(\text{HL})]^+$ complex

cation and a perchlorate anion. The Mn atom in the $[\text{MnL}(\text{HL})]^+$ complex cation is coordinated by two pyridine N, two imine N, and two enolate O atoms from one deprotonated form of the hydrazone ligand and one zwitterionic form of the hydrazone ligand, forming an octahedral geometry. The hydrazones act as tridentate ligands, forming two five-membered chelate rings with the Mn atom. The bond distances subtended at the Mn atom are comparable to those observed in the similar manganese(II) complexes with Schiff bases.¹⁵ The *cis* and *trans* coordinate bond angles are range from $70.38(15)$ to $125.52(15)^\circ$ and from $141.99(14)$ to $155.58(17)^\circ$, respectively, indicating the distortion of the octahedral coordination from ideal geometry. In the crystal structure of the compound, the $[\text{MnL}(\text{HL})]^+$ complex cations and the perchlorate anions are linked through hydrogen bonds (Table 3), to form a three-dimensional network (Fig. 4).

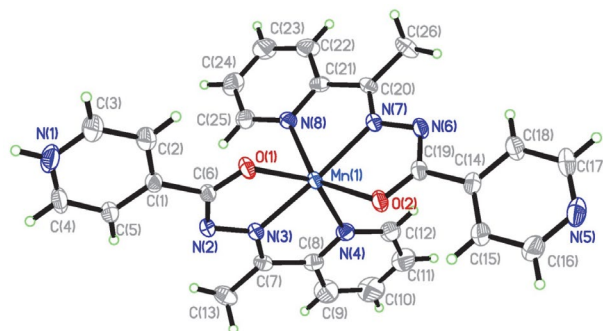


Fig. 3. Perspective view of complex 2 with 30% probability thermal ellipsoids.

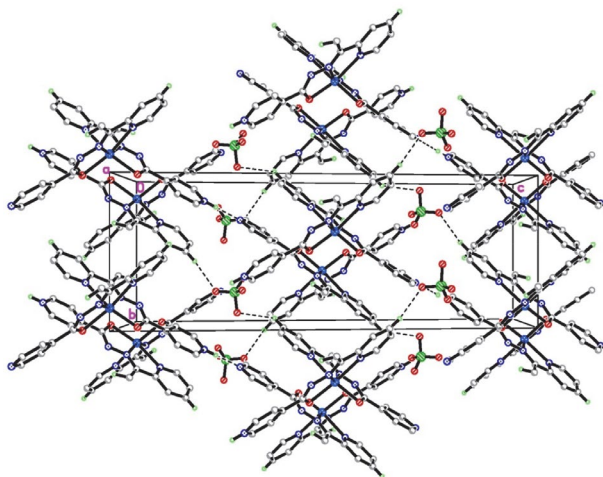


Fig. 4. Molecular packing structure of complex 2, with hydrogen bonds drawn as dashed lines.

3. 5. Antimicrobial Activity

The results are summarized in Table 4. A comparative study of minimum inhibitory concentration (MIC) values of the hydrazone and the metal complexes indicates that the complexes have better activity than the free hy-

drazone. Generally, this is caused by the greater lipophilic nature of the complexes than the ligand. Such increased activity of the metal chelates can be explained on the basis of chelating theory.¹⁶ On chelating, the polarity of the metal atoms will be reduced to a greater extent due to the overlap of the ligand orbital and partial sharing of positive charge of the metal atoms with donor atoms. Further, it increases the delocalization of *p*-electrons over the whole chelate ring and enhances the lipophilicity of the complexes. This increased lipophilicity enhances the penetration of the complexes into lipid membrane and blocks the metal binding sites on enzymes of microorganisms.

From Table 4, it is obvious that the two complexes have higher antibacterial and antifungi activities against *Staphylococcus aureus*, *Escherichia coli*, and *Candida albicans* when compared to the free hydrazone. Complex **1** has strong activity against *Escherichia coli*, with MIC value of 0.20 µg/mL, which is comparable to Tetracycline. Complex **1** has medium activity against *Staphylococcus aureus* and weak activity against *Candida albicans*. Complex **2** has effective activity against *Escherichia coli*, and weak activity against *Staphylococcus aureus* and *Candida albicans*. In general, the zinc complex has stronger activity against *Staphylococcus aureus*, *Escherichia coli*, and *Candida albicans* than the manganese complex. So, the metal type of the complexes can influence the antimicrobial activity.

Table 4. MIC values (µg/mL) for the antimicrobial activities of the tested compounds

Compounds	<i>Staphylococcus aureus</i>	<i>Escherichia coli</i>	<i>Candida albicans</i>
The hydrazone	64	32	> 512
1	8.0	2.0	64
2	16.0	8.0	128
Tetracycline	0.32	2.12	> 1024

4. Supplementary Material

CCDC 1871743 for **1**, and 1871744 for **2** contain the supplementary crystallographic data for this paper. These data can be obtained free of charge at <http://www.ccdc.cam.ac.uk/const/retrieving.html> or from the Cambridge Crystallographic Data Centre, 12 Union Road, Cambridge CB2 1EZ, UK; fax: +44(0)1223-336033 or email: deposit@ccdc.cam.ac.uk.

5. Acknowledgments

This research was supported by the Top-class foundation of Pingdingshan University (no. PXY-BSQD-2018006 and PXY-PYJJ-2018002).

6. References

- (a) K. J. Davis, N. M. O. Assadawi, S. Q. T. Pham, M. L. Birrento, C. Richardson, J. L. Beck, A. C. Willis, S. F. Ralph, *Dalton Trans.* **2018**, 47, 13573–13591; DOI:10.1039/C8DT02727G
(b) S. Banerjee, R. Patra, P. Ghorai, P. Brandao, S. G. Chowdhury, P. Karmakar, A. Saha, *New J. Chem.* **2018**, 42, 16571–16582; DOI:10.1039/C8NJ02235F
(c) S. Asadzadeh, M. Amirnasr, F. F. Tirani, A. Mansouri, K. Schenk, *Inorg. Chim. Acta* **2018**, 483, 310–320. DOI:10.1016/j.ica.2018.08.037
- (a) Y. Salman, F. B. Barlas, M. Yavuz, K. Kaya, S. Timur, F. C. Telli, *Inorg. Chim. Acta* **2018**, 483, 98–105; DOI:10.1016/j.ica.2018.08.010
(b) A. S. Burlov, V. G. Vlasenko, Y. V. Koshchienko, N. I. Makarova, A. A. Zubenko, Y. D. Drobin, L. N. Fetisov, A. A. Kolodina, Y. V. Zubavichus, A. L. Trigub, S. I. Levchenkov, D. A. Garnovskii, *Polyhedron* **2018**, 154, 65–76; DOI:10.1016/j.poly.2018.07.034
(c) S. Alyar, C. H. Sen, H. Alyar, S. Adem, A. Kalkanci, U. O. Ozdemir, *J. Mol. Struct.* **2018**, 1171, 214–222. DOI:10.1016/j.molstruc.2018.06.004
- (a) A. K. Ghosh, C. S. Purohit, R. Ghosh, *Polyhedron* **2018**, 155, 194–201; DOI:10.1016/j.poly.2018.08.021
(b) Y.-T. Li, J.-W. Dong, Y. Lu, Y.-T. Gu, C.-N. Shang, F.-Y. Li, Y. Xin, C.-L. Jing, Z.-L. You, *Chinese J. Inorg. Chem.* **2018**, 34, 1192–1198;
(c) L. W. Xue, G. Q. Zhao, Y. J. Han, Y. X. Feng, *Russ. J. Coord. Chem.* **2011**, 37, 262–269; DOI:10.1134/S1070328411030110
(d) L. W. Xue, Y. J. Han, G. Q. Zhao, Y. X. Feng, *Russ. J. Coord. Chem.* **2012**, 38, 24–28. DOI:10.1134/S1070328411120104
- (a) M. Zhang, D.-M. Xian, H.-H. Li, J.-C. Zhang, Z.-L. You, *Aust. J. Chem.* **2012**, 65, 343–350; DOI:10.1071/CH11424
(b) E. W. Ainscough, A. M. Brodie, A. J. Dobbs, J. D. Ranford, J. M. Waters, *Inorg. Chim. Acta* **1998**, 267, 27–38; DOI:10.1016/S0020-1693(97)05548-5
(c) R. N. Patel, S. P. Rawat, M. Choudhary, V. P. Sondhiya, D. K. Patel, K. K. Shukla, D. K. Patel, Y. Singh, R. Pandey, *Inorg. Chim. Acta* **2012**, 392, 283–291. DOI:10.1016/j.ica.2012.03.040
- (a) W. Cao, Y.-M. Liu, T. Zhang, J.-P. Jia, *Polyhedron* **2018**, 147, 62–68; DOI:10.1016/j.poly.2018.03.012
(b) A. A. El-Sherif, A. Fetoh, Y. K. Abdulhamed, G. M. Abu El-Reash, *Inorg. Chim. Acta* **2018**, 480, 1–15; DOI:10.1016/j.ica.2018.04.038
(c) Q.-Y. Mo, J.-G. Deng, Y.-N. Liu, G.-D. Huang, Z.-W. Li, P. Yu, Y. Gou, F. Yang, *Eur. J. Med. Chem.* **2018**, 156, 368–380; DOI:10.1016/j.ejmech.2018.07.022
(d) R. Fekri, M. Salehi, A. Asadi, M. Kubicki, *Inorg. Chim. Acta* **2019**, 484, 245–254; DOI:10.1016/j.ica.2018.09.022
(e) Z.-Y. Hao, Q.-W. Liu, J. Xu, L. Jia, S.-B. Li, *Chem. Pharm. Bull.* **2010**, 58, 1306–1312. DOI:10.1248/cpb.58.1306
- H.-Q. Chang, L. Jia, J. Xu, W.-N. Wu, T.-F. Zhu, R.-H. Chen, T.-L. Ma, Y. Wang, Z.-Q. Xu, *Transition Met. Chem.* **2015**, 40, 485–491.

7. (a) G.-P. Cheng, L.-W. Xue, C.-X. Zhang, *Acta Chim. Slov.* **2017**, *64*, 261–265; DOI:10.17344/acsi.2016.3036
 (b) L. Wang, Y.-J. Han, Q.-B. Li, L.-W. Xue, *Acta Chim. Slov.* **2016**, *63*, 822–826; DOI:10.17344/acsi.2016.2699
 (c) Q.-B. Li, Y.-J. Han, G.-Q. Zhao, L.-W. Xue, *Acta Chim. Slov.* **2017**, *64*, 500–505. DOI:10.17344/acsi.2017.3416
8. M. R. Maurya, S. Khurana, W. Zhang, D. Rehder, *Dalton Trans.* **2002**, 3015–3023. DOI:10.1039/b202852m
9. *SMART and SAINT. Area Detector Control and Integration Software*, Madison (WI, USA): Bruker Analytical X-ray Instruments Inc., 1997.
10. G. M. Sheldrick, *SADABS, Program for Empirical Absorption Correction of Area Detector Data*, Göttingen (Germany): Univ. of Göttingen, 1997.
11. A. C. T. North, D. C. Phillips, F. S. Mathews, *Acta Crystallogr. A* **1968**, *24*, 351–359. DOI:10.1107/S0567739468000707
12. G. M. Sheldrick, *SHELXL-97, Program for the Refinement of Crystal Structures*, Göttingen (Germany): Univ. of Göttingen, 1997.
13. (a) A. Barry, *Procedures and Theoretical Considerations for Testing Antimicrobial Agents in Agar Media*, In: *Antibiotics in Laboratory Medicine*, Lorian, V. (Ed.), Baltimore: Williams and Wilkins, 1991;
 (b) T. Rosu, M. Negoiu, S. Pasculescu, E. Pahontu, D. Poirier, A. Gulea, *Eur. J. Med. Chem.* **2010**, *45*, 774–781. DOI:10.1016/j.ejmech.2009.10.034
14. (a) S. Konar, A. Jana, K. Das, S. Ray, S. Chatterjee, S. K. Kar, *Polyhedron* **2012**, *47*, 143–150; DOI:10.1016/j.poly.2012.07.080
 (b) Z. He, C. He, Z.-M. Wang, E.-Q. Gao, Y. Liu, C.-H. Yan, *Dalton Trans.* **2004**, 502–504; DOI:10.1039/b315281b
 (c) C.-F. Chow, S. Fujii, J.-M. Lehn, *Chem. Asian. J.* **2008**, *3*, 1324–1335. DOI:10.1002/asia.200800101
15. (a) C.-F. Wang, Z.-J. Chen, K.-D. Zhao, X.-F. Chen, C.-Y. Zhang, G.-H. Sheng, H.-L. Zhu, *J. Coord. Chem.* **2016**, *69*, 2656–2665; DOI:10.1080/00958972.2016.1213819
 (b) N. A. Mangalam, S. R. Sheeja, M. R. P. Kurup, *Polyhedron* **2010**, *29*, 3318–3323; DOI:10.1016/j.poly.2010.09.007
 (c) S. Banerjee, A. Ray, S. Sen, S. Mitra, D. L. Hughes, R. J. Butcher, S. R. Batten, D. R. Turner, *Inorg. Chim. Acta* **2008**, *361*, 2692–2700. DOI:10.1016/j.ica.2008.01.019
16. J. W. Searl, R. C. Smith, S. Wyard, *J. Proc. Phys. Soc.* **1961**, *78*, 1174–1181. DOI:10.1088/0370-1328/78/6/311

Povzetek

Sintetizirali smo dve enojedrni cinkovi(II) in manganovi(II) spojini, $[\text{ZnL}_2]$ (**1**) in $[\text{MnL}(\text{HL})]\text{ClO}_4$ (**2**), kjer je L mon-oanionska oblika N^2 -(1-(piridin-2-il)etiliden)izonikotinohidrazida (HL) in HL ion dvojček HL, ter ju okarakterizirali z elementno analizo, IR in UV-Vis spektroskopijo ter monokristalno rentgensko strukturno analizo. Spojina **1** je nevtralen $[\text{ZnL}_2]$ kompleks. Spojina **2** je zgrajena iz $[\text{MnL}(\text{HL})]^+$ kompleksnega iona in enega perkloratnega aniona. Kovinski ioni v obeh kompleksih so oktaedrično koordinirani. Hidrazonski ligand se koordinira na kovinski ion preko piridinskega N, iminskega N in enolatnega O atoma. Spojinama smo določili antimikrobno aktivnost proti *Staphylococcus aureus*, *Escherichia coli* in *Candida albicans*.

Scientific paper

Evaluation of DNA/BSA Binding and Chemical Nuclease Activity of L-Tyrosine-Based Mn(III) and Fe(III) Metallo-Intercalators

Biju Bennie Rajaretnam,¹ Joel Chellappa,¹ Daniel Abraham Solomon,² Iyyam Pillai Subramanian³ and Theodore David Manickam Selvanayagam^{4,*}

¹ Postgraduate Department of Chemistry, St. John's College, Tirunelveli-627002, Tamil Nadu, India.

² Department of Chemistry, Madras Christian College, Chennai-600059, Tamil Nadu, India.

³ Postgraduate and Research Department of Chemistry, Pachaiyappa's College, Chennai-600030, Tamil Nadu, India.

⁴ Department of Applied Chemistry, PSN College of Engineering and Technology, Tirunelveli-627152, Tamil Nadu, India.

* Corresponding author: E-mail: s.theodore.david@gmail.com

Mobile: +91 9366705118

Received: 10-11-2018

Abstract

A novel class of Mn(III) and Fe(III) complexes of L-tyrosine-based ligand has been synthesized and characterized through various analytical and spectroscopic techniques. These complexes were found to exhibit efficient binding properties with the biomolecules *viz.* calf thymus DNA and BSA. The ability of complexes to bind with such biomolecules has been explored through absorption, emission and viscosity measurements. Based on spectroscopic techniques we can conclude that the complexes could bind to DNA *via* intercalation. It was observed that these complexes can cleave pBR322 DNA in gel-electrophoresis technique through oxidative mechanism. The BSA was quenched by the complexes around 340 nm adopting a mechanism of static mode. The binding constants, thermodynamic parameters and the donor to acceptor distance were calculated. Besides, molecular docking simulations were carried out for the complexes with human DNA topoisomerase and BSA protein. The docked poses are visualized to provide supportive evidence to the interaction of the synthesized complexes with DNA/BSA.

Keywords: BSA; CT DNA; Coordination complex; L-Tyrosine; Molecular docking

1. Introduction

Biomolecules such as proteins or nucleic acids are particularly interesting as the target since they act as the key molecules in the metabolic pathways associated with a specific disease.¹ A drug is a molecule designed in order to obstruct the target function in the particular disease modifying pathway. The transition metal complexes containing multidentate aromatic ligands play important role in different biological processes which eventually helps to develop different structural and more importantly functional model systems.^{2–4} DNA is known to be an important cellular receptor. Interactions of small metal complexes with DNA and proteins are the key research areas of current years as there are enough potentials of development of new therapeutic agent particularly showing anti-

tumor properties and possibility of the transportation of these molecules throughout the physiological system via protein binding.^{5–8} The metal complexes–nucleic acid interaction has gained the attention of researchers due to their excellent biological activity. The activity of the complexes is described based on their mode and affinity of binding with DNA.^{9–11} Generally, DNA has been considered as a target molecule for a wide range of disease therapies such as anticancer and antiviral. Any disorder in gene expression may cause diseases and plays a secondary role in the outcome and severity of human diseases.¹² Therefore, various metal-based drugs have been opted with improved pharmacological properties and aimed at different targets. Proteins play fundamental roles in sustaining life and are an integral part of origin, evolution,

and metabolism. Being one of the most abundant proteins in blood constituent, serum albumin aids in the transportation of various molecules (ligands) including fatty acids, steroids and metal ions.¹³ Hence the binding of these molecules to serum albumins is taken under consideration in various fields.¹⁴ The homology of 76% in structures between the bovine serum albumin (BSA) and the human serum albumin (HSA) makes it a unique one for the researchers to be studied more comprehensively.¹⁵ Serum albumins are model globular proteins found abundant in plasma. Serum albumins exhibit a character of reversible binding with various molecules through hydrophobic, hydrophilic and electrostatic interactions. The binding of metal complexes with BSA can be detected by the decrease in intensity of the fluorescence emitted by one of the amino acid residues called tryptophan 212, which is exposed outwards. It is expected that the ligand could bind into the two binding sites of BSA marked as site I and site II located in the hydrophobic cavities of subdomains IIA and IIIA, respectively. The binding of drug molecules to BSA on a particular site can be probed through various selective site markers.¹⁶ Serum albumin also binds metal ions, predominantly soft/intermediate metal ions at one or more of at least four proposed specific sites. Albumin binds hard metals in chelate form. For example, albumin scavenges hemein, the ferric state of heme, to avoid the formation of reactive oxygen species. Albumin binding affects the pharmacokinetics, trafficking and efficacy of metal-based therapeutics.¹⁷ Amino acids are small molecules capable of metal complexation via amino and carboxylate groups.¹⁸ It has been reported that transition metal complexes of amino acids could possess better fungicidal, anti-bacterial, antiviral and anti-tubercular activities.¹⁹ Hence, we herein report the synthesis of Mn(III) and Fe(III) complexes of L-tyrosine-based ligand and their interaction with CT-DNA/BSA using various spectral methods.

2. Experimental

All the chemicals utilized in this research work are of AR grade and also 99% pure solvents are used. The ligands employed in our present investigation, viz. 9,10-phenanthrenequinone (Aldrich) and L-tyrosine (Loba Chemie) were purchased in pure form and used as such. CT-DNA and pBR322 DNA was purchased from Genei, Bengaluru, India. The protein bovine serum albumin (BSA) used in this experiment was purchased from Sigma whereas Tris buffer from HIMEDIA. Carlo Erba 1108 elemental analyzer was involved in analysing the elemental content (C, H, N) of the ligand as well as its Mn(III) and Fe(III) complexes. The percentage of metal ions in the complexes were estimated as per the procedure given in the book.²⁰ Nuclear magnetic study was performed on Bruker Advance DRX 300 FT-NMR spectrometer in CDCl_3 solvent and the refer-

ence material taken was TMS. JEOL DX-303 EI mass spectrometer and Bruker-Daltonics micro TOF-Q II mass spectrometer were used to record EI mass spectrum of the ligand and electrospray ionization mass spectra (ESI) of the complexes respectively. Vibrational spectral analysis of the ligand and its manganese and iron complexes were carried out on JASCO FT-IR/4100 Spectrometer, involving KBr disc method. The UV-vis spectra of both the synthesised complexes were taken in 200–800 nm wavelength range on a Perkin Elmer Lambda 35 spectrophotometer using the solvent DMSO. Hertz SG8-5HJ model Gouy magnetic balance was employed to study the magnetic susceptibility measurements by taking $\text{CuSO}_4 \cdot 5\text{H}_2\text{O}$ as the calibrant. The molar conductivities of MnL and FeL were measured using Elico model SX 80 conductivity-bridge taking DMSO as solvent.

2. 1. Synthesis of Ligand

About 2.08 g of 9,10-phenanthrenequinone (10.0 mmol) dissolved in 50 mL of ethanol was taken in a two-neck flat bottomed flask. To this, 3.62 g of L-tyrosine (20.0 mmol) dissolved in 20 mL of 1 M sodium hydroxide was added. The reaction mixture was subjected to stirring for 10 hours to give a bright yellow colored precipitate of the Schiff base ligand (L). After washing the precipitate repeatedly with water and diethyl ether, it was then dried *in vacuo* over anhydrous calcium chloride. The dried product obtained (Scheme 1) was then characterized using IR, EI-MS and ^{13}C NMR spectroscopic tools.

Yield: 75%, m.p.: 178 °C, Anal. Found (%): C, 71.84; H, 4.88; N, 5.20; Calc.: C, 71.90; H, 4.91; N, 5.22; EI-MS: m/z , 534.46; IR (KBr, cm^{-1}): $\nu_{(\text{C}=\text{N})}$ 1673, $\nu_{\text{asy}(\text{COOH})}$ 1589, $\nu_{\text{sy}(\text{COOH})}$ 1450, $\nu_{(\text{OH})}$ 3205; ^{13}C NMR (δ , ppm in CDCl_3): 163.19 (C=N), 180.47 (COOH).

2. 2. Synthesis of Metal Complexes

1.0 mmol (0.58 g) of finely powdered Schiff base ligand was dissolved in 20 mL ethanol. To this, 20 mL ethanolic solution of 1.0 mmol metal salts (manganese(III) acetate 0.27g / iron(III) chloride 0.40 g) were added drop wise (Scheme 2). Then the mixture was subjected to stirring as well as refluxing at 50 °C for 12 hours. The resulting homogenous solution was subjected to slow evaporation at room temperature and the product obtained was washed with ethanol and dried and stored in air tight container for further analysis.

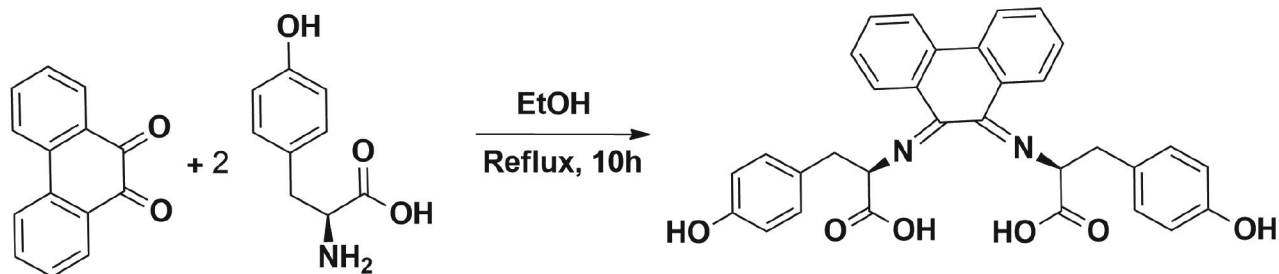
MnL: Yield: 57%; Brown color; Molecular weight: 623.51; Molecular formula $\text{C}_{32}\text{H}_{28}\text{MnN}_2\text{O}_8$; Anal. Found (%): C, 61.57; H, 4.46; N, 4.82 and Mn, 8.76. Calc.: C, 61.6; H, 4.5; N, 4.9 and Mn, 8.81, ESI-MS: m/z , 624.25; IR (KBr, cm^{-1}): $\nu_{(\text{C}=\text{N})}$ 1598, $\nu_{\text{asy}(\text{COO}^-)}$ 1512, $\nu_{\text{sy}(\text{COO}^-)}$ 1435, $\nu_{(\text{M}-\text{O})}$ 547, $\nu_{(\text{M}-\text{N})}$ 423; $\Lambda_m(\text{S mol}^{-1} \text{cm}^2)$ 51.78; μ_{eff} (BM) 4.89; UV-Vis (DMSO, nm, transition): 280 (LMCT), 530 and 720 (d-d).

FeL: Yield: 52%; Green color; Molecular weight: 624.42; Molecular formula $C_{32}H_{28}FeN_2O_8$; Anal. Found (%): C, 61.46; H, 4.44; N, 4.47 and Fe, 8.87. Calc.: C, 61.5; H, 4.5; N, 4.5 and Fe, 8.94, ESI-MS: m/z , 625.91; IR (KBr, cm^{-1}): $\nu_{(C=N)}$ 1611, $\nu_{asy(COO^-)}$ 1513, $\nu_{sy(COO^-)}$ 1402, $\nu_{(M-O)}$ 528, $\nu_{(M-N)}$, 435; $\Lambda_m(S\ mol^{-1}\ cm^2)$ 51.56; μ_{eff} (BM) 5.93; UV-Vis (DMSO, nm, transition): 275 (LMCT), 525 and 670 (d-d).

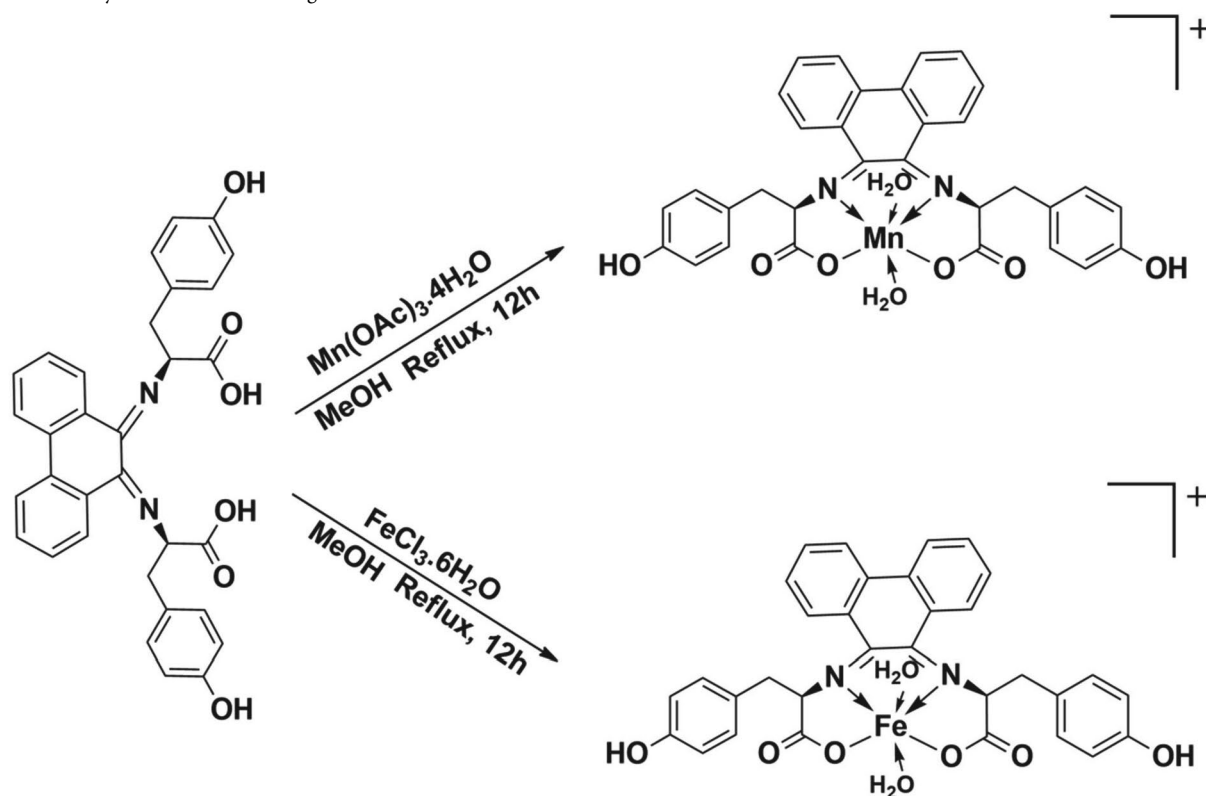
3. Results and Discussion

3.1. Scheme

The schematic representation of the Schiff Base ligand synthesized from the effective condensation of 9,10-phenanthrenequinone and L-tyrosine is shown in Scheme 1 and Scheme 2 represents the complexation of the ligand with Mn(III)/Fe(III) ions.



Scheme 1: Synthesis of Schiff base ligand



Scheme 2: Synthesis of Mn(III)/Fe(III) complexes

3.2. FTIR Spectra

The FTIR spectrum of the ligand L (Fig. S1a) exhibit the imine stretching $\nu(-C=N)$ vibration at $1673\ cm^{-1}$. The peaks due to (COOH) asymmetric stretching and (COOH) symmetric stretching vibration are observed in the regions of $1589\ cm^{-1}$ and $1450\ cm^{-1}$ respectively. The less intense and weak band at $3570\ cm^{-1}$ corresponds to phenolic $-OH$ stretching. In the vibrational spectra of complexes (Fig S1b and S1c), the imino (C=N) stretching frequency has been shifted to lower frequency regions 1598 and $1611\ cm^{-1}$, respectively, when compared to the imino stretching frequency of ligand ($1673\ cm^{-1}$). This indicates the coordination of nitrogens in the imino group to the metal ions.²¹ Moreover, the asymmetric stretching and the symmetric stretching vibrations of COO^- group has been shifted down to $1512\ cm^{-1}$, $1513\ cm^{-1}$ and $1435\ cm^{-1}$, $1402\ cm^{-1}$, respectively, which confirms the bonding of the metal ions by the carboxylato oxygen atom.²² This is further support-

ed by the presence of Mn–N, Fe–N and Mn–O, Fe–O bands at 423 cm^{-1} , 435 cm^{-1} and 547 cm^{-1} , 528 cm^{-1} , respectively.²³ The –OH stretching vibrations exhibits broad band at 3423 cm^{-1} and 3200 cm^{-1} for the MnL and FeL complexes, respectively. The peaks around 750 cm^{-1} and 650 cm^{-1} correspond to $\rho_r(\text{H}_2\text{O})$ and $\rho_w(\text{H}_2\text{O})$ of coordinated water molecules, respectively.

3. 3. ^{13}C NMR Spectra

The ^{13}C NMR spectrum of the ligand L (Fig S2) shows a signal at δ 155.98 assigned to two –OH attached carbons. The signal at δ 36.13 is assigned to –CH₂ carbons present in between azomethine groups. The signal for the methane carbon of L-tyrosine appears at δ 67.10. The signals in the range δ 114.12–136.16 are due to aromatic carbon²⁴ atoms of L-tyrosine as well as 9,10-phenanthrenequinone. The signal at δ 163.19 corresponds to the two azomethine carbons.²⁵ The signal at δ 180.47 is due to the two carboxylate carbons.

3. 4. Mass Spectra

The EI mass spectrum of ligand L (Fig S3a) posses a molecular ion (M^+) peak at $m/z = 534$ which is meant to the molecular weight of the ligand. The peaks at $m/z = 485, 440, 383, 305, 253, 236, 204, 181, 154, 136, 108, 78$ and 58 corresponds to various fragments $\text{C}_{31}\text{H}_{23}\text{N}_2\text{O}_4$, $\text{C}_{26}\text{H}_{20}\text{N}_2\text{O}_5$, $\text{C}_{20}\text{H}_{18}\text{N}_2\text{O}_6$, $\text{C}_{18}\text{H}_{13}\text{N}_2\text{O}_3$, $\text{C}_{16}\text{H}_{13}\text{NO}_2$, $\text{C}_{15}\text{H}_9\text{NO}_2$, $\text{C}_{14}\text{H}_8\text{N}_2$, $\text{C}_{12}\text{H}_9\text{NO}$, $\text{C}_{12}\text{H}_{10}$, $\text{C}_7\text{H}_6\text{NO}_2$, $\text{C}_7\text{H}_7\text{O}$, C_6H_4 and $\text{C}_2\text{H}_2\text{O}_2$, respectively, which confirms the structure of the ligand. The structure of the complexes was corroborated with ESI-MS studies. The ESI mass spectra of the complexes exhibit the molecular ion peak which is in correct accordance with their molecular weights. The various other peaks in the spectra correspond to different fragments of the complexes. In the spectrum of MnL (Fig S3b), the molecular ion peak is observed at $m/z = 624.25$ and for the complex FeL (Fig S3c), the molecular ion peak is obtained at $m/z = 625.91$ which are in correct coherency with the molecular weight of the complexes. Therefore, the mass spectral analysis substantiates well with the proposed chemical structure of the complexes MnL and FeL.

3. 5. Electronic Spectra, Molar Conductance, and Magnetic Measurements

The UV-Vis spectrum of MnL (Fig 1a) exhibit ligand field absorption at 280 nm and two d-d bands at 530 nm and 720 nm corresponding to $^5\text{B}_{1g} \rightarrow ^5\text{E}_g$ and $^5\text{B}_{1g} \rightarrow ^5\text{B}_{2g}$ transitions, respectively. Normally these two weak transitions are expected for tetragonally distorted octahedral MnL complex.²⁶ The electronic spectra of FeL (Fig 1b) complex show three absorption maxima at 670 nm, 525 nm, and 275 nm. The transitions corresponding to the aforesaid absorption bands are $^6\text{A}_{1g}(\text{S}) \rightarrow ^4\text{T}_{1g}(\text{G})$, $^6\text{A}_{1g}(\text{S}) \rightarrow$

$^4\text{T}_{2g}(\text{G})$ and $^6\text{A}_{1g}(\text{S}) \rightarrow ^4\text{E}_g$ respectively, suggesting the octahedral geometry for FeL complex.²⁷ The magnetic moment values of 4.86 BM and 5.91 BM for MnL and FeL, respectively, further confirms the octahedral geometry.²⁸ The values obtained for molar conductance (51.78 and 51.56) of MnL and FeL complexes, respectively, reveals that the complexes are 1:1 electrolytes.²⁹

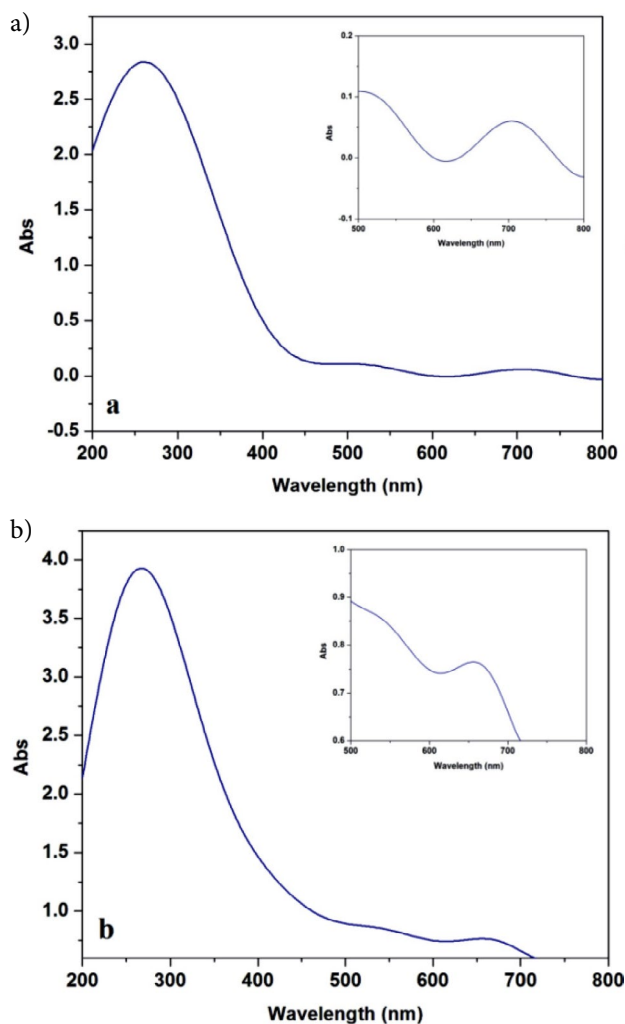


Fig. 1 (a) Electronic spectra of MnL complex (b) FeL complex

3. 6. DNA Binding Studies

3. 6. 1. Absorption Spectral Studies

The binding ability of the MnL and FeL complexes in DMSO solutions with CT-DNA were studied by measuring their effects on the absorption spectral method. In this method, the titrations were done at fixed complex concentration against different concentrations of DNA. If only could the complexes bind intercalatively to DNA helix, it shows hypochromism and also bathochromism. Since there exists a stacking interaction of an aromatic chromophore between the base pairs of nucleic acid, hy-

pochromism arises³⁰ whereas the bathochromic shift is a characteristic of coupling of π^* orbital of the complexes with the π orbital of the DNA nucleotide pairs which in turn causes decrease of the $\pi \rightarrow \pi^*$ transition energy.³¹ Hypochromism is generally a measure of the extend of intercalative mode of binding.³² An aqueous solution of the complexes showed intra-ligand charge transition bands at 276 nm (MnL) and 264 nm (FeL) which resulted in hypochromism on addition of increasing concentration of CT-DNA (Fig S4a and S4b) from which the binding constants K_b of the complexes were evaluated. The intrinsic equilibrium binding constant K_b was found to be $1.22 \times 10^5 \text{ M}^{-1}$ and $1.56 \times 10^5 \text{ M}^{-1}$ for MnL and FeL complexes, respectively, which is in compliance with the observed trend in hypochromism. These experimentations conclude that both the complexes could interact through intercalation with DNA.

3. 6. 2. EB Fluorescence Displacement Assay

A competitive binding titrations using ethidium bromide have been performed to substantiate the above results. Being a non-fluorescent compound in Tris-buffer, ethidium bromide (EB) shows fluorescence when combined with DNA, because of its strong intercalation between the nucleotides of DNA.³³ It is reported that the emission of DNA pretreated with EB is being quenched by some complexes resulting in the reduction of emission intensity. On addition of the complexes MnL and FeL to EB-DNA, the fluorescence intensity at 615 nm was decreased with increasing the concentration of the complexes without any shift in the position of emission maxima³⁴ as seen in (Fig 2a and 2b). From the classical Stern–Volmer equation, the apparent binding constant values (K_{app}) for the complexes MnL and FeL were calculated and it is found to be $4.8 \times 10^6 \text{ M}^{-1}$ and $12.3 \times 10^6 \text{ M}^{-1}$. From the observed

results, it may be concluded that both the complexes interact with CT-DNA via intercalative mode.

3. 6. 3 Viscosity Experiments

Viscosity experiments provide additional information regarding the intercalative nature of complexes between the nucleotide pairs of CT-DNA (Fig 3). The increase in complex concentration enhances the DNA viscosity as the base pairs of DNA get separated at its intercalation sites causing increase in the overall DNA length.³⁵ The viscosity of the DNA increases gradually with increase in complex concentration. These results indicate that both the complexes under study can intercalate the adjacent DNA base pairs, causing an expansion in the helix, and thus enhance the viscosity of DNA. Thus, the intercalative binding of the

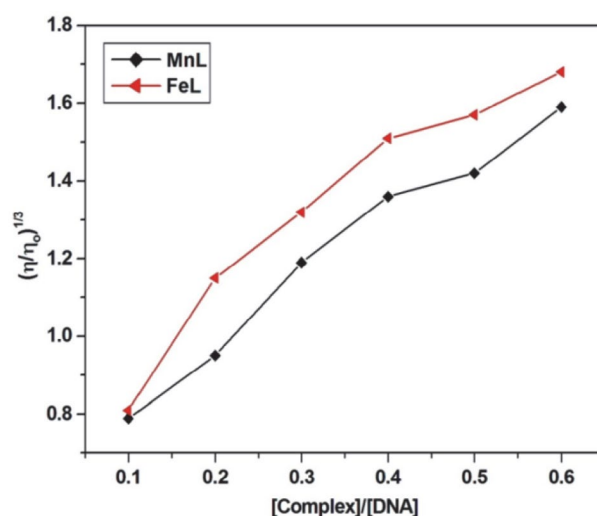


Fig. 3: Effect of increasing amounts of MnL and FeL on the relative viscosities of CT-DNA at room temperature in 5 mM Tris-HCl buffer

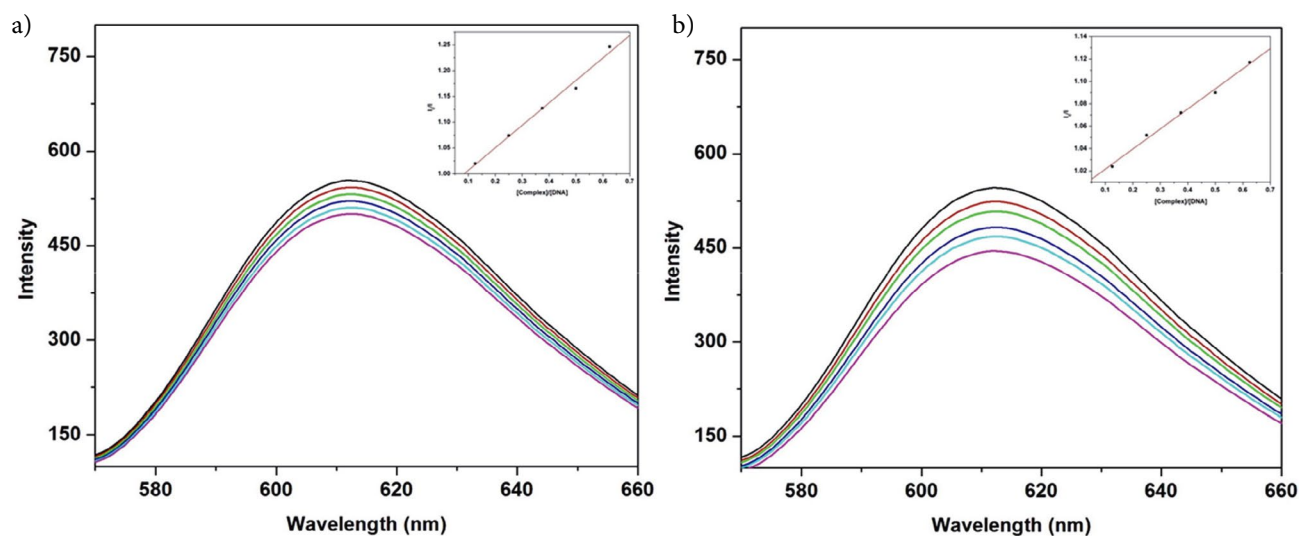


Fig. 2: Emission spectrum of EB bound to DNA in the presence of complexes ([EB] = 3.3 μM , [DNA] = 40 μM , [complex] = 0–30 μM , λ_{ex} = 430 nm). Inset shows the plots of emission intensity I_0/I vs [DNA] / [complex]. (a) Emission spectra of MnL complex (b) Emission spectra of FeL complex

complexes to CT-DNA is determined as established through absorption and fluorescence measurements.

3. 7. DNA Cleavage Analysis

The cleavage efficiency of the complexes was studied on pBR322 plasmid DNA using agarose gel electrophoresis so as to identify the conformational changes of the DNA. When electrophoresis is performed on circular plasmid pBR322 DNA (Fig. 4), there occurs a rapid migration for the supercoiled SC form (Form I). The super coiled form of the DNA was relaxed to slow moving open circular OC form (Form II) in the presence of oxidant H_2O_2 which indicates that one strand is being cleaved.³⁶ Both the MnL and FeL complexes possess the tendency to cleave the DNA from SC form to OC form on various concentrations (10, 20 and 30 μg). From the Figure 4 it is observed that no cleavage occurred in the case of control DNA (lane 1) and control DNA/ H_2O_2 (lane 2). The complex MnL shows no cleavage at 10 μg (lane 3) but partial cleavage is observed at 20 μg (lane 4) and 30 μg (lane 5) from SC form (Form I) to OC (Form II) in the presence of H_2O_2 . Similarly, the complex FeL does not cleave the DNA at 10 μg (lane 6) but in the presence of the oxidant it exhibits partial cleavage from SC form (Form I) to OC (Form II) at 20 μg (lane 7) and 30 μg (lane 8). An effective cleavage is visualized as the concentration of the complexes increases. Both the MnL and FeL complexes could cleave DNA more effectively in the presence of an oxidant (H_2O_2) which may be attributed to the involvement of hydroxyl free radicals. In oxidative cleavage, the hydroxyl free radicals formed oxidize the deoxyribose moiety and further hydrolytic cleavage of sugar phosphate back bone occurs.³⁷

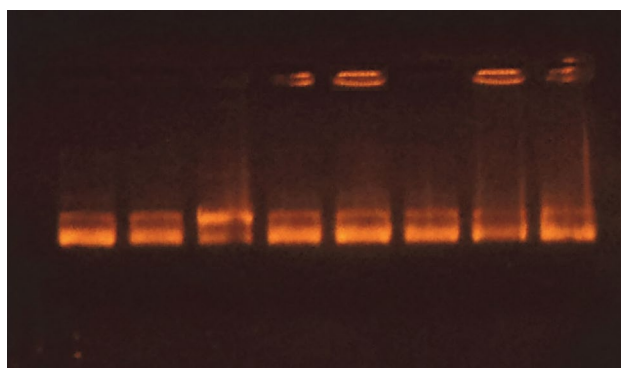


Fig. 4: DNA cleavage analysis. 1st well- Control only pBR322; 2nd well- pBR322+ H_2O_2 and Buffer; 3rd well- Sample (MnL)-10 μg ; 4th well- Sample (MnL)-20 μg ; 5th well-sample (MnL)-30 μg ; 6th well-sample (FeL)-10 μg ; 7th well- sample (FeL)-20 μg ; 8th well- sample (FeL)-30 μg

3. 8. BSA Binding Studies

3. 8. 1 Fluorescence Spectroscopy

The intrinsic BSA fluorescence at 340 nm due to tryptophan moiety³⁸ is quenched on addition of drug mol-

ecules. The mechanistic process involved in quenching is categorized to be static or dynamic. The molecular collisions results in dynamic quenching while static quenching arises as a result of complex formation in ground-state between the protein and the quencher. Dynamic quenching values are found to increase along with temperature whereas the static quenching constants decrease with temperature.³⁹ This quenching mechanism can be explored from Stern-Volmer equation.⁴⁰

$$\frac{F_0}{F} = 1 + K_{sv}[Q] = 1 + K_q\tau_0[Q] \quad (1)$$

The emission maxima *in-absentia* and presence of quencher molecules are denoted as F_0 and F , respectively. K_{sv} being Stern-Volmer quenching constant and the quencher concentration is designated as $[Q]$ with τ_0 , the mean life time of protein and for BSA it is found to be 10^{-8} s.⁴¹ K_q is

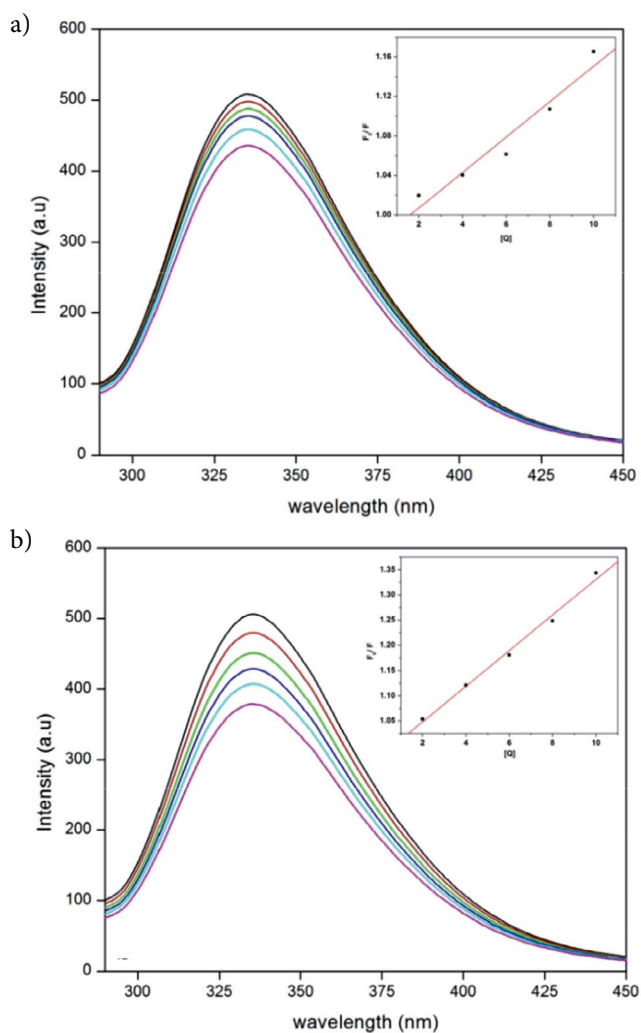


Fig. 5: Emission spectra of BSA in the presence of various concentrations of metal complexes in DMSO ($T = 298$ K), $c(\text{BSA}) = 2.0 \times 10^{-6}$ mol L^{-1} , $c(\text{Metal complex}) = 2, 4, 6, 8, 10 \times 10^{-6}$ mol L^{-1} . Insert: Stern-Volmer plot for quenching of BSA by metal complexes (a) Emission spectra of BSA with MnL complex (b) Emission spectra of BSA with FeL complex

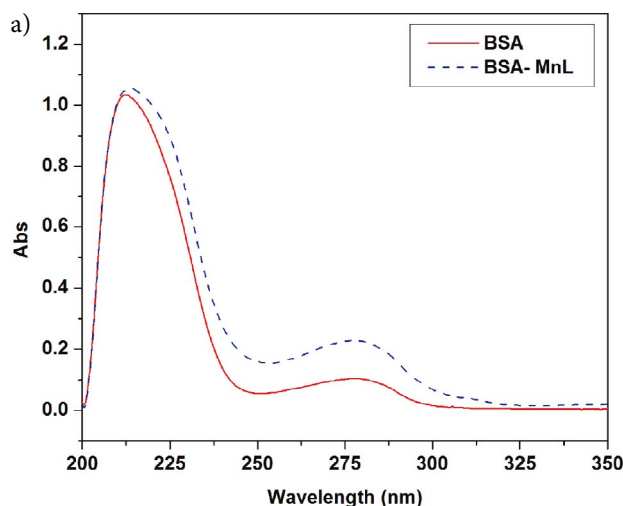
the quenching rate constant of the protein and it is equal to K_{sv}/τ_0 . The K_{sv} values are obtained from the slope of linear fitting plots F_0/F vs $[Q]$. The Stern-Volmer plots for MnL and FeL complexes at three different temperatures 298 K, 304 K and 310 K are provided in Figs. 5, S5 and S6 and their K_q values are presented in Table 1. The results conclude that Stern-Volmer quenching constants (K_{sv}) decreases with increasing temperature. Also, it was found that the K_q values are greater than $2.0 \times 10^{10} \text{ L mol}^{-1} \text{ s}^{-1}$ and this value is attributed to the maximum scattering collision quenching constant of various quenchers for dynamic quenching.⁴² This exposes that the BSA quenching by MnL and FeL is due to ground-state complex formation i.e., static and not dynamic quenching.

Table 1: K_{sv} and K_q values of MnL and FeL complexes

Complexes	T (K)	K_{sv} ($\times 10^4 \text{ L mol}^{-1}$)	K_q ($\times 10^{12} \text{ L mol}^{-1} \text{ s}^{-1}$)
MnL	298	2.10	2.10
	304	1.39	1.39
	310	1.07	1.07
FeL	298	3.53	3.53
	304	2.69	2.69
	310	2.29	2.29

3. 8. 2. Absorption Spectroscopy

Ground state interaction of MnL and FeL with BSA is further proved by UV-vis absorption spectra. The absorption spectra were recorded both for the BSA and BSA-MnL/FeL system in the range of 200–350 nm (Fig. 6). A bathochromic shift occurs at the absorption maxima compared to that of BSA which confirms the static quenching mechanism.⁴³



3. 8. 3. Analysis of Binding Constants and Binding Sites

From the binding of complexes MnL and FeL with BSA, the binding constants (K_b) and the binding sites (n) can be calculated from the following equation.⁴⁴

$$\log\left(\frac{F_0 - F}{F}\right) = \log K_b + n \log [Q] \quad (2)$$

The values of K_b and n are obtained (Table 2) from the intercepts and slopes of the linear fitting plots of $\log F_0 - F/F$ vs $\log [Q]$ at 298 K are displayed in Fig. 7 for MnL and FeL complexes, respectively. Similarly, the plots for BSA-MnL complex at 304 K and 310 K and for BSA-FeL complex at 304 K and 310 K are shown in Figs. S7 and S8, respectively. The binding site values approximated to 1 reveals the existence of only one binding site in BSA where the complexes could bind. The BSA molecule possess two tryptophan residues, i.e., Trp-134 in sub-domain IA and Trp-212 in hydrophobic sub-domain IIA. Any molecules which bind to sub-domain IIA can result in conformational changes.⁴⁵ These results confirm that the complexes could fit into the hydrophobic pocket in sub-domain IIA.

Table 2: Binding constant (K_b) and Binding site (n) values of MnL and FeL complexes

Complexes	T (K)	Binding constant (10^4 L mol^{-1})	Binding site
MnL	298	5.72	1.31
	304	4.95	1.16
	310	4.37	1.06
FeL	298	5.17	1.12
	304	4.71	1.05
	310	4.66	1.02

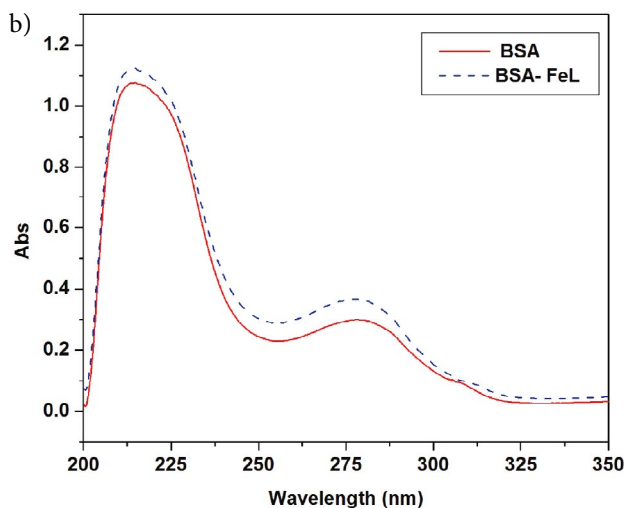


Fig. 6: UV-Vis absorption spectra of BSA and BSA-Metal complex solutions: $c(\text{BSA}) = c(\text{Metal complex}) = 2 \times 10^{-6} \text{ mol L}^{-1}$. (a) BSA-MnL solution (b) BSA-FeL solutions

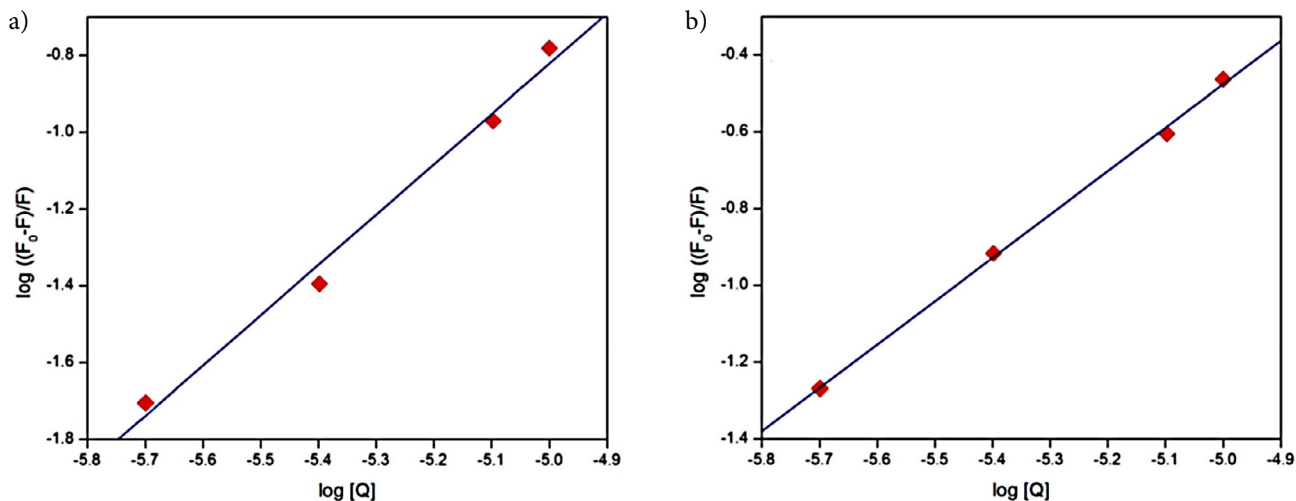


Fig. 7: Double logarithm plot for BSA-metal complexes at 298 K (a) Double logarithm plot for BSA-MnL (b) Double logarithm plot for BSA-FeL

3. 8. 4 Thermodynamic Parameters

The interactions between the complexes and BSA could be hydrophobic, hydrogen bonds, van der Waals forces and electrostatic interactions.⁴⁶ It can be found out from the thermodynamic parameters such as enthalpy (ΔH) and entropy (ΔS). The thermodynamic parameters were investigated at 298 K, 303 K and 310 K and the result shows no structural degradation was observed in BSA. The values for ΔH and ΔS can be obtained from the following van't Hoff equation.

$$\ln k = \frac{-\Delta H}{RT} + \frac{\Delta S}{R} \quad (3)$$

The free energy changes can be obtained from,

$$\Delta G = -RT \ln K \quad (4)$$

The ΔH and ΔS values can be obtained from the slopes and ordinates of linear fitting plots of $\ln K$ vs $1/T$

(Fig. 8). The positive values of ΔH and ΔS are attributed to hydrophobic interactions. The ΔH and ΔS values being negative shows the existence of hydrogen bonding and van der Waals forces, very low positive or negative ΔH value and positive ΔS values are attributed to electrostatic interactions.⁴⁷ From the thermodynamic parameters (Table 3), the negative enthalpy (ΔH) and positive entropy (ΔS) values ascertain that electrostatic interactions played an important role between BSA and MnL/FeL. The negative ΔG values calculated, proves the spontaneous binding process.

3. 8. 5 Energy Transfer Between Metal Complexes and BSA

The binding of metal complexes to BSA becomes effective only when there is considerable transfer of energy between the donor and the acceptor which can be calculated from Forster's resonance energy transfer theory.⁴⁸ For an effective energy transfer, the following conditions must be

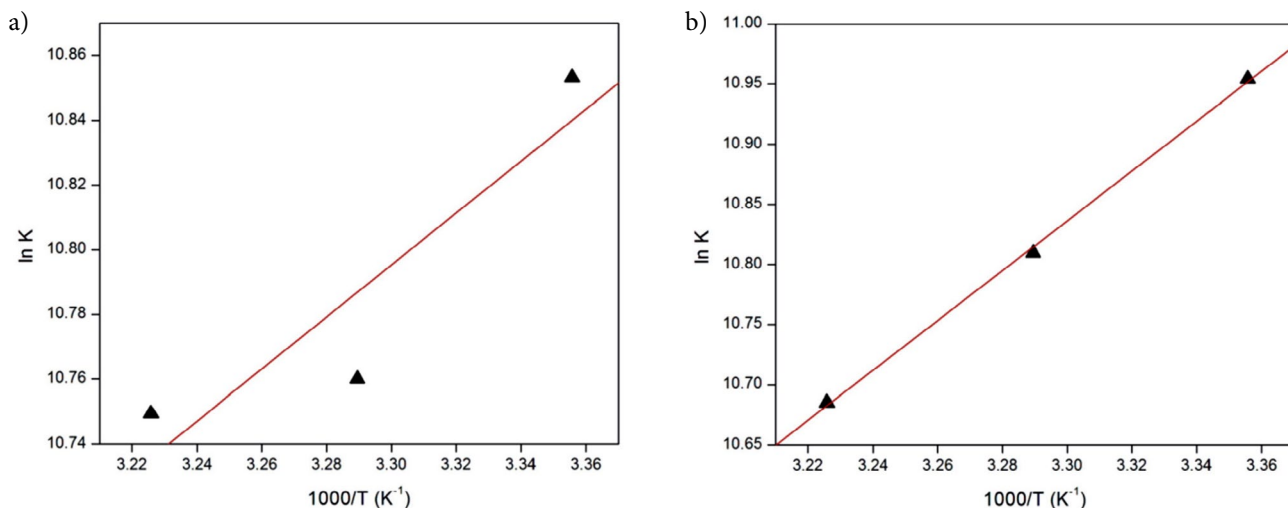


Fig. 8: van't Hoff plot for the interaction of BSA with (a) MnL complex (b) FeL complex

Table 3: Thermodynamic parameters of the binding interaction of metal complexes with BSA

Complexes	T (K)	ΔH (kJ mol ⁻¹)	ΔS (J mol ⁻¹ K ⁻¹)	ΔG (kJ mol ⁻¹)
MnL	298	-17.23	33.22	-27.14
	304			-27.33
	310			-27.54
FeL	298	-6.68	67.72	-26.89
	304			-27.20
	310			-27.71

satisfied: a) the donor must be a fluorescent in nature b) there must be a spectral overlap between the emission of donor and the absorption of acceptor; c) the donor-acceptor distance should be less than 8 nm. From the following equation, the efficiency of energy transfer can be calculated.⁴⁹

$$E = 1 - \frac{F}{F_0} = \frac{R_0^6}{R_0^6 + r^6} \quad (5)$$

Where r is the donor-acceptor distance, R_0 is the critical distance at which 50% energy transfer occurs and is given by,⁵⁰

$$R_0^6 = 8.8 \times 10^{-25} K^2 n^{-4} \Phi J \quad (6)$$

K^2 the orientation factor whose value is found to be 2/3 for random alignment in fluid medium; n being the average refractive index of the medium in the wavelength region of significant spectral overlap ($n = 1.336$); Φ is denoted for the quantum efficiency for emission of donor and for BSA it is 0.15;⁵¹ J is found to be the overlap integral amid the emission and absorbance spectra of donor/acceptor which is calculated as follows

$$J = \frac{\sum \varepsilon(\lambda) F(\lambda) \lambda^4 \Delta \lambda}{\sum F(\lambda) \Delta \lambda} \quad (7)$$

$F(\lambda)$ is represented for corrected donor fluorescence intensity in wavelength range λ , $\varepsilon(\lambda)$ is the acceptor's ab-

sorptivity at wavelength λ . The spectral overlap between the emission of BSA and absorption of MnL and FeL are shown in Fig. 9 along with the energy transfer parameters given in Table 4. The donor-acceptor distance (r) is calculated to be lesser than 8 nm,⁵² ascribing the occurrence of transfer energy from BSA to metal complexes with high possibility.

Table 4: Energy transfer parameters for the interaction of metal complexes with BSA

Complexes	J (cm ³ L mol ⁻¹)	R_0 (nm)	E	r (nm)
MnL	6.47×10^{-14}	3.44	0.037	5.91
FeL	2.27×10^{-15}	1.96	0.051	3.20

3. 9. Molecular Docking Studies of Human DNA Topoisomerase I and BSA

The molecular docking system can add normal medication outline by putting a little particle into the coupling site of the DNA/BSA targets particularly in a non-covalent mode. The most suitable binding mode, binding site and possible interactions of the complexes with DNA/BSA could be probed using this study. By using X-ray structural pattern of the human DNA topoisomerase I and BSA

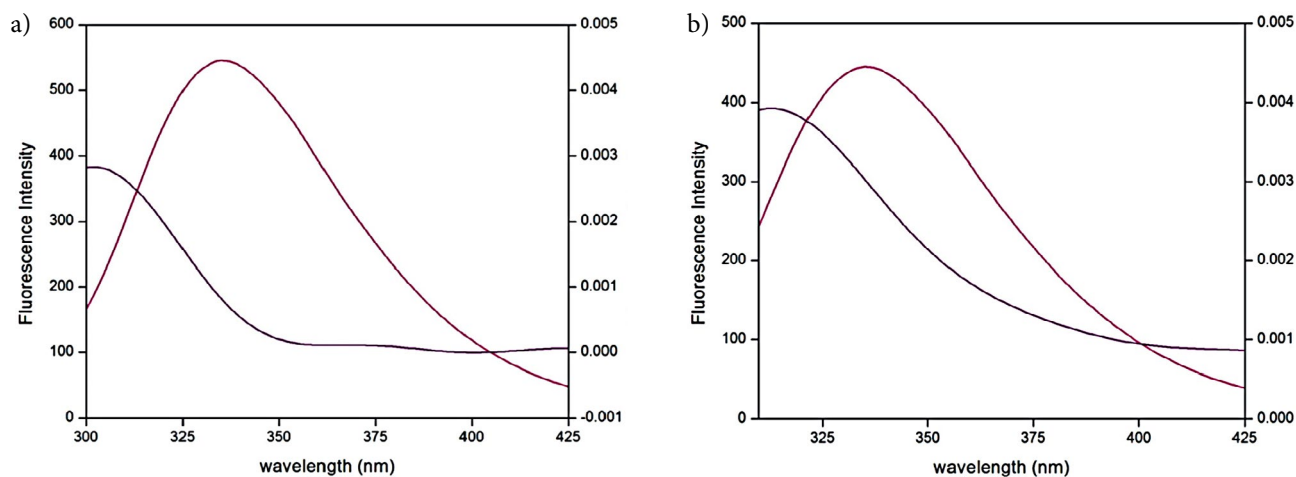


Fig 9: Spectral overlap of UV-Vis absorption spectrum of metal complexes with the fluorescence emission spectrum of BSA. $c(\text{BSA}) = c(\text{Metal complex}) = 2 \times 10^{-6}$ mol L⁻¹, $T = 298$ K (a) Spectral overlap of MnL (b) Spectral overlap of FeL

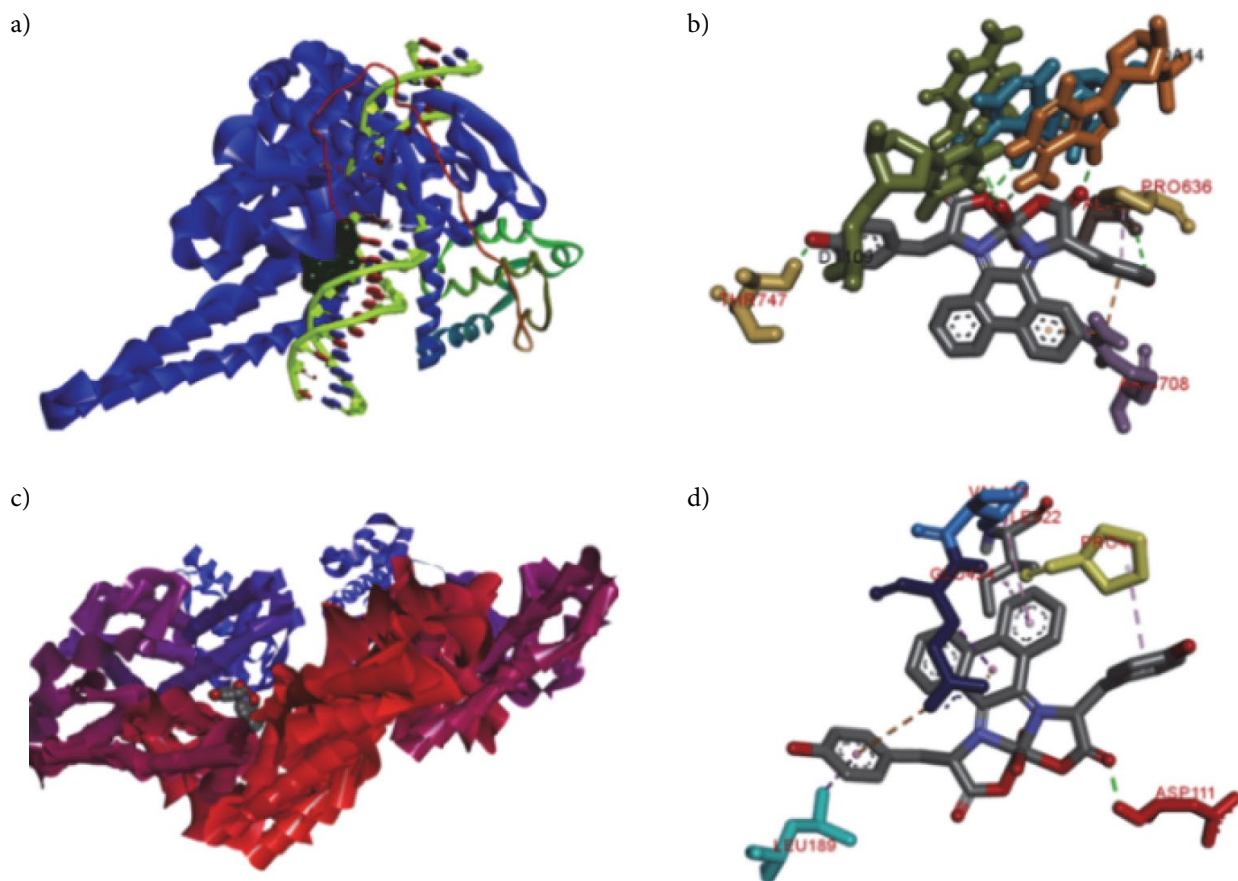


Fig. 10: (a) Molecular docked model of MnL with DNA. (b) specific interaction of MnL with DNA (c) Molecular docked model of MnL with BSA. (d) specific interaction of MnL with BSA

(downloaded from RCSB PDB)⁵³ the molecular docking of the complexes were carried out. Interactions of the complexes with the receptors DNA-topoisomerase I and BSA along with most preferable binding sites are given in Fig. 10 for MnL and Fig. 11 for FeL. The binding energies of the MnL and FeL complexes with DNA were found to be -11.8 and -11.7 kcal mol⁻¹, respectively. Also it was observed that the binding energies of the MnL and FeL complexes with BSA were -10.9 and -10.8 kcal mol⁻¹, respectively. The possible binding modes, bond distances and binding sites for both the complexes are provided in Tables S1–S4.

4. Conclusion

A tetradentate Schiff base ligand involving L-tyrosine and 9,10-phenanthrenequinone along with its Mn(I-II)/Fe(III) complexes has been synthesized and characterized using various analytical and spectroscopic tools. The absorption and emission spectra and viscosity measurement provides information on intercalative mode of interaction of the metal complexes with CT-DNA. The interaction of the complexes with BSA was studied at three varying temperatures and observed that the fluorescence

quenching process may be accomplished as static quenching. The changes in enthalpy and entropy are ascertained to electrostatic interaction between the Mn(III)/Fe(III) complexes and BSA. The distance between the BSA and MnL and FeL was found to be 5.91 and 3.20, respectively, which indicates that the energy transfer occurs with high possibility. These results reveal that the synthesised Mn(I-II)/Fe(III) complexes could be promising compounds as target-based drugs.

5. Supporting Information Summary

The experimental details of DNA/BSA binding and chemical nuclease activity, spectral techniques used such as FTIR, ¹³C NMR, Mass, absorption and emission titrations and tables for binding energy values of this work can be found in supplementary information.

6. Acknowledgement

The authors thank SAIF, Indian Institute of Technology, Madras for providing EI-mass spectra. The authors

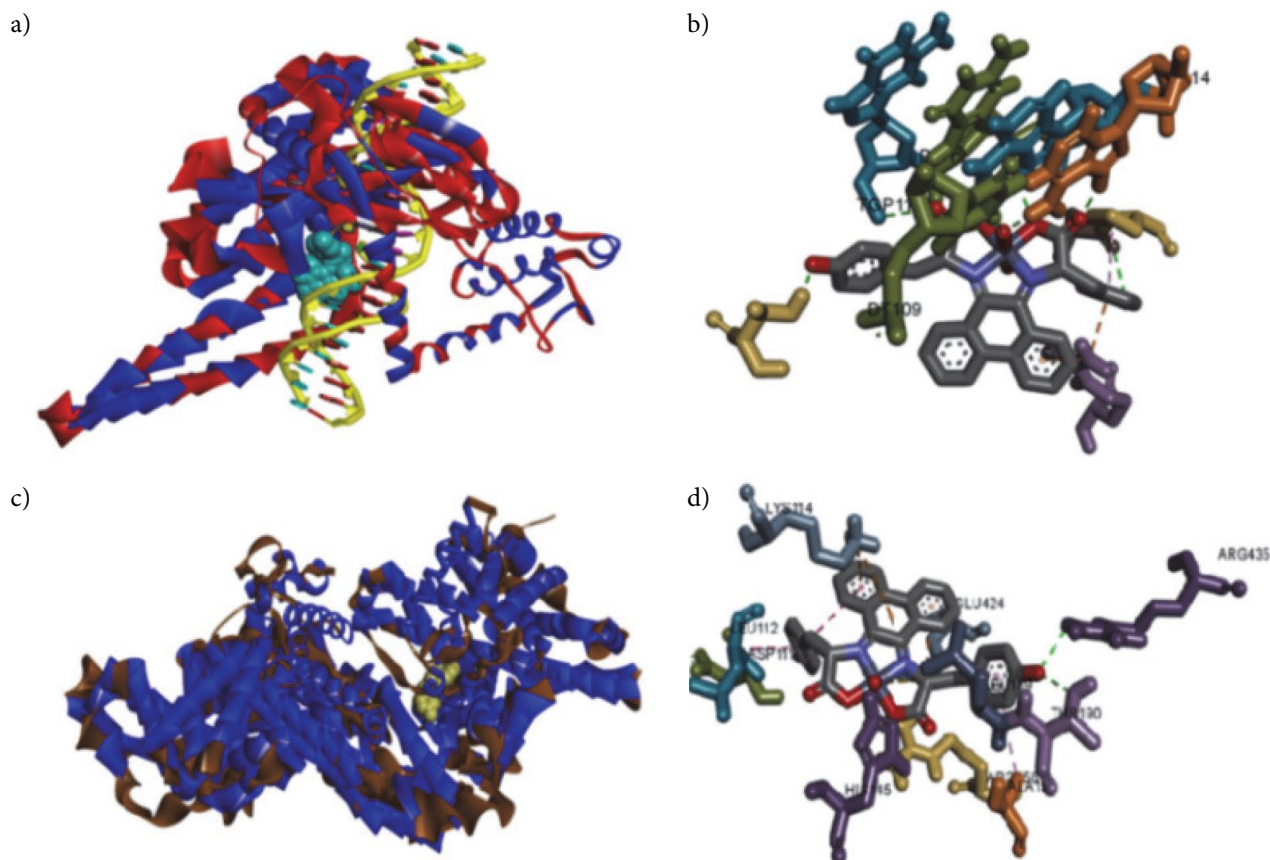


Fig. 11: (a) Molecular docked model of FeL with DNA (b) specific interaction of FeL with DNA (c) Molecular docked model of FeL with BSA (d) specific interaction of FeL with BSA

are thankful to the Vellore Institute of Technology for recording ^{13}C NMR spectra. Also the authors thank BioGenics, Hubli, for the DNA cleavage analysis.

5. References

1. S. J. Dixon, B. R. Stockwell, *Curr. Opin. Chem. Biol.* **2009**, *13*, 549–555. DOI: 10.1016/j.cbpa.2009.08.003.
2. D. Tietze, M. Tischler, S. Voigt, D. Imhof, O. Ohlenschlager, M. Gorchach, Buntkonwsky, *Chem. Eur. J.* **2010**, *16*, 7572–7578. DOI: 10.1002/chem.200903306.
3. S. M. Barnett, K. I. Goldberg, J. M. Mayer, *Nat. Chem.* **2012**, *4*, 498–502. DOI: 10.1038/nchem.1350.
4. S. Shaik, *Nat Chem.* **2010**, *2*, 347–349. DOI: 10.1038/nchem.638.
5. L. J. K. Boerner, J. M. Zaleski, *Curr. Opin. Chem. Biol.* **2005**, *9*, 135–44. DOI: 10.1016/j.cbpa.2005.02.010.
6. V. C. Silveira, M. P. Abbott, M. Cavicchioli, M. B. Goncalves, H. M. Petrilli, L. De Rezende, A. T. Amaral, D. E. P. Fonseca, G. F. Caramori, A. M. da Costa Ferreira, *Dalton Trans.* **2013**, *42*, 6386–6396. DOI: 10.1039/C3DT00108C.
7. A. Patra, T. K. Sen, A. Ghorai, G. T. Musie, S. K. Mandal, U. Ghosh, M. Bera, *Inorg. Chem.* **2013**, *52*, 2880–2890. DOI: 10.1021/ic302099y.
8. X.-W. Li, L. Tao, Y.-T. Li, Z.-Y. Wu, C.-W. Yan, *Eur. J. Med. Chem.* **2012**, *54*, 697–708. DOI: 10.1016/j.ejmech.2012.06.022.
9. Y. B. Zeng, N. Yang, W. S. Liu, N. Tang, *J. Inorg. Biochem.* **2003**, *97*, 258–264. DOI: 10.1016/S0162-0134(03)00313-1.
10. R. Nagane, T. Koshigoe, M. Chikira, *J. Inorg. Biochem.* **2003**, *93*, 204–212. DOI: 10.1016/S0162-0134(02)00619-0.
11. A. Silvestri, G. Barone, G. Ruisi, M. Giudice, S. Tumminello, *J. Inorg. Biochem.* **2004**, *98*, 589–594. DOI: 10.1016/j.jinorgbio.2004.01.010.
12. C. Gokce, N. Dilek, R. Gup, *Inorg. Chim. Acta* **2015**, *432*, 213–220. DOI: 10.1016/j.ica.2015.03.040.
13. P. Bolel, N. Mahapatra, M. Halder, *J. Agric. Food Chem.* **2012**, *60*, 3727–3734. DOI: 10.1021/jf205219w.
14. B. P. Kamat, J. Seetharamappa, *J. Pharm. Biomed. Anal.* **2004**, *35*, 655–664. DOI: 10.1016/j.jpba.2004.02.008.
15. B. X. Huang, H. Y. Kim, C. Dass, *J. Am. Soc. Mass Spectrom.* **2004**, *15*, 1237–1247. DOI: 10.1016/j.jasms.2004.05.004.
16. S. Ghosh, S. Jana, N. Guchhait, *J. Phys. Chem. B* **2012**, *116*, 1155–1163. DOI: 10.1021/jp2094752.
17. D. A. Tinoco, V. E. Eames, D. C. Incarvito, M. A. Valentine, *Inorg. Chem.* **2008**, *47*, 8380–8390. DOI: 10.1021/ic800529v.
18. M. Shamsi, S. Yadav, F. Arjmand, *J. Photochem. Photobiol. B* **2014**, *136*, 1–11. DOI: 10.1016/j.jphotobiol.2014.04.009.

19. J. Dong, L. Li, G. Liu, T. Xu, D. Wang, *J. Mol. Struct.* **2011**, *986*, 57–63. DOI: 10.1016/j.molstruc.2010.11.036.
20. A. Vogel, Text Book of Quantitative Inorganic Analysis, third ed., ELBS, Longman, London, **1969**.
21. L. J. Bellamy, The Infrared Spectra of Complex Molecules, Second ed., Chapman & Hall, Methuen, London, **1958**.
22. S. Cakir, E. Coskun, P. Naumov, E. Bicer, *J. Mol. Struct.* **2002**, *608*, 101–107. DOI: 10.1016/S0022-2860(01)00939-5.
23. J. R. Ferraro, Low Frequency Vibrations of Inorganic and Coordination Compounds, Plenum Press, New York, **1971**.
24. P. Anitha, R. Manikandan, P. Vijayan, G. Prakash, P. Viswanathamurthi, R. J. Butcher, *J. Chem. Sci.* **2015**, *127*, 597–608. DOI: 10.1007/s12039-015-0811-4
25. A. Gubendran, M. P. Kesavan, S. Ayyanaar, L. Mitu, P. Athapan, J. Rajesh, *Spectrochim. Acta A* **2017**, *181*, 39–46. DOI: 10.1016/j.saa.2017.03.031
26. E. W. Hatfield, E. W. Parker, *Inorg. Nucl. Chem. Lett.* **1965**, *1*, 7–9. DOI: 10.1016/S0020-1650(65)80029-0
27. T. Davis, J. Fackler, M. Weeks, *Inorg. Chem.* **1968**, *7*, 1994–2002. DOI: 10.1021/ic50068a007.
28. C. Joel, R. Biju Bennie, S. Daniel Abraham, S. Iyyam Pillai, S. Theodore David, *Appl. Organometal. Chem.* **2018**; e4516. DOI: 10.1002/aoc.4516.
29. W. J. Geary, *Coord. Chem. Rev.* **1971**, *7*, 81–122. DOI: 10.1016/S0010-8545(00)80009-0.
30. N. Raman, A. Selvan, S. Sudharsan, *Spectrochim. Acta A*, **2011**, *79*, 873–883. DOI: 10.1016/j.saa.2011.03.017.
31. Y. Li, Z. Y. Yang, Z. Liao, Z. Han, Z. C. Liu, *Inorg. Chem. Commun.* **2010**, *13*, 1213–1216. DOI: 10.1016/j.inoche.2010.07.005.
32. J. K. Barton, A. T. Danishefsky, J. M. Goldberg, *J. Am. Chem. Soc.* **1984**, *106*, 2172–2176. DOI: 10.1021/ja00319a043.
33. R. Senthil Kumar, S. Arunachalam, *Biophys. Chem.* **2008**, *136*, 136–144. DOI: 10.1016/j.bpc.2008.05.007.
34. L. Jia, P. Jiang, J. Xu, Z. Hao, X. Xu, L. Chen, J. Wu, N. Tang, Q. Wang, J. J. Vittal, *Inorg. Chim. Acta* **2010**, *363*, 855–865. DOI: 10.1016/j.ica.2009.12.047.
35. C. Joel, S. Theodore David, R. Biju Bennie, S. Daniel Abraham, S. Iyyam Pillai, *J. Chem. Pharm. Res.*, **2015**, *7*, 1159–1176.
36. P. Anitha, N. Chitrapriya, Y. J. Jang, P. Viswanathamurthi, *J. Photochem. Photobiol. B: Biol.* **2013**, *129*, 17–26. DOI: 10.1016/j.jphotobiol.2013.09.005.
37. L. Shi, Y.-Y. Jiang, T. Jiang, W. Yin, J.-P. Yang, M.-L. Cao, Y.-Q. Fang, H.-Y. Liu, *Molecules*, **2017**, *22*, 1084, 1–17. DOI: 10.3390/molecules22071084.
38. S. Bi, Y. Sun, C. Qiao, H. Zhang, C. Liu, *J. Lumin.* **2009**, *129*, 541–547. DOI: 10.1016/j.jlumin.2008.12.010.
39. H. X. Zhang, X. Huang, P. Mei, K.H. Li, C. N. Yan, *J. Fluoresc.* **2006**, *16*, 287–294. DOI: 10.1007/s10895-006-0087-7.
40. E. L. Gelamo, C. H. T. P. Silva, H. Imasato, M. Tabak, *Biochim. Biophys. Acta* **2002**, *1594*, 84–99. DOI: 10.1016/S0167-4838(01)00287-4.
41. J. R. Lakowicz, G. Weber, *Biochemistry*, **1973**, *12*, 4161–4170. DOI: 10.1021/bi00745a020.
42. R. E. Maurice, A. G. Camillo, *Anal. Biochem.* **1981**, *114*, 199–227. DOI: 10.1016/0003-2697(81)90474-7.
43. Y. J. Hu, Y. Liu, R. M. Zhao, J. X. Dong, S. S. Qu, *J. Photochem. Photobiol. A: Chem.* **2006**, *179*, 324–329. DOI: 10.1016/j.jphotochem.2005.08.037.
44. Y. J. Hu, W. Li, Y. Liu, J. X. Dong, S. S. Qu, *J. Pharm. Biomed. Anal.* **2005**, *39*, 740–745. DOI: 10.1016/j.jpba.2005.04.009.
45. M. Gharagozlou, M. D. Boghaei, *Spectrochim. Acta A* **2008**, *71*, 1617–1622. DOI: 10.1016/j.saa.2008.06.027.
46. Y. Zhang, B. Zhou, X. Zhang, P. Huang, C. Li, Y. Liu, *J. Hazard. Mater.* **2009**, *163*, 1345–1352. DOI: 10.1016/j.jhazmat.2008.07.132.
47. D. P. Ross, S. Subramanian, *Biochemistry* **1981**, *20*, 3096–3102. DOI: 10.1021/bi00514a017.
48. T. Forster, Modern Quantum Chemistry, Academic Press, New York, **1965**, *3*, 93–137.
49. W. D. Horrocks, W. E. Collier, *J. Am. Chem. Soc.* **1981**, *103*, 2856–2862. DOI: 10.1021/ja00400a061.
50. L. A. Sklar, B. S. Hudson, R. D. Simoni, *Biochemistry* **1977**, *16*, 819–828. DOI: 10.1021/bi00624a002.
51. A. Mahammed, H. B. Gray, J. J. Weaver, K. Sorasaene, Z. Gross, *Bioconjugate Chem.* **2004**, *15*, 738–746. DOI: 10.1021/bc034179p.
52. D. J. Li, J. F. Zhu, J. Jin, X. J. Yao, *J. Mol. Struct.* **2007**, *846*, 34–41. DOI: 10.1016/j.molstruc.2007.01.020.
53. Protein Data Bank (<http://www.rcsb.org/pdb>).

Povzetek

Sintetizirali smo nova Mn(III) in Fe(III) kompleksa z ligandom, ki vsebuje motiv L-tirozina, ter ju okarakterizirali z različnimi analznimi in spektroskopskimi tehnikami. Kompleksa izkazujeta učinkovite vezne lastnosti z biomolekulami, kot npr. CT-DNA in BSA. Sposobnost kompleksov, da se vežejo na biomolekule, smo raziskovali z absorpcijskimi in emisijskimi metodami in z viskozimetrijo. Na podlagi spektroskopskih tehnik lahko zaključimo, da se kompleksa interkalirata na DNA. Kompleksa lahko cepita pBR322 DNA pri gelski elektroforezi preko oksidativnega mehanizma. BSA je bil kvinčiran s kompleksoma pri približno 340 nm preko statičnega mehanizma. Določili smo tudi vezne konstante, termodinamske parametre in razdalje donor-akceptor. Nadalje smo z dokingom simulirali nastanek interakcij med kompleksoma in DNA topoizomerazo in BSA proteinom. Simulirane pozicije omogočajo vizualizacijo, ki podpira nastanek interakcij med kompleksoma in DNA/BSA.

Scientific paper

Adsorption of Cr (III) and Cd (II) Ions using Mesoporous Cobalt-Ferrite Nanocomposite from Synthetic Wastewater

Iman Khoshkerdar¹ and Hossein Esmaeili^{2,*}¹ Department of Chemical Engineering, Dashtestan Branch, Islamic Azad University, Dashtestan, Iran² Department of Chemical Engineering, Bushehr Branch, Islamic Azad University, Bushehr, Iran* Corresponding author: E-mail: esmaeili.hossein@gmail.com & esmaeili.hossein@iaubushehr.ac.ir

Received: 10-18-2018

Abstract

In this study, cobalt-ferrite nano-composite (CFNC) is used to adsorb chromium and cadmium ions from synthetic wastewater. Adsorptive characteristics of CFNC are determined by various analysis including SEM, FTIR, VSM and BET. Also, effect of different parameters such as solution pH, buffer volume, electrolyte dose, the initial ion concentration, contact time, the adsorbent dose and temperature were studied on adsorption process. The results showed that the maximum recovery of Cd(II) and Cr(III) ions were determined as $C_0 = 20 \text{ mg/L}$, $t = 50 \text{ min}$, $T = 25 \text{ }^\circ\text{C}$, CFNC dosage = 20 g/L , and pH = 7 (for Cr(III)) and 6 (for Cd(II)). In these conditions, the amount of 100% Cr(III) and Cd(II) were removed from the aqueous solution. Also, the equilibrium study showed that the adsorption process followed the Langmuir model and the maximum adsorption capacity for Cr(III) and Cd(II) ions were obtained 217 and 303 mg/g, respectively which show very high adsorption capacities. In addition, adsorption kinetics showed that the pseudo first-order kinetic model was better than the pseudo second-order kinetic model. Moreover, thermodynamic studies showed that the adsorption process was possible, spontaneous and endothermic.

Keywords: Nano-composite; cobalt-ferrite; heavy metals; synthesis wastewater

1. Introduction

After fast growth of population and industrialized societies, releasing heavy metals in water ecosystem is one of the most important concerns of the environment. Although most of the noxious chemical materials when they are in the atmosphere after some years are less hazardous, when pollution is made by heavy metals ions, removing them are very difficult and maybe gradually accumulated and enter to our body throughout food chains.^{1,2} Important heavy metals such as cadmium, zinc, chromium, lead, and copper penetrate to the water throughout industrial wastewater. Cr (III) ions are in modern industrial as leather and oil purification and also Cd (II) ion is widely used in various industries like as metallurgy, dye industry, and making battery, so that wastewater of these industries is polluted by a lot of Cr (III) and Cd (II) ions.³ Environmental protection agency (EPA) and world health organization (WHO) identify the admissible value of Cr (III) and Cd (II) ions in drinking water as 0.1 and 0.003 mg/L, respec-

tively.^{4,5} In oxidation state, Cr (III) is completely insoluble, and then it deposits easily. This ion is less detrimental in nature, but a high concentration of chromium ion (III) is hazardous.⁶ Increasing heavy metals concentration in water cause that health on a human is in danger. For example, the presence of heavy metal Cr (III) in the body can cause some illness as skin illness, liver, lung, kidney, brain failure, pancreas, and injuring bowels. Also, Cd(II) can cause some injuries to kidneys, tay-tay, increased blood pressure, and emphysema.^{7,8} Therefore, suitable and cheap methods to remove these ions from water are essential.^{9,10} There are various methods such as chemical precipitation, ionic exchange, membrane filtration, reverse osmosis, electrical coagulation, solvent extracting and adsorption to recovering and removing ion of heavy metal and pollutions from synthesis wastewater.^{11,12} Adsorption is one of the most common methods to remove heavy metals ion due to high efficiency, easy recovery and its cheap cost. Nevertheless, adsorption capacity, selectivity, equilibrium time and recovery depend on characteristics of sorbent materials.

Therefore, recently researches about applications of new materials such as nano-adsorbents are focused on adsorption of heavy metals from aqueous solutions.^{13,14} Nano-structured adsorbents have strong effects for treatment of contaminants from wastewaters due to a large specific surface area, high adsorption capacities and short diffusion paths.¹⁵ However, it is difficult for recovery of nano-sized adsorbents from aqueous media.¹⁶ The application of nanostructured magnetic adsorbents (such as; Fe₃O₄ nano-particles) is a new technology which has recently received important attention; because of their potency to be easily separated from wastewater using an external magnetic field after adsorption, in this way, their reconstruction and reuse are essential. For practical application of nanoparticles in various potential fields, their surface modification is vital.¹⁷ To improve the magnetic features of adsorbents, we can combine magnetic nanoparticles with different materials such as Co, CaO, MgO and etc. Different methods such as impregnation, ball milling and chemical co-precipitation have been expanded to combine them together to produce magnetic nano-composite. Among them, chemical co-precipitation is the most important method, because of simple procedure and no need of special chemicals.¹⁴ Until now, there are a lot of research to remove heavy metals by using composite that we can note some of them such as CaO/Fe₃O₄ magnetic composite,¹⁴ oxide graphite nanocomposite based on polymer,¹⁸ chitosan/Sulfydryl-functionalized graphene oxide composites,¹⁹ nanofibre membrane of chitosan/hydroxyapatite composite,²⁰ magnetized nanocomposite coated with manganese oxide,²¹ bentonite composite/reformed poly acryl amide by amines acids of humic acids²² that show very high efficiencies.

The purpose of this study is to investigate the effect of cobalt-ferrite nanocomposite (CFNC) as a magnetic adsorbent for the removal of chromium (III) and cadmium (II) ions from synthesis wastewater. Cobalt-ferrite (Co-Fe₂O₄) is regarded as an attractive magnetic material, because it has moderate saturated magnetic, terrific chemical stability and mechanical strength.²³ CFNC is used to destroy environmental various contaminants as sorbent and photo-catalyzer.²⁴ Hence, the effect of important parameters like pH, type and volume of buffer, type and concentration of the electrolyte, initial concentration, contact time, sorbent dose and temperature on adsorption process is investigated. Also, kinetic, equilibrium and thermodynamic behaviors of the adsorbent were studied.

2. Material and Methods

2.1. Preparation of Solutions

To prepare stock solutions containing chromium (III) and cadmium (II) ions sequentially Cr(NO₃)₃ and 3CdSO₄·8H₂O with the weight of 0.228 and 0.37 g were added to deionized distilled water to reach the volume of

1000 mL. Then, solutions with lower concentrations were made by dilution of these solutions.

Also, the buffer solution was used to keep the pH of the solutions at the optimized pH. To this end, four buffers such as citrate, phosphate, maleic acid and potassium hydrogen phthalate was used. To prepare buffer solutions of maleic acid, citrate, phosphate and potassium hydrogen phthalate in a pH value of 7, the amounts of 1.16, 2.14, 138 and 2.04 g of maleic acid, sodium citrate and potassium hydrogen phthalate salts were added to the 100 mL balloon containing distilled water and the pH values was regulated by NaOH solution (1 molar).

2.2. Synthesis of CFNC

A mixture of 25mL of Fe(NO₃)₃ with the molarity of 0.4 Mol L⁻¹ and 25 mL of Co(NO₃)₂ with the molarity of 0.2 Mol L⁻¹ was produced and the mixture was stirred with a magnetic stirrer and NaOH solution (3 Mol L⁻¹) was added to the solution until the mixture pH reached 11–12. Then, 0.6mL of olive oil was added to it as a surfactant and was heated at 80 °C for 1 h. The obtained black sediment was separated from the solution using a magnet due to a magnetic property and washed with water and ethanol several times to neutralize its pH. After pulverizing, a soft powder was obtained.²⁵

2.3. Analysis Methods

The concentration of Cr (III) and Cd (II) ions after adsorption process was identified by flame atomic absorption instrument which was equipped with air-acetylene fuel (PLUS SPECTRAA- 10, VARIAN). Also, Scanning Electron Microscopy (SEM) (TESCAN VEGA II, Czech Republic), Fourier Transform Infrared (FTIR) (Perkin-Elmer, Germany), Vibrating Sample Magnetometer (VSM) (Lakeshore VSM 7410, Germany) and Brunauer–Emmett–Teller (BET) (ASAP 2020, USA) analyzers were used to investigate the change of sorbent surface, functional groups in sorbent, magnetic characteristics and specific surface area before and after adsorption process.

2.4. Batch Experiments

First, 20 mg of CFNC and 10 mL of surfactant were placed into a beaker to reduce surface tension and more adsorption of heavy metals on the sorbent surface²⁶ and placed on the magnetic stirrer for 3 min until nano-particles distribute uniformly in solution. Produced mixture was transferred to a 100 mL balloon, and then 20 mL of cadmium (II) and chromium (III) solution with the concentration of 100mg/L was added to that. Then, 0.5 mL of hydroxide sodium (0.1 Mol L⁻¹) was added to the solution and finally, 1.5 mL of the maleic acid buffer with the pH value of 6 was added to the solution and the balloon was filled to the marked line with double distilled water. After

shaking balloon and unifying solution, the content of balloon was transferred to a beaker with the working volume of 200 mL. Then, to do adsorption process, this solution was located on the magnetic stirrer and the specified value of the adsorbent was added to the solution. After adsorption process, this solution was filtered by Whatman filter paper (No. 42) and centrifuge for 2 min and it then was moved to a test tube. Eventually, the concentration of metal ions in the solution was measured.

2. 5. Desorption Experiment and Reuse of Adsorbent

To study desorption process, 20 mg of magnetic nanocomposite of cobalt-ferrite, 10 mL surfactant (Triton X-100), 0.5 mL solution of 0.1 Mol L⁻¹ chloride sodium, and 20 mL of cadmium (II) and chromium (III) solution (with the concentration of 100 mg/L) were added to the 100 mL balloon. After that 1.5 mL of maleic acid buffer with pH of 6 for chromium (III) and pH of 7 for cadmium (II) was added until its volume reached to the mark line (100 mL). After shaking the balloon, the contents of the balloon were transferred to a 200 mL beaker. To perform desorption process, this solution was stirred at different times. Then, the solution filtered by filter paper and was centrifuged for 2 min and it then was transferred to a test tube and concentration of metal ions in final solution were measured by flame atomic absorption apparatus. After that, achieved sorbent was washed with 30 mL acetone/methanol and the aforementioned steps were repeated again on the adsorbent with a solution consist of same cadmium (II) and chromium (III) ions.

3. Results and Discussion

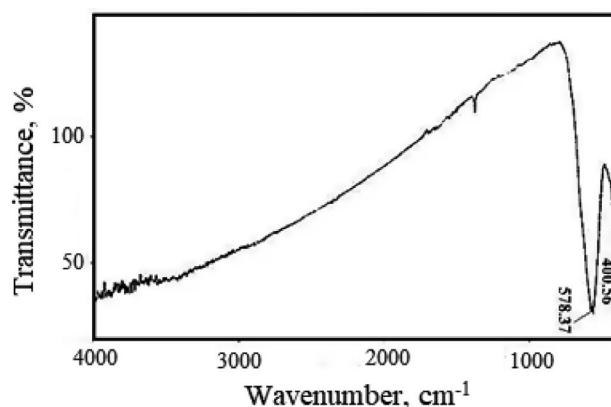
3. 1. Characteristics

In Fig. 1, the morphology of the adsorbent surface has been shown using SEM. Fig. 1-A shows nano-particles of cobalt-ferrite that they are the as disordered polygon

and are accumulated, that the reason of accumulating assign to the magnetic character of nano-particles. The pores and empty spaces are clearly seen in the surface of CFNC. The presence of small grains of magnetic nano-particles is indicating the porous structure and high adsorption capacity. Also, the presence of a lot of pores with disordered sizes in the surface of cobalt-ferrite is suitable to take cadmium (II) and chromium (III) heavy metals ion. Additionally, the morphology and the pores of the adsorbent surface after adsorption of metal ions are shown in Fig. 1-B and C.

Also, Fig. 2 shows FT-IR spectra and functional groups of synthesized cobalt-ferrite at different wavenumbers. As shown in this Fig., two vibration peaks of 578 and 406 cm⁻¹ exist that first peak is powerful and related to tension vibration of Fe⁺³O⁻² in quadrilateral situation and peak with less intensity assign to tension link Fe³⁺O²⁻ in octagon situation. As a result, FTIR spectra can prove structure of reverse spinel in synthesized cobalt-ferrite.

Fig. 2. FTIR analysis of CFNC



Additionally, VSM analysis of CFNC is shown in Table 1. The amount of the saturation magnetization (M_s), residual magnetism (M_r) and coercivities (H_c) are 50.5, 23.45 and 848.09 emu g⁻¹, sequentially. The amount of saturated magnetism is based on particles size and is de-

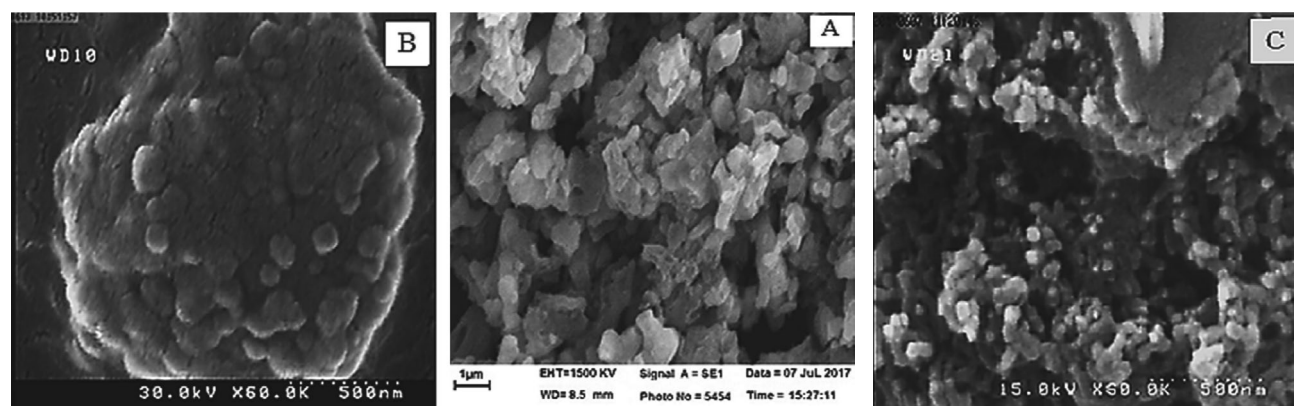


Fig. 1: SEM images (A) CFNC before adsorption of metal ions on a scale of 500 nm, (B) adsorbent after adsorption of chromium(III) ions on a scale of 1 μm, (C) adsorbent after adsorption of Cadmium(II) ions on a scale of 500 nm.

creased with particle size reduction.²⁷ The values of M_s and M_r are high due to the presence of magnetic properties. Achieved values showed that this material can separate from solution easily by external magnetic force. Also, considering achieved values from Table 1, CFNC is hard based on the type of magnetic material.

Table 1: VSM analysis of CFNC

Hc (Oe)	Mr (emu g ⁻¹)	Ms (emu g ⁻¹)
848.1	23.5	50.5

Eventually, the specific surface area of the adsorbent was measured by BET analysis. The BET results are shown in Table S-1. As can be seen in this table, the specific surface area of cobalt-ferrite adsorbent is obtained 17.84 m²/g and the average diameter of pores achieved 7.53 nm which shows this adsorbent is mesoporous.

3. 2. Effect of pH

Solution pH has a crucial role in the adsorption process.^{28,29} Figure 3 shows the effect of pH on chromium (III) and cadmium (II) ion adsorption using CFNC. At low pH values, H⁺ ion concentration is much more than the metal ions, in this case, H⁺ ion competes with heavy metal ions to locate on active sites of adsorbent, and creates repulsive force by locating on the adsorbent surface which prevents locating ions on the adsorbent surface and adsorption efficiency decreases. By increasing pH, H⁺ ion concentration decreases in solution and therefore enough surfaces create to locate heavy metal ions. Increasing solution pH to pH near to 7, the value of the hydrogen ion (H⁺) into the aqueous solution is decreased and concentration of hydroxide (OH⁻) will increase. On the other hand, by increasing pH, accessibility of heavy metal ion of chromium (III) and cadmium (II) ion to active sites is increased and therefore adsorption efficiency has been in-

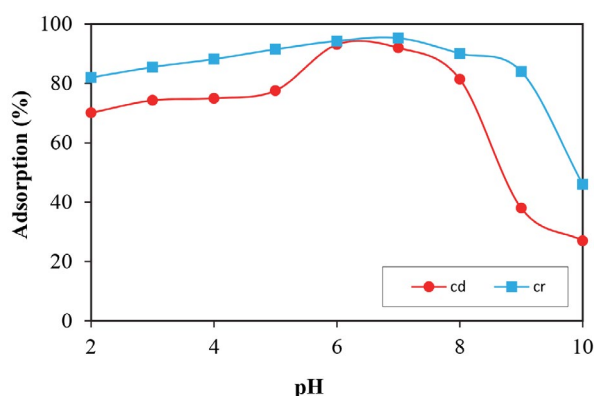


Fig. 3: Effect of pH on chromium (III) and cadmium (II) ion adsorption using CFNC

creased. So, adsorption of chromium (III) and cadmium (II) ions sequentially at pH value of 7 and 6 were optimized with 95.3% and 93.1%. At pH larger than optimized values, it is shown that hydroxide ion (OH⁻) in solution is precipitated as insoluble and cause to decrease of adsorption efficiency.

3. 3. Effect of Buffer Type and Volume

The buffer plays an important role to keep the pH of the solution at a constant value.³⁰ Effect of different buffers such as citrate, phosphate, maleic acid, potassium hydrogen phthalate was studied on adsorption efficiency of chromium (III) and cadmium (II) ion and results are shown in Table S-2. Among the four types of buffers, it is shown maleic acid has highest adsorption efficiency to chromium (III) and cadmium (II) ion sequentially with 96.4% and 95%, while potassium hydrogen phthalate has the least adsorption efficiency to chromium (III) and cadmium (II) ion with 87.4% and 88.9%. Reducing the adsorption efficiency of Cr (III) and Cd (II) ions by different buffers can be attributed the formation of Cr (III) and Cd (II) ions deposition with anions in the buffer structure.

To determine an optimum volume of maleic acid, various amounts of this buffer were studied in the range of 0, 1, 1.5, 2, 3 and 4 mL based on adsorption efficiency of chromium and cadmium. In Fig. 4, effects of buffer volume on chromium (III) and cadmium (II) ion adsorption have been shown by CFNC. It is seen that by increasing volume of maleic acid, adsorption efficiency of chromium (III) and cadmium (II) ions will be increased. In volume higher than 1.5 mL of maleic acid, the value of adsorption is not change for cadmium ion but efficiency value of adsorption for chromium ion is decreased. Therefore, buffer volume of 1.5 mL is obtained from aqueous solution as optimum value to chromium (III) and cadmium (II) ion adsorption.

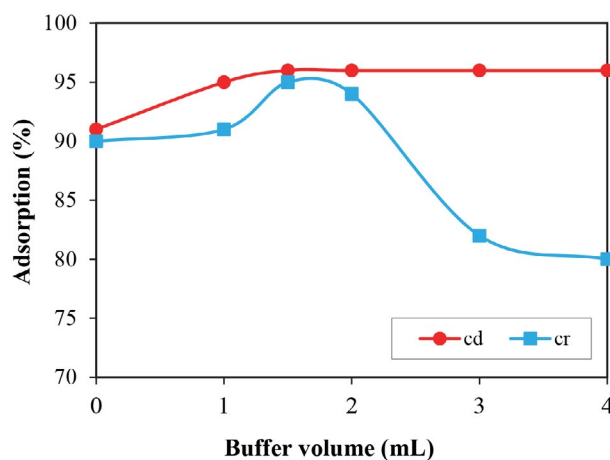


Fig. 4: Effect of buffer volume on removal of chromium (III) and cadmium (II) ions from aqueous solution using CFNC

3. 4. Effects of Electrolyte Type and Concentration

In this study, effects of various electrolytes such as CaCl_2 , NaCl , KCl , and NaNO_3 were investigated on adsorption efficiency of chromium (III) and cadmium (II) ions. The results are given in Table S-3. Among the various electrolytes, NaCl , KCl , and NaNO_3 electrolytes had a better adsorption efficiency to remove chromium (III) and cadmium (II) ions with single capacity cations than CaCl_2 with bivalency cations. The difference in adsorption efficiency is due to capacities difference between Ca^{2+} , K^+ and Na^+ electrolytes with chromium (III) and cadmium (II) ions existed in solution to fill the active sites. The displacement of ions on active sites cause a competition between them and it reduces adsorption efficiency. Among these materials, NaCl was chosen as a better electrolyte. On the other hand, ions of NaCl , make chromium (III) and cadmium (II) ions to accumulate and from this way increase adsorption efficiency of chromium (III) and cadmium (II) heavy metals ion on the adsorbent.

After determining types of electrolyte, effects of electrolyte NaCl concentration on adsorption efficiency of chromium (III) and cadmium (II) cations were studied in the range of 0.0004 to 0.001 molar that the result has been shown in Fig. 5.

As seen in Fig. 5, after concentration of 0.001, the slope of the Fig. 5 is reduced by increasing concentration of electrolyte NaCl . In fact, by increasing concentration of electrolyte NaCl in aqueous solution, increasing ionic strength cause increasing dissolution of solvent in aquatic phase and as a result adsorption efficiency is decreased. Therefore, the molar concentration of 0.001 is obtained as an optimum concentration for electrolyte NaCl .

3. 5. Effect of Metal Ion Concentration

To investigate the effect of initial ion concentration, adsorption of Cr (III) and Cd (II) ions was studied

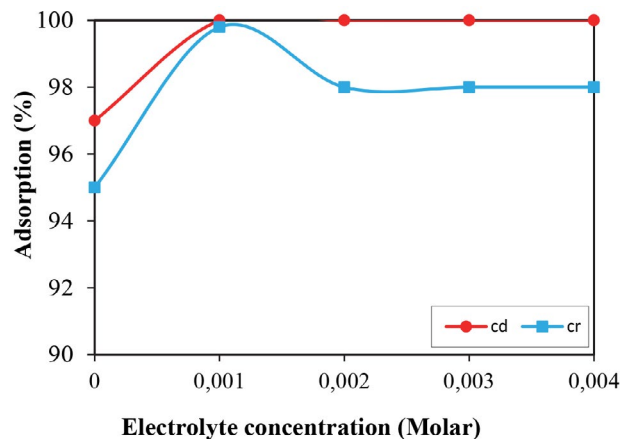


Fig. 5: Effect of electrolyte concentration on removal of Cr (III) and Cd (II) from aqueous solution using CFNC

by CFNC sorbent in the concentration of 10, 20, 30 and 50 mg/L. Fig. 6 shows the effect of initial ion concentration of chromium and cadmium using CFNC sorbent. The other conditions are including an adsorbent dose of 20 g/L, contact time of 50 min and temperature of 25 °C and pH for Cr (III) = 7 and for Cd (II) = 6. Increasing concentration from 10 to 20 mg/L, adsorption efficiency of chromium (III) and cadmium (II) ion has been increased. Because increasing the concentration of chromium (III) and cadmium (II) ions creates the required force for mass transfer between the solid and liquid phase in the solution. For concentrations greater than 20 mg/L, adsorption efficiency of chromium (III) and cadmium (II) ion is changed very slightly because of a high amount of chromium (III) and cadmium (II) ion to saturate active sites on the adsorbent surface of CFNC. Therefore, at low concentrations of metal ion, adsorption process is equilibrated sooner and initial concentration of 20 mg/L for chromium (III) and cadmium (II) ions was optimized sequentially by adsorption efficiency of 91% and 93%.

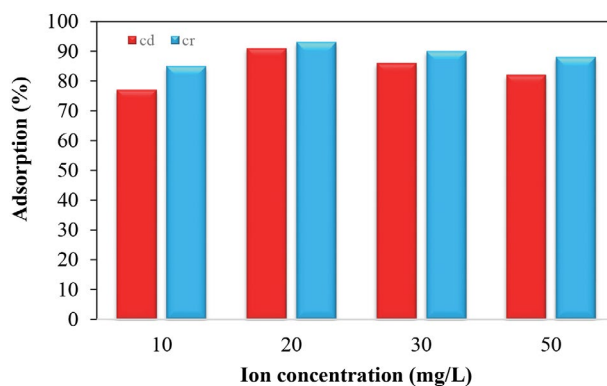


Fig. 6: The effect of initial concentration of cadmium and chromium in conditions in terms of (cadmium pH: 6, chromium pH: 7, adsorbent dosage 20 g/L, time 50 min and temperature 25 °C)

3.6. Effect of Contact Time

The contact time is one of the most important factors that plays an important role in batch adsorption tests.¹⁴ The removal efficiency of chromium (III) and cadmium (II) ions by CFNC in contact period times 10–80 min has been shown in Fig. 7. As can be seen, adsorption efficiency is fast in the beginning and after that process goes forward slowly and after 50 min, the adsorption efficiency remained constant. Increasing adsorption efficiency at early times (time <50 min) is due to the availability of sufficient surfaces and the number of adsorbent unsaturated active sites.¹⁰ At this time, the removal efficiencies of Cr (III) and Cd (II) ions were 100%. So, the contact time of 50 min is selected as optimum time.

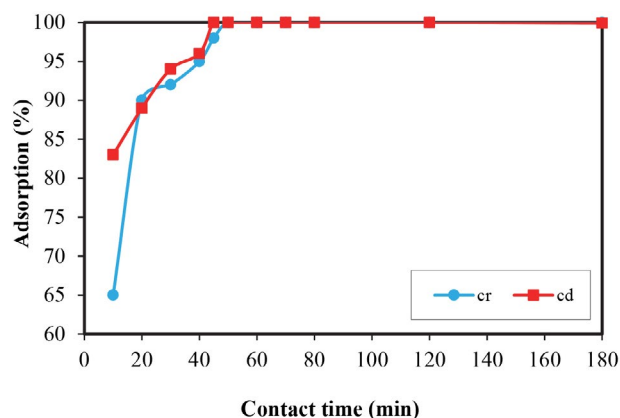


Fig. 7: The effects of time on the cadmium and chromium in conditions in terms of (cadmium pH: 6, chromium pH: 7, initial concentration of metal ions 20 mg/L, adsorbent dosage 20 g/L and temperature 25 °C)

3. 7. Effect of Sorbent Dose

Another important parameter in adsorption processes is the adsorbent dose. This parameter determines the potential and capacity of an adsorbent to adsorb metal ions from aqueous solutions.¹⁴ Effect of CFNC dose is studied in conditions: pH chromium ion (III):7 and cadmium ion (II): 6, initial concentration of metal ions of 20 mg/L, contact time of 50 min and temperature of 25 °C in adsorbent doses of 10, 15, 20, 25 and 30 g/L and results can be seen in Fig. 8. As shown in this Fig., in an adsorbent dose range of 10–15 g/L, adsorption efficiency of chromium (III) and cadmium (II) ion is low due to the lack of sufficient active sites to replace heavy metal ions. On the other hand, adsorption efficiency was increased by increasing sorbent dose of CFNC. At concentrations higher than 20 g/L, adsorption efficiency was not changed. Therefore, an adsorbent dose of 20 g/L was reported as the optimum value. In optimum adsorbent dose, the removal efficiency was obtained 100% for both metal ions.

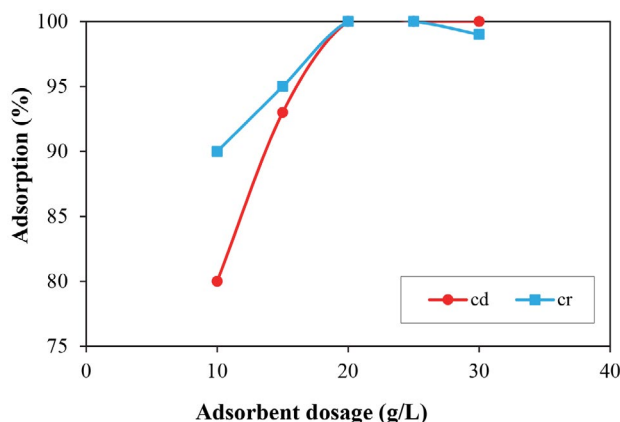


Fig. 8: The effect of cobalt-ferrite magnetic nanocomposite on the percentage remove of cadmium and chromium in conditions in terms of (cadmium pH: 6, chromium pH: 7, initial ion concentration 20 mg/L, time 50 min and temperature 25 °C)

3. 8. Effect of Temperature

To investigate the effect of temperature on adsorption of chromium (III) and cadmium (II) ions by CFNC sorbent, various temperatures such as 25, 30, 40, 50 and 60 °C were checked that the results have been drawn in Fig. 9. Regarding Fig. 9, adsorption efficiency of metal ions was decreased with increasing temperature due to the endothermic adsorption process and destructing active sites. Also, it may be due to the high tendency of metal ions to separate from the adsorbent and release in the solution with the increase of the solution temperature.¹⁴ So, 25 °C was selected as an optimum value for temperature.

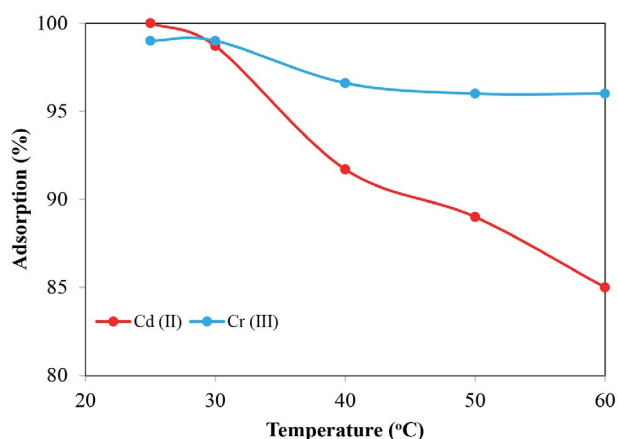


Fig. 9: The effect of temperature on the cadmium and chromium in conditions in terms of (cadmium pH: 6, chromium pH: 7, initial concentration of metal ions 20 mg/L, time 50 min and adsorbent dosage 20 g/L)

3. 9. Study of Adsorption Isotherms

To explain the interaction between sorbent and contaminants, adsorption isotherms are used widely and play an important role in the optimal use of adsorbents.²⁸ In this study, Langmuir and Freundlich isotherm models are used to explain adsorption process of chromium (III) and cadmium (II) ions using CFNC.^{31–33} The details are given in supplementary material.

As it is shown in Table 2, correlation coefficient in Langmuir isotherm model to cadmium (II) and chromium (III) ion is 0.9948 and 0.9999 sequentially. Also, the value of R_L achieved from Langmuir isotherm to remove cadmium (II) and chromium (III) ion from aqueous solution by using CFNC sorbent is obtained 0.049 and 0.083 sequentially that show removing of cadmium (II) and chromium (III) ion by using CFNC is desirable. Additionally, maximum adsorption capacity (q_{max}) of cadmium (II) and chromium (III) ions by using Langmuir isotherm is achieved 303 and 217 mg/g sequentially which are significant amounts. Cadmium (II) and chromium (III) ion have correlation coefficient sequentially 0.9268 and 0.9959 for the Freundlich isotherm model. Moreover, the value of n for cadmium (II) and chromium (III) ion are obtained

Table 2: Langmuir and Freundlich isotherm constants for adsorption of cadmium (II) and chromium (III) using CFNC from aqueous solutions.

Isothermic models	parameters	cadmium	chromium
	q_{\max} (mg/g)	217	303
	K_L (L/g)	0.95	0.55
Langmuir isotherm model	R^2	0.99	0.99
	R_L	0.05	0.08
Freundlich isotherm model	n	0.48	2.36
	R^2	0.93	0.99
	K_f	8.15	7.21

0.48 and 2.36 that show the Freundlich isotherm model is sequentially desirable and undesirable to remove cadmium (II) and chromium (III) ions by using of CFNC.

3. 10. Kinetic Study

Kinetic studies of adsorption processes show the interactions between metal ions in aqueous solution and the adsorbent. Also, the kinetic study describes the mechanism of the adsorption process³⁴. In this study, in order to explain adsorbent kinetic behavior, pseudo first-order and pseudo second-order kinetic models were applied.^{32–34} The details are given in Supplementary material.

Fig. S-3 shows the effect of time (t) against $\log(q_e - q_t)$ for pseudo first-order kinetic model. Also, the effect of time (t) against t/q_t for the pseudo second-order kinetic model is shown in Fig. S-4. Additionally, constants and parameters of pseudo first-order and pseudo second-order kinetic models for adsorption of cadmium (II) and chromium (III) ions using CFNC are tabulated in Tables S-4 and S-5. Based on the obtained values for correlation coefficient (R^2), adsorption process of Cr (III) and Cd (II) ions using CFNC follow up the pseudo-first order kinetic model and this model has higher R^2 in comparison to pseudo-second order kinetic model. In other word, the pseudo first-order kinetic model is fitted well with the experimental data.

3. 11. Thermodynamic Studies

In this work, a thermodynamic study of cadmium (II) and chromium (III) ions removal using CFNC was

done at temperatures of 5, 15, 25, 30, 40, 50 and 60 °C. The other conditions were constant including pH of cadmium ion: 6 and chromium ion (III): 7, sorbent dose of 20 g/L, the initial concentration of 20 mg/L and contact time of 70 min. The details are given in Supplementary material. Constants and thermodynamic parameters are presented in Table 3.

A positive value of enthalpy ΔH° shows that adsorption process of cadmium (II) and chromium (III) ions using CFNC sorbent is endothermic. Also, the value of ΔS° was positive that shows at the solid/liquid interface an increase of randomness occurs after adsorption of Cd(II) and Cr(III) using CFNC adsorbent.³³ Moreover, a negative value of Gibbs free energy shows that cadmium (II) and chromium (III) ions adsorption using ferrite-cobalt sorbent is spontaneous.

3. 12. Desorption

Desorption process gives useful data about the possibilities of adsorbent regeneration after it saturates with heavy metals, and this process is necessary to enhance the economical feasibility of the adsorption process³⁴. Fig. 10 shows adsorption efficiency of cadmium (II) and chromium (III) ions due to reusing of CFNC in consecutive adsorption. Desorption process was done in 8 cycles. Adsorption efficiency of heavy metal ions due to desorption in the first eight steps, the peak of the graphs was constant, and after each repetition, no significant change was observed with the ferrite-cobalt magnetic nanocomposite. These results indicate the ability to reuse ferrite-cobalt

Table 3: Thermodynamic properties for cadmium (II) and chromium (III) adsorption

heavy metal ion	Temperature/K	K_C	ΔG (kJ/mol)	ΔH (kJ/mol)	ΔS (J/mol K)
cadmium (II)	278	2.25	-1.82	39.37	147.85
	288	3.86	-3.23		
	293	5.92	-4.31		
	298	10.17	-5.73		
chromium (III)	278	2.25	-2.86	34.36	133.91
	288	3.86	-4.2		
	293	5.92	-4.87		
	298	10.17	-5.54		

magnetic nanocomposite to recover cadmium (II) and chromium (III) ions from aqueous solutions. Also, the advantage of the CFNC sorbent is that it can be used 4 times consecutively by washing it with 30mL of acetone/methanol (1:1).

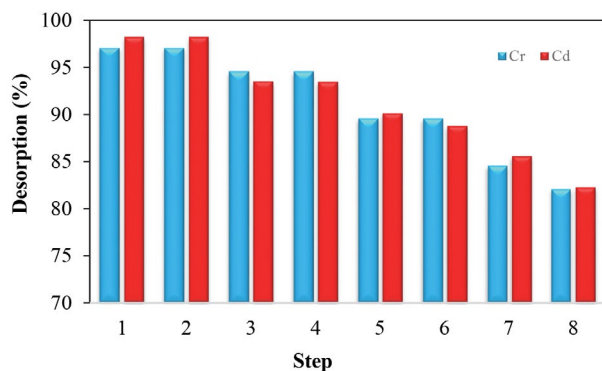


Fig. 10: Desorption of cadmium (II) and chromium (III) ions from solution using acetone/ethanol (1:1)

4. Conclusion

To remove cadmium (II) and chromium (III) ions, cobalt-ferrite nanocomposite (CFNC) was used as a new magnetic adsorbent. To determine characteristics of CFNC sorbent, various analyses such as SEM, FTIR, VSM, and BET were used. By BET analysis, the specific surface area of CFNC was measured 17.84 m²/g. Also, various parameters such as pH of the solution, type and volume of buffer, type and concentration of the electrolyte, the initial concentration of metal ions in solution, contact time, sorbent dose and temperature were studied on the removal of chromium and cadmium ions from aqueous solution using CFNC. The results showed that the optimum value of pH to remove cadmium (II) and chromium (III) ions were achieved 7 and 6, respectively. The other optimum conditions were including: temperature = 25 °C, initial ion concentration = 20 mg/L, contact time = 50min, type of buffer = maleic acid, type of electrolyte = NaCl and adsorbent dose = 20 g/L. To study adsorption process of cadmium (II) and chromium (III) ions, CFNC sorbent of Langmuir and Freundlich isotherm models were used. Adsorption data follow Langmuir isotherm and show that cadmium (II) and chromium (III) ions adsorption are happened on monolayer surface and homogeneous of CFNC. Moreover, maximum adsorption capacity (q_{max}) of cadmium (II) and chromium (III) is achieved from Langmuir adsorption isotherm model 217 and 303 mg/g, sequentially. In order to study the kinetic behavior of adsorption, pseudo first-order and pseudo second-order kinetic models were used and the results showed that the pseudo first-order kinetic model was more desirable than the pseudo second-order model because of its higher correlation coefficient (R^2). The thermodynamic study also

showed that the adsorption of chromium and cadmium ions using CFNC adsorbent is spontaneous and endothermic. Additionally, the desorption process showed that the adsorbent can be used consecutively 4 times by washing it with 30mL of acetone/methanol solution (1:1).

Conflict of Interests Statement

The authors declare that there is no conflict of interests.

5. References

- L. Jiang, P. Liu, S. Zhao. *Colloids Surf. A Physicochem. Eng. Asp.* **2015**, 470, 31–38. DOI:10.1016/j.colsurfa.2015.01.078.
- X. Luo, J. Zeng, S. Liu, L. Zhang. *Bioresour. Technol.* **2015**, 194, 403–406. DOI:10.1016/j.biortech.2015.07.044.
- F. G. L. M. Borsagli, A. A. P. Mansur, P. Chagas, L. C. A. Oliveira, H. S. Mansur. *React. Funct. Polym.* **2015**, 97, 37–47. DOI:10.1016/j.reactfunctpolym.2015.10.005.
- L. P. Lingamdinne, Y. Y. Chang, J. K. Yang, J. Singh, E. H. Choi, M. Shiratani, J. R. Koduru, P. Attri. *Chem. Eng. J.* **2017**, 307, 74–84. DOI:10.1016/j.cej.2016.08.067.
- T. S. Anirudhan, F. Shainy. *J. Ind. Eng. Chem.* **32** (2015) 157–166. DOI:10.1016/j.jiec.2015.08.011.
- G. Sharma, M. Naushad, A. H. Al-Muhtaseb, A. Kumar, M. R. Khan, S. Kalia, Shweta, M. Bala, A. Sharma. *Int. J. Biol. Macromol.* **2017**, 95, 484–493. DOI:10.1016/j.ijbiomac.2016.11.072.
- W. R. García-Niño, J. Pedraza-Chaverri. *Food Chem. Toxicol.* **2014**, 69, 182–201. DOI:10.1016/j.fct.2014.04.016.
- E. Igberease, P. Osifo. *J. Ind. Eng. Chem.* **2015**, 26, 340–347. DOI:10.1016/j.jiec.2014.12.007.
- F. Ge, M. M. Li, H. Ye, B. X. Zhao. *J. Hazard. Mater.* **2012**, 211–212, 366–372. DOI:10.1016/j.jhazmat.2011.12.013.
- H. Esmaeili, R. Foroutan. *J. Dispers. Sci. Technol.* **2018**. DOI:10.1080/01932691.2018.1489828.
- R. Foroutan, H. Esmaeili, M. Abbasi, M. Rezakazemi, M. Mesbah. *Environ. Technol.* **2018**, 39, 2792–2800. DOI:10.1080/09593330.2017.1365946.
- R. Mahini, H. Esmaeili, Rauf Foroutan. *Turk. J. Biochem.* **2018**. DOI:10.1515/tjb-2017-0333.
- M. I. Shariful, S. Bin Sharif, J. J. L. Lee, U. Habiba, B. C. Ang, M. A. Amalina. *Carbohydr. Polym.* **2017**, 157, 57–64. DOI:10.1016/j.carbpol.2016.09.063.
- F. S. Khoo, H. Esmaeili. *J. Serb. Chem. Soc.* **2018**, 83, 237–249. DOI:10.2298/JSC170704098S.
- R. D. Ambashta, M. Sillanpää. *J. Hazard. Mater.* **2010**, 180, 38–49. DOI:10.1016/j.jhazmat.2010.04.105.
- X. Zhao, L. Lv, B. Pan, W. Zhang, S. Zhang, Q. Zhang. *Chem. Eng. J.* **2011**, 170, 381–394. DOI:10.1016/j.cej.2011.02.071.
- A. M. Muliwa, T. Y. Leswif, M. S. Onyango, A. Maity. *Sep. Purif. Technol.* **2016**, 158, 250–258. DOI:10.1016/j.seppur.2015.12.021.
- Y. L. F. Musico, C. M. Santos, M. L. P. Dalida, D. F. Rodrigues.

- J. Mater. Chem. A.* **2013**, *1*, 3789–3796.
DOI:10.1039/C3TA01616A.
19. X. Li, H. Zhou, W. Wu, S. Wei, Y. Xu, Y. Kuang. *J. Colloid Interface Sci.* **2015**, *448*, 389–397.
DOI:10.1016/j.jcis.2015.02.039.
20. M. Aliabadi, M. Irani, J. Ismaeili, S. Najafzadeh. *J. Taiwan Inst. Chem. Eng.* **2014**, *45*, 518–526.
DOI:10.1016/j.jtice.2013.04.016.
21. E. J. Kim, C. S. Lee, Y. Y. Chang, Y. S. Chang. *ACS Appl. Mater. Interfaces.* **2013**, *5*, 9628–9634. DOI:10.1021/am402615m.
22. T. S. Anirudhan, P. S. Suchithra. *Chem. Eng. J.* **2010**, *156*, 146–156. DOI:10.1016/j.cej.2009.10.011.
23. K. S. Thangamani, N. Muthulakshmi Andal, E. Ranjith Kumar, M. Saravanabhavan. *J. Environ. Chem. Eng.* **2017**, *5*, 2820–2829. DOI:10.1016/j.jece.2017.05.030.
24. S. Yavari, N. M. Mahmodi, P. Teymouri, B. Shahmoradi, A. Maleki. *J. Taiwan Inst. Chem. Eng.* **2016**, *59*, 320–329.
DOI:10.1016/j.jtice.2015.08.011.
25. K. Maaz, A. Mumtaz, S. K. Hasanain, A. Ceylan. *J. Magn. Magn. Mater.* **2007**, *308*, 289–295.
DOI:10.1016/j.jmmm.2006.06.003.
26. L. C. Shen, X. T. Nguyen, N. P. Hankins. *Sep. Purif. Technol.* **2015**, *152*, 101–107. DOI:10.1016/j.seppur.2015.07.065.
27. V. Srivastava, Y. C. Sharma, M. Sillanpää. *Appl. Surf. Sci.* **2015**, *338*, 42–54. DOI:10.1016/j.apsusc.2015.02.072.
28. F. S. Sarvestani, H. Esmaeili, B. Ramavandi. *3 Biotech.* **2016**, *6*, 251. DOI:10.1007/s13205-016-0570-z.
29. R. Foroutan, H. Esmaeili, S. M. D. Rishehri, F. Sadeghzadeh, S. R. Mirahmadi, M. Kosarifar, B. Ramavandi. *Data Brief.* **2017**, *12*, 485–492. DOI:10.1016/j.dib.2017.04.031.
30. S.M. Mousavi, S.A. Hashemi, H. Esmaeili, A.M. Amani, F. Mojoudi. *Acta Chim. Slov.* **2018**, *65*, 750–756.
DOI:10.17344/acsi.2018.4536.
31. M. Venkata Subbaiah, Y. Vijaya, A. Subba Reddy, G. Yuvaraja, A. Krishnaiah. *Desalination*, **2011**, *276*, 310–316.
DOI:10.1016/j.desal.2011.03.067.
32. B. S. Zadeh, H. Esmaeili, R. Foroutan. *Indones. J. Chem.* **2018**, *18*, 265–271. DOI:10.22146/ijc.28789.
33. A. Teimouri, H. Esmaeili, R. Foroutan, B. Ramavandi. *Korean J. Chem. Eng.* **2018**, *35*, 479–488.
DOI:10.1007/s11814-017-0311-y.
34. L. N. Nemeş, L. Bulgariu. *Open Chem.* **2016**, *14*, 175–187.
DOI:10.1515/chem-2016-0019

Povzetek

Študija preučuje možnost uporabe kobalto-feritnih nano-kompozitov (CFNC) za adsorpcijo kromovih in kadmijevih ionov iz odpadnih voda. Adsorpcijske lastnosti smo določali z različnimi tehnikami kot so SEM, FTIR, VSM in BET. Prav tako smo preučevali kako vplivajo na adsorpcijo pH vrednost, volumen pufru, dodatek elektrolitov, začetna koncentracija ionov, kontaktni čas in temperatura. Rezultati so pokazali, da je maksimalna adsorpcija Cd(II) in Cr(III) ionov dosežena pri začetni koncentraciji $C_0 = 20 \text{ mg/L}$, $t = 50 \text{ min}$, $T = 25 \text{ °C}$, CFNC koncentraciji 20 g/L ter pH vrednosti $\text{pH} = 7$ (za Cr(III)) oziroma 6 (za Cd(II)). Pod temi pogoji je bila dosežena 100 % odstranitev ionov iz vodne raztopine. Študija je pokazala, da lahko adsorpcijsko ravnotežje opišemo z Langmuirjevo izotermo, pri čemer dosežemo visoke maksimalna adsorpcijske kapacitete, ki znašajo 217 mg/g za Cr(III) ione in 303 mg/g za Cd(II) ione. Kinetiko adsorpcije lahko bolje opišemo z reakcijo psevdo-prvega reda kot z reakcijo psevdo-drugega reda. Adsorpcija je pod preučevanimi pogoji spontana in endotermna.

Scientific paper

Release of Halophilic Extremozymes by Mechanical Cell Disruption

Mateja Primožič,¹ Maja Čolnik,² Željko Knez,^{1,2} and Maja Leitgeb^{1,2}¹ University of Maribor, Faculty of Chemistry and Chemical Engineering, Laboratory for Separation Processes and Product Design, Smetanova 17, 2000 Maribor, Slovenia² University of Maribor, Faculty of Medicine, Taborska ulica 8, 2000 Maribor, Slovenia

* Corresponding author: E-mail: maja.leitgeb@um.si

Received: 10-19-2018

Abstract

Trimastroma salinum, *Walleimia ichthyophaga*, *Hortaea werneckii* and *Phaeotheca triangularis* are halophilic fungi, which can thrive in a wide range of salinity. They present a source of valuable bioactive compounds, enzymes and proteins interesting for food and pharmaceutical industry. To separate enzymes from halophilic fungi cells, the mechanical method was used. Obtained results and new findings are important from the biotechnological point of view, since the separation of in the form of cocktail from halophilic fungi is interesting for industrial applications, especially for cascade reactions. Enzymes from extremophiles namely possess improved properties and can be used at harsh conditions where non-extremophilic enzymes may deactivate.

Keywords: Activity; enzymes; halophilic fungi; mechanical method; proteins

1. Introduction

The great importance of the biotechnology industry is shown in the use of microbial intracellular proteins that possess catalytic or biological activity. For the manufacture of recombinant proteins, the release of catalytic active proteins and enzymes from living cells presents a key unit operation. Any living organism contains biologically active enzymes that can be extracted from them. The importance of microbial cells as a source of commercially useful chemicals, antibiotics and enzymes has been recognized for a very long time. They have several advantages over plant and animal cells with many good physiological characteristics, such as high growth rate, capability to grow on simple media, no requirements of expensive additives, generation of high yields on the chosen carbon substrate, ability to grow at high cell densities and stable growth in continuous culture.¹

The most common source of industrial enzymes are microbial cells. The production of microbial enzymes takes place inside their cells (intracellular enzymes), although some may be secreted from outside the cell (extracellular enzymes). Extracellular enzymes are often soluble in water, which facilitates their extraction from the culture medium and purification. Obtaining an intracellular enzyme from

microbial cells consists of two steps: harvesting microbial cells (by physical, chemical or enzymatic methods) from the culture and breaking the microbial cells to release the enzymes.² Several intracellular enzymes are produced industrially. The necessity of harvesting the producing cells, in order to subsequently extract an intracellular product, is a major economic disadvantage. Simultaneous isolation of intracellular products following cell disruption could lead to cost reduction.² The mechanical disruption method is based on disrupting cells and tissues by applying a force not inherent to the sample. Lysates obtained by using mechanical forces and those produced by chemical lysis have different characteristics.

Various methods of mechanical cell disruption (such as bead mills, French press, high-pressure homogenizer, ultrasonication etc.) are currently commercially available for processing minute samples (<1 mL) to larger production quantities and are well documented as to the advantages and disadvantages of each method by Goldberg³ and Flickinger.⁴ Effective methods for disruption of the fungi or bacterial cell walls are fundamental to obtain higher intracellular compound extraction efficiencies. By using mechanical methods, non-selective destruction is usually achieved. These processes are easy to scale up and relatively cheaper to operate and are therefore often favoured

for large-scale cell disruption. Non-mechanical methods (enzymatic, physical or chemical) are more selective and mostly used on the laboratory scale owing to their operational and economic limitations.

Detergents and chaotropes can destabilize protein structures during the release of them from the cell. Therefore, they are not suitable tools for cell wall disruption for isolating proteins, while mechanical homogenization in combination with denaturing reagents is a useful tool for rapid cell and tissue disruption (especially during RNA isolation). When applying mechanical methods of cell disruption, the resulting stresses and strains disrupt the cell walls of the microorganisms. In mechanical disruption devices, load is transmitted to the cells. Cells are mainly stressed by shear and compressive stress and stress transmitted from the fluid medium.⁴ Mechanical methods are most effective for the disintegration of yeast and filamentous fungi⁵ and can lead to enzymatically active cell-free extracts. Moreover, intracellular enzymes of interest can be isolated and purified. A broad spectrum of experimental work on mechanical disruption of yeast cell,^{3,6–8} *Escherichia coli*, *Bacillus subtilis*⁹ and algae^{10,11} using different methods in research and industry has been published. The purpose of these studies was recovering of the large volumes of intracellular substances inside cells. There are very few published studies on other organisms.

One reason for preferring mechanical methods to chemical and enzymatic methods for cell disruption on the industrial scale is to avoid the increase in unit operation steps during downstream processing.¹²

Bead mills represents the most effective ways for mechanical disruption of microbial cells with high disruption efficiency, good temperature control and easy scale-up procedure. High-pressure homogenizers are most commonly used for bacteria and yeast disruption in the pharmaceutical and biotechnological industries. The main drawback is the non-selective release of the products, which complicates the purification process, its price and operating costs. Ultrasonication is another common mechanical cell disruption method in which, because of high frequency ultrasound, high shear forces are created which cause cell disruption.

Halim et al.¹⁰ studied the influence of varied mechanical methods for *Chlorococcum* sp. cell disruption expressed by disruption efficacy. They found that the highest disruption efficacy was achieved using high-pressure homogenization (73.8%); with the sulfuric acid treatment, 33.2% disruption efficacy was detected, and by usage of bead beating (33.2%) and ultrasonics (4.5%), the lowest disruption efficacies were detected.

A positive effect on protein activity was determined during ultrasonication of some commercially purified enzyme preparations. On the other hand, biological tissue denaturation at high intensity ultrasonication could appear.¹³ Therefore, the selection of operational parameters during ultrasonication can strongly affect the activity and

stability of bioactive components in the cell. Therefore, operational parameters (such as time and intensity) of the sonifier should be optimised specifically for each enzyme or biological tissue, since degradation of the released enzyme during the disruption of cells could appear.

However, there is no general rule regarding the use of a particular method for cell opening; the choice of disruption method is therefore dependent on the selected microorganism and the desired results.

Homogenization is a process where homogeneity throughout a product is achieved by particle size modification. It can be divided into three major categories: ultrasonic pressure homogenization, pressure homogenization and mechanical homogenization. Applications of homogenization are diverse in the food industry, pharmaceuticals and the chemical industry. Selection criteria for homogenizers depend on the particular application. High-pressure homogenizers and mechanical homogenizers have been for many years the most commonly used equipment for disruption of microbial cells.^{14–17}

Organisms such as halophilic fungi that survive and thrive under conditions that are detrimental to the majority of other species have become an increasing scientific attention over the last few years.¹⁸ The role of halophilic fungi in industrial and biotechnological areas become more and more important especially since they contain industrially important enzymes that are resistant to harsh conditions. Halophilic and halotolerant fungi can act as valuable. In the past, halophilic fungi have been used for production of fermentation-based foods such as soy sauce and fish sauce. Nowadays, their applications extend from bacteriorhodopsin production for optical and optoelectronic devices¹⁹ to biopolymers such as biosurfactants and exopolysaccharides for oil recovery and compatible solutes as stress protectants.²⁰ Halotolerant fungi can act as valuable sources of transgenes for imparting tolerance to microbes such as *Saccharomyces cerevisiae* which present a very important microorganisms for industrially application, which are subjected to various abiotic stresses.

W. ichthyophaga is a halophilic basidiomycetous fungus,^{21,22} *P. triangularis* is an obligate halophile, while *H. werneckii* and *T. salinum* are facultatively halotolerant. These fungi were first isolated from the hypersaline water of the Slovenian Sečovlje solar salterns, an environment characterised by high concentrations of NaCl, occasional rapid changes in water activity, low oxygen concentrations and high UV radiation.^{21,23,24} Halophilic *T. salinum* was the first fungal species that was shown to thrive in the low water potential environment created by pure salt.^{25,26} *H. werneckii* is the most salt-adaptable fungus known, as it can grow without NaCl and in almost saturated NaCl solutions, and its plasma membrane is rigid.²⁷ The saline and nonsaline conditions for growth enable the presence of the dark pigment melanin in their cell walls. Melanin plays a very important role not only in UV-protection, but also

in desiccation and radiation tolerance.^{28–30} *W. ichthyophaga* has an obligate halophilic character, as it grows only in media with NaCl above 1.7 M and still shows growth to 5.2 M NaCl.^{21,23}

To release enzymes from halophilic fungi cells, a mechanical homogenizer (rotor-stator homogenizer) was used. Homogenizing the black yeast cell suspensions allows the achievement of more rapid and effective results. It is an affordable, simple and reliable method, which enables the extraction of intracellular substances without needing to use solvents or other chemicals to break down the cell walls. During homogenization, protein deactivation could appear, owing to shearing at the molecular level or the thermal denaturation, caused by local overheating of the cell suspension. However, the degree of possible denaturation of proteins is dependent on the type of protein. Some proteins are easily deactivated and are very influenced by process parameters (e.g. homogenization time), whereas others are more stable.³¹

So far no publication regarding release of enzymes from studied halophilic fungi using homogenization method and the study of their activity was published. Since the studied halophilic fungi are adapted to the high salinity and their cells selectively accumulate compatible solutes such as glycerol, the cell wall of those fungi is more rigid and release of intracellular enzymes can be more difficult. These fungi can occur in stressful environments that are hostile to most eukaryotes and are therefore interesting and important for evolutionary processes. Extremophiles such as *T. salinum*, *W. ichthyophaga*, *H. werneckii* and *P. triangularis* are considered as a source of chemically diverse and often novel metabolites and proteins (e.g. enzymes such as protease, α -amylase, β -glucosidase and cellulase) which are interesting for food and pharmaceutical industry in a form of a cocktail, especially when the cascade reactions are required.

Therefore, the influence of homogenization time on various factors, such as the viability of black yeast cells, residual activity of enzymes (protease, α -amylase, β -glucosidase and cellulase), and the residual protein concentration was studied.

2. Experimental

2. 1. Materials

The halophilic fungi *H. werneckii* EXF- 225, *P. triangularis* EXF-206, *T. salinum* EXF-295 and *W. ichthyophaga* EXF-5676 were kindly donated by the University of Ljubljana, Biotechnical Faculty, Department of Biology (Ljubljana, Slovenia). Peptone from meat, potassium phosphate, potassium dihydrogen phosphate, sodium carbonate, sodium bicarbonate and acetic acid were purchased from Merck (Darmstadt, Germany). Sodium pyrophosphate decahydrate ($\geq 99.0\%$), sodium phosphate monobasic ($\geq 99.0\%$), sodium phosphate dibasic ($\geq 99.0\%$),

albumin from bovine serum (BSA) ($\geq 98.0\%$), malt extract, agar, D-(+)-glucose, sodium acetate, Sigmacell, glucose assay reagent, Casein, Hammarsten bovine, trichloroacetic acid (TCA), D-(–)-Salicin ($\geq 99.0\%$), starch azure and sodium chloride were supplied by Sigma (Schnelldorf, Germany).

2. 2. Preparation of Halophilic Fungi Suspension

The microbial strains used in this study were *H. werneckii*, *P. triangularis*, *T. salinum*, and *W. ichthyophaga*. *H. werneckii*, *P. triangularis* and *T. salinum* were grown on solid malt extract agar (MEA) for 5–7 days at room temperature, while cells of *W. ichthyophaga* were grown on MEA with 17% NaCl under the same conditions. Black yeast cells were suspended in sterile saline solutions, incubated at 25 °C and stirred at 300 rpm for 10 min to achieve homogeneity of the cell suspension. All cultures were freshly prepared by the same procedure.

2. 3. Disintegration of Halophilic Fungi Cells

Rotor-stator homogenizers consist of two parts: a fast-spinning inner rotor and a stator (a stationary outer sheath). Their function is to homogenize samples based on the action of mechanical tearing, shear fluid forces, and/or cavitation (the rapid forming and collapsing of bubbles). Rotor-stator homogenizers are broadly capable of homogenizing a wide variety of tissues or cells.

The experiments were conducted in a 100 mL glass centrifuge tube. The sterile centrifuge tube was filled with a fresh cell suspension of selected black yeasts, mixed and then placed into a water bath at a fixed temperature of 35 °C. For black yeast cell disruption, a rotor-stator homogenizer (Homogenizer, Polytron Pt1200, Kinematica AG, Switzerland) for volumes from 1 mL to 1 L was used. The cell suspension was homogenized from 10 to 100 min at 25,000 rpm, and at a predetermined time, samples were taken for subsequent analysis. The experiments were repeated three times.

2. 4. Survivor Colony Count

The number of colonies of *H. werneckii*, *T. salinum* and *P. triangularis* was determined before and after the defined homogenization time. The initial concentration (N_0) was around 10^5 CFU mL⁻¹ (colony forming units mL⁻¹) for each fungus. Parameters for determination of CFU mL⁻¹ were volume of sample 100 μ L, an incubation temperature of 25 °C and an incubation time of 5 to 7 days.

2. 5. Bradford Assay

A Bradford assay is a highly sensitive colorimetric method, with perceived linearity, and it presents high

speed of analysis.^{32–35} Bovine serum albumin (BSA) was used as the standard protein.

2. 6. Determination of Enzymatic Activity

The optical density of halophilic fungi cell suspensions was determined at 600 nm by the UV-Vis spectrophotometer and were between 0.47 and 0.54 before homogenization. Samples of halophilic fungi cell suspensions after homogenization were centrifuged for 2 min, and the supernatant without cells and debris was analyzed spectrophotometrically. The amount of total proteins was determined with the Bradford method.³² Activities of the cellular enzymes of halophilic fungi, α -amylase, cellulase, β -glucosidase and protease, which are the most commonly used enzymes in applied biocatalysis were determined by the UV-Vis spectrophotometer at wavelengths of 595 nm, 340 nm and 280 nm, before and after homogenization of the black yeast culture.

2. 6. 1. Assay of Cellulase Enzyme Activity

Cellulase activity was defined at 340 nm (25 °C) with a UV-Vis spectrophotometer using the method with a Sigmacell solution as a substrate.³⁶

2. 6. 2. Assay of α -amylase Enzyme Activity

α -Amylase activity was defined spectrophotometrically at 595 nm, using starch azure as a substrate. The activity was expressed as the change in absorbance at 595 nm per minute per mL of cell suspension.³⁶

2. 6. 3. Assay of Protease Enzyme Activity

Protease enzyme activity was determined at 280 nm on a UV-Vis spectrophotometer, using the TCA method.³⁶

2. 6. 4. Assay of β -glucosidase Enzyme Activity

β -glucosidase enzyme activity was determined at 340 nm with a UV-Vis spectrophotometer, using salicin as a substrate.³⁶

2. 6. 5. Statistical Method

For the statistical evaluation of the deviation of individual measurements, the standard deviation method was used, and for regression analysis, the coefficient of determination (R^2) for linear regression was determined.

For the calculation of standard deviation, the following equation was used:

$$s = \sqrt{\frac{\sum(x - \bar{x})^2}{n - 1}} \quad (1)$$

Symbols: x – each value in the population; \bar{x} – the mean value of the sample; $n-1$ – the number of values in the sample minus 1.

3. Results and Discussion

3. 1. Viability of Halophilic Fungi Exposed to Mechanical Forces

Structural damage or physiological dysfunction of the cell are often associated with the reason for its death. Other effects that influence or lead to cell death are disruption of the envelopes, DNA conformational changes, ribosome alterations or protein aggregation, as well as physiological disorders (membrane selective permeability alteration or loss of key enzyme function).³⁷ In addition, elevated temperatures can also affect the cellular structure; therefore, it is very difficult to determine which parameter contributes most to cell death. For that reason, in our study a low temperature (35 °C) was chosen for exposure of the fungi to mechanical forces. The influence of mechanical forces on the viability of *H. werneckii*, *P. triangularis*, *T. salinum* and *W. ichthyophaga* cells in the cell suspension was a subject of interest (Figure 1).

Cell division, growth and morphogenesis are phases during which the fungal cell structure dynamic is changing. No similarity in the composition and mechanical properties of the cell wall is expected either between genera, or even within closely related species. Moreover, growth conditions and genetic modifications could affect the fungal cell structure.^{38,39}

Therefore, it was interesting to study the influence of homogenization on cell death of these four halophilic fungi.

Before homogenization of the halophilic fungi, the number of viable cells was cca. 10^5 CFU mL⁻¹ for *H. werneckii*, *T. salinum* and *W. ichthyophaga*, and 10^2 CFU mL⁻¹ for *P. triangularis*.

The viability of all four treated halophilic fungi after 10 minutes of homogenization was relatively high, from

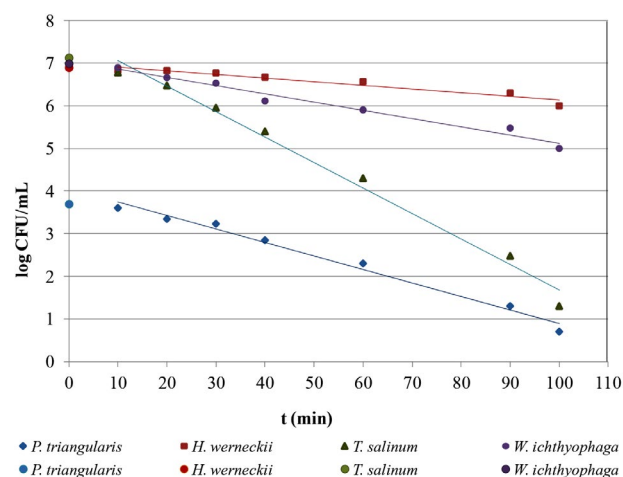


Figure 1: Survivor lines for *H. werneckii*, *P. triangularis*, *T. salinum*, and *W. ichthyophaga* after homogenization of cell suspension at 35 °C in relation to homogenization time. Experiments were repeated three times. Coefficients of determination (R^2) for linear regression are 0.985 (for *P. triangularis*); 0.942 (for *H. werneckii*); 0.987 (for *T. salinum*); and 0.974 (for *W. ichthyophaga*).

88% (corresponding to the $68 \cdot 10^5$ CFU mL⁻¹ for *H. werneckii*), to 99% (corresponding to the $79 \cdot 10^5$ CFU mL⁻¹ for *W. ichthyophaga*). With further increases in homogenization, a rapid decline in the viability of *T. salinum* and *P. triangularis* cells was observed. In comparison to *T. salinum* and *P. triangularis*, *W. ichthyophaga* and *H. werneckii* cells are more resistant to the influence of mechanical forces. After 100 minutes of homogenization of the *W. ichthyophaga* cell suspension, 1% of the cells (corresponding to the $1 \cdot 10^5$ CFU mL⁻¹ for *W. ichthyophaga*) had survived, and for the same time of treatment, 13% (corresponding to the $10 \cdot 10^5$ CFU mL⁻¹ for *H. werneckii*) of the *H. werneckii* cells had survived. In our earlier studies, it was also found that the black yeasts *W. ichthyophaga* and *H. werneckii* were highly resistant to high pressure.^{36,40} On the basis of the survivor lines constructed for these halophilic fungi, decimal reduction times (D-values) were determined. The times required to kill 90% of tested microorganisms exposed to mechanical forces at 35 °C, expressed as D-values. The greatest resistance to mechanical forces was observed for the *H. werneckii* cells (D-value = 115.0 min), while the least resistant were the *T. salinum* cells (D-value = 17.0 min). D-values for *W. ichthyophaga* and *P. triangularis* were following; 51.5 min and 31.7 min.

After treatment of the halophilic fungi cell suspensions by mechanical forces, the shape of the cells was examined under an environmental scanning electron microscope (ESEM).

Kralj Kunčič et al.⁴¹ reported that at low salinity (15% NaCl), the cell walls of *W. ichthyophaga* cells were threefold thicker than the cell walls of the hyphae of both *W. muriae* and *W. sebi* (both belong also to the halophilic fungal genus *Walleimia*). This could be the reason for the

very high D-values for *W. ichthyophaga* and *H. werneckii* that were obtained in our study.

Figure 2 shows the ESEM figures for these fungi before (Figures 2 a, c, e, g) and after (Figures 2 b, d, f, h) exposure to mechanical forces, using the homogenization method. As can be seen from Figure 2, untreated halophilic fungi cells had a smooth surface and typical shape. Homogenized halophilic fungi cells were damaged and deformed. Slightly wrinkled cell walls of dead halophilic fungi cells were detected, especially among the treated cells of *T. salinum* (Figure 2d). Ruptures and broken pieces of the cell walls were also detected. All these morphological changes indicate damage to the cell walls of the treated fungi. Therefore, the release of intracellular proteins could be predicted.

3. 2. Residual Protein Concentration

Besides the cell types, the appropriate time of exposure of the biological material to homogenization is also a critical parameter influencing the activity of the intracellular compounds. The residual protein concentration in the selected halophilic fungi suspensions increased linearly with the increase in homogenization time (Figure 3). The highest residual protein concentration (330%), which is equivalent to $8.7780 \text{ mg}_{\text{proteins}} \text{ mL}^{-1}$ of cell suspension, was detected after 100 min of homogenization in the *P. triangularis* cell suspension. The lowest protein concentration after 100 min of homogenization was observed in the *H. werneckii* cell suspension.

These results coincide with those obtained by determination of the survivor curves in selected halophilic fungi. The lowest D-value was obtained for *P. triangularis*,

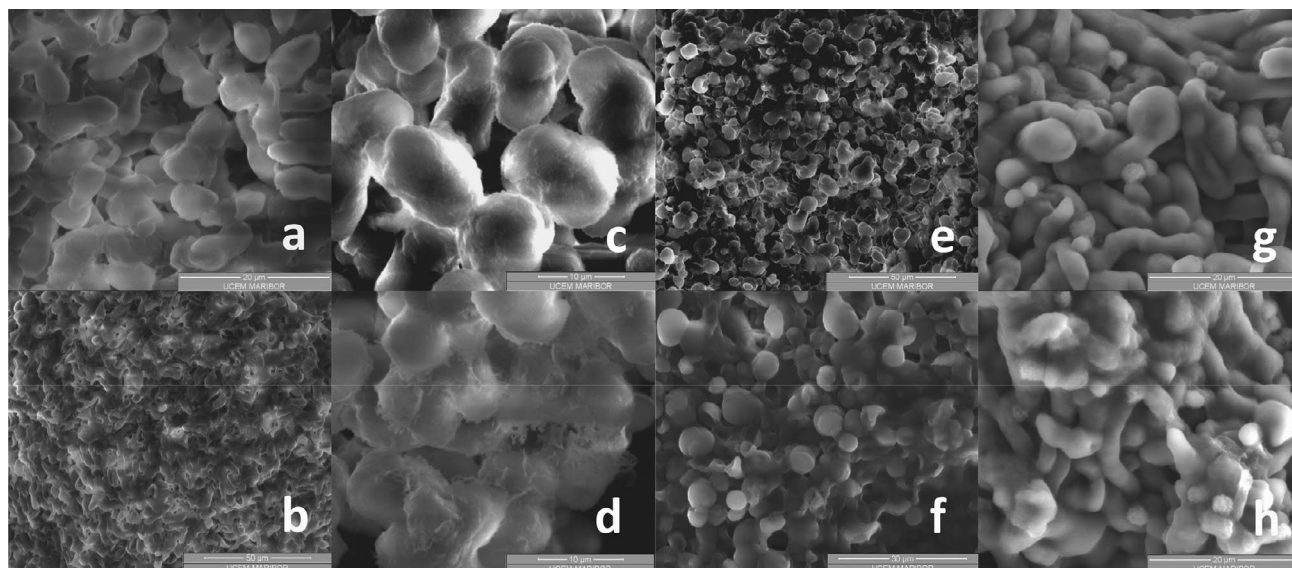


Figure 2: Halophilic fungi cells observed under an environmental scanning electron microscope (ESEM). *H. werneckii* cells a) before (magnification: 3000 X) and b) after 100 min of homogenization, *T. salinum* cells (magnification: 1000 X) c) before (magnification: 4000 X) and d) after 100 min of homogenization, *P. triangularis* cells (magnification: 4000 X) e) before (magnification: 1000 X) and f) after 100 min of homogenization and *W. ichthyophaga* (magnification: 2000 X) g) before (magnification: 3500 X) and h) after 100 min of homogenization (magnification: 3500 X).

where the highest protein concentration in the cell suspension was also detected. In contrast, the highest D-value and greatest viability was observed for *H. werneckii*, where the residual concentration of proteins in the cell suspension was the lowest. Obviously, intracellular proteins were extracted from the cells and consequently, the total protein concentration in selected halophilic fungi cell suspensions was increased.

The strength of the fungal cell wall is defined by its structure, which comprises glycoproteins and polysaccharides, mainly glucan and chitin. Several studies suggest that chitin is a primary effector for melanin deposition within the fungal cell wall.⁴² It has an enormous tensile strength and significantly contributes to the overall integrity of the cell wall. However, chitin microfibrils account for only 1–2% of the yeast cell walls by dry weight.⁴³ This could be the reason for the very high level of proteins released under variable conditions during the homogenization disruption procedure.

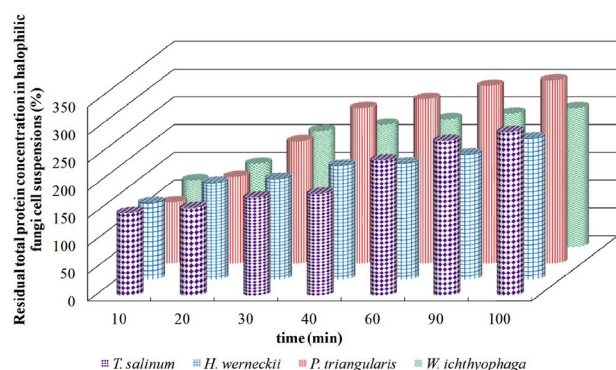


Figure 3: Residual total protein concentration in halophilic fungi cell suspensions in relation to homogenization time at 35 °C and a homogenization speed of 25,000 rpm. Experiments were repeated three times. Standard deviation for all measurements was less than $\pm 3\%$.

Initial concentration of the proteins in the halophilic fungi cell suspensions before homogenization are presented in Table 1 and were set to a value of 100%.

Table 1: Initial concentration of proteins in halophilic fungi cell suspensions before homogenization and standard deviation of measurements (SD).

Halophilic fungi	c (mg _{proteins} mL ⁻¹ of cell suspension)	SD (mg _{proteins} mL ⁻¹ of cell suspension)
<i>T. salinum</i>	0.0341	± 0.0010
<i>H. werneckii</i>	0.0472	± 0.0014
<i>P. triangularis</i>	0.0266	± 0.0007
<i>W. ichthyophaga</i>	0.0114	± 0.0003

Nucleic acids and their related compounds, such as pyrimidines and purines, are known to absorb UV light at a wavelength of 260 nm. Nucleic acids and proteins

have absorbance maxima at 260 and 280 nm, respectively. The ratio of absorbances at 260 nm and at 280 nm could be used as a measure of purity in both nucleic acid and protein extractions. A 260/280 ratio is generally accepted as “pure” for DNA; a ratio of ~ 2.0 is generally accepted as “pure” for RNA. A ratio lower than ~ 1.8 may indicate the presence of protein, phenol or other compounds, which are characterized by an absorption maximum at 280 nm.⁴⁴ The absorbic ratio of the UV-absorbing materials was measured after the mechanical treatment of the halophilic fungi cell suspensions. Figure 4 shows the absorbic ratio of the absorbance 260 nm and 280 nm. The highest absorbic ratio was determined for *T. salinum* cell suspension after 100 min of homogenization ($A_{260/280} = 1.9$). Obviously, during the homogenization of the *T. salinum* cell suspension, pure DNA was also extracted. Absorbic ratios $A_{260/280}$ for the other halophilic fungi (*P. triangularis*, *W. ichthyophaga* and *H. werneckii*) were lower than 1.8. Regarding the trend

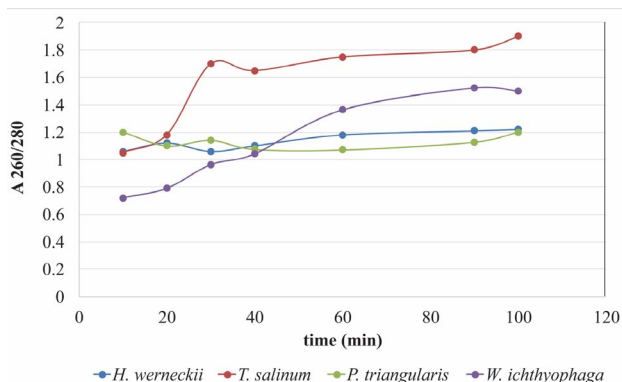


Figure 4: Absorbic ratio ($A_{260/280}$) after homogenization of halophilic fungi cell suspensions at 35 °C and a homogenization speed of 25,000 rpm. Experiments were repeated three times. Standard deviation for all measurements was less than ± 0.004 .

curves for other studied halophilic fungi, it is expected that with prolongation of homogenization time, pure DNA will also be extracted from other halophilic fungi cells.

3. 3. Influence of Homogenization Time on Residual Activity of Different Enzymes from the *T. Salinum* Cell Suspension

T. salinum is a melanized meristematic fungus that was isolated from saltern water along the Adriatic coast.²⁵ The influence of homogenization time on the residual activity of a range of extracellular and intracellular enzymes, α -amylase, β -glucosidase, protease and cellulose, from the *T. salinum* cell suspension was studied.

As can be seen from Figure 5, the highest residual enzyme activity (440%) in the *T. salinum* cell suspension, which is equivalent to the enzyme activity of 1.6720 U mL⁻¹ of cell suspension, was determined for α -amylase

ase after 60 min of homogenization time. α -Amylase belongs to the group of endoamylases that catalyse initial hydrolysis of starch into shorter oligosaccharides through the cleavage of interval α -D-(1-4) glycosidic bonds, resulting in α -anomeric product.^{45,46} Therefore, it is a very important enzyme in industrial processes such as starch saccharification, the textile, paper and food industries and pharmaceuticals.^{47–49} Since α -amylase from *T. Salinum* is an intracellular enzyme⁵⁰, an increase in its residual activity was expected after the defined time of homogenization. By prolonging the exposure of the *T. salinum* cell suspension to mechanical forces, the cell walls were damaged and intracellular enzymes were released in the cell suspension. A similar trend was detected for protease (maximal residual activity was determined after 30 min of homogenization), which is also an intracellular enzyme of *T. salinum*.⁵⁰ Prolongation of homogenization time results in a decrease of α -amylase and protease activity. Probably, the overly long exposure to shear forces caused disruption in the enzyme tertiary structure and, consequently, its deactivation.

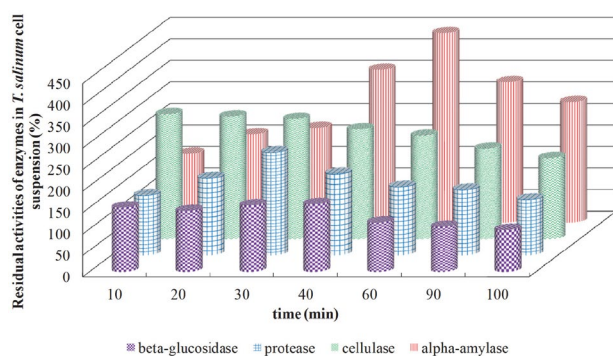


Figure 5: Residual activity of various enzymes in the *T. salinum* cell suspension in relation to homogenization time at 35 °C and a homogenization speed of 25,000 rpm. Experiments were repeated three times. Standard deviation for all measurements was less than $\pm 3\%$.

Initial activity of the studied enzymes in the *T. salinum* cell suspension before homogenization are presented in Table 2 and were set to the value of 100%.

Table 2: Initial activity of the studied enzymes in the *T. salinum* cell suspension before homogenization and standard deviation of measurements (SD).

Enzyme	Enzyme activity (U mL ⁻¹ of cell suspension)	SD (U mL ⁻¹ of cell suspension)
β -glucosidase	0.0035	± 0.0001
protease	0.0108	± 0.0003
cellulase	0.0350	± 0.0010
α -amylase	0.0038	± 0.0001

β -Glucosidase and cellulase are extracellular enzymes of *T. salinum*. The residual activity of β -glucosidase in the *T. salinum* cell suspension after 10 min of homogenization was detected to be 150% (the enzyme activity was 0.5250 U mL⁻¹ of cell suspension), and it remained unchanged until 40 min of homogenization time, when by prolonging the homogenization time, a decrease in β -glucosidase activity was detected. A similar trend was observed for cellulase. Cellulases are of great interest in the field of organic acids and biotechnology industries. They have remarkable applications in areas such as alternate energy, detergent, textile, food, the pharmaceutical industry, nutrition and the agriculture industry.⁵¹ The reason for a decline in the residual activity of β -glucosidase and cellulase after a longer homogenization time could lie in the denaturation of both enzymes as a result of longer exposure to shear forces.

3. 4. Influence of Homogenization Time on Residual Activity of Various Enzymes from the *W. Ichthyophaga* Cell Suspension

Wallemia belongs to the cosmopolitan xerophilic fungi and can be found in habitats with low a_w and high concentrations of toxic inorganic ions.⁵⁰ When a fungal cell is exposed to a high salinity environment, it uses common molecular mechanisms as well as specific molecular mechanisms to react rapidly to the consequent loss of water. In *W. ichthyophaga* and *H. werneckii*, this is achieved by the synthesis of glycerol.⁵²

The *W. ichthyophaga* cell suspension was homogenized from 10 to 100 min, and the residual activity of α -amylase, β -glucosidase, protease and cellulase vs. the time of homogenization was studied (Figure 6).

Initial activity of the studied enzymes in *W. ichthyophaga* cell suspension before homogenization are presented in Table 3 and were set to the value of 100%.

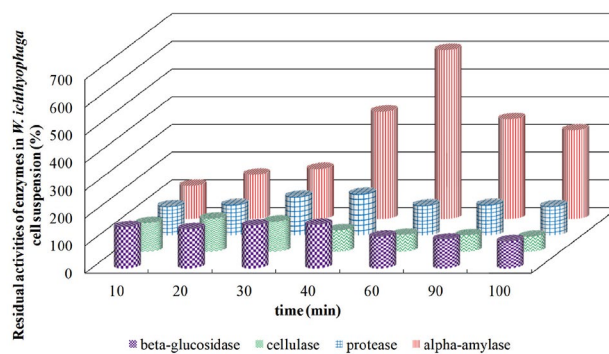


Figure 6: Residual activity of various enzymes in the *W. ichthyophaga* cell suspension in relation to homogenization time at 35 °C and a homogenization speed of 25,000 rpm. Experiments were repeated three times. Standard deviation for all measurements was less than $\pm 3\%$.

Table 3: Initial activity of various enzymes in the *W. ichthyophaga* cell suspension before homogenization and standard deviation of measurements (SD).

Enzyme	Enzyme activity (U mL ⁻¹ of cell suspension)	SD (U mL ⁻¹ of cell suspension)
β -glucosidase	0.0279	± 0.0008
protease	0.0082	± 0.0002
cellulase	1.2200	± 0.0317
α -amylase	0.0074	± 0.0002

With the increase in homogenization time, the activity of the intracellular enzymes α -amylase, cellulase and protease also increased. The highest residual activity of α -amylase (610%), which is equivalent to an enzyme activity of 4.5140 U mL⁻¹ of cell suspension, was detected after 60 min of homogenization, and with a further increase in homogenization time, its residual activity decreased. A slight increase in the activity of protease from 0 to 40 min homogenization time and cellulase from 0 to 20 min was also observed. *W. ichthyophaga* cells are obviously rich in α -amylase, while concentrations of the other enzymes were much lower. An increase in homogenization time up to 100 min caused a rapid decrease in all enzyme activity. Longer exposure to shear forces resulted in conformation changes to the proteins' molecular structure, which led to their activity loss.

3. 5. Influence of Homogenization Time on Residual Activity of Various Enzymes from the *H. Werneckii* Cell Suspension

The living environments of *H. werneckii* are seawater and natural or man-made saltpans with reduced water activity⁵³, but it can also be present in house dust.⁵⁴ It is a halophilic species with the capacity to survive in environments with high salt concentrations (3–30% NaCl). This microorganism has been used as a model for conditions of extremotolerance studies (e.g. oxidative stress, osmotic ad-

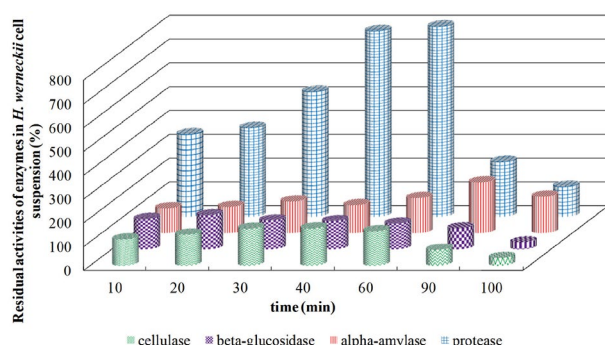


Figure 7: Residual activity of various enzymes in the *H. werneckii* cell suspension in relation to homogenization time at 35 °C and a homogenization speed of 25,000 rpm. Experiments were repeated three times. Standard deviation for all measurements was less than $\pm 3\%$.

aptation and melanisation).^{55–57} The influence of homogenization time on residual activity of selected enzymes in the *H. werneckii* cell suspension was studied (Figure 7).

Initial activity of the enzymes in the *H. werneckii* cell suspension before homogenization are presented in Table 4 and were set to the value of 100%.

Table 4: Initial activity of various enzymes in the *H. werneckii* cell suspension before homogenization and standard deviation of measurements (SD).

Enzyme	Enzyme activity (U mL ⁻¹ of cell suspension)	SD (U mL ⁻¹ of cell suspension)
β -glucosidase	0.0042	± 0.0001
protease	0.0164	± 0.0004
cellulase	0.0320	± 0.0008
α -amylase	0.0029	± 0.0001

An immense increase in residual activity of protease was detected in the *H. werneckii* cell suspension (800%), which is equivalent to the enzyme activity of 13.1200 U mL⁻¹ of cell suspension, after 60 min of homogenization. As expected, with the increase in homogenization time, the viability of *H. werneckii* cells decreased, and intracellular enzymes were released in the cell suspension. Among the selected enzymes, *H. werneckii* cells contain mostly protease (intracellular enzyme).⁵⁰ Proteases are among the three largest groups of industrial enzymes and represent about 60% of the total worldwide sale of enzymes, where approximately 40% of sales comprise microbial proteases.⁵⁸

A slight increase in the residual activity of α -amylase in the *H. werneckii* cell suspension in relation to homogenization time was also detected. The highest residual activity of α -amylase was observed after 90 min of homogenization, when the viability of the *H. werneckii* cell was also low (less than 25%, corresponding to the $20 \cdot 10^5$ CFU mL⁻¹). Since α -amylase is an intracellular enzyme,⁵⁰ sufficient destruction of the cell walls was needed to release α -amylase in the cell suspension and, consequently, a higher residual activity was reached after 90 min of homogenization. Obviously, enzymes released in the suspension (α -amylase, as well as protease) were less resistant to mechanical forces, since a rapid decrease in residual activity was determined after only an additional 10 min of homogenization. The highest residual activity of β -glucosidase and cellulase was observed after 10 min and 30 min of homogenization, and with an additional increase in homogenization time, a decrease in their residual activity was also determined.

3. 6. Influence of Homogenization Time on Residual Activity of Various Enzymes from the *P. Triangularis* Cell Suspension

P. triangularis is an obligate halophile meristematic black yeast that can live in humidifiers.⁵⁹ Meristematic growth of the *P. triangularis* cell is slow, and it possesses

very thick, darkly pigmented cell walls.³⁰ The *P. triangularis* cell suspension was treated with a rotor-stator homogenizer to disintegrate the halophilic fungus cells. Residual activity of various enzymes from *P. triangularis* was studied in relation to homogenization time (Figure 8).

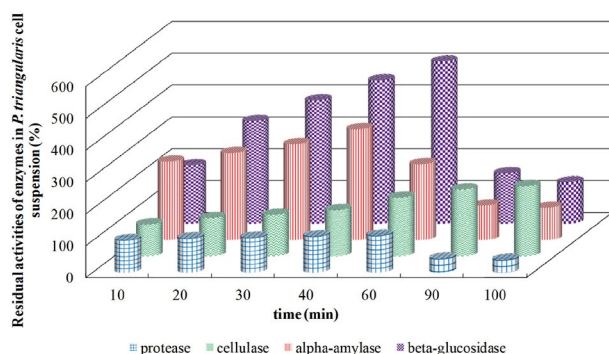


Figure 8: Residual activity of various enzymes in the *P. triangularis* cell suspension in relation to homogenization time at 35 °C and a homogenization speed of 25,000 rpm. Experiments were repeated three times. Standard deviation for all measurements was less than $\pm 3\%$.

Initial activity of the enzymes in the *P. triangularis* cell suspension before homogenization is presented in Table 5 and was set to the value of 100%.

Table 5: Initial activity of various enzymes in the *P. triangularis* cell suspension before homogenization and standard deviation of measurements (SD).

Enzyme	Enzyme activity (U mL ⁻¹ of cell suspension)	SD (U mL ⁻¹ of cell suspension)
β -glucosidase	0.0040	± 0.0001
protease	0.0648	± 0.0019
cellulase	0.0237	± 0.0007
α -amylase	0.0064	± 0.0002

As can be seen from Figure 10, the highest residual activity was detected for β -glucosidase. By prolonging the homogenization time from 10 min to 60 min, an increase in β -glucosidase residual activity was observed, while additional prolongation of the homogenization yielded a decrease in its residual activity. Many bacteria, yeasts and filamentous fungi can produce β -glucosidase,⁶⁰ which is an essential component of the cellulose complex, since it relieves the glucanases from product inhibition by hydrolysing cellobiose to glucose and thus is crucial for rapid and efficient saccharification of cellulose.⁶¹

High residual activity of α -amylase, which is an intracellular enzyme of *P. triangularis*, after only a short time of homogenization indicates that *P. triangularis* has low resistance to mechanical forces (D-value *P. triangularis* was 31.7 min). The cell walls were damaged, resulting in the release of intracellular enzymes into the cell suspension. The

influence of mechanical forces on the released enzymes in the suspension was high, since with an increase in homogenization time, a rapid decrease in their residual activity was detected, except for cellulase, where a slight increase in its residual activity with increase in homogenization time was observed. No significant increase was detected in the residual activity for protease (an extracellular enzyme) after 60 min of homogenization.

Too long exposure of enzymes in the cell suspension to mechanical force may result in enzyme inactivation.

4. Conclusion

The influence of a mechanical cell-disruption method (use of a rotor-stator homogenizer) on the viability of the halophilic fungi *T. salinum*, *W. ichthyophaga*, *H. werneckii* and *P. triangularis* and residual activity of selected enzymes were studied. The homogenization method was successfully used for the destruction of selected halophilic fungi cell walls. The greatest resistance to mechanical forces was observed for the *H. werneckii* cells (D-value = 115.0 min), while the least resistant were the *T. salinum* cells (D-value = 17.0 min). Due to the damage of cell walls, the residual concentration of proteins and residual activity of the intracellular enzymes from extremophilic fungi were increased.

McMillan et al.¹¹ reported about 92.95% efficiency of algae cell disruption using mechanical solid shear, while ultrasonication was less efficient.

Recovery of intracellular enzymes using homogenization is a challenging problem because the released enzymes can be inactivated in the homogenizer. Another challenge is to keep the activity of extracellular enzymes unchanged during the homogenization method, while at the same time obtaining a high level of active intracellular enzymes.

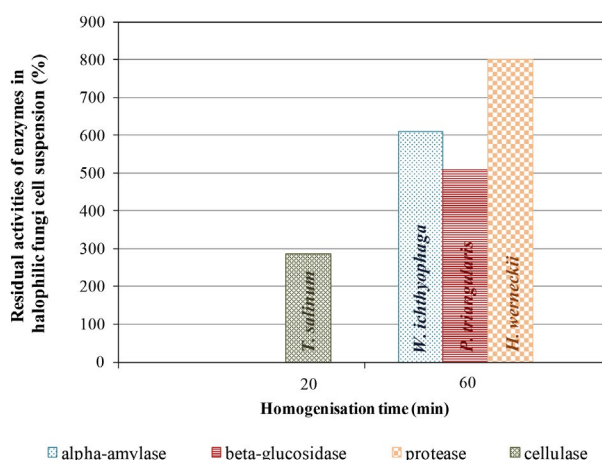


Figure 9: The highest residual activity of α -amylase, β -glucosidase, cellulase and protease obtained in various halophilic fungi cell suspensions vs. optimal homogenization time.

The highest residual activity among the selected enzymes was detected for protease in the *H. werneckii* cell suspension (800%), with 13.1200 U mL⁻¹ of cell suspension, after 60 min of homogenisation time (Figure 9).

Furthermore, the highest residual activity of β -glucosidase in the *P. triangularis* cell suspension (509%) of 2.0360 U mL⁻¹ of cell suspension, and α -amylase in *W. ichthyophaga* cell suspension (610%) of 4.5140 U mL⁻¹ of cell suspension, was also detected after 60 min of cell suspension treatment with the rotor-stator homogenizer. *T. salinum* cells are rich in cellulase, since after 20 min of homogenization, the highest residual activity of cellulase among the tested halophilic fungi was detected in the *T. salinum* cell suspension.

The level of proteins released under variable conditions and with these specific disruption method is usually higher in the case of yeast cells than fungi. Different strengths and structures of the fungal cell walls, which comprise glycoproteins and polysaccharides, mainly glucan and chitin, are the reason for the lower levels of protein released from fungi in comparison to those from yeast.

Due to the diversity of environmental sources of isolation and the cultivation conditions for these individual halophilic fungi, the content of individual enzymes may vary. Therefore, the results of our study did not turn out as expected. Moreover, no standard trend of enzyme release from the cells that would apply to all microbial cells could be determined.

The appropriate time of exposure of the biological material to certain forces causing cell lysis is a critical parameter that could influence the activity of the intracellular compounds. Klimek-Ochab et al.⁵ reported that the prolongation of sonication cycles from 11 to 30s admittedly resulted in a decrease in the amount of proteins released from *P. citrinum*, but allowed a higher level of specific activity of G6P dehydrogenase. In contrast, for the *A. fumigatus* cells, the short period of sonication enables the release of a high amount of protein, and a high specific activity of G6P dehydrogenase was detected.

Table 6 shows the highest residual activity of the enzymes related to viability of the halophilic fungi and residual protein concentration obtained in the cell suspensions.

While the α -amylase in these four halophilic fungi is an intracellular enzyme, whose residual activity increased after exposure to mechanical forces, regardless of the treated fungi, β -glucosidase belongs to the group of extracellular enzymes not exhibiting the expected significant increase in its residual activity after homogenization. Nevertheless, its residual activity significantly increased when the cells from *P. triangularis* were disrupted by the homogenization method. Most likely, the β -glucosidase in this fungus is located on the inner edge of the cell wall, and only after exposure to shear forces is released from the cell wall, which is reflected in the increase in its residual activity. Consequently, no uniform estimate of the content and activity of each enzyme can be given, and results thus did not turn out as mostly expected.

An essential first step in the enzyme extraction process from a microbial cell is its rupture. Homogenization is an important and widespread method for acquiring intracellular enzymes and organelles from microbial, plant and animal sources. It enables extraction of intracellular substances without the presence of solvents or other chemicals to break down the cell wall.

Although some studies of cell wall disintegration and extraction of intracellular components privilege the use of non-mechanical methods and advise the use of a homogenizer for fungus cell disruption, it has been demonstrated that even using mechanical methods such as homogenization, many intracellular enzymes from the halophilic fungal cells can be released while their activity is maintained.

Extremophiles such as *T. salinum*, *W. ichthyophaga*, *H. werneckii* and *P. triangularis* present a source of chemically diverse and often novel metabolites and proteins (e.g. enzymes such as protease, α -amylase, β -glucosidase and cellulase) which are interesting for food and pharmaceutical industry and offer new catalytic alternatives for industrial applications and represent the basis for the development of environmentally friendly, efficient, sustainable and cleaner industrial technologies.

Therefore, obtained results represent significant new findings, which are of broad biotechnological importance and are especially interesting for industrial application and useful also for a wider scientific sphere working in bio-

Table 6: Correlation between the viability of halophilic fungi, residual protein concentration and residual enzyme activity for selected enzymes (α -amylase, β -glucosidase, cellulase and protease) in the halophilic fungi cell suspensions.

Halophilic fungi	α -amylase			β -glucosidase			cellulase			protease		
	RPC (%)	VHP (%)	REA (%)	RPC (%)	VHP (%)	REA (%)	RPC (%)	VHP (%)	REA (%)	RPC (%)	VHP (%)	REA (%)
<i>T. salinum</i>	245	0.15	440	185	2	158	150	44	290	178	7	240
<i>W. ichthyophaga</i>	230	8	610	100	100	100	150	47	120	220	13	150
<i>H. werneckii</i>	226	25	213	175	87	143	206	61	156	210	47	800
<i>P. triangularis</i>	280	14	348	296	4	509	330	0.1	220	296	4	116

Legend: RPC (%) – Residual protein concentration (%); VHP (%) – Viability of halophilic fungi (%); REA (%) – Residual enzyme activity (%). Red color – intracellular enzyme; Blue color – extracellular enzyme

technology on protein purification. Based on the obtained results, studied halophilic fungi contain industrial important enzymes with high catalytic activity which can be released from the cells with a cheap and simple method and are suitable for different industrial applications as batch or continuous operations e.g. reduction of mixed wastes, leading in reduction of environmental impacts.

5. Acknowledgments

The authors acknowledge the financial support of the Slovenian Research Agency (research core funding No. P2-0046 – “Separation Processes and Product Design”). Special thanks goes to Prof. Dr. Nina Gunde-Cimerman, University of Ljubljana, Biotechnical Faculty, Slovenia for the donation of halophilic fungi. The authors would like to thank Kaja Grobelnik, Laura Kolednik, Jadranka Švigelj and Marko Kresnik for technical support.

6. References

- R. C. Kuhad, A. Singh, K. K. Tripathi, R. K. Saxena, K. E. Eriksson, *Nutr. Rev.* **1997**, *55*, 65–75. DOI:10.1111/j.1753-4887.1997.tb01599.x
- Y. Chisti, M. Mooyoung, *Enzyme Microb. Technol.* **1986**, *8*, 194–204. DOI:10.1016/0141-0229(86)90087-6
- S. Goldberg, *Methods Mol. Biol.* Clifton NJ, 2008, **424**, 3–22. DOI:10.1007/978-1-60327-064-9_1
- In: M. C. Flickinger (Ed.): Downstream industrial biotechnology recovery and purification, John Wiley & Sons Inc., Hoboken, N.J., **2013**.
- M. Klimek-Ochab, M. Brzezińska-Rodak, E. Żymanić-Duda, B. Lejczak, P. Kafarski, *Folia Microbiol. (Praha)* **2011**, *56*, 469–475. DOI:10.1007/s12223-011-0069-2
- D. Liu, X.-A. Zeng, D.-W. Sun, Z. Han, *Innov. Food Sci. Emerg. Technol.* **2013**, *18*, 132–137. DOI:10.1016/j.ifset.2013.02.006
- L. E. N. Ekpeni, K. Y. Benyounis, F. F. Nkem-Ekpeni, J. Stokes, A. G. Olabi, *Energy* **2015**, *81*, 74–83. DOI:10.1016/j.energy.2014.11.038
- M. Sudar, D. Valinger, Z. Findrik, D. Vasic-Racki, Z. Kurtanek, *Appl. Biochem. Biotechnol.* **2013**, *169*, 1039–1055. DOI:10.1007/s12010-012-0056-3
- J. Geciova, D. Bury, P. Jelen, *Int. Dairy J.* **2002**, *12*, 541–553. DOI:10.1016/S0958-6946(02)00038-9
- R. Halim, R. Harun, M. K. Danquah, P. A. Webley, *Appl. Energy* **2012**, *91*, 116–121. DOI:10.1016/j.apenergy.2011.08.048
- J. R. McMillan, I. A. Watson, M. Ali, W. Jaafar, *Appl. Energy* **2013**, *103*, 128–134. DOI:10.1016/j.apenergy.2012.09.020
- J. R. Kar, R. S. Singhal, *Biotechnol. Rep.* **2015**, *5*, 89–97. DOI:10.1016/j.btre.2014.12.005
- B. Ozbek, K. O. Ulgen, *Process Biochem.* **2000**, *35*, 1037–1043. DOI:10.1016/S0032-9592(00)00141-2
- A. Middelberg, *Biotechnol. Adv.* **1995**, *13*, 491–551. DOI:10.1016/0734-9750(95)02007-P
- C. R. Thomas, J. D. Stenson, Z. Zhang, in: S. Muller, T. Bley (Eds.): High Resolution Microbial Single Cell Analytics, Springer-Verlag Berlin, Berlin, **2011**, vol. 124, pp. 83–98. DOI:10.1007/10_2010_84
- D. Liu, L. Ding, J. Sun, N. Boussetta, E. Vorobiev, *Innov. Food Sci. Emerg. Technol.* **2016**, *36*, 181–192. DOI:10.1016/j.ifset.2016.06.017
- P. Dhankhar, *IOSR J. Eng.* **2014**, *4*, 01–08.
- C. Gostinčar, M. Grube, S. De Hoog, P. Zalar, N. Gunde-Cimerman, *FEMS Microbiol. Ecol.* **2009**, *71*, 2–11. DOI:10.1111/j.1574-6941.2009.00794.x
- B. Xi, K. J. Wise, J. A. Stuart, R. R. Birge, in: V. Renugopalakrishnan, R. V. Lewis (Eds.): Bionanotechnology, Springer, Dordrecht, **2006**, pp. 39–59. DOI:10.1007/978-1-4020-4375-8_4
- R. Margesin, F. Schinner, *Extrem. Life Extreme Cond.* **2001**, *5*, 73–83. DOI:10.1007/s007920100184
- M. Lenassi, J. Zajc, C. Gostinčar, A. Gorjan, N. Gunde-Cimerman, A. Plemenitas, *Fungal Biol.* **2011**, *115*, 959–970. DOI:10.1016/j.funbio.2011.04.001
- S. Jancic, P. Zalar, D. Kocev, H.-J. Schroers, S. Dzeroski, N. Gunde-Cimerman, *Fungal Divers.* **2016**, *76*, 97–118. DOI:10.1007/s13225-015-0333-x
- N. Gunde-Cimerman, J. Ramos, A. Plemenitas, *Mycol. Res.* **2009**, *113*, 1231–1241. DOI:10.1016/j.mycres.2009.09.002
- M. Kralj Kuncic, J. Zajc, D. Drobne, Z. Pipan Tkalec, N. Gunde-Cimerman, *Fungal Biol.* **2013**, *117*, 466–478. DOI:10.1016/j.funbio.2013.04.003
- P. Zalar, G. S. de Hoog, N. Gunde-Cimerman, *Stud. Mycol.* **1999**, 57–62.
- T. Kogej, A. A. Gorbushina, N. Gunde-Cimerman, *Mycol. Res.* **2006**, *110*, 713–724. DOI:10.1016/j.mycres.2006.01.014
- M. Turk, A. Plemenitas, N. Gunde-Cimerman, *Fungal Biol.* **2011**, *115*, 950–958. DOI:10.1016/j.funbio.2011.04.006
- K. Sterflinger, D. Tesei, K. Zakharova, *Fungal Ecol.* **2012**, *5*, 453–462. DOI:10.1016/j.funeco.2011.12.007
- M. J. Najafzadeh, V. A. Vicente, J. Sun, J. F. Meis, G. S. De Hoog, *Fungal Biol.* **2011**, *115*, 1066–1076. DOI:10.1016/j.funbio.2011.06.007
- T. Kogej, M. H. Wheeler, T. L. Rizner, N. Gunde-Cimerman, *Fems Microbiol. Lett.* **2004**, *232*, 203–209. DOI:10.1016/S0378-1097(04)00073-4
- A. Carlson, M. Signs, L. Liermann, R. Boor, K. Jem, *Biotechnol. Bioeng.* **1995**, *48*, 303–315. DOI:10.1002/bit.260480403
- M. Bradford, *Anal. Biochem.* **1976**, *72*, 248–254. DOI:10.1016/0003-2697(76)90527-3
- C. V. Sapan, R. L. Lundblad, N. C. Price, *Biotechnol. Appl. Biochem.* **1999**, *29*, 99–108.
- P. Nicolas, V. L. Lassalle, M. L. Ferreira, *Enzyme Microb. Technol.* **2017**, *97*, 97–103. DOI:10.1016/j.enzmictec.2016.11.009
- M. A. Redmile-Gordon, E. Armenise, R. P. White, P. R. Hirsch, K. W. T. Goulding, *Soil Biol. Biochem.* **2013**, *67*, 166–173. DOI:10.1016/j.soilbio.2013.08.017
- M. Čolnik, M. Primožič, Ž. Knez, M. Leitgeb, *Front. Bioeng. Biotechnol.* **2016**, *4*, 33. DOI:10.3389/fbioe.2016.00033
- P. Manas and R. Pagan, *J. Appl. Microbiol.* **2005**, *98*, 1387–1399. DOI:10.1111/j.1365-2672.2005.02561.x

38. A. Firon, G. Lesage, H. Bussey, *Curr. Opin. Microbiol.* **2004**, *7*, 617–623. DOI:10.1016/j.mib.2004.10.015
39. F. M. Klis, A. Boorsma, P. W. J. De Groot, *Yeast* **2006**, *23*, 185–202. DOI:10.1002/yea.1349
40. M. Leitgeb, M. Čolnik, M. Primožič, P. Zalar, N. G. Cimerman, Ž. Knez, *J. Supercrit. Fluids* **2013**, *78*, 143–148. DOI:10.1016/j.supflu.2013.03.029
41. M. K. Kuncic, T. Kogej, D. Drobne, N. Gunde-Cimerman, *Appl. Environ. Microbiol.* **2010**, *76*, 329–337. DOI:10.1128/AEM.02318-09
42. J. D. Nosanchuk, R. E. Stark and A. Casadevall, *Front. Microbiol.* **2015**, *6*.
43. S. M. Bowman, S. J. Free, *Bioessays* **2006**, *28*, 799–808. DOI:10.1002/bies.20441
44. R. Hassan, A. Husin, S. Sulong, S. Yusoff, M. F. Johan, B. H. Yahaya, C. Ang, S. Ghazali, S. K. Cheong, *Malays. J. Pathol.* **2015**, *37*, 165–173.
45. R. Visvanathan, C. Jayathilake, R. Liyanage, *Food Chem.* **2016**, *211*, 853–859. DOI:10.1016/j.foodchem.2016.05.090
46. Y. J. Yoo, J. Hong, R. T. Hatch, *Biotechnol. Bioeng.* **1987**, *30*, 147–151. DOI:10.1002/bit.260300120
47. A. Sundarram, T. P. K. Murthy, *J. Appl. Environ. Microbiol.* **2014**, *2*, 166–175.
48. S. Afrisham, A. Badoei-Dalfard, A. Namaki-Shoushtari, Z. Karami, *J. Mol. Catal. B Enzym.* **2016**, *132*, 98–106. DOI:10.1016/j.molcatb.2016.07.002
49. P. M. de Souza, P. de Oliveira Magalhães, *Braz. J. Microbiol.* **2010**, *41*, 850–861. DOI:10.1590/S1517-83822010000400004
50. P. Zalar, G. S. de Hoog, H. J. Schroers, J. M. Frank, N. Gunde-Cimerman, *Antonie Van Leeuwenhoek Int. J. Gen. Mol. Microbiol.* **2005**, *87*, 311–328.
51. S. Shajahan, I. G. Moorthy, N. Sivakumar, G. Selvakumar, *J. King Saud Univ. – Sci.* **2017**, *29*, 302–310.
52. A. Plemenitas, M. Lenassi, T. Konte, A. Kejzar, J. Zajc, C. Gostinčar, N. Gunde-Cimerman, *Front. Microbiol.* **2014**, *5*, 199.
53. P. Zalar, G. S. de Hoog, N. Gunde-Cimerman, *Stud. Mycol.* **1999**, 38–48.
54. H. Uezato, M. Gushi, K. Hagiwara, S. Kayo, A. Hosokawa, S. Nonaka, *J. Dermatol.* **2006**, *33*, 23–29. DOI:10.1111/j.1346-8138.2006.00004.x
55. U. Petrovic, *Fems Yeast Res.* **2006**, *6*, 816–822. DOI:10.1111/j.1567-1364.2006.00063.x
56. T. Kogej, M. Stein, M. Volkmann, A. A. Gorbushina, E. A. Galinski, N. Gunde-Cimerman, *Microbiol.-Sgm* **2007**, *153*, 4261–4273. DOI:10.1099/mic.0.2007/010751-0
57. A. Bonifaz, H. Badali, G. S. de Hoog, M. Cruz, J. Araiza, M. A. Cruz, L. Fierro, R. M. Ponce, *Stud. Mycol.* **2008**, 77–82. DOI:10.3114/sim.2008.61.07
58. In: T. Godfrey, J. Reichelt (Eds.): *Industrial enzymology: the application of enzymes in industry*, Macmillan, London, **1983**.
59. G. S. de Hoog, H. Beguin, W. H. B. de Vegte, *Antonie Van Leeuwenhoek* **1997**, *71*, 289–295. DOI:10.1023/A:1000156820793
60. A. Abdella, T. E.-S. Mazeed, A. F. El-Baz, S.-T. Yang, *Process Biochem.* **2016**, *51*, 1331–1337. DOI:10.1016/j.procbio.2016.07.004
61. S. Chamoli, P. Kumar, N. K. Navani, A. K. Verma, *Int. J. Biol. Macromol.* **2016**, *85*, 425–433. DOI:10.1016/j.ijbiomac.2016.01.001

Povzetek

Trimatostroma salinum, *Walleimia ichthyophaga*, *Hortaea werneckii* in *Phaeothea triangularis* so halofilne glive, ki lahko uspevajo v širokem razponu slanosti. Predstavljajo vir dragocenih bioaktivnih spojin, encimov in beljakovin, ki so zanimivi za živilsko in farmacevtsko industrijo. Za ločevanje encimov iz celic halofilnih gliv smo uporabili mehansko metodo. Dobljeni rezultati in nova spoznanja so pomembna z biotehnoškoga vidika, saj je ločevanje encimov v obliki koktajla iz halofilnih gliv zanimivo za industrijsko uporabo, zlasti za kaskadne reakcije. Encimi iz ekstremofilov imajo namreč izboljšane lastnosti in se lahko uporabljajo v težkih pogojih, pri katerih se lahko neekstremofilni encimi deaktivirajo.

Scientific paper

Characterization and Atmospheric Implication of Hydrotrioxy Radical-Water-Methylamine-Formic Acid-Sulphuric Acid Complexes

Matjaž Dlouhy and Antonija Lesar*

Department of Physical and Organic Chemistry, Jožef Stefan Institute, Jamova c. 39, SI-1000 Ljubljana, Slovenia

* Corresponding author: E-mail: antonija.lesar@ijs.si

Received: 10-26-2018

Presented at the 24th Annual Meeting of the Slovenian Chemical Society

Abstract

New particle formation is an important source of atmospheric aerosols, but the nucleation phenomena is still poorly understood. Here the formation of bimolecular complexes of HOOO• radical with H₂O, CH₃NH₂, HCOOH and H₂SO₄ has been investigated by quantum chemical methods. The stabilising effect of methylamine is found to be close to that of sulphuric acid, both complexes are formed spontaneously at studied atmospheric conditions. In addition, the hydration of the four most stable 1:1 complexes forming the 1:1:1 complexes have been considered. Water stabilises a HOOO•...H₂SO₄ complex, the most effectively. Complexation process is spontaneous as well. Complex formations induced significant red-shift and enhancement of the IR intensity for the OH stretching vibration relative to that of the free radical. Equilibrium constants have been examined and the relative abundance of complexes in the troposphere is discussed.

Keywords: Hydrotrioxy radical; atmospheric acids; amine; water; nucleation precursors; quantum chemistry

1. Introduction

Hydrotrioxy (HOOO•) radical, or hydridotrioxygen according to IUPAC nomenclature,¹ belongs to the group of polyoxides with general molecular formula, RO_nR, where R stands for hydrogen, any other atom or chemical group and $n \geq 3$.^{2,3} It is believed that such polyoxides, especially the HOOO• radical, play an important role in atmospheric processes in Earth's troposphere and environmental reactions as well as in biological oxidation reactions.⁴ Hence the understanding of its structure, stability and reactivity with other atmospheric species is a matter of the utmost importance.

The HOOO• radical can be regarded as an adduct of HO• and O₂, and represents a temporary reservoir of OH• radicals.⁵ Many theoretical and experimental data suggest that the formation of HOOO• radical in the atmosphere can be described by the following reactions^{5,6}:



Reaction 3 is exothermic with the activation energy of around 3 kcal mol⁻¹ implying that a certain amount of the radical is indeed formed.⁶

The first mention of the hydrotrioxy radical dates back to the 1970's and ever since it has been a subject of *pomum Eridis*.⁷ Despite its long postulated existence, the HOOO• radical was inadvertently predicted in 1996 by Speranza⁸ and was first detected three years later by Cacace et al.⁹ in the gas phase experiments based on neutralization-reionization/collisionally activated dissociation mass spectrometry. At the turn of the millennium, Nelander et al.¹⁰ investigated and detected HOOO• radical in argon matrices using infrared spectroscopy. A few years later, in 2005 Suma et al.¹¹ reported the rotational spectrum and structure of the radical. Their experimental study was the first to confirm the planar geometry of the radical, suggesting *trans*-HOOO• conformation with inner O–O bond length of 1.688 Å.

Numerous theoretical studies on the structure and stability of the radical have been published, but there is still no consensus on its planar structure (*cis*-HOOO• or *trans*-HOOO•) as the quantum chemical calculations are strongly dependent on the level of theoretical method and basis sets used in the calculations.^{1,4,12,13,14}

HOOO• is a reactive molecule and can form complexes by interaction with other species present in the atmosphere. Recent works of Kim et al.¹⁵ show that the hydrated radical may be 20 to 500 times more stable compared to the isolated HOOO• structure. Furthermore, Cannon et al.¹⁶ have reported that the radical forms a stable binary and ternary complexes with water and sulphuric acid, which are up to 800 times more stable than the isolated radical.

Water is the most abundant species in the atmosphere, its concentration varies between 1–4 %¹⁷, and can form strong hydrogen bonds with other molecules and radical species. Such interactions can lead to the formation of new atmospheric particles that serve as a predecessors of secondary aerosols.^{18,19} In addition to the water, sulphuric acid is the main molecular species in new particle formation.¹⁹ Many recent studies reported the importance of gaseous amines (especially methyl-, dimethyl- and trimethylamine) in nucleation processes.¹⁶ Nucleation is enhanced also by organic compounds, formic acid is an important trace constituent of the troposphere.¹⁸ The abundance of these species varies, but experimental data proposes that the concentration of sulphuric acid and methylamine is hovering around 1×10^7 molecule cm^{-3} ^{18,20}, while a concentration of formic acid is higher, around 2×10^{11} molecule cm^{-3} ¹⁸. Their concentration can significantly increase in urban and industrial areas (up to a few orders of magnitude) and varies pretty much by daytime and season.²⁰

In this paper we have performed a study on electronic structure calculations of possible conformations of the hydrotrioxy radical and its complexes with water, sulphuric acid, methylamine and formic acid molecules. Further, the hydration of the most stable 1:1 complexes were investigated. Based on these calculations, we reported valuable properties of complexes, such as the equilibrium structure, stability, the nature of interaction between each component and the IR spectral features. Thermodynamic properties of the clusters were calculated at four temperatures relevant to the atmospheric conditions. The computed Gibbs free energies were used to estimate the relative concentration of the formed complexes.

2. Computational Methods

All calculations were performed out with the GAUSSIAN 16 software package²¹ using default convergence criteria. Equilibrium geometry of monomers and complexes were optimised using the Becke three-parameter non-local exchange functional with the non-local correlation of Lee, Yang, and Parr (B3LYP)^{22,23} and the People-type 6-311++G(3df,3pd)²⁴ basis set. The harmonic and anharmonic frequencies of all species were computed at the same level of theory in order to confirm the nature of the stationary points. The final energies of the complexes were improved by a multi-step composite method using the CBS-QB3 level of theory.²⁵ The selection of above

methods was based on the comparison of test calculations for hydrotrioxy radical, and available experimental structural, spectroscopic and binding parameters. These calculations included B3LYP, M06-2X²⁶ density functional methods and CCSD(T) wave function method²⁷ in combination with the 6-311++G(2df,2pd), 6-311++G(3df,3pd) and aug-cc-pVDZ basis sets. The results of these computations are summarised in the next section.

Binding energy (D_0) of the complexes has been estimated as a negative difference between the zero-point corrected energy of the complexes ($E_{0, \text{complex}}$) and monomers ($E_{0, \text{monoi}}$). Specifically, for three-body complex the equation is written as:

$$D_0 = -(E_{0, \text{complex}} - E_{0, \text{mono1}} - E_{0, \text{mono2}} - E_{0, \text{mono3}}). \quad (4)$$

Thermochemical parameters, i.e. Gibbs free energies, are calculated at four atmospherically relevant conditions: at the surface, 298.15 K and 278.15 K, 1atm; at altitude 5km, 255.15 K, 0.533 atm and at altitude 8 km, 235.15 K, 0.351 atm. Further, the equilibrium constants, K_c , of the complex formations were calculated according to equation 5:

$$K_c(T) = \sigma \frac{10^3 RT}{N_A} e^{-\frac{\Delta G_T}{RT}}. \quad (5)$$

In this equation σ is the symmetry number, R is the universal gas constant, T is the temperature, N_A is the Avogadro's number and ΔG_T is the complex formation Gibbs free energy change.

3. Results and Discussion

Let us first consider the HOOO• radical, the optimised structures of *cis* and *trans* conformations denoted as c-HTO and t-HTO, respectively, are presented in Figure 1 with the atom enumeration. Our calculations confirm that both conformations exhibit planar geometry. Due to a very low isomerization energy barrier the rotation around inner O²–O³ bond is nearly spontaneous.

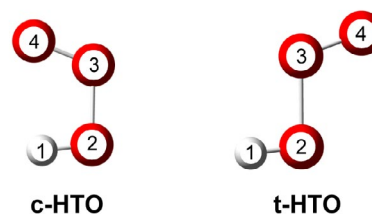


Figure 1: Optimised structures of *cis*-HOOO• (c-HTO) and *trans*-HOOO• (t-HTO) configuration of radical.

Structural parameters obtained at different levels of theory are summarised in Table 1. Calculated values for bond lengths and angles are in good agreement with available experimental data also presented in the Table. In general, c-HTO has longer bond lengths and narrower angles in

Table 1: Optimised geometry parameters for c-HTO and t-HTO. Bond distances are given in Å and angles in degrees. For comparison, experimental data are included.

Method/basis set:	$d(\text{H}^1\text{O}^2)$	$d(\text{O}^2\text{O}^3)$	c-HTO		
			$d(\text{O}^3\text{O}^4)$	$\alpha(\text{H}^1\text{O}^2\text{O}^3)$	$\alpha(\text{O}^2\text{O}^3\text{O}^4)$
M06-2X/aug-cc-pVTZ	0.973	1.434	1.251	100.8	111.6
B3LYP/aug-cc-pVTZ	0.974	1.505	1.250	99.9	112.7
B3LYP/6-311++G(2df,2pd)	0.973	1.503	1.249	100.0	112.7
B3LYP/6-311++G(3df,3pd)	0.973	1.501	1.247	99.9	112.7
CCSD(T)/ aug-cc-pVTZ	0.973	1.500	1.241	99.8	111.9
t-HTO					
M06-2X/aug-cc-pVTZ	0.969	1.458	1.240	100.0	109.4
B3LYP/aug-cc-pVTZ	0.971	1.546	1.233	98.5	110.2
B3LYP/6-311++G(2df,2pd)	0.970	1.454	1.232	98.6	110.2
B3LYP/6-311++G(3df,3pd)	0.970	1.544	1.230	98.6	110.2
CCSD(T)/ aug-cc-pVTZ	0.970	1.542	1.231	100.2	109.1
experiment ^a	0.913	1.684	1.235	92.4	110.7
experiment ^b	0.972	1.688	1.225	90.0	111.0
experiment ^c	0.970	–	1.208	–	–

^a McCathy et al., FTMW spectrometry¹, ^b Suma et al., FTMW spectrometry¹¹, ^c Huber et al., Photoionization mass spectrometry²⁸

comparison to the same parameters in t-HTO. Interestingly, for inner O²–O³ bond length we detected largest differences between calculated and experimental values, absolute deviation is between 0.14 Å and 0.25 Å. Calculations at B3LYP/6-311++G(3df,3pd) show good agreement with available experimental data for t-HTO, even for the most variable inner bond length, with a discrepancy of around 8 %.

Calculated binding energies for both stable conformations of the radical are represented in Table 2. The energy difference between them is rather small, but D_0 is strongly dependent on the method and basis set used for calculations. Results computed at M06-2X/aug-cc-pVTZ level show no correlation between experimental and computed value. Pople's B3LYP method, CCSD(T) method and CBS-QB3 composite method show a stronger correlation with the experiment, with the latter being the most reliable. At the CBS-QB3 level of calculation t-HTO is slightly more stable, by 0.12 kcal mol⁻¹, than the *cis* conformation. The predicted energy difference is at the limit of computational accuracy, and for this reason, we decided to take both stable conformations into account in our study.

Table 2: Binding energies (D_0 ; eq. 4) in kcal mol⁻¹ for c-HTO and t-HTO.

Method/basis set:	c-HTO	t-HTO
M06-2X/aug-cc-pVTZ	1.23	1.36
B3LYP/aug-cc-pVTZ	3.07	3.20
B3LYP/6-311++G(2df,2pd)	2.82	2.94
B3LYP/6-311++G(3df,3pd)	2.80	2.88
CCSD(T)/ aug-cc-pVTZ	2.71	2.83
CBS-QB3	2.69	2.81
experiment ^a	–	2.94

^a Picard et al., CRESU experiment²⁹

Harmonic and anharmonic frequencies for both configurations of the radical along with the IR absorption intensities at the B3LYP/6-311++G(3df,3pd) level of theory are presented in Table 3 and graphically illustrated in Figures S1 and S2 of Supplementary Material. The radical has six different vibrational modes. The comparison between calculated harmonic and anharmonic vibrational frequencies shows that OH stretching absorption peaks for t-HTO and c-HTO differ for 160 cm⁻¹ and 166 cm⁻¹, respectively; while all the others are shifted to higher energies on average by 24 cm⁻¹ in t-HTO and 31 cm⁻¹ in c-HTO. Calculated anharmonic frequencies for t-HTO and c-HTO show reasonable agreement with observed gas-phase spectra. Predicted HO stretching peak in t-HTO appears 13 cm⁻¹ lower than experimentally observed; implying that the calculated OH stretching mode for the complexes should be adequate. The differences between anharmonic and experimental values for other vibrations are slightly more significant.

3.1 Structure, Intramolecular Interaction and Binding Energy

Binary complexes

A systematic sampling was used to search for global minima of the complexes. Nearly a hundred initial guess structures were generated where all rational interaction of radical with water (W), methylamine (MA), formic acid (FA) and sulphuric acid (SA) molecules were considered. After full geometry optimization and on the basis of the Boltzmann probability distributions two stable low-energy structures for the HTO-W, two for HTO-MA, six for HTO-FA and three for HTO-SA complexes were identified. All these structures are shown in Supplementary Material, Figure S3, while the most stable structure for each type of com-

Table 3: B3LYP/6-311++G(3df,3pd) calculated harmonic and anharmonic frequencies (ν) in cm^{-1} and IR absorption intensities (I) in km mol^{-1} of *c*-HTO and *t*-HTO. Available experimental values are given.

	Mode:	harmonic		anharmonic		experimenta
		ν	I	ν	I	ν
t-HTO	H ¹ O ² srt.	3742	70	3582	59	3569
	O ³ O ⁴ str.	1389	22	1353	36	–
	H ¹ O ² O ³ bend.	1239	136	1199	113	1202
	O ² O ³ O ⁴ bend.	659	64	636	53	482
	O ² O ³ str.	460	76	445	74	244
	H ¹ O ² O ³ O ⁴ tor.	183	109	193	98	129
c-HTO	H ¹ O ² srt.	3687	49	3521	42	–
	O ³ O ⁴ str.	1413	72	1362	72	–
	H ¹ O ² O ³ bend.	1240	12	1219	8	–
	O ² O ³ O ⁴ bend.	715	150	691	138	–
	O ² O ³ str.	463	19	450	22	–
	H ¹ O ² O ³ O ⁴ tor.	230	106	163	93	148

^a Murray et al., values for isolated radical in gas-phase³⁰

plex is illustrated in Figure 2. The binding energies D_0 , are given in the figure to present the complex's stability.

***c*-HTO-*W* complex.** After complexation a planar structure of radical moiety in the complex is preserved. The inner O–O bond in the radical unit is shortened by 0.03 Å compared to that in the isolated radical. The hydrogen atom from the radical and the electron rich oxygen atom from the water molecule form one strong H-bond with the length of 1.782 Å. Our calculated binding energy for this structure is 4.80 kcal mol⁻¹, which is in good agreement with the previously reported value of 4.86 kcal mol⁻¹ by Kim et al.¹⁵

***c*-HTO-*MA* complex.** The formation of a binary complex between *c*-HTO and MA forced the radical out of a planar geometry. The inner O–O bond in the *c*-HTO-MA complex is shortened by 0.04 Å in comparison to the isolated radical. The hydrogen bond, 1.725 Å in length, is formed between the hydrogen atom from the radical and the nitrogen atom of the methylamine. Binding energy of this complex is 9.85 kcal mol⁻¹.

***c*-HTO-*FA* complex.** Due to the interaction between *c*-HTO and FA, the radical moiety undergoes a structural change, its geometry in the complex is no longer planar and

the inner bond is shortened by 0.05 Å. The complex is found to be of a cyclic structure with two H-bonds. A shorter hydrogen bond, 1.734 Å, is formed between the carbonyl oxygen atom of the formic acid and the hydrogen atom of the radical, but the radical can also act as a proton acceptor, resulting in a second H-bond, 1.885 Å, with the acid proton. The calculated binding energy for this complex is 8.14 kcal mol⁻¹.

***t*-HTO-*SA* complex.** When *t*-HTO interacts with SA, the inner O–O bond in the HOOO moiety of the complex is by 0.03 Å shorter than that in the free radical. Two H-bonds with the length of 1.790 Å and 2.080 Å are formed resulting in a cyclic structure with a planar *t*-HTO unit in the complex. In the shorter H-bond SA acts as a proton donor while in the second, rather longer H-bond, the hydroxyl oxygen atom from the radical interacts with a lone oxygen electron pair of SA. Our calculated binding energy for this structure is 10.09 kcal mol⁻¹, which is in good agreement with the previously reported value of 10.00 kcal mol⁻¹ by Cannon et al.¹⁶

Ternary complexes

In addition, we carried out an extensive search of a possible structure of the ternary complexes formed by hy-

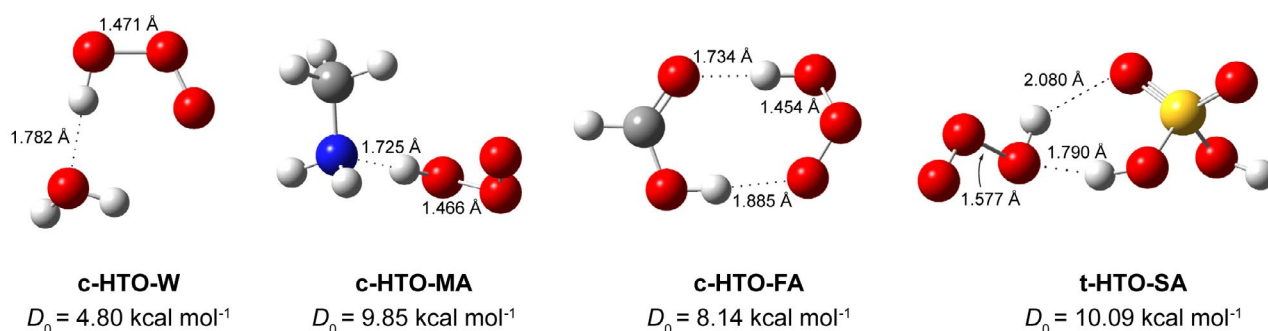


Figure 2: Optimised structures of the most stable *c*-HTO-*W*, *c*-HTO-*MA*, *c*-HTO-*FA* and *t*-HTO-*SA* complexes with the B3LYP/6-311++G(3d-f,3pd) bond lengths and the CBS-QB3 binding energies. Dotted lines represent intermolecularly formed H-bonds.

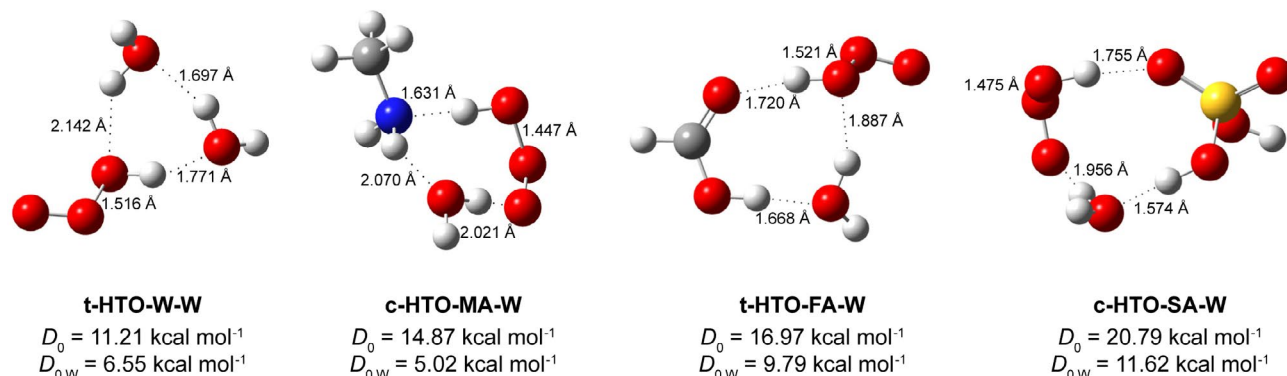


Figure 3: Optimised structures of the most stable t-HTO-W-W, c-HTO-MA-W, t-HTO-FA-W and c-HTO-SA-W complexes with the B3LYP/6-311++G(3df,3pd) bond lengths and the CBS-QB3 binding energies. Dotted lines represent intermolecularly formed H-bonds.

dration of the four stable binary complexes described above. Around two hundred initial guess structures were full geometry optimised and three, five, three and six stable low-energy structures of the HTO-W, HTO-MA, HTO-FA and HTO-SA complexes with water, respectively, were selected. The identified most stable structures of the HTO-W-W, HTO-MA-W, HTO-FA-W and HTO-SA-W are shown in Figure 3, whereas all structures are found in Figure S4 of the Supplementary Material. The binding energies D_0 and $D_{0,W}$ displayed in the figure are related to the monomer interaction process and the process of hydration of corresponding binary complex, respectively.

t-HTO-W-W complex. In the most stable ternary complex the conformation of the hydrotrioxy radical unit is changed to the *trans* arrangement compared to that in the most stable binary structure being *cis* (c-HTO-W). The inner O–O bond of the radical subunit is approximately 0.03 Å shorter than that in the isolated radical. Three H-bonds are formed by the association of the radical with two water molecules. The shortest H-bond with a length of 1.697 Å is formed between two water molecules. Next, the 1.771 Å long H-bond is a result of an interaction between the radical proton and the lone electron pair of oxygen from the water molecule. The longest H-bond at 2.142 Å results from an interaction of the hydroxyl radical oxygen atom being an electron acceptor and water hydrogen being a proton donor. t-HTO-W-W is quite stable with a binding energy of 11.21 kcal mol⁻¹. When comparing energies of the ternary complex and the corresponding binary one, we observe that the additional water molecule contributes around 6.55 kcal mol⁻¹ to the stability of the t-HTO-W-W complex.

c-HTO-MA-W complex. *Cis* configuration of the radical moiety is retained in the hydrogenation of the HTO-MA complex. The radical inner O–O bond is again shortened by 0.05 Å. The c-HTO-MA-W complex is a cyclic structure with three H-bonds. The shortest intermolecular H-bond at 1.631 Å results from an interaction between the radical hydrogen and the electron rich amino nitrogen atom. The water molecule acts as an H-donor to

the terminal radical oxygen atom, and as an H-acceptor from the amine group, the formed H-bonds are 2.021 and 2.070 Å long, respectively. Further, calculated binding energy for this complex related to the monomer interaction process is 14.87 kcal mol⁻¹, whereas the additional water contributes 5.02 kcal mol⁻¹ to the stability of the complex.

t-HTO-FA-W complex. The hydrotrioxy radical moiety in the complex changes the orientation of atoms when the water molecule is added to the binary HTO-FA complex. The inner O–O bond is shortened by 0.02 Å. Three stable intermolecular bonds are formed, resulting in an eight-membered ring structure. The water molecule acts as a proton donor and proton acceptor and forms two 1.887 Å and 1.668 Å long H-bonds, respectively. The lone electron pair on the carbonyl oxygen atom participates in the 1.720 Å long H-bond with the hydrogen atom from the HOOO subunit. The binding energy is predicted to be 16.96 kcal mol⁻¹. Additional water stabilises the most stable HTO-FA complex even further, by 9.06 kcal mol⁻¹.

c-HTO-SA-W complex. Similar to the t-HTO-W-W and t-HTO-FA-W complexes, the radical moiety changes the orientation in comparison to the corresponding binary complex. As in all the other cases, the inner O–O bond in the HTO unit is shortened, in this case by 0.03 Å. A strong H-bond, 1.574 Å long, is formed between the hydrogen atom of SA and the lone electron pair on the water oxygen atom, whereas the H-bond with the acid being a proton acceptor is 1.755 Å long. The third intermolecular H-bond is longer, 1.956 Å, where water acts as the proton donor and terminal oxygen contributes a lone electron pair to the bond. The c-HTO-SA-W complex with the binding energy of 20.79 kcal mol⁻¹ is predicted to be the most stable ternary structure reported in this study. Water stabilises the HTO-SA significantly, as it contributes 11.62 kcal mol⁻¹ to the stability of the c-HTO-SA-W complex.

3. 2. Vibrational Spectra

The complete set of harmonic and anharmonic frequencies with IR absorption intensities calculated at

B3LYP/6-311++G(3df,3pd) level of theory for the both HOOO• conformers and the precursor molecules is collected in Table S1 of the Supplementary Material, where available experimental data for gas-phase molecules of precursors are given for comparison. Figures 4 and 5 show harmonic vibrational spectra for the four most stable binary and the four most stable ternary complexes, respectively.

The intermolecular interactions in complex formation induced new degrees of freedom and consequently new intermolecular vibrational modes which are not present in monomer spectra. An examination of the calculated data shows that the frequencies and IR absorption intensities of H-bonded OH stretching regions are the most significantly affected by complexation. As expected, a large frequency red-shift is mainly observed for vibration of OH bonds involved in H-bond formation.

Binary complexes

c-HTO-W complex. The complex has 15 fundamental vibrational modes, 6 of them are related to the free radical and three are related to modes in an isolated water molecule. The remaining six are present due to intermolecular interactions. The most noticeable change in the IR

spectrum is a red-shift of 314 cm^{-1} related to the OH stretching of the HOOO• radical subunit. This stretching vibration is decreased to 3207 cm^{-1} in the complex relative to the 3521 cm^{-1} in the isolated *c*-HTO, while the intensity of the transition increases to the maximum in the spectra of the complex.

c-HTO-MA complex. This particular complex has even more vibrational modes due to more participating atoms and bonds in the complex formation. When the OH group from the radical subunit in the complex is compared to the isolated HOOO•, it is seen that frequency is red-shifted by 472 cm^{-1} and is accompanied by a substantial increase in IR absorption.

c-HTO-FA complex. When the anharmonic vibrational frequencies of the OH symmetric stretch mode of cyclic *c*-HTO-FA is considered, a shift of 454 cm^{-1} to the red region of the spectra with increased intensity is observed. The OH vibration of the formic acid subunit is also shifted to the higher energy by 229 cm^{-1} .

t-HTO-SA complex. In this complex, the OH stretching vibration of the enol HTO and sulphuric acid subunits are also red-shifted compared to the isolated monomers, the shifts are 150 cm^{-1} and 537 cm^{-1} , respectively.

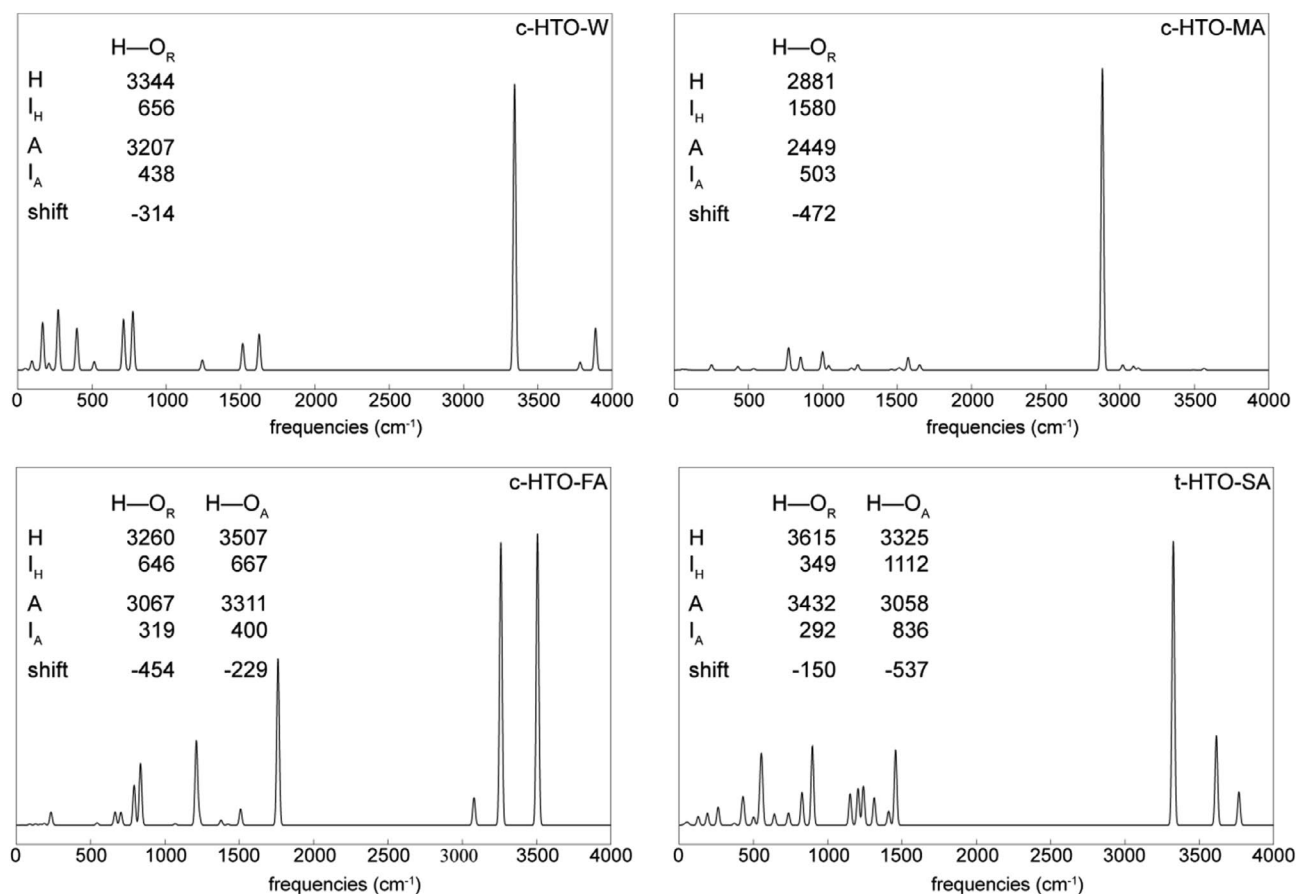


Figure 4: B3LYP/6-3++1G(3df,3pd) calculated IR absorption spectra for the most stable binary complexes. Graphs represent the harmonic absorption spectra, while in the inserted tables the relevant harmonic and anharmonic absorption peaks as well as calculated shifts of anharmonic frequencies in cm^{-1} are summarised.

Ternary complexes

In general, ternary complexes have even more vibrational modes due to the three body molecules interactions forming stable complexes.

t-HTO-W-W complex. The radical and both water OH stretching frequencies are moderately red-shifted; the shifts are 419 cm^{-1} , 198 cm^{-1} and 87 cm^{-1} compared to the OH symmetric stretching motions of the radical and water subunits. The vibrational modes are all accompanied by increased intensity.

c-HTO-MA-W complex. The most pronounced change in the vibrational spectrum of the complex with regard to the isolated species is the 419 cm^{-1} red-shift of the OH anharmonic stretching frequency in the HOOO moiety. The OH and NH stretching of the water and amine moieties are decreased only by 87 cm^{-1} and 48 cm^{-1} , respectively, implying the less strong participation of water and amino groups in the bonding.

t-HTO-FA-W complex. When the OH-stretching anharmonic frequencies of the OH-stretching in the t-HTO-FA-W complex are considered and compared to the isolated species, the red-shifts of 671 cm^{-1} , 511 cm^{-1} and 237 cm^{-1} are observed for the OH modes of the radical, formic

acid and water moiety, respectively, all involved in the H-bond formation.

c-HTO-SA-W complex. In this specific complex, shifts in three OH vibrational modes are observed due to participation in the H-bond formation. The OH stretching in HOOO moiety is shifted by 304 cm^{-1} . Sulphuric acid OH bond related vibration is decreased by 30 cm^{-1} , and symmetric OH vibrational mode of water moiety is red-shifted by 180 cm^{-1} .

Evaluated data provides strong evidence that the complex formation of the hydrotrioxy radical with water, methylamine, formic acid and sulphuric acid introduces new intermolecular vibrations. The vibration frequencies of those OH bonds that participate in H-bonding interaction are generally shifted to lower frequencies, while their intensity absorption bands strongly increase. The other modes in the complexes are similar to that in the isolated monomers.

3. 3. Atmospheric Implication

Binding energies are important parameters related to the stability of the complexes formed, and the vibrational

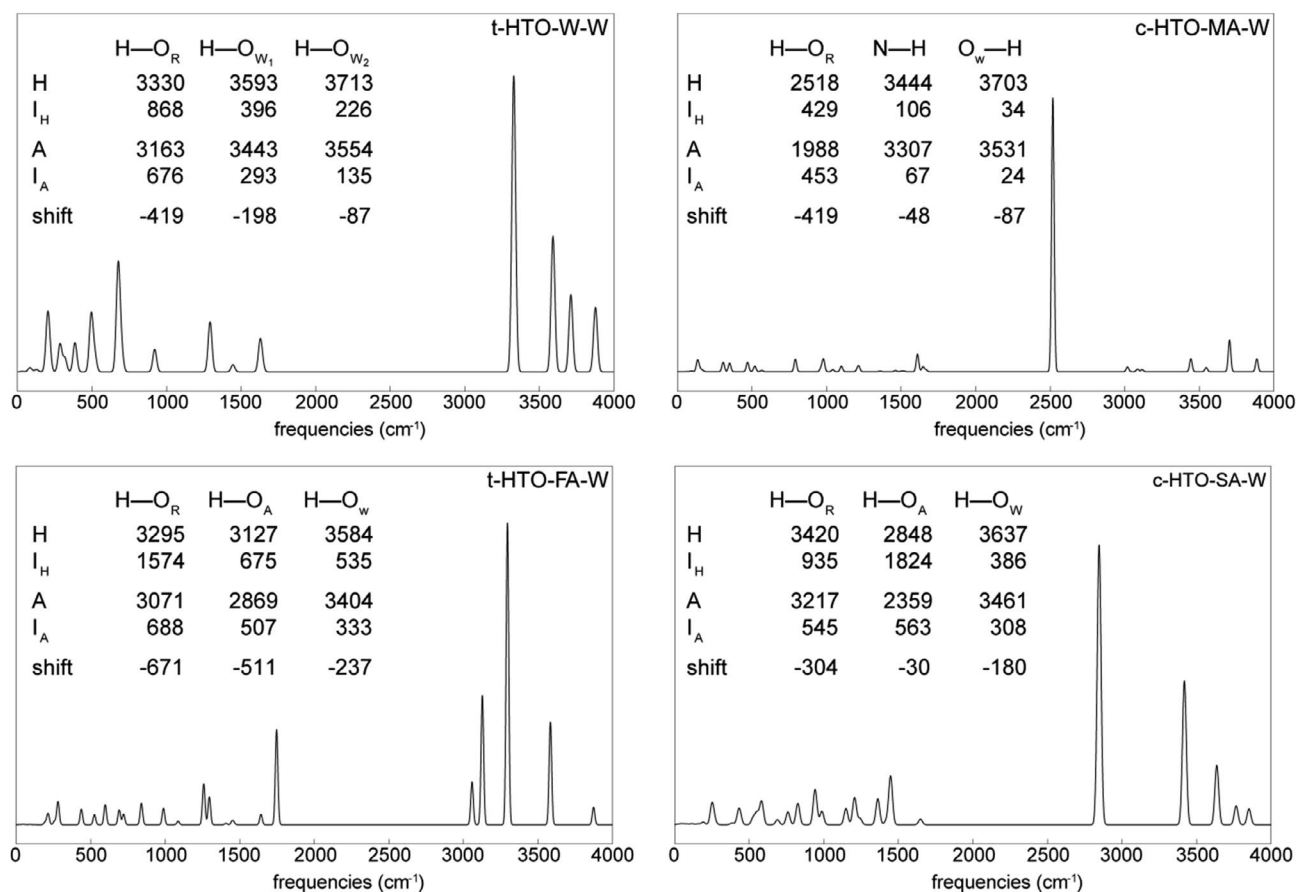


Figure 5: B3LYP/6-311++G(3df,3pd) calculated IR absorption spectra for the most stable ternary complexes. Graphs represent harmonic absorption spectra, while in the inseted tables the relevant harmonic and anharmonic absorption peaks as well as calculated shifts for anharmonic frequencies in cm^{-1} are summarised.

Table 4: Thermodynamic properties (ΔH , $T\Delta S$ and ΔG) in kcal mol⁻¹ and calculated K_c values in cm³ molecules⁻¹ at different altitude (h) [km], temperature (T) [K] and pressure (p) [atm].

Complex	h	T	p	ΔH	$T\Delta S$	ΔG	K_c
Binary Complexes							
c-HTO-W	0	298.15	1	-5.42	-8.40	2.98	2.8×10^{-22}
	0	278.15	1	-5.44	-7.84	2.40	5.1×10^{-22}
	5	255.15	0.533	-5.46	-7.53	2.07	6.1×10^{-22}
	8	236.15	0.351	-5.47	-7.18	1.71	8.8×10^{-22}
c-HTO-MA	0	298.15	1	-9.94	-9.24	-0.70	1.4×10^{-19}
	0	278.15	1	-9.97	-8.64	-1.33	4.4×10^{-19}
	5	255.15	0.533	-9.99	-8.25	-1.74	1.1×10^{-18}
	8	236.15	0.351	-10.01	-7.84	-2.16	3.4×10^{-18}
c-HTO-FA	0	298.15	1	-8.37	-10.29	1.92	1.7×10^{-21}
	0	278.15	1	-8.40	-9.63	1.23	4.3×10^{-21}
	5	255.15	0.533	-8.44	-9.19	0.75	8.3×10^{-21}
	8	236.15	0.351	-8.47	-8.72	0.26	1.9×10^{-20}
t-HTO-SA	0	298.15	1	-10.02	-9.45	-0.56	1.1×10^{-19}
	0	278.15	1	-10.06	-8.86	-1.20	3.5×10^{-19}
	5	255.15	0.533	-10.10	-8.49	-1.61	8.8×10^{-19}
	8	236.15	0.351	-10.13	-8.08	-2.05	2.7×10^{-18}
Ternary Complexes							
t-HTO-W-W	0	298.15	1	-12.66	-18.04	5.38	4.8×10^{-24}
	0	278.15	1	-12.70	-16.86	4.16	2.1×10^{-23}
	5	255.15	0.533	-12.72	-16.13	3.41	4.4×10^{-23}
	8	236.15	0.351	-12.74	-15.33	2.59	1.3×10^{-22}
c-HTO-MA-W	0	298.15	1	-15.59	-18.29	2.70	4.5×10^{-22}
	0	278.15	1	-15.65	-17.12	1.47	2.8×10^{-21}
	5	255.15	0.533	-15.71	-16.40	0.69	9.3×10^{-21}
	8	236.15	0.351	-15.75	-15.61	-0.14	4.5×10^{-20}
t-HTO-FA-W	0	298.15	1	-17.94	-19.69	1.75	2.2×10^{-21}
	0	278.15	1	-17.99	-18.42	0.43	1.8×10^{-20}
	5	255.15	0.533	-18.04	-17.58	-0.46	8.9×10^{-20}
	8	236.15	0.351	-18.07	-19.69	-1.38	6.3×10^{-19}
c-HTO-SA-W	0	298.15	1	-21.45	-18.89	-2.56	3.2×10^{-18}
	0	278.15	1	-21.50	-17.67	-3.83	4.1×10^{-17}
	5	255.15	0.533	-21.55	-16.69	-4.66	3.6×10^{-16}
	8	236.15	0.351	-21.58	-16.06	-5.53	4.4×10^{-15}

spectra provide valuable data for laboratory and atmospheric identification. To provide insightful information into the atmospheric relevance of the complexes the thermochemical properties have also to be evaluated.

The enthalpy (ΔH), entropy ($T\Delta S$) and Gibbs free energy (ΔG) changes for global minimum structures of binary and ternary complexes were calculated as a difference between the values for the complex and infinity separated constituents. These quantities at different atmospheric conditions as noted in the introduction section together with calculated K_c values according to the equation 5 are gathered in Table 4.

An inspection of the table illustrates that both the binary and ternary complex formations are exothermic processes at all studied conditions. The ΔH value decreases

with increasing atmospheric height, but according to the ΔG value, not all processes are spontaneous. The c-HTO-MA and t-HTO-SA binary complexes, are spontaneously formed at all conditions with $\Delta G_{236.15} = -2.16$ kcal mol⁻¹ and -2.05 kcal mol⁻¹, respectively. Only the c-HTO-SA-W ternary complex is formed spontaneously at all studied altitudes with $\Delta G_{236.15} = -5.53$ kcal mol⁻¹, while c-HTO-MA-W and t-HTO-FA-W have a negative Gibbs free energy value at higher levels of the troposphere. K_c values of the complexes increase with height, probably due to lower pressure and lower concentration of the reactive species. From the equilibrium constants and the gas-phase concentration of molecular species, we have evaluated relative abundance of the particular binary complexes. The reported atmospheric concentrations at 298 K are as fol-

lows: $[\text{H}_2\text{O}] = 8 \times 10^{17}$ molecules cm^{-3} ¹⁷, $[\text{CH}_3\text{NH}_2] = 1 \times 10^7$ molecules cm^{-3} ²⁰, $[\text{HCOOH}] = 2 \times 10^{11}$ molecules cm^{-3} ¹⁸ and $[\text{H}_2\text{SO}_4] = 1 \times 10^7$ molecules cm^{-3} ¹⁸. For example, 0.002 % of the $\text{HO}\text{O}\cdot$ radical is bounded into the c-HTO-W complex at the Earth's surface, while only 4×10^{-4} % of the radical forms a binary complex with water at an altitude of 8 km and 100 % relative humidity. For other complexes the values of relative abundance can go as far as ten decades lower than those calculated for water.

Figure 6 illustrates the computed equilibrium constants at the different temperatures at the ground level and different altitudes of the Earth's atmosphere for the all spontaneous processes. The equilibrium constants for the formation of the bimolecular t-HTO-SA and c-HTO-MA complexes are comparable. A formation of the ternary c-HTO-SA-W complex from monomes appears to be more favourable than the hydration of binary c-HTO-SA complex. The equilibrium constant for the hydration of binary complexes is one decade lower than for the monomer interaction process resulting in the same ternary c-HTO-SA-W complex formation. Thermodynamic quantities for the hydration process of binary complexes are listed in the Table S2 of the Supplementary Material.

drotrioxy radical with lengths of around 1.75 Å, while the complexes with both acids have a cyclic structure with two H-bonds, the second H-bonds are somewhat longer. The binding energies of complexes with methylamine and sulphuric acid are comparable, they approach to 10 kcal mol⁻¹. The addition of water to the most stable dimer complexes resulted in multiple H-bonded cyclic structures with H-bonds of lengths between 1.6 Å and 2.1 Å and stabilised the most effectively the complex with sulphuric acid, with binding energy of 20.8 kcal mol⁻¹.

The present calculations confirmed that large spectral red-shift and enhancement of IR intensities could be used for spectroscopic identification in the atmosphere. In particular, the most substantial red-shift of 671 cm⁻¹ is observed for the H-bonded OH stretching vibrational mode of HOOO moiety in the hydrated complex involved formic acid.

From the calculated thermodynamic quantities, it should be concluded that a binary complex with methylamine and sulphuric acid, and a ternary complex with sulphuric acid are all formed spontaneously at the Earth's surface to the height of 8 km in the troposphere. Equilibrium constants of the complexes increase with increasing altitude.

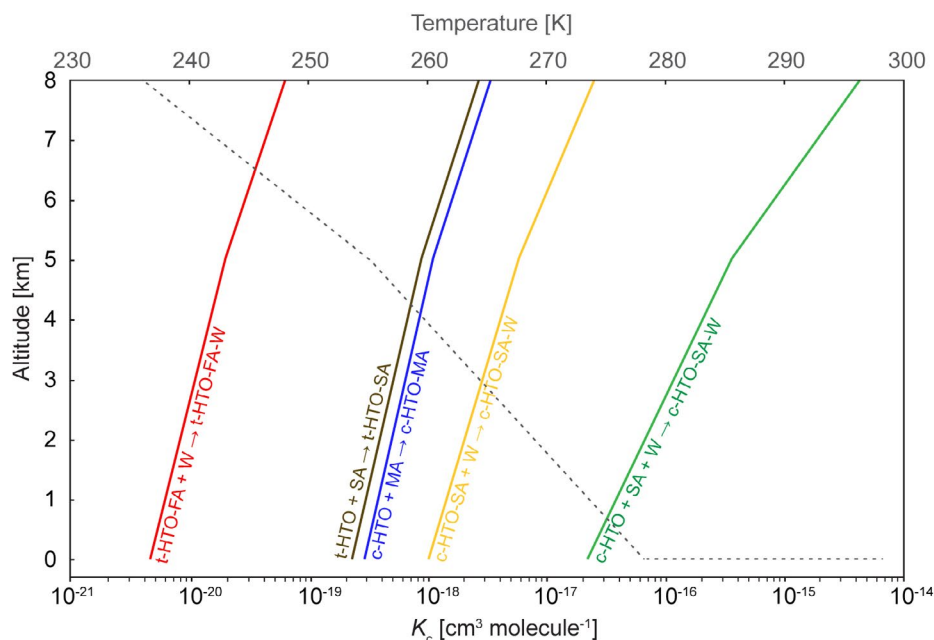


Figure 6: Calculated equilibrium constants, K_c , as a function of the altitude of Earth's atmosphere for the formation of selected processes indicated along each curve on the figure above. The dashed line represents a variation of temperature.

4. Conclusion

The hydrogen-bonded complexes of hydrotrioxy radical with water, methylamine, formic acid and sulphuric acid were studied using the B3LYP/6-311++G(3df,3pd) and CBS-QB3 methods. Our results indicate that due to the negligible energy difference, 0.1 kcal mol⁻¹, either the *cis* or *trans* isomer is involved in the complexation. Water and methylamine formed one strong H-bond with the hy-

5. Acknowledgment

This research was funded by the Slovene Research Agency, Program grant number P2-0393 and, partly, PR-08976. M. D. is grateful to prof. Tomaž Urbič for his contribution to the master's work.

6. References

1. M. C. McCarthy et al., *J. Chem. Phys.* **2012**, *136*, 034303. DOI:10.1063/1.3673875
2. D. G. Semes'ko, S.L. Khursan, *Russ. J. Phys. Chem. A* **2008**, *82*, 1277–1282. DOI:10.1134/S0036024408080074
3. K. Bhattacharjee, P. K. Shukla, *Struct. Chem.* **2018**, *29*, 1109–1118. DOI:10.1007/s11224-018-1095-3
4. S. Chalmet, M. F. Ruiz-Lopez, *Chem. Phys. Chem.* **2006**, *7*, 463–467. DOI:10.1002/cphc.200500326
5. S. L. Khursan, *PATAI'S Chem. of Func. Group* **2014**, *1*, 1–72.
6. C. Murray, E. L. Derro, T. D. Sechler, M. I. Lester, *Acc. Chem. Res.* **2008**, *42*, 419–427. DOI:10.1021/ar8001987
7. R. J. Blint, M. D. Newton, *J. Chem. Phys.* **1973**, *59*, 6220–6228. DOI:10.1063/1.1680001
8. M. Speranza, *Inorg. Chem.* **1996**, *35*, 6140–6151. DOI:10.1021/ic960549s
9. F. Cacace, G. De Petris, F. Pepi, A. Troiani, *Science* **1999**, *285*, 81–82. DOI:10.1126/science.285.5424.81
10. B. Nelander, A. Engdahl, T. Svensson, *Chem. Phys. Lett.* **2000**, *332*, 403–408. DOI:10.1016/S0009-2614(00)01280-X
11. K. Suma, Y. Sumiyoshi, Y. Endo, *Science* **2005**, *308*, 1885–1886. DOI:10.1126/science.1112233
12. J. M. Anglada, S. Olivella, A. Sole, *J. Chem. Theory Comput.* **2010**, *6*, 2743–2750. DOI:10.1021/ct100358e
13. J. M. Beames, et al., *J. Chem. Phys.* **2011**, *134*, 044304. DOI:10.1063/1.3518415
14. M. C. McCarthy, et al., *J. Chem. Phys.* **2012**, *136*, 034303. DOI:10.1063/1.3673875
15. J. M. Kim, S. Y. Hong, S. J. Kim, *J. Korean Chem. Soc.* **2015**, *59*, 387–396. DOI:10.5012/jkcs.2015.59.5.387
16. D. Cannon, T. Tuttle, J. Koller, B. Plesničar, *Comput. Theor. Chem.* **2013**, *1010*, 19–24. DOI:10.1016/j.comptc.2013.01.009
17. M. B. McElroy: The atmospheric environment: effects of human activity. Princeton University Press, Princeton, United States, **2002**, pp. 205–211.
18. R. Zhang et al., *Science* **2004**, *304*, 1487–1490. DOI:10.1126/science.1095139
19. L. Yao et al., *Science* **2018**, *361*, 278–281. DOI:10.1126/science.aao4839
20. F. Yu, G. Luo, *Atmos. Chem. Phys.* **2014**, *14*, 12455–12464. DOI:10.5194/acp-14-12455-2014
21. M. J. Frisch et al., Gaussian 16, Revision B.01. Gaussian, Inc., Wallingford CT, **2016**.
22. C. Lee, W. Yang, R. G. Parr, *Phys. Rev. B* **1988**, *37*, 785–789. DOI:10.1103/PhysRevB.37.785
23. B. Miehlich, A. Savin, H. Stoll, H. Preuss, *Chem. Phys. Lett.* **1989**, *157*, 200–206. DOI:10.1016/0009-2614(89)87234-3
24. Krishnan, J. S. Binkley, R. Seeger, J. A. Pople, *J. Chem. Phys.* **1980**, *7*, 650–654. DOI:10.1063/1.438955
25. J. A. Montgomery, M. J. Frisch, J. W. Ochterski, G. A. Petersson, *J. Chem. Phys.* **1999**, *110*, 2822–2827. DOI:10.1063/1.477924
26. Y. Zhao, D. G. Truhlar, *Acc. Chem. Res.* **2008**, *41*, 157. DOI:10.1021/ar700111a
27. K. Raghavachari, G. W. Trucks, J. A. Pople, M. Head-Gordon, *Chem. Phys. Lett.* **1989**, *157*, 479–483. DOI:10.1016/S0009-2614(89)87395-6
28. K. P. Huber, G. Herzberg: Molecular Spectra and Molecular Structure, Van Nostrand Reinhold Company, New York, United States, **1979**, pp. 463. DOI:10.1007/978-1-4757-0961-2
29. S. D. Le Picard et al., *Science* **2010**, *328*, 1258–1262. DOI:10.1126/science.1184459
30. C. Murray, E. L. Derro, T. D. Sechler, M. I. Lester, *J. Phys. Chem. A* **2007**, *111*, 11592. DOI:10.1021/jp071473w

Povzetek

Delo povzema študij kompleksov hidrotrioksi radikala z vodo, metilaminom, mravljinčno kislino in žveplovo kislino z metodama B3LYP/6-311++G(3df, 3pd) in CBS-QB3. Rezultati kažejo, da je razlika energije med *cis* in *trans* izomero radikala le 0,1 kcal mol⁻¹, zato smo obe izomeri vključili v preučevanje kompleksov. Voda in metilamin sta v interakciji z radikalom tvorili eno močno H-vez z dolžino okoli 1,75 Å, medtem ko imata kompleksa z obema kislinama ciklično strukturo z dvema H-vezema, dolžini druge H-vezi v kompleksih pa sta nekoliko daljši. Vezavni energiji kompleksov z metilaminom in žveplovo kislino sta med seboj primerljivi, približujeta se 10 kcal mol⁻¹. Dodana molekula vode najbolj stabilnim dimernim kompleksom vodi do tvorbe cikličnih struktur z več H-vezmi z dolžinami med 1,6 in 2,1 Å. Najbolj se stabilizirana kompleks z žveplovo kislino, njegova vezavna energija je 20,8 kcal mol⁻¹.

Z izračuni anharmonskih frekvenc smo pokazali, da je komplekse v ozračju mogoče identificirati z IR spektroskopijo. Zlasti velik premik v rdeči del spektra, pomik 671 cm⁻¹, se pojavi pri OH-nazteznem nihanju v hidratiranem kompleksu z mravljinčno kislino. Na osnovi izračunananih termodinamskih količin zaključimo, da se binarna kompleksa z metilaminom in žveplovo kislino ter kompleks z žveplovo kislino in vodo tvorijo spontano od površja zemlje do višine 8 km v troposferi. Ravnotežne konstante kompleksov naraščajo z večanjem nadmorske višine.

Scientific paper

Determination of Dissolved Iron Redox Species in Freshwater Sediment using DGT Technique Coupled to BDS

Hanna Budasheva,^{1,*} Aleksander Kravos,² Dorota Korte,¹ Arne Bratkič,^{3,4} Yue Gao³ and Mladen Franko¹

¹ University of Nova Gorica, Laboratory for Environmental and Life Sciences, Vipavska 13, SI-5000 Nova Gorica, Slovenia

² University of Ljubljana, Faculty of Chemistry and Chemical Technology, Večna pot 113, SI-1000 Ljubljana, Slovenia

³ Vrije Universiteit Brussel, Analytical, Environmental and Geo-Chemistry, Boulevard de la Plaine 2, 1050 Brussels, Belgium

⁴ Université de Liège, Chemical Oceanography Unit, Allée du 6 Août 17, 4000 Liège, Belgium

* Corresponding author: E-mail: hanna.budasheva@ung.si
+386 70 718 204

Received: 11-13-2018

Abstract

In this work we have developed a novel method for determination of iron redox species by the use of diffusive gradients in thin-film (DGT) technique coupled to photothermal beam deflection spectroscopy (BDS). The combination of both methods achieved low limit of detection (LOD) of 0.14 μM for Fe (II) ions. The total Fe concentration determined in the Vrtojba river sediment (Slovenia, Rožna Dolina, 5000 Nova Gorica) was 49.3 μgL^{-1} . The Fe (II) and Fe (III) concentration amounted to 12.8 μgL^{-1} and 39.9 μgL^{-1} , respectively. Such an approach opens new opportunities for monitoring the content of iron species in natural waters and sediments and provides highly sensitive chemical analysis and an accurate qualitative and quantitative characteristic of the materials under study.

Keywords: Beam deflection spectroscopy; diffusive gradients in thin-film technique; iron redox species; photothermal techniques; sediment

1. Introduction

Metals in trace amounts are natural components of the environment, but at high concentrations they can become toxic to living organisms since they act as conservative pollutants. All trace elements (including iron, Fe) that are essential for supporting various life processes have a fairly narrow “concentration window” between their biogenic and toxic levels. Iron is a vital constituent of plant life since it is essential for photosynthetic and respiratory electron transport, nitrate reduction, chlorophyll synthesis, and detoxification of reactive oxygen species.¹ At low concentrations, Fe plays an important role in metabolic and fermentation processes, as an enzyme activator, stabilizer and functional component of proteins, and may be limiting for growth of organisms. Its redox state will also have influence on being available for the uptake.

Human populations in areas contaminated by iron and other heavy metals could be significantly exposed to

these contaminants due to their bioaccumulation properties. They can accumulate in bone, hair and in some soft tissues, such as the liver, kidney and lungs. Prolonged exposure and high concentration levels can lead to heart disease, the development of cancer, as well as other complications such as arthritis, diabetes or liver disease.²

As a result of these health concerns various methods have been developed for determination of iron concentration in the environmental samples, including UV-Vis spectrophotometry,³ atomic absorption spectrometry,⁴ ion chromatography⁵ and high-performance liquid chromatography.⁶ Unfortunately, the information about the bioavailable fraction content of its redox species is very difficult to measure and is in most cases lacking, although it is very important for understanding Fe toxicity.^{7,8} This is partly due to complex Fe geochemistry; either of the two redox states (Fe(II), Fe(III)) may be present in various

complexes and size fractions (e.g. as truly dissolved, in soluble coordination complexes with inorganic ligands and organic ligands, or in a variety of colloidal and/or particulate forms). Investigation of the fractions accessible to biota (bioavailable) is often hampered by their extremely low environmental concentrations, which requires the use of contamination-prone detection methods (e.g. voltammetry and potentiometry).^{9–11} Studying Fe cycling in the environment is further complicated also because the distribution of its chemical species often changes during sampling and storage. Since the above methods are not sensitive enough to satisfy the requirements associated with detection of ultra-trace amounts of Fe, thus, there is need to develop new sensitive techniques that provide reliable measurement of Fe redox species in natural environments.

Diffusive gradients in thin-film (DGT) technique has been increasingly used for monitoring of environmental pollution due to its robustness, versatility, precision and capacity of pre-concentrating trace-level metal pollutants. In the uptake process, metals diffuse from natural waters through the diffusive layer to the binding layer (commonly Chelex-100 resin), which is selective to transition metals and their species,^{12,13} such as Fe(II) and Fe(III). It is important to point out that DGT technique advantage is capability of pre-concentrating Fe species from the dissolved phase. It samples labile fraction passively, which is without external pressures, sample manipulation, transport, derivations, etc. It provides also a time-average of environmental species concentrations during the deployment time.

In contrast to the above enumerated methods, optothermal methods provide high-sensitivity measurements for spectroscopic characterization and detection of low-absorption transparent samples.^{14–17} The high sensitivity of the optothermal methods has already been repeatedly improved by combining with other methods.^{18–22} In this work the detection of iron species strongly bound in the resin gel was performed by the photothermal beam deflection spectroscopy (BDS).

In the theoretical approach to the coupled DGT-DBS method, an intensity modulated beam of light illuminates (excitation beam EB) the absorbing sample with iron species. As a result of nonradiative deexcitation processes, thermal waves are generated. They diffuse into the sample and the adjacent medium inducing the thermal oscillations (TOs) called the temperature field. Causing the intensity change of another light beam (probe beam PB) passing through the samples adjacent medium and grazing its surface.^{23,24} Intensity changes are correlated to the iron concentration bonded in the examined gel.²⁵ Presumably, the BDS technique would provide a highly sensitive chemical analysis, will be non-invasive and will retain optical and structural characteristics of the sample, thus, offering new possibilities for determination of iron species in natural water environments.

The goal of this work was therefore to couple DGT and BDS methods, and to determine dissolved Fe redox species concentration as well as the amount of dissolved total Fe in the river sediments.

2. Experimental

2. 1. Solutions and Reagents

The solution of 3 mM 1.10-phenanthroline (PHN) was prepared by adding 2.61 g of PHN (Merck) to 5.0 mL of 6 M HCl and dissolving both in 500 mL of double-deionized water (18 MΩ m⁻¹, NANOPURE), then diluted 10-times in 100 mL flasks. While 6 M of hydrochloric acid (HCl) solution was prepared by dissolving 5.9 mL of 32% pure HCl (Sigma-Aldrich) in 10 mL of double-deionized water.

The solution of 5.1 mM of L-ascorbic acid (Sigma-Aldrich) was prepared in 100 mL flask by dissolution of 9 mg of solid L-ascorbic acid in 0.1 M acetic acid. While 0.1 M acetic acid solution was prepared by dissolving 0.6 mL of 99.8% pure acetic acid (Merck) in 100 mL flask and diluted with double-deionized water.

Working solutions of Fe(II) and Fe(III) to construct the calibration curves were prepared using concentrations of 4, 8, 12, 16 and 20 μmol L⁻¹ in 25 mL flasks by proper dilution of stock solution in the double-deionized water (18 MΩ m⁻¹, NANOPURE).

The Fe(II) stock solution was prepared by dissolving 695 mg of ferrous sulphate heptahydrate (FeSO₄ 7H₂O) reagent (Merck) in 250 mL of 0.1 M HCl solutions (Sigma-Aldrich). The Fe(II) concentration of stock solution was than 10 mmol L⁻¹. While the 0.1 M of HCl prepared by dissolving 4.9 mL of 32% HCl in 500 mL of double-deionized H₂O.

The Fe(III) stock solution was prepared by dissolving 677.6 mg of Iron (III) chloride hexahydrate (FeCl₃ 6H₂O) reagent (Riedel de Haen) in 250 mL of 0.1 M HCl solutions. The Fe(III) concentration of stock solution was than 10 mmol L⁻¹.

All reagents and solvents were used as purchased without further purification.

2. 2. Preparation of DGT

The procedure for DGT probe preparation is in depth described elsewhere.²⁶ Briefly, the probe base was overlaid in the following order with 1) ground Chelex-100 resin gel, 2) polyacrylamide diffusive gel (APA, 0.8 mm final thickness) and 3) acid-precleaned 0.45 μm HVLP filter (Millipore). The layers were secured by the probe cover with a fixed-area window for diffusion (Figure 1).

To avoid contamination of the samplers, all used equipment, as well as DGT sediment probes were pre-cleaned in 5% HNO₃. Before assembling DGT sampler, its parts were thoroughly washed with double-deionized wa-

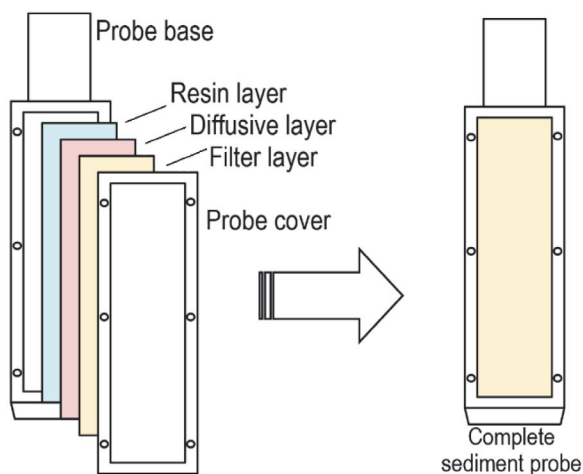


Figure 1. The components and assembled DGT probe for sediment deployment.

ter ($18 \text{ M}\Omega \text{ m}^{-1}$, NANOPURE) to protect from acid coming into contact with the gels. Both polyacrylamide gel and Chelex-100 resin were stored in closed plastic vials in double-deionized water before use to prevent them from drying. The gels were cut with Teflon-covered blade to fit the sediment probe.

One day before field work, the assembled DGT probe was inserted into a bottle filled with double-deionized water and purged with nitrogen to expel oxygen, which could affect redox speciation. Immediately before sampling, the bottle was tightly closed and transferred to the sampling site, where the sampler was inserted into the sediment.

2. 3. Field Work

DGT sediment probes were used for accumulation and pre-concentration of the Fe redox species *in situ* in the Vrtojba River sediment. Vrtojba flows through an anthropogenically-impacted environment of the city of Nova Gorica and its sedimentary Fe content is expected to be sufficiently high for reliable analysis. Two assembled DGT sediment probes were placed back-to-back in the river sediment for 5 days (from 18.07.2018 to 23.07.2018), reaching approximately 7.5 cm deep. The water temperature recorded at the beginning and the end of the experiment ranged between $23.5 \text{ }^{\circ}\text{C}$ and $24.5 \text{ }^{\circ}\text{C}$.

After sampling, the DGT probes were carefully recuperated from the sediment, rinsed with a double-deionized water, inserted into the plastic bag and transferred to the laboratory.

2. 4. Laboratory Analysis

In the laboratory the diffusive layer and filter were discarded, and resin layer was transferred into clean vial with double-deionized water until analysis. One probe gel was

used to determine the dissolved Fe(II) concentration, whereas the second one to determine the total dissolved amount of iron. Fe(III) was calculated as the difference between dissolved total and Fe(II) values. The procedure for total Fe determination was the same as described below (see 2.3).

After determination of Fe redox values in the gel, DGT equation was applied to calculate the concentration of Fe species (C) in the sediment pore waters:

$$C = \frac{M \Delta d}{D A t}, \quad (1)$$

where M is the mass of accumulated Fe species, t is the time of exposure, A is the area of exposed surface ($A = 0.15 \times 10^{-3} \text{ m}^2$), Δd is the diffusive layer thickness and D is the diffusive coefficient of the labile Fe species ($D = 5.9 \times 10^{-6} \text{ m}^2/\text{s}$).

The determination of Fe redox species is based on colorimetric reaction of the Fe(II) and PHN, accompanied by the formation of a stable orange complex, named Ferroin ($[\text{Fe}(\text{phen})_3]^{2+}$), with high absorptivity at 508 nm (Figure 2). For the total iron content, the Fe(III) was reduced to Fe(II) with L-ascorbic acid, followed by determination of total Fe as Fe(II).

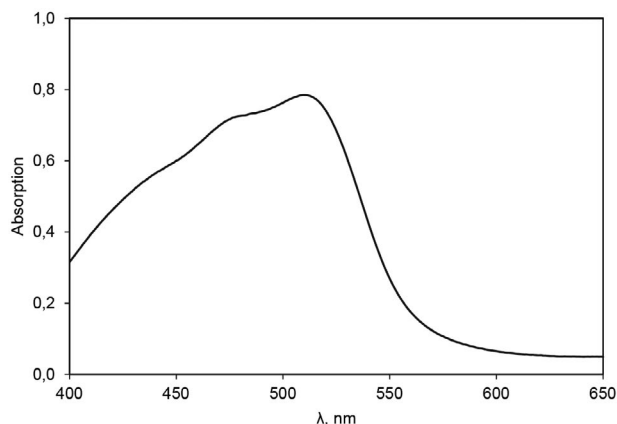


Figure 2. The Ferroin complex absorption spectrum.

For a comprehensive understanding of how Fe ions are distributed in the aqueous phase of the sediments using of the sampler described above, the binding gel was cut into smaller pieces vertically and horizontally by Teflon-covered blade. They were then separately, piece by piece, immersed directly in the 3 mM solution of PHN for the formation of a coloured complex. Before immersing in the PHN solution the pieces of gel from the second sampler were enriched by 5.1 mM L-ascorbic acid for reduction reaction of Fe(III) to Fe(II) for determination of the total Fe content. After 24 hours of soaking in the PHN solution, the gels were dried between clean glass layers for another 24 hours before performing the BDS measurements.

2. 5. Experimental Setup for BDS Method

For determination of Fe concentration, the dried gels on glass support was placed on the sample's holder in BDS system (Figure 3, 4).

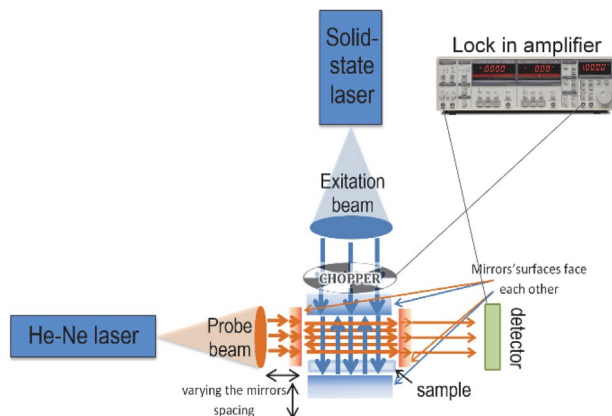


Figure 3. Experimental setup of BDS system.

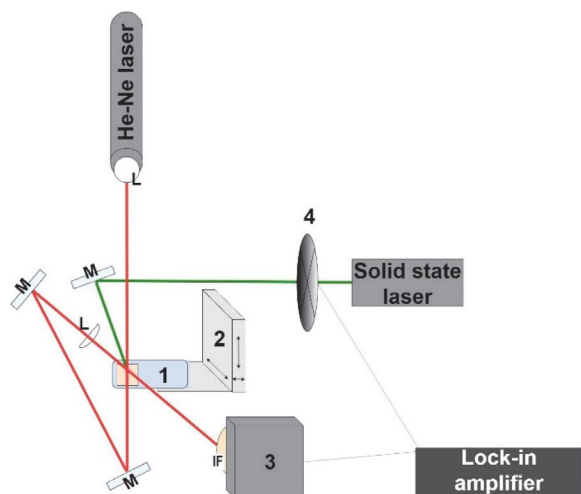


Figure 4. The scheme of BDS system with view from above, where: 1 - glass layer with a sample; 2 - 3D translation stage; 3 - detector; M - mirror; IF- interference filter; L - lens.

As EB (excitation beam) was chosen a solid-state laser at 532 nm output wavelength because the absorption maximum of Ferriin complex is close to it (508 nm), and 30 mW output power (CST-H-532nm-1000 MW). He-Ne laser (Uniphase, Model 1103P) was used as PB (probe beam) source at 633 nm output wavelength and 3 mW output power since this wavelength is not absorbed by Ferriin complex. Both beams were focused by a set of lenses (Bi-Convex, AR Coated: 350–700 nm, EDMUND OPTICS). A variable-speed mechanical chopper (SCIENTIC INSTRUMENTS, Control unit model 300C, chopping head model 300CD, chopping disks model 300H) at frequency of 3.0 Hz was used to modulate the EB. The used frequency range was chosen to ensure the TOs penetration only within the sample (the thickness of the dried gel is

0.04 mm) to get the information only from it without the influence of the support. The sensitivity of the BDS system was improved by using additional mirrors (400–750 nm, Thorlabs) that directed PB through the TOs to increase its intensity change and thus enhance the BDS signal. The intensity change of PB was measured by a quadrant photodiode (RBM-R. Braumann GmbH, Model C30846E) equipped with an interference filter (633 nm, Edmund Optics) and connected to the lock-in amplifier (Stanford research instruments, Model SR830 DSP). The examined sample was placed on a 3D translation stage (CVI, Model 2480M/2488) to vary its position in x, y and z direction and optimize the experimental configuration.

3. Results and Discussion

3. 1. Determination of Fe(II) Content

The calibration curve obtained for the Chelex-100 resin spiked with different concentration of Fe(II) including best fit equation is shown on the Figure 5. After immersing the gels in the Fe(II) solution for 5 days, the gels were transferred to the PHN solution for 1 day to form a coloured Ferriin complex, then transferred to the glass layers for drying. The achieved limit of detection was 0.14 $\mu\text{mol L}^{-1}$.

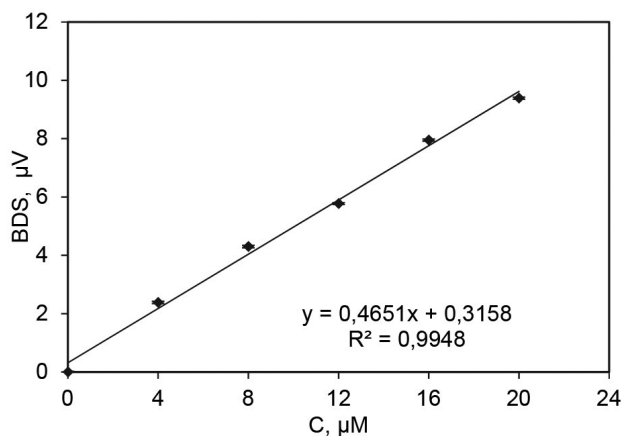


Figure 5. Calibration curve for Fe(II) determination.

A linear relationship between Fe concentration and BDS signal was obtained between 0 and 20 μM of Fe(II). All our samples fit in this concentration range.

To determine the 2D distribution of Fe redox species in the gels, the binding gel was cut into 4 parts horizontally and into 3 parts vertically. In each part, Fe(II) concentration was determined. The gel concentrations from Vrtojba River sediment are presented in Table 1 and Figure 7a.

The lower horizontal part was damaged during the deployment, so the data for Fe (II) (respectively for Fe (III) also) in this layer at the depth 7.5 cm is not available.

Table 1. Concentrations of the Fe(II) ions in the Chelex-100 resin. (The “–” sign indicates data lower than the LOD.)

Vertical position in the sample, cm	Horizontal position in the sample, cm			Average, $\mu\text{mol L}^{-1}$
	0.6	1.2	1.8	
0	2.1±0.2	1.9±0.4	1.9±0.4	2.0±0.3
–2.5	2.3±0.2	–	–	2.3±0.2
–5.0	2.5±0.4	1.5±0.4	–	2.0±0.3
Average, $\mu\text{mol L}^{-1}$	2.3±0.3	1.7±0.4	1.9±0.4	2.0±0.3

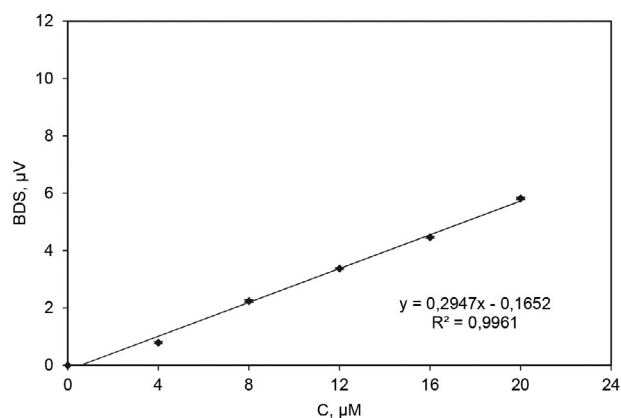
The obtained data indicate that the concentrations of Fe(II) do not vary much in the sediment pore waters. Generally, the absence of Fe(II) indicates oxidative environment and the presence implies reductive conditions. There is an increase on the left side of the investigated area, which could imply more reductive localized condition during the time of the sampling. Considering that DGT binds the dissolved and labile fractions of total Fe(II), our data suggest there was a constant amount of Fe(II) available for geochemical transformations and as well for organisms. Surprisingly, no decrease in Fe(II) concentrations were observed at the sediment-water interface (SWI), suggesting that there might be a loss of this species to the water. Also interestingly and somewhat contrary to general behaviour of reduced metals species, the values around –2.5 and –5 cm were below LOD on the right side of the gel. Usually, in the sediments the anoxia begins somewhere below SWI and extends in the interior of the sediment, where the reduced species dominate²⁶. The Vrtojba River however, is a quickly flowing stream of water, hence the absence of Fe(II) in the part of the sediment of might represent a well aerated sediment.

3. 2. Determination of Total Fe Content

Dissolved total Fe was determined by conversion of the Fe (III) to Fe (II) with L-ascorbic acid as a reducing agent, using this method previously described in the literature for photothermal techniques.^{18–19}

The calibration curve obtained for the Chelex-100 resin spiked with different concentration of Fe(III) re-

duced into Fe(II) including best fit equation is shown in the Figure 6. The achieved limit of detection in this case was $0.21 \mu\text{mol L}^{-1}$.

**Figure 6.** Calibration curve for total Fe determination.

Using a linear equation of the calibration curve the total Fe concentrations in river water and sediment were calculated. The results are presented in Table 2 and its distribution in the gels in Figure 7b.

The distribution of the total dissolved Fe in the sediment of the Vrtojba River is quite uniform. This suggests stable conditions during the deployment, and also a stable pool of labile, dissolved Fe species that was continuously present in the sediment during the time of the sampling.

Table 2. Concentrations of total Fe in the Chelex-100 resin.

Vertical position in the sample, cm	Horizontal position in the sample, cm			Average, $\mu\text{mol L}^{-1}$
	0.6	1.2	1.8	
0	3.0±0.4	8.4±0.3	2.3±0.0	4.6±0.2
–2.5	10.1±0.0	10.8±0.2	7.8±0.1	9.6±0.1
–5.0	9.8±0.3	8.3±0.3	8.4±0.2	8.8±0.3
–7.5	8.5±0.1	6.9±0.1	9.7±0.2	8.3±0.1
Average, $\mu\text{mol L}^{-1}$	7.9±0.2	8.6±0.2	7.0±0.2	7.8±0.2

At the SWI, the concentration of total dissolved Fe species is lower than inside of the sediments, clearly indicating general loss to the water of both redox species. The increase of dissolved species in the sediment interior is associated with dissolved Fe(III) increase (see 3.3).

3.3. Determination of Fe(III) Content

One of the goals of the study was to determine the concentration of Fe(III) ions in the sediment since it is one of the species in which iron as essential metal appears in the nature. Numerous factors contribute to the environmental ratios of Fe(II) and Fe(III), e.g. pH, temperature and reductive-oxidative environmental conditions, presence of sulphide ions, ammonia and oxygen. Furthermore, the ratio is also dependant on geological features of the river sediment.

The content of Fe(III) was calculated as a difference between the total Fe content (Table 2) and Fe (II) (Table 1). The results are given in the Table 3 and presented in the Figure 7c.

Generally, the distribution of the Fe(III) in the sediment follows the distribution of total dissolved Fe. There is an increase of Fe(III) below the SWI at the depth of ap-

proximately 2.5 – 5 cm in the centre of the gel. This might indicate a geological source dissolving and releasing Fe(I-II) into the pore waters, or a local oxidation hotspot that would oxidize any Fe(II) to Fe(III). The oxidation source might be geochemical or microbial. Very likely this feature indicates sediment heterogeneity, which we were able to observe as a result of the newly developed method.

The coupling of DGT and BDS methods enables the determination of the distribution of Fe redox species in two dimensions. While Fe(III) is present over all investigated area and occurs simultaneously with Fe(II), Fe(III) is exclusively present on the right side of the gel. Combined with the Fe(II) results, this part of the sediment appears to be fully oxygenated and/or excludes formation of Fe(II), at least during the sampling period. As the DGT technique reports time-average values, this indicates very stable conditions in the time of the sampling.

The DGT-BDS method does not require intensive manipulation after the sampling, which renders the possibility of transport or storage artefacts that could influence Fe speciation less likely and increases the reliability of the obtained results. Therefore, the observed patterns of Fe redox species likely accurately represent the sedimentary conditions. To summarize the data obtained in Figure 7

Table 3. Concentrations of the Fe (III) ions in the Chelex-100 resin.

Vertical position in the sample, cm	Horizontal position in the sample, cm			Average, $\mu\text{mol L}^{-1}$
	0.6	1.2	1.8	
0	1.0±0.3	6.5±0.3	0.4±0.2	2.6±0.3
-2.5	7.8±0.1	10.8±0.3	7.8±0.2	8.8±0.2
-5.0	7.3±0.4	6.9±0.4	8.4±0.2	7.5±0.3
Average, $\mu\text{mol L}^{-1}$	5.3±0.3	8.1±0.3	5.5±0.2	6.3±0.3

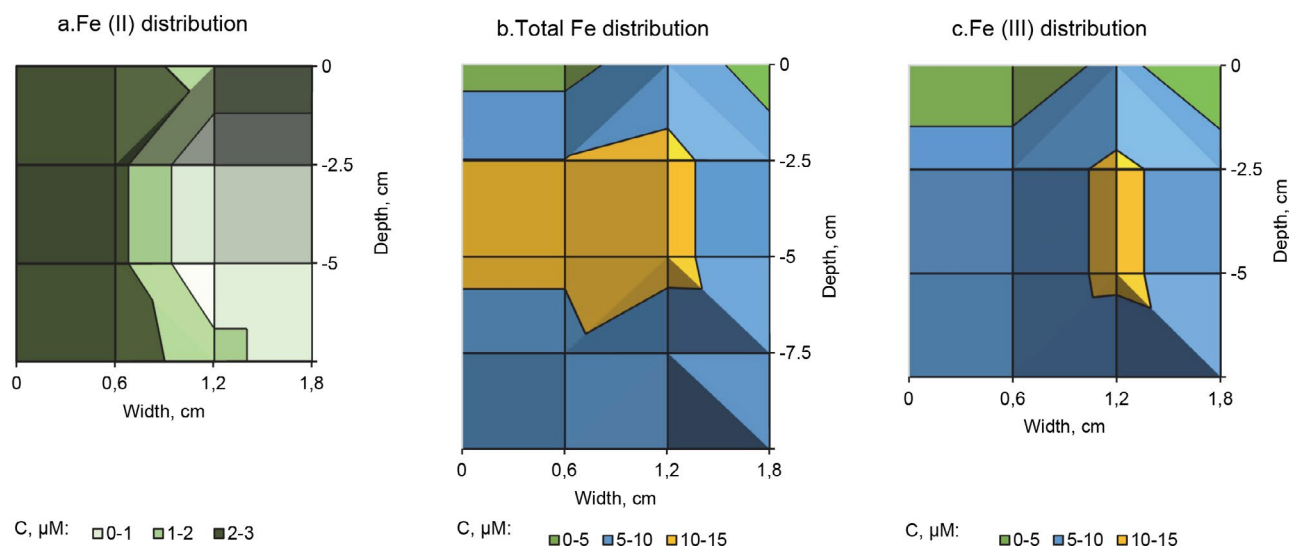


Figure 7. Graphical presentation of Fe redox species distribution in the Chelex-100 resin.

presents the Fe (II), total Fe and Fe (III) distribution in the Chelex-100 resin, respectively.

Although our preliminary results are not accompanied with a suite of other geochemical parameters, they clearly demonstrate the potential and applicability of the newly developed method to be used for two-dimensional imaging of dissolved, bioavailable Fe redox species in natural environments.

3. 4. Concentrations of the Fe Redox Species in the River Sediment

Using the equation (1) we calculated the concentration of Fe species in the sediment pore waters (Table 4).

Although not much data exist for comparison of DGT-derived Fe redox species concentrations, our data fit in the range of the published results for pristine environments.¹⁸ Total concentrations obtained from polluted or strongly impacted river sediments are higher for factor of 10 or 100.^{28–30} Nonetheless, the distribution of dissolved, labile and potentially bioavailable fraction of Fe redox species in the Vrtojba River indicates a dynamic sediment system. As observed before, the low values at SWI indicate sediments are a source of both Fe redox species to the river water. The observed increases in dissolved Fe(II) and dissolved total Fe in the sediment interior could be attributable either to geochemical and microbial interactions with Fe-rich minerals, or both. Since these are the first data on iron speciation in this system, it cannot be said with cer-

tainty if the concentrations are representative of this particular environment. However, despite its city location, Vrtojba river sediment is far from polluted and not likely to increase river water Fe concentration to above WHO guidelines on Fe in drinking water (0.3 mg/L). Together with low SWI concentration our data suggests that anthropogenic activity might have not affected the river and that the sediment does not act as a sink for Fe. Simultaneously, however, it is also yet unclear which factors have highest influence on the redox state of dissolved Fe in the sediment.

4. Conclusions

We report for the first time the dissolved Fe redox species distribution in freshwater sediments measured by coupled DGT technique and BDS method.

The average total iron concentration in the Vrtojba River river sediment was found to be 49.3 $\mu\text{g/L}^{-1}$. The average amount of Fe(III) was 3 times higher than the average Fe(II) concentration and reached the value of 39.9 $\mu\text{g/L}^{-1}$ and 12.8 $\mu\text{g/L}^{-1}$, respectively.

The obtained results show the potential of using DGT method coupled to BDS technique for monitoring biologically relevant Fe species at environmental concentrations in natural waters and sediments. The information received from the newly coupled method will advance our understanding of the basic biogeochemical processes gov-

Table 4. Concentrations of the Fe redox species in the Vrtojba sediment.

Vertical position in the sample, cm	Horizontal position in the sample, cm			Average, $\mu\text{g/L}$
	0.6	1.2	1.8	
	Fe(II) in pore waters, $\mu\text{g/L}$			
0	13.2±1.3	12.0±2.5	12.0±2.5	12.4±2.1
-2.5	14.5±1.3			14.5±1.3
-5.0	15.7±2.5	9.4±2.5		12.6±2.5
Average	14.5±1.7	10.7±2.5	12.0±2.5	12.8±2.1
	Total Fe in pore waters, $\mu\text{g/L}$			
0	18.9±2.5	52.9±1.9	14.5±0.0	28.7±1.5
-2.5	63.6±0.0	68.0±1.3	49.1±0.6	60.2±0.6
-5.0	61.7±1.9	52.2±1.9	52.9±1.3	55.6±1.7
-7.5	53.5±0.6	43.4±0.6	61.0±1.3	52.7±0.8
Average	49.4±1.3	54.1±1.4	44.4±0.8	49.3±2.0
	Fe(III) in pore waters, $\mu\text{g/L}$			
0	6.3±1.9	40.9±1.9	2.5±1.3	16.6±1.7
-2.5	49.1±0.6	68.6±1.9	49.1±1.3	55.6±1.3
-5.0	45.9±2.5	43.4±1.9	52.9±1.3	47.4±1.9
Average, $\mu\text{g/L}$	33.8±1.7	51.0±1.9	34.8±1.3	39.9±2.2

erning trace metal behaviour in pristine and anthropogenically-impacted environments. Its results may be well incorporated in the existing mathematical models, which are currently based primarily on one-dimensional profiles, thereby increasing reliability of the model predictions. Further development, application and testing of the DGT-BDS is warranted, since it is reliable, precise, resistant to contamination, inexpensive, and time-saving analytical method.

5. Acknowledgements

This work was supported by Slovenian Research Agency within the research program P2-0393; Advanced materials for low-carbon and sustainable society.

6. References

1. W. G. Sunda, S. A. Huntsman, *Mar. Chem.* **1995**, *50*, 189–206.
2. S. Tautkus, L. Steponieniene, R. Kazlauskas, *J. Serb. Chem. Soc.* **2004**, *69*(5), 393–402. DOI:10.1016/0304-4203(95)00035-P
3. A. T. Pilipeko, V. G. Safronova, L. V. Zakrevskaya, *Zavod. Lab.* **1998**, *1*, 54.
4. M. Feng, Y. Yang, P. He, Y. Fang, *Spectrochim. Acta A* **2000**, *56*(3), 581–587. DOI:10.1016/S1386-1425(99)00157-2
5. B. Divjak, M. Franko, M. Novic, *J. Chromatogr. A* **1998**, *829*, 167–174. DOI:10.1016/S0021-9673(98)00837-1
6. H. Z. Senyuva, D.Y. Sarica, T. Ozden, *Turk. J. Chem.* **2002**, *26*, 425–430.
7. K. W. Bruland, E. L. Rue, in: K. A. Hunter and D. R. Turner (Ed.): Iron: Analytical methods for the determination of concentrations and speciation. The Biogeochemistry of Iron in Seawater, NY: John Wiley & Sons, New York, USA, **2001**, pp. 255–289.
8. W. W. Gregg, P. Ginoux, P. S. Schopf, N. W. Casey, *Deep-Sea Res. Pt. II* **2003**, *50*(22–26), 3143–3169. DOI:10.1016/j.dsr2.2003.07.013
9. L. M. Laglera, D. Monticelli, *Curr. Opin. Electrochem.* **2017**, *3*, 123–129. DOI:10.1016/j.coelec.2017.07.007
10. Y. Dai et al., *Chemosphere*. **2018**, *191*, 183–189. DOI:10.1016/j.chemosphere.2017.10.035
11. X. Pan, B. Yan, H. Zhu, L. Wang, *Acta Sci. Circumst.* **2010**, *30*, 1087–1092.
12. W. Bennett, M. Arsic, J. G. Panther, D. T. Welsh, P. R. Teasdale, in: W. Davison (Ed.): Diffusive Gradients in Thin-Films for Environmental Measurements. 1.ed. Cambridge University Press, Cambridge, UK, **2016**, pp. 66–92. DOI:10.1017/CBO9781316442654.005
13. W. Li, C. Li, J. Zhao, R. J. Cornett, *Anal. Chim. Acta* **2007**, *592*(1), 106–113. DOI:10.1016/j.aca.2007.04.012
14. M. Pawlak, S. Pal, A. Ludwig, A. D. Wieck, *J. Appl. Phys.* **2017**, *122*(22), 135109-1–135109-7. DOI:10.1063/1.5013305
15. D. Korte, M. Franko, *J. Opt. Soc. Am. A. Opt.* **2015**, *32*(1), 61–74. DOI:10.1364/JOSAA.32.000061
16. M. Pawlak, S. Pal, S. Scholz, A. Ludwig, A. D. Wieck, *Thermochim. Acta* **2018**, *662*, 69–74. DOI:10.1016/j.tca.2018.02.009
17. Ł. Chrobak, M. Malinski, J. Zakrzewski, *Thermochim. Acta* **2018**, *606*, 84–89. DOI:10.1016/j.tca.2015.03.014
18. L. Gojat, M. Martelanc, V. Vinatier, A. Delort, M. Franko, *23th YISAC*. **2016**, 44.
19. L. Gojat, M. A. Proskurnin, I. V. Mikheev, M. Franko, *Euroanalysis XIX*. 2017, 203.
20. H. Cabrera, D. Korte, M. Franko, *Int. J. Thermophys.* 2015, *36*(9), 2434–2440. DOI:10.1007/s10765-015-1933-0
21. E. Cedeño, H. Cabrera, A. E. Delgadillo-López, O. Delgado-Vasallo, A. M. Mansanares, A. Calderón, and E. Marín, *Talanta*. 2017, *170*, 260–265. DOI:10.1016/j.talanta.2017.04.008
22. H. Cabrera, J. Akbar, D. Korte, E. E. Ramírez-Miquet, E. Marín, J. Niemela, Z. Ebrahimpour, K. Mannatunga, and M. Franko, *Talanta*. 2018, *183*, 158–163. DOI:10.1016/j.talanta.2018.02.073
23. M. Maliński, Ł. Chrobak, L. Bychto, *Solid State Commun.* **2010**, *150*(9–10), 424–427. DOI:10.1016/j.ssc.2009.12.002
24. M. Maliński, Ł. Chrobak, *Arch. Acoust.* **2009**, *34*(4), 727–734.
25. M. Maliński, Ł. Chrobak, M. Pawlak, *Appl. Phys. A-Mater.* **2015**, *118*(3), 1009–1014.
26. Y. Gao, S. van de Velde, P. N. Williams, W. Baeyens, H. Zhang, *TrAC*. **2015**, *66*, 63–71.
27. S. V. Pakhomova et al., *Mar. Chem.* **2007**, *107*, 319–331. DOI:10.1016/j.marchem.2007.06.001
28. F. Leermakers, J. C. Eriksson, H. Lyklema, *Fundamentals of Interface and Colloid Science* **2005**, *5*, 1–123. DOI:10.1016/S1874-5679(05)80014-5
29. F. Gao et al., *J. Exp. Bot.* **2006**, *57*, 3259–3270. DOI:10.1093/jxb/erl090
30. C. Montalvo et al., *Environ. Pollut.* **2014**, *3*.

Povzetek

Scientific paper

Development of a Dispersive Liquid-Liquid Microextraction Followed by LC-MS/MS for Determination of Benzotriazoles in Environmental Waters

Ida Kraševc* and Helena Prosen

Faculty of Chemistry and Chemical Technology, University of Ljubljana, Večna pot 113, Ljubljana, Slovenia

* Corresponding author: E-mail: ida.krasevec@fkkt.uni-lj.si

Received: 12-18-2018

Abstract

Emerging environmental pollutants are becoming a global concern, since the acceptable concentrations are currently not set by legislation in EU or elsewhere. Benzotriazoles are an important group of emerging pollutants found in low $\mu\text{g/L}$ concentrations, entering the environment through wastewater treatment facilities due to their insufficient removal, and through industrial and other use. Two new dispersive liquid-liquid microextraction (DLLME) methods were developed for the extraction of hydrophilic and hydrophobic benzotriazoles from environmental waters. Liquid chromatographic method coupled to tandem mass spectrometric detection (LC-MS/MS) was developed and validated for surface water. Validation parameters were satisfactory and the overall DLLME-LC-MS/MS method was found to be applicable to analysis of the chosen analytes in environmental waters. It was used to determine benzotriazoles in surface water and wastewater from a municipal wastewater treatment plant. In surface waters, concentration was below the limit of detection, while concentrations determined in wastewater were estimated between 2.7 and 12.0 $\mu\text{g/L}$.

Keywords: Benzotriazoles; dispersive liquid-liquid microextraction; liquid chromatography-mass spectrometry; natural water; wastewater

1. Introduction

Benzotriazole and its derivatives are heterocyclic compounds used as anti-corrosive agents in industrial fluids, household dishwasher detergents, de-icing liquids, cooling systems, and hydraulic fluids, while less polar derivatives are used as UV stabilizers in plastics and cosmetics.¹ Their widespread use has led to a ubiquitous presence in the environment: surface fresh and sea water,^{2–4} groundwater and drinking water,^{5–7} river sediments,⁸ soils,⁹ sewage sludge,¹⁰ indoor dust,¹¹ and air.¹² Their main point of entry to environmental waters is through the wastewater treatment plants (WWTP) effluents where they are insufficiently removed.^{13–14} A survey from European Union in 2013¹⁵ has shown their presence in 97–100% of effluent wastewaters (90 WWTPs with various sources) with concentrations in low $\mu\text{g/L}$ range, while concentrations in untreated wastewaters were up to ten times higher.¹⁴ Nevertheless, no environmental limit concentrations are set for benzotriazoles in EU yet.

Benzotriazoles are classified as emerging pollutants with low acute toxicity, but their chronic effects are less well known:

possible endocrine-disrupting activity,¹⁶ toxicity for plants and some aquatic organisms,¹⁷ and suspected human carcinogenesis.¹⁸ Measurable concentrations of benzotriazoles have been found in human urine and amniotic fluid.^{19–21}

The concentrations of benzotriazoles in environmental matrices are in the ng/L to $\mu\text{g/L}$ range, therefore it is necessary to perform some form of extraction and pre-concentration before the analysis. The most frequently used method is solid-phase extraction (SPE).^{3,6,21–25} Stir-bar sorptive extraction (SBSE)²⁶ and solid-phase microextraction (SPME)^{21–27} have also been applied.

More recently, liquid-phase microextractions were introduced as an alternative to sorbent-based extraction, but with a very low solvent consumption. One of the most popular is dispersive liquid-liquid microextraction (DLLME), which has to date been applied to the extraction of benzotriazoles only in few instances,^{28–29} in both cases with the use of lighter-than-water solvents, which requires the use of special glassware to collect the solvent. Air-assisted liquid-liquid microextraction, a variant of DLLME, with lighter-than-water solvent, has also been developed for benzotriazoles in water samples.³⁰

Following the extraction, benzotriazoles are usually determined by chromatographic techniques. HPLC coupled to MS or MS/MS detection is the most frequently applied technique,^{2,3,7,10,19,22,23,25–27} with LODs in the range 0.2–200 ng/L (depending also on the extraction method), occasionally also with UV detection,^{28,30} which is usually leading to higher LODs. GC-MS or GC-MS/MS methods, either with or without derivatization of analytes, are less frequently encountered,^{6,13,21,25,29} their LODs tend to be comparable or a bit higher than with LC-MS/MS.

In the present work, two DLLME methods were developed and optimized for the extraction of six hydrophilic and two hydrophobic benzotriazoles from aqueous samples. The optimization of DLLME for extraction from water samples with heavier-than-water solvents was done stepwise and with a two-level fractional factorial experimental design. The extracts were analysed with LC-MS/MS. The method for hydrophilic benzotriazoles was evaluated in terms of the analytical parameters and the efficiency to determine analytes in the environmental aqueous samples. The validated method was applied to the determination of selected benzotriazoles in Slovenian environmental waters.

2. Experimental

2.1. Materials

Solid standards of the analytes in this study (Table 1) were purchased from Sigma-Aldrich, USA (OHBZ, CIBZ, BTZ, TBZMF, and BZPF), from Fluka, Switzerland (4MBZ, 5MBZ, and DMBZ), or from Santa Cruz Biotechnology, USA (BTZ-d4 as internal standard – IS). Ultrapure water (MQ) was prepared by Milli-Q water system (Millipore, USA). HPLC grade solvents acetonitrile (Fisher Chemical, UK), methanol (J. T. Baker, UK), acetone (Honeywell, USA), and isopropanol (Sigma-Aldrich, USA) were used. Other chemicals were of p.a. or higher purity from various producers: formic acid and CS₂ from Sigma-Aldrich (USA), 25% NH₃ from Gram-mol (Croatia), HCl, ethanol, and CCl₃ from Honeywell (USA), NaOH and CCl₄ from Merck (USA), NaCl from Scharlau (Spain), chlorobenzene from Fluka (USA), and 1,1,1-trichloroethane from Codex (Italy).

2.2. DLLME Extraction

Extensive optimization of DLLME procedure with heavier-than-water solvents was performed, partially with a two-level fractional factorial experimental design and partially stepwise.

The final conditions for DLLME of hydrophilic and hydrophobic benzotriazoles were: pH of an aqueous sample (3 mL) in a conical test tube was adjusted to 3.5 with HCl, and solid NaCl was added up to 8% w/v. A mixture of 80 µL CHCl₃, 20 µL CCl₄, and 700 µL acetonitrile was quickly injected into the sample. After shaking for 5 s, the mixture was centrifuged at 3000 rpm for 5 min. The extract was collected from the bottom of the tube with a syringe and transferred to a vial, dried under nitrogen and re-dissolved in 50 µL of MQ:ACN (3:7).

The final conditions for DLLME of hydrophilic benzotriazoles were: pH of an aqueous sample (5 mL) in a conical test tube was adjusted to 4.0 with HCl, and solid NaCl was added up to 10 % w/v. A mixture of 160 µL CHCl₃ and 800 µL acetonitrile was quickly injected into the sample. After shaking for 5 s, the mixture was centrifuged at 3000 rpm for 5 min.

Extract was collected from the bottom of the tube with a syringe and transferred to a vial, dried under nitrogen and re-dissolved in 25 µL of MQ.

2.3. HPLC-DAD and LC-MS/MS Analysis

DLLME conditions were optimized using an HPLC-DAD method with the following parameters: an Agilent 1100 Series HPLC-DAD instrument (Agilent, USA) equipped with autosampler was used. LC separation was performed on a Kinetex XB-C18 column (Phenomenex, USA, 150 × 4.6 mm, 5 µm) at room temperature and flow rate of 0.7 mL/min. The mobile phase was composed of acetonitrile (A) and 0.1% HCOOH in MQ (B), with the following gradient profile: 5% A, increased to 50% A in 5.0 min, then to 100% A in 9.0 min and retained at 100% A for 11.0 min. The injection volume was 20 µL. UV spectra were recorded in 200–400 nm range, and detection wavelengths for quantification were set at 260, 304, and 350 nm.

LC-MS/MS method for hydrophilic benzotriazoles: a PerkinElmer LC system, coupled with TurboSpray ESI ionization and 3200 QTRAP mass analyser (Sciex, USA)

Table 1: Analyte abbreviations, molecular weights, logK_{ow} and pK_a.

Abbrev.	Name	M (g/mol)	logK _{ow}	pK _a
OHBZ	4-hydroxy-1H-benzotriazole	135.12	0.80	7.25
BTZ	1H-benzotriazole	119.12	1.44	8.38
4MBZ	4-methyl-1H-benzotriazole	133.15	1.82	8.74
5MBZ	5-methyl-1H-benzotriazole	133.15	1.98	8.74
CIBZ	5-chloro-1H-benzotriazole	153.57	2.13	7.46
DMBZ	5,6-dimethyl-1H-benzotriazole	147.18	2.28	8.92
TBZMF	2-tert-butyl-6-(5-chloro-2H-benzotriazol-2-yl)-4-methylphenol	315.80	6.81	9.31
BZPF	2-(2H-benzotriazol-2-yl)-4,6-di-tert-pentylphenol	351.49	7.87	8.85

was used. LC separation was performed on the same column and with same parameters as for HPLC-DAD, except for the mobile phase gradient, which was as follows: 5% A, increased to 15% A in 0.5 min, then to 35% A in 12.5 min, then to 100% A in next 7 min. The injection volume was 10 μ L.

Ionization was performed with the electrospray in positive mode with the curtain gas pressure at 30 psi, ion spray voltage of 4 kV, drying gas temperature at 450 $^{\circ}$ C, sheath gas 1 at 50 psi and sheath gas 2 at 50 psi. Nitrogen, supplied by Messer (Germany), was used both as drying and collision cell gas. The mass spectrometer was operated in selected reaction monitoring (SRM) mode; the declustering potential, entrance potential and collision cell exit potential were fixed at 40 V, 10 V, and 3 V, respectively. Transition parameters were optimized for each analyte separately by injecting separate solutions directly into the ion source by flow-injection; two fragment ions were monitored for each compound (Table 2). Quantification was performed as analyte/IS signal ratio, using the first transition for each analyte and BTZ-d4 as the IS, while the second transition and the fragment ion ratio were used for identity confirmation. During sample analysis, the calibration standard at 0.1 mg/L level and a MQ blank were injected every 12 samples to check for drift in response and carryover effect.

2. 4. Samples

Grab samples of surface water were taken from the Glinščica (46,050972 $^{\circ}$ N, 14,468536 $^{\circ}$ E), Soča (46,152460 $^{\circ}$ N, 13,739944 $^{\circ}$ E), and Idrijca (46,04803 $^{\circ}$ N, 14,02272 $^{\circ}$ E) rivers (Slovenia) and two groundwater samples were taken at two different drinking water sources (Roje, PIS) of Ljubljana, Slovenia. Samples were stored in the dark at 4 $^{\circ}$ C. Influent and effluent municipal wastewater samples in the form of 24 h composite samples were taken at Central wastewater treatment plant in Ljubljana, Slovenia, and stored at -20° C. Due to high matrix effect, which was ob-

servable with the use of the internal standard, the influent wastewater sample was diluted 5 times before extraction procedure.

3. Results and Discussion

3. 1. Optimization of HPLC-DAD and LC-MS/MS Method

Two different reverse-phase columns were initially tested to separate polar and hydrophobic analytes in the same run: Kinetex XB-C18 column (Phenomenex, USA, 150 \times 4.6 mm, 5 μ m, 100 \AA) and Gemini C18 column (Phenomenex, USA, 150 \times 4.6 mm, 3 μ m, 110 \AA). The Kinetex column provided better resolution of the peaks, which was expected since the sorbent is prepared with core-shell technology, and was selected for further use. The optimization of mobile phase gradient was challenging due to very different polarities of the analytes (Table 1). Therefore, the final gradient started at low acetonitrile percentage (5%), which was then steeply increased to 50% and then to 100% to reach the conditions that were favourable for the elution of hydrophobic benzotriazoles (TBZMF, BZPF). Still, the separation of methyl isomers 4MBZ and 5MBZ could not be achieved. These conditions were chosen as final since HPLC-DAD was used only for the optimization of DLLME extraction parameters and the later use of LC-MS/MS in SRM mode enabled us to tolerate the less than satisfactory separation. Wavelengths for quantification were set at 260, 304, and 350 nm due to different UV spectra of analytes. Under these conditions, the calibration curves for the selected benzotriazoles were linear in the 0.5–50.0 mg/L range with $R^2 > 0.99$. An interesting finding was that the standard solutions had to be prepared in a mixture with high percentage of organic solvent to achieve repeatable peak areas for hydrophobic analytes (Figure 1), possibly due to their low solubility in water and adsorption to the walls of the glassware. For this reason all

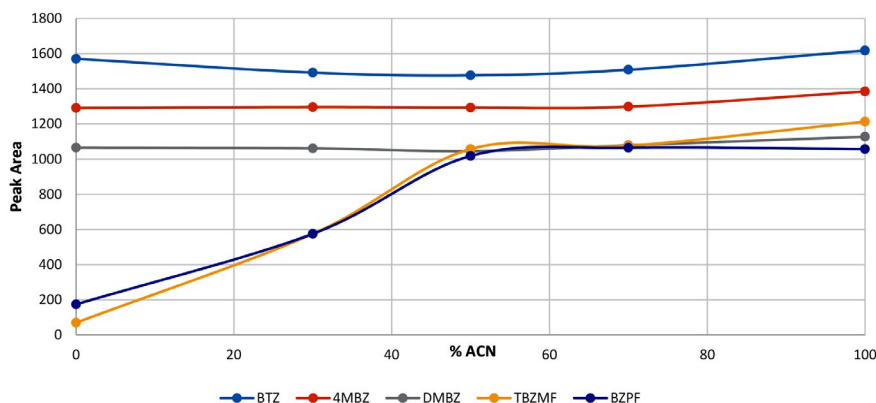


Figure 1: Peak area of different analytes at various compositions of solvent (MQ and acetonitrile) for 50 mg/L standard solution.

solutions were prepared in 70% ACN. A chromatogram of standard solution is given in Supplementary Information SI 1.

Although it would be possible to determine all selected analytes with LC-MS/MS and it was also possible to achieve favourable DLLME extraction conditions for all of them, we decided to omit the two most hydrophobic analytes (TBZMF, BZPF) from further method development since it was highly unlikely that they would be present in aqueous samples due to their hydrophobicity. Therefore, the LC-MS/MS method was optimized only for the hydrophilic benzotriazoles. At this point, a deuterated internal standard (IS; 1*H*-benzotriazole-*d*₄, BTZ-*d*₄) was also introduced. The same chromatographic column was used and the elution gradient started with very low concentration of organic solvent with the slow increase in its percentage (35% ACN in 12.5 min) to achieve the best separation of methyl isomers 4MBZ and 5MBZ. Even so, their peaks were not baseline separated (see Table 2). A chromatogram of standard solution under final conditions is given in Supplementary Information SI 2.

For MS parameters, electrospray conditions were optimized by flow-injection of analyte solution. Positive ESI ionization was chosen because the signals were of a much higher intensity than with negative ionization, which is in agreement with other published methods.^{7,22,23} The optimized SRM transition conditions are presented in Table 2. The first transition was used for quantification, while the second transition and the fragment ion ratio were used for the identification of analytes.

Table 2: Retention times (t_R), observed SRM transitions, their collision energies (CE) and fragment ion ratios.

analyte	t_R (min)	SRM1	CE1 (V)	SRM2	CE2 (V)	Ion ratio
OHBZ	6.96	136>80	29	136>90	27	9.74
BTZ	8.63	120>65	30	120>92	25	2.74
4MBZ	11.3	134>77	34	134>79	25	1.46
5MBZ	11.5	134>77	34	134>79	25	1.40
CIBZ	13.7	154>99	32	154>73	46	2.05
DMBZ	14.0	148>77	37	148>91	31	1.75
IS	8.55	124>69	33	124>96	24	

Instrumental limits of detection (ILOD) and quantification (ILOQ) were calculated from calibration curves in standard solutions with added IS, using formulae $ILOD = 3.3 \times s(\text{res})/k$ and $ILOQ = 10 \times s(\text{res})/k$, where $s(\text{res})$ is the residual sum of squares and k the slope of the calibration curve. ILOD were at 5–30 $\mu\text{g/L}$, while ILOQ were determined in the range 16–91 $\mu\text{g/L}$. Acceptable linearity of the calibration curve was observed in the range from ILOQ to 10 mg/L.

3. 2. Optimization of DLLME Extraction

DLLME extraction was studied in MQ water with added analytes at 1 mg/L level. Two sets of conditions were optimized: for both hydrophilic and hydrophobic benzotriazoles; and for hydrophilic analytes only. The following parameters were changed: choice and volume of extraction solvent; choice and volume of dispersive solvent; volume, pH and ionic strength of aqueous sample; time and speed of centrifugation. All of the tested extraction solvents were denser than water: dichloromethane, 1,1,1-trichloroethane, CHCl_3 , CS_2 , CCl_4 , and chlorobenzene. Solvents with lower density than water (lighter-than-water) can also be applied,^{28–30} but after centrifugation, a thin layer of solvent with extracted compounds is formed on the surface of aqueous phase, which is impossible to collect. For that reason, special glassware with narrow neck should be used to allow for formation of a thicker upper layer of solvent.^{28–30} To avoid the need for special equipment, heavier-than-water solvents were used to form an easy-to-collect drop at the bottom of the vessel after centrifugation. For dispersive solvent, methanol, acetonitrile, acetone, isopropanol, and ethanol were tested. The extract was dried and re-dissolved in MQ or MQ/ACN because of the incompatibility of the chlorinated solvents with the LC column.

Out of all tested extraction solvents, the best recoveries were achieved with CHCl_3 for hydrophilic and CCl_4 for hydrophobic analytes. A mixture of these solvents was used, the ratios determined in further steps. Acetonitrile proved to be the best dispersive solvent for all analytes.

Optimization of the previously listed parameters was first performed by two-level fractional factorial experimental design, the values of parameters investigated are presented in Table 3. 8 different experiments with parameters set at these levels (with 4 repetitions) were performed to estimate the significance of influences of the parameters. For most analytes the only significant parameter seemed to be the pH value (Figure 2), which could be due to its broad range investigated (4–10). As it is well known that other parameters can also influence the extraction efficiency, we decided to further perform a stepwise optimization.

Table 3: Values of parameters, investigated with fractional factorial design.

Parameter	Level –	Level +
Sample volume (mL)	2	5
CHCl_3 volume (μL)	20	100
CCl_4 volume (μL)	20	100
ACN volume (mL)	0,3	1
Sample pH	4	10
NaCl (% w/v)	0	10
rpm	1500	3000

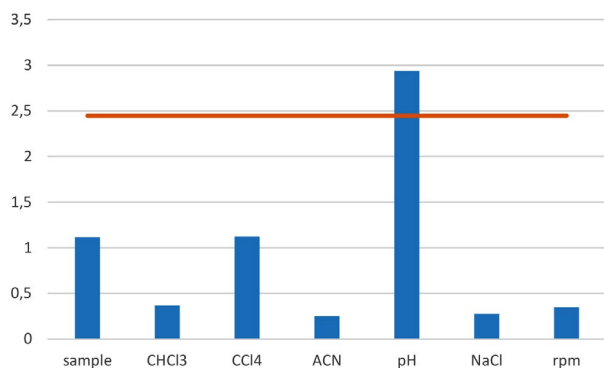


Figure 2: Influence of investigated parameters on 4MBZ extraction efficiency, the line denotes significant influence.

In the stepwise optimization it turned out, that sample pH below 6 was necessary for efficient extraction of hydrophilic compounds and that the addition of salt up to 10 % *w/v* improved the extraction for the hydrophilic analytes, while the hydrophobic analytes remained unaffected. Variations in centrifugation speed and time had almost no effect on extraction efficiency, while smaller sample volumes and larger solvent volumes increased the efficiency for all analytes. Due to aiming for higher enrichment factors (not recoveries), the ratio between sample and extract volume was adjusted further, with sample volume set at 3 mL and final solvent volumes 80 μ L CHCl₃, 20 μ L CCl₄, and 700 μ L acetonitrile, which resulted in 200–220 μ L of extract before drying. With the parameters set as described in Experimental, the enrichment factors ranged between 9.5 and 28.7. Further experimental data on this optimization is given in Supplementary Information (SI3–5).

For hydrophilic analytes, only CHCl₃ was used as the extraction solvent, as the addition of CCl₄ was unnecessary. The best enrichment factors in general were obtained with the CHCl₃/acetonitrile ratio 1:5 (Figure 3) and the highest available sample volume (5 mL). Relatively high volumes of solvents contributed to higher enrichment factors due to the additional concentrating step (drying and re-dissolving). Again, the acidic pH and salt addition in-

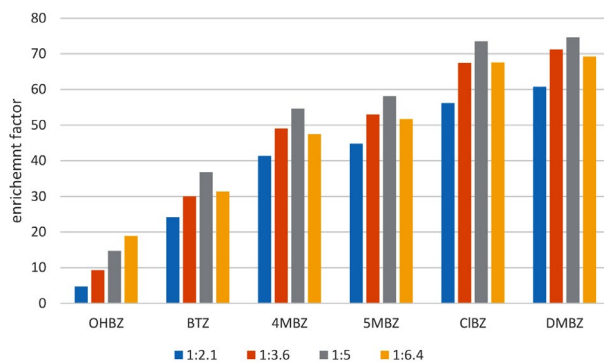


Figure 3: The effect of solvent ratios (CHCl₃:ACN) on enrichment factors for hydrophilic analytes.

creased the efficiency, while the centrifugation speed and time had negligible effect. While the addition of 15 % *w/v* of NaCl further increased the efficiency, the density of the sample increased to such amount, that the extract floated to the surface, and the repeatability dropped drastically. With the final parameters, the obtained enrichment factors ranged from 9.5 to 84.7.

3. 3. Validation of the Method in Environmental Samples

DLLME method for hydrophilic analytes in surface water in combination with LC-MS/MS analytical method was evaluated for enrichment factor, linearity, repeatability, limit of detection, and limit of quantification, using matrix matched calibration. River water was spiked with analytes in the range 0.01–50 μ g/L and 1 μ g/L of IS, and then extracted by the optimized DLLME procedure. The repeatability was estimated at two concentration levels (0.5 and 10 μ g/L) in at least 3 replicates, and blank river water extracts were also prepared. All signals were calculated as the ratio of peak areas of analytes and IS. The validation results are shown in Table 4. High linearity was observed from LOQ to 10 μ g/L for all analytes (R^2 0.9901–0.9985, except for OHBZ 0.9827). Moreover, the matrix effect (ME) was estimated by comparing the signal of the blank extract, spiked with the analytes and IS (post-extraction spiking), and the signal of the standard solutions in MQ water at the same theoretical concentration. Negative values of ME indicate ionization suppression in ESI, while positive ME values indicate ionization enhancement. Interestingly, ME is in the range +15% to +31%, except for BTZ (–19%). Matrix effect is commonly explained by the co-elution of compounds from the sample matrix that are still present in the sample extract and compete with analytes during the ESI ionization process. Positive ME values are in fact favourable because lower LODs can be achieved, but nevertheless, matrix-matched calibration should be used for the quantitative determination of analytes in real samples. As seen from Table 4, LODs and LOQs are sufficiently low to cover the expected range of concentrations in wastewater,^{14,15} while using only 5 mL of sample, which is much lower compared to sample volumes usually required for SPE.^{3,6,21–25} Extraction efficiency, given as enrichment factor (EF), is calculated by comparing concentration in the extract and initial concentration in sample. It is obvious that EFs for the most polar analytes (OHBZ, BTZ) are lower than EFs for the other analytes, which results from their lower solubility in the non-polar extraction solvent. Repeatability is acceptable at higher spiking level, but it is obvious that DLLME is a manual technique requiring a highly skilled operator. On the lower spiking level, the repeatability decreases, even with the use of an internal standard, but this is understandable, since this level is close to or below LOQs.

Table 4: Method validation parameters in surface water.

	OHBZ	BTZ	4MBZ	5MBZ	CIBZ	DMBZ
LOD ($\mu\text{g/L}$)	0.07	0.14	0.75	0.19	0.06	0.04
LOQ ($\mu\text{g/L}$)	0.23	0.47	2.51	0.62	0.19	0.14
%RSD (10 $\mu\text{g/L}$)	19.4	4.4	8.8	10.7	12.1	16.2
%RSD (0.5 $\mu\text{g/L}$)	44.0	42.4	35.2	24.4	16.8	14.3
EF ^a	10	34	75	66	81	70

^aEF – enrichment factors, determined at spiking concentration 5 $\mu\text{g/L}$

3. 4. Comparison to Other DLLME Methods for Benzotriazoles

Three other DLLME or similar methods were found in the literature for the determination of polar benzotriazoles. The comparison of methods from the analytical standpoint is presented in Table 5. Pena et al.²⁸ used 100 μL of the ionic liquid tri-butyl-phosphate as the extraction solvent, but due to the high viscosity of the ionic liquid, the extract had to be diluted 10-times before injection into LC-Flu-UV. In our method, the recoveries are lower, but no ionic liquids are used, so it is not necessary to dilute the extract and further preconcentration is gained with the drying step and the LOQs achieved are quite similar. Casado et al.²⁹ used 60 μL of toluene as the extraction solvent with 100 μL of acetic anhydride added for simultaneous acetylation of the analytes, which were then analysed by GC-MS. With this method, they obtained very low LOQs, but the recoveries are comparable to those obtained with our method, with the exception of the most polar analyte (OHBZ) which was not analysed in their study. Lu et al.³⁰ used 80 μL of 1-hexanol extraction solvent, which was dispersed with the assistance of air instead of a dispersive solvent. The extracts were analysed by HPLC-UV, which also contributes to the higher LOQs in comparison to our method's.

In general, our method is comparable to those from the literature. For all of these methods, the extracts were lighter-than-water, which demanded either special glassware or a twofold transferring of the extract for exact separation of the phases. In this work, we managed to avoid these disadvantages connected to the use of heavier-than-water solvents.

In comparison to conventional SPE methods, for which the reported LOQs range from 1 to 100 ng/L ,^{3,6,22,23,25} the LOQs obtained with all of these DLLME methods are quite higher. This is a direct consequence of lower sample volumes, which reduces the possible preconcentration factors.

3. 5. Determination of Benzotriazoles in Environmental Samples

The developed and validated method was applied to the determination of analytes in environmental water samples. The quantification was performed with matrix-matched calibration. In groundwater and rivers Glinščica, Idrijca, and Soča, all analytes were below LOD of the method, while BTZ, 4MBZ, and 5MBZ were found in influent and effluent wastewaters from the Central wastewater treatment plant in Ljubljana. Estimated concentrations in effluent wastewater ranged from 4.8 to 7.3 $\mu\text{g/L}$. In influent wastewater, the same analytes were present in estimated concentrations 2.7 to 12.0 $\mu\text{g/L}$. Influent water was diluted 1:5 with MQ water before extraction due to enhanced matrix effect compared to surface water. However, for accurate quantification, matrix-matched calibration for wastewater should be applied.

The concentrations for wastewater are in good agreement with those usually determined in European wastewaters.^{14,15} In a recent study on micropollutants in surface and groundwater from the area of Maribor, Slovenia, where SPE extraction was performed (LOQs 3–7 ng/L), two benzotriazoles (2-methyl-2H-benzotriazole, 2,4-dimethyl-2H-benzotriazole) were found in concentrations 1.4 to 273.3 ng/L in groundwater, and in concentrations 5.8 to 27.9 ng/L in surface water.³¹ These two compounds were not considered in our method.

4. Conclusions

In this study, two DLLME microextraction methods were developed for the determination of either hydrophilic benzotriazoles, or hydrophilic and hydrophobic benzotriazoles together. Especially the hydrophilic benzotriazoles are emerging pollutants present in the aquatic system. Microextraction methods for benzotriazoles are rarely encountered in literature, and to our best knowledge, this is

Table 5: Comparison of analytical performance in pure water with DLLME methods from literature (EF – enrichment factor, RSD – repeatability).

Analytes	EF	Absolute recovery (%)	RSD (%) (at spiking level)	LOQ	Ref.
OHBZ, BTZ, 4MBZ, 5MBZ, CIBZ, DMBZ	ND	67–86	5.0–7.8 (18 $\mu\text{g/L}$)	0.1–7.3 $\mu\text{g/L}$	28
BTZ, 4MBZ, 5MBZ, CIBZ, DMBZ	93–172	24–46	2–8 (0.2 $\mu\text{g/L}$)	7–80 ng/L	29
BTZ, 5MBZ, CIBZ	43–87	ND	3.0–4.3 (50 $\mu\text{g/L}$)	2.9–4.8 $\mu\text{g/L}$	30
OHBZ, BTZ, 4MBZ, 5MBZ, CIBZ, DMBZ	10–85	5–42	4.7–13 (50 $\mu\text{g/L}$)	0.1–2.5 $\mu\text{g/La}$	This work

ND – no data available; ^a In surface water

the first time a DLLME method with denser-than-water extracts for benzotriazoles has been developed. The developed methods use smaller volumes of samples and solvents than classical methods and in this aspect contribute to a more environmentally friendly chemistry. The DLLME method for hydrophilic benzotriazoles was validated in surface water. Matrix effect was compensated for in sample analysis with the usage of matrix matched calibration.

The method was applied for determination of analytes in groundwater, surface water and wastewater samples. However, in wastewater samples the matrix effect was more pronounced than in surface water. Therefore, matrix-matched calibration using wastewater matrix should be applied for accurate quantification. This study was also one of the very few investigating the presence of benzotriazoles in Slovenian water environment. We confirmed their presence in the wastewater at $\mu\text{g/L}$ levels, comparable to other European samples, but the analytes were <LOD in river and groundwater samples.

Both DLLME methods could also be applied in analysis of solid samples, such as sediments and soil, where more hydrophobic analytes can be expected. In this case, the analytes from solid samples would be first extracted into a liquid phase (with one of conventional methods), and then these extracts would be cleaned and preconcentrated through the use of DLLME.

5. Acknowledgments

The authors acknowledge the financial support from the Slovenian Research Agency (research core funding No. P1-0153). I. Kraševc has received the grant from Slovenian Research Agency (MR 38132). We would also like to express our thanks to Primož Auersperger, MSc, and Vlasta Kramarič Zidar at JP Vodovod-Kanalizacija, who supplied us with groundwater and wastewater samples.

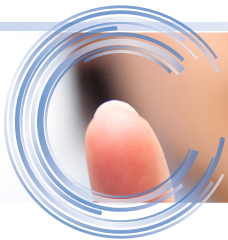
6. References

- P. Herrero, F. Borrull, E. Pocurull, R. M. Marcé, *Trends Anal. Chem.* **2014**, *62*, 46–55. DOI:10.1016/j.trac.2014.06.017
- S. Weiss, T. Reemtsma, *Anal. Chem.* **2005**, *77*, 7415–7420. DOI:10.1021/ac051203e
- P. Herrero, F. Borrull, E. Pocurull, R. M. Marcé, *J. Chromatogr. A* **2013**, *1309*, 22–32. DOI:10.1016/j.chroma.2013.08.018
- A. Kiss, E. Fries, *Environ. Sci. Pollut. Res.* **2009**, *16*, 702–710. DOI:10.1007/s11356-009-0179-4
- H. Janna, M. D. Scrimshaw, R. J. Williams, J. Churchley, J. P. Sumpter, *Environ. Sci. Technol.* **2011**, *45*, 3858–3864. DOI:10.1021/es103267g
- Y.-S. Liu, G.-G. Ying, A. Shareef, R. S. Kookana, *J. Chromatogr. A* **2011**, *1218*, 5328–5335. DOI:10.1016/j.chroma.2011.05.100
- L. Wang, J. Zhang, H. Sun, Q. Zhou, Q. *Environ. Sci. Technol.* **2016**, *50*, 2709–2717. DOI:10.1021/acs.est.5b06093
- M. G. Cantwell, J. C. Sullivan, D. R. Katz, R. M. Burgess, J. Bradford Hubeny, J. King, *Mar. Pollut. Bull.* **2015**, *101*, 208–218. DOI:10.1016/j.marpolbul.2015.10.075
- A. Speltini, M. Sturini, F. Maraschi, A. Porta, A. Profumo, *Talanta* **2016**, *147*, 322–327. DOI:10.1016/j.talanta.2015.09.074
- P. Herrero, F. Borrull, R. M. Marcé, E. Pocurull, *J. Chromatogr. A* **2014**, *1355*, 53–60. DOI:10.1016/j.chroma.2014.05.086
- L. Wang, A. G. Asimakopoulos, H. B. Moon, H. Nakata, K. Kannan, *Environ. Sci. Technol.* **2013**, *47*, 4752–4759. DOI:10.1021/es305000d
- J. Xue, Y. Wan, K. Kannan, *Toxicol. Environ. Chem.* **2017**, *99*, 402–414. DOI:10.1080/02772248.2016.1196208
- Y. S. Liu, G. G. Ying, A. Shareef, R. S. Kookana, *Environ. Pollut.* **2012**, *165*, 225–232. DOI:10.1016/j.envpol.2011.10.009
- T. Reemtsma, U. Miehe, U. Duennbier, M. Jekel, *Water Res.* **2010**, *44*, 596–604. DOI:10.1016/j.watres.2009.07.016
- R. Loos, R. Carvalho, D. C. Antonio, S. Cornero, G. Locoro, S. Tavazzi, B. Paracchini, M. Ghiani, T. Lettieri, L. Blaha, *Water Res.* **2013**, *47*, 6475–6487. DOI:10.1016/j.watres.2013.08.024
- C. A. Harris, E. J. Routledge, C. Schaffner, J. V. Brian, W. Giger, J. P. Sumpter, *Environ. Toxicol. Chem.* **2007**, *26*, 2367–2372. DOI:10.1897/06-587R.1
- A. Seeland, M. Oetken, A. Kiss, E. Fries, J. Oehlmann, *Environ. Sci. Pollut. Res.* **2012**, *19*, 1781–1790. DOI:10.1007/s11356-011-0705-z
- Health Council of the Netherlands, 1,2,3-Benzotriazole. Health-based recommended occupational exposure limit. The Hague: Health Council of the Netherlands, publication no. 2000/14OSH-2000.
- A. G. Asimakopoulos, A. A. Bletsou, Q. Wu, N. S. Thomaidis, K. Kannan, *Anal. Chem.* **2013**, *85*, 441–448. DOI:10.1021/ac303266m
- X. Li, L. Wang, A. G. Asimakopoulos, H. Sun, Z. Zhao, J. Zhang, L. Zhang, Q. Wang, *Chemosphere* **2018**, *199*, 524–530. DOI:10.1016/j.chemosphere.2018.02.076
- A. Naccarato, E. Gionfriddo, G. Sindona, A. Tagarelli, *J. Chromatogr. A* **2014**, *1338*, 164–173. DOI:10.1016/j.chroma.2014.02.089
- D. Salas, F. Borrull, R. M. Marcé, N. Fontanals, *J. Chromatogr. A* **2016**, *1444*, 21–31. DOI:10.1016/j.chroma.2016.03.053
- J. A. van Leerdam, A. C. Hogenboom, M. M. van der Kooi, P. de Voigt, *Int. J. Mass Spectrom.* **2009**, *282*, 99–107. DOI:10.1016/j.ijms.2009.02.018
- I. Kraševc, H. Prosen, *Molecules* **2018**, *23*, 2501–2514. DOI:10.3390/molecules23102501
- E. Jover, V. Matamoros, J. M. Bayona, *J. Chromatogr. A* **2009**, *1216*, 4013–4019. DOI:10.1016/j.chroma.2009.02.052
- N. Gilart, P. A. G. Cormack, R. M. Marcé, F. Borrull, N. Fontanals, *J. Chromatogr. A* **2013**, *1295*, 42–47. DOI:10.1016/j.chroma.2013.04.067
- J. Casado, I. Rodríguez, M. Ramil, R. Cela, *J. Chromatogr. A* **2013**, *1299*, 40–47. DOI:10.1016/j.chroma.2013.05.061
- M. T. Pena, X. Vecino-Bello, M. C. Casais, M. C. Mejuto, R. Cela, *Anal. Bioanal. Chem.* **2012**, *402*, 1679–1695.

- DOI:10.1007/s00216-011-5598-7
29. J. Casado, R. Nescatelli, I. Rodríguez, M. Ramil, F. Marini, R. Cela, *J. Chromatogr. A* **2014**, 1336, 1–9. DOI:10.1016/j.chroma.2014.01.068
30. J. Lu, M.-M. Wang, Q. Wang, H.-P. Li, Z.-G. Yang, *Chinese J. Anal. Chem.* **2018**, 46, e1817–e1824.
31. A. Koroša, P. Auersperger, N. Mali, *Sci. Total Environ.* **2016**, 571, 1419–1431. DOI:10.1016/S1872-2040(17)61082-X

Povzetek

Nova okoljska onesnaževala postajajo svetovni problem, tudi zato, ker EU ali druga zakonodaja ne predpisuje meja njihovih sprejemljivih koncentracij. Benzotriazoli so pomembna skupina novih onesnaževal, ki jih v okolju najdemo v koncentracijskem območju nizkih $\mu\text{g/L}$, vanj pa vstopajo pretežno skozi čistilne naprave zaradi slabe razgradnje, pa tudi preko industrijske in druge rabe. V tem delu smo razvili dve novi disperzivni tekočinski mikroekstrakcijski metodi (DLLME) za ekstrakcijo hidrofilnih in hidrofobnih benzotriazolov iz okoljskih voda. Razvili in validirali smo tudi analizo metodo s tekočinsko kromatografijo sklopljeno s tandemsko masno spektrometrijo (LC-MS/MS) za določitve v površinski vodi. Validacijski parametri so bili zadovoljivi in celotna DLLME-LC-MS/MS metoda se je izkazala za primerno za analizo izbranih analitov v okoljskih vodah. Z njo smo določali benzotriazole v površinskih in odpadnih vodah iz komunalne čistilne naprave. V površinskih vodah so bile koncentracije pod mejo zaznave, koncentracije v odpadnih vodah pa smo ocenili na 2,7–12 $\mu\text{g/L}$.



Donau Lab d.o.o., Ljubljana
Tbilisjska 85
SI-1000 Ljubljana
www.donaulab.si
office-si@donaulab.com



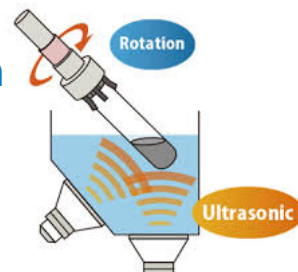
THINKY

Nano PREMIXER PR-1

Uniformna disperzija in deaglomeracija nanomaterialov (CNT, Graphene, drugi)

Dual-Sonic ultrazvočni sistem

Aktivno hlajenje kopeli



BODITE NEUSTAVLJIVI

MAGNEZIJ Krka 300



Granulat za pripravo napitka vsebuje magnezijev citrat in vitamin B₂.



Magnezij in vitamin B₂ prispevata k zmanjšanju utrujenosti in izčrpanosti ter normalnemu delovanju živčnega sistema.



Magnezij prispeva tudi k delovanju mišic.



www.magnezijkrka.si

- ✔ Okus po pomaranči in limeti. ✔ Brez konzervansov.
- ✔ Brez umetnih barvil, arom in sladil. ✔ Ena vrečka na dan.

Prehransko dopolnilo ni nadomestilo za uravnoteženo in raznovrstno prehrano. Skrbite tudi za zdrav življenjski slog.

NOVO

 KRKA

ActaChimicaSlovenica

ActaChimicaSlovenica

The crystal structure of the human cathepsin B-human stefin B complex demonstrates that the occluding loop residues of the native cathepsin B are displaced, thus allowing interaction with inhibitors in the binding region (page 5)



Year 2019, Vol. 66, No. 1

